University of Nottingham



School of Mathematical Sciences

Multiscale modelling of nutrient and water uptake by plants

Jakub Köry

A thesis submitted to the University of Nottingham for the degree of

Doctor of Philosophy

September 2017

Dedicated to my parents and siblings
for their unending love and support

Abstract

Growing populations in combination with the effects of climate change make the task of ensuring global food security in the future challenging. Water and various nutrients contained in soils are essential for the growth and survival of crop plants. Processes governing the dynamics of these substances are often highly complex and occur at various spatial scales. Because of that, and also due to limited possibilities for direct studies of soil processes in general, the ability to model such processes across these scales will most likely be crucial to address the food security challenge. Therefore, in this thesis, we model water and nutrient uptake by plant roots at various spatial scales.

As all our models will be simulated numerically, we first test whether the software used throughout this thesis (FEniCS) gives us reliable numerical results (Chapter 2).

We then proceed with the central part of this thesis, where we study nutrient uptake by root hairs using the method of homogenisation (introduced in Section 1.4.4). In Chapter 3, we first rederive the homogenisation result from [80] using a framework of periodic arrays of uptaking cylinders (hairs). Noticing that this framework can also be used to model nutrient or water uptake by a field of crops, we further study how well the homogenisation result compares with full-geometry numerics using various continuity equations and boundary conditions. In Chapter 4, we study the case where the radius of the root hair is much smaller than the inter-hair distance, which eventually leads us to a distinguished limit. In Chapter 5, we first establish that the framework from Chapters 3 and 4 is a suitable geometry for modelling nutrient uptake by root hairs, if the hair length is much smaller than the root radius. However, this is rarely the case. Therefore, we then investigate the effects of root surface curvature and hair length on the homogenised equation, and obtain a better approximation for the case where the hair length is comparable to the root radius.

In the final two chapters, we introduce different complex problems relating to uptake by plants, and show how even simple multiscale techniques can provide us with useful insights into these problems. In Chapter 6, we show how to upscale nitrate uptake kinetics from a single transporter level to a root segment level, and then propose a model for nitrate uptake via low and high affinity transporters (see Section 6.1.2). Model predictions for the time of depletion, and a threshold nitrate concentration at which uptake ceases, are both in accordance with empirical values (Section 6.3.6). Finally, we demonstrate that under certain conditions, three-dimensional descriptions of the root system architecture are not necessary to estimate overall water and nitrate uptake, and that simple one-dimensional models can be used instead (Chapter 7).

Acknowledgements

First of all, I would like to thank my supervisors, Professor John King and Professor Markus Owen, for giving me the opportunity to work on this project, providing me with many compelling ideas, and for their guidance and patience with me. I am very thankful to John for giving me plenty of freedom in choosing the topic of my research, for all the comments and feedback he provided me with, and for introducing me to the beauty of asymptotic analysis. I am also very thankful to Markus for all of his support, and for his many helpful corrections and comments on mathematical, computational, writing and other issues with my work. I would like to thank The School of Mathematical Sciences and The University of Nottingham for funding my research. I am further grateful to my internal assessors, Dr Ruediger Thul and Dr Bindi Brook for their useful feedback over the years, and to Dr Rebecca Shipley for her critical appraisal of my thesis as an external assessor during my final examination.

My thanks go to Dr Larry York, for introducing me to and collaborating with me on the problem of nitrate uptake via transporters, for giving lots of background biological information and ideas necessary for the modelling, and for commenting on Chapter 6 of this thesis. Similarly, I would like to thank Dr Nathan Mellor for all his help with SimRoot, for writing major parts of the python scripts extracting the root length as well as the average water content distributions with depth (and helping me to write the remaining parts), and for his comments on Chapter 7. Thanks must also go to Dr Mariya Ptashnyk for giving me many useful corrections and suggestions on Chapter 4, to Adam George-Wood for his detailed corrections in Chapter 1, to Dr Matúš Benko for his comments on Chapter 3, and to Vladimir Toussaint for his comments on Chapter 6. Moreover, I would like to thank Andrew Krause for his help, suggestions and support during the time I worked on the final version of this thesis.

Next, I would like to express gratitude to the FutureRoots team within The Centre for Plant Integrative Biology at The University of Nottingham, especially Professor Malcolm Bennett, Professor Sacha Mooney, and my fellow PhD students Marcus Griffiths, Andrew Hyde, Jim Johnson, Ernst Schäfer, Shaunagh Slack and Mark Thompson for many useful and exciting conversations during and outside our monthly meetings, which provided me with a lot of help in my own research.

My thanks further extend to Dr Arnd Korn for introducing me to and greatly helping me with FEniCS, to Dr Mattia Colombo for making his University of Nottingham thesis latex template available to me, to Dave Parkin for providing extremely efficient IT support, as well as to Helen Cunliffe and Sarah Burton for being great PGR Administrators. I would also like to thank many of my friends from The School of Mathematical Sciences (especially Agne, Andrea, Mirka and Sarah) for their help with the practicalities of PhD study.

It makes me happy to think of how many great people I met in Nottingham, and these people made my stay here very enjoyable. Because of this, I would like to thank all my friends from The Catholic Community, The Slovak and Czech Society, and The School of Mathematical Sciences at The University of Nottingham (Ambrus, Samanthika, Robert, Vlad, Martin, Roman and many others).

Finally, I would like to thank God and my parents without whom none of this would have been possible.

CONTENTS

1 INTRODUCTION AND LITERATURE REVIEW 1

1.1 Introduction . . . 1

1.2 Roots and soil . . . 3

1.2.1 Roots and root systems . . . 3

1.2.2 Soil . . . 8

1.2.3 Plant uptake . . . 9

1.2.4 Root-soil interactions. Rhizosphere . . . 13

1.3 Modelling . . . 14

1.3.1 Simple root-like geometries . . . 14

1.3.2 Modelling growth and development of root systems . . . 15

1.3.3 Soil water and nutrient dynamics . . . 18

1.3.4 Modelling water and nutrient uptake . . . 25

1.3.5 Non-root boundary conditions . . . 31

1.4 Solution methods . . . 31

1.4.1 Numerical analysis . . . 31

1.4.2 Asymptotic analysis and nondimensionalisation . . . 32

1.4.3 Multiscale methods . . . 33

1.4.4 Homogenisation . . . 34

1.5 Available software tools . . . 43

1.5.1 SimRoot . . . 44

1.6 Thesis plan . . . 44

2 WATER UPTAKE BY SIMPLE ROOT STRUCTURES 46

2.1 Introduction . . . 46

2.2 Equations, geometries and software . . . 47

2.2.1 Continuity equation . . . 47

2.2.2 Boundary conditions . . . 48

2.2.3 Software 51
2.3 Brief introduction to the finite difference method 52
2.4 Brief introduction to the finite element method 55
2.5 Numerical checking and simulations - toy problems 59
2.5.1 Linear diffusion equation 59
2.5.2 Linear advection-diffusion equation 73
2.6 More realistic models 83
2.6.1 Single root: no uptake 85
2.6.2 Water uptake by a single cylindrical root 96
2.6.3 Water uptake by branching structures 106

3 NUTRIENT UPTAKE BY PERIODIC ARRAYS OF CYLINDERS. 121
3.1 Introduction 121
3.2 Linear diffusion equation 124
3.2.1 Homogenisation 125
3.2.2 One-dimensional modelling 138
3.2.3 Three-dimensional modelling 147
3.3 Model with convection 150
3.4 Michaelis-Menten boundary condition 154
3.4.1 One-dimensional results 156
3.5 Nonlinear model for water dynamics 157
3.5.1 One-dimensional results 163
3.6 Summary 163

4 NUTRIENT UPTAKE AND HOMOGENISATION: SPARSE HAIRS LIMIT 166
4.1 Introduction - three spatial scales 166
4.2 Informal approach 167
4.3 Simpler problem - full circular symmetry 169
4.3.1 Leading order 169
4.3.2 $O(\epsilon)$ 170
4.3.3 $O(\epsilon^2)$ 171
4.3.4 Boundary and outer layer solutions for v 177
4.3.5 Matching for v 179

4.3.6 Different scalings for $K(a)$ . . . 182
4.4 Periodic boundary conditions . . . 185
4.4.1 u_0 . . . 185
4.4.2 u_1 . . . 186
4.4.3 u_2 . . . 189
4.4.4 Different scalings for $K(a)$ . . . 192
4.5 Checking . . . 195
4.5.1 Consistency between matching procedures . . . 195
4.5.2 Checking numerics for Dirac delta function . . . 198
4.6 First nonuniformity: $\epsilon = \frac{\lambda}{\ln \frac{1}{a}}$ . . . 201
4.7 Next nonuniformity: $\epsilon^2 = \frac{\lambda}{\ln \frac{1}{a}}$ . . . 204
4.8 Testing the new limit . . . 206
4.8.1 Approximation using higher orders . . . 209
4.8.2 Time evolution . . . 216
4.9 Summary . . . 216

5 EFFECTS OF ROOT CURVATURE ON HAIR UPTAKE MODELS 218
5.1 Introduction . . . 218
5.2 Short root hairs . . . 219
5.2.1 Transforming the hair boundary condition . . . 221
5.2.2 Homogenisation . . . 223
5.3 $\delta = O(1)$ . . . 241
5.3.1 Leading order . . . 244
5.3.2 $O(\epsilon)$ . . . 245
5.3.3 $O(\epsilon^2)$ . . . 246
5.4 Simulations . . . 248
5.4.1 Robin boundary condition . . . 249
5.4.2 More realistic models . . . 260
5.5 Summary . . . 267

6 NITRATE TRANSPORTERS AND UPTAKE 269
6.1 Introduction . . . 269
6.1.1 Michaelis-Menten . . . 269

6.1.2 Low and high affinity transporters . . . 270
6.1.3 Efflux . . . 271
6.2 Derivation of $\bar{I}_{max}$ and $\bar{K}_m$ . . . 272
6.2.1 Nutrient uptake by phytoplankton - literature review . . 272
6.2.2 Application to root uptake modelling . . . 273
6.3 Derivation of $\bar{c}_{min}$ . . . 277
6.3.1 General Michaelis-Menten boundary condition . . . 277
6.3.2 High and low affinity transport modelling . . . 281
6.3.3 Steady state scenario . . . 282
6.3.4 Time evolution to the steady state . . . 286
6.3.5 Toy model . . . 287
6.3.6 Model with realistic parameters . . . 292
6.4 Summary . . . 302

7 HORIZONTALLY AVERAGED MODELS OF ROOT SYSTEM UPTAKE 303
7.1 Introduction . . . 303
7.2 Extraction of data from root images . . . 305
7.3 Water uptake by static root systems . . . 307
7.4 Nitrate uptake . . . 313
7.4.1 Averaged model for nitrate . . . 318
7.4.2 Single cylindrical root . . . 320
7.4.3 Real root systems . . . 324
7.5 Summary . . . 327

8 SUMMARY AND FUTURE WORK 328
8.1 Summary . . . 328
8.2 Future work . . . 330

A APPENDIX A 333
A.1 Justification of scalings . . . 333

B APPENDIX B 339

C APPENDIX C 346

LIST OF FIGURES

Figure 1.1 Branching structure of a wheat root system (in centimetres), obtained using X-ray imaging (see Section 1.2.1). Grown in a soil column in Hounsfield facility at the University of Nottingham (for a more-detailed description of how this image was obtained, see Section 7.1). 4

Figure 1.2 Root hairs of four different plant species, taken from [87]. The scale bars on the bottom right of all images represent 200 micrometres. Average hair length is indicated above the images. Note that in a different experiment, the average length of root hairs for certain wheat and barley cultivars exceeded 1 millimetre (see [51]); we will model uptake by such root hairs in Chapters 2 and 5. 5

Figure 1.3 Root hair geometry, taken from [80]. In (a) we see various scales used in the method of homogenisation (see Section 1.4.4) - the microscopic scale given by the inter-hair distance and the macroscopic scale given by the length of the root segment under consideration. Figure (b) shows a rolled-out root surface and root hairs orthogonal to it. 16

Figure 2.1 Coarsely meshed geometry without a side branch. . . . 49

Figure 2.2 Slice through a (coarsely) meshed geometry with a side branch. 50

Figure 2.3 MATLAB simulation (the linear diffusion equation (60) equipped with the boundary conditions (63), (62), and the initial condition (65)). The parameters are chosen as follows: $D = 2.5$, $\Phi_{ff} = 0.5$, $I = 0.17$, $r_0 = 2.0$, $r_\infty = 20.0$ and $dt = 10.0$. The root surface ($r = 2.0$) takes up water from its neighbourhood, and thus the water content is decreasing here. Comparison with the analytic result (Equation (64); in red) is also shown. The arrow represents the time evolution. 64

Figure 2.4 Evolution to the steady state (FEniCS simulation, the linear diffusion equation (60), equipped with the boundary conditions (74), (62), and the initial condition (65)). The parameters are chosen as follows: $D \approx 0.2$, $r_0 = 0.1$, $r_\infty = 2.0$, $\Phi_{ff} = 0.36$ and $dt = 2.0$. Comparison with the analytic steady-state solution (in red) is also shown. . . 66

Figure 2.5 The log-log plot of the L^2 norm of $\Phi_A^\infty - \Phi_N^\infty$ as a function of the maximal mesh size. FEniCS simulation, Equation (61), equipped with the same boundary conditions and parameters as in Figure 2.4. 67

Figure 2.6 Steady state on the two-dimensional geometry (same problem as in Figure 2.5). 67

Figure 2.7 Analytic solution (75) does not satisfy the outer boundary condition (62) on the meshed domain exactly. The parameters are: $r_0 = 0.1$, $r_\infty = 2.0$, $D \approx 0.2$ and $\Phi_{ff} = 0.36$. 69

Figure 2.8 Log-log plot of the L^2 norm of $\Phi_A^\infty - \Phi_N^\infty$ as a function of the maximal mesh size. Mesh refined on the boundaries. Three-dimensional simulations (same problem as in Figure 2.5). 72

Figure 2.9 Comparison of the integrals from Equation (76) at the steady state for a decreasing maximal mesh size (same problem as in Figure 2.5). Three-dimensional simulations. 73
Figure 2.10 Time evolution to the steady state in FEniCS: Equation (45), equipped with the initial condition (77), and the boundary conditions (49), (47) and (20). The parameters are chosen as follows: $\theta_r = 0.0$, $D = 1.0$, $K = 1.0$ and $h_0 = 1.0$. The maximal mesh size is 0.4. The polynomial degree is 1. 78
Figure 2.11 Comparison of the integrals from Equation (76) at the steady state for a decreasing maximal mesh size (same problem as summarised in the caption for Figure 2.10). 79
Figure 2.12 MATLAB simulation: same problem as in Figure 2.10. Colours indicate local water content. 81
Figure 2.13 Absolute value of the error between the two implementations (same problem as in Figure 2.10). 82
Figure 2.14 The shape of (van Genuchten) $D(\Theta)$ and $k(\Theta)$ for $m = 0.5$ 84
Figure 2.15 Diffusivity and conductivity functions for different values of m. 87
Figure 2.16 The (three-dimensional) single-root-geometry mesh. . . 89
Figure 2.17 Steady-state water distribution using Equation (92) with van Genuchten nonlinearities $D(S)$ and $k(S)$ (defined in equations (85) and (86)), equipped with the zero-flux boundary condition (93) everywhere. Parameters are summarised in Table 2.8, the only change being $m = 0.35$ here. 91
Figure 2.18 Evolution to the steady state for the same problem as in Figure 2.17, using the initial condition (95). The geometry is stretched in the r direction for visualisation purposes. 92

Figure 2.19 Evolution to the steady state for the same problem as in Figure 2.18, except for $m = 0.85$. The geometry is stretched in the r direction for visualisation purposes. . 93

Figure 2.20 Evolution to the steady state for the same problem as in Figure 2.19, except for $m = 0.5$. 94

Figure 2.21 Evolution to the steady state for the same problem as in Figure 2.20 using the nonhomogeneous initial condition 96. 95

Figure 2.22 Difference between the two steady states (same problem as in Figure 2.20). 95

Figure 2.23 Results using Equation (92) with van Genuchten nonlinearities $D(S)$ and $k(S)$ (defined in equations (85) and (86)), equipped with the boundary conditions (102) – (105), and the initial condition (95). Parameters are summarised in Table 2.8. For the chosen uptake rate (see Equation (98)), the watering rate of $C_w = 6\,\mathrm{cm\,d^{-1}}$ is too high, and the simulation crashes at $t \approx 0.73$ (note that the solution seems nearly uniform in r, which is caused by the diffusion acting very fast on such short length scales). 99

Figure 2.24 The watering rate of $C_w = 4\,\mathrm{cm\,d^{-1}}$ yields a steady state close to full saturation (keeping everything else unchanged compared to Figure 2.23). 99

Figure 2.25 The steady state for $C_w = 4\,\mathrm{cm\,d^{-1}}$ (same problem as in Figure 2.24). Note the changed colorbar limits. 100

Figure 2.26 No watering (same problem as in Figure 2.24, except for $C_w = 0\,\mathrm{cm\,d^{-1}}$) leads to the drying out of the soil and the subsequent crash of the simulation. 103

Figure 2.27 Comparison of simulations for two values close to the critical watering rate (same problem as in Figure 2.24; the only changed parameter is the watering rate C_w). . 105

Figure 2.28 Steady state for the same problem as in Figure 2.25, except for $C_w = 0.09\,\mathrm{cm\,d^{-1}}$. Note the changed colorbar limits. 106

Figure 2.29 Boundary parts for the geometry with the hair. The main root is coloured green and the hair is coloured red. As the domain is very thin in the x_3 direction, we stretched it 10 times. 111

Figure 2.30 Time evolution for the geometry with the hair. Equation (119) using the van Genuchten nonlinearity $D(S)$ (see Equation (85)), equipped with the initial condition (123), boundary conditions (120), (121), (122) (using C_2 from Equation (117)), and the zero-flux boundary condition applied at $r = \frac{r_\infty}{h_0}$. Geometric parameters are summarised in Table 2.11. 113

Figure 2.31 Steady state for the same problem as in Figure 2.30, except that we use a Dirichlet condition $S(r = \frac{r_\infty}{h_0}) = 0.99$. 114

Figure 2.32 Steady state for the same problem as in Figure 2.30, except that we use a Dirichlet condition $S(r = \frac{r_\infty}{h_0}) = 0.04$. 114

Figure 2.33 Comparison of steady states for varying inter-hair distance h_0 (and fixed r_0). x_3 direction is stretched 10 times to capture the changing inter-hair distance better. Same problem as in Figure 2.32, except that we have 4 root hairs in the unit cell, and at $r_\infty = 0.2$ cm, we assume $S = 0.02$. 117

Figure 3.1 The domain with periodically-spaced cylinders and the two characteristic length scales. In the case of root hairs, one has $l \approx 0.01$ cm, $L \approx 1$ cm [80]. 123

Figure 3.2 The (meshed) microscale geometry. 126

Figure 3.3 Two-dimensional micro-geometry C as defined in Equation (133). 127

Figure 3.4 The steady state solution using the Dirichlet boundary conditions at $x_3 = 0$ and $x_3 = d$. 140

Figure 3.5 The steady state solution using the Dirichlet boundary conditions at $x_3 = 0$ and $x_3 = d$. In order to obtain the aspect ratio of (approximately) 1, the x_1 and x_2 axes are stretched. 141
Figure 3.6 Comparison between the full-geometry numerics and the homogenisation solution for the steady-state scenario. 141
Figure 3.7 Comparison between the analytic and the numerical solutions of the homogenised equation (steady states). . . 142
Figure 3.8 The unit-cell simulations with and without the uptake. 142
Figure 3.9 Comparison with $K = 0$; solutions plotted along the edge of the unit cell. 143
Figure 3.10 Comparison between the full-geometry numerics and the homogenisation solution (steady states). The zero-flux boundary condition is applied at $x_3 = d$. 144
Figure 3.11 Comparison between the analytic and the numerical solution of the homogenised equation (steady states). The zero-flux boundary condition is applied at $x_3 = d$. . . . 145
Figure 3.12 Investigating how C_1 depends on K for $a = 0.25$ (fixed). 146
Figure 3.13 Investigating how C_1 depends on a for $K = 1$ (fixed). . 146
Figure 3.14 Introducing the plane view. Solution at $t = 0.1$. 147
Figure 3.15 Introducing the new camera view. 147
Figure 3.16 Comparison between the full-geometry solution and the homogenisation solution (time evolution). 148
Figure 3.17 Model with a macroscopic gradient in x_1 (steady state). 149
Figure 3.18 Normalised solution to the unit cell problem for λ_1. The solution is independent of y_3, as shown before. 150
Figure 3.19 Comparison between the full-geometry numerics and the homogenisation solution: model with a macroscopic variation in x_1 (steady state). 151

Figure 3.20 Comparison between the full-geometry numerics and the homogenisation solution: model with a macroscopic variation in x_1 (steady state). Slices at $x_3 = const$. Note that $x_3 = 0.90$ is located outside of the root-hair zone. . 152

Figure 3.21 Comparison between the full-geometry numerics and the homogenisation solution plotted along the diagonal within the $x_3 = 0.0$ slice. The $x-$axis represents the distance (measured on the macroscale) from one corner of this slice (-0.5,-0.5) to the opposite corner (0.5,0.5). . . . 153

Figure 3.22 Comparison between the full-geometry numerics and the homogenisation solution for the model with convection. 155

Figure 3.23 Comparison between the models with and without convection. 156

Figure 3.24 Comparison between the full-geometry numerics and the homogenisation solution: model with the Michaelis-Menten boundary condition. 158

Figure 3.25 Comparison between the models with different cylindrical surface boundary conditions. 159

Figure 3.26 Comparison between the full-geometry numerical solution and the homogenisation result for the model with van Genuchten nonlinearities. 164

Figure 4.1 The schematic representation of the depletion gradients close to the hair surfaces ($a \ll 1$). 168

Figure 4.2 Behaviour of $\tilde{v}(r_y; a)$ as $a \ll 1$ 185

Figure 4.3 Numerical solution for ψ (FEniCS). 199

Figure 4.4 Comparison between the FEniCS solution and the analytic solution for ψ. 200

Figure 4.5 Comparison between the FEniCS solution and the analytic solution for ψ (zoom). 200

Figure 4.6 The domain geometry for $a = 0.01$ and $\epsilon = 0.5$. 207

Figure 4.7 The steady-state solutions of the full-geometry model for decreasing a deviate from the solution of Equation (211) (clipped domain). 208
Figure 4.8 Comparison of the steady-state solutions at the root surface. 210
Figure 4.9 Comparison of the steady-state solutions out of the hair zone. 211
Figure 4.10 Comparison of the steady-state solutions at the root surface using the higher-order microscopic behaviour (decreasing a). 214
Figure 4.11 Comparison of the steady-state solutions at varying distance from the root surface using the higher-order microscopic behaviour ($a = 0.001$). 215
Figure 4.12 Comparison between the models at different times ($x_3 = 0.0$). We used $a = 0.001$, $C = 1.0$, and assumed a zero-flux boundary condition at $x_3 = 1.0$ (instead of the Dirichlet boundary condition; this can be used to model inter-root competition). 217
Figure 5.1 The curved root surface and the most important parameters in this chapter. The four hairs per each layer are chosen rather arbitrarily, and this parameter will be changed in future. 219
Figure 5.2 The solution of the first unit cell problem and its derivative with respect to y_1. 229
Figure 5.3 The solution of the second unit cell problem and its derivative with respect to y_1. 230
Figure 5.4 The solution of the λ_1^1 (unit cell) problem and its derivative with respect to y_1. 233
Figure 5.5 The solution of the λ_2^1 (unit cell) problem and its derivative with respect to y_1. 234
Figure 5.6 Restricting attention to the single wedge. Using the clipped domain, we see the (finely-meshed) hair surfaces. 252

Figure 5.7 Comparison between the full-geometry numerics and the short-hairs homogenisation result at $t = 1$ ($\delta = 0.5, 1.0$). 255
Figure 5.8 Comparison between the full-geometry numerics and the short-hairs homogenisation result at $t = 1$ ($\delta = 2.0, 5.0$). 256
Figure 5.9 The depletion gradients at the tips of the hairs for varying δ ($t = 1$). 257
Figure 5.10 The domain is divided into 6 subdomains. Colour indicates the subdomain number. 258
Figure 5.11 Different unit cell geometries for varying x_{3,h_1} ($\delta = 5$). . 259
Figure 5.12 Comparison with the new model in which the sink term is dependent on the distance from the root surface. Errors in the short-hairs limit simulation are obvious for $\delta = 5.0$ ($t = 1.0$). 261
Figure 5.13 Assessing the validity of the linear approximation. . . . 263
Figure 5.14 Comparison with the new effective equation for $\delta = 5.0$ (the model with efflux; $t = 1.0$). 264
Figure 5.15 Comparison with the new effective equation for $\delta = 5.0$ (the Michaelis-Menten model; $t = 1.0$). 266
Figure 5.16 The linear model takes up more nutrient. 267
Figure 5.17 Comparison with the new effective equation for $\delta = 5.0$ using $\bar{u}_{in} = 3K_m$ (the Michaelis-Menten model; $t = 1.0$). 268
Figure 6.1 Comparison of the Michaelis-Menten functions for LATs and HATs assuming $\frac{K_m^L}{K_m^H} = 20$ and $\frac{I_{max}^L}{I_{max}^H} = 5$. 283
Figure 6.2 Comparison of the Michaelis-Menten functions for LATs and HATs assuming $\frac{K_m^L}{K_m^H} = 2$ and $\frac{I_{max}^L}{I_{max}^H} = 5$. 284

Figure 6.3 For $I^H_{max} = 0.01085$ (blue), the steady-state concentration (for any value of N^L; solid line) is greater than c^* (dashed line), and therefore it is advantageous for the plant to produce LATs only. However, a slight increase in I^H_{max} gives the opposite outcome (red), and HATs-only becomes the optimal strategy for minimising c_{ss}. 285

Figure 6.4 Time evolution to the steady state for the toy model of nitrate uptake by HATs and LATs. 288

Figure 6.5 Time evolution to the steady state for the toy model of nitrate uptake by HATs and LATs (zoom). 289

Figure 6.6 The external nitrate concentration as a function of time and N^L for the toy model of nitrate uptake by HATs and LATs. 289

Figure 6.7 Global minimum in depletion time for the toy model is achieved for a nontrivial low/high affinity transporters distribution - at $N^L \approx 505$ (which corresponds to $N^H = 495$). 290

Figure 6.8 Remaining nitrate concentration at the reference time and the corresponding steady states for the toy model. 290

Figure 6.9 Depletion times for $I^H_{max} = 0.02$ and $I^H_{max} = 0.05$ (toy model). 291

Figure 6.10 Time evolution to the steady state for the model of nitrate uptake by LATs and HATs. 298

Figure 6.11 Steady state concentration as a function of N^L for the model of nitrate uptake by LATs and HATs. 298

Figure 6.12 Depletion time as a function of N^L for the model of nitrate uptake by LATs and HATs. 299

Figure 6.13 Steady state concentration as a function of N^L (zoomed-in to the relevant region). 299

Figure 6.14 Depletion time as a function of N^L for $c_{in} = 30$ mM and $c_{in} = 300$ mM. 300

Figure 6.15 Time evolution to the steady state for $c_{in} = 100$ mM. . . 301

Figure 6.16 Steady state concentrations as a function of N^L for $c_{in} =$ 100 mM. 301
Figure 6.17 Depletion time as a function of N^L for $c_{in} = 100$ mM. . 302
Figure 7.1 A wheat root system numbered as 600 (in centimetres). 305
Figure 7.2 The root length distribution with depth for the root system 600. 306
Figure 7.3 Water depletion zones close to root surfaces in the modified SimRoot; a slice through the soil domain. Colours represent the varying water content - blue indicates the driest soil. 308
Figure 7.4 Comparison between the models without transpiration for an increasing time. 312
Figure 7.5 Comparison with the Boolean model. The root length distribution is clearly relevant. 314
Figure 7.6 Other root systems used in simulations. 314
Figure 7.7 Comparison between the models with water uptake. . . 315
Figure 7.8 The results of nitrate uptake simulation in SimRoot using the simple root system. 321
Figure 7.9 Comparison of nitrate models for the simple root system using a finer mesh in SimRoot. 322
Figure 7.10 Comparison of nitrate models for the simple root system using a finer mesh in SimRoot, and a finer root geometry definition. 323
Figure 7.11 Remaining soil nitrate concentration after 6 days of uptake (the simple root system). 324
Figure 7.12 The nitrate concentration distributions with depth after 6 hours of uptake (real root system geometries). Root length distributions with depth (separately for different root classes) of these root systems are shown for comparison. 326

Figure 7.13 Using $c_{in} = 4\,\mathrm{mM}$, after 6 hours, the depletion can still be neglected in the nitrate uptake calculations (root system 555). 327
Figure A.1 Nutrient concentration distribution at time $t = 1.0$ for $\epsilon = 1.0$ and $K = 1$. 335
Figure A.2 The isosurfaces for nutrient concentration at time $t = 1.0$ for $\epsilon = 1.0$ and $K = 1$. 336
Figure A.3 Slice through the domain at $x_3 = 0.0$ for a decreasing value of ϵ. Notice the varying concentration range as well as the varying size of the unit cell. 337
Figure A.4 The nutrient concentration at the cylindrical surface at time $t = 1.0$ as a function of ϵ for varying m. 338

LIST OF TABLES

Table 1.1 The Michaelis-Menten and efflux parameters for phosphate uptake by mildly phosphate starved plants; reproduced from [80]. 40

Table 2.1 Numerical error for increasing resolution (same problem as in Figure 2.5). 68

Table 2.2 Numerical error for the increasing polynomial degree (same problem as in Figure 2.5). 69

Table 2.3 Numerical error for an increasing resolution with a refined boundary mesh (same problem as in Figure 2.5). 70

Table 2.4 Comparison of the two integrals from Equation (76) for an increasing resolution (same problem as in Figure 2.5). 71

Table 2.5 Comparison of the two integrals from Equation (76) for an increasing polynomial degree (same problem as in Figure 2.5). 72

Table 2.6 Comparison of the two integrals from Equation (76) for an increasing polynomial degree (same problem as in Figure 2.5). Three-dimensional simulations. 74

Table 2.7 Comparison of the two integrals from Equation (76) for the same problem as summarised in the caption for Figure 2.10. Increasing the polynomial degree in the three-dimensional simulations. 80

Table 2.8 The default parameter values for the single root water uptake model. The soil parameters are taken from [142], and the root parameters are approximated from [70] (as discussed in the main text). 86

Table 2.9 Numerically computed integrals at the steady state for an increasing mesh resolution (same problem as in Figure 2.25). The polynomial degree is 1. 102

Table 2.10 Numerically computed integrals at the steady state for an increasing polynomial degree (same problem as in Figure 2.25). $N_r = 25$. 102

Table 2.11 Geometry parameters for the model with the hair. . . . 108

Table 2.12 Comparison between the total flux entering the root surfaces and the influx from the far-field at the steady state for varying maximal mesh size (same problem as in Figure 2.32). Polynomial degree is 1. 115

Table 2.13 Searching for the optimal inter-hair distance h_0 (r_0 is fixed). The optimisation is based on the same problem as described in Figure 2.33. $F(h_0)$ is the (numerically computed) total flux into the (unit cell) root surfaces, whereas $F^*(h_0)$ denotes the (numerically computed) influx from the far field. $E(h_0)$ is defined in Equation (125) and $E^*(h_0)$ is defined in Equation (126). Polynomial degree is 2. 119

Table 3.1 Numerical confirmation that $\int_C \frac{\partial \lambda_1}{\partial y_2} dS = \int_C \frac{\partial \lambda_2}{\partial y_1} dS = 0$ and $\int_C \frac{\partial \lambda_1}{\partial y_1} dS = \int_C \frac{\partial \lambda_2}{\partial y_2} dS \approx -0.13$ 137

Table 5.1 The parameter values for phosphate uptake by wheat. Most values are estimated from [80]. The values for μ_r, μ_h, r_∞ and H are justified in the main text. 251

Table 5.2 Numerically-computed integral values. 259

Table 6.1 Toy model parameter values. 287

Table 6.2 Realistic parameter values for nitrate uptake by oilseed rape plant. Various sources (see the main text). 297

Table 7.1 Default geometric parameters for water uptake. 311

Table 7.2 Default soil water parameters. 311

Table 7.3 Default nitrate dynamics parameters in SimRoot. 321

Table A.1 $u_{cyl}(1, \epsilon)$ for different uptake scalings $\psi(\epsilon) = \epsilon^m$ 336

1

INTRODUCTION AND LITERATURE REVIEW

1.1 INTRODUCTION

In the middle of the 20th century, food security problems arose as food production could not keep pace with growing populations and also because of the limited responsiveness of cereals to fertilisers (cereals would lodge i.e. bend/-fall over at high fertility) [85]. Norman Borlaug and others solved this problem by developing dwarf genotypes of rice and wheat which responded to fertilisers without lodging. Even though this resulted in a large increase in grain production (which became known as the Green Revolution), since chemical fertilisers are getting more expensive (which mostly affects third-world farmers) we still need a second Green Revolution which would increase yields at lower fertility [85]. In other words, the most important goals of agriculture nowadays are to increase nutrient use efficiency and simultaneously decrease the usage of fertilizers [61].

The world's population reached 7 billion in 2011 [149], and it is predicted to reach 9 billion by 2050 [55]. In order to keep pace with this population change, and correct for the current shortage of food supply, it has been suggested that crop production must double by this time [115] (compared to 2013 production). We face an immense food crisis - 854 million people are malnourished and 6 million children under the age of 5 die each year from hunger [85].

Progress in food security can be introduced in many ways, of which the most direct would be increased food production in developing nations [85]. To obtain this improvement, many processes involved in plant growth and develop-

ment must be understood qualitatively and quantitatively. Acquisition of plant nutrients (e.g. nitrate) from the soil is of particular importance. As nutrient intake takes place at the root surfaces below the ground, it is often not amenable to direct measurements. Furthermore, due to the complexity of the root systems as well as of the soil, uptake processes are inherently multiscale. To give just one example, the distance between two neighbouring root hairs - which significantly contribute to nutrient uptake (see Section 1.2.1) - is often much smaller than the length of the root that these hairs grow on. The former is typically of order 10^{-2} cm, while the latter can be over 100 cm for many plant species, including wheat (see [80] and [58]). For these reasons, mathematical modelling offers a desirable alternative. This thesis presents various examples of how to solve multiscale problems arising from plant nutrient uptake studies.

In Section 1.2, we introduce some basic knowledge about roots and soil, which will be important for the purposes of this thesis, briefly mentioning some of the factors influencing plant proliferation such as the presence of hormones, fungi, and microbes. In Section 1.3, we discuss some aspects of mathematical modelling. First, we introduce basic geometries often used for representing roots in nutrient uptake modelling, after which we briefly discuss modelling root growth and root system development. Then we present the basic ideas behind conservation laws, which give us better understanding of important concepts used in water and nutrient uptake modelling, such as the reaction-convection-diffusion equations, Darcy's law, and Richards' equation. Next, we focus on reviewing up to date modelling of water and nutrient uptake, and we finish this section with a discussion of standard non-root boundary conditions. In Section 1.4, we discuss how differential equations (such as those from Section 1.3) can be solved using either numerical (finite difference or finite element) or asymptotic (homogenisation) methods. In Section 1.5, we review some software tools that have been used to model water and nutrient uptake by plants.

1.2 ROOTS AND SOIL

1.2.1 *Roots and root systems*

The root systems of plants can be highly complex and irregular structures (see Figure 1.1). Roots are cylindrically shaped below-ground organs of plants (which taper towards their tips; for simplicity, we will neglect these effects in this thesis) responsible primarily for the anchorage of the plant in the soil and ensuring that the plant gets enough essential nutrients (nitrogen, phosphorus, water etc.) from the soil, but also for many other functions [143]. When studying root architecture, roots are often described by their order (as in [48]). This simply means that roots emerging from the seed have order 0 (seminal roots), roots emerging from zeroth-order roots have order 1 (first order lateral roots or branches) and so on. Roots of cereal plants (wheat, barley, maize or rice are among the most important representatives of this group for agricultural purposes) usually have three or four orders of branches [122]. In general, water and nutrient uptake can occur on the surface of roots of arbitrary order, and the corresponding uptake rate is influenced by many factors (for readers interested in variation of nitrate uptake rates in maize root system, we recommend [150]).

Root system architecture is crucial for a plant's survival. For nitrogen acquisition, it is advantageous for a plant to have deeper roots, as nitrate leaches deep into the soil [50]. On the other hand, phosphate accumulates in the top soil (approximately top 30 centimetres), and thus more shallow-angled roots may be needed to satisfy plant's phosphate demand [54]. Therefore, different root traits imply different resource accessibility.

Root hairs (shown in Figure 1.2) are cylindrically-shaped lateral extensions of epidermal (i.e. outer layer) cells that increase the surface area of the root system, and therefore play a significant role in nutrient acquisition [30]. Evidence of this role is nicely summarized in [152] - studies of soil depletion zones (zones of low nutrient concentration) using autoradiography and studies with hair mutants (plants without the root hairs) serve as proof.

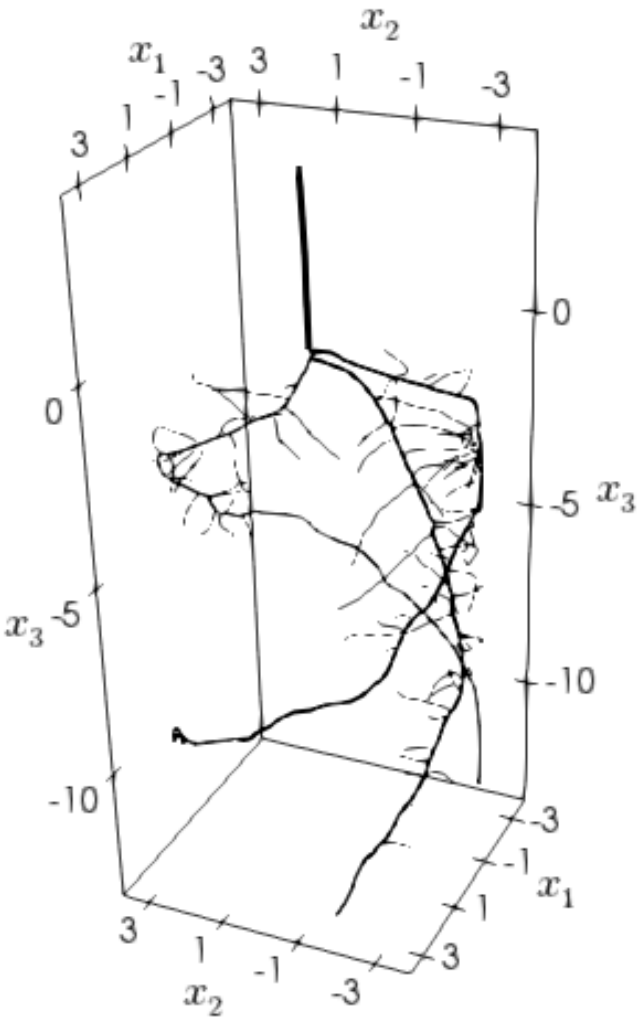


Figure 1.1.: Branching structure of a wheat root system (in centimetres), obtained using X-ray imaging (see Section 1.2.1). Grown in a soil column in Hounsfield facility at the University of Nottingham (for a more-detailed description of how this image was obtained, see Section 7.1).

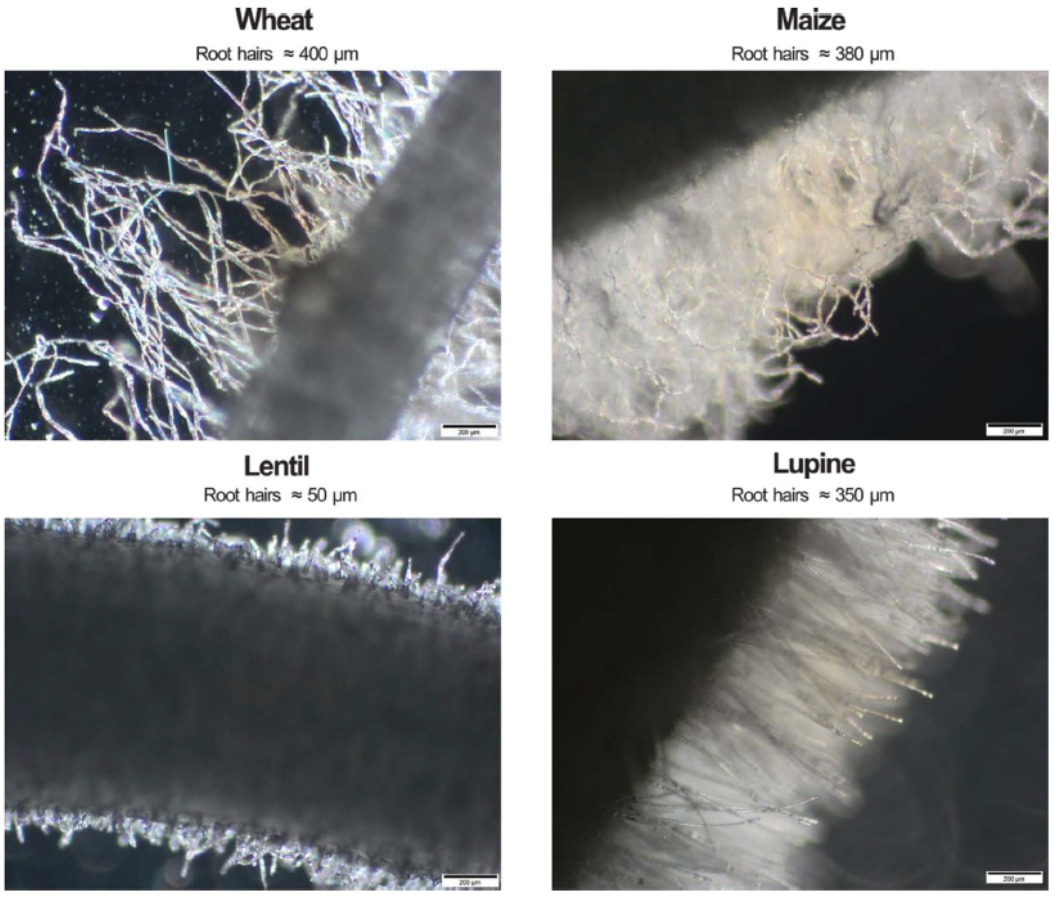


Figure 1.2.: Root hairs of four different plant species, taken from [87]. The scale bars on the bottom right of all images represent 200 micrometres. Average hair length is indicated above the images. Note that in a different experiment, the average length of root hairs for certain wheat and barley cultivars exceeded 1 millimetre (see [51]); we will model uptake by such root hairs in Chapters 2 and 5.

Imaging methods

The most heavily used tools for visualisation of root systems in soils up to date include X-ray computed tomography (X-ray CT; see [132], [4], and Figure 1.1) and magnetic resonance imaging (MRI, see [141] or [105]). In [92], these two tools were directly compared using pots of different sizes. While finer details of roots were better captured using X-ray CT due to its higher spatial resolution, in the largest pot, more roots were detected using MRI, which was attributed to its stronger root-to-soil contrast [92]. The presence of magnetic materials in soils often limits the applicability of MRI [94].

Recently, X-ray CT has been used for three-dimensional visualisation of soil structure and quantification of hydraulic properties of such structure [139], as well as for three-dimensional visualisation of root systems and quantification of water uptake by these systems [27].

The final tools worth mentioning when discussing the imaging of root-soil interactions at the root-system scale (due to their increased popularity in recent years) are neutron radiography (two-dimensional) and neutron tomography (three-dimensional), which were used for visualisation of root system architecture and water content distribution in soil (see [18], [94] and [100]). The main advantage of these tools (in comparison with X-ray CT) is their ability to capture small changes in water content [94].

For plants grown outside of the soil, the geometry of root hairs is often obtained using microscopy imaging techniques (see [74], [87], and Figure 1.2). As this geometry can be different for plants grown in soils and also because one may wish to study interactions between root hairs and soil particles, it is often desirable to visualise root hairs embedded in a soil environment. Substantial progress in this direction was made by an imaging group led by Professor Tiina Roose at The University of Southampton using synchrotron radiation X-ray computed tomography (SRXCT), which yields images of high resolution with significant reduction in exposure times compared to microfocus X-ray scanning systems (for more details, see [71]). In recent years, this tool has also been used to visualise water content distributions in the root-hair zone (see [26] and [72]).

Quantitative descriptions of root system architecture

Due to the mentioned complexity of some root systems, statistical methods are often employed to give better description of a root system.
Certain root system characteristics have been extensively measured in experiments and subjected to statistical analysis. Among these, the important characteristics which have been found to have a significant effect on (various) uptake processes are root length density (total root length per unit volume of soil), root:shoot ratio (root mass per unit shoot mass), specific root length (length of the root divided by its dry mass), rooting depth, and elongation rate of different root classes (seminal root, first order lateral roots, and so on). A good overview of how these features affect water uptake can be found in [145].

FRACTAL ANALYSIS

Fractals are self-similar objects, which means that they contain the same shapes on various (all) scales. A plant root system with its branches exhibits self-similarity and therefore, fractal analysis has often been used in root system research. While one is often familiar with the notion of a spatial dimension as being a natural number (a line has a dimension of 1, a plane has a dimension of 2, etc.), fractal dimension is often non-integer [143].

SUBCELLULAR SCALES - HORMONAL DYNAMICS

As in any living system, many different hormones interact in often a highly complex manner to create root anatomy as well as to influence root architecture by affecting root growth and branching (e.g. gravitropic response - bending of roots in the direction of gravity). Amongst hormones that have a major impact on root system development are auxin, gibberellin and cytokinin. [62] presents a thorough review of both genetic and environmental determinants of root system growth, and discusses recent developments in modelling as well. For an interested reader, we also recommend an article [9], which reviews mathematical models of growth at the organ (root) scale using information upscaled from subcellular scales. We will not discuss these topics anymore in this thesis, as our modelling will mostly be on larger scales.

1.2.2 *Soil*

Soil affects plant proliferation in different ways. For instance, it introduces a mechanical impedance to the growth of a plant's root (see e.g. [70]). Most of the definitions in this section are taken from [14].

Soil texture is defined by the proportions of particles of different sizes that a given soil contain. The most common practice is to divide soil particles with respect to their size into particles larger than 2 mm (referred to as gravel), sand (diameter d is smaller than 2 mm but larger than 0.05 mm), silt ($0.002\,\text{mm} < d < 0.05\,\text{mm}$) and clay ($d < 0.002$ mm). A soil containing a mixture of fine and coarse particles is commonly referred to as loam [59].

A particular arrangement of these particles into soil aggregates is called soil structure. Typical examples include plate-like, block-like or spheroidal soil structure (for more details, see [14]).

Mass of a unit volume of dry soil is commonly referred to as bulk density. Pore space is the part of the soil which is occupied by fluids (note that this is distinct from void, which is vacant space), and porosity is defined as a quotient of the pore space volume divided by the overall soil volume.

From soil hydrology perspective, two zones are usually present in a soil. An unsaturated zone (in which the pores are not fully occupied by water mostly due to plant uptake and gravity; also referred to as the zone of aeration or the vadose zone) stretches down to a certain depth, whereas below this depth, the soil is fully-saturated (the zone of saturation) [59]. The upper boundary of the saturation zone is often called the water table [138]. Capillarity generally refers to the upward motion of a fluid placed inside a thin (glass) tube due to adhesion (attraction between the fluid and the tube material) and cohesion (attraction between the water molecules themselves) [14]. As the zone of saturation is located below the unsaturated zone, capillary rise often takes place in soils (with the soil pores playing the role of the thin tube).

Water retention refers to the strength with which water is held within soil pores, and it depends on the amount of water present, the size and the shape of the pore. As a result, soil water-holding capacity is a function of porosity

and the pore size distribution [143]. In this way, soil texture strongly affects water mobility (as well as mobility of various nutrients dissolved in the water), and thus influences plant nutrient availability. We will discuss soil water dynamics in more detail in Section 1.3.3.
Let us note that for experimental purposes, plants are often grown in solution culture, i.e. in nutrient solutions with no soil (often referred to as hydroponics; see [14]).

1.2.3 *Plant uptake*

Plants need water and many nutrients in order to grow and reproduce [119].

Transpiration and water uptake

Plants need carbon dioxide from the atmosphere for photosynthesis in their leaves. To obtain the carbon dioxide, leaf stomata (pores used to control exchange of gases) must be open which means that the leaf loses its water vapour. The evaporation creates negative water pressure, which is transmitted through the above-ground plant organs down to its roots, and this drives water flux from the surrounding soil [143]. This process is called transpiration.
Maximum transpiration rate depends on atmospheric moisture [136]. Water lost due to transpiration needs to be replaced via root uptake, and the overall plant water demand is thus dependent on both the size (as well as arrangement) of the leaf surfaces and the weather conditions [136].
In [7], the relationship between the evaporation, leaf water potential (see Section 1.3.3) and root system water uptake was studied experimentally. Leaf water potential responded very slightly to large changes in weather conditions, which suggests an equality between the evaporation and the root uptake. This balance is established via stomatal changes, which seem to happen in response to root water status [7]. Therefore, the quotient of actual to potential (maximum) transpiration rate (when stomata are fully open) often plays a crucial role in transpiration models [140]. If water content decreases significantly in the root's neighbourhood, plants can close their stomata completely, so that

they preserve water.

There are multiple timescales involved in soil water extraction by plant roots - while extraction by a single root can be in the order of minutes, changes in root system architecture in response to localised resource patches can take months [34].

For a more-detailed explanation of transpiration-related processes, see also [97].

Note, that the movement of water from moist to dry soil through plant roots is commonly referred to as hydraulic redistribution. It affects transpiration, photosynthetic rates and the life span of roots [96]. If hydraulic redistribution happens in an upward direction, it is often called hydraulic lift [36].

For a more-detailed treatment of various water-related processes occurring in the soil-plant-atmosphere continuum including flow within the root system as well as in the soil, we recommend classical articles [107] and [103].

Nutrient dynamics influencing uptake

Elements crucial for plant growth are usually divided into two groups - those used in large amounts ($> 0.1\%$ of dry plant tissue) and those used in small amounts ($< 0.1\%$ of dry plant tissue). Elements from the former group can be subdivided into those obtained from air and water (carbon, hydrogen and oxygen), and those obtained from soil (nitrogen, phosphorus, potassium, calcium, magnesium and sulphur; these are often called macronutrients). Elements from the latter group (usually referred to as micronutrients) are obtained from soil, and include iron, zinc, and many others [14].

For nutrient uptake to occur, plant roots must encounter soil nutrients, which can happen either via the root growing into previously unexplored soil volumes (i.e. by root interception), or via movement of nutrient towards root surfaces [14]. Influential soil scientist Stanley Arthur Barber proposed to distinguish between two main concepts by which nutrients are driven towards root surfaces - mass flow and diffusion [10]. Mass flow is a convective transport of soil solution caused by transpiration or drainage [136], while diffusion is movement of a nutrient from areas of higher concentration to those of lower

concetration, which occurs as a consequence of random motion of nutrient ions or molecules (often described by Brownian motion) [14].

Mass flow is often dominant in providing plant roots with some of the essential nutrients, which are easily dissolved in soil solution (nitrogen, calcium) [11]. Diffusion is usually the primary factor for movement of poorly soluble nutrients [11]. In the aforementioned paper, Barber also introduced a method of determining which of these processes is likely to be dominant [10]. Briefly, if one observes an accumulation of a nutrient close to a root surface (compared to the surrounding medium), then the mass flow contribution is sufficient to satisfy plant's demand for the nutrient (represented here by the nutrient uptake rate), and diffusion actually drives the nutrient away from the root surface. However, if the nutrient is depleted close to the root surface, then diffusion can play an important role as well. To quantify the respective contributions of these processes, one usually estimates the mass flow contribution by measuring plant transpiration and an average nutrient concentration in the medium, and then estimates the contribution of diffusion by measuring the total nutrient content of the plant (see [11]).

Some nutrients are strongly adsorbed to soil particles, which makes them poorly mobile with the mass flow. The adsorbed nutrients can become desorbed and vice-versa. In most of the modelling literature (e.g. [122], [80]) however, it is assumed that these reactions reach equilibrium much faster compared to the time scales of nutrient transport through soil. In such cases, concentration of the nutrient bound to solid soil surfaces is simply assumed to be proportional to that of nutrient dissolved in the soil solution, and the constant of proportionality is called soil buffer power (see [122]). In other words, highly buffered nutrients are those strongly bound to soil particles, and the soil's ability to resupply these nutrients from the solid fraction is high [61]. For a more general definition as well as more detailed treatment of the soil buffer power, see [136]. We will come back to the soil buffer power, when we discuss soil nutrient dynamics modelling in Section 1.3.3.

A nutrient is often called limiting if its availability affects the growth of plants in the given ecosystem (in other words, if a small change in its concentration re-

sults in a non-negligible change in the growth). Naturally, nutrients that limit the growth of crops in most agricultural ecosystems are most heavily applied as fertilisers. It is generally agreed that the two most-often-limiting nutrients are nitrogen and phosphorus (see [12], [134] or [135]).

NITROGEN

Nitrogen is an important building block of many molecules essential for plant development. Most notably, it is contained in all amino acids (the building blocks of proteins, and therefore enzymes), as well as in nucleic acids (encoding genetic information) and in chlorophyll (which is essential for photosynthesis) [14].

Soil nitrogen exists in various forms: soil nitrate, soil ammonium, and as part of live or dead roots, organic matter and litter. Transitions between these compartments were modelled in [117].

We will model nitrate uptake in Chapters 6 and 7. The most important parameter values for nitrate uptake (derived from experiments) are summarised in Table 6.2.

PHOSPHORUS

Plants cannot grow without phosphorus either, as it is an important building block of adenosine triphosphate (ATP; which is used in many biochemical reactions that require energy), phospholipids (which are crucial component of cell membranes), and nucleic acids (see above). Roots uptake phosphorus dissolved in the soil solution, mainly in the form of phosphate ions (HPO_4^{2-} and $H_2PO_4^-$) [14].

In Chapter 5, we will model uptake of a nutrient by root hairs, and the approach there is applicable (amongst other nutrients) to phosphate (for a more-detailed discussion on the applicability, see Section 1.4.4). Due to its importance (from the discussed perspective of growth limitation), we will use parameter values for phosphate. These values (obtained from experiments for different plant species) are summarised in Table 1.1.

1.2.4 *Root-soil interactions. Rhizosphere*

Having discussed the ways soil properties affect growth and proliferation of roots, it is important to mention that roots impact on the soil in which they grow. According to [29], a rhizosphere is an immediate vicinity of a root that is affected by root processes.

Studying legumes (plants in the family Fabaceae, e.g. peas, beans, lupins, etc.)in 1904, Lorenz Hiltner deduced the existence of interacting processes occurring at the root–soil interface [57]. A volume of soil existed that was shared by roots and soil bacteria.

Release of organic and inorganic compounds from roots into the rhizosphere is called rhizodeposition [148] (other definitions of rhizodeposition can be found in [136]). These compounds include (among others) sloughed root cells, root exudates (substances released from intact cells, such as citrate and protons [61]) and root mucilage (gelatinous material containing polysaccharide exuded from the outer layers of the root cap [146]) [32]. Phospholipid surfactants (lecithin) in the root mucilage affect the properties of rhizosphere. Lecithin can be exuded into the rhizosphere, lowering the adsorption of phosphate to soil particles which makes phosphate more available to the root [39]. Moreover, experimental studies have shown that the hydraulic properties of the rhizosphere are different from those of the bulk soil [18], and the main reason for that seems to be the excretion of mucilage by plant roots [94].

Root development and growth, respiration (production of carbon dioxide), rhizodeposition, water and nutrient uptake result in biochemical and physical changes in soils over different distances from the root surface. Thus the rhizosphere has various dimensions depending on which process is being considered [57].

Many authors emphasise the huge importance of mycorrhizas (fungi that live in symbiosis with roots [143]) on the uptake of nutrients. For readers interested in modelling of these mutualistic associations as well as associations with other rhizosphere microorganisms (bacteria), we recommend articles, such as

[62], [124], [137], [61] and [78]. We will not model these interactions in this thesis.

1.3 MODELLING

Mathematical models can be used to describe a huge variety of physical, chemical, engineering or biological processes. One can model root system growth and development with a specified set of (stochastic or deterministic) rules describing these. More importantly, we can use differential equations to describe many different processes in the root-soil environment. Differential equations can be ordinary, partial, delayed, stochastic etc. Often, one needs to couple differential equations together in different ways. In this thesis, we will mostly make use of partial differential equations describing nutrient flows and plant uptake.

Due to recent advances in numerical computations, it has now become possible to model some root-soil processes using an explicit root system geometry embedded in a soil dynamics simulation (see Section 1.5). However, these simulations become much more challenging as we add additional processes, or as we make a numerical mesh finer (in an attempt to decrease the simulation errors). Moreover, as the number of simulated processes or the complexity of the root system increases, it may become more difficult to interpret results clearly. In many cases, simulations using simpler geometries are computationally cheaper, and understanding of the underlying mechanisms is much easier to gain. Therefore, whenever possible, we will choose this modelling approach. In general, the choice of the modelling framework should always be motivated by specific biological questions one wishes to answer.

1.3.1 *Simple root-like geometries*

Early papers by Philip [106] and Gardner [52] describe a root as a cylindrical, isolated structure, which appears to be the simplest model [103]. This approach, although seemingly simplistic, allows modifications (e.g. adding root

branches), and thus it gives rise to many of the models in use.
Often, one wishes to model branching structures. Many software tools have now been developed to model the growth and development of such structures (as well as the interactions with their environment) (see Section 1.5).
A very important framework (for the purposes of this thesis) for modelling nutrient uptake by root hairs was first introduced in [112] and [80]. Root hairs are distributed periodically and orthogonal to the root surface which is flattened out [112]. Figure 1.3 presents the arrangement of root hairs as modelled in [80]. This geometry will be our starting point in Chapters 3 and 4.

1.3.2 *Modelling growth and development of root systems*

Roots grow axially as well as radially [62]. Apart from the growth of individual roots, a root system develops via branching - the emergence of lateral roots as described in Section 1.2.1. In order to model this process, one at least needs to have (plant-specific) information on number of seminal roots, maximum root order, branching density (number of lateral roots per unit root length of the root they emerge from; this would usually depend on the root order), branching angles, and growth rates of roots of different orders (this is, again, dependent on the root order). This information can either be given as a set of deterministic [119], or stochastic rules [69]. Moreover, one can either take into account the geometry of each individual root explicitly, or model the growth and development of the root system using a continuum approach, in which the root system is represented using certain distributions (e.g. root density distribution; see [41]).

Explicit root architecture modelling

In an attempt to model root architecture explicitly, many software tools have been developed in recent decades. We will discuss these in Section 1.5.

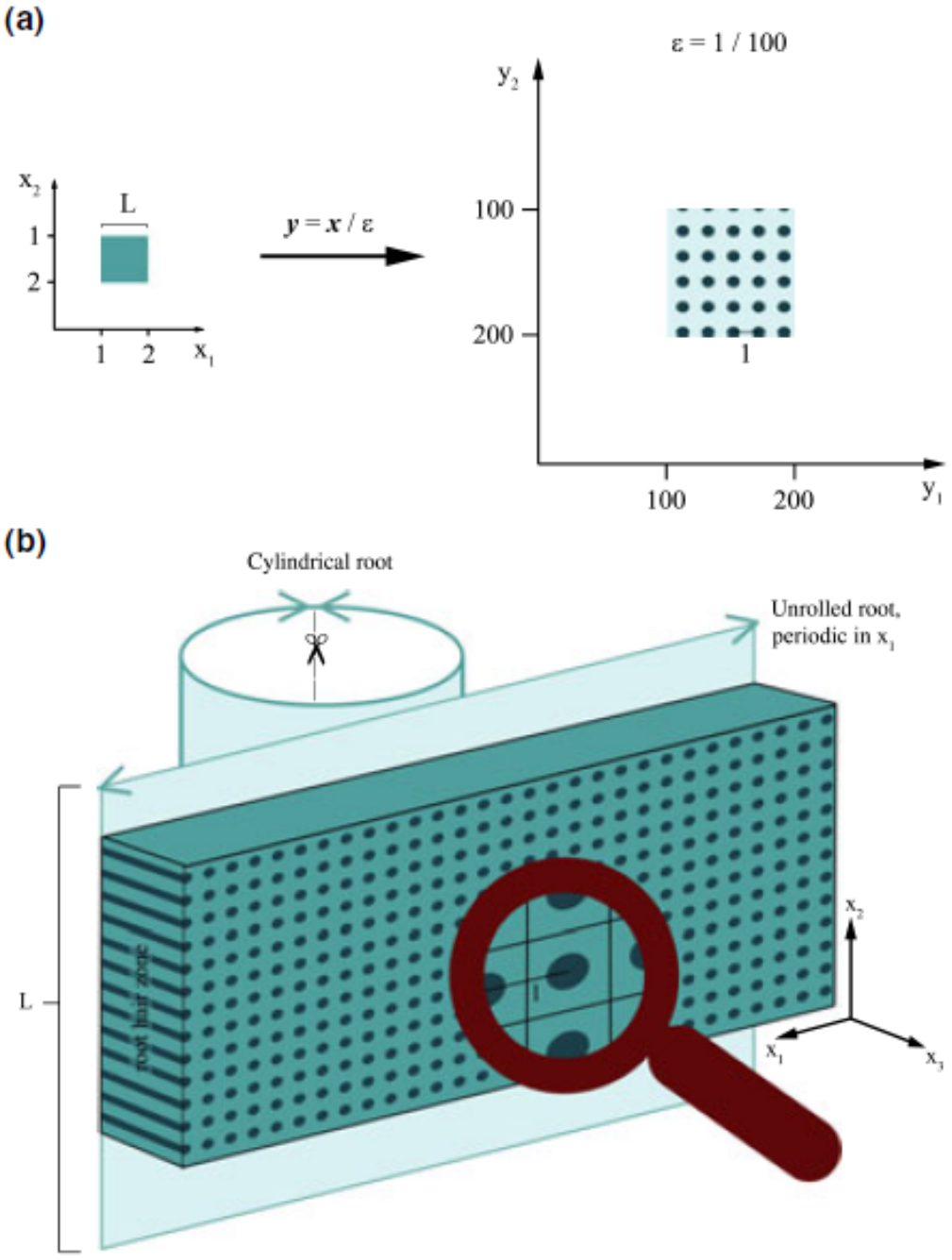


Figure 1.3.: Root hair geometry, taken from [80]. In (a) we see various scales used in the method of homogenisation (see Section 1.4.4) - the microscopic scale given by the inter-hair distance and the macroscopic scale given by the length of the root segment under consideration. Figure (b) shows a rolled-out root surface and root hairs orthogonal to it.

Density-based models

In [41], the authors studied how the dynamics of root system growth depend on individual root developmental parameters (e.g. rates of lateral root elongation) using root density distributions, namely root length density, root branching density and root meristem (tissue of undifferentiated cells, where root growth occurs) density. The simulations suggested that the root system growth occurs in travelling wave patterns of meristems [41].

ROOT-SHOOT INTERACTIONS

As discussed in Section 1.2.3, apart from root uptake, a plant also acquires nutrients essential for its survival from the air (carbon, hydrogen, oxygen). Both types of nutrients (i.e. those acquired from the soil as well as those acquired from the air) are then redistributed throughout the whole plant according to the plant's needs. Absence of any of these nutrients often has severe consequences for one or more plant functions. Therefore, in recent years, many authors tried to couple the below-ground and the above-ground models. For a recent review of the most relevant models, we recommend [40].

NEGLECTING GROWTH

When modelling nutrient uptake by a young (small, fast-growing) root system over longer time scales (weeks or months), the root system growth is significant and needs to be taken into account. However, for the later stages of plant development when the root growth has nearly ceased and the root system is well-established (for instance, according to [3], the root growth slows down significantly in the last two months of a wheat life cycle), the growth can often be disregarded. The same applies when modelling over short timescales (e.g. a few hours), simply because the root growth over these timescales can be considered negligible (even for non-mature plants).

All modelling in this thesis will be concerned with static (non-growing) roots and root systems.

1.3.3 *Soil water and nutrient dynamics*

Conservation laws and continuity equations

Conservation laws are used for modelling many situations where some quantity is conserved. Suppose we have a certain amount of some substance (water, nutrient, or anything else) which moves in space. We denote $c(t, x, y, z)$ to be the distribution of the substance, and $\mathcal{J}(t, x, y, z)$ to be the flux of this substance at time t and at a spatial point with coordinates (x, y, z). Assuming no substance is created or destroyed, i.e. the total amount (more generally it can be any quantity we are interested in - e.g. mass) of the substance remains constant, we can express the conservation law mathematically as:

$$\frac{\partial c}{\partial t} + \nabla \cdot \mathcal{J} = 0, \tag{1}$$

which is often referred to as the equation of continuity. In this thesis, we will mostly be interested in diffusive and advective fluxes.

DIFFUSIVE FLUX Diffusion is the net movement of a substance from places of higher to places of lower concentration. Fick's first law of diffusion states that the net flux of a substance ($\mathcal{J}_d$) is proportional to the gradient of the substance concentration (∇c), and the constant of proportionality (D) is called a diffusion coefficient (or diffusivity) [24]. This can be mathematically expressed as:

$$\mathcal{J}_d = -D\nabla c, \tag{2}$$

where the minus suggests that the net flux is from regions of higher concentration to those of lower concentration (we always take D to be positive). Substituting Fick's first law (2) into the continuity equation (1), we get the diffusion equation:

$$\frac{\partial c}{\partial t} = \nabla \cdot \{D\nabla c\}. \tag{3}$$

Note that this equation can also be derived using a random walk model describing Brownian motion (see [42]).

In the simplest case, D is a constant, and this gives:

$$\frac{\partial c}{\partial t} = D\nabla^2 c,$$

which is sometimes referred to as the heat equation [45]. However, if the medium is inhomogeneous, then D can be taken to be a (scalar) function of spatial variables $D(x, y, z)$. Moreover, if D depends on concentration c, we get a nonlinear diffusion equation (e.g. soil water dynamics, where diffusivity is dependent on local water content; see 1.3.3). Finally, when modelling an anisotropic medium (i.e. diffusion is different in different directions), D is taken to be a symmetric, positive-definite, $n \times n$ matrix (in n dimensions).

ADVECTIVE FLUX Sometimes, a substance is carried along with a bulk motion. This is called advection. For instance, a nutrient dissolved in the soil solution is advected by the mass flow. Advective flux is often written as $\mathcal{J}_c = c\mathcal{V}$, where $\mathcal{J}_c$ is the advective flux, c is the concentration of (movable) nutrient and $\mathcal{V}$ is the velocity field of the carrying substance. Substituting in the continuity equation (1) gives:

$$\frac{\partial c}{\partial t} = -\nabla \cdot \{c\mathcal{V}\}. \tag{4}$$

Advection-diffusion equation: soil water dynamics

In this section, we will be guided by soil water theory, as introduced in [136] and [114].

The continuity equation for volumetric water content θ states:

$$\frac{\partial \theta}{\partial t} = -\nabla \cdot \mathcal{J} \tag{5}$$

In most cases, water potential in the soil (porous medium) is defined as a sum of matric potential (which occurs due to adhesive forces between water and solid soil surfaces; sometimes also called a capillary pressure head potential) and gravitational potential. The central idea in the theory of soil water flow is that for water to flow, a difference in water potential must exist. Darcy's law states that the rate of water flow is proportional to the gradient in water potential (here denoted by Φ and having the units of cm (head of water); for a discussion on other units used in water potential theory and conversions

between these, see [136]), and this proportionality factor is called hydraulic conductivity. Mathematically, this can be expressed as:

$$\mathcal{J} = -k\nabla\Phi = -k\big(\nabla h - \nabla x_3\big),$$

where $\mathcal{J}$ is called the volumetric Darcy flux (cm s^{-1}), k is the hydraulic conductivity (cm s^{-1}), h is the capillary pressure head (cm head of water) and x_3 is the vertical coordinate (positive downward) [114]. Note, that in its structure, Darcy's law is very similar to Fick's law of diffusion as well as to Fourier's law of thermal conduction [136]. In all these, the spatial flux of some substance (or heat) is proportional to the concentration (or temperature) gradient[1].
The velocity of water $\boldsymbol{V}$ is obtained using the formula $\boldsymbol{V} = \frac{\mathcal{J}}{\theta}$.
In saturated flow, the prevailing potential is the gravitational potential. A problem with Darcy's law is that the saturated state is rarely achieved. As the soil drains (water content decreases), hydraulic conductivity decreases, and we write:

$$\mathcal{J} = k(\theta)\big(-\nabla h + \nabla x_3\big).$$

Amongst the $k(\theta)$ relationships most frequently used in the modelling literature are the so-called van Genuchten [142] and Brooks-Corey functions [15]. We will discuss these in more detail in Chapter 2 (see Section 2.6), and we also refer interested readers to a good overview contained in [114].
In the theory of unsaturated water flow, it is further assumed that as the soil drains, the water remaining in pores is more tightly held in these pores. Therefore, the matric potential of water in the soil h can be considered to be an increasing function of the remaining water content θ [2]. As a consequence, we get:

$$\mathcal{J} = k(\theta)\big(-\nabla h(\theta) + \nabla x_3\big),$$

which gives:

$$\mathcal{J}_D = k(\theta)\big(-\frac{dh}{d\theta}\nabla\theta + \nabla x_3\big) = -\hat{D}(h(\theta))\nabla\theta + k(\theta)\nabla x_3, \tag{6}$$

1 For a broader discussion on the experiments leading to the formulation of Darcy's law, see [59]

2 Note, that this is only true if we neglect hysteresis (the fact that one empirically gets slightly different $h(\theta)$ functions for drying and for wetting soils).

where we denoted $\hat{D}(h(\theta)) = k(\theta)\frac{\partial h(\theta)}{\partial \theta}$ to be soil water diffusivity and the subscript $_D$ indicates that we are dealing with the Darcy flux [136].
Finally, we define $D(\theta) = \hat{D}(h(\theta))$ and substitute the flux from Equation (6) into the continuity equation (5) to get:

$$\frac{\partial \theta}{\partial t} = \nabla \cdot \Big(D(\theta)\nabla\theta - k(\theta)\nabla x_3 \Big). \tag{7}$$

This equation is called Richards' equation [118]. As $D(\theta)$ and $k(\theta)$ are often nonlinear functions of θ (see [142], [15]), this is a nonlinear advection-diffusion equation (water is being advected with gravity in this case), which we wish to solve analytically or (more often) numerically for θ.

Advection-diffusion equation: nutrient dynamics

When dealing with the movement of dissolved nutrient in soil, we need to consider two processes taking place - the whole solution is moving with a velocity (which usually has to be calculated in advance using Richards' equation (7)) and the nutrient is diffusing within the solution. This again leads to the advection-diffusion equation (coupled to Richards' equation for water dynamics).
If the equilibration between the adsorption and desorption of a nutrient to soil particles is much faster than the diffusion and uptake processes, one can obtain a quasi-steady-state (QSS) approximation for the governing equations. We now repeat the derivation of this approximation as presented in [122]. Furthermore, we closely follow [99] and [11].
Let us now denote the concentration of nutrient dissolved in water as c and the concentration in solid form as c_s (mass per unit volume of solid phase). The continuity equation from the Nye-Tinker-Barber model [99] goes as follows:

$$\frac{\partial c_s}{\partial t} = d_s \qquad\qquad \frac{\partial}{\partial t}(\theta c) + \nabla \cdot \Big(c\boldsymbol{\mathcal{J}}_D - \theta D \nabla c \Big) = -d_s. \tag{8}$$

The concentration of nutrient in the solid form can change only via the adsorption of some pore water nutrients or via the reverse process (desorption), which explains the d_s term in the first equation. The second equation describes (except for the previously explained $-d_s$ term, which simply ensures

the overall nutrient conservation) an advection-diffusion process for the movable nutrient. D is the diffusion coefficient of nutrient in pore water. As c denotes the concentration of nutrient dissolved in the soil solution, we need to multiply it by the water content θ, so that we get concentration relative to unit soil volume. $\boldsymbol{\mathcal{J}}_D$ is the Darcy flux from Equation (6).

Technically speaking, this is a system of reaction-convection-diffusion equations because of the adsorption and desorption term d_s. However, in this section, we will show how to obtain the QSS approximation. Having done that, these terms will no longer be present, and thereafter we only study the resulting advection-diffusion equation.

To obtain the QSS approximation, one assumes:

$$d_s = k_a c - k_d c_s, \tag{9}$$

where k_a is the constant of adsorption and k_d is the constant of desorption. Substituting (9) into Nye-Tinker-Barber model (8) gives:

$$\frac{\partial c_s}{\partial t} = k_a c - k_d c_s \qquad \frac{\partial}{\partial t}(\theta c) + \nabla \cdot \Big(c\boldsymbol{\mathcal{J}}_D - \theta D \nabla c \Big) = -k_a c + k_d c_s. \tag{10}$$

Assuming k_d is large (more precisely, that $\frac{1}{k_d}$ is small relative to the timescale of diffusion), the QSS assumption for (10) reads $k_a c - k_d c_s = 0$, which implies:

$$c_s = bc, \tag{11}$$

where $b = \frac{k_a}{k_d}$ is the previously mentioned soil buffer power [11].

Adding the two equations from (10), the adsorption-desorption terms cancel out, and using Equation (11), we get:

$$(\theta + b)\frac{\partial c}{\partial t} + c\frac{\partial \theta}{\partial t} = -\nabla c \cdot \boldsymbol{\mathcal{J}}_D - c\nabla \cdot \boldsymbol{\mathcal{J}}_D + \nabla \cdot \big(\theta D \nabla c\big),$$

which using the continuity equation for water (5) yields:

$$(\theta + b)\frac{\partial c}{\partial t} = -\nabla c \cdot \boldsymbol{\mathcal{J}}_D + \nabla \cdot \big(\theta D \nabla c\big). \tag{12}$$

If we assume that θ is independent of the spatial variables (which serves as a good approximation when modelling uptake close to full water saturation, see

[11]) and that the same is true for D (we do not wish to model the effects of heterogeneity in the porous structure of soil in this thesis), we get:

$$(\theta + b)\frac{\partial c}{\partial t} + \nabla c \cdot \boldsymbol{\mathcal{J}}_D = \theta D \nabla^2 c. \tag{13}$$

Thus, we have obtained the promised advection-diffusion equation.
Now, following [122], we study convection and diffusion of a nutrient close to a single cylindrical root of radius r_0, and introduce the important notion of a Péclet number. Assuming a steady-state condition for water dynamics (i.e. $\frac{\partial \theta}{\partial t} = 0$), we get from the continuity equation (5):

$$\nabla \cdot \boldsymbol{\mathcal{J}}_D = 0,$$

which (using cylindrical coordinates) assuming independence of the azimuthal angle φ and well as of the longitudinal position z gives:

$$\frac{1}{r}\frac{\partial \left(r \mathcal{J}_{D,r}\right)}{\partial r} = 0,$$

where r denotes the radial distance. This gives:

$$\mathcal{J}_{D,r} = \frac{C}{r} \tag{14}$$

for a constant C, which is determined from the boundary condition at the root surface. Here, imposition of $\mathcal{J}_{D,r}(r = r_0) = -\mathcal{V}$ (where $\mathcal{V}$ is the root influx) yields:

$$C = -r_0 \mathcal{V},$$

which after substituting back to Equation (14) gives:

$$\mathcal{J}_{D,r} = -\frac{r_0 \mathcal{V}}{r}. \tag{15}$$

Thus, we can rewrite the continuity equation (13) in cylindrical coordinates as:

$$(\theta + b)\frac{\partial c}{\partial t} - \frac{r_0 \mathcal{V}}{r}\frac{\partial c}{\partial r} = \frac{\theta D}{r}\frac{\partial}{\partial r}(r\frac{\partial c}{\partial r}), \tag{16}$$

which is equivalent to Equation (2.7) from [122].
Nondimensionalising space with respect to the root radius r_0 (taken as the typical length scale for this geometry; for more details see [119]), time with respect to the diffusional time scale for this length scale, and concentration

with respect to any nutrient concentration (e.g. initial nutrient concentration c_{in}), i.e.:

$$r = r_0 R \quad t = \frac{(\theta + b) r_0^2}{\theta D} T \quad c = c_{in} C$$

we get:

$$\frac{\partial C}{\partial T} - Pe \frac{1}{R} \frac{\partial C}{\partial R} = \frac{1}{R} \frac{\partial}{\partial R} \left(R \frac{\partial C}{\partial R} \right),$$

where:

$$Pe = \frac{r_0 \mathcal{V}}{\theta D} \tag{17}$$

is a Péclet number [122]. It is a dimensionless quantity which gives an indication of the relative importance of advection and diffusion.

In [123], the Péclet number is defined as $Pe = \frac{r_0 \mathcal{V}}{D}$. Typical values of $\mathcal{V}$, D and r_0 for soil nutrient modelling give $Pe < 10^{-2}$ [123], [136]. This means that in most of these cases, the Péclet number can be neglected and the advection-diffusion equation reduces to a diffusion equation. The impact of advection is small compared to that of diffusion.

Reaction terms

If the substance is created or destroyed by some mechanism (chemical reaction, adsorption/desorption of nutrient to/from solid surfaces, and many others), we get a general continuity equation:

$$\frac{\partial c}{\partial t} + \nabla \cdot \boldsymbol{\mathcal{J}} = s \tag{18}$$

where $s(t, x, y, z, c)$ is referred to as a reaction term (also called a sink or a source term, depending on its sign). By changing the form of the sink/source function s, one can model a large variety of processes.

One example of a reaction term is the adsorption-desorption term, which we have introduced in the previous section. Other soil processes that can be modelled using reaction terms include release or fixation of solutes by the organic matter transformation as well as degradation of organic solutes by chemical or microbial action [136].

Most importantly for the purposes of this thesis, sink terms can be used to model water or nutrient uptake (usually when considering larger spatial scales). We will discuss these sink terms in more detail in the next section.

1.3.4 *Modelling water and nutrient uptake*

A slightly older review of models of water transport in plant tissue at cellular and subcellular scales can be found in [93].
However, in this thesis, we will only be interested in modelling uptake processes at scales larger than subcellular. The uptake can be represented in two ways - either by a boundary condition applied at an explicitly-modelled root (or hair) surface (via this boundary condition, soil water model can be coupled with a model of water dynamics inside the root system, which often needs to be solved independently) or by adding a sink term to the equation of continuity. Whether we use the former or the latter depends on the scale of the processes under consideration. The first method is generally preferred when dealing with smaller scales (prescribed flux at the root-soil interface), while the second is preferable at larger scales (a single plant scale or a field scale) [114].

Water uptake

ROOT SURFACE BOUNDARY CONDITION According to [114], water uptake is supposed to switch (at some critical time) from demand-driven to supply-dependent. As the simplest model neglecting root architecture as well as soil water status, for a sufficiently wetted soil, one usually considers a constant water influx condition:

$$-\{D(\theta)\nabla\theta - k(\theta)\nabla x_3\} \cdot \hat{\boldsymbol{n}} = C_1 \tag{19}$$

applied at the root surfaces [114], where $\hat{\boldsymbol{n}}$ is the unit outward pointing vector normal to the root surface. However, for soils under drought conditions, one would normally impose:

$$\theta = \theta_r, \tag{20}$$

where θ_r is an irreducible (residual) water content (water content below which no uptake occurs; see [15]). For simplicity, it is often assumed that $\theta_r = 0$, and

we will make use of this simplification too.
Furthermore, we introduce a Robin-type boundary condition:

$$-\{D(\theta)\nabla\theta - k(\theta)\nabla x_3\} \cdot \hat{\boldsymbol{n}} = C_2\theta \tag{21}$$

at the root surfaces, which states that the water flux into the root is proportional to local water content. This condition can be thought of as an interpolation between the constant influx condition (for fully-saturated soils) and the condition of residual water content at the root surface (for very dry soils).
More sophisticated models (such as those introduced in [121], [36] and [67]) model water dynamics within the root system alongside the dynamics in the soil, and they assume that the water flux at the root surface is proportional to the difference between the water potential in the soil and that inside the root. As we will not model water dynamics inside the root system explicitly in this thesis (for the sake of simplicity), in the next paragraph, we will only briefly discuss how these small-scale boundary conditions have been scaled up to the root system level.

UPSCALING THE ROOT SURFACE BOUNDARY CONDITION - SINK TERMS

When modelling at the root system or a field scale, one does not have to be concerned with an explicit root system geometry. Instead, one often introduces some averaging considerations. Thus, it is customary to model water uptake with a sink (extraction) function in the Richard's equation (7). The main question is, what kind of extraction function to use.
In [121], the Richards' equation (7) as a soil water model was first combined with a model for water pressure inside a single cylindrical root via a root surface boundary condition. A sink term, representing the water uptake by a root system consisting of seminal and first order lateral roots, was subsequently derived by upscaling this root surface boundary condition, and the resulting equation was solved numerically.
A mathematical model combining locally measured root hydraulic conductance with root system architecture is presented in [35] to give a more-detailed description of water uptake and intra-plant water flow. This framework is

further extended in [36], where this hydraulic architecture model is coupled with the Richards' equation modelling soil water transfer (Equation (7)). Subsequent simulations confirm the occurrence of hydraulic lift (see Section 1.2.3).

The previously mentioned article [93] lists several such functions developed up to the beginning of 1980s. For a more recent review of models at both smaller and larger scales, we recommend [114].

ONE-DIMENSIONAL MODELS

Fully three-dimensional models can be computationally demanding even if we use sink terms to represent water uptake. Therefore, it is often more convenient to model water uptake using (spatially) one-dimensional models. The most obvious choice is to study models dependent on depth x_3 only, as this is the direction of gravity (which strongly affects water dynamics) as well as the direction of gravitropic response (gravitropism denotes the tendency of roots to grow in the direction of gravity; see [54]). Uptake is then modelled using sink terms dependent on some root characteristic, which is a function of x_3 only (most often root length distribution with depth [28]).

Therefore, as discussed in [53], water uptake models are often written as some variation of equation:

$$\frac{\partial \theta}{\partial t} = \frac{\partial}{\partial x_3}\left(\frac{D(\theta)\partial\theta}{\partial x_3}\right) - \frac{\partial k(\theta)}{\partial x_3} - s(t, x_3, \theta, R), \tag{22}$$

which is a one-dimensional Richards' equation (7), enriched with the sink term $-s(t, x_3, \theta, R)$, which models water uptake, and $R(t, x_3)$ represents root length distribution with depth at time t. These sink terms are often unrealistic because they neglect the importance of depth in the uptake process [53]. In accordance with experimental data, it was assumed in [53], that the uptake takes place in a relatively narrow zone, which moves down through the soil at a specified speed (corresponding to the root system growth rate).

A model using sink terms dependent on root length density taking into account energy expenditure on water uptake was examined in [2]. While for wet soils, the patterns of water extraction followed root length densities very closely, these similarities were not present under drought conditions.

In [82], the authors studied two models. In the first model, the root length density decreased linearly with depth while in the second model, this relationship was exponential (which usually yields a better match with experiments). The exponential model was shown to perform better when compared to empirical data.
In [66] a three-dimensional characterisation of a tree root system was added to a three-dimensional architectural representation of a tree crown. To simplify the computations, a model consisting of a one-dimensional soil water flow model and a one-dimensional plant xylem (transport tissue) water flow model (both being porous medium equations) was introduced.
For further information on the one-dimensional water uptake models and their relation to climate models, we recommend reading [46].

Nutrient uptake

MICHAELIS-MENTEN BOUNDARY CONDITION

This model was first proposed by Michaelis and Menten when they studied enzymatic reactions [95]. Enzymes catalyse (i.e. speed up) many chemical reactions. In brief, if a substrate needs to be bound to an enzyme in order to be changed into a product later on, then the maximum overall rate of this chemical reaction is limited by the number of available enzyme molecules. In the case of nutrient uptake, the role of enzymes is played by certain molecules transporting the nutrients from the soil into the roots, called transporters (or porters). Therefore, the Michaelis-Menten condition has been used heavily in nutrient uptake models [21] [116] [5].
Michaelis-Menten formalism models a situation in which uptake is (approximately) a linear function of concentration for low nutrient concentrations and saturates at a finite value as nutrient concentration goes to infinity. Hence the Michaelis-Menten function usually has a form ([98]):

$$\frac{I_{max}c}{K_m + c}. \tag{23}$$

One can readily see the meaning of constants I_{max} and K_m: K_m is the nutrient concentration at which the uptake rate is half of its saturation value and I_{max}

is the saturation value itself.

In [122], which we discussed in Section 1.3.3, this led to the root surface boundary condition:

$$\theta D\frac{\partial c}{\partial r} + \mathcal{V}c = \frac{I_{max}c}{K_m + c} \quad at\ \ r = r_0.$$

In reality, there exists a nonzero level of nutrient concentration below which no uptake occurs [122]. To model this, some authors (e.g. [39]) modify the Michaelis-Menten function as follows:

$$\frac{I_{max}(c - c_{min})}{K_m + (c - c_{min})}, \tag{24}$$

where c_{min} is the minimum nutrient concentration below which no uptake occurs. However, for concentrations below c_{min} this model predicts a small efflux from the root. If we want to ensure that below this concentration the flux is zero (and not negative), impose

$$\frac{H(c - c_{min})I_{max}(c - c_{min})}{K_m + (c - c_{min})},$$

where $H(c)$ is Heaviside function defined as:

$$H(c) = \{^{1}_{0} \quad ^{c\geq 0}_{c<0}.$$

However, the expression (24) is phenomenological, and a more mechanistic model is often preferable. Therefore, one often finds root influx modelled as:

$$\frac{I_{max}(c)}{K_m + c} - E,$$

where E models efflux from the root, which is often empirically observed [80]. It is then not difficult to model any mechanism (potentially) underlying the observed efflux, by choosing the appropriate E term.

The one-dimensional equation (16) (modelling nutrient diffusion and advection with the mass flow) together with the Michaelis-Menten boundary condition at the root surface $r = r_0$, form the so-called Barber-Cushman model for nutrient uptake developed in the early 1980s [11].

HAIRS UPTAKE MODELLING Chapters 3, 4 and 5 of this thesis will be concerned with the modelling of nutrient uptake by root hairs using the method

of homogenisation. Before we introduce this method and show how it can be used in the uptake modelling (see Section 1.4.4), we briefly mention two papers which approach the problem of hair uptake in different ways.

In [65], the authors modified the Barber-Cushman model from the previous section by including a sink term representing the uptake by the hairs. However, this sink term was derived using the assumption of steady-state diffusion towards the root surface, and thus it is not always applicable. Furthermore, this model is not capable of capturing the effects of inter-hair competition on the overall uptake.

In [88], the impact of the root hair length, density and other traits on phosphorus uptake was studied. Here, the effects of the inter-hair competition were included via estimating the radius of the phosphorus depletion zones, and calculating the overlapping volume between the neighbouring root hairs. However, using this approach, we do not gain any information on how the presence of the hairs affects the effective diffusion coefficient of phosphorus (as we do with the method of homogenisation). Furthermore, it is impossible to model the case of heterogeneous phosphorus supply (i.e. gradients of phosphorus concentration along the root axis) using this approach. We will show how the method of homogenisation solves these problems in Chapter 3.

Modelling simultaneous water and nutrient uptake

As discussed in Section 1.2.3 and 1.3.3, when modelling nutrient uptake, one often has to model water dynamics at the same time, because plant takes up nutrient dissolved in the soil solution.

One of the best reviews of mathematical models of water and nutrient uptake (and plant-soil interactions in general) was given in [124]. First, modelling at a single root scale is described. Later on, the way this information should be transferred to the whole-plant and field levels is discussed.

In [38], the interaction between root system growth (carried out using a three-dimensional root architecture growth model called ROOTMAP, see Section 1.5) and water as well as nitrate capture was studied. A regulation mechanism linking the root system growth with plant demand as well as the external

supply of resources was introduced. Experimental data for lupins agreed with the computer simulation very well.
In [120], simultaneous uptake of water and a highly buffered nutrient (e.g. phosphate) by branching structures from partially saturated soil was modelled.

1.3.5 *Non-root boundary conditions*

Boundary conditions vary substantially from one problem to another.
When modelling nutrient uptake at the scale of a single cylindrical root, one often assumes a fixed far-field concentration (i.e. $c(r) \to c_\infty$ as $r \to \infty$) [123]. It is even more customary to impose a zero-flux boundary condition at $r = r_\infty$, which models either soil stored in a pot, or competition for a nutrient with a neighbouring root.
Standard boundary conditions for water dynamics (in the field or laboratory experiments) are discussed in Section 2.2.2.

1.4 SOLUTION METHODS

Equations discussed in the previous section need to be solved using numerical or analytical methods.

1.4.1 *Numerical analysis*

Commonly used numerical methods for solving differential equations include finite difference methods and finite element methods. These methods will also be used in this thesis. While in the finite difference method one approximates all derivatives in the studied equation with the so-called finite difference schemes, in the finite element methods, one completely changes the definition of the solution to the differential equation under consideration. We will introduce both methods in Chapter 2.

1.4.2 *Asymptotic analysis and nondimensionalisation*

When obtaining the exact solution to some equation is non-trivial or even impossible, one can sometimes derive approximate solutions which are only valid for a certain time or spatial range. If a small parameter is present in the problem being studied, one is often interested in finding the limiting behaviour of the solutions of such problems as the small parameter decreases to 0. If this limit is found and the relevant parameter is small enough, one hopes that the limit solution is (in some sense) close to the solution of the problem with this parameter. Asymptotic analysis allows us to determine such approximate solutions for small (or large) time or for certain ranges of the spatial coordinates (e.g. boundary layers). Furthermore, one can often obtain a composite solution, which holds everywhere [60].

The small parameter is usually uncovered in the process of nondimensionalisation, i.e. scaling all the dimensional variables in the equation with some dimensional values. Nondimensionalisation helps us reduce the number of parameters in the equation (which in turn means reduction in computing time when scanning a parameter space or estimating a parameter). It can also lead to a (desirable) change from a differential to an algebraic equation.

As one example, we used nondimensionalisation in Section 1.3.3 when studying models of nutrient dynamics. In this case, as mentioned in [122], the Péclet number is small in most cases, which leads to the reduction from the advection-diffusion equation to the diffusion equation (i.e. mass flow is negligible compared to the diffusion).

As another example, in the same paper, an explicit formula for a single cylindrical root uptake is derived by solving the diffusion equation equipped with the Michaelis-Menten boundary condition asymptotically in a large time limit.

Finally, in [120], nondimensionalisation uncovered two distinct time scales - for a highly-buffered nutrient (see Section 1.3.3), water dynamics settle to a steady state very quickly compared to the slow mobility of the nutrient.

1.4.3 *Multiscale methods*

In order to study processes such as water or nutrient uptake, one must work at different scales, ranging from the microscopic scale of root hairs (or even cellular and subcellular scales), through the mesoscopic scale of a single cylindrical root, to the macroscopic scale of a single plant (or even a field of plants). To derive a reliable model, one must be able to determine how processes at smaller scales affect macroscopic properties. It is often crucial to choose an appropriate representative elementary volume (i.e. the smallest volume of soil one needs to take into account in order to fully capture all the important microscopic root-soil interactions).

This transition between the scales causes much trouble. In [120], it was shown that different mathematical techniques for upscaling nutrient uptake can theoretically lead to 30 per cent differences between the computed uptakes [124]. It is therefore necessary to use and further develop suitable upscaling techniques to make models mathematically rigorous and scientifically useful. Otherwise, wrong conclusions about the overall behaviour could be drawn [124].

In [39], water and nutrient uptake by wheat roots was studied using a two-dimensional (finite element) rhizosphere model, information from which was then upscaled to ROOTMAP (see Section 1.5). Comparison between the wheat and lupin root systems showed that the highly-branched wheat root structure acquired relatively more P in the presence of lecithin (see Section 1.2.4) than the sparsely-branched lupin root system.

Upscaling from the rhizosphere scale to the root system scale was reviewed in [29], taking into account the impact of inter-root competition as well as of heterogeneity at both the rhizosphere and the root system scale.

1.4.4 *Homogenisation*

Brief introduction to homogenisation

Homogenisation is one of the most important upscaling methods used in root-soil modelling. This theory was first introduced in the 1960s, and it was mostly concerned with estimating averaged properties of composite materials, i.e. materials which seem homogeneous at the macroscale but have heterogeneities at smaller scales. These heterogeneities can have periodic, random or some other nature. However, in this thesis we will only consider periodic media.
In homogenisation, the task is to derive effective macroscopic material properties (heat/electrical conductivity, Young's modulus, etc.) taking into account microscale information. Usually, tensors involved in partial differential equations are rapidly oscillating functions which causes numerical problems. Our goal is then to obtain a sensible approximation to the solution by sending ϵ to 0, where ϵ is a small parameter representing the quotient between characteristic microscopic and macroscopic length scales. Homogenisation is concerned with this limit process, and the resulting equations are usually much easier to solve than the full-detail equations [68].
As discussed in [20], a lot of effort has been put into rigorous mathematical justifications for the method of homogenisation. However, in this thesis we will only use the formal method of multiscale asymptotic expansions. This method is discussed in [19]. We will introduce it using our own simple examples in the following section.

Simple examples of homogenisation

In this section, we introduce the method of two-scale asymptotic expansions using a toy problem in the form of a one-dimensional advection-diffusion equation with a highly-oscillatory sink term. This may serve as a (largely simplified) model for nutrient uptake of a hairy root where rapid oscillations are caused by the root hairs.

LINEAR MODEL WITHOUT CONVECTION

Let $t, x_3 \in \mathbb{R}_0^+$ and consider a linear equation:

$$\frac{\partial S}{\partial t} = \begin{cases} \frac{\partial^2 S}{\partial x_3^2} - f(x_3, \frac{x_3}{\epsilon})S & \text{for } 0 < x_3 < 1 \\ \frac{\partial^2 S}{\partial x_3^2} & \text{for } 1 < x_3 < \infty, \end{cases} \tag{25}$$

where $f(x_3, y_3)$ is $1-$periodic in y_3[3] with a boundary condition:

$$S(x_3 = 0) = 1, \tag{26}$$

and continuity conditions at the interface between the two parts of the domain ($x_3 = 1$):

$$[S]_-^+ = [\frac{\partial S}{\partial x_3}]_-^+ = 0, \tag{27}$$

where $[A]_-^+ = \lim_{x_3 \to 1+} A(z) - \lim_{x_3 \to 1-} A(z)$ (in other words, S should be a C^1 function on $(0, \infty)$)[4].

Assuming $\epsilon \ll 1$, $y_3 = \frac{x_3}{\epsilon}$ is considered to be an independent (microscale) variable, and we search for a solution in the form:

$$S(t, x_3; \epsilon) = \begin{cases} S_0(t, x_3, \frac{x_3}{\epsilon}) + \epsilon S_1(t, x_3, \frac{x_3}{\epsilon}) + \\ \epsilon^2 S_2(t, x_3, \frac{x_3}{\epsilon}) + O(\epsilon^3) & \text{for } 0 < x_3 < 1 \\ S(t, x_3) & \text{for } 1 < x_3 < \infty, \end{cases} \tag{28}$$

where we require all $S_i(t, x_3, y_3)$ to be $1-$periodic in y_3. We apply two-scale differential operators:

$$\frac{\partial}{\partial x_3}(S_i) = (\frac{\partial}{\partial x_3} + \frac{1}{\epsilon}\frac{\partial}{\partial y_3})S_i, \tag{29}$$

and

$$\frac{\partial^2}{\partial x_3^2}(S_i) = (\frac{\partial^2}{\partial x_3^2} + \frac{2}{\epsilon}\frac{\partial^2}{\partial y_3 \partial x_3} + \frac{1}{\epsilon^2}\frac{\partial^2}{\partial y_3^2})(S_i). \tag{30}$$

3 This can serve as a simple model of uptake by a structure that is periodic with the period equal to ϵ.

4 This setting can be used as a very simplified model of nutrient uptake by a single cylindrical root (with $x_3 = 0$ corresponding to the base of the root and $x_3 = 1$ corresponding to the tip of the root) covered with root hairs. Microscopic variation in the sink term (i.e. the dependence of f on y_3) then reflects the presence of root hairs.

Therefore, Equation (25) becomes:

$$\begin{cases} \frac{\partial(S_0+O(\epsilon))}{\partial t} = [\frac{\partial^2}{\partial x_3^2} + \frac{2}{\epsilon}\frac{\partial^2}{\partial x_3 \partial y_3} + \frac{1}{\epsilon^2}\frac{\partial^2}{\partial y_3^2}][S_0 + \epsilon S_1 + \\ \epsilon^2 S_2 + O(\epsilon^3)] - f(x_3, y_3)[S_0 + O(\epsilon)] & \text{for } 0 < x_3 < 1 \\ \frac{\partial S}{\partial t} = \frac{\partial^2 S}{\partial x_3^2} & \text{for } 1 < x_3 < \infty \end{cases} \tag{31}$$

The boundary condition (26) becomes:

$$S_0(t, 0, y_3) + O(\epsilon) = 1, \tag{32}$$

and the interface condition (27) reads:

$$\begin{gathered} S(t, 1+) - S_0(t, 1-, y_3) - O(\epsilon) = 0 = \\ \frac{\partial S(t, 1+)}{\partial x_3} - [\frac{\partial}{\partial x_3} + \frac{1}{\epsilon}\frac{\partial}{\partial y_3}][S_0(t, 1-, y_3) + \epsilon S_1(t, 1-, y_3) + O(\epsilon^2)]. \end{gathered} \tag{33}$$

The leading order inside the two-scale region in Equation (31) gives (using the periodicity of S_0 in y_3) $S_0 = S_0(t, x_3)$[5].

Solving (31) at order $O(\epsilon^{-1})$ gives (using periodicity of S_1 in y_3) $S_1 = S_1(t, x_3)$.

At order $O(1)$ in Equation (31), we get:

$$\begin{cases} \frac{\partial S_0}{\partial t} = \frac{\partial^2 S_0}{\partial x_3^2} + \frac{\partial^2 S_2}{\partial y_3^2} - f(x_3, y_3) S_0 & \text{for } 0 < x_3 < 1 \\ \frac{\partial S}{\partial t} = \frac{\partial^2 S}{\partial x_3^2} & \text{for } 1 < x_3 < \infty. \end{cases} \tag{34}$$

Integrating Equation (34) with respect to y_3, and using the periodicity condition yields:

$$\begin{cases} \frac{\partial S_0}{\partial t} = \frac{\partial^2 S_0}{\partial x_3^2} - S_0 \int_0^1 f(x_3, y_3) dy_3 & \text{for } 0 < x_3 < 1 \\ \frac{\partial S}{\partial t} = \frac{\partial^2 S}{\partial x_3^2} & \text{for } 1 < x_3 < \infty, \end{cases} \tag{35}$$

which is the effective macroscale equation that we searched for. This homogenised equation is equipped with the following macroscopic boundary condition (derived from $O(1)$ in Equation (32)):

$$S_0(t, 0) = 1, \tag{36}$$

and the following interface conditions (derived from $O(1)$ in Equation (33)):

$$S(t, 1+) - S_0(t, 1-) = 0 = \frac{\partial S(t, 1+)}{\partial x_3} - \frac{\partial S_0(t, 1-)}{\partial x_3}. \tag{37}$$

5 This is because we get $\frac{\partial^2 S_0}{\partial y_3^2} = 0$, which yields $S_0(t, x_3, y_3) = S_0(t, x_3) + B(t, x_3) y_3$, and the periodicity condition gives $B(t, x_3) = 0$.

NONLINEAR ADVECTION-DIFFUSION IN ONE DIMENSION

Let us consider a general nonlinear model with advection now:

$$\frac{\partial S}{\partial t} = \begin{cases} \frac{\partial}{\partial x_3}\left[\lambda_2(S)\frac{\partial S}{\partial x_3} - \lambda_1(S)\right] - f(x_3, \frac{x_3}{\epsilon})S & \text{for } 0 < x_3 < 1 \\ \frac{\partial}{\partial x_3}\left[\lambda_2(S)\frac{\partial S}{\partial x_3} - \lambda_1(S)\right] & \text{for } 1 < x_3 < \infty, \end{cases} \tag{38}$$

where $\lambda_1(S)$ and $\lambda_2(S)$ are nonlinear functions of S. We need to write the asymptotic expansions of $\lambda_1(S(t, x_3, \epsilon))$ and $\lambda_2(S(t, x_3, \epsilon))$ in ϵ. Using Taylor expansions gives:

$$\lambda_1(S(\epsilon)) = (\lambda_1 \circ S)(0) + \epsilon(\lambda_1 \circ S)'(0) + \epsilon^2 \frac{(\lambda_1 \circ S)''(0)}{2} + O(\epsilon^3),$$

where the prime denotes differentiation with respect to ϵ. Searching for S in the form of ansatz (28), we have:

$$(\lambda_1 \circ S)'(0) = [\lambda_1'(S(\epsilon))S'(\epsilon)]|_{\epsilon=0} = \lambda_1'(S_0)S_1$$

$$(\lambda_1 \circ S)''(0) = [\lambda_1''(S(\epsilon))(S'(\epsilon))^2 + \lambda_1'(S(\epsilon))S''(\epsilon)]|_{\epsilon=0} =$$

$$\lambda_1''(S_0)S_1^2 + \lambda_1'(S_0)2S_2.$$

Therefore:

$$\lambda_1(S) = \lambda_1(S_0) + \epsilon\lambda_1'(S_0)S_1 + \frac{\epsilon^2}{2}(\lambda_1''(S_0)S_1^2 + \lambda_1'(S_0)2S_2) + O(\epsilon^3),$$

and an analogous formula applies to λ_2. Substituting these expansions into the continuity equation (38) yields:

$$\begin{cases} \frac{\partial(S_0+O(\epsilon))}{\partial t} = (\frac{\partial}{\partial x_3} + \frac{1}{\epsilon}\frac{\partial}{\partial y_3})\Big\{\big[\lambda_2(S_0) + \epsilon\lambda_2'(S_0)S_1 + \\ \frac{\epsilon^2}{2}\big(\lambda_2''(S_0)S_1^2 + \lambda_2'(S_0)2S_2\big) + O(\epsilon^3)\big]\big[\frac{\partial}{\partial x_3} + \\ \frac{1}{\epsilon}\frac{\partial}{\partial y_3}\big]\big[S_0 + \epsilon S_1 + \epsilon^2 S_2 + O(\epsilon^3)\big] - \big[\lambda_1(S_0) + \\ \epsilon\lambda_1'(S_0)S_1 + O(\epsilon^2)\big]\Big\} - f(x_3, y_3)\big[S_0 + O(\epsilon)\big] & \text{for } 0 < x_3 < 1 \\ \frac{\partial S}{\partial t} = \frac{\partial}{\partial x_3}\big[\lambda_2(S)\frac{\partial S}{\partial x_3} - \lambda_1(S)\big] & \text{for } 1 < x_3 < \infty. \end{cases} \tag{39}$$

At $O(\epsilon^{-2})$, we get $0 = \frac{\partial}{\partial y_3}(\lambda_2(S_0)\frac{\partial S_0}{\partial y_3})$, which for everywhere positive λ_2 gives (using the periodicity conditions) $S_0 = S_0(t, x_3)$[6].

6 This can be shown using Kirchhoff transform method, see Section 3.5

At $O(\epsilon^{-1})$, we get $0 = \frac{\partial}{\partial y_3}(\lambda_2(S_0)\frac{\partial S_1}{\partial y_3})$, which again gives $S_1 = S_1(t, x_3)$. At $O(1)$, we get:

$$\begin{cases} \frac{\partial S_0}{\partial t} = \frac{\partial}{\partial x_3}[\lambda_2(S_0)\frac{\partial S_0}{\partial x_3} - \lambda_1(S_0)] + \\ \frac{\partial}{\partial y_3}[\lambda_2(S_0)\frac{\partial S_2}{\partial y_3}] - f(x_3, y_3)S_0 & \text{for } 0 < x_3 < 1 \\ \frac{\partial S}{\partial t} = \frac{\partial}{\partial x_3}[\lambda_2(S)\frac{\partial S}{\partial x_3} - \lambda_1(S)] & \text{for } 1 < x_3 < \infty, \end{cases} \tag{40}$$

which after integration with respect to y_3 yields an effective equation:

$$\begin{cases} \frac{\partial S_0}{\partial t} = \frac{\partial}{\partial x_3}[\lambda_2(S_0)\frac{\partial S_0}{\partial x_3} - \lambda_1(S_0)] - S_0 \int_0^1 f(x_3, y_3)dy_3 & \text{for } 0 < x_3 < 1 \\ \frac{\partial S}{\partial t} = \frac{\partial}{\partial x_3}[\lambda_2(S)\frac{\partial S}{\partial x_3} - \lambda_1(S)] & \text{for } 1 < x_3 < \infty. \end{cases} \tag{41}$$

Homogenisation and nutrient uptake by root hairs

To our knowledge, homogenisation was first used for modelling nutrient uptake by a single cylindrical root periodically covered with root hairs in [80]. The root surface with hairs was rolled out to give a structure periodic in two dimensions (see Figure 1.3 in Section 1.3.1)[7]. Denoting l to be the inter-hair distance and L to be the root length, we set $\epsilon = \frac{l}{L}$ as the small parameter. The Michaelis-Menten boundary condition with an efflux term (see Section 1.3.4) was used at all the root surfaces (including the root hairs). Two-scale analysis is performed and three different models depending on the relative importance of the uptake and the diffusion processes are obtained. In the first case, the uptake is negligibly small compared to the diffusion and thus, no change is observed at the leading order in the effective equation. In the critical case, in which the uptake and the diffusion are comparable in strength, one can replace an explicit root hair geometry with a sink term in the continuity equation via homogenisation. In the last case, the uptake is much faster than the diffusion, and one can replace the root hairs with an enlarged root radius.

JUSTIFICATION OF HOMOGENISATION APPROACH IN HAIR UPTAKE MODELS

7 Note that a similar problem was rigorously studied in [112].

In chapters 3, 4 and 5 of this thesis, we will model uptake of a diffusing nutrient by root hairs using the method of homogenisation. It therefore seems worthwhile to look at nondimensional groupings of parameters that are assumed to be $O(1)$ in the homogenisation approach, and see how close to (or far from) $O(1)$ these really are.

Following [80], we consider diffusion of a nutrient described in dimensional variables as:

$$\frac{\partial c}{\partial t} = \nabla \cdot \{D \nabla c\},$$

and uptake of this nutrient at the (cylindrical) hair surfaces described by a Michaelis-Menten boundary condition with efflux:

$$-D \nabla c \cdot \hat{\boldsymbol{n}} = \frac{F_h c}{K_h + c} - E_h.$$

Following Supporting Information to [80], we nondimensionalise space with respect to the length of the root on which the hairs grow (L), time with respect to the corresponding timescale of diffusion ($\frac{L^2}{D}$), and concentration with respect to the Michaelis constant (K_h), i.e.:

$$\boldsymbol{x} = L\boldsymbol{X} \qquad t = \frac{L^2}{D} T \qquad c = K_h C.$$

This yields a dimensionless continuity equation:

$$\frac{\partial C}{\partial T} = \nabla^2 C$$

and a dimensionless hair boundary condition:

$$-\nabla C \cdot \hat{\boldsymbol{n}} = \frac{F_h L}{K_h D} \frac{C}{1 + C} - \frac{E_h L}{K_h D} = \alpha \frac{C}{1 + C} - \beta, \tag{42}$$

where we have defined $\alpha = \frac{F_h L}{K_h D}$ and $\beta = \frac{E_h L}{K_h D}$. In Chapters 3 and 5, we will assume that $\alpha = O(\epsilon)$ and $\beta = O(\epsilon)$, so that the leading order equation will contain contributions from all processes involved (the diffusion as well as the uptake; see Equation (132) for instance). Using Table 1.1 and the following values from [80]: $D = 10^{-5}$ cm^2 s^{-1} (standard value for diffusion of small molecules in water; see [97]), $L = 1$ cm and $l = 0.01$ cm (this value seems to be a good approximation for most of the species included in [80]), we see that α tends to be $O(10^1)$ or $O(10^2)$, with arabidopsis, ryegrass, russian thistle and wheat being close to $O(10^1)$.

Plant	$F_h(\mu\text{mol cm}^{-2}\text{ s}^{-1})$	$K_h(\text{mM})$	$E_h(\mu\text{mol cm}^{-2}\text{ s}^{-1})$
Arabidopsis	5.03×10^{-7}	3.92×10^{-3}	2.08×10^{-8}
Barley	$15 - 29.7 \times 10^{-7}$	$2.9 - 4.7 \times 10^{-3}$	$0.58 - 0.71 \times 10^{-8}$
Bean	2.76×10^{-7}	0.4×10^{-3}	6.9×10^{-8}
Carrot	12.7×10^{-7}	3.1×10^{-3}	5.8×10^{-8}
Lettuce	10.6×10^{-7}	2×10^{-3}	11.35×10^{-8}
Onion	2.68×10^{-7}	0.4×10^{-3}	6.7×10^{-8}
Rape	4.26×10^{-7}	0.4×10^{-3}	10.65×10^{-8}
Ryegrass	1.54×10^{-7}	1.3×10^{-3}	1.18×10^{-8}
Russian Thistle	3.9×10^{-7}	2.7×10^{-3}	3.42×10^{-8}
Spinach	4.10×10^{-7}	0.4×10^{-3}	10.25×10^{-8}
Tomato	9×10^{-7}	0.4×10^{-3}	22.5×10^{-8}
Wheat	2.21×10^{-7}	2.3×10^{-3}	0.96×10^{-8}

Table 1.1.: The Michaelis-Menten and efflux parameters for phosphate uptake by mildly phosphate starved plants; reproduced from [80].

This is rather far from $O(\epsilon) = O(10^{-2})$ assumed in Chapters 3 and 5. However, considering other nutrients, we see that for a maize plant, the quotient $\frac{F_h}{K_h}$ is of order 10^{-5} cm s^{-1} for sulphur and magnesium, and of order 10^{-7} cm s^{-1} for calcium (see [119]). This yields $\alpha = O(1)$ for sulphur and magnesium, and $\alpha = O(10^{-2})$ for calcium, which is already of the order assumed in Chapters 3 and 5. Finally, by choosing $c(t = 0) = c_{in}$ to be significantly smaller than K_h (e.g. $c_{in} = 0.1 \times K_h$), we get that $C(T = 0) = 0.1$ and (assuming $\frac{F_h c_{in}}{K_h + c_{in}} > E_h$) that $C < 0.1$ for any $T > 0$. This then gives $\frac{C}{1+C} < 0.1$ for any $T > 0$, which reduces the strength of the Michaelis-Menten (uptake) term by another order. Using the values from Table 1.1, we further see that β tends to be $O(10^{-1})$, $O(10^{0})$ or $O(10^{1})$, with arabidopsis, barley and wheat being the closest to $O(10^{-1})$. This is reasonably close to the $O(10^{-2})$ value used in Chapters 3 and 5. These values suggest that our analysis should give a reasonable approximation for some plants and nutrients, and may be more widely applicable.

MODIFICATIONS OF THE MODEL FROM [80]

If one wants to model nutrient sorption to soil particles, the assumption of homogeneous soil may not be valid at such small scales [152]. For these reasons, in [113], homogenisation was used to derive a dual porosity (soil is composed of micro-aggregates which are porous collections of soil particles) model of solute sorption and diffusion. Comparison was made with a single porosity model, which was shown to exhibit significant errors [113].

A typical inter-hair distance is roughly the same size as a typical soil micro-aggregates. Therefore, in [152], the dual porosity approach for nutrient diffusion and sorption from [113] was combined with the root hair uptake model from [80] to produce a more realistic model (especially for highly-sorbed nutrients - see Section 1.2.3).

However, in both [80] and [152], the root surface was considered to be flattened out from the very beginning and cartesian geometry was used instead of the cylindrical one. This, as the authors themselves mention, is justified as long as the average distance between the root hairs along the root surface ($\frac{2\pi r_0}{n}$ where r_0 is the root radius, and n is the number of root hairs in a root cross-section) is

comparable to the distance between the root hair tips ($\frac{2\pi(r_0+L_h)}{n}$ where L_h is the root hair length). Dividing these two expression we get $\frac{r_0+L_h}{r_0}$. We found the following values for winter Kraka wheat: $r_0 \approx 0.085\,\text{mm}$ and $L_h \approx 1.27\,\text{mm}$ [51], which suggests that the quotient can be as large as 16. In other words, the root hair length can play a very important role and therefore we conclude that it is not always justifiable to flatten the root surface out. We will study this problem in Chapter 5.

OTHER APPROACHES

It is important to note that the geometry of a root covered with root hairs is not exactly periodic (see Figure 1.2). As a consequence, one might want to approach the problem of hair uptake modelling using different methods (such as volume averaging or stochastic homogenisation), and study how the resulting effective equation deviates from the periodic homogenisation result.

In the method of volume averaging, one directly integrates the given partial differential equation over the so-called representative volume element (RVE), which is a small part of the domain that captures the material properties of the entire domain sufficiently [147]. Writing the solution as a sum of a value averaged over a RVE and a local perturbation, one then uses theorems allowing the averaging and differential operators to be interchanged, and uses additional assumptions to obtain a relationship between the perturbation and the averaged term, which finally yields a closed form macroscopic problem (for more details, see [31] or [84]). However (as also discussed in [31]), the volume averaging yields the same effective equation as periodic homogenisation for a linear diffusion equation, and this generally extends to other settings.

Alternatively, stochastic homogenisation assumes prescribed random fields for the domain, and determines effective equations as a function of these (see [126] or [125]). However, it is not clear what spatial probability distribution of root hairs one might expect in our case. Furthermore, as shown in [16], stochastic homogenisation results are often in good agreement with the periodic homogenisation approaches when studying diffusion in porous media with small volume fraction of obstacles.

Let us also note that as discussed in [30] (see Fig. 2), the geometric arrangements of root hairs on root surfaces fall into three categories. While for plants belonging to the first category, any outer layer cell can become either a hair or a non-hair cell, for plants belonging to the remaining two categories, the arrangement of root hairs is much more regular, and exhibits varying levels of periodicity along the root length (type 1 pattern) or around the circumference of the root (type 2 pattern) [30]. This observation further supports the periodic homogenisation approach (even though the actual path that a particular root hair takes when growing into the surrounding soil depends on its interactions with soil particles and other soil constituents [72]).

To summarise, even though periodic homogenisation presents the greatest simplification of the geometry from all these methods, it offers us a more systematic framework than the volume averaging [31], it is more intuitive than stochastic homogenisation, and normally gives the same effective equations as these two methods. Therefore, and also for the sake of brevity, we will only use periodic homogenisation in this thesis.

1.5 AVAILABLE SOFTWARE TOOLS

Due to the high complexity of root systems as well as that of root-soil interactions, many software tools have been developed in recent decades to model root system growth and its interactions with the environment explicitly.

ROOTMAP - a computer model simulating the growth of fibrous root systems and incorporating features such as growing time, growth rates and branching properties of the root system - was introduced in [33]. Locations of branches and root tips are recorded and the root system develops in discrete time.

Other commonly used software tools include RootTyp [101], RootBox [81] and SimRoot [86]. We focus on the one we will use in the last chapter of this thesis, i.e. SimRoot.

1.5.1 *SimRoot*

In [86], the SimRoot model is introduced. The root system is represented in the form of a graph - a set of nodes connected by edges. SimRoot was novel in introducing spatial heterogeneity of processes such as water and nutrient uptake or respiration into the model, which can vary along the roots as well as among different roots [86]. SimRoot was used to estimate fractal properties (see Section 1.2.1) of simulated root systems in [86], and to study soil exploration by roots using fractal analysis methods in [144].
Apart from simulating root system growth and development, SimRoot has been coupled with an $SWMS-3D$ code, which models water (Richards' equation with a sink term) and nutrient (reaction-advection-diffusion equation) dynamics in soil [129] (for a model coupling the soil model $SWMS-3D$ with a computer model of flows within the root network, see $R-SWMS$ [67]). Therefore, SimRoot is now capable of simulating water and nutrient (nitrate, phosphate and other) uptake by a growing root system.

1.6 THESIS PLAN

In Chapter 2, we provide various accuracy checks for numerical solutions of water uptake by simple root-like structures. These checks are desirable, because simulations using similar geometries will be used in Chapters 3, 4 and 5. Soil water dynamics is modelled using Richards' equation (7), and we use various boundary conditions at the root surfaces (including the Robin-type boundary condition; see Section 1.3.4). Later on in this chapter, we show that even though these models are simplistic and the main purpose of this chapter is validation of the numerics, they still can be used to address real agricultural problems.
In Chapter 3, we introduce a key framework - a periodic array of uptaking cylinders (as in Figure 1.3) - and show how homogenisation can give us an effective equation here. The same geometry was used in [80]. However, we present this framework in a rather general setting, noting that apart from mod-

elling root hairs, it can also be used to model uptake by a field of crops. Moreover, we show how to homogenise this problem using various continuity equations and boundary conditions often found in root-soil modelling (discussed in Sections 1.3.3 and 1.3.4), we compare the full-geometry numerics with the homogenisation results for all these cases, and thus we directly see how homogenisation averages out microscopic heterogeneities.

As can be seen from this literature review, many authors modelled water and nutrient uptake at a single root as well as a single plant scale (see Section 1.3.4). However, less attention was paid to modelling root hairs' contribution to overall nutrient uptake (those few exceptions are summarised in Section 1.4.4). Therefore, in Chapter 4, we study the limit of very sparse root hairs, in which the root hair thickness is much smaller than the distance between the neighbouring hairs. This introduces another small parameter to the model, and therefore, a separate asymptotic analysis is needed. To our knowledge, no one has studied this problem in the context of root hairs before us.

As mentioned in Section 1.4.4, the authors of [80] neglected the role of the root hair length, and the way it affects the root surface unrolling (also see Figure 1.3). As we have not seen any attempt to study these effects in the available literature, we will study this problem in Chapter 5.

Even though the central chapters of this thesis (i.e. chapters 3, 4 and 5) are concerned with homogenisation and its role in modelling nutrient uptake by root hairs, we believe that multiscale (and averaging) methods will be crucial in many other areas of plant uptake research. Therefore, in the remaining two chapters of this thesis we will introduce other challenging problems related to the uptake processes, and show how even simple upscaling (and averaging) techniques can give us useful insight into such problems. In Chapter 6, we upscale nitrate intake from a single transporter scale to a root segment scale simply by multiplying the single transporter uptake with the transporters density. Finally, in Chapter 7, we study how depth-dependent (horizontally averaged) models of water and nitrate uptake (similar to those discussed in Section 1.3.4) compare with a fully three-dimensional architectural model (SimRoot; see Section 1.5.1) using realistic root system geometries.

2

WATER UPTAKE BY SIMPLE ROOT STRUCTURES

2.1 INTRODUCTION

In this chapter, we study the models of water uptake by structures similar to those found in root systems. These models are often nonlinear, hence we often have to solve the corresponding equations numerically. After introducing standard partial differential equations that govern water dynamics in the soil and a few simple root geometries that will be used throughout this chapter, we present the basics of the finite difference and the finite element methods.
As we will use numerical simulations in FEniCS (a computing platform that uses finite element methods - see Section 2.4 - for solving partial differential equations) throughout chapters 3, 4 and 5 of this thesis, accuracy checks for these are highly desirable. Therefore, in this chapter, we compare the FEniCS results with numerics in MATLAB, and provide further numerical checks using various geometries and governing equations. This gives us numerical evidence that the results of our simulations are valid.
Up to this point, we need not be concerned too much with the specific values of physiological or physical parameters used, as we are mostly interested in making sure that our understanding of FEniCS is correct, and thus the modelling outcomes are trustworthy. In later sections of this chapter, we show how the mentioned simulations can be used for studying real agricultural problems. This includes the estimation of a minimal watering rate needed for keeping the soil from drying out (see Section 2.6.2). Moreover, we will also study a geometry with a branch (see Figure 2.2), which provides us with a very general

framework - one can use it to model an uptake by a seminal root with periodically spaced branches as well as an uptake by a root covered with root hairs. Thus, we conclude this chapter with an attempt to optimise a water uptake by a single root with respect to the root hair density, for which we will use biologically realistic parameters.

2.2 EQUATIONS, GEOMETRIES AND SOFTWARE

2.2.1 *Continuity equation*

To model water dynamics in the soil, let us start with the equation of continuity (see Section 1.3.3) for the volumetric water content $\theta(t, \boldsymbol{x})$ without any sink terms:

$$\frac{\partial \theta}{\partial t} + \nabla \cdot \boldsymbol{\mathcal{J}} = 0, \tag{43}$$

where t is time, θ is the volumetric water content, and $\boldsymbol{\mathcal{J}}$ is the water flux, i.e. $\int_S \boldsymbol{\mathcal{J}} \cdot \hat{\boldsymbol{n}} dS$ is the volume of water passing through any surface S ($\hat{\boldsymbol{n}}$ is a unit vector normal to that surface).

Moreover, it is easy to see that $\boldsymbol{\mathcal{J}} = \theta \boldsymbol{\mathcal{V}}$, where $\boldsymbol{\mathcal{V}}$ is the velocity of water. Following [114], for processes not involving hysteresis [1], Darcy's law can be expressed as:

$$\boldsymbol{\mathcal{J}} = \theta \boldsymbol{\mathcal{V}} = -D(\theta)\nabla\theta + k(\theta)\nabla x_3, \tag{44}$$

where the $-D(\theta)\nabla\theta$ term models flux caused by a difference in matric potential, and the $+k(\theta)\nabla x_3$ term models flux caused by a difference in gravitational potential (with $D(\theta)$ being the soil water diffusivity, $k(\theta)$ being the hydraulic conductivity and x_3 the vertical coordinate taken positive downwards; see Equation (6) and Section 1.3.3). Note that both $D(\theta)$ and $k(\theta)$ can be highly nonlinear functions of the local water content θ [114], which models reduction

1 In standard Darcy's law, the water flux is proportional to the pressure head gradient (see Section 1.3.3). Hysteresis means that the relationship between the water content and the pressure head is different for a wetting and a drying soil. Therefore, we can only express the pressure head gradient in terms of the water content gradient, provided we neglect hysteresis. For more details, see Section 1.3.3

in water mobility due to a decreased water content known from experiments [121]. We postpone the discussion regarding the exact forms of $D(\theta)$ and $k(\theta)$ to Section 2.6. Substituting Equation (44) into the continuity equation (43), we get:

$$\frac{\partial \theta}{\partial t} = \nabla \cdot \{D(\theta)\nabla\theta - k(\theta)\nabla x_3\}, \tag{45}$$

which is exactly the same as Equation (7) from the previous chapter.

2.2.2 *Boundary conditions*

When using partial differential equations to model biological systems, one normally deals with finite spatial domains, and therefore a boundary condition is imposed at some finite distance from the process of interest (water uptake at the root surface in this case). Here, we will often impose a zero-flux condition:

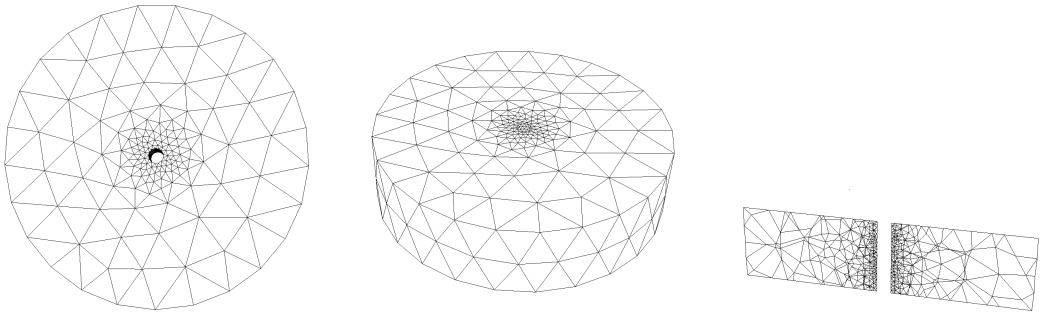
$$-\{D(\theta)\nabla\theta - k(\theta)\nabla x_3\} \cdot \hat{\boldsymbol{n}} = 0, \tag{46}$$

which can either be used to model an impermeable layer (e.g. plants stored in a pot), or to model competition with a neighbouring plant/root (the imposition of this boundary condition can also be thought of as a symmetry argument). Alternatively, we will sometimes impose a fixed water content:

$$\theta = \theta_{ff} \tag{47}$$

at the far-field distance.

We do not model water transport within the root system in this thesis. Instead, we wish to model water intake, and to do that, we either need to add a sink term to the continuity equation, or we model the uptake explicitly via a boundary condition specified on the root surface (this choice usually depends on the spatial scale under consideration - see Section 1.3.4). In this chapter, we choose the latter option, and we consider two distinct root system geometries. In attempt to keep the geometry as simple as possible, we first assume a single cylindrical root surrounded by a cylindrical column of soil, and then add one lateral root branching off perpendicularly from this root.



(a) View from above (b) Side view (c) Vertical slice

Figure 2.1.: Coarsely meshed geometry without a side branch.

A single cylinder geometry

In the first case, our geometry consists of a thick cylinder of finite height (representing the soil) with a thinner cylinder of the same height (representing the root) cut out of it. Different views of the (meshed) geometry are presented in Figure 2.1. Note that in this chapter, the main axis of the cylindrical root is always oriented in the direction of gravity.

On the length scale of the rooting depth, the gravity term cannot be neglected. Therefore, if the length of the modelled root is of this order, the imposed boundary conditions at the top and the bottom parts of the boundary become decisive for the model outcomes. Normally, water content increases as we move into the deeper soil layers (see Section 1.2.2). Therefore, as a default case, we impose a full-saturation Dirichlet boundary condition:

$$\theta = \phi \tag{48}$$

at the bottom part of the boundary (defined as $x_3 = h_0$), where ϕ is the soil porosity from Section 1.2.2. This way, we can model a water table located at $x_3 = h_0$ (see [121] and Section 1.2.2).

Furthermore, one may sometimes wish to impose a zero-flux boundary condition:

$$-\{D(\theta)\nabla\theta - k(\theta)\nabla x_3\} \cdot \hat{\boldsymbol{n}} = 0 \tag{49}$$

at the top ($x_3 = 0$) or the bottom ($x_3 = h_0$) part of the boundary. This can represent an impermeable layer at the bottom boundary (modelling a soil overlying

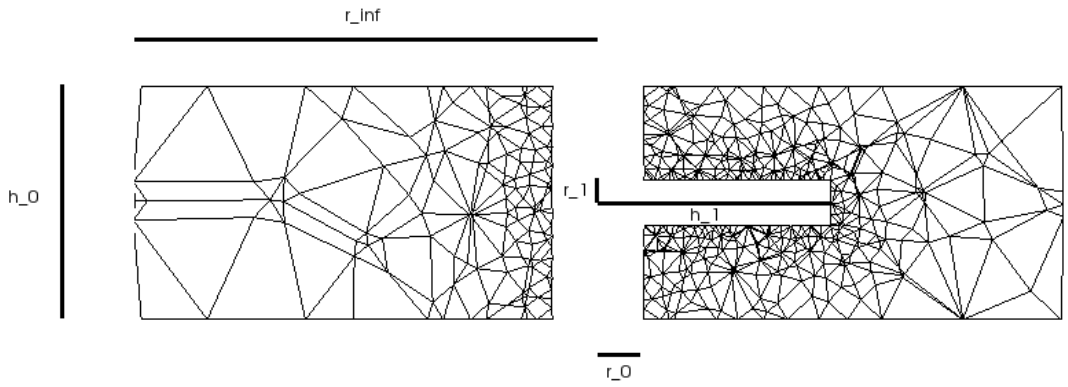


Figure 2.2.: Slice through a (coarsely) meshed geometry with a side branch.

an aquitard - a zone of low hydraulic conductivity - see [121], or simply a soil stored in a sealed pot). When applied at the top boundary, this condition can model the absence of precipitation (as well as evaporation).
In this chapter, we also implement a free-drainage boundary condition:

$$-\{D(\theta)\nabla\theta - k(\theta)\nabla x_3\} \cdot \hat{\boldsymbol{n}} = k(\theta) \tag{50}$$

at the bottom boundary, which is often found to be a good approximation in field studies with the water table lying far below the rooting depth [129].
Another possible modification could be in the form of a prescribed influx at the top boundary (modelling rainfall or watering). However, we will not impose this boundary condition in this chapter.

Branching structure

The single cylindrical root geometry is not an ideal description of sometimes highly complex structures that are found in root systems. As the simplest modification towards simulating more realistic root geometries, we consider the case with another (thinner) cylinder cut out from the domain (which can represent a root hair or a lateral root branching off the main root). A vertical slice through such domain is shown in Figure 2.2. This allows us to model water uptake on smaller scales. However, if the difference in water content between the two ends of the main root is negligible, we can upscale the outcomes of this setting, and model water uptake by a root with periodically-spaced branches

(or root hairs). To do this, we imagine that the geometry from Figure 2.2 is repeated in the x_3 direction, and we impose periodic boundary conditions, i.e. a periodic value condition:

$$\theta(t, x_1, x_2, 0) = \theta(t, x_1, x_2, h_0) \quad \forall t, x_1, x_2, \tag{51}$$

and a periodic flux condition:

$$\left(D\big(\theta(t, x_1, x_2, 0)\big) \nabla \theta(t, x_1, x_2, 0) - \left(0, 0, k\big(\theta(t, x_1, x_2, 0)\big)\right)\right) \cdot \left(0, 0, 1\right) =$$
$$\left(D\big(\theta(t, x_1, x_2, h_0)\big) \nabla \theta(t, x_1, x_2, h_0) - \left(0, 0, k\big(\theta(t, x_1, x_2, h_0)\big)\right)\right) \cdot \left(0, 0, 1\right)$$
$$\forall t, x_1, x_2 \tag{52}$$

which in this case reduces to the periodic value of the derivative with respect to x_3:

$$\frac{\partial \theta(t, x_1, x_2, 0)}{\partial x_3} = \frac{\partial \theta(t, x_1, x_2, h_0)}{\partial x_3} \quad \forall t, x_1, x_2. \tag{53}$$

Similar conditions are frequently imposed in the method of homogenisation, which will be the key concept in the next three chapters of this thesis. Therefore, even though we will not use homogenisation in this chapter, confidence in the numerical simulations using the periodic boundary condition will be essential in the next three chapters.

2.2.3 *Software*

If we assume the root to be an infinitely long cylinder located in an infinite soil, neglect the gravity (advection) term in Equation (45), and impose initial and boundary conditions dependent only on the polar radius ($r = \sqrt{x_1^2 + x_2^2}$), then our model is effectively one-dimensional, i.e. its solution is only dependent on r. If we add the advection to the model, it becomes two-dimensional. These situations can be easily solved in MATLAB using the finite difference method (as introduced in Section 2.3), and we will use this approach in Section 2.5. However, adding a branch to the main root, the problem becomes essentially three-dimensional. The finite difference methods (that one can easily implement in MATLAB) are not well-suited for more complex geometries like this

anymore. We used finite element solvers (implemented in FEniCS [83]) to solve these geometrically more challenging problems in Section 2.6.
However, we need to provide FEniCS with meshed geometries in the form of .xml files. First, we write a .geo file (describing the geometry of our domain using simple primitives - e.g. cylinders - and Boolean operations - complement, union and intersection [127]). We then use NetGen [127] to generate the meshed domain with a specified maximal mesh size, in the form of an .msh file. Finally, we use DOLFIN-CONVERT (a python script [83]) to convert the .msh file into an .xml file, which can be used as an input for FEniCS.
We first sketch the basic principles of the finite difference method, and then do the same with the finite element method. Later on, we compare MATLAB and FEniCS results for linear models with and without the advection.

2.3 BRIEF INTRODUCTION TO THE FINITE DIFFERENCE METHOD

In this chapter, we will deal with advection-diffusion equations (see Equation (45)). Therefore, we introduce finite difference schemes for this type of equation.
Suppose we have a nonlinear, inhomogeneous diffusion equation:

$$\frac{\partial u}{\partial t} = \nabla \cdot [D(x_1, x_2, x_3, u)\nabla u], \tag{54}$$

which we wish to solve in a cubic domain:

$$\Omega = \left\{ (x_1, x_2, x_3) \in \mathbb{R}^3, 0 \leq x_1, x_2, x_3 \leq L \right\}$$

for $t \in [0, T]$. We discretise the spatial as well as the temporal domain. Let $M, N \in \mathbb{N}$ be fixed, reasonably large (this will affect the accuracy of the numerical solution) numbers. Denote $\delta t = \frac{T}{M}$, $h = \frac{L}{N}$, $t_n = n\delta t$ for $n \in \{0, 1, ..., M\}$, and $x_1^i = ih$, $x_2^j = jh$, $x_3^k = kh$ for $i, j, k \in \{0, 1, ..., N\}$. We want to find a numerical approximation for the values of the exact solution u at specified points in space and time - $u(t_n, x_1^i, x_2^j, x_3^k)$, and we denote these values as u_{ijk}^n. Furthermore, we denote ∇u_{ijk}^n to be our numerical approximation for the gradient and similar notation is used for other derivatives. Finally, we denote

$D^n_{ijk} = D(x^i_1, x^j_2, x^k_3, u^n_{ijk})$. Any first-order spatial derivative (e.g. derivative with respect to x_1) can be approximated either by a forward Euler method:

$$\frac{\partial u^n_{ijk}}{\partial x_1} \approx \frac{u^n_{(i+1)jk} - u^n_{ijk}}{h},$$

or by a backward Euler method:

$$\frac{\partial u^n_{ijk}}{\partial x_1} \approx \frac{u^n_{(i)jk} - u^n_{(i-1)jk}}{h}.$$

Let us focus on the expression:

$$\nabla \cdot \left[D(x_1, x_2, x_3, u) \nabla u(t, x_1, x_2, x_3) \right]. \tag{55}$$

First, we approximate the first component of $\frac{\partial [D(x_1,x_2,x_3,u)\nabla u(t,x_1,x_2,x_3)]}{\partial x_1}$ as:

$$\frac{\partial \left[D(x^i_1, x^j_2, x^k_3, u^n_{ijk}) \frac{\partial u^n_{ijk}}{\partial x_1} \right]}{\partial x_1} \approx \frac{1}{h} \left\{ D^n_{(i+\frac{1}{2})jk} \frac{\partial u^n_{(i+\frac{1}{2})jk}}{\partial x_1} - D^n_{(i-\frac{1}{2})jk} \frac{\partial u^n_{(i-\frac{1}{2})jk}}{\partial x_1} \right\} \approx$$

$$\frac{1}{h} \left\{ \frac{D^n_{(i+1)jk} + D^n_{ijk}}{2} \quad \frac{u^n_{(i+1)jk} - u^n_{ijk}}{h} - \frac{D^n_{(i-1)jk} + D^n_{ijk}}{2} \quad \frac{u^n_{ijk} - u^n_{(i-1)jk}}{h} \right\}.$$

Similarly, the approximation of the second term in the divergence Expression (55) gives:

$$\frac{1}{h} \left\{ \frac{D^n_{i(j+1)k} + D^n_{ijk}}{2} \quad \frac{u^n_{i(j+1)k} - u^n_{ijk}}{h} - \frac{D^n_{i(j-1)k} + D^n_{ijk}}{2} \quad \frac{u^n_{ijk} - u^n_{i(j-1)k}}{h} \right\},$$

and the final term is approximated by:

$$\frac{1}{h} \left\{ \frac{D^n_{ij(k+1)} + D^n_{ijk}}{2} \quad \frac{u^n_{ij(k+1)} - u^n_{ijk}}{h} - \frac{D^n_{ij(k-1)} + D^n_{ijk}}{2} \quad \frac{u^n_{ijk} - u^n_{ij(k-1)}}{h} \right\}.$$

Adding these term, we obtain an approximation for Expression (55), and Equation (54) becomes:

$$\frac{du^n_{ijk}}{dt} = \frac{1}{2h^2} \Big\{$$

$$\left(D^n_{(i+1)jk} + D^n_{ijk}\right) \left(u^n_{(i+1)jk} - u^n_{ijk}\right) - \left(D^n_{(i-1)jk} + D^n_{ijk}\right) \left(u^n_{ijk} - u^n_{(i-1)jk}\right) +$$

$$\left(D^n_{i(j+1)k} + D^n_{ijk}\right) \left(u^n_{i(j+1)k} - u^n_{ijk}\right) - \left(D^n_{i(j-1)k} + D^n_{ijk}\right) \left(u^n_{ijk} - u^n_{i(j-1)k}\right) +$$

$$\left(D^n_{ij(k+1)} + D^n_{ijk}\right) \left(u^n_{ij(k+1)} - u^n_{ijk}\right) - \left(D^n_{ij(k-1)} + D^n_{ijk}\right) \left(u^n_{ijk} - u^n_{ij(k-1)}\right) \Big\}.$$

If we impose a Dirichlet condition everywhere on the boundary, this can be treated as the system of $(N-1) \times (N-1) \times (N-1)$ ordinary differential equations in time. This is called a semi-discretisation (so far we only discretised in space), and it is often useful when performing the stability analysis. We discretise in time using the forward Euler method (for simplicity [2]), and get:

$$u_{ijk}^{n+1} = u_{ijk}^n + \delta t \frac{1}{2h^2} \Big\{ \left(D_{(i+1)jk}^n + D_{ijk}^n\right) \left(u_{(i+1)jk}^n - u_{ijk}^n\right) - \left(D_{(i-1)jk}^n + D_{ijk}^n\right) \left(u_{ijk}^n - u_{(i-1)jk}^n\right) + \left(D_{i(j+1)k}^n + D_{ijk}^n\right) \left(u_{i(j+1)k}^n - u_{ijk}^n\right) - \left(D_{i(j-1)k}^n + D_{ijk}^n\right) \left(u_{ijk}^n - u_{i(j-1)k}^n\right) + \left(D_{ij(k+1)}^n + D_{ijk}^n\right) \left(u_{ij(k+1)}^n - u_{ijk}^n\right) - \left(D_{ij(k-1)}^n + D_{ijk}^n\right) \left(u_{ijk}^n - u_{ij(k-1)}^n\right) \Big\}.$$

Thus, we can calculate the solution at time t_{n+1} if we know its values at time t_n. As we know the values at time $t_0 = 0$ from the initial condition, we can in principle calculate the numerical solution at any time in future.

Having introduced the finite difference method for the diffusion equation, let us briefly discuss the advection-diffusion equation. Recall Equation (45). We approximate the diffusion term $\nabla \cdot \{D(\theta)\nabla\theta\}$, using the centered difference method as above. The advection term becomes:

$$-\nabla \cdot \{k(\theta)\nabla x_3\} = -\frac{\partial(k(\theta))}{\partial x_3} = -k'(\theta)\frac{\partial\theta}{\partial x_3}.$$

The key question here is whether one should approximate the advection term using the forward or the backward Euler method. The standard procedure in numerical studies is to use the so-called upwinding: one should choose the side from which 'the wind is blowing' (which in this case means to go against gravity). As mentioned in Section 1.3.3, the hydraulic conductivity $k(\theta)$ is always assumed to be an increasing function of the local water content θ, which means that $k'(\theta) > 0$. Therefore, if we approximate $\frac{\partial\theta}{\partial t} \approx \frac{\theta_{ijk}^{n+1} - \theta_{ijk}^n}{\delta t}$, then the upwinding gives $-k'(\theta)\frac{\partial\theta}{\partial x_3} \approx -k'(\theta_{ijk}^n)\frac{\theta_{ijk}^n - \theta_{ij(k-1)}^n}{h}$.

2 Without going into much detail, we mention that this method is often unstable. Therefore, the backward Euler method is often used for time discretisation, and it yields a system of algebraic equations to be solved.

2.4 BRIEF INTRODUCTION TO THE FINITE ELEMENT METHOD

To solve a differential equation using the finite element method, we first need to change our equation into a so-called weak form. Following [83], we first discretise in time. Then, we multiply the equation with a test function, integrate over the whole domain, and use integration by parts. We explain this procedure in more detail with a few simple examples.

First, consider the geometry from Figure 2.1 and assume that gravity can be neglected so that the solution depends only on one spatial coordinate (the polar radius r). Denoting $\Phi(t, r) = \theta(t, \boldsymbol{x})$, we get:

$$\frac{\partial \Phi}{\partial t} = \frac{1}{r}\frac{\partial}{\partial r}\left[rD(\Phi)\frac{\partial \Phi}{\partial r}\right].$$

Approximating the time derivative using the backward Euler scheme (see Section 2.3), we get:

$$\frac{\Phi^n - \Phi^{n-1}}{\delta t} = \frac{1}{r}\frac{d}{dr}\left[rD(\Phi^n)\frac{d\Phi^n}{dr}\right].$$

Rearranging this, we obtain:

$$\Phi^n - \delta t\frac{1}{r}\frac{d}{dr}\left[rD(\Phi^n)\frac{d\Phi^n}{dr}\right] = \Phi^{n-1}, \tag{56}$$

for $n = 1, 2, 3, ..., N$, where $N \in \mathbb{N}$, and:

$$\Phi^0 = \Phi(0, r),$$

Our strategy is to calculate the solution at time t_n (Φ^n) from the known solution at time t_{n-1} (Φ^{n-1}). In order to do that, we write our equation in the previously mentioned weak form. We multiply Equation (56) by a test function v, and we integrate over the truncated domain $\Omega = (r_0, r_\infty)$ where r_∞ is some (reasonably large) positive real number. Using integration by parts, we arrive at:

$$\int_{r_0}^{r_\infty} \Phi^n v dr - \delta t\left\{\left[D(\Phi^n)v\frac{d\Phi^n}{dr}\right]_{r_0}^{r_\infty} - \int_{r_0}^{r_\infty} rD(\Phi^n)\frac{d\Phi^n}{dr}\frac{d}{dr}\left(\frac{v}{r}\right)dr\right\} = \int_{r_0}^{r_\infty} \Phi^{n-1} v dr \tag{57}$$

Suppose the boundary is divided into two parts - at one of them (Γ_D), we assume a Dirichlet boundary condition ($\theta(t, \boldsymbol{x}) = f(t, \boldsymbol{x})$), while at the other ($\Gamma_N$), we assume a Neumann boundary condition ($[D(\theta)\nabla\theta - k(\theta)\nabla x_3] \cdot \hat{\boldsymbol{n}} =$

$g(t, \boldsymbol{x})$, where $\hat{\boldsymbol{n}}$ is the outward pointing unit normal vector). For instance, we may want to impose a fixed root influx at $r = r_0$ (i.e. $D(\Phi^n)\frac{d\Phi^n}{dr} = I$; Equation (19)), and a fixed water content at the outer boundary (i.e. $\Phi(t, r_\infty) = \Phi_{ff}$; Equation (47)). We only admit test functions v which are zero at Γ_D (see [83]). Therefore, Equation (57) can be written as:

$$a(\Phi^n, v) = L(v),$$

where:

$$a(\Phi^n, v) = \int_{r_0}^{r_\infty} \Phi^n v dr + \delta t \int_{r_0}^{r_\infty} rD(\Phi^n)\frac{d\Phi^n}{dr}\frac{d}{dr}\left(\frac{v}{r}\right)dr$$

is linear in v (and is a bilinear form, if $D(\Phi^n)$ is constant), and:

$$L(v) = \int_{r_0}^{r_\infty} \Phi^{n-1} v dr - \delta t I v(r_0)$$

is a linear functional.

Denote $H = \{h \in H^1(\Omega) : h = \Phi_{ff} \ at \ r = r_\infty\}$ and $J = \{j \in H^1(\Omega) : j = 0 \ at \ r = r_\infty\}$, where $H^1(\Omega) = W^{1,2}(\Omega)$ is a well-known Sobolev space [45]. Using these spaces, we can finally state the weak formulation in its fullness - we look for $\Phi^n \in H$ such that $a(\Phi^n, v) = L(v)$ for all $v \in J$.

However, the spaces H and J are infinite-dimensional. Therefore, in the finite element method, one constructs finite-dimensional subspaces of these spaces H^m and J^m, and searches for $\Phi \in H^m$ such that $a(\Phi, v) = L(v)$ for all $v \in J^m$. The domain is divided into a finite number of subdomains, and the finite-dimensional subspaces are chosen to be the spaces of piecewise (with respect to the chosen domain division) polynomial functions (with their degree constrained from above) [83]. We do not need to go into the details of how exactly the solutions are found in the finite element method, because FEniCS does that for us automatically; we only need to provide FEniCS with the mesh, the weak formulation, and the maximal polynomial degree.

In this chapter, we will also study problems in two and three spatial dimensions. Therefore, let us go back to Equation (45) in cartesian coordinates (x_1, x_2, x_3). In the case of $D(\theta)$ and $k(\theta)$ being nonlinear functions of θ [114],

this can rarely be solved analytically, and we need to use numerical methods. Time discretisation using the backwards Euler method yields:

$$\frac{\theta^n - \theta^{n-1}}{\delta t} = \nabla \cdot \left[D(\theta^n) \nabla \theta^n - k(\theta^n) \nabla x_3 \right],$$

or:

$$\theta^n - \delta t \nabla \cdot \left[D(\theta^n) \nabla \theta^n - k(\theta^n) \nabla x_3 \right] = \theta^{n-1}$$

for $n = 1, 2, 3, ..., N$, where $N \in \mathbb{N}$. Impose an initial condition:

$$\theta^0 = \theta_0.$$

Multiplying by the test function v, integrating over

$$\Omega = \{(x_1, x_2, x_3) \in \mathbb{R}^3 : r_1^2 \geq x_1^2 + x_2^2 \geq r_0^2, 0 \leq x_3 \leq h_1\},$$

and integrating by parts, we get:

$$\begin{aligned} &\int_\Omega \theta^n v dx - \delta t \int_{\partial\Omega} v \left[D(\theta^n) \nabla \theta^n - k(\theta^n) \nabla x_3 \right] \cdot \hat{\boldsymbol{n}} dS + \\ &\delta t \int_\Omega \left[D(\theta^n) \nabla \theta^n - k(\theta^n) \nabla x_3 \right] \cdot \nabla v dx = \int_\Omega \theta^{n-1} v dx, \end{aligned} \tag{58}$$

where $\hat{\boldsymbol{n}}$ is an outward pointing unit normal vector.

The boundary is again divided according to the type of a boundary condition used. We consider the two distinct geometries from Figures 2.1 and 2.2 in this section.

We first consider a long vertical root stretching from the ground down to deeper soil layers (see Figure 2.1). Assume that we keep the water content at the bottom boundary fixed, i.e. $\theta(t, x_1, x_2, h_0) = \theta_b$ (generalised Equation (48)). At $r = r_\infty$, we impose Equation (46), i.e. the zero-flux boundary condition. We further assume imposed fluxes $[D(\theta)\nabla\theta - k(\theta)\nabla x_3] \cdot \hat{\boldsymbol{n}} = g_1(t, \boldsymbol{x})$ at the root-soil interface ($r = r_0$) modelling the water uptake (generalised Equation (19)), and $[D(\theta)\nabla\theta - k(\theta)\nabla x_3] \cdot \hat{\boldsymbol{n}} = g_2(t, \boldsymbol{x})$ at the soil-atmosphere interface ($x_3 = 0$) modelling precipitation or evaporation (generalised Equation (49)). As the test functions vanish at Γ_D (the standard step in the finite element method), we get:

$$\int_\Omega \theta^n v dx + \delta t \int_\Omega \left[D(\theta^n) \nabla \theta^n - k(\theta^n) \nabla x_3 \right] \cdot \nabla v dx =$$

$$\int_\Omega \theta^{n-1} v dx + \delta t \{ \int_{r=r_0} v g_1 dS + \int_{x_3=0} v g_2 dS \}.$$

Denote:

$$H = \{h \in H^1(\Omega) : h = \theta_b \ \ at \ \ x_3 = h_0\},$$

and:

$$J = \{j \in H^1(\Omega) : j = 0 \ \ at \ \ x_3 = h_0\}.$$

We wish to find $\Phi^n \in H$ such that $a(\Phi^n, v) = L(v)$ for all $v \in J$ where a and L are linear in v, and a may be nonlinear in Φ^n.

Because of their importance in the method of homogenisation, in the last example, we show how the periodic boundary conditions are imposed.

We study the model with a branch (see Figure 2.2), and we impose the periodic boundary conditions in the x_3 direction, namely the periodic value condition (51) (which leads to $v(t, x_1, x_2, 0) = v(t, x_1, x_2, h_0) \ \ \forall t, x_1, x_2$ for all test functions v), and the periodic flux condition (52). The only remaining type of boundary condition important for this thesis that was not discussed yet (in relation to its finite element implementation) is the Robin boundary condition, and thus we impose Equation (21) at the root-soil interface (which now includes the surface of the branch/hair; let us denote it by RS). To get a non-trivial steady state, we assume $\theta = \theta_{ff}$ at $r = r_\infty$, and the weak formulation (58) becomes:

$$\begin{aligned} &\int_\Omega \theta^n v dx + \delta t C_2 \int_{RS} v \theta^n dS - \delta t \int_{\partial\Gamma_P} v \big[D(\theta^n) \nabla \theta^n - k(\theta^n) \nabla x_3 \big] \cdot \hat{\boldsymbol{n}} dS + \\ &\delta t \int_\Omega \big[D(\theta^n) \nabla \theta^n - k(\theta^n) \nabla x_3 \big] \cdot \nabla v dx = \int_\Omega \theta^{n-1} v dx, \end{aligned} \tag{59}$$

where Γ_P denotes the part of the boundary, at which the periodic boundary conditions are imposed. The periodic boundary conditions cause the integrals over the upper and the lower part of the periodic boundary to cancel out. Therefore, the weak formulation goes as follows: find $\theta^n \in H = \{h \in H^1(\Omega) : h(r = r_\infty) = \theta_{ff}, h(x_1, x_2, 0) = h(x_1, x_2, h_0) \ \ \forall x_1, x_2\}$ such that for all $v \in J = \{j \in H^1(\Omega) : j(r = r_\infty) = 0, j(x_1, x_2, 0) = j(x_1, x_2, h_0) \ \ \forall x_1, x_2\}$, we have $a(\theta^n, v) = L(v)$, where

$$a(\theta, v) = \int_\Omega \theta v dx + \delta t \int_\Omega \big[D(\theta) \nabla \theta - k(\theta) \nabla x_3 \big] \cdot \nabla v dx + \delta t C_2 \int_{RS} v \theta dS,$$

$$L(v) = \int_{\Omega} \theta^{n-1} v dx,$$

and θ^{n-1} is known from the previous time step.

2.5 NUMERICAL CHECKING AND SIMULATIONS - TOY PROBLEMS

Before we draw any conclusions from our models, we need to make sure that we can control the errors which are inevitably created in the process of solving any equation numerically (by the finite element method in this case). Therefore, we now study these errors.

Note that no biological conclusions will be drawn in this section, and therefore, exact parameter values and their units are not important here. We will introduce biologically relevant parameters in Section 2.6.

We start with the geometry without a branch (see Figure 2.1). Because of the cylindrical nature of the geometry, we will use cylindrical coordinates.

2.5.1 *Linear diffusion equation*

Assume first, that the advection can be neglected, and thus we omit the second term on the right-hand side of Equation (45). Assuming a constant initial condition and zero-flux boundary conditions at the top and the bottom part of the boundary, we get that the solution is independent of the azimuthal angle φ as well as of the depth x_3, i.e. $\Phi(t, r) = \theta(t, x_1, x_2, x_3)$ (where $r = \sqrt{x_1^2 + x_2^2}$ is the polar radius). Equation (45) (without the advection term) becomes:

$$\frac{\partial \Phi}{\partial t} = \frac{1}{r} \frac{\partial}{\partial r} \left(rD \frac{\partial \Phi}{\partial r} \right), \tag{60}$$

and we assume that the diffusivity D is independent of the local water content Φ.

Analytical solutions

STEADY STATE

As we are dealing with a linear equation, it is easy to analytically find the

steady state (denoted as Φ^{∞}), to which the solution converges as time goes to infinity. To obtain this steady state, we simply set:

$$\frac{1}{r}\frac{d}{dr}\left(rD\frac{d\Phi^{\infty}}{dr}\right) = 0. \tag{61}$$

This means that $r\frac{d\Phi^{\infty}}{dr} = C_1$, where C_1 is a constant. This leads to $\Phi^{\infty}(r) = C_1 \ln r + C_2$ for some constants C_1 and C_2. Using the following boundary condition:

$$\Phi^{\infty}(r_{\infty}) = \Phi_{ff} \tag{62}$$

as well as the assumption of a constant influx:

$$D\frac{d\Phi^{\infty}}{dr} = I \tag{63}$$

at the root surface $r = r_0$[3], we arrive at:

$$\Phi_A^{\infty}(r) = \Phi_{ff} + \frac{Ir_0}{D}\ln\frac{r}{r_{\infty}}, \tag{64}$$

where the subscript A is used to denote the analytical steady state from now onwards.

TIME-DEPENDENT PROBLEM

Here, we will attempt to find an analytical solution for Equation (60) equipped with the Dirichlet boundary condition (62) at $r = r_{\infty}$, the constant-flux boundary condition (63) at $r = r_0$, and a constant initial condition:

$$\Phi(0, r) = \Phi_{ff}. \tag{65}$$

We write Φ in the form:

$$\Phi(t, r) = \xi(t, r) + \Phi_A^{\infty}(r), \tag{66}$$

where Φ_A^{∞} is the steady-state solution from Equation (64) (which satisfies both boundary conditions). Using separation of variables, we then write:

$$\xi(t, r) = T(t)R(r), \tag{67}$$

3 Note that this is a good approximation for highly wetted soils so that the transpirational demand is easily met by the available water content. Other uptake regimes - see [114] - will be considered as well.

and impose boundary conditions:

$$R'(r_0) = 0 \qquad\qquad R(r_\infty) = 0. \tag{68}$$

Substituting the ansatz (66) (with ξ defined by (67)) into Equation (60), we get:

$$\frac{T'}{DT} = \frac{R'' + \frac{1}{r}R'}{R} = -\lambda, \tag{69}$$

and it follows that:

$$R'' + \frac{1}{r}R' + \lambda R = 0. \tag{70}$$

By defining $P(r, \varphi) = R(r)$ for all $\varphi \in [0, 2\pi]$, we therefore have:

$$-\nabla^2 P = \lambda P. \tag{71}$$

We will now show that this problem equipped with a zero-flux boundary condition at $r = r_0$ and a Dirichlet boundary condition $P = 0$ at $r = r_\infty$ (see the boundary conditions for R, i.e. equations (68)) only admits positive eigenvalues (i.e. $\lambda > 0$).

Multiplying Equation (71) by P, and integrating over an annulus Ω_A with the inner radius of r_0 and the outer radius of r_∞, we get:

$$\int_{\Omega_A} \lambda P^2 dS = -\int_{\Omega_A} P\nabla^2 P dS =$$

$$-\left\{ \int_{\partial\Omega_A} P\nabla P \cdot \hat{\boldsymbol{n}} dl - \int_{\Omega_A} \|\nabla P\|^2 dS \right\} = \int_{\Omega_A} \|\nabla P\|^2 dS,$$

where we used Green's first identity (see [130]), and the imposed boundary conditions caused the boundary integral to vanish. This yields $\lambda \geq 0$. The $\lambda = 0$ case leads to $\nabla P = 0$ everywhere, which gives P constant everywhere, and using the boundary condition at $r = r_\infty$, we conclude $P = 0$ everywhere. Therefore, from now onwards, we only assume $\lambda > 0$, and we write $\lambda = \mu^2$ for some positive μ.

Equation (70) can therefore be written as:

$$r^2 R'' + rR' + \mu^2 r^2 R = 0.$$

Defining $\rho = \mu r$ and $S(\rho) = R(r)$, this becomes:

$$\rho^2 S'' + \rho S' + \rho^2 S = 0,$$

which is known as Bessel's differential equation of order 0 (see [130]). We can choose two linearly independent solutions of this linear second-order differential equation to be the Bessel function of the first kind $J_0(\rho)$ and the Bessel function of the second kind $Y_0(\rho)$ (for more details, see [1]), which gives a general solution to the R equation in the form:

$$R = AJ_0(\mu r) + BY_0(\mu r).$$

For this solution to satisfy our boundary conditions (68), we need to impose:

$$AJ_0(\mu r_\infty) + BY_0(\mu r_\infty) = 0, \tag{72}$$

and

$$AJ_0'(\mu r_0) + BY_0'(\mu r_0) = 0, \tag{73}$$

which can be regarded as a system of 2 linear equations in A and B. For this system to give a nontrivial solution (A, B), the determinant of its matrix needs to be 0, i.e.:

$$J_0(\mu r_\infty)Y_0'(\mu r_0) - J_0'(\mu r_0)Y_0(\mu r_\infty) = 0,$$

and this introduces a constraint on possible values of μ (and therefore on $\lambda = \mu^2$).

Upon rewriting Equation (70) in a form:

$$\frac{1}{r}\Big(rR'\Big)' = -\lambda R,$$

this becomes an eigenvalue problem, and we can apply Sturm-Liouville theory (for details and proofs, see [75]). This tells us that the eigenvalues form a sequence $\{\lambda_k\}_{k=1}^{\infty}$ with $\lim_{k\to\infty} |\lambda_k| = \infty$, and that eigenfunctions associated with distinct eigenvalues are orthogonal (with weight r) [75]. As we have already shown that $\lambda_k > 0$, it follows that $\lim_{k\to\infty} \lambda_k = \infty$. Finally, looking back into Equation (69), these eigenvalues give the corresponding time-dependent functions of the form $T_k(t) = T_k(0)e^{-\lambda_k Dt}$.

To summarise, we can write the solution $\Phi(t, r)$ as an infinite series:

$$\Phi(t, r) = \Phi_A^\infty(r) + \sum_{k=1}^{\infty} e^{-\lambda_k Dt}\Big\{A_k J_0(\sqrt{\lambda_k}r) + B_k Y_0(\sqrt{\lambda_k}r)\Big\},$$

and using Equation (72), this can be written as:

$$\Phi(t,r) = \Phi_A^\infty(r) + \sum_{k=1}^{\infty} A_k e^{-\lambda_k Dt}\left\{ J_0(\sqrt{\lambda_k}r) - \frac{J_0(\sqrt{\lambda_k}r_\infty)}{Y_0(\sqrt{\lambda_k}r_\infty)} Y_0(\sqrt{\lambda_k}r)\right\},$$

It remains to determine constants A_k, which is achieved using the initial condition. For $t = 0$, we get:

$$\Phi_{ff} - \Phi_A^\infty(r) = \sum_{k=1}^{\infty} A_k\left\{ J_0(\sqrt{\lambda_k}r) - \frac{J_0(\sqrt{\lambda_k}r_\infty)}{Y_0(\sqrt{\lambda_k}r_\infty)} Y_0(\sqrt{\lambda_k}r)\right\}.$$

Multiplying both sides by $r\left\{ J_0(\sqrt{\lambda_i}r) - \frac{J_0(\sqrt{\lambda_i}r_\infty)}{Y_0(\sqrt{\lambda_i}r_\infty)} Y_0(\sqrt{\lambda_i}r)\right\}$, and integrating over (r_0, r_∞) gives:

$$\int_{r_0}^{r_\infty} r\left\{ J_0(\sqrt{\lambda_i}r) - \frac{J_0(\sqrt{\lambda_i}r_\infty)}{Y_0(\sqrt{\lambda_i}r_\infty)} Y_0(\sqrt{\lambda_i}r)\right\}\left\{\Phi_{ff} - \Phi_A^\infty(r)\right\}dr = \int_{r_0}^{r_\infty} r\left\{ J_0(\sqrt{\lambda_i}r) - \right.$$

$$\left. \frac{J_0(\sqrt{\lambda_i}r_\infty)}{Y_0(\sqrt{\lambda_i}r_\infty)} Y_0(\sqrt{\lambda_i}r)\right\}\left\{ \sum_{k=1}^{\infty} A_k\left\{ J_0(\sqrt{\lambda_k}r) - \frac{J_0(\sqrt{\lambda_k}r_\infty)}{Y_0(\sqrt{\lambda_k}r_\infty)} Y_0(\sqrt{\lambda_k}r)\right\}\right\}dr =$$

$$A_i \int_{r_0}^{r_\infty} r\left\{ J_0(\sqrt{\lambda_i}r) - \frac{J_0(\sqrt{\lambda_i}r_\infty)}{Y_0(\sqrt{\lambda_i}r_\infty)} Y_0(\sqrt{\lambda_i}r)\right\}^2 dr,$$

where we used the mentioned fact, that eigenfunctions corresponding to distinct eigenvalues are orthogonal with weight r. This yields:

$$A_i = \frac{\int_{r_0}^{r_\infty} r\left\{ J_0(\sqrt{\lambda_i}r) - \frac{J_0(\sqrt{\lambda_i}r_\infty)}{Y_0(\sqrt{\lambda_i}r_\infty)} Y_0(\sqrt{\lambda_i}r)\right\}\left\{\Phi_{ff} - \Phi_A^\infty(r)\right\}dr}{\int_{r_0}^{r_\infty} r\left\{ J_0(\sqrt{\lambda_i}r) - \frac{J_0(\sqrt{\lambda_i}r_\infty)}{Y_0(\sqrt{\lambda_i}r_\infty)} Y_0(\sqrt{\lambda_i}r)\right\}^2 dr}.$$

Convergence to steady state in MATLAB

In order to avoid calculating such integrals and working with infinite sums, we only solve our problem numerically in MATLAB (the code is presented in Appendix *B*) using the finite difference method (as introduced in Section 2.3) and see if the solution converges to the analytically-obtained steady state. We impose the initial condition (65). Figure 2.3 shows discrete time steps as well as the steady-state solution. We see that the time evolution truly approaches the analytic steady state, which is our first numerical check.

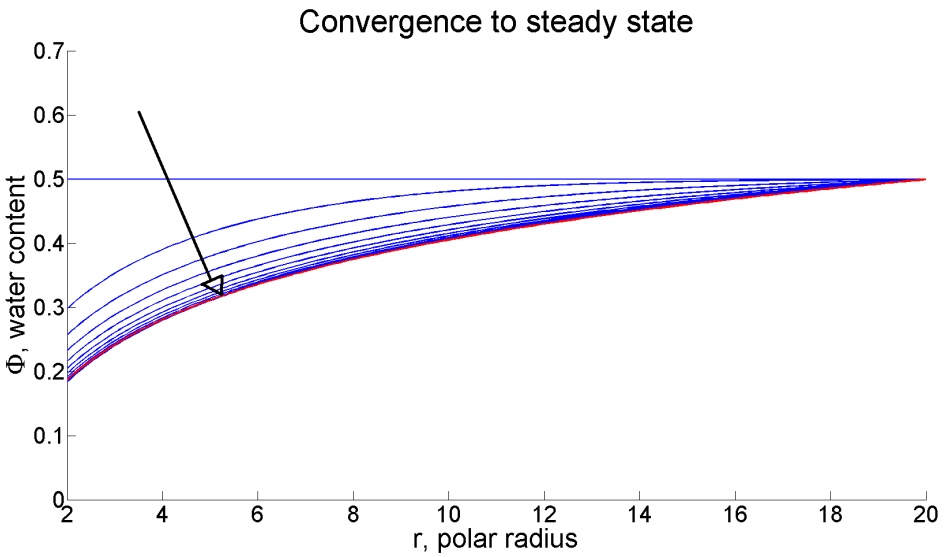


Figure 2.3.: MATLAB simulation (the linear diffusion equation (60) equipped with the boundary conditions (63), (62), and the initial condition (65)). The parameters are chosen as follows: $D = 2.5$, $\Phi_{ff} = 0.5$, $I = 0.17$, $r_0 = 2.0$, $r_\infty = 20.0$ and $dt = 10.0$. The root surface ($r = 2.0$) takes up water from its neighbourhood, and thus the water content is decreasing here. Comparison with the analytic result (Equation (64); in red) is also shown. The arrow represents the time evolution.

Convergence to steady state in FEniCS

Impose zero-flux boundary conditions at $x_3 = 0$ and $x_3 = h_0$ (such boundary conditions result in a solution independent of x_3, as nothing forces variations in this direction). To demonstrate our ability to model various soil water conditions, we change the root surface boundary condition to a Dirichlet condition:

$$\Phi(r = r_0) = 0, \tag{74}$$

and thus we end up with an analytic steady-state solution:

$$\Phi_A^{\infty}(r) = \Phi_{ff} \frac{\ln \frac{r}{r_0}}{\ln \frac{r_\infty}{r_0}}. \tag{75}$$

We run the numerical simulation in FEniCS (in the three-dimensional geometry), and check if this time evolution converges to the steady state as calculated by FEniCS. We also compare this steady state with the analytic solution, and the results are shown in Figure 2.4. We used Lagrange polynomials of degree one (for details, see [83]). Even though the numerically calculated steady state seems close to the analytic result, we wish to compare these results quantitatively and see how they depend on the prescribed maximal mesh size. Thus, we vary the maximal mesh size h (as imposed in NetGen), and compare the numerically obtained steady state with the analytic steady state to check that the numerical steady-state solution is accurate. Figure 2.5 shows the log-log plot of the (numerically computed) L^2 norm of a function $\Phi_A^{\infty} - \Phi_N^{\infty}$ where Φ_N^{∞} is the numerical approximation of the steady-state solution in FEniCS. Overall, the errors appear to be $O(h)$. However, we observe that the error occasionally increases (jumps) with the decreased mesh size. In order to understand these jumps, we also perform simulations using a two-dimensional geometry (where we do not use the x_3 coordinate) in FEniCS as illustrated in Figure 2.6. In the two-dimensional case, we do not generate the mesh using NetGen. Instead, we use generate_mesh function, which is a part of a mesh-generation component in FEniCS called mshr [79]. This function requires an input parameter called "resolution", which can be interpreted as the quotient of the domain size divided by the size of a single cell from the mesh.

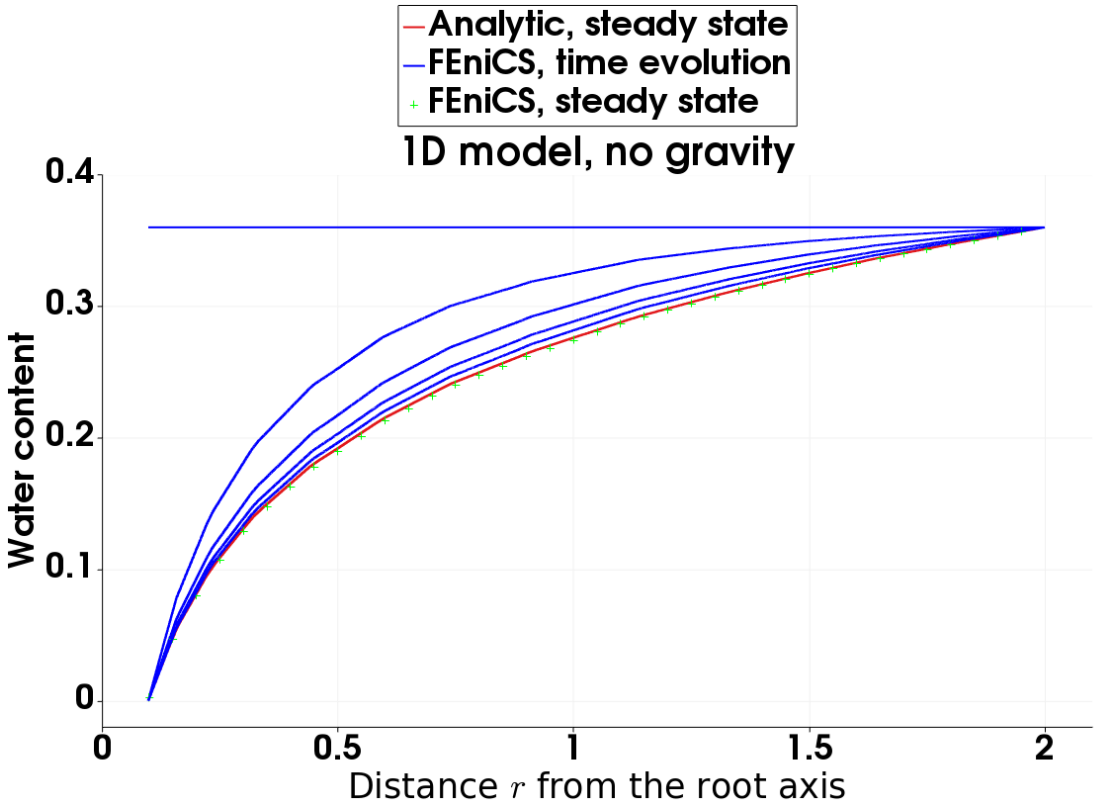


Figure 2.4.: Evolution to the steady state (FEniCS simulation, the linear diffusion equation (60), equipped with the boundary conditions (74), (62), and the initial condition (65)). The parameters are chosen as follows: $D \approx 0.2$, $r_0 = 0.1$, $r_\infty = 2.0$, $\Phi_{ff} = 0.36$ and $dt = 2.0$. Comparison with the analytic steady-state solution (in red) is also shown.

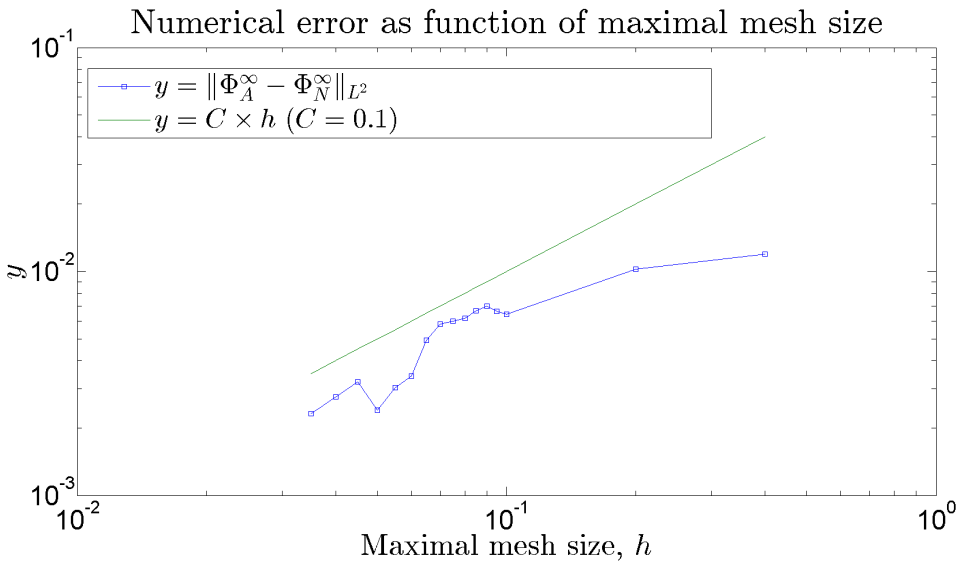


Figure 2.5.: The log-log plot of the L^2 norm of $\Phi_A^\infty - \Phi_N^\infty$ as a function of the maximal mesh size. FEniCS simulation, Equation (61), equipped with the same boundary conditions and parameters as in Figure 2.4.

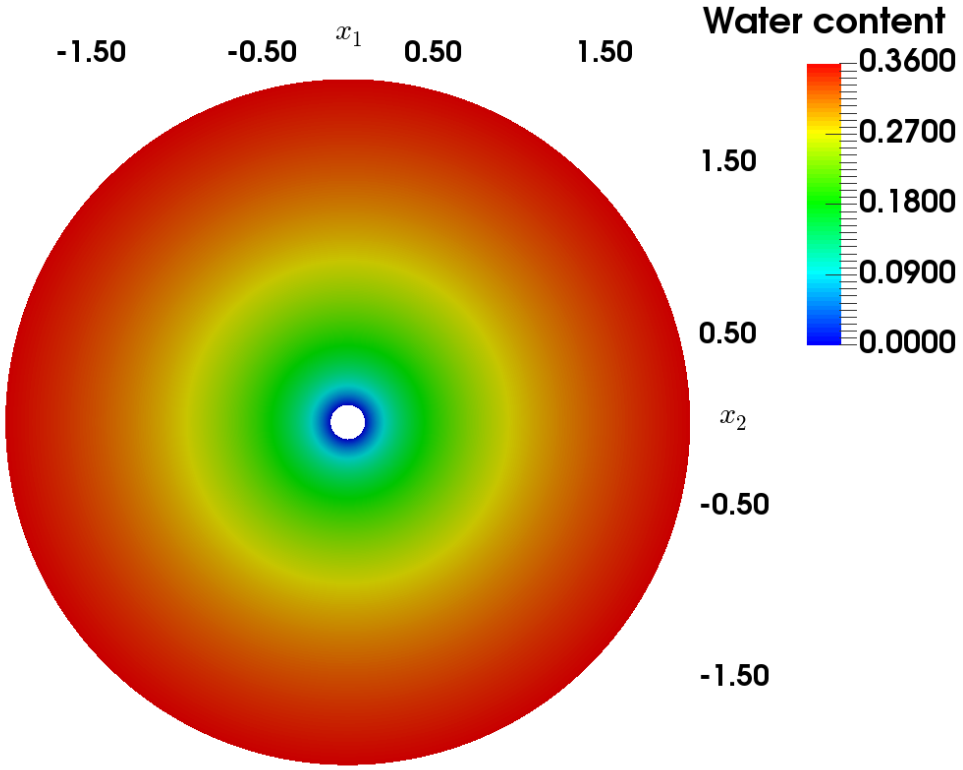


Figure 2.6.: Steady state on the two-dimensional geometry (same problem as in Figure 2.5).

resolution	error
5	0.0316631149109
10	0.0191333066483
20	0.00973923196781
40	0.00422586931327
80	0.00241039446918
160	0.00301086267964
320	0.00333357765744
640	0.0034313164863

Table 2.1.: Numerical error for increasing resolution (same problem as in Figure 2.5).

Doubling this parameter thus (roughly) halves the mesh size [79], and the resulting error (measured as L^2 norm) in the numerical steady-state approximation as function of the resolution parameter is presented in Table 2.1. Even though we observe a decreasing numerical error initially, starting around resolution equal to 100, the error begins to approach a non-zero value (close to 0.003). To confirm this from a different perspective, we fix the resolution parameter (e.g. 50), and increase the degree of Lagrange polynomials. The results summarised in Table 2.2 confirm our conclusions. We see that something is still wrong with our numerics. The reason is that the resolution of the boundary mesh is not sufficient. In our numerical simulations, the outer and inner boundary will always be a polygon (rather than a perfect circle). Interpolating the analytic solution onto such meshes does not result in a homogeneous Dirichlet boundary condition, as illustrated in Figure 2.7 (where we zoom-in on the outer boundary, and adjust the color scales so that we can notice the small changes in the local water content). To improve the accuracy of our method, we impose a separate resolution parameter on the outer and on the root boundary. Having tried different sets of values, we finally let the resolution of the outer and the root boundary be $10-$times higher than that for the domain itself. The results are shown in Table 2.3.

order	error
1	0.00323603774225
2	0.00341211591267
3	0.00345552072241
4	0.00346323948502
5	0.00346602628248
6	0.00346719918931
7	0.00346774874067
8	0.00346803997911

Table 2.2.: Numerical error for the increasing polynomial degree (same problem as in Figure 2.5).

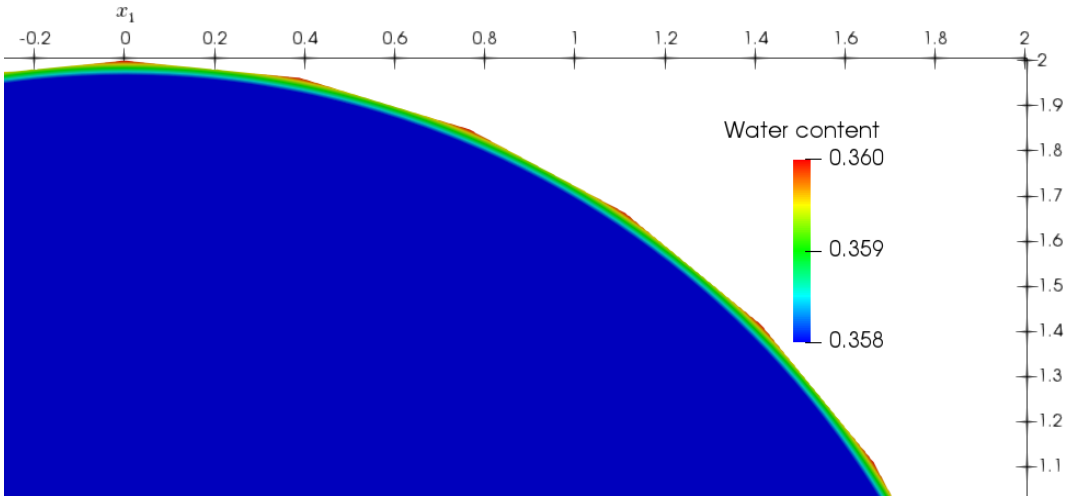


Figure 2.7.: Analytic solution (75) does not satisfy the outer boundary condition (62) on the meshed domain exactly. The parameters are: $r_0 = 0.1$, $r_\infty = 2.0$, $D \approx 0.2$ and $\Phi_{ff} = 0.36$.

resolution	error
5	0.0324269777621
10	0.0211199863018
20	0.0110826434076
40	0.0046261632921
80	0.0016982457868
160	0.0005344314533
320	0.0001549112265
640	0.0000411403528

Table 2.3.: Numerical error for an increasing resolution with a refined boundary mesh (same problem as in Figure 2.5).

We see that the error is decreasing with the increasing resolution. Another way of checking the accuracy of our method is based on the divergence theorem [130]. In our case, this gives:

$$\int_{\Omega} \frac{\partial \theta}{\partial t} dx = \int_{\Omega} \nabla \cdot (D \nabla \theta) dx = \int_{\partial \Omega} D \nabla \theta \cdot \hat{\boldsymbol{n}} dS =$$

$$\int_{x_3=0} D \nabla \theta \cdot \hat{\boldsymbol{n}} dS + \int_{x_3=h_0} D \nabla \theta \cdot \hat{\boldsymbol{n}} dS + \int_{r=r_0} D \nabla \theta \cdot \hat{\boldsymbol{n}} dS + \int_{r=r_\infty} D \nabla \theta \cdot \hat{\boldsymbol{n}} dS =$$

$$\int_{r=r_0} D \nabla \theta \cdot \hat{\boldsymbol{n}} dS + \int_{r=r_\infty} D \nabla \theta \cdot \hat{\boldsymbol{n}} dS,$$

due to the zero-flux boundary condition applied at the top and bottom part of the boundary ($\hat{\boldsymbol{n}}$ is the outward pointing unit normal vector as usual). As time goes to infinity, the system settles towards the steady state, which means that $\int_{\Omega} \frac{\partial \theta}{\partial t} dx = 0$. Therefore:

$$\int_{r=r_0} D \nabla \theta \cdot \hat{\boldsymbol{n}} dS = - \int_{r=r_\infty} D \nabla \theta \cdot \hat{\boldsymbol{n}} dS.$$

In other words, at the steady state, the total flux into the root equals the total flux into the domain coming from the far-field. Assuming constant D, this yields:

$$- \int_{r=r_0} \nabla \theta \cdot \hat{\boldsymbol{n}} dS = \int_{r=r_\infty} \nabla \theta \cdot \hat{\boldsymbol{n}} dS. \tag{76}$$

resolution	$-\int_{r=r_0} \nabla\theta \cdot \hat{\boldsymbol{n}} dS$	$\int_{r=r_\infty} \nabla\theta \cdot \hat{\boldsymbol{n}} dS$
5	0.710411615882	0.921894446094
10	0.736475128648	0.833853802836
20	0.743890065365	0.791861248044
40	0.747775504761	0.772364015175
80	0.750742342397	0.763025266518
160	0.752596353888	0.758659771464
320	0.753670590672	0.756725008428
640	0.754329464734	0.755859509199

Table 2.4.: Comparison of the two integrals from Equation (76) for an increasing resolution (same problem as in Figure 2.5).

We now check if this condition holds. Using the refined mesh at the root and the outer part of the boundary in the two-dimensional simulation, we increased the overall domain resolution, and obtained the results summarised in Table 2.4. Having done that, we fixed the resolution (50), and increasing the polynomial degree we obtained results shown in Table 2.5. We see that both approaches (increasing the mesh resolution as well as increasing the polynomial degree) lead to the same result:

$$-\int_{r=r_0} \nabla\theta \cdot \hat{\boldsymbol{n}} dS \approx 0.755.$$

It seems that refining the mesh on the boundary helps the accuracy of our numerics. Keeping this in mind, we go back to the three-dimensional simulations, and impose a (5 times) smaller maximal mesh size on the root and the outer boundary surfaces. The log-log plot of the error is shown in Figure 2.8. The jumps, that we observed in Figure 2.5, are smoothed out, and the overall behaviour resembles the $O(h)$ line more closely.

Keeping the polynomial degree 1, we now compare the fluxes from Equation (76) for a decreasing maximal mesh size. The results are found in Figure 2.9 and they suggest that the two integrals converge to the same value for $h \to 0$ as expected.

degree	$-\int_{r=r_0} \nabla\theta \cdot \hat{\mathbf{n}} dS$	$\int_{r=r_\infty} \nabla\theta \cdot \hat{\mathbf{n}} dS$
1	0.74915178333	0.768723608931
2	0.75472495996	0.755288745268
3	0.754728135741	0.755369810449
4	0.754745764992	0.755352038755
5	0.754802906976	0.755297216986
6	0.754869410283	0.755234096992
7	0.754920029591	0.755185979386
8	0.754951670126	0.755155634977
9	0.754971969202	0.75513612266
10	0.754986760251	0.755122043719

Table 2.5.: Comparison of the two integrals from Equation (76) for an increasing polynomial degree (same problem as in Figure 2.5).

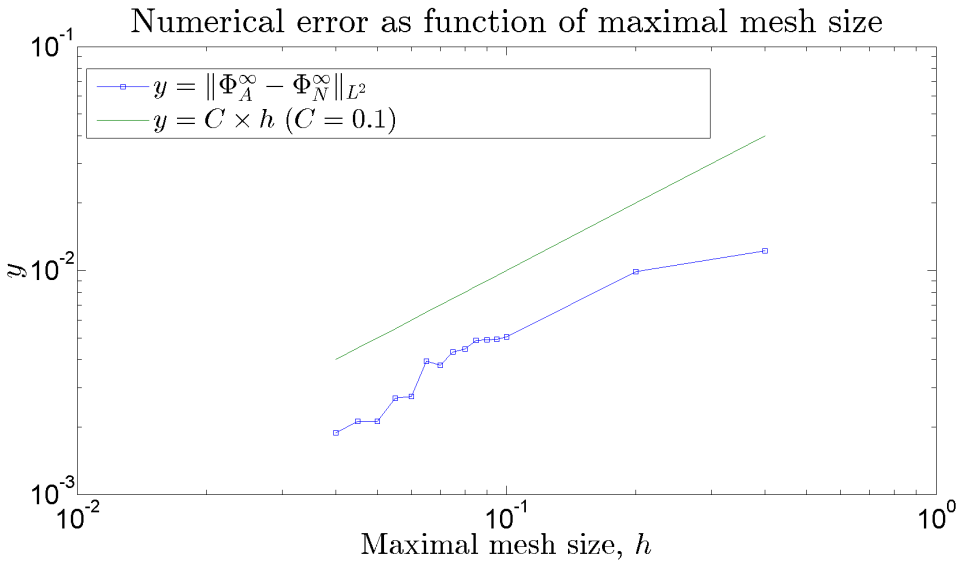


Figure 2.8.: Log-log plot of the L^2 norm of $\Phi_A^\infty - \Phi_N^\infty$ as a function of the maximal mesh size. Mesh refined on the boundaries. Three-dimensional simulations (same problem as in Figure 2.5).

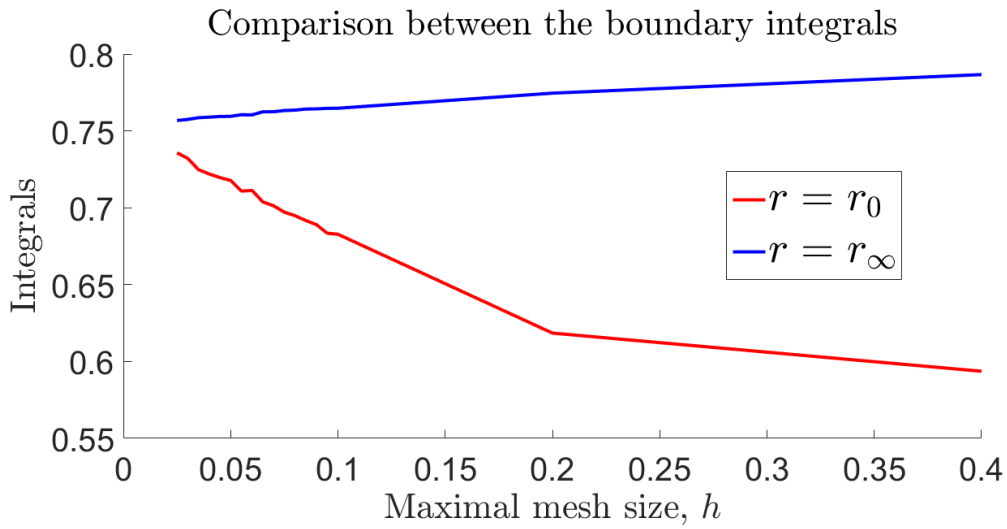


Figure 2.9.: Comparison of the integrals from Equation (76) at the steady state for a decreasing maximal mesh size (same problem as in Figure 2.5). Three-dimensional simulations.

As the final check, we fix the maximal mesh size ($h = 0.4$), and vary the polynomial degree d. Table 2.6 shows the results, and we see that the difference between the integrals decreases with the increased order of polynomials.

2.5.2 *Linear advection-diffusion equation*

We now study Equation (45). We impose the zero-flux boundary conditions at the top and the bottom part of the boundary (Equation (49)), the Dirichlet condition (47) at the outer boundary, and the Dirichlet condition (20) at the root surface. We choose a constant initial condition:

$$\theta(t = 0, \boldsymbol{x}) = \theta_{ff} = 0.25. \tag{77}$$

This way, the initial and the boundary conditions are independent of the azimuthal angle φ, and this yields effectively a two-dimensional model (the solution only depends on the polar radius r and the depth x_3). To keep the model linear in this section, we assume a constant diffusivity D (i.e. independent of the water content θ), and the conductivity function $k(\theta)$ is assumed to be a linear function of the local water content, i.e. $k(\theta) = K\theta$.

degree	$-\int_{r=r_0} \nabla\theta \cdot \hat{\mathbf{n}} dS$	$\int_{r=r_\infty} \nabla\theta \cdot \hat{\mathbf{n}} dS$	$\int_{r=r_\infty} \nabla\theta \cdot \hat{\mathbf{n}} dS + \int_{r=r_0} \nabla\theta \cdot \hat{\mathbf{n}} dS$
1	0.687289349	0.784050304	0.096760955
2	0.746815162	0.754760325	0.007945163
3	0.750249953	0.754959199	0.004709246
4	0.751066678	0.754934729	0.003868051
5	0.752019434	0.754735436	0.002716002
6	0.752689788	0.754617198	0.001927410

Table 2.6.: Comparison of the two integrals from Equation (76) for an increasing polynomial degree (same problem as in Figure 2.5). Three-dimensional simulations.

Analytical solution of the steady-state problem

We first study the steady-state problem

$$0 = \nabla \cdot \left\{ D\nabla\theta^\infty - K\theta^\infty \nabla x_3 \right\} = \frac{D}{r}\frac{\partial}{\partial r}\left(r\frac{\partial \theta^\infty}{\partial t} \right) + D\frac{\partial^2 \theta^\infty}{\partial x_3^2} - K\frac{\partial \theta^\infty}{\partial x_3}$$

using analytical approach. We search for the solution in a form:

$$\theta^\infty = \theta_1(r) + \theta_2(r, x_3),$$

where we define $\theta_1(r) = \theta_r + (\theta_{ff} - \theta_r)\frac{\ln \frac{r}{r_0}}{\ln \frac{r_\infty}{r_0}}$, so that it satisfies an equation:

$$0 = \nabla \cdot \left\{ D\nabla\theta_1 - K\theta_1 \nabla x_3 \right\}$$

and boundary conditions:

$$\theta_1(r = r_0) = \theta_r \qquad \theta_1(r = r_\infty) = \theta_{ff}.$$

Using separation of variables $\theta_2(r, x_3) = R(r)Z(x_3)$, we get:

$$\frac{\frac{K}{D}Z' - Z''}{Z} = \frac{R'' + \frac{1}{r}R'}{R} = -\lambda. \tag{78}$$

For $R(r)$, this gives Equation (70), now equipped with boundary conditions:

$$R(r_0) = R(r_\infty) = 0. \tag{79}$$

Following similar reasoning as in Section 2.5.1, we get that only $\lambda > 0$ are admissible, and writing $\lambda = \mu^2$, we can write a general solution as:

$$R(r) = AJ_0(\mu r) + BY_0(\mu r).$$

The boundary conditions (79) imply:

$$0 = AJ_0(\mu r_0) + BY_0(\mu r_0) \quad \text{and} \quad 0 = AJ_0(\mu r_0) + BY_0(\mu r_0),$$

and this system allows a nontrivial solution only if:

$$J_0(\mu r_0)Y_0(\mu r_\infty) - J_0(\mu r_\infty)Y_0(\mu r_0) = 0.$$

The Sturm-Liouville theory then again gives a sequence $\{\lambda_k\}_{k=1}^{\infty}$, with $\lambda_k \to \infty$ as $k \to \infty$. Finally, using the boundary condition at $r = r_0$, we get a sequence of eigenfunctions (mutually orthogonal with weight r) corresponding to these eigenvalues:

$$R_k(r) = A_k\left\{J_0(\sqrt{\lambda_k}r) - \gamma_k Y_0(\sqrt{\lambda_k}r)\right\},$$

where $\gamma_k = \frac{J_0(\sqrt{\lambda_k}r_0)}{Y_0(\sqrt{\lambda_k}r_0)}$. Looking back at the separation of variables (78), we wish to find a sequence $\{Z_k\}_{k=1}^{\infty}$ satisfying:

$$Z_k'' - \frac{K}{D}Z_k' - \lambda_k Z_k = 0.$$

The general solution reads:

$$Z_k(x_3) = C_k e^{\nu_k^1 x_3} + D_k e^{\nu_k^2 x_3},$$

where $\nu_k^{1,2} = \frac{1}{2}\left\{\frac{K}{D} \pm \sqrt{(\frac{K}{D})^2 + 4\lambda_k}\right\}$. Recalling that $K, D, \lambda_k > 0$, we see that the two solutions $\nu_k^{1,2}$ are always real, one of them being positive and another negative. To summarise, we can write our analytical solution as the following series:

$$\theta^{\infty} = \theta_1(r) + \sum_{k=1}^{\infty}\left\{J_0(\sqrt{\lambda_k}r) - \gamma_k Y_0(\sqrt{\lambda_k}r)\right\}\left\{E_k e^{\nu_k^1 x_3} + F_k e^{\nu_k^2 x_3}\right\}, \tag{80}$$

and it remains to determine constants E_k and F_k. To do this, we use the zero-flux boundary conditions at the top and bottom parts of the boundary, which now read:

$$\frac{\partial\theta^{\infty}(x_3 = 0)}{\partial x_3} = \frac{K}{D}\theta^{\infty}(x_3 = 0) \qquad \frac{\partial\theta^{\infty}(x_3 = h_0)}{\partial x_3} = \frac{K}{D}\theta^{\infty}(x_3 = h_0),$$

which using $h_0 = 1$ and Equation (80) give:

$$\sum_{k=1}^{\infty}\Big\{J_0(\sqrt{\lambda_k}r)-\gamma_k Y_0(\sqrt{\lambda_k}r)\Big\}\Big\{E_k\nu_k^1+F_k\nu_k^2\Big\}=$$

$$\frac{K}{D}\left(\theta_1(r)+\sum_{k=1}^{\infty}\Big\{J_0(\sqrt{\lambda_k}r)-\gamma_k Y_0(\sqrt{\lambda_k}r)\Big\}\Big\{E_k+F_k\Big\}\right),$$

and

$$\sum_{k=1}^{\infty}\Big\{J_0(\sqrt{\lambda_k}r)-\gamma_k Y_0(\sqrt{\lambda_k}r)\Big\}\Big\{E_k\nu_k^1e^{\nu_k^1}+F_k\nu_k^2e^{\nu_k^2}\Big\}=$$

$$\frac{K}{D}\left(\theta_1(r)+\sum_{k=1}^{\infty}\Big\{J_0(\sqrt{\lambda_k}r)-\gamma_k Y_0(\sqrt{\lambda_k}r)\Big\}\Big\{E_ke^{\nu_k^1}+F_ke^{\nu_k^2}\Big\}\right).$$

These equations can be rewritten as follows:

$$\sum_{k=1}^{\infty}\Big\{J_0(\sqrt{\lambda_k}r)-\gamma_k Y_0(\sqrt{\lambda_k}r)\Big\}\Big\{E_k\big(\nu_k^1-\frac{K}{D}\big)+F_k\big(\nu_k^2-\frac{K}{D}\big)\Big\}=\frac{K}{D}\theta_1(r), \quad (81)$$

$$\sum_{k=1}^{\infty}\Big\{J_0(\sqrt{\lambda_k}r)-\gamma_k Y_0(\sqrt{\lambda_k}r)\Big\}\Big\{E_k\big(\nu_k^1-\frac{K}{D}\big)e^{\nu_k^1}+F_k\big(\nu_k^2-\frac{K}{D}\big)e^{\nu_k^2}\Big\}=\frac{K}{D}\theta_1(r). \quad (82)$$

Multiplying both equations by $r\Big\{J_0(\sqrt{\lambda_i}r)-\gamma_i Y_0(\sqrt{\lambda_i}r)\Big\}$, integrating over (r_0, r_∞), and using the orthogonality of eigenfunctions, we get:

$$\Big\{E_i\big(\nu_i^1-\frac{K}{D}\big)+F_i\big(\nu_i^2-\frac{K}{D}\big)\Big\}\int_{r_0}^{r_\infty} r\big(J_0(\sqrt{\lambda_i}r)-\gamma_i Y_0(\sqrt{\lambda_i}r)\big)^2dr=$$

$$\frac{K}{D}\int_{r_0}^{r_\infty} r\theta_1(r)\big(J_0(\sqrt{\lambda_i}r)-\gamma_i Y_0(\sqrt{\lambda_i}r)\big)dr,$$

$$\Big\{E_ie^{\nu_i^1}\big(\nu_i^1-\frac{K}{D}\big)+F_ie^{\nu_i^2}\big(\nu_i^2-\frac{K}{D}\big)\Big\}\int_{r_0}^{r_\infty} r\big(J_0(\sqrt{\lambda_i}r)-\gamma_i Y_0(\sqrt{\lambda_i}r)\big)^2dr=$$

$$\frac{K}{D}\int_{r_0}^{r_\infty} r\theta_1(r)\big(J_0(\sqrt{\lambda_i}r)-\gamma_i Y_0(\sqrt{\lambda_i}r)\big)dr.$$

Denoting:

$$\delta_i=\frac{\frac{K}{D}\int_{r_0}^{r_\infty} r\theta_1(r)\big(J_0(\sqrt{\lambda_i}r)-\gamma_i Y_0(\sqrt{\lambda_i}r)\big)dr}{\int_{r_0}^{r_\infty} r\big(J_0(\sqrt{\lambda_i}r)-\gamma_i Y_0(\sqrt{\lambda_i}r)\big)^2dr},$$

we can write this system of equations as:

$$E_i(\nu_i^1 - \frac{K}{D}) + F_i(\nu_i^2 - \frac{K}{D}) = \delta_i \tag{83}$$

$$E_i e^{\nu_i^1}(\nu_i^1 - \frac{K}{D}) + F_i e^{\nu_i^2}(\nu_i^2 - \frac{K}{D}) = \delta_i. \tag{84}$$

Multiplying Equation (83) by $e^{\nu_i^1}$, and subtracting Equation (84) from the result leads to:

$$F_i = \frac{\delta_i(e^{\nu_i^1} - 1)}{(\nu_i^2 - \frac{K}{D})(e^{\nu_i^1} - e^{\nu_i^2})}.$$

Similarly, multiplying Equation (83) by $e^{\nu_i^2}$, and subtracting Equation (84) from the result leads to:

$$E_i = \frac{\delta_i(e^{\nu_i^2} - 1)}{(\nu_i^1 - \frac{K}{D})(e^{\nu_i^2} - e^{\nu_i^1})},$$

which completes our task of determining the constants.

Numerical solution - convergence to steady state

We see that finding the steady state analytically is rather cumbersome in this case, and that the solution is not very insightful. Furthermore, adding time dependency only adds to the complexity of the problem. As in Section 2.5.1, we therefore solve this problem numerically. We start with its weak formulation (58). Equation (58) becomes:

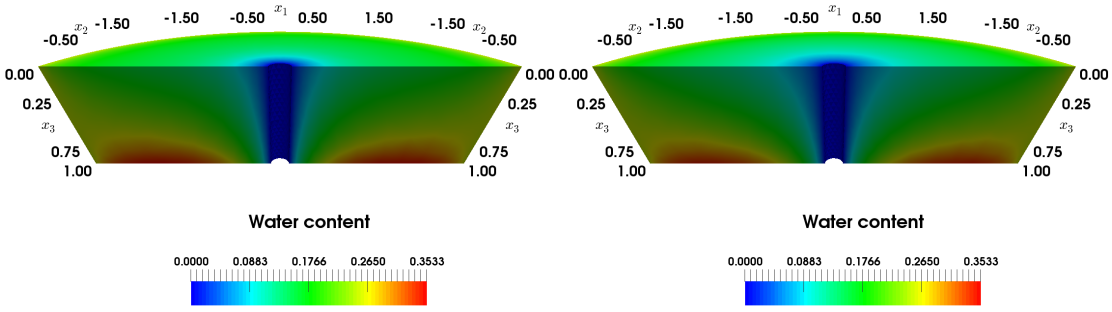
$$\int_\Omega \theta^n v dx - \delta t \int_{\partial\Omega} v(D\nabla\theta^n - K\theta^n \nabla x_3) \cdot \hat{\boldsymbol{n}} dS +$$

$$\delta t \int_\Omega \{D\nabla\theta^n - K\theta^n \nabla x_3\} \cdot \nabla v dx = \int_\Omega \theta^{n-1} v dx$$

Using the boundary conditions as described in Section 2.5.2, we get:

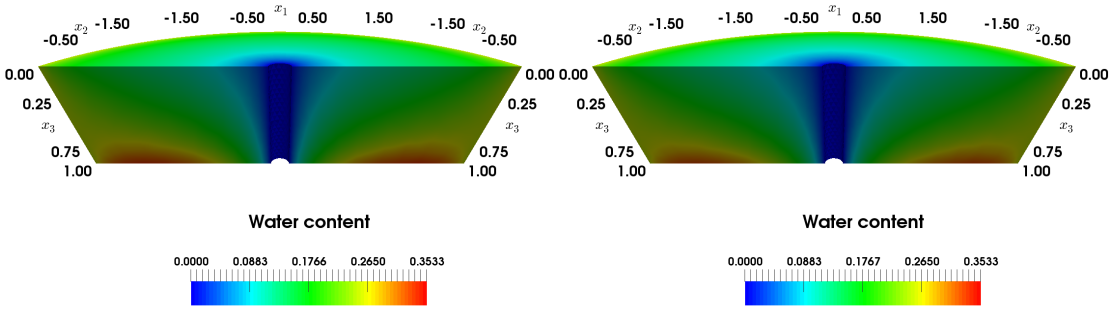
$$\int_\Omega \theta^n v dx + \delta t \int_\Omega \{D\nabla\theta^n - K\theta^n \nabla x_3\} \cdot \nabla v dx = \int_\Omega \theta^{n-1} v dx.$$

The time evolution (using $\theta(t = 0, \boldsymbol{x}) = \theta_{ff} = 0.25$) and the steady state (all obtained in FEniCS) are shown in Figure 2.10.



(a) Time=0.3

(b) Time=0.6



(c) Time=0.9

(d) Steady state.

Figure 2.10.: Time evolution to the steady state in FEniCS: Equation (45), equipped with the initial condition (77), and the boundary conditions (49), (47) and (20). The parameters are chosen as follows: $\theta_r = 0.0$, $D = 1.0$, $K = 1.0$ and $h_0 = 1.0$. The maximal mesh size is 0.4. The polynomial degree is 1.

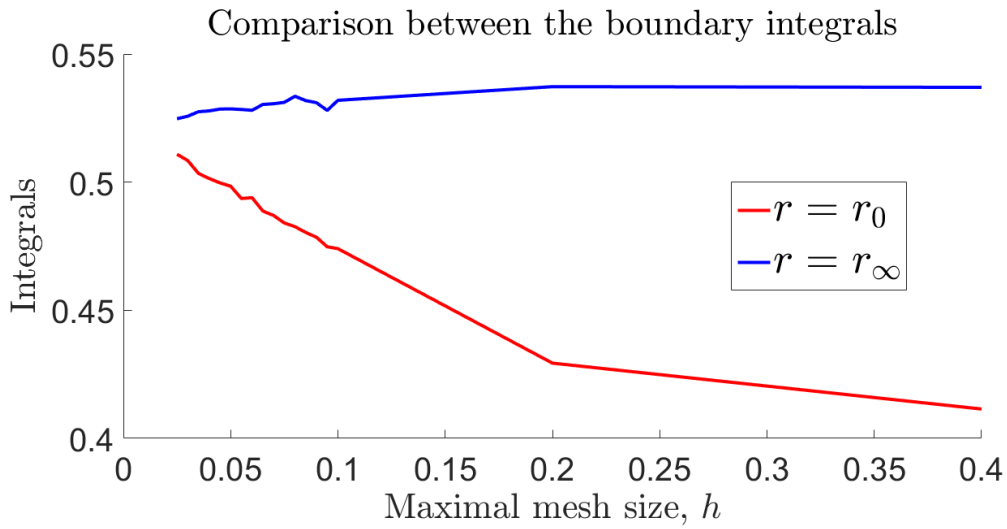


Figure 2.11.: Comparison of the integrals from Equation (76) at the steady state for a decreasing maximal mesh size (same problem as summarised in the caption for Figure 2.10).

The advection term pulls water down the soil profile, and thus the soil regions close to $x_3 = h_0 = 1.0$ are wetter compared to those close to $x_3 = 0.0$. As before, we compare the boundary integrals resulting from the divergence theorem (applied at the steady state). In the case of the linear model with advection, we get:

$$\int_{\Omega} \frac{\partial \theta}{\partial t} dx = \int_{\Omega} \nabla \cdot \{D\nabla\theta - K\theta\nabla x_3\} dx =$$

$$\int_{\partial\Omega} \{D\nabla\theta - K\theta\nabla x_3\} \cdot \hat{\boldsymbol{n}} dS = \int_{x_3=0} \{D\nabla\theta - K\theta\nabla x_3\} \cdot \hat{\boldsymbol{n}} dS +$$

$$\int_{x_3=h_0} \{D\nabla\theta - K\theta\nabla x_3\} \cdot \hat{\boldsymbol{n}} dS + \int_{r=r_0} \{D\nabla\theta - K\theta\nabla x_3\} \cdot \hat{\boldsymbol{n}} dS +$$

$$\int_{r=r_\infty} \{D\nabla\theta - K\theta\nabla x_3\} \cdot \hat{\boldsymbol{n}} dS = \int_{r=r_0} D\nabla\theta \cdot \hat{\boldsymbol{n}} dS + \int_{r=r_\infty} D\nabla\theta \cdot \hat{\boldsymbol{n}} dS$$

due to the zero-flux boundary conditions applied at the upper and the lower parts of the boundary, and the fact that the vectors $\hat{\boldsymbol{n}}$ and ∇x_3 are perpendicular at the root surface as well as at the outer boundary. Thus, at steady state, we again recover Equation (76), and the results for a decreasing maximal mesh size are presented in Figure 2.11. The small jumps from the previous section are slightly more pronounced here. Keeping the maximal mesh size fixed (0.4)

degree	$-\int_{r=r_0} \nabla\theta \cdot \hat{\mathbf{n}} dS$	$\int_{r=r_\infty} \nabla\theta \cdot \hat{\mathbf{n}} dS$	$\int_{r=r_\infty} \nabla\theta \cdot \hat{\mathbf{n}} dS + \int_{r=r_0} \nabla\theta \cdot \hat{\mathbf{n}} dS$
1	0.41145	0.53698	0.12553
2	0.49898	0.51768	0.01870
3	0.51104	0.52173	0.01069
4	0.51375	0.52222	0.00847
5	0.51589	0.52201	0.00612
6	0.51747	0.52194	0.00447

Table 2.7.: Comparison of the two integrals from Equation (76) for the same problem as summarised in the caption for Figure 2.10. Increasing the polynomial degree in the three-dimensional simulations.

and increasing the polynomial degree, we obtain the results summarised in Table 2.7. We see that both procedures (decreasing the maximal mesh size as well as increasing the polynomial degree) lead to approximately the same integral value (≈ 0.52). Therefore, we consider our numerics to be trustworthy.

Comparison of MATLAB and FEniCS results: linear advection-diffusion equation

We implemented the same model in MATLAB (see Appendix *B*). The results are shown in Figure 2.12. To quantify the difference between these solutions, we extract the values of the FEniCS solution at certain points located within a half-plane defined by $x_2 = 0$ and $x_1 > 0$. Then, we interpolate the MATLAB solution onto these points using *interp*2 function (as implemented in MATLAB). The absolute value of the difference between these two-dimensional functions at different time points is shown in Figure 2.13. As expected, there is no difference between the results of the two implementations on the Dirichlet part of the boundary. The biggest errors seem to occur close to the bottom part of the boundary, which is probably linked to the direction of convection in this case.

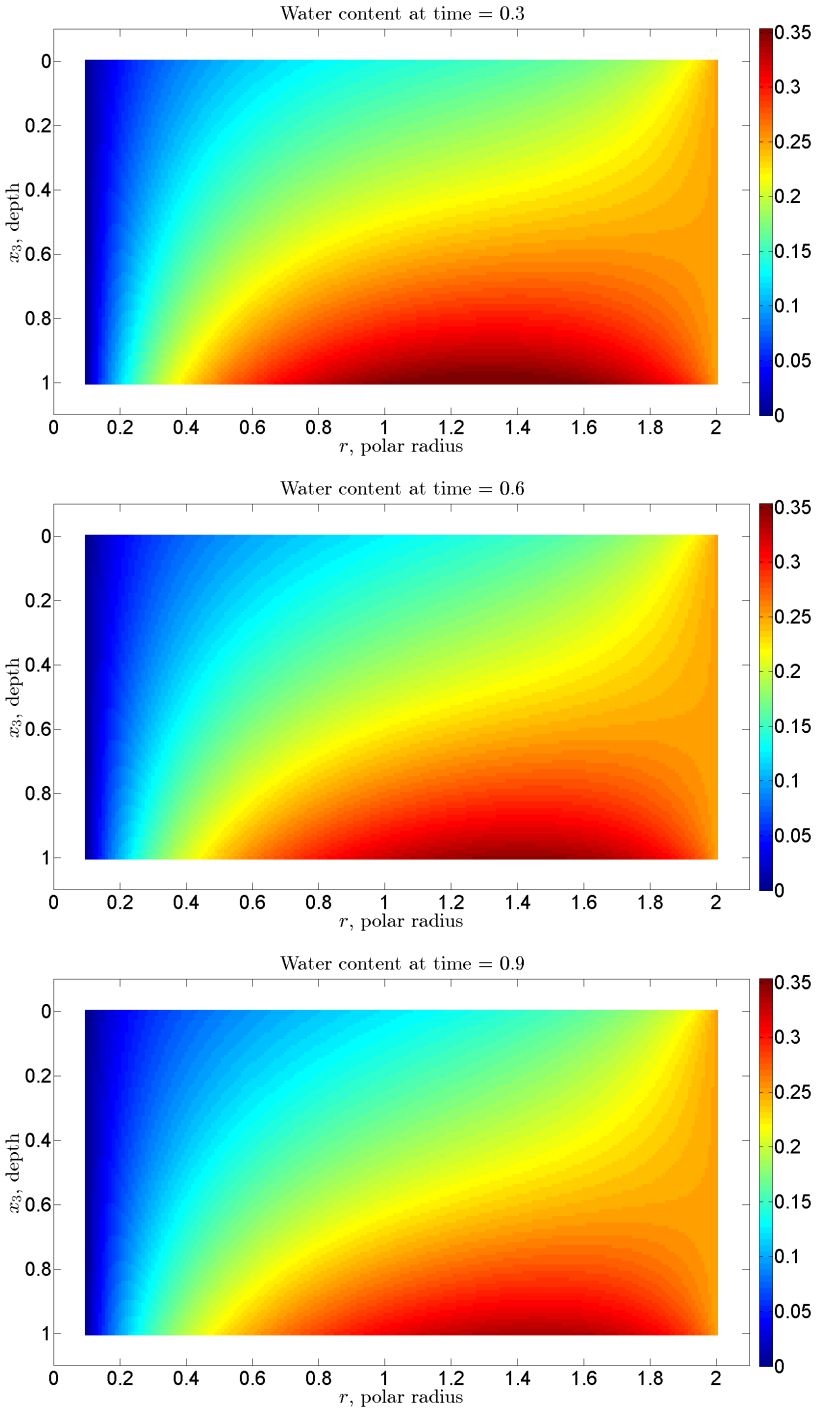


Figure 2.12.: MATLAB simulation: same problem as in Figure 2.10. Colours indicate local water content.

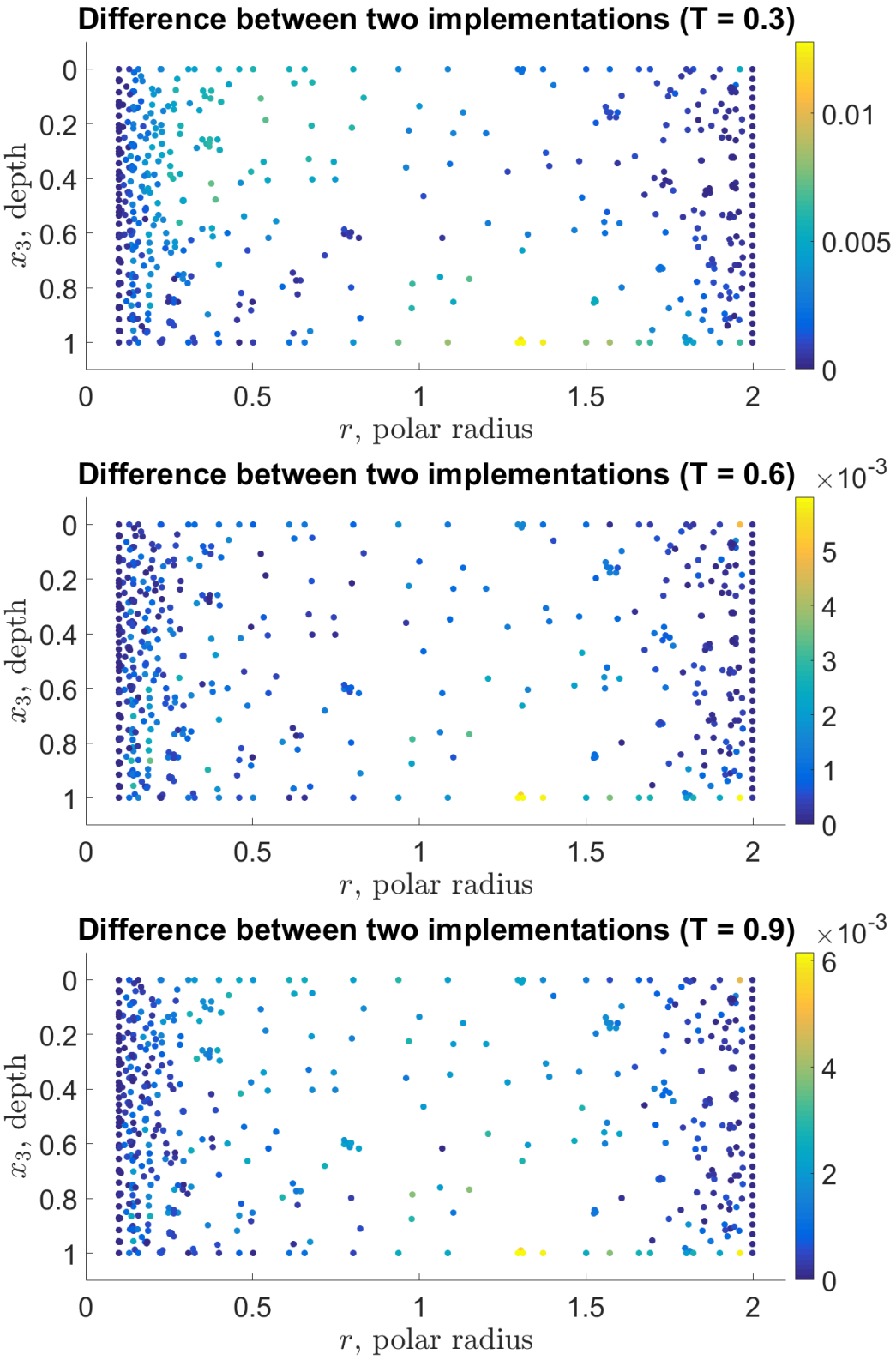


Figure 2.13.: Absolute value of the error between the two implementations (same problem as in Figure 2.10).

These errors are usually below 10^{-2} (with the exception of $T = 0.3$), and might be caused by the different numerical methods used for the computations (FEniCS uses finite element methods whereas in MATLAB, we used a finite difference method), or different mesh sizes. We consider these errors to be small enough for us to proceed towards more realistic problems. From now onwards, we only perform simulations in FEniCS.
Note further, that the comparisons obtained in this section serve only as validations of the FEniCS simulations, and we do not discuss specific parameter values here. The only important thing here was that the parameters were the same for both implementations.

2.6 MORE REALISTIC MODELS

The linear model is usually not an adequate description of water dynamics due to the porous nature of the soil (see Section 1.3.3). According to [114], expressions describing the diffusivity ($D(\theta)$) and the conductivity functions ($k(\theta)$) fall into two categories, both of which have been used frequently in the soil water modelling.
Models belonging to the first category can be solved analytically; this includes the linear models with $D(\theta)$ constant and $k(\theta) = K\theta$ (leading to the linear advection-diffusion equation) as well as Brooks–Corey power function soils (for more details, see [15]), where D and k are power functions of θ (these result from fractal models of the porous structure [114]).
Expressions from the second category are based on more mechanistic assumptions about water dynamics within porous networks. Typically, these models are less amenable to mathematical analysis [114]. The most important member of this class (for the purposes of this thesis) is the van Genuchten (or van Genuchten-Mualem) model. This model was first derived by a soil hydrologist Martinus Th. van Genuchten in [142]. Introducing the dimensionless water content:

$$\Theta = \frac{\theta - \theta_r}{\phi - \theta_r},$$

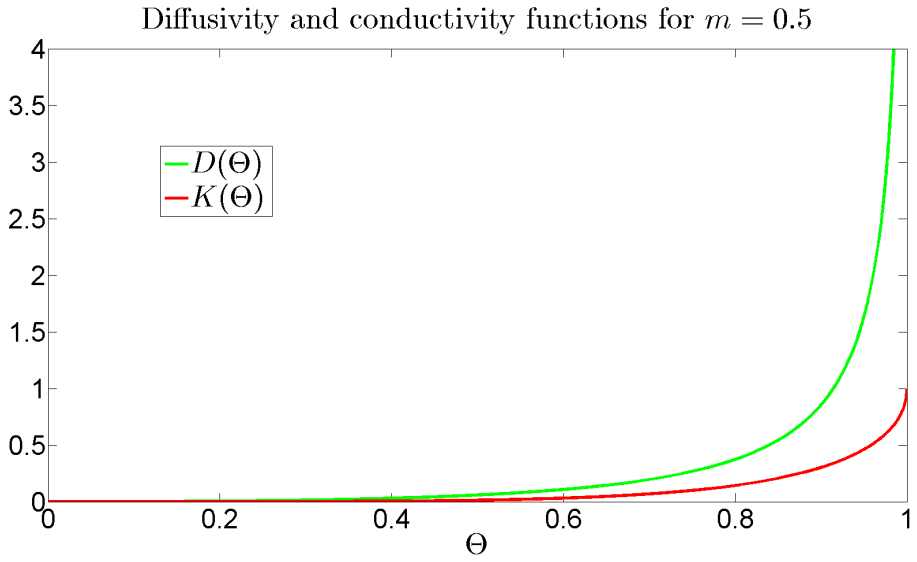


Figure 2.14.: The shape of (van Genuchten) $D(\Theta)$ and $k(\Theta)$ for $m = 0.5$

where ϕ is the soil porosity and θ_r is the residual water content (as introduced in Section 1.3.4), the derived diffusivity function is of a form:

$$D(\Theta) = \Theta^{\frac{1}{2}-\frac{1}{m}}[(1-\Theta^{\frac{1}{m}})^{-m} + (1-\Theta^{\frac{1}{m}})^{m} - 2] \tag{85}$$

and the conductivity function is of a form:

$$k(\Theta) = \Theta^{\frac{1}{2}}[1-(1-\Theta^{\frac{1}{m}})^{m}]^2, \tag{86}$$

where $0 < m < 1$ is an experimentally determined parameter, which varies for different soils (we will mostly use $m = 0.5$, which is a good estimate for a Silt Loam soil [121]; for details and derivation of these formulas, see [142]). In Section 2.6.1, we will briefly study the effect of the parameter m on the mobility of water in the soil. Figure 2.14 shows $D(\Theta)$ and $k(\Theta)$ for $m = 0.5$. Substituting $\Theta = 0$ into $D(\Theta)$ yields the expression of the $0 \times \infty$ type, and as $\lim_{\Theta\to 0} D(\Theta) = 0$, we define $D(0) = 0$. Note further, that $\lim_{\Theta\to 1} D(\Theta) = \infty$.
As discussed in [76], the van Genuchten model is usually found to be in better agreement with experimental data compared to the Brooks-Corey model, even though it is more difficult to approach with mathematical analysis, which is caused by its complicated functional form. Therefore, we will use the van Genuchten expressions from now onwards.
The exact form of the continuity equation in the remainder of this chapter

is taken from [121], where water uptake by a growing branching structure is modelled using a sink term (derived from an explicit root surface boundary condition). The resulting equation states:

$$\phi \frac{\partial S}{\partial t} = \nabla \cdot \left[D_0 D(S) \nabla S - K_s k(S) \hat{\boldsymbol{k}} \right] - F_w \tag{87}$$

where S is the relative water saturation ($S = \frac{\phi_l}{\phi}$ where ϕ_l is the volumetric water fraction, i.e. water content θ; S is identical to the dimensionless water content Θ from [142] provided $\theta_r = 0$), D and k are the functions from the equations (85) and (86), $\hat{\boldsymbol{k}}$ is the downwards pointing unit vector ($(0,0,1)$ in our coordinate system; same as ∇x_3), and F_w is the water sink term [121]. D_0 and K_s are constants dependent on soil parameters in a way detailed in [121] (or [142]). Omitting the sink term, we get:

$$\phi \frac{\partial S}{\partial t} = \nabla \cdot \left[D_0 D(S) \nabla S - K_s k(S) \nabla x_3 \right], \tag{88}$$

which will be our starting point here, and which we will equip with suitable boundary conditions (including the root surface boundary condition).

2.6.1 *Single root: no uptake*

Assume the geometry from Figure 2.1. First, we focus our attention to the water mobility solely, imposing the zero-flux boundary condition:

$$-\left[D_0 D(S) \nabla S - K_s k(S) \nabla x_3 \right] \cdot \hat{\boldsymbol{n}} = 0$$

at all the boundary parts (even at the root-soil interface; i.e. we impose no water uptake). We now introduce the new values of geometric parameters, which will be more closely related to the physical and biological reality.

The cylinder from Figure 2.1 can either represent a single root (here, r_∞ represents a half-distance to the nearest root within the same root system), or it can be thought of as an overall representation of the entire root system under consideration (in which case r_∞ represents a half-distance to the neighbouring plant). We choose the former case here, and impose the zero-flux boundary

Parameter	value	units
ϕ	0.4	-
D_0	432.0	$\mathrm{cm}^2\ \mathrm{d}^{-1}$
K_s	4.96	$\mathrm{cm\ d}^{-1}$
m	0.5	-
r_0	0.01	cm
r_∞	1.0	cm
h_0	50.0	cm

Table 2.8.: The default parameter values for the single root water uptake model. The soil parameters are taken from [142], and the root parameters are approximated from [70] (as discussed in the main text).

condition (46) at $r = r_\infty$ (modelling an intra-plant competition). In dimensional variables, we define the domain as:

$$\Omega = \left\{(x_1, x_2, x_3) \in \mathbb{R}^3, r_0^2 < x_1^2 + x_2^2 < r_\infty^2, 0 < x_3 < h_0\right\}. \tag{89}$$

Parameter values that will be used as default throughout this section for the single root geometry are summarised in Table 2.8. Most of these represent typical biological or physical values for a Silt Loam soil as presented in [142] or [121] (the porosity $\phi = 0.396$ is rounded up to 0.4, $m = 0.51$ is rounded down to 0.5, $D_0 = 0.5 \times 10^{-6}\,\mathrm{m}^2\,\mathrm{s}^{-1} = 432\,\mathrm{cm}^2\,\mathrm{d}^{-1}$, $K_s = 4.96\,\mathrm{cm\,d}^{-1}$). We assume $r_0 = 0.01$ cm (which is a good approximation for wheat or barley; see [70] or [51]), and we set the outer boundary to be at $r_\infty = 1$ cm. The length of the root is chosen to be $h_0 = 50$ cm.

Clearly, some of these parameters vary greatly from one soil type to another (or from one plant species to another). Noting that our modelling can easily be applied to any parameter set, we will from now onwards (for the sake of brevity) mostly use parameters from Table 2.8.

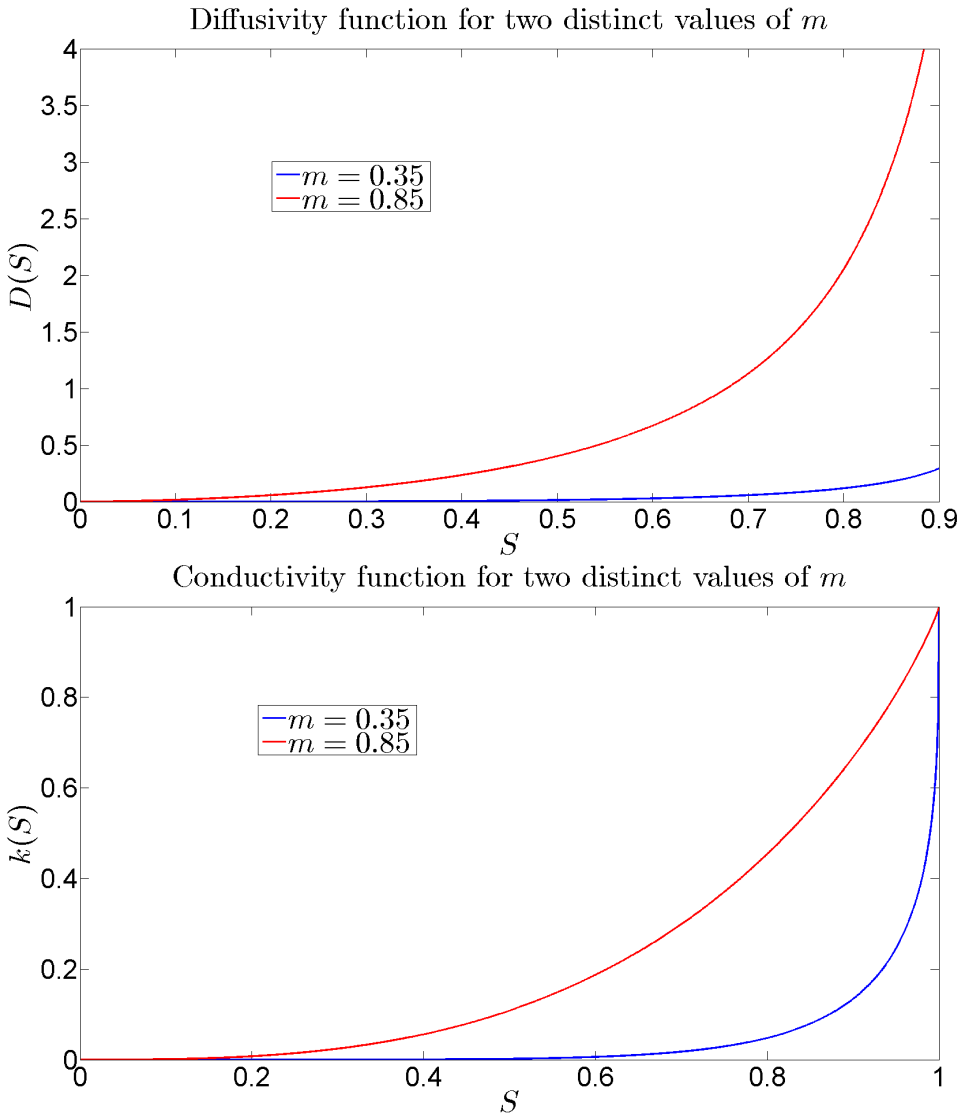


Figure 2.15.: Diffusivity and conductivity functions for different values of m.

Studying the effect of m

As our first numerical check, we study the effect of m on the water mobility in the soil. From [142] and [121], we see that m varies considerably (between 0.15 and 0.90) among different soil types. The $D(S)$ and $k(S)$ functions for two distinct values of m ($m = 0.35$ and $m = 0.85$) are plotted in Figure 2.15. Both $D(S)$ and $k(S)$ are greater for $m = 0.85$ than for $m = 0.35$. This suggests that an overall water mobility in the soil with $m = 0.35$ will be much lower than that in the soil with $m = 0.85$. Imposing a constant initial condition, we numerically simulate these two scenarios to see if the steady state for $m = 0.85$ is reached faster than the one for $m = 0.35$, as predicted from Figure 2.15.

NONDIMENSIONALISATION

We proceed with the nondimensionalisation of this model. Multiplying Equation (88) by $\frac{h_0^2}{D_0}$, we get:

$$\frac{h_0^2\phi}{D_0}\frac{\partial S}{\partial t} = h_0^2\nabla\cdot\left[D(S)\nabla S - \frac{K_s}{D_0}k(S)\nabla x_3\right]. \tag{90}$$

Both sides of the equation are now dimensionless. Therefore, we nondimensionalise time as $t = \frac{h_0^2\phi}{D_0}\tau$ (where τ is dimensionless). Furthermore, we nondimensionalise the space variables as $x_{1,2,3} = h_0\tilde{x}_{1,2,3}$, and get:

$$\frac{\partial S}{\partial \tau} = h_0^2\frac{1}{h_0}\tilde{\nabla}\cdot\left[D(S)\frac{1}{h_0}\tilde{\nabla}S - \frac{K_s}{D_0}k(S)\nabla x_3\right] = \tilde{\nabla}\cdot\left[D(S)\tilde{\nabla}S - \alpha k(S)\nabla x_3\right], \tag{91}$$

where $\alpha = \frac{h_0 K_s}{D_0} > 0$ is a dimensionless parameter[4]. From [121], we get ranges $D_0 \sim (10^{-7} - 10^{-5})\,\mathrm{m^2\,s^{-1}}$, $K_s \sim (10^{-8} - 10^{-4})\,\mathrm{m\,s^{-1}}$, and $h_0 = 0.5\,\mathrm{m}$ gives $\alpha \sim (0.05 - 5)$. Thus, the gravity term can be as important as the diffusion term at this length scale.

The zero-flux boundary conditions become $\hat{\boldsymbol{n}}\cdot\left[-D(S)\tilde{\nabla}S + \alpha k(S)\nabla x_3\right] = 0$ in the new coordinates. To summarise, after dropping tildes and returning to t as the time variable, equation

$$\frac{\partial S}{\partial t} = \nabla\cdot\left[D(S)\nabla S - \alpha k(S)\nabla x_3\right] \tag{92}$$

with $\alpha = \frac{h_0 K_s}{D_0}$, is to be satisfied inside the domain:

$$\Omega = \left\{(x_1, x_2, x_3) \in \mathbb{R}^3, (\frac{r_0}{h_0})^2 < x_1^2 + x_2^2 < (\frac{r_\infty}{h_0})^2, 0 < x_3 < 1\right\},$$

and the zero-flux boundary condition:

$$\hat{\boldsymbol{n}}\cdot\left[-D(S)\nabla S - \alpha k(S)\nabla x_3\right] = 0 \tag{93}$$

is applied at every boundary part.

A slice through the (dimensionless) meshed domain is shown in Figure 2.16. Even such (rather coarsely meshed) domain contains more than two million elements. This is due to the fact that the root radius is much smaller than the half-distance between the roots.

4 Thus, we nondimensionalised space with respect to the length of the root, and we nondimensionalised time with respect to the corresponding timescale of diffusion.

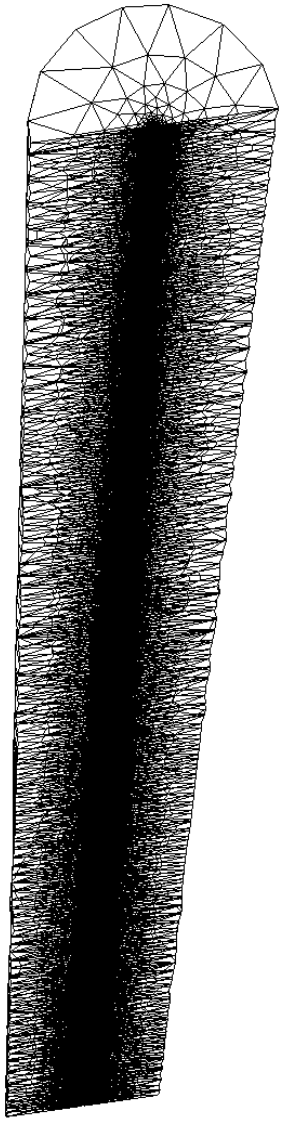


Figure 2.16.: The (three-dimensional) single-root-geometry mesh.

Therefore, the three-dimensional simulations (especially for time-dependent problems with nonlinear diffusion and advection terms) are challenging. However, in this section we will only impose boundary and initial conditions, which do not introduce any variation in the azimuthal angle (φ) direction. Thus, the model becomes (effectively) two-dimensional (in space), with possible dependencies on r and x_3 only. The dimensionless domain becomes:

$$\Omega_{2D} = \left\{(r, x_3) \in \mathbb{R}^2, \frac{r_0}{h_0} < r < \frac{r_\infty}{h_0}, 0 < x_3 < 1\right\} \tag{94}$$

TWO-DIMENSIONAL SIMULATIONS

We simulate time evolution for both $m = 0.35$ and $m = 0.85$, until the difference between the solution at time t and $t + 1$ (measured as the L^∞ norm) is smaller than 10^{-8}. When this happens, we conclude that the steady state has been reached. As an initial condition, we impose:

$$S(t = 0, r, x_3) = 0.5 \tag{95}$$

to avoid the singularities of the van Genuchten model at both $S = 0.0$ and $S = 1.0$. Having performed the computation, we always go back to the water content variable $\theta = \phi \times S$ (using the constant porosity ϕ). The steady-state solution for $m = 0.35$ is shown in Figure 2.17. With our parameter choice, the aspect ratio is very small. Therefore, from now on in this section, when plotting results of the simulations, we stretch the r direction so that the resulting aspect ratio is close to 1.0 (in this case we stretch it 50 times). Thus, we have to keep in mind that the size of the domain in the r direction is actually much smaller than suggested by the figures. Another consequence of the small aspect ratio is that we need to be careful about the accuracy of our numerical approximations. Therefore, further accuracy checks will be provided in this section.

Time evolution for the two values of m can be found in Figures 2.18 and 2.19.

As predicted, the steady state is approached much faster ($t \approx 6.5$) for the $m = 0.85$ case compared to the $m = 0.35$ case ($t \approx 120$).

From now onwards, we fix $m = 0.5$.

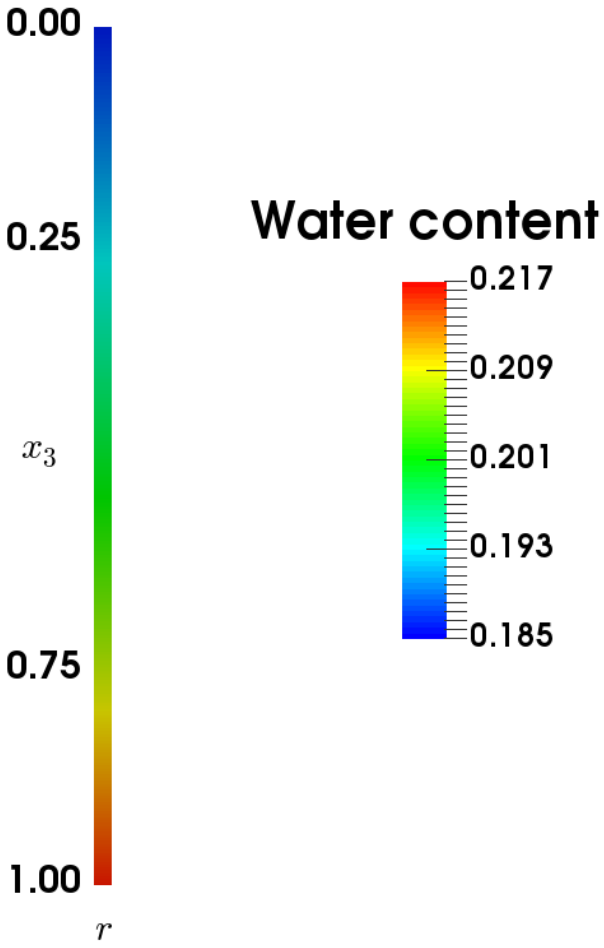
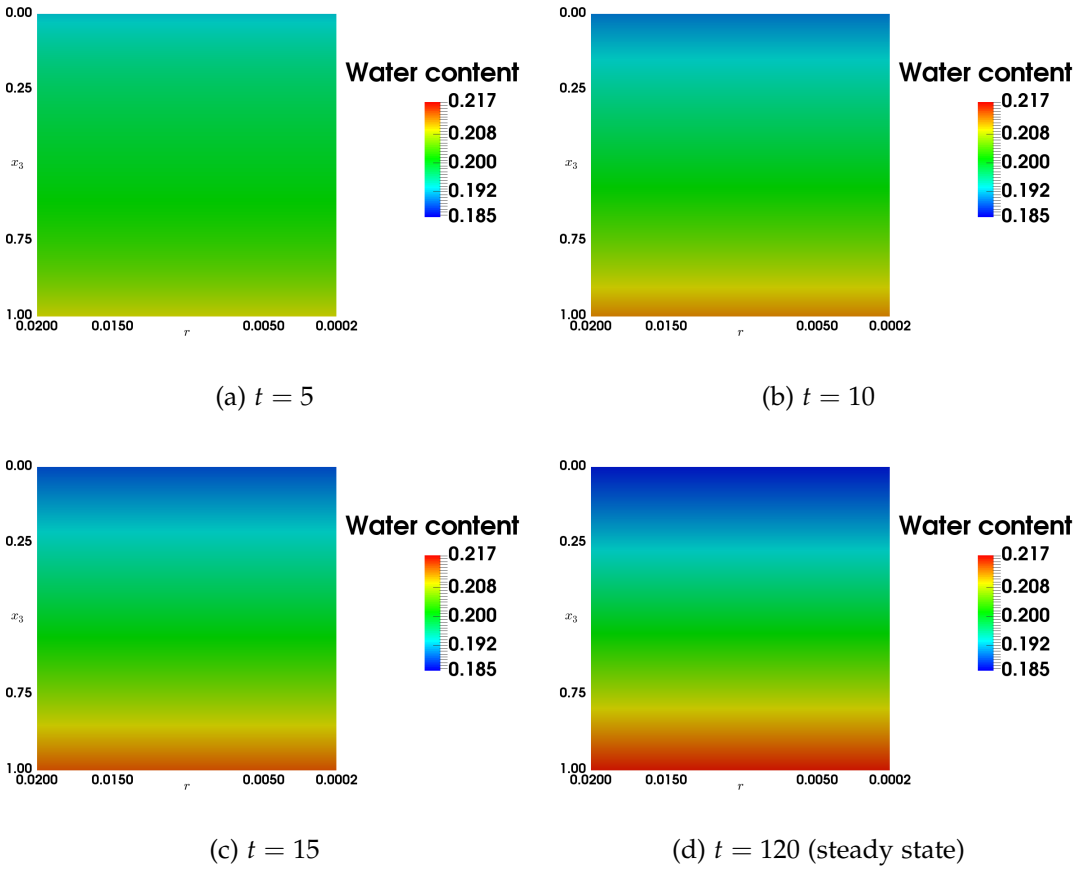


Figure 2.17.: Steady-state water distribution using Equation (92) with van Genuchten nonlinearities $D(S)$ and $k(S)$ (defined in equations (85) and (86)), equipped with the zero-flux boundary condition (93) everywhere. Parameters are summarised in Table 2.8, the only change being $m = 0.35$ here.



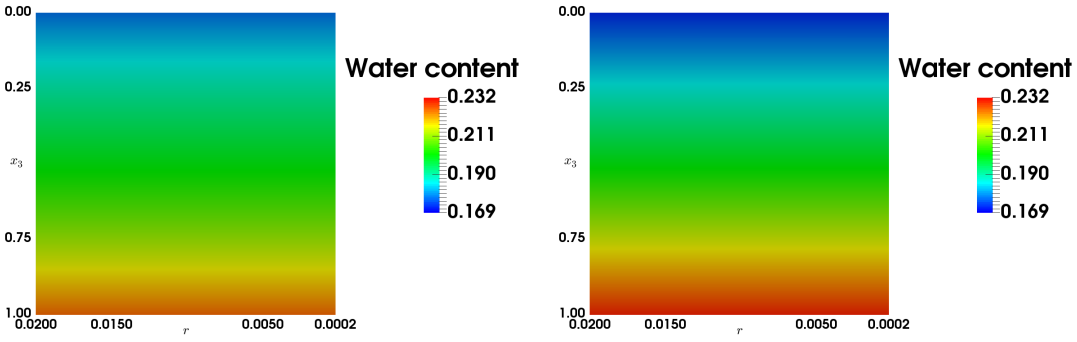
(a) $t = 5$

(b) $t = 10$

(c) $t = 15$

(d) $t = 120$ (steady state)

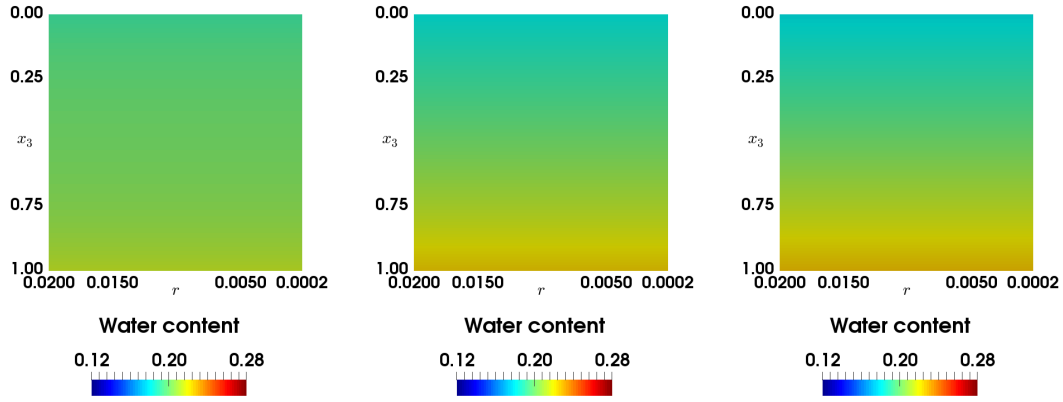
Figure 2.18.: Evolution to the steady state for the same problem as in Figure 2.17, using the initial condition (95). The geometry is stretched in the r direction for visualisation purposes.



(a) $t = 0.5$ (b) $t = 1.0$

(c) $t = 1.5$ (d) $t = 6.5$ (steady state)

Figure 2.19.: Evolution to the steady state for the same problem as in Figure 2.18, except for $m = 0.85$. The geometry is stretched in the r direction for visualisation purposes.



(a) $t = 1$ (b) $t = 5$ (c) $t = 25$

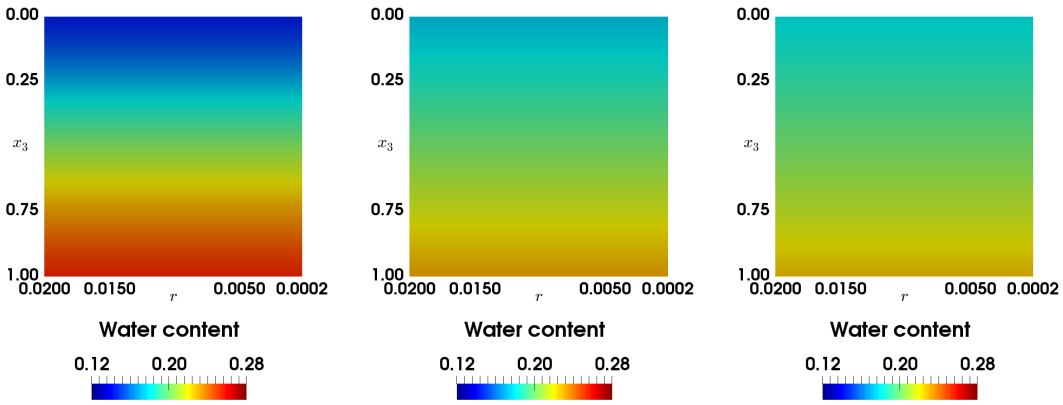
Figure 2.20.: Evolution to the steady state for the same problem as in Figure 2.19, except for $m = 0.5$.

Nonhomogeneous initial conditions

Keeping the zero-flux boundary conditions at all boundary parts, we now solve the same problem with a nonhomogeneous initial condition, so that the total water content in the domain is the same as in the constant-initial-condition case ($S(t, r, x_3) = 0.5$). We impose:

$$S(t = 0, r, x_3) = 0.3 + 0.4 * x_3, \tag{96}$$

and the solutions are compared in Figures 2.20 and 2.21. The colorbar range was changed to $\theta \in (0.12, 0.28)$ (which corresponds to $S \in (0.3, 0.7)$) to accommodate for the changed initial conditions, and we also adjusted the colormap to be able to capture the differences in water content close to $\theta = 0.2$ (corresponding to $S = 0.5$). It seems that both solutions approach the same steady state. To test this hypothesis, we find the two steady states (using the same procedure as described in Section 2.6.1), and their difference is shown in Figure 2.22. The maximal difference seems to be of order 10^{-8}, which is the same as our tolerance for finding the steady states. We conclude that the two steady states obtained using different initial conditions are identical.



(a) $t = 1$ (b) $t = 5$ (c) $t = 25$

Figure 2.21.: Evolution to the steady state for the same problem as in Figure 2.20 using the nonhomogeneous initial condition 96.

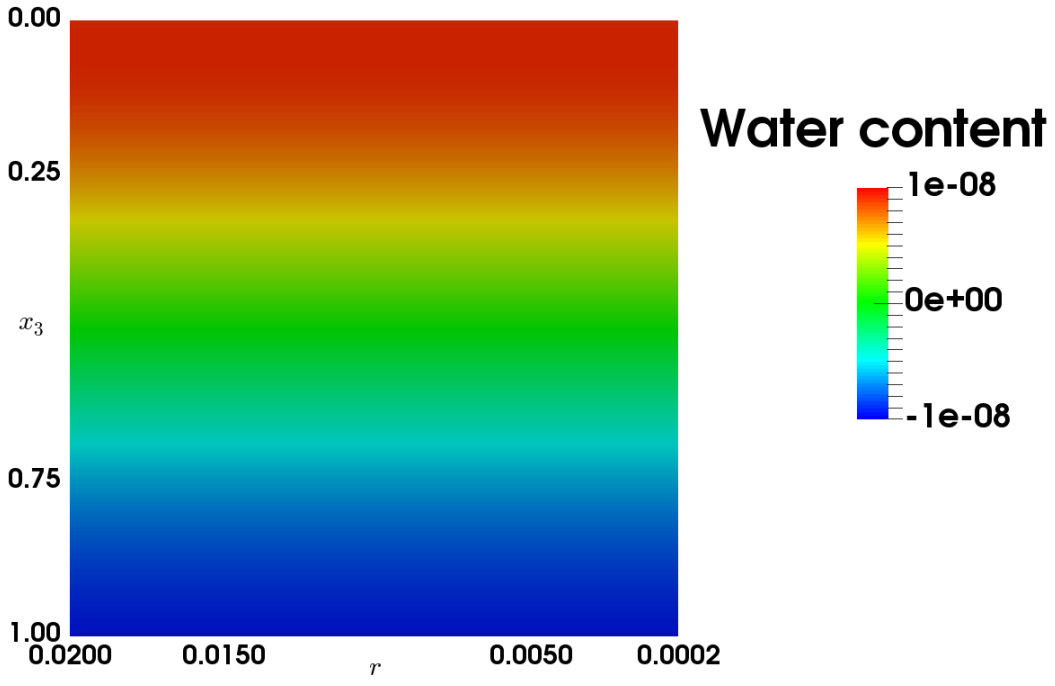


Figure 2.22.: Difference between the two steady states (same problem as in Figure 2.20).

2.6.2 *Water uptake by a single cylindrical root*

Even though the primary purpose of this chapter consists in validating numerical simulations in FEniCS, we now explore the possible implications of the outcomes of such modelling.

Assume the geometry from Figure 2.1, the parameter values from Table 2.8, the dimensionless continuity equation (92), the constant initial condition $S(t = 0, \boldsymbol{x}) = 0.5$, and the zero-flux boundary condition applied at $r = \frac{r_\infty}{h_0}$. Imposing a constant root influx condition (see also Equation (19)):

$$-\left[D_0 D(S)\nabla S - K_s k(S)\nabla x_3\right] \cdot \hat{\boldsymbol{n}} = C_1,$$

we get a dimensionless boundary condition:

$$-\left[D(S)\nabla S - \alpha k(S)\nabla x_3\right] \cdot \hat{\boldsymbol{n}} = \frac{C_1 h_0}{D_0} = \beta \tag{97}$$

applied at $r = \frac{r_0}{h_0}$. As discussed in Section 1.3.4, this condition is valid provided we avoid drought conditions. From [7], we get a possible range for the water uptake rate:

$$C_1 \in (0.1, 2.0)\ \mu\text{g s}^{-1}\ \text{cm}^{-2}$$

for barley. We set $C_1 = 1\ \ \mu\text{g s}^{-1}\ \text{cm}^{-2}$, which is equivalent to:

$$C_1 = 0.0864\ \text{cm d}^{-1}. \tag{98}$$

We further imposed a free-drainage boundary condition (see Equation (50)):

$$-\left[D_0 D(S)\nabla S - K_s k(S)\nabla x_3\right] \cdot \hat{\boldsymbol{n}} = K_s k(S),$$

which is often observed in field studies (see [90] or Section 2.2.2). The dimensionless form of this equation:

$$-\left[D(S)\nabla S - \alpha k(S)\nabla x_3\right] \cdot \hat{\boldsymbol{n}} = \alpha k(S) \tag{99}$$

is applied at $x_3 = 1$. Finally, we impose a constant watering rate:

$$-\left[D_0 D(S)\nabla S - K_s k(S)\nabla x_3\right] \cdot \hat{\boldsymbol{n}} = -C_w,$$

at the top surface, the dimensionless form of which:

$$-\left[D(S)\nabla S - \alpha k(S)\nabla x_3\right] \cdot \hat{\boldsymbol{n}} = -\frac{C_w h_0}{D_0} = -\gamma \tag{100}$$

is applied at $x_3 = 0$. We study the impact of the watering rate C_w on the water dynamics in the soil.

Cylindrical coordinates

With such continuity equation, initial and boundary conditions, our problem becomes effectively two-dimensional - the relative water saturation S is independent of the azimuthal angle φ. Writing Equation (92) in cylindrical coordinates, and realising no dependence on φ, we get:

$$\begin{aligned}\frac{\partial S}{\partial t} =& \frac{1}{r}\frac{\partial}{\partial r}\big(rD(S)\frac{\partial S}{\partial r}\big) + \frac{1}{r^2}\frac{\partial}{\partial \varphi}\big(D(S)\frac{\partial S}{\partial \varphi}\big) + \frac{\partial}{\partial x_3}\big(D(S)\frac{\partial S}{\partial x_3}\big) - \frac{\partial}{\partial x_3}\big(\alpha k(S)\big) = \\ & \big(\frac{\partial}{\partial r}, \frac{\partial}{\partial x_3}\big) \cdot \left[D(S)\big(\frac{\partial S}{\partial r}, \frac{\partial S}{\partial x_3}\big) - \alpha k(S)\big(0,1\big)\right] + \frac{1}{r}D(S)\frac{\partial S}{\partial r}.\end{aligned} \tag{101}$$

The root surface boundary condition (97) in cylindrical coordinates becomes:

$$D(S)\frac{\partial S}{\partial r} = \beta \tag{102}$$

applied at $r = \frac{r_0}{h_0}$, and analogously, we get a zero-flux boundary condition:

$$D(S)\frac{\partial S}{\partial r} = 0 \tag{103}$$

at $r = \frac{r_\infty}{h_0}$. The free-drainage condition (99) states:

$$-D(S)\frac{\partial S}{\partial x_3} + \alpha k(S) = \alpha k(S) \tag{104}$$

at $x_3 = 1$, and similarly, the watering condition (100) (at $x_3 = 0$) can be written as:

$$D(S)\frac{\partial S}{\partial x_3} - \alpha k(S) = -\gamma. \tag{105}$$

Dimensional values of boundary fluxes

For any physically realistic simulation, the relative water saturation must be between 0 and 1. This yields a minimal drainage efflux rate of $K_s k(S = 0) = 0\,\mathrm{cm\,d^{-1}}$, and a maximal drainage efflux rate of $K_s k(S = 1) = K_s = 4.96\,\mathrm{cm\,d^{-1}}$. Integrating over the bottom boundary gives a minimal (overall) drainage efflux of $0\,\mathrm{cm\,d^{-1}}$ and a maximal (overall) drainage efflux of:

$$4.96 \times \pi \times (r_\infty^2 - r_0^2)\,\mathrm{cm^3\,d^{-1}} \approx 15.58\,\mathrm{cm^3\,d^{-1}}.$$

Integrating the root boundary condition gives an overall water influx of:

$$C_1 \times 2\pi \times r_0 \times h_0\,\mathrm{cm^3\,d^{-1}} = 0.0864\pi\,\mathrm{cm^3\,d^{-1}} \approx 0.27\,\mathrm{cm^3\,d^{-1}}. \tag{106}$$

If we choose the watering rate so that the overall influx from the watering is higher than a threshold value:

$$15.85\,\mathrm{cm}^3\,\mathrm{d}^{-1}, \tag{107}$$

which is the sum of the upper bound for the drainage efflux ($15.58\,\mathrm{cm}^3\,\mathrm{d}^{-1}$) and the root influx ($0.27\,\mathrm{cm}^3\,\mathrm{d}^{-1}$), then we expect the overall water content to increase without bounds. Thus, the simulated values of relative water saturation are expected to approach full saturation $S = 1$ in finite time, and the simulation will eventually crash due to the singularity of the diffusivity function $D(S)$ at $S = 1$. The choice of $C_w = 6\,\mathrm{cm}\,\mathrm{d}^{-1}$ leads to an overall watering influx of:

$$C_w \times \pi \times (1 - 0.0001)\,\mathrm{cm}^3\,\mathrm{d}^{-1} \approx 18.85\,\mathrm{cm}^3\,\mathrm{d}^{-1},$$

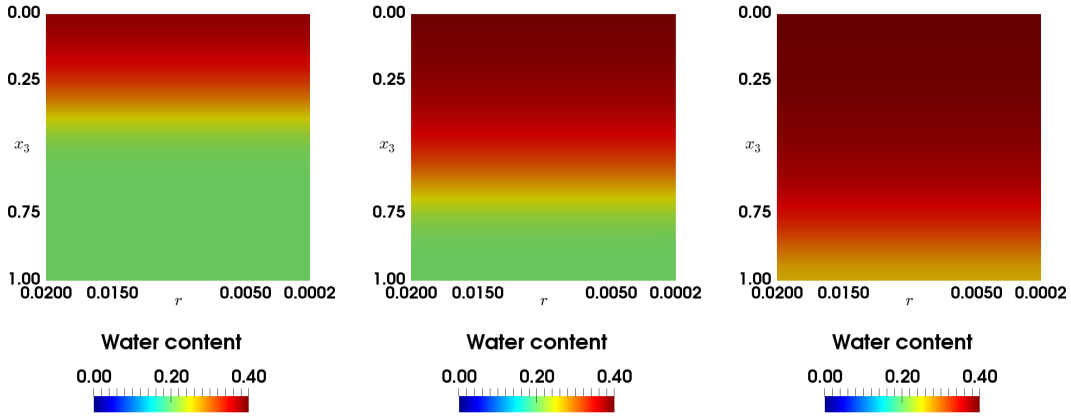
which is higher than the threshold value (107). With $C_w = 6\,\mathrm{cm}\,\mathrm{d}^{-1}$, the simulation crashes at $t \approx 0.73$, and the situation preceding this moment is shown in Figure 2.23. In reality, we would observe surface ponding [121]. On the other hand, $C_w = 4\,\mathrm{cm}\,\mathrm{d}^{-1}$ yields an overall watering influx of approximately $12.57\,\mathrm{cm}^3\,\mathrm{d}^{-1}$ which is below the threshold value (107). As shown in Figure 2.24, the time evolution is similar, and we again approach the full-saturation conditions. However, the simulation does not crash, and eventually (at $t \approx 2.39$), we reach a steady state, which is shown in Figure 2.25.

Dimensionless flux balance

Once we have reached the steady state, we can check whether the integrals resulting from the divergence theorem balance each other out. To be precise, we integrate the steady state version of Equation (101):

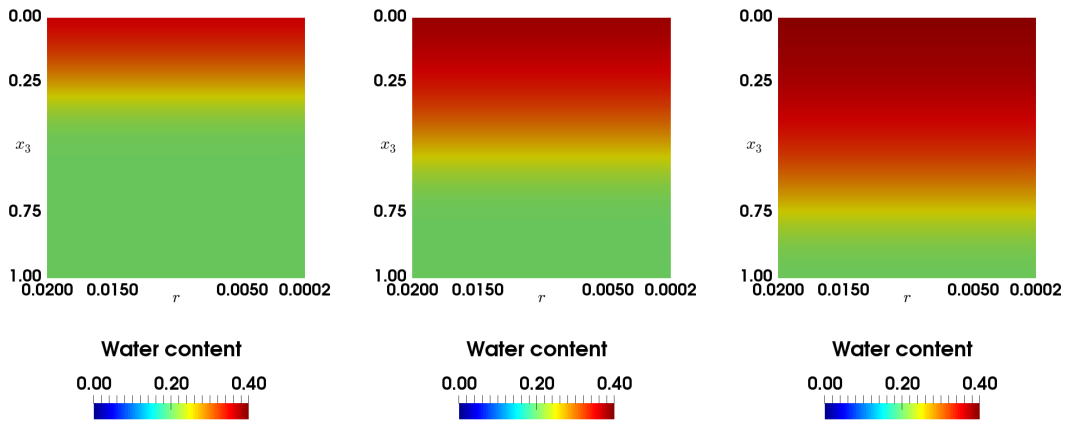
$$0 = \left(\frac{\partial}{\partial r}, \frac{\partial}{\partial x_3}\right) \cdot \left[D(S)\left(\frac{\partial S}{\partial r}, \frac{\partial S}{\partial x_3}\right) - \alpha k(S)\,(0,1)\right] + \frac{1}{r} D(S) \frac{\partial S}{\partial r}$$

over the two-dimensional domain Ω_{2D} (as defined in Equation (94)), and use the divergence theorem.



(a) $t = 0.2$ (b) $t = 0.4$ (c) $t = 0.6$

Figure 2.23.: Results using Equation (92) with van Genuchten nonlinearities $D(S)$ and $k(S)$ (defined in equations (85) and (86)), equipped with the boundary conditions (102) – (105), and the initial condition (95). Parameters are summarised in Table 2.8. For the chosen uptake rate (see Equation (98)), the watering rate of $C_w = 6\,\mathrm{cm\,d^{-1}}$ is too high, and the simulation crashes at $t \approx 0.73$ (note that the solution seems nearly uniform in r, which is caused by the diffusion acting very fast on such short length scales).



(a) $t = 0.2$ (b) $t = 0.4$ (c) $t = 0.6$

Figure 2.24.: The watering rate of $C_w = 4\,\mathrm{cm\,d^{-1}}$ yields a steady state close to full saturation (keeping everything else unchanged compared to Figure 2.23).

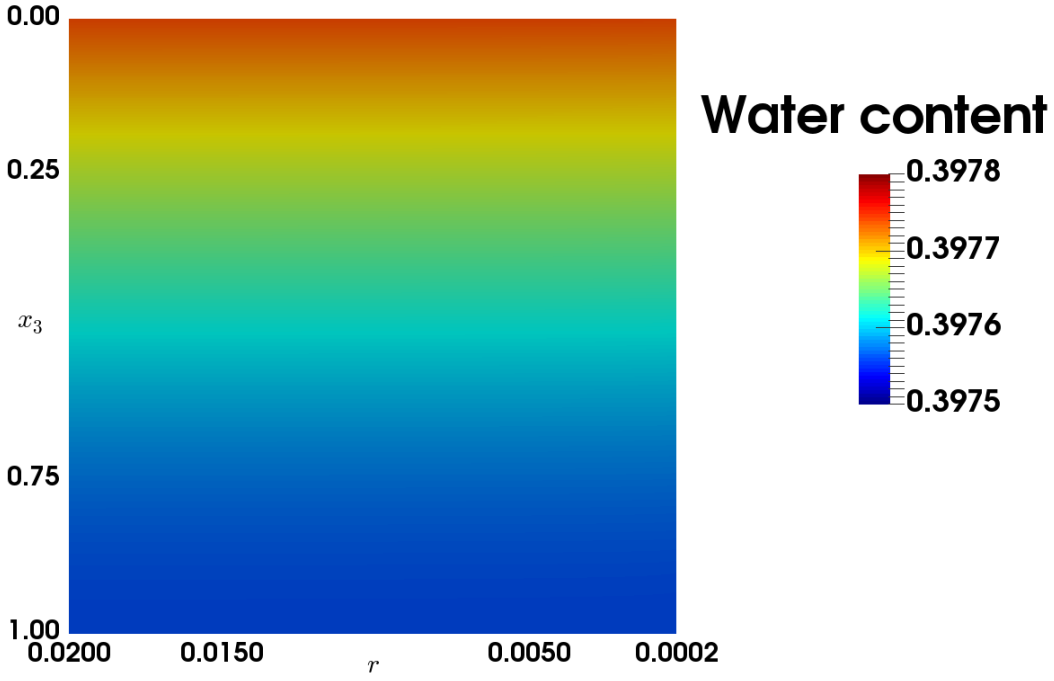


Figure 2.25.: The steady state for $C_w = 4\,\mathrm{cm\,d^{-1}}$ (same problem as in Figure 2.24). Note the changed colorbar limits.

We get:

$$0 = \int_{\Omega_{2D}} \left\{ \left(\frac{\partial}{\partial r}, \frac{\partial}{\partial x_3}\right) \cdot \left[D(S)\left(\frac{\partial S}{\partial r}, \frac{\partial S}{\partial x_3}\right) - \alpha k(S)(0,1) \right] + \frac{1}{r} D(S) \frac{\partial S}{\partial r} \right\} dS =$$

$$\int_{\partial\Omega_{2D}} \left[D(S)\left(\frac{\partial S}{\partial r}, \frac{\partial S}{\partial x_3}\right) - \alpha k(S)(0,1) \right] \cdot \hat{\boldsymbol{n}} dl +$$

$$\int_{\Omega_{2D}} \frac{1}{r} D(S) \frac{\partial S}{\partial r} dS = \int_{\Omega_{2D}} \frac{1}{r} D(S) \frac{\partial S}{\partial r} dS + \int_{r=\frac{r_0}{h_0}} -D(S) \frac{\partial S}{\partial r} dl +$$

$$\int_{x_3=1} \left[D(S) \frac{\partial S}{\partial x_3} - \alpha k(S) \right] dl + \int_{x_3=0} \left[-D(S) \frac{\partial S}{\partial x_3} + \alpha k(S) \right] dl,$$

where we have already used the fact that the zero-flux boundary condition is applied at $r = \frac{r_\infty}{h_0}$. Putting all the boundary fluxes on the left-hand side of this equation, we get:

$$\int\limits_{r=\frac{r_0}{h_0}} D(S)\frac{\partial S}{\partial r}dl - \int\limits_{x_3=1}\left[D(S)\frac{\partial S}{\partial x_3} - \alpha k(S)\right]dl + \int\limits_{x_3=0}\left[D(S)\frac{\partial S}{\partial x_3} - \alpha k(S)\right]dl = \int\limits_{\Omega_{2D}} \frac{1}{r}D(S)\frac{\partial S}{\partial r}dS. \tag{108}$$

Furthermore, using the boundary conditions (102), (104) and (105), we get:

$$I_1 = \int\limits_{r=\frac{r_0}{h_0}} D(S)\frac{\partial S}{\partial r}dl = \beta \times 1 = \beta, \tag{109}$$

$$\int\limits_{x_3=1}\left[D(S)\frac{\partial S}{\partial x_3} - \alpha k(S)\right]dl = -\alpha \int\limits_{x_3=1} k(S)dl, \tag{110}$$

and:

$$I_2 = \int\limits_{x_3=0}\left[D(S)\frac{\partial S}{\partial x_3} - \alpha k(S)\right]dl = -\gamma(\frac{r_\infty}{h_0} - \frac{r_0}{h_0}). \tag{111}$$

Substituting these results into Equation (108), we get:

$$I_3 = \int\limits_{\Omega_{2D}} \frac{1}{r}D(S)\frac{\partial S}{\partial r}dS - \alpha \int\limits_{x_3=1} k(S)dl = \beta - \gamma(\frac{r_\infty}{h_0} - \frac{r_0}{h_0}). \tag{112}$$

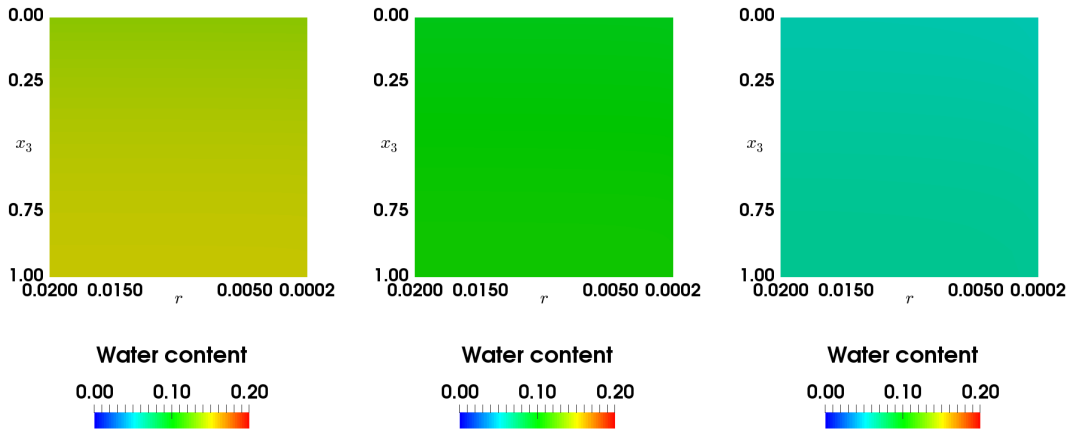
We now check the conditions $(109) - (112)$ for the steady state obtained in FEniCS using an increasing mesh resolution and an increasing polynomial degree. We ran this simulation with the domain meshed so that the number of elements in the r direction is the same (10) as the number of elements in the x_3 direction. It seemed that the largest errors occured in the evaluation of the root surface integral ($\int\limits_{r=\frac{r_0}{h_0}} D(S)\frac{\partial S}{\partial r}dl \approx 0.0035$ whereas $\beta = 0.01$ - compare with Equation (109)). Therefore, we changed the meshing so that the number of elements in the r direction is larger (5 times) than the number of elements in the x_3 direction. Numerical results for these integrals using an increasing number of elements in the r direction (N_r), as well as the values that these integrals should approximate, are summarised in Table 2.9. Table 2.10 shows results for an increasing polynomial degree and a fixed resolution ($N_r = 25$).

N_r	I_1	I_2	I_3
25	0.005035	−0.009142	0.000833
50	0.006142	−0.009159	0.000833
100	0.007263	−0.009164	0.000833
200	0.008249	−0.009166	0.000833
400	0.008977	−0.009166	0.000833
Exact	0.01	−0.009167	0.000833

Table 2.9.: Numerically computed integrals at the steady state for an increasing mesh resolution (same problem as in Figure 2.25). The polynomial degree is 1.

degree	I_1	I_2	I_3
1	0.005035	−0.009142	0.000833
2	0.007599	−0.009173	0.000833
3	0.008942	−0.009166	0.000833
4	0.009588	−0.009177	0.000833
5	0.009825	−0.009167	0.000833
Exact	0.01	−0.009167	0.000833

Table 2.10.: Numerically computed integrals at the steady state for an increasing polynomial degree (same problem as in Figure 2.25). $N_r = 25$.



(a) $t = 10.0$ (b) $t = 20.0$ (c) $t = 30.0$

Figure 2.26.: No watering (same problem as in Figure 2.24, except for $C_w = 0\,\text{cm}\,\text{d}^{-1}$) leads to the drying out of the soil and the subsequent crash of the simulation.

The error decreases with both the increased mesh resolution and the increased polynomial degree. Therefore, we can be confident about the accuracy of our numerical method.

No watering

If $C_w = 0\,\text{cm}\,\text{d}^{-1}$ (i.e. there is no watering from $x_3 = 0.0$), no water is flowing into the domain, and the water is flowing out of the domain at the rate of at least $0.27\,\text{cm}^3\,\text{d}^{-1}$ (this is the overall water uptake rate - see Equation (106); drainage only adds to this water loss). Therefore, in finite time, all the water is depleted from the domain. We reach negative water content, which is non-physical and the simulation crashes[5]. Keeping all the parameters same as in the previous section (except for C_w), the simulation crash occurs close to $t = 35$. The simulation results are presented in Figure 2.26. We used polynomial degree 2 and $N_r = 50$, because these choices lead to significant increases in the accuracy in the previous section, while keeping the simulation time short.

5 Note that in reality, when the local water content reaches the residual water content θ_r (equivalent to $S = 0$), the plant closes its stomata and the uptake rate starts declining. We do not model these processes in this thesis.

Minimal watering rate preventing soil from drying

We have shown that without the watering, soil water content reaches 0 in finite time and the simulation crashes, while for $C_w = 4\,\mathrm{cm\,d^{-1}}$, we approach a steady state close to the full saturation. This suggests that there should exist a minimal rate of watering that still leads to a steady state, and we now try to find it.

In this extremal case, the soil would dry down to 0 but not below. The overall drainage for $S \approx 0$ is very close to 0, and therefore we simply impose that the overall uptake is equal to the overall watering, i.e.:

$$C_w \times \pi \times (1 - 0.0001)\,\mathrm{cm^3\,d^{-1}} = 0.0864 \times 2 \times \pi \times 0.01 \times 50\,\mathrm{cm^3\,d^{-1}},$$

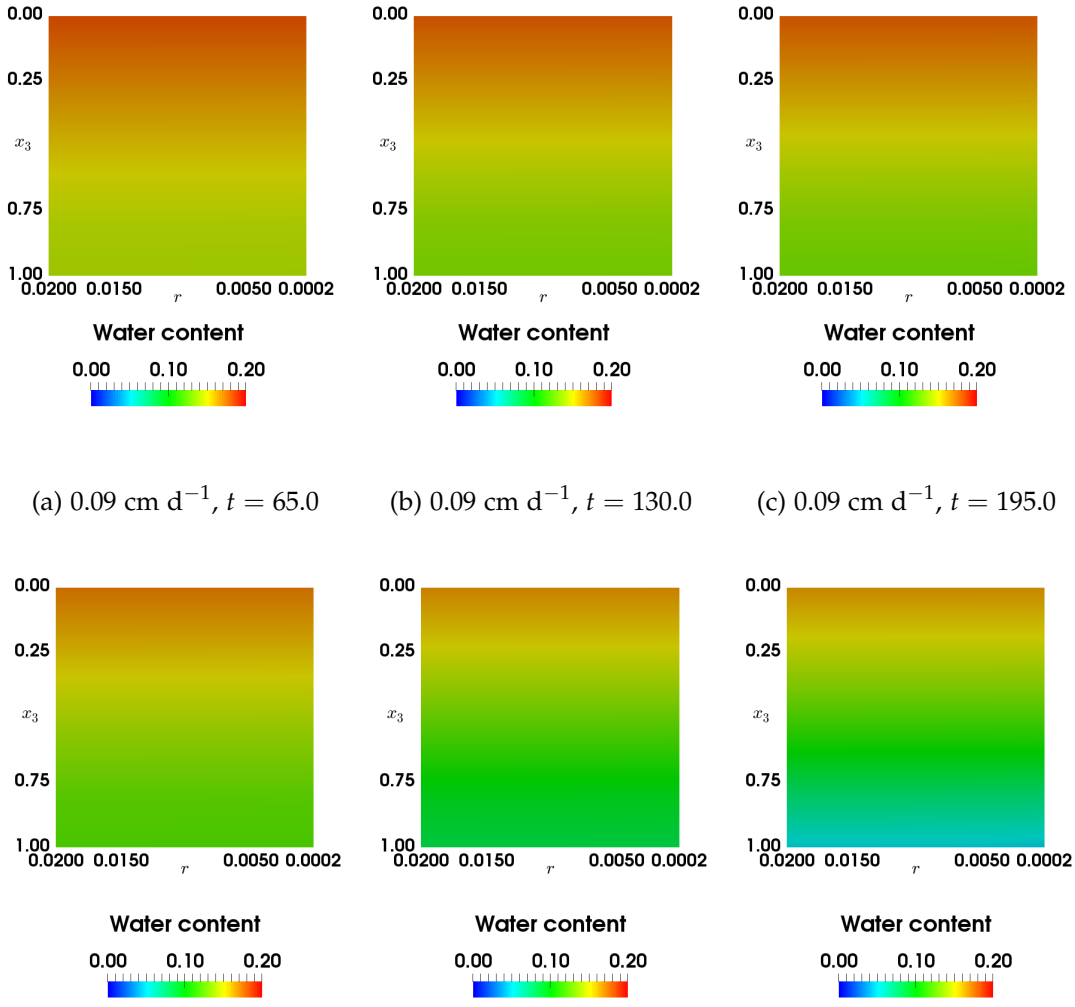
or:

$$C_w = \frac{0.0864}{0.9999}\,\mathrm{cm\,d^{-1}} \approx 0.0864\,\mathrm{cm\,d^{-1}}.$$

Thus, we run 2 simulations, with C_w either side of this critical value. In the case of $C_w = 0.09\,\mathrm{cm\,d^{-1}}$, the time evolution reaches a steady state with (relatively) low water content (as shown in Figure 2.28), while in the case of $C_w = 0.08\,\mathrm{cm\,d^{-1}}$, the soil dries down to 0 in finite time and the simulation crashes (at $t \approx 200$). We used a polynomial degree 2 and $N_r = 25$. Time evolution for both values can be seen in Figure 2.27.

Single root simulations - conclusions

Thus we have shown that even using a geometry as simple as that of a single cylindrical root, one can study problems of agricultural importance. In this setting, we managed to estimate the minimal watering rate which keeps the soil from drying, as well as the minimal watering rate, which results in surface ponding. There are many other ways this setting can be used. Imagine for instance, that we have information on the minimal water content at which the plant transpiration still equals the potential (maximal) transpiration, and thus the plant is not stressed and proliferates as desired (e.g. for agricultural use). Then, we can estimate the overall drainage efflux, and thus adjust the watering strategy so that the water content does not fall below that value.



(a) 0.09 cm d^{-1}, $t = 65.0$ (b) 0.09 cm d^{-1}, $t = 130.0$ (c) 0.09 cm d^{-1}, $t = 195.0$

(d) 0.08 cm d^{-1}, $t = 65.0$ (e) 0.08 cm d^{-1}, $t = 130.0$ (f) 0.08 cm d^{-1}, $t = 195.0$

Figure 2.27.: Comparison of simulations for two values close to the critical watering rate (same problem as in Figure 2.24; the only changed parameter is the watering rate C_w).

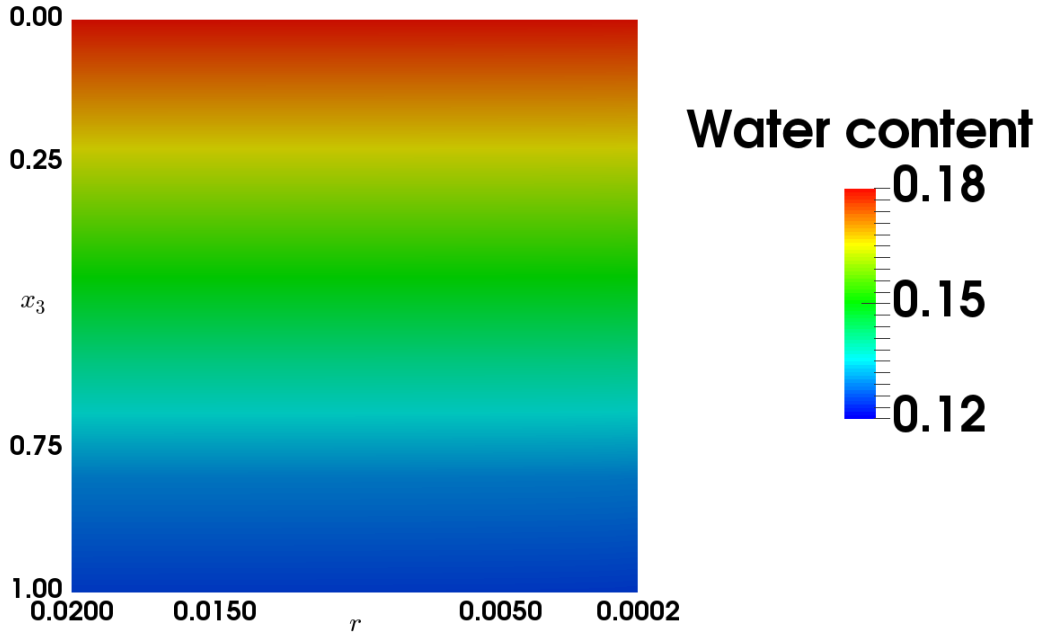


Figure 2.28.: Steady state for the same problem as in Figure 2.25, except for $C_w = 0.09\,\mathrm{cm\,d^{-1}}$. Note the changed colorbar limits.

Alternatively, we can impose the Dirichlet boundary condition $S = 1$ at the bottom boundary ($x_3 = h_0$) which represents a water table at a fixed depth and is often used in agricultural modelling (see Section 1.2.2 or [121]). This would allow us to study the effects of the capillary rise on plant water uptake (see Section 1.2.2).

2.6.3 *Water uptake by branching structures*

In this section, we model water uptake by a structure consisting of a thicker cylinder (the main root) and a thinner cylinder (the hair/branch) that branched off this cylinder as shown in Figure 2.2.
Note that for any nontrivial governing equations, this problem cannot be reduced to a two-dimensional geometry as it was often done in the previous section. Therefore, three-dimensional simulations are necessary.
As mentioned in Section 2.6, this geometry can be successfully upscaled to a larger scale using the periodic boundary conditions, provided that the gradi-

ent in water content at the larger scale is negligible. However, as we observed in previous sections, these gradients can be significant for a root of length 50 cm.

Assuming a root segment of length 1 cm, the dimensionless parameter α from Equation (92) is equal to $\frac{h_0 K_s}{D_0} \approx 0.0115$, and thus, the gravity effects are likely to be negligible in most cases. From [151], we deduce that a typical branching density for maize is between 5 and 10 branches per cm of root length, which can still be directly simulated. On the other hand, [51] gives a typical value of about 300 root hairs per cm of root length for wheat and barley (for data on other species, see [80] and references therein). Therefore, imposing the periodic boundary conditions to the geometry from Figure 2.2 seems to be a very useful approach for modelling uptake by root hairs, and from now onwards, we focus on this case.

Root with a hair

Let the cylinder from previous sections represent a segment of the main root so that the height of this cylinder corresponds to an inter-hair distance (h_0). We assume that the hair is perpendicular to the main root and is defined as $A^d \setminus B^d$, where A^d is a cylinder (with radius r_1 and height $r_0 + h_1$; positioned so that the centres of its end faces are at points $(0, 0, h_0/2)$ and $(h_1 + r_0, 0, h_0/2)$), B^d is the main root, and $\setminus$ is the set difference (superscript d indicates that the dimensional variables are used). We assume that $r_1 < r_0$ (see Figure 2.2). As before, we do not model the water flows within the root system. The surrounding soil is defined as $\Omega_H^d = C^d \setminus D^d$ (the subscript H it used to represent the geometry with the hair), where $C^d = \{(x_1, x_2, x_3) \in \mathbb{R}^3, x_1^2 + x_2^2 < r_\infty^2, 0 < x_3 < h_0\}$, and $D^d = B^d \bigcup A^d$. Therefore, the boundary of Ω_H^d (denoted by $\partial\Omega_H^d$) consists of five parts, which we denote as E^d, F^d, G^d, H^d and I^d. Let E^d be the part of the boundary for which $x_3 = 0$, and F^d the one satisfying $x_3 = h_0$. Furthermore, suppose that the points belonging to G^d satisfy $x_1^2 + x_2^2 = r_\infty^2$, points belonging to H^d satisfy $x_1^2 + x_2^2 = r_0^2$, and let $I^d = \partial\Omega_H \setminus (E^d \bigcup F^d \bigcup G^d \bigcup H^d)$. The dimensionless geometry is shown in Figure 2.29.

parameter	meaning	value	units
r_0	root radius	80	µm
r_∞	far-field distance	10000	µm
r_1	root hair radius	6	µm
h_0	inter-hair distance	130	µm
h_1	hair length	920	µm

Table 2.11.: Geometry parameters for the model with the hair.

PARAMETER SURVEY

We need to adjust the parameters so that they correspond to the physical reality of a root hair geometry. Table 2 from [51] gives us the following estimates for wheat: $r_0 = 0.008$ cm, $r_1 = 0.0006$ cm, $h_1 = 0.092$ cm[6]. The mentioned estimate of 300 hairs per cm of the root length leads to 300 hairs per 0.05 cm^2 of the root surface (using $r_0 = 0.008$ cm), and assuming the root hairs are spaced periodically on the root surface with the same period along the main axis of the root and around the circumference of the root (this assumption will be used throughout Chapters 3, 4 and 5), we conclude that the average inter-hair distance (measured along the root surface) is approximately 0.013 cm. Finally, we choose the far-field distance r_∞ to be 1 cm.

These parameter values and their units are summarised in Table 2.11. The height of the unit cell (i.e. the inter-hair distance) will be varied in future.

Governing equations

To model the soil water dynamics, we start with the continuity equation (88). At the length scale of $h_0 = 0.013$ cm, the dimensionless parameter $\alpha = \frac{h_0 K_s}{D_0} \approx 1.5 \times 10^{-4}$ is very small, and thus we neglect the gravity term. We get:

$$\phi \frac{\partial S}{\partial t} = \nabla \cdot \left[D_0 D(S) \nabla S \right]. \tag{113}$$

6 These values can serve as good estimates for barley as well (see [51])

We impose the periodic boundary conditions in the x_3 direction (see Equations (51) and (53)), i.e. the periodic value condition:

$$S(t, x_1, x_2, 0) = S(t, x_1, x_2, h_0) \quad \forall t, x_1, x_2, \tag{114}$$

and the periodic derivative condition:

$$\frac{\partial S(t, x_1, x_2, 0)}{\partial x_3} = \frac{\partial S(t, x_1, x_2, h_0)}{\partial x_3} \quad \forall t, x_1, x_2. \tag{115}$$

At the root surfaces (this now includes the hair surface as well), we impose the Robin boundary condition (see Equation (21)):

$$\hat{\boldsymbol{n}} \cdot \Big[- D_0 D(S) \nabla S \Big] = C_2 S. \tag{116}$$

We choose the value of C_2 so that the uptake rate per unit root surface at full saturation ($S = 1$) is equal to the value $C_1 = 0.0864\,\mathrm{cm\,d^{-1}}$ found in Section 2.6.2, i.e.:

$$C_2 = 0.0864\,\mathrm{cm\,d^{-1}}. \tag{117}$$

As we could not find any data on the water uptake rate of the root hairs, we simply consider C_2 to be the same constant for both the root and the hair surfaces.

Soon, we will study water uptake for a changing inter-hair distance. For the nonlinear model under consideration (Equation (113)) in combination with the nontrivial geometry from Figure 2.2, solving the time-dependent problem can be computationally expensive. Therefore, we will simplify our task by restricting our attention to the steady-state conditions. If we (as before) assumed the zero-flux boundary condition:

$$\hat{\boldsymbol{n}} \cdot \big[D_0 D(S) \nabla S \big] = 0 \tag{118}$$

at $r = r_\infty$, the water would be extracted from the soil by the root surfaces, and we would not have any water source balancing this water loss. As a consequence, for large times, the water content in the domain would approach a trivial steady state $S = 0$ (plus we would have to deal with the singularity of the diffusivity function $D(S)$ as $S \to 0$). Therefore, we impose the Dirichlet boundary condition (see Equation (47)):

$$S = 1$$

at $r = r_\infty$ instead, and this represents the full-saturation condition far from the root surfaces, and introduces a water source to balance out the water uptake at the (nontrivial) steady state.
As an initial condition, we impose full saturation ($S = 1$) everywhere.

Nondimensionalisation

We nondimensionalise the problem in the same way as in the single-cylinder case, and obtain the dimensionless continuity equation (92) without the gravity term:

$$\frac{\partial S}{\partial t} = \nabla \cdot \big[D(S)\nabla S\big]. \tag{119}$$

This equation is to be satisfied in the dimensionless domain $\Omega_H = X \setminus Y$, where $X = \{(x_1, x_2, x_3) \in \mathbb{R}^3, (\frac{r_0}{h_0})^2 < x_1^2 + x_2^2 < (\frac{r_\infty}{h_0})^2, 0 < x_3 < 1\}$ and $Y = \{(x_1, x_2, x_3) \in \mathbb{R}^3, 0 < x_1 < \frac{h_1 + r_0}{h_0}, x_2^2 + (x_3 - \frac{1}{2})^2 < (\frac{r_1}{h_0})^2\}$ (see Figure 2.29). The dimensionless periodic boundary conditions state:

$$S(t, x_1, x_2, 0) = S(t, x_1, x_2, 1) \quad \forall t, x_1, x_2, \tag{120}$$

and:

$$\frac{\partial S(t, x_1, x_2, 0)}{\partial x_3} = \frac{\partial S(t, x_1, x_2, 1)}{\partial x_3} \quad \forall t, x_1, x_2. \tag{121}$$

Analogous to the dimensional case, we denote by E the part of the boundary satisfying $x_3 = 0$, and by F the one satisfying $x_3 = 1$.
The Robin condition (116) in the dimensionless variables attains a form:

$$\hat{\boldsymbol{n}} \cdot \big[- D(S)\nabla S\big] = \frac{C_2 h_0}{D_0} S, \tag{122}$$

and it is imposed at all the root surfaces. The main root boundary is given by $x_1^2 + x_2^2 = (\frac{r_0}{h_0})^2$, and we denote it by H. We denote the hair part of the boundary by I.

Time evolution (zero flux at $r = \frac{r_\infty}{h_0}$)

First, we simulate this problem with a zero-flux boundary condition at $r = \frac{r_\infty}{h_0}$ to clearly see the water being extracted from the domain (no water source).

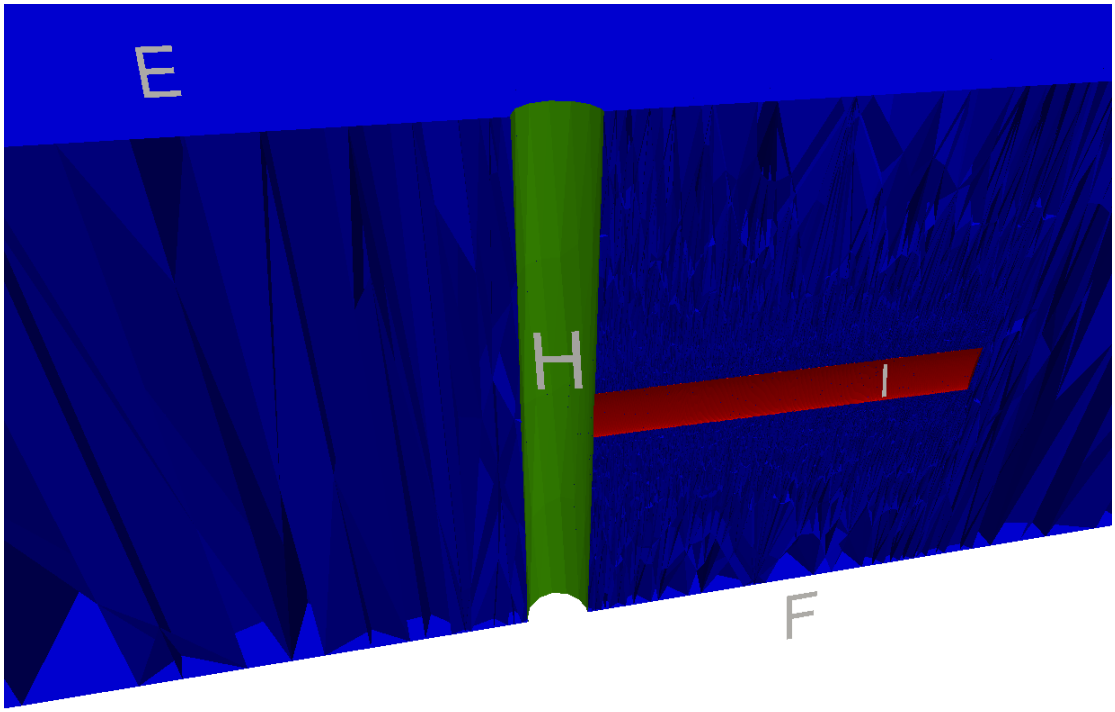


Figure 2.29.: Boundary parts for the geometry with the hair. The main root is coloured green and the hair is coloured red. As the domain is very thin in the x_3 direction, we stretched it 10 times.

To avoid the singularity of the diffusivity function $D(S)$ at $S = 1$, we start with the initial water content distribution:

$$S = 0.99 \tag{123}$$

everywhere. The time evolution is shown in Figure 2.30. Note that the dimensionless time $\tau = 10^8$ corresponds dimensionally to $t = \frac{h_0^2 \phi}{D_0} \tau \approx 15.65$ d.

Steady state

If we impose the Dirichlet boundary condition $S = 0.99$ at $r = \frac{r_\infty}{h_0}$, we obtain a (non-trivial) steady state, which is shown in Figure 2.31. We observe the expected water depletion close to the root surfaces. However, the gradients in water content are almost negligible. This is due to the water content being very close to the full saturation. Therefore, we now impose a much lower water content ($S = 0.04$) at $r = \frac{r_\infty}{h_0}$, and the (zoomed-in) steady state is shown in Figure 2.32.

Checking

The steady-state version of Equation (119) reads:

$$0 = \nabla \cdot \big[D(S) \nabla S \big].$$

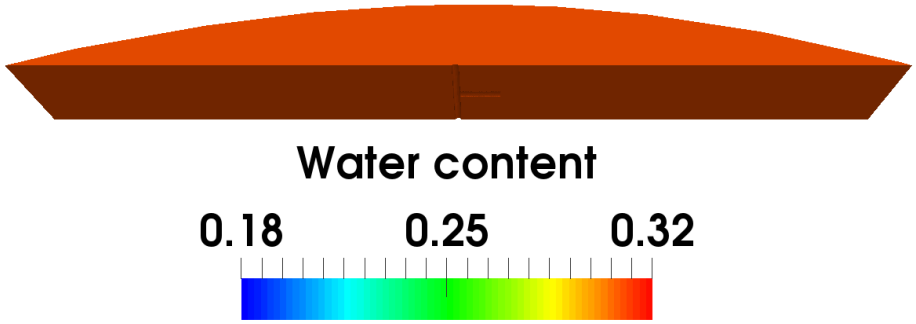
Integrating over the entire domain and using the divergence theorem yields:

$$0 = \int_{\Omega_H} \nabla \cdot \big[D(S) \nabla S \big] dx = \int_{\partial \Omega_H} \big[D(S) \nabla S \big] \cdot \hat{\boldsymbol{n}} dS,$$

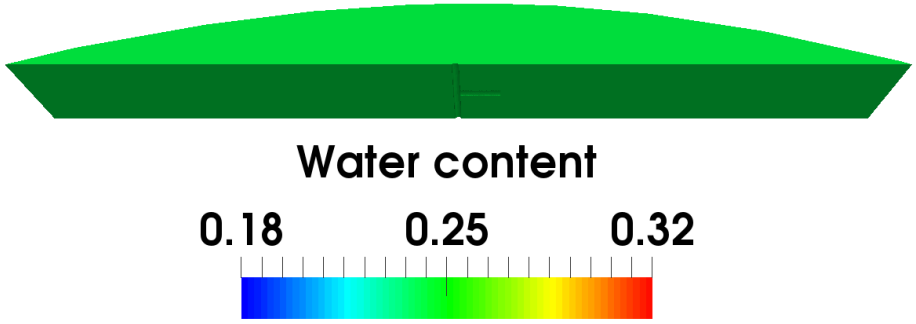
which using the periodic boundary conditions at the top and the bottom part of the boundary reduces to:

$$\int_{\partial \Omega_H} \big[D(S) \nabla S \big] \cdot \hat{\boldsymbol{n}} dS = \int_{H \cup I} \big[D(S) \nabla S \big] \cdot \hat{\boldsymbol{n}} dS + \int_{G} \big[D(S) \nabla S \big] \cdot \hat{\boldsymbol{n}} dS.$$

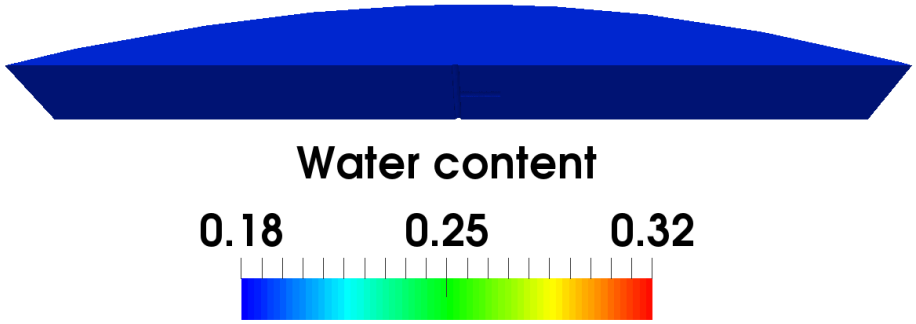
Therefore, by calculating these integrals, we can check if the influx from the far-field balances the flux into the root surfaces at the steady state.



(a) $\tau = 3 \times 10^8$



(b) $\tau = 6 \times 10^8$



(c) $\tau = 9 \times 10^8$

Figure 2.30.: Time evolution for the geometry with the hair. Equation (119) using the van Genuchten nonlinearity $D(S)$ (see Equation (85)), equipped with the initial condition (123), boundary conditions (120), (121), (122) (using C_2 from Equation (117)), and the zero-flux boundary condition applied at $r = \frac{r_\infty}{h_0}$. Geometric parameters are summarised in Table 2.11.

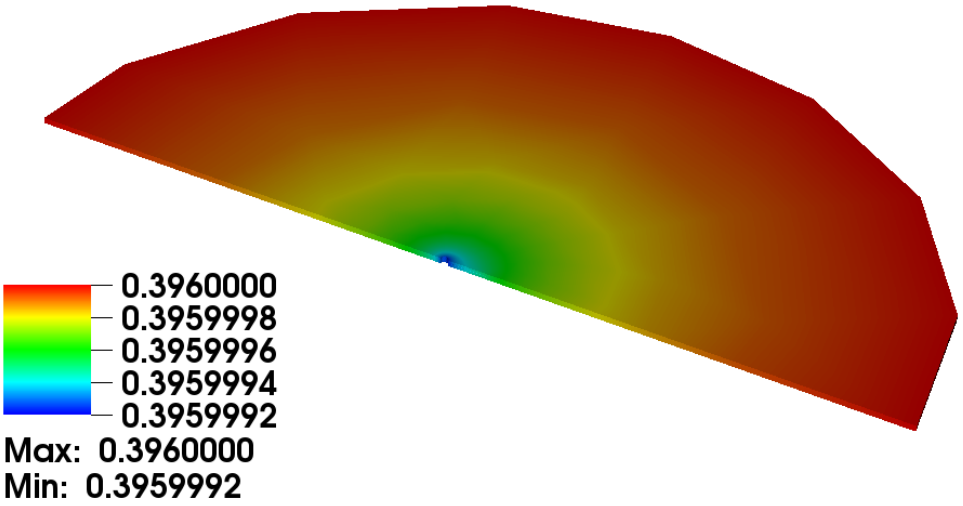


Figure 2.31.: Steady state for the same problem as in Figure 2.30, except that we use a Dirichlet condition $S(r = \frac{r_\infty}{h_0}) = 0.99$.

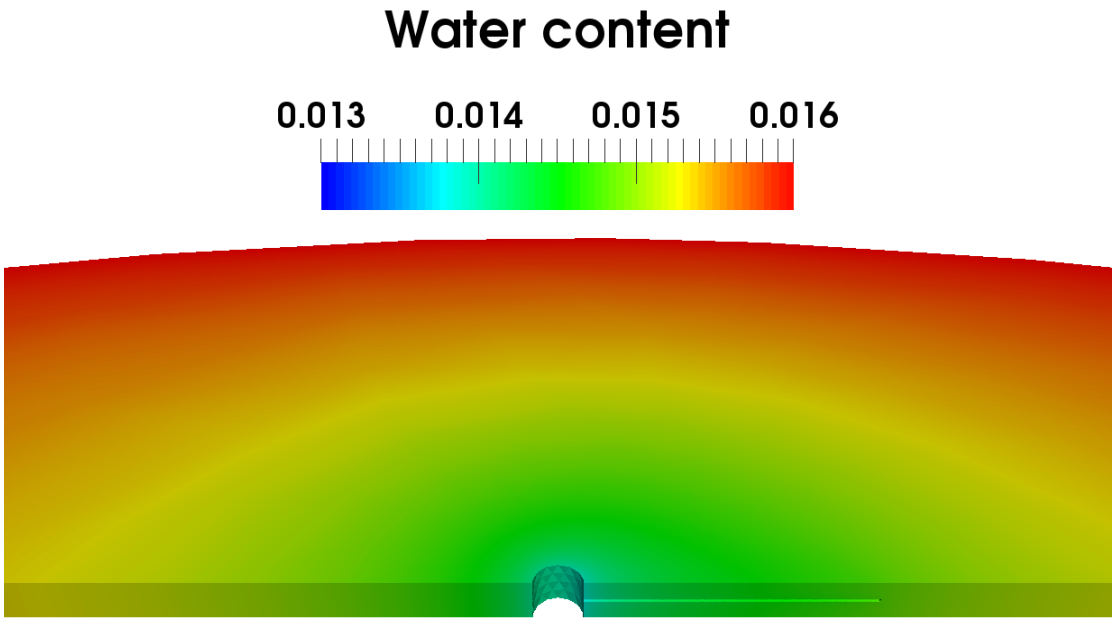


Figure 2.32.: Steady state for the same problem as in Figure 2.30, except that we use a Dirichlet condition $S(r = \frac{r_\infty}{h_0}) = 0.04$.

maximal mesh size	flux into root surfaces	flux from far-field
8.0	4.231×10^{-7}	5.458×10^{-7}
4.0	4.386×10^{-7}	5.415×10^{-7}
2.0	4.454×10^{-7}	5.392×10^{-7}
1.0	4.886×10^{-7}	5.397×10^{-7}
0.5	5.133×10^{-7}	5.394×10^{-7}

Table 2.12.: Comparison between the total flux entering the root surfaces and the influx from the far-field at the steady state for varying maximal mesh size (same problem as in Figure 2.32). Polynomial degree is 1.

Guided by our experience from previous sections, we are led to generate meshes for which the maximal mesh size at various parts of the boundary is distinct from the maximal mesh size imposed for the whole domain. NetGen [127] allows us to do that for a three-dimensional domain like this. After trying different scenarios, we imposed the maximal mesh size at the outer (root surface, hair surface) boundary to be 4 (20, 100) times smaller than the maximal mesh size of the entire domain.

We varied the overall maximal mesh size, and the results are shown in Table 2.12. Fixing the maximal mesh size at 4.0 and increasing the polynomial degree to 2 leads to the root surfaces influx of 5.253×10^{-7} and the far-field flux of 5.367×10^{-7}.

We see that the error in the divergence theorem decreases both with the decreasing maximal mesh size and with the increasing polynomial degree. Moreover, using both procedure, we seem to approach the same value. Therefore, we conclude that the numerical simulations perform well enough to continue with our water uptake studies.

Note that setting the polynomial degree to 3 results in computer memory problems. Furthermore, notice from Table 2.11, that the root radius of 80 µm implies the circumference of $2\pi \times 80\,\mu\text{m} \approx 502.655\,\mu\text{m}$. Assuming the inter-hair

distance of 130 µm gives roughly 4 hairs in each layer (i.e. 4 hairs within the region defined by $0 < x_3 < 1$).

Pipeline

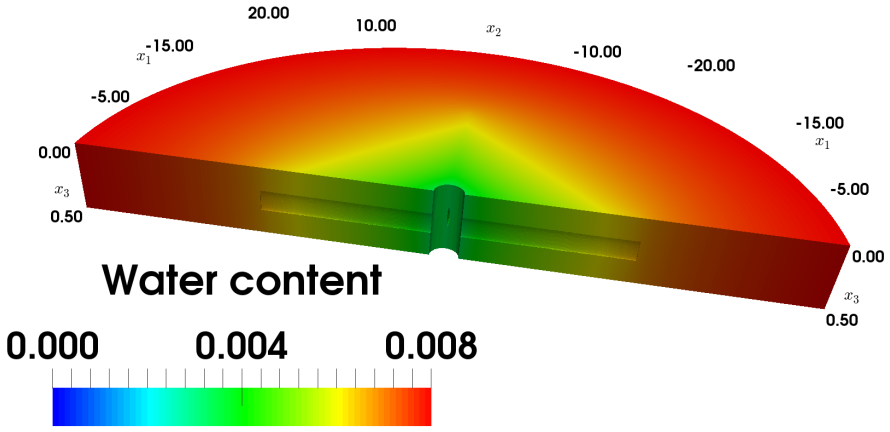
In this section, our aim is to study how changes in the inter-hair distance along the root length h_0 affect the overall water uptake. The main idea is that using a fix volume of root material, one can create a greater absorbing surface area with root hairs compared to the roots due to their smaller radius. On the other hand, it seems possible that if we produce too many hairs, less material is available for the growth of the main root, and the overall uptake may be smaller than in the lower-hair-density case, due to the larger volume of soil explored by the (longer) main root (and potentially also due to a decreased inter-hair competition for water in the lower-hair-density case).

We wish to vary h_0, which corresponds to changing the number of root hairs per unit root length (keeping 4 hairs in each layer from now on in this chapter). Therefore, we need to change the nondimensionalisation; we nondimensionalise with respect to r_0, i.e. $(x_1, x_2, x_3) = r_0(\tilde{x}_1, \tilde{x}_2, \tilde{x}_3)$, and $t = \frac{\phi r_0^2}{D_0}\tau$. We arrive at a dimensionless continuity equation:

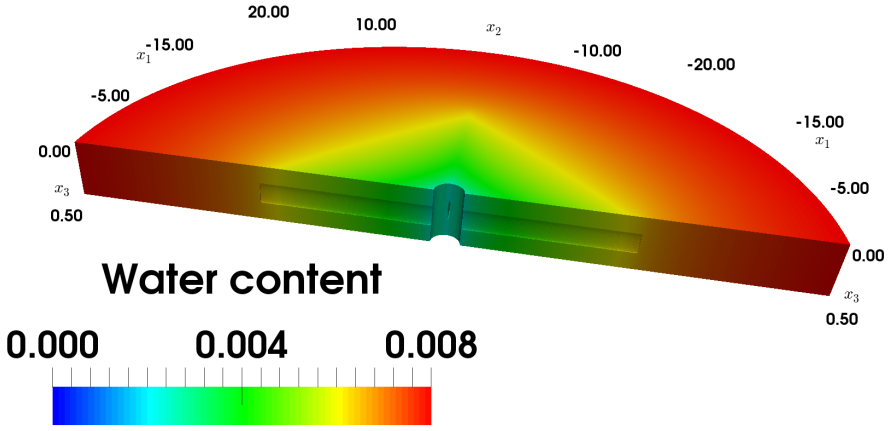
$$\frac{\partial S}{\partial \tau} = \tilde{\nabla} \cdot [D(S)\tilde{\nabla} S - \alpha_r k(S) \nabla x_3], \tag{124}$$

where the dimensionless parameter is $\alpha_r = \frac{r_0 K_s}{D_0} > 0$. The boundary conditions are nondimensionalised accordingly. To simplify the numerics, we decreased the far-field distance to $r_\infty = 0.2$ cm, and we imposed a Dirichlet boundary condition $S = 0.02$ here.

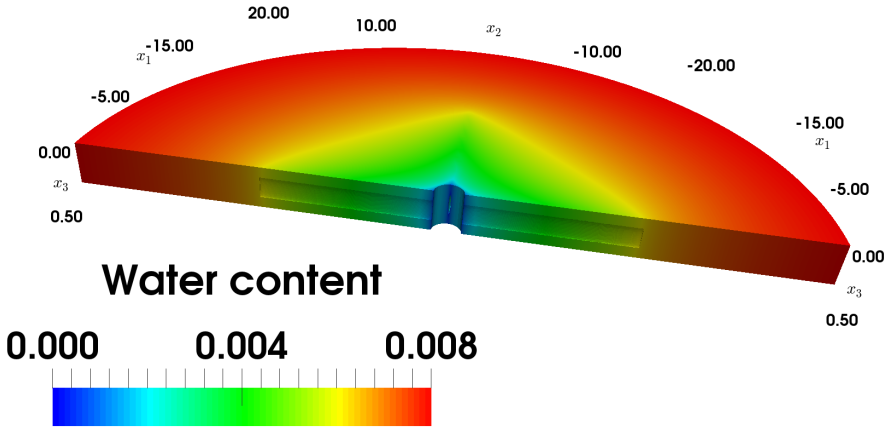
To study the effect of the new dimensionless inter-hair distance $\frac{h_0}{r_0}$ on the overall uptake, we need to be able to perform a series of steps for each value of this parameter. These steps include writing a separate .geo file, meshing the geometry in NetGen, converting .msh file to .xml file so that it can be uploaded into FEniCS, and then solve the problem using FEniCS. In order to automate this process, we created a pipeline using bash scripts. Results shown in Figure 2.33 were obtained using the described procedure (using polynomial degree 2).



(a) $\frac{h_0}{r_0} = 0.5$



(b) $\frac{h_0}{r_0} = 0.4$



(c) $\frac{h_0}{r_0} = 0.3$

Figure 2.33.: Comparison of steady states for varying inter-hair distance h_0 (and fixed r_0). x_3 direction is stretched 10 times to capture the changing inter-hair distance better. Same problem as in Figure 2.32, except that we have 4 root hairs in the unit cell, and at $r_\infty = 0.2$ cm, we assume $S = 0.02$.

We observe that for very small inter-hair distance h_0, the steady-state water content at the root surfaces is very close to zero and therefore, the influx per unit root surface area becomes small.

Optimisation

So far, a very important fact that a plant has only a limited supply of nutrients (e.g. carbon) was little discussed. Therefore, we may assume that although it is possible to change the average inter-hair distance (h_0), this will have implications for carbon allocation to different parts of the plant. Here, we simply assume, that a change in h_0 leads to the corresponding change in the length of the root (L_r) from which the hairs grow, so that the total volume of this system is fixed (V_t). In other words, if the hair density is very high, then the length of the main root must be small given only a fixed amount of carbon is available and vice versa. This means that:

$$C = V_t = \pi r_0^2 L_r(h_0) + 4\pi r_1^2 h_1 \frac{L_r(h_0)}{h_0}$$

(keeping 4 hairs in every layer), or:

$$L_r(h_0) = \frac{C}{\pi(r_0^2 + 4r_1^2\frac{h_1}{h_0})}.$$

If we denote $F(h_0)$ to be the overall (dimensionless) flux into the unit cell root surfaces, and this unit cell is periodically repeated in the x_3 direction, then $\frac{F(h_0)}{h_0}$ is the total (dimensionless) influx per unit length of the main root (at the steady state). Therefore, $\frac{F(h_0)}{h_0}L_r(h_0)$ is the total (dimensionless) flux into this system, and we wish to maximise:

$$\frac{F(h_0)}{h_0}\frac{C}{\pi(r_0^2 + 4r_1^2\frac{h_1}{h_0})} = D\frac{F(h_0)}{r_0^2 h_0 + 4r_1^2 h_1}$$

with respect to h_0, where $D = \frac{C}{\pi}$. We aim to find the optimal inter-hair distance h_0, and our task can thus be reduced to maximising the expression:

$$E(h_0) = \frac{F(h_0)}{r_0^2 h_0 + 4r_1^2 h_1}. \tag{125}$$

The results of the numerical simulations are shown in Table 2.13. Here, we denote $F^*(h_0)$ to be the numerical approximation of the total influx from the

$\frac{h_0}{r_0}$	$F(h_0)$	$E(h_0)$ (cm^{-3})	$F^*(h_0)$	$E^*(h_0)$ (cm^{-3})
2.00	2.829×10^{-7}	0.245	2.907×10^{-7}	0.251
1.50	2.502×10^{-7}	0.278	2.569×10^{-7}	0.285
1.00	2.112×10^{-7}	0.328	2.174×10^{-7}	0.337
0.80	1.917×10^{-7}	0.354	1.976×10^{-7}	0.365
0.60	1.677×10^{-7}	0.382	1.729×10^{-7}	0.393
0.50	1.518×10^{-7}	0.391	1.571×10^{-7}	0.405
0.45	1.430×10^{-7}	0.394	1.480×10^{-7}	0.408
0.40	1.332×10^{-7}	0.395	1.379×10^{-7}	0.409
0.35	1.214×10^{-7}	0.390	1.265×10^{-7}	0.406
0.30	1.093×10^{-7}	0.382	1.139×10^{-7}	0.398

Table 2.13.: Searching for the optimal inter-hair distance h_0 (r_0 is fixed). The optimisation is based on the same problem as described in Figure 2.33. $F(h_0)$ is the (numerically computed) total flux into the (unit cell) root surfaces, whereas $F^*(h_0)$ denotes the (numerically computed) influx from the far field. $E(h_0)$ is defined in Equation (125) and $E^*(h_0)$ is defined in Equation (126). Polynomial degree is 2.

far-field boundary at the steady state (which we have shown to be equal to the overall root surfaces influx using the divergence theorem in this section). Analogously:

$$E^*(h_0) = \frac{F^*(h_0)}{r_0^2 h_0 + 4 r_1^2 h_1}. \tag{126}$$

From Table 2.13 we see that both methods of the overall root influx calculation give approximately the same value of the optimal dimensionless inter-hair distance - 0.4 (which in dimensional terms corresponds to the inter-hair distance of 32 µm).

Unfortunately, the numerical error in our calculations (the difference between $F(h_0)$ and $F^*(h_0)$ for a fixed value of h_0) is still too large to draw any definitive conclusions. At the same time, with the fully three-dimensional numerics for a nonlinear problem close to drought, we are reaching the limits of a simple

desktop computer computations. If we wanted more precise numerical results, we would probably need to use a supercomputer.

Summary

In this chapter, we introduced and studied the standard equations and geometries involved in root water (and nutrient) uptake modelling. We checked the accuracy of numerical simulations in FEniCS for such equations and geometries, as these will be used repeatedly in this thesis. We further sketched how these simulations, although rather simplistic, may still be used to address important problems in agriculture.

It is important to note, that we did not find experimental evidence on how much root hairs really contribute to the overall water uptake[7]. Therefore, the boundary conditions we used may be of little biological relevance. It is now widely accepted within the scientific community, that the root hairs are particularly important for the uptake of poorly-mobile nutrients such as phosphate (see [26] or [61]). It would not be difficult to change the continuity equation and the boundary conditions to model the uptake of such nutrients using the existing geometry 2.2.

However, if a gradient in water content (or nutrient concentration) along the main root axis exists, then the usage of the periodic boundary conditions cannot be justified anymore. Non-negligible gradients in (e.g.) water content are expectable especially in very dry soils [11]. Numerical simulations using the full geometry are rather expensive, and a different upscaling method is desirable. In the next chapter, we show how the method of homogenisation can be used to upscale uptake from the single hair scale to the root segment scale.

7 Note that the imaging and quantification of water content distribution in the rhizosphere has only become possible in recent years, and to our knowledge, quantitative data on water uptake rates at this scale are not available yet (see Section 1.2.1).

3

NUTRIENT UPTAKE BY PERIODIC ARRAYS OF CYLINDERS.

3.1 INTRODUCTION

In this chapter, we study uptake of a substance (which we will refer to as a nutrient from now onwards) by an array of periodically spaced cylinders of finite length (see Figure 3.1). A similar framework was rigorously studied in [20], was used to model nutrient uptake by growing root systems in [17], and was analysed as a model for nutrient uptake by hairy roots (dense root structures caused by a bacterium) in [112]. Furthermore, this approach has also been used to model uptake by cluster roots (short and dense lateral roots occuring in some plants) in [153].

Most importantly for the purposes of this thesis, the same arrangement can be used to model nutrient uptake by root hairs after one flattens out the root surface on which they grow. To our knowledge, this was first studied using the asymptotic expansions method (as introduced in Section 1.4.4) in [80]. Here, a linear diffusion equation (modelling a nutrient diffusing in a soil) was equipped with a Michaelis-Menten boundary condition at the root surfaces (including root hairs; for more details, see Figure 1.3).

In this chapter, we extend the approach from [80] to the case where a nontrivial macroscopic gradient in the nutrient concentration exists in the direction of periodicity (Section 3.2.3), to the case where the dynamics of the nutrient is governed by a convection-diffusion equation (Section 3.3), and also to the case where the dynamics of water in the soil is modelled using the (nonlinear) van

Genuchten model (Section 3.5). Furthermore, in all these cases, we directly compare the full-geometry results with the homogenisation results.

We keep the setting as general as possible and our main goal is to demonstrate how homogenisation can be used with this framework to derive macroscopic equations using information from the microscale. Therefore, exact parameter values are not important in this chapter. In the following chapters, we will use this framework with biologically realistic parameters to model nutrient uptake by root hairs. In all cases, we use the method of asymptotic expansions.

The domain of interest is a cuboid (usually representing a soil) minus the cylinders (representing the roots or the root hairs depending on context). We do not model water or nutrient flows within the root system in this thesis. We assume that the distance between the cylinders is much smaller than the size of the cuboid in the direction in which the structure is periodic, which introduces two characteristic length scales - a microscopic length scale determined by the distance between the cylinders l and a macroscopic length scale determined by the size of the cuboid L (in the direction of periodicity). This way, we stay consistent with the notation introduced in [80]. Moreover, we define a to be a quotient of the cylinder radius divided by the distance between the cylinders. Note that in this chapter, we assume $a = O(1)$ (in the following chapter, we will extend this analysis to the cases where $a \ll 1$). Two different views of the domain are presented in Figure 3.1.

In Section 3.2, we will show how the method of homogenisation is used in the case of a linear diffusion equation equipped with a Robin boundary condition at the cylindrical surfaces. A homogenised equation for this problem will be derived (see Equation (155)), and the analytical as well as numerical solutions of this equation will be obtained using different sets of boundary conditions. These solutions will subsequently be compared with numerical simulations on the full-geometry, and we will observe that homogenisation gives us a behaviour averaged over the microscale. The same approach will then be extended to the case of a convection-diffusion equation (Section 3.3), the case of the Michaelis-Menten boundary condition (Section 3.4), and the case of a nonlinear continuity equation (Section 3.5).

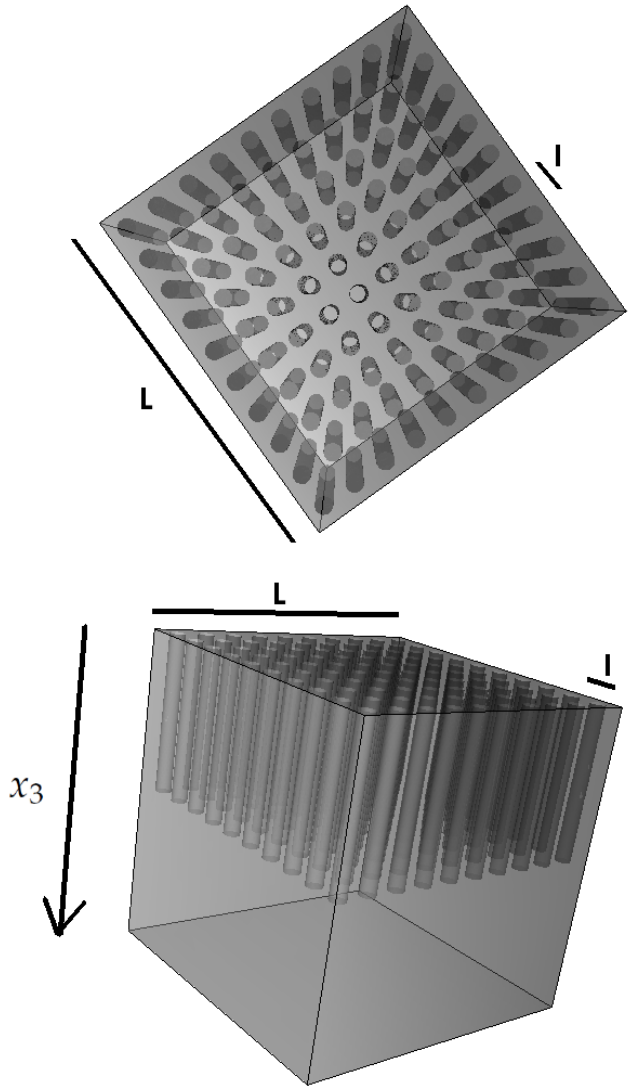


Figure 3.1.: The domain with periodically-spaced cylinders and the two characteristic length scales. In the case of root hairs, one has $l \approx 0.01$ cm, $L \approx 1$ cm [80].

3.2 LINEAR DIFFUSION EQUATION

To make things simpler at the beginning, we start with a nutrient diffusing within the domain not assuming any advection with the mass flow (this is a good approximation for most nutrients anyway, as shown in Section 1.3.3) and being taken up by the cylinders using a Robin boundary condition (which has already been introduced for water uptake modelling in previous chapter - see Equation (21)). Therefore, we start with a dimensional linear (isotropic) diffusion equation:

$$\frac{\partial \bar{u}}{\partial \bar{t}} = \bar{\nabla} \cdot \left(D \bar{\nabla} \bar{u} \right) \tag{127}$$

inside the domain from Figure 3.1, and a Robin boundary condition:

$$D \bar{\nabla} \bar{u} \cdot \hat{\boldsymbol{n}} = -B \bar{u} \tag{128}$$

at the cylindrical surfaces (note again that the domain is external to the cylinders)[1]. Here, D is a diffusion coefficient of the nutrient in the given environment, $\bar{u}(\bar{t}, \bar{x}_1, \bar{x}_2, \bar{x}_3)$ is a nutrient concentration at time $\bar{t}$ at point $(\bar{x}_1, \bar{x}_2, \bar{x}_3)$ in space, and B is an uptake constant. Note that the bars indicate the use of dimensional variables. For simplicity, we assume a zero-flux boundary condition at the end planes of the cylinders. The boundary conditions at the remaining boundary parts will vary depending on the problem we want to study.
We nondimensionalise the spatial variables according to the macroscale, and the time variable according to the corresponding diffusion timescale:

$$\bar{u} = u_{in} u \qquad (\bar{x}_1, \bar{x}_2, \bar{x}_3) = L(x_1, x_2, x_3) \qquad \bar{t} = \frac{L^2}{D} t,$$

where u_{in} denotes an initial nutrient concentration and L the size of the domain in the direction in which the structure is periodic. Thus, we arrive at a dimensionless (macroscale) diffusion equation:

$$\frac{\partial u}{\partial t} = \nabla^2 u, \tag{129}$$

a dimensionless initial condition:

$$u(t = 0) = 1, \tag{130}$$

1 In the context of root hairs, this can be thought of as a linearised Michaelis-Menten boundary condition without an efflux term.

and a dimensionless boundary condition:

$$\nabla u \cdot \hat{\boldsymbol{n}} = -\frac{BL}{D}u \tag{131}$$

at the cylindrical surfaces. In order to proceed with the two-scale analysis, we introduce a small parameter $\epsilon = \frac{l}{L} \ll 1$, and from now onwards, $u(t, x_1, x_2, x_3, \epsilon)$ is parameterised by ϵ. We rewrite Equation (131) as:

$$\nabla u \cdot \hat{\boldsymbol{n}} = -\frac{BL}{D}u = -\frac{BL^2}{lD}\frac{l}{L}u = -K\epsilon u, \tag{132}$$

where we have introduced $K = \frac{BL^2}{lD}$ and we assume it to be $O(1)$ as $\epsilon \to 0$ (in the context of root hairs, the justification for this assumption is discussed in Section 1.4.4).

Notice further, that we have introduced the factor ϵ in Equation (132) so that the multiscale procedure leads to a homogenisation limit, and a nontrivial sink term appears in the effective equation (a more detailed reasoning can be found in Appendix *A*; the same scaling was used in [80]).

3.2.1 *Homogenisation*

Let H denote the dimensional length of the cylinders, so that their dimensionless (macroscopic) length is $h = \frac{H}{L}$, and we assume this to be $O(1)$. Furthermore, assume that we truncate the domain at $x_3 = d > h$, and that d is $O(1)$ too. Now, we present a derivation of the effective equation using homogenisation theory. It is important to note that the two-scale analysis which follows applies only to region $x_3 < h$. Outside this region ($x_3 > h$), the situation is much simpler - diffusion is the only process taking place here. On the interface between these two regions ($x_3 = h$), we want the concentration as well as its flux to be continuous.

We use microscopic variables $(y_1, y_2, y_3) = \frac{(x_1, x_2, x_3)}{\epsilon}$ to describe local behaviour. To better understand the microscopic variables, imagine we have blown up the geometry close to a point on the surface of one of the cylinders. Sending ϵ to 0, we get the microscale geometry - $Y = Y_1 \setminus Y_2$, where $Y_1 = \{(y_1, y_2, y_3) \in \mathbb{R}^3, -0.5 \leq y_1, y_2 \leq 0.5\}$ and $Y_2 = \{(y_1, y_2, y_3) \in \mathbb{R}^3, y_1^2 + y_2^2 \leq a^2\}$.

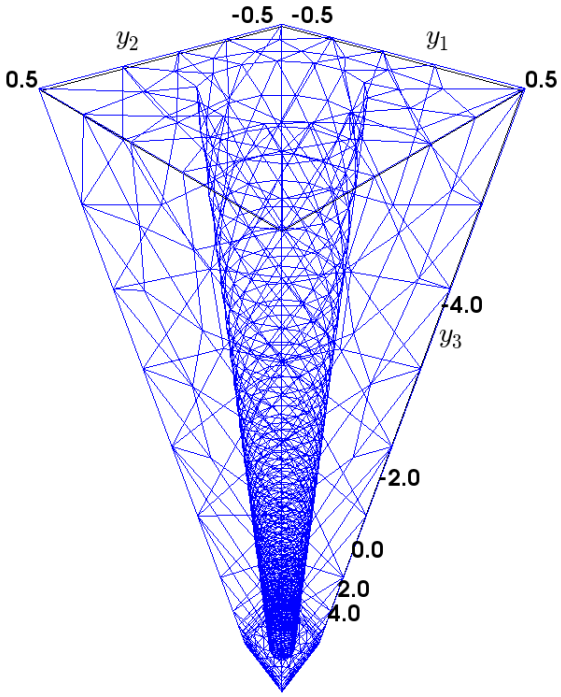


Figure 3.2.: The (meshed) microscale geometry.

As it is impossible to mesh an infinitely large domain, Figure 3.2 shows (meshed) $Y^* = Y \cap Y_3$, where $Y_3 = \{(y_1, y_2, y_3) \in \mathbb{R}^3, -5 \leq y_3 \leq 5\}$. As the analysis in this section will confirm, u_0, u_1 and u_2 (introduced in Ansatz (136)) are independent of y_3, which means that the microscale geometry is effectively two-dimensional. Therefore, the two-dimensional micro-geometry (shown in Figure 3.3) is defined as

$$C = S \setminus \{(y_1, y_2) \in \mathbb{R}^2, y_1^2 + y_2^2 \leq a^2\}, \tag{133}$$

where

$$S = (-0.5, 0.5) \times (-0.5, 0.5). \tag{134}$$

The meshed domain is shown in Figure 3.3. Assuming the independence of the microscopic and the macroscopic scales (which is the central assumption in the method of multiple scales), and using standard multiscale asymptotics rules (as introduced in Section 1.4.4), we get from Equation (129):

$$\frac{\partial u}{\partial t} = \nabla_x^2 u + \frac{2}{\epsilon} \nabla_x \cdot \nabla_y u + \frac{1}{\epsilon^2} \nabla_y^2 u, \tag{135}$$

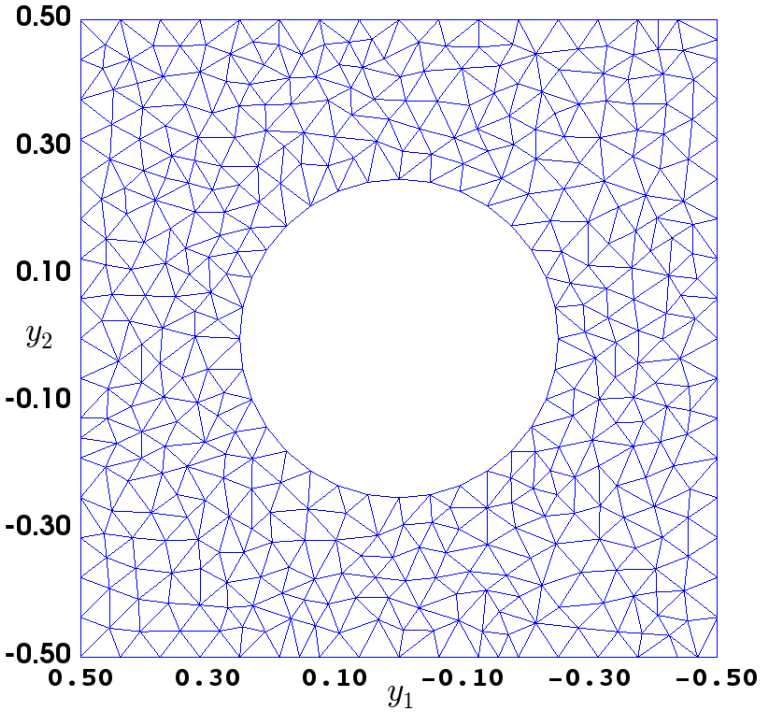


Figure 3.3.: Two-dimensional micro-geometry C as defined in Equation (133).

where we have introduced an operator $\nabla_y = (\frac{\partial}{\partial y_1}, \frac{\partial}{\partial y_2}, \frac{\partial}{\partial y_3})$. We search for a solution in the form of a two-scale ansatz:

$$u(t, \boldsymbol{x}; \epsilon) = u_0(t, \frac{\boldsymbol{x}}{\epsilon}, \boldsymbol{x}) + \epsilon u_1(t, \frac{\boldsymbol{x}}{\epsilon}, \boldsymbol{x}) + \epsilon^2 u_2(t, \frac{\boldsymbol{x}}{\epsilon}, \boldsymbol{x}) + o(\epsilon^2), \tag{136}$$

where we require $u_i(t, y_1, y_2, y_3, \boldsymbol{x})$ to be $1-$periodic in y_1 and y_2 (in this and the following two chapters, we will refer to these conditions as the periodic boundary conditions, or the periodicity conditions). Furthermore, in order to eliminate any possibility of unbounded (also called secular) growth in y_3, at each order in ϵ, we will impose certain conditions as $y_3 \to \pm\infty$. Note that for the simplicity of notation, from now onwards, we do not always explicitly write out the dependencies of functions on the macroscopic variables $\boldsymbol{x}$ and the time variable t.

Multiplying Equation (135) by ϵ^2, we get:

$$\begin{aligned} \epsilon^2 \frac{\partial \big[u_0 + o(1)\big]}{\partial t} =& \epsilon^2 \nabla_x^2 \big[u_0 + o(1)\big] + 2\epsilon \nabla_x \cdot \nabla_y \big[u_0 + \epsilon u_1 + o(\epsilon)\big] + \\ & \nabla_y^2 \big[u_0 + \epsilon u_1 + \epsilon^2 u_2 + o(\epsilon^2)\big], \end{aligned} \tag{137}$$

and from (132), we obtain the cylindrical surface boundary condition:

$$\begin{aligned}\epsilon\nabla_x\big[u_0+\epsilon u_1+o(\epsilon^2)\big]\cdot\hat{\boldsymbol{n}}+\nabla_y\big[u_0+\epsilon u_1+\epsilon^2u_2+o(\epsilon^2)\big]\cdot\hat{\boldsymbol{n}}=\\ -K\epsilon^2\big[u_0+o(1)\big].\end{aligned}\tag{138}$$

Note again, that this boundary condition applies only in the region occupied by the cylinders ($x_3 < h$).

Next, we study the continuity equation (137) and the boundary condition (138) at different orders of ϵ.

Leading order

At $O(1)$ in Equation (137), we find:

$$0=\nabla_y^2u_0=\frac{\partial^2u_0}{\partial y_1^2}+\frac{\partial^2u_0}{\partial y_2^2}+\frac{\partial^2u_0}{\partial y_3^2},$$

equipped with the periodic boundary conditions in y_1 and y_2, and the same order in boundary condition (138) gives $\nabla_y u_0\cdot\hat{\boldsymbol{n}}=0$ at $y_1^2+y_2^2=a^2$. We see, that a linear growth in y_3 is a possible far-field ($y_3\to\pm\infty$) behaviour. This would mean that the solution becomes unbounded, and thus the secularity conditions at this order must state:

$$\lim_{y_3\to\infty}\frac{\partial u_0(t,\boldsymbol{y},\boldsymbol{x})}{\partial y_3}=0=\lim_{y_3\to-\infty}\frac{\partial u_0(t,\boldsymbol{y},\boldsymbol{x})}{\partial y_3}.\tag{139}$$

Clearly, this problem admits a solution independent of the microscopic variables:

$$u_0=u_0(t,\boldsymbol{x}).\tag{140}$$

Note that later on in the homogenisation procedure, we will uncover an effective (homogenised) equation, which u_0 solves. Next, we show the uniqueness of solution (140).

Assume for the sake of contradiction that there exists a function $g(\boldsymbol{y})$ satisfying the Laplace's equation and all the (microscopic) boundary conditions, which is nontrivially dependent on $\boldsymbol{y}$. Multiplying the Laplace's equation for g by g, we get $g\nabla_y^2g=0$. Defining

$$Y^N=[-0.5,0.5]\times[-0.5,0.5]\times[-N,N],\tag{141}$$

integrating over Y^N, and using Green's first identity (see [130]), we get:

$$0 = \int_{Y^N} g\nabla_y^2 g d\Omega = \int_{\partial Y^N} g\nabla_y g \cdot \hat{\boldsymbol{n}} dS - \int_{Y^N} \nabla_y g \cdot \nabla_y g d\Omega =$$

$$\int_C g(y_3 = N)\frac{\partial g(y_3 = N)}{\partial y_3} dS - \int_C g(y_3 = -N)\frac{\partial g(y_3 = -N)}{\partial y_3} dS +$$

$$\int_{\partial Y^N_{per}} g\nabla_y g \cdot \hat{\boldsymbol{n}} dS - \int_{Y^N} \left\|\nabla_y g\right\|^2 d\Omega,$$

where ∂Y^N_{per} is the part of the boundary of Y^N at which we impose the periodic boundary conditions. Thus, the integral over this boundary part is zero and we are left with:

$$\int_{Y^N} \left\|\nabla_y g\right\|^2 d\Omega = \int_C g(y_3 = N)\frac{\partial g(y_3 = N)}{\partial y_3} dS -$$

$$\int_C g(y_3 = -N)\frac{\partial g(y_3 = -N)}{\partial y_3} dS$$

Using the secularity conditions (139), the $N \to \infty$ limit yields:

$$\int_Y \left\|\nabla_y g\right\|^2 d\Omega = 0.$$

As $\left\|\nabla_y g\right\|^2$ is always non-negative, we conclude that $\nabla_y g = \mathbf{0}$ everywhere, and thus g is independent of the microscopic variables. We arrived at a contradiction, and thus we know that there exists no microscopically-nontrivial solution to the cell problem at this order.

$O(\epsilon)$

At $O(\epsilon)$, we obtain a continuity equation $\nabla_y^2 u_1 = 0$, a cylindrical surface boundary condition $\nabla_y u_1 \cdot \hat{\boldsymbol{n}} = -\nabla_x u_0 \cdot \hat{\boldsymbol{n}}$, and the usual periodic boundary conditions in y_1 and y_2. The cylindrical surface boundary condition at this order impels us to search for solution in the form:

$$u_1(t, y_1, y_2, y_3, \boldsymbol{x}) = f(t, \boldsymbol{x}) + \nabla_x u_0(t, \boldsymbol{x}) \cdot \boldsymbol{\lambda}(y_1, y_2, y_3), \tag{142}$$

where the microscopically-nontrivial term comes from the cylindrical surface boundary condition, $\boldsymbol{\lambda}(y_1, y_2, y_3) = \big(\lambda_1(y_1, y_2, y_3), \lambda_2(y_1, y_2, y_3), \lambda_3(y_1, y_2, y_3)\big)$,

and f is an as yet undetermined function of t, x_1, x_2, x_3. In order to satisfy the continuity equation, we impose:

$$\nabla_y^2 \lambda_1 = \nabla_y^2 \lambda_2 = \nabla_y^2 \lambda_3 = 0, \tag{143}$$

and to avoid the secular growth in y_3 (compare with the previous section), we impose the secularity conditions:

$$\lim_{y_3 \to \infty} \frac{\partial \lambda_i}{\partial y_3} = 0 = \lim_{y_3 \to -\infty} \frac{\partial \lambda_i}{\partial y_3}$$

for $i \in \{1, 2, 3\}$. Using Ansatz (142) in the cylindrical surface boundary condition, we get:

$$(-\frac{\partial u_0}{\partial x_1}, -\frac{\partial u_0}{\partial x_2}) \cdot (n_1, n_2) = (-\frac{\partial u_0}{\partial x_1}, -\frac{\partial u_0}{\partial x_2}, -\frac{\partial u_0}{\partial x_3}) \cdot (n_1, n_2, 0) = -\nabla_x u_0 \cdot \hat{\boldsymbol{n}} =$$

$$\nabla_y u_1 \cdot \hat{\boldsymbol{n}} = (\frac{\partial u_0}{\partial x_1}\frac{\partial \lambda_1}{\partial y_1} + \frac{\partial u_0}{\partial x_2}\frac{\partial \lambda_2}{\partial y_1} + \frac{\partial u_0}{\partial x_3}\frac{\partial \lambda_3}{\partial y_1}, \frac{\partial u_0}{\partial x_1}\frac{\partial \lambda_1}{\partial y_2} +$$

$$\frac{\partial u_0}{\partial x_2}\frac{\partial \lambda_2}{\partial y_2} + \frac{\partial u_0}{\partial x_3}\frac{\partial \lambda_3}{\partial y_2}, ...) \cdot (n_1, n_2, 0) =$$

$$(\frac{\partial u_0}{\partial x_1}\frac{\partial \lambda_1}{\partial y_1} + \frac{\partial u_0}{\partial x_2}\frac{\partial \lambda_2}{\partial y_1} + \frac{\partial u_0}{\partial x_3}\frac{\partial \lambda_3}{\partial y_1}, \frac{\partial u_0}{\partial x_1}\frac{\partial \lambda_1}{\partial y_2} + \frac{\partial u_0}{\partial x_2}\frac{\partial \lambda_2}{\partial y_2} + \frac{\partial u_0}{\partial x_3}\frac{\partial \lambda_3}{\partial y_2}) \cdot (n_1, n_2),$$

which is satisfied, provided we impose:

$$\nabla_y \lambda_1 \cdot \hat{\boldsymbol{n}} = \frac{y_1}{a} = -n_1 \qquad \nabla_y \lambda_2 \cdot \hat{\boldsymbol{n}} = \frac{y_2}{a} = -n_2 \qquad \nabla_y \lambda_3 \cdot \hat{\boldsymbol{n}} = 0 \tag{144}$$

for (y_1, y_2, y_3) belonging to the cylindrical surface. The conditions for λ_3 are the same as those for g from the previous order. Therefore, we know that constant λ_3 (i.e. independent of the microscopic variables) is the only possible solution. We now show that the solution to the λ_1 problem exists, it does not depend on y_3, and it is unique up to a constant.

First, we show that a certain problem defined in the two-dimensional unit cell C (see Figure 3.3) has a solution. Assume Laplace's equation $\nabla_y^2 \zeta = 0$ in C equipped with the cylindrical surface condition $\nabla_y \zeta \cdot \hat{\boldsymbol{n}} = -n_1$ and with the periodic boundary conditions in y_1 and y_2. If we add a normalisation condition $\int_C \zeta dS = 0$, the Lax-Milgram theorem[2] ensures the existence of a unique

2 This is a theorem from functional analysis, and the explanation of how it can be used to prove the existence of a unique solution of our problem is beyond the scope of this thesis; for more information, we refer interested readers to [19].

solution to this problem. It is therefore clear that ζ satisfying the required conditions exists.

This implies, that the solution to the λ_1 problem exists as well, as we can simply write it as $\lambda_1(y_1, y_2, y_3) = \zeta(y_1, y_2)$, and clearly, this solution is independent of y_3. Let λ_1^1 and λ_1^2 be two distinct solutions, and define $\lambda_1^* = \lambda_1^1 - \lambda_1^2$. Then λ_1^* satisfies the same conditions as g from the previous order, which implies that λ_1^* is constant, and thus the solution to the λ_1 problem is unique up to a constant.

By the same reasoning, $\lambda_2(y_1, y_2, y_3) = \lambda_2(y_1, y_2)$, and the solution to this problem is unique up to a constant. We conclude that u_1 is independent of y_3.

Note that solving the cell problems for λ_1 and λ_2 analytically is a difficult task, because the domain is multiply-connected. If we assumed that instead of cylinders, the root hairs were rectangular cuboids, and that the resulting root hair boundary in the unit cell setting satisfied either $y_1 = \pm a$ or $y_2 = \pm a$, then we could analyse the problems fully in cartesian coordinates. The hair surface boundary conditions for the cell problems would become:

$$\nabla_y \lambda_1 \cdot \hat{\boldsymbol{n}} = \begin{cases} 1 & \text{at } y_1 = a \\ -1 & \text{at } y_1 = -a \\ 0 & \text{elsewhere.} \end{cases} \tag{145}$$

$$\nabla_y \lambda_2 \cdot \hat{\boldsymbol{n}} = \begin{cases} 1 & \text{at } y_2 = a \\ -1 & \text{at } y_2 = -a \\ 0 & \text{elsewhere.} \end{cases} \tag{146}$$

However, in this case, one still cannot write the resulting unit-cell domain as a product of two intervals (and therefore, the x and y dependencies of these solutions are not separable). The only analytical approach known to us is to map the domain conformally to a domain which consists of two concentric circles having different radii, with the smaller circle being cut out from the larger one. We then would wish to obtain the analytical solution using separation of variables (namely the polar radius r and the azimuthal angle φ), analogously to what we did in Section 2.5.1 (separated variables being r and t) as well as in

Section 2.5.2 (separated variables being r and x_3). However, the boundary conditions (145) and (146) would introduce inhomogeneity onto the inner (now circular) boundary, which would yield dependency of the boundary conditions for $R(r)$ on φ, and the transformed periodic boundary conditions would further complicate the solution process. Therefore, these problems are much more difficult to solve analytically than those discussed in the previous chapter, and we will only solve them numerically in this chapter.

$O(\epsilon^2)$

Moving to $O(\epsilon^2)$, we get:

$$\nabla_y^2 u_2 = \frac{\partial u_0}{\partial t} - \nabla_x^2 u_0 - 2\nabla_x \cdot \nabla_y u_1, \tag{147}$$

a cylindrical surface boundary condition:

$$\nabla_y u_2 \cdot \hat{\boldsymbol{n}} = -K u_0 - \nabla_x u_1 \cdot \hat{\boldsymbol{n}}, \tag{148}$$

and the periodic boundary conditions in y_1 and y_2. Integrating the continuity equation over Y^N (as defined in Equation (141)) gives:

$$2N(1-\pi a^2)\frac{\partial u_0}{\partial t} = 2N(1-\pi a^2)\nabla_x^2 u_0 + \int_{Y^N} \nabla_y \cdot \nabla_y u_2 d\Omega + 4N \int_C \nabla_x \cdot \nabla_y u_1 dS,$$

where C is the two-dimensional unit cell (see Figure 3.3), and dividing by $2N(1-\pi a^2)$ yields:

$$\frac{\partial u_0}{\partial t} = \nabla_x^2 u_0 + \frac{1}{2N(1-\pi a^2)} \int_{Y^N} \nabla_y \cdot \nabla_y u_2 d\Omega + \frac{2}{1-\pi a^2} \int_C \nabla_x \cdot \nabla_y u_1 dS. \tag{149}$$

The divergence theorem gives:

$$\begin{aligned} \int_{Y^N} \nabla_y \cdot \nabla_y u_2 d\Omega = \int_{\partial Y^N} \nabla_y u_2 \cdot \hat{\boldsymbol{n}} dS = \int_{P^N} \nabla_y u_2 \cdot \hat{\boldsymbol{n}} dS + \\ \int_{U^N} \nabla_y u_2 \cdot \hat{\boldsymbol{n}} dS + \int_C \frac{\partial u_2(y_3 = N)}{\partial y_3} dS - \int_C \frac{\partial u_2(y_3 = -N)}{\partial y_3} dS, \end{aligned} \tag{150}$$

where we split the boundary into a part P^N at which the periodic boundary conditions are imposed (i.e. $y_1 = \pm 0.5$, $y_2 = \pm 0.5$), an uptaking part U^N ($y_1^2 +$

$y_2^2 = a^2$), and the remaining parts are located at $y_3 = N$ and $y_3 = -N$. Due to the periodic boundary conditions, the integral over P^N vanishes. Applying (148) to the second integral, we get:

$$\frac{1}{2N(1-\pi a^2)} \int\limits_{Y^N} \nabla_y \cdot \nabla_y u_2 d\Omega = \frac{1}{2N(1-\pi a^2)} \int\limits_{U^N} \{-Ku_0 - \nabla_x u_1 \cdot \hat{\boldsymbol{n}}\} dS +$$

$$\frac{1}{2N(1-\pi a^2)} \int\limits_{C} \frac{\partial u_2(y_3 = N)}{\partial y_3} dS - \frac{1}{2N(1-\pi a^2)} \int\limits_{C} \frac{\partial u_2(y_3 = -N)}{\partial y_3} dS =$$

$$-\frac{2\pi Ka}{1-\pi a^2} u_0 - \frac{1}{1-\pi a^2} \int\limits_{U} \nabla_x u_1 \cdot \hat{\boldsymbol{n}} dl +$$

$$\frac{1}{2N(1-\pi a^2)} \int\limits_{C} \frac{\partial u_2(y_3 = N)}{\partial y_3} dS - \frac{1}{2N(1-\pi a^2)} \int\limits_{C} \frac{\partial u_2(y_3 = -N)}{\partial y_3} dS,$$

where:

$$U = \{(y_1, y_2) \in \mathbb{R}^2, y_1^2 + y_2^2 = a^2\}. \tag{151}$$

Substituting this result into Equation (149) leads to:

$$\frac{\partial u_0}{\partial t} = \nabla_x^2 u_0 - \frac{2\pi Ka}{1-\pi a^2} u_0 - \frac{1}{1-\pi a^2} \int\limits_{U} \nabla_x u_1 \cdot \hat{\boldsymbol{n}} dl +$$

$$\frac{2}{1-\pi a^2} \int\limits_{C} \nabla_x \cdot \nabla_y u_1 dS + \frac{1}{2N(1-\pi a^2)} \int\limits_{C} \frac{\partial u_2(y_3 = N)}{\partial y_3} dS -$$

$$\frac{1}{2N(1-\pi a^2)} \int\limits_{C} \frac{\partial u_2(y_3 = -N)}{\partial y_3} dS.$$

In order to obtain the homogenised equation, we send N to ∞, and we use secularity conditions:

$$\lim_{y_3 \to \infty} \frac{\partial u_2}{\partial y_3} = 0 = \lim_{y_3 \to -\infty} \frac{\partial u_2}{\partial y_3}$$

(ensuring the bounded growth of u_2) to get:

$$\frac{\partial u_0}{\partial t} = \nabla_x^2 u_0 - \frac{2\pi Ka}{1-\pi a^2} u_0 + \frac{2}{1-\pi a^2} \int\limits_{C} \nabla_x \cdot \nabla_y u_1 dS - \frac{1}{1-\pi a^2} \int\limits_{U} \nabla_x u_1 \cdot \hat{\boldsymbol{n}} dl. \tag{152}$$

Now, we show that the two integrals in this equation are actually equal. First, using symmetries of the unit cell geometry, we get:

$$\int\limits_{P} \nabla_x f(t, \boldsymbol{x}) \cdot \hat{\boldsymbol{n}} dl = 0 = \int\limits_{U} \nabla_x f(t, \boldsymbol{x}) \cdot \hat{\boldsymbol{n}} dl,$$

where $P = \partial S$ is the boundary of the unit square S given by Equation (134). Using symmetry of second derivatives and Ansatz (142) for u_1, we have:

$$\int_C \nabla_x \cdot \nabla_y u_1 dS = \int_C \nabla_y \cdot \nabla_x u_1 dS = \int_C \nabla_y \cdot \nabla_x \big[\nabla_x u_0(t, \boldsymbol{x}) \cdot \boldsymbol{\lambda}(y_1, y_2)\big] dS,$$

which, taking into account the divergence theorem, becomes:

$$\int_P \nabla_x \big[\nabla_x u_0(t, \boldsymbol{x}) \cdot \boldsymbol{\lambda}(y_1, y_2)\big] \cdot \hat{\boldsymbol{n}} dl + \int_U \nabla_x \big[\nabla_x u_0(t, \boldsymbol{x}) \cdot \boldsymbol{\lambda}(y_1, y_2)\big] \cdot \hat{\boldsymbol{n}} dl.$$

Thanks to the periodicity conditions on λ_1, λ_2 and λ_3), it can be easily shown that:

$$\int_P \nabla_x \big[\nabla_x u_0(t, \boldsymbol{x}) \cdot \boldsymbol{\lambda}(y_1, y_2)\big] \cdot \hat{\boldsymbol{n}} dl = 0,$$

and thus we conclude:

$$\int_U \nabla_x u_1 \cdot \hat{\boldsymbol{n}} dl = \int_C \nabla_x \cdot \nabla_y u_1 dS.$$

Applying this result to Equation (152) gives:

$$\frac{\partial u_0}{\partial t} = \nabla_x^2 u_0 - \frac{2\pi K a}{1 - \pi a^2} u_0 + \frac{1}{1 - \pi a^2} \int_C \nabla_x \cdot \nabla_y u_1 dS.$$

Finally, we use our knowledge of u_1 (Ansatz (142) as well as the fact that λ_3 is constant) to get:

$$\int_C \nabla_x \cdot \nabla_y u_1 dS = \nabla_x \nabla_x u_0 : B,$$

where

$$\nabla_x \nabla_x u_0 = \begin{pmatrix} \frac{\partial^2 u_0}{\partial x_1^2} & \frac{\partial^2 u_0}{\partial x_1 \partial x_2} & \frac{\partial^2 u_0}{\partial x_1 \partial x_3} \\ \frac{\partial^2 u_0}{\partial x_2 \partial x_1} & \frac{\partial^2 u_0}{\partial x_2^2} & \frac{\partial^2 u_0}{\partial x_2 \partial x_3} \\ \frac{\partial^2 u_0}{\partial x_3 \partial x_1} & \frac{\partial^2 u_0}{\partial x_3 \partial x_2} & \frac{\partial^2 u_0}{\partial x_3^2} \end{pmatrix}$$

is a Hessian matrix,

$$B = \begin{pmatrix} \int_C \frac{\partial \lambda_1}{\partial y_1} dS & \int_C \frac{\partial \lambda_2}{\partial y_1} dS & 0 \\ \int_C \frac{\partial \lambda_1}{\partial y_2} dS & \int_C \frac{\partial \lambda_2}{\partial y_2} dS & 0 \\ 0 & 0 & 0 \end{pmatrix} \tag{153}$$

is a constant matrix, and : is an inner product between two matrices defined as $M : N = \sum_{ij} M_{ij} N_{ij}$ (see [104]).

Thus, we have arrived at the effective macroscale equation:

$$\frac{\partial u_0}{\partial t} = \nabla_x \nabla_x u_0 : D_{eff} - \frac{2\pi K a}{1 - \pi a^2} u_0,$$

where

$$D_{eff} = \frac{1}{1 - \pi a^2} B + I \tag{154}$$

is an effective (anisotropic) diffusion tensor and

$$I = \begin{pmatrix} 1 & 0 & 0 \\ 0 & 1 & 0 \\ 0 & 0 & 1 \end{pmatrix}$$

is the identity matrix. This can also be rewritten as:

$$\frac{\partial u_0}{\partial t} = \nabla_x \cdot \left(D_{eff} \nabla_x u_0 \right) - \frac{2\pi K a}{1 - \pi a^2} u_0. \tag{155}$$

We now briefly summarise the homogenisation procedure. From $O(1)$, we concluded that the leading order solution u_0 is independent of the microscale. From $O(\epsilon)$, $u_1(t, y_1, y_2, \boldsymbol{x}) = f_1(t, \boldsymbol{x}) + \left(\frac{\partial u_0(t,\boldsymbol{x})}{\partial x_1}, \frac{\partial u_0(t,\boldsymbol{x})}{\partial x_2} \right) \cdot \left(\lambda_1(y_1, y_2), \lambda_2(y_1, y_2) \right)$ was concluded, with λ_1 and λ_2 satisfying Laplace's equation in C (from Figure 3.3), the boundary conditions (144) at the circular boundary, and the periodicity conditions. Using this information, integration of the continuity equation at $O(\epsilon^2)$ yielded the homogenised equation (155). The $-\frac{2\pi K a}{1-\pi a^2} u_0$ term from this equation is a sink term representing uptake by the cylinders. The diffusion tensor D_{eff} captures the effects of impedance to the diffusion due to the presence of the cylinders, and is dependent on λ_1 and λ_2 via matrix B (153).

Using symmetry arguments, we now show that:

$$\int_C \frac{\partial \lambda_1}{\partial y_1} dS = \int_C \frac{\partial \lambda_2}{\partial y_2} dS. \tag{156}$$

First, recall the λ_1 problem, i.e. the continuity equation $\frac{\partial^2 \lambda_1}{\partial y_1^2} + \frac{\partial^2 \lambda_1}{\partial y_2^2} = 0$ in C, the boundary condition $\frac{\partial \lambda_1}{\partial y_1} n_1 + \frac{\partial \lambda_1}{\partial y_2} n_2 = -n_1$ at U, and the periodic boundary conditions at $y_1, y_2 = \pm 0.5$. Upon swapping the coordinate axes y_1 and y_2, we get a continuity equation $\frac{\partial^2 f}{\partial y_2^2} + \frac{\partial^2 f}{\partial y_1^2} = \frac{\partial^2 f}{\partial y_1^2} + \frac{\partial^2 f}{\partial y_2^2} = 0$ in C, the same periodic

boundary conditions at $y_1, y_2 = \pm 0.5$, and the boundary condition $\frac{\partial f}{\partial y_2} n_2 + \frac{\partial f}{\partial y_1} n_1 = \frac{\partial f}{\partial y_1} n_1 + \frac{\partial f}{\partial y_2} n_2 = -n_2$ at U. These are exactly the conditions that define the λ_2 problem. In other words, defining:

$$f(s,t) = \lambda_1(t,s) \qquad \forall (s,t) \in C,$$

we see that f satisfies all conditions on λ_2, and due to our uniqueness result, we get:

$$\lambda_2(s,t) = \lambda_1(t,s) \qquad \forall (s,t) \in C \tag{157}$$

up to a constant. As a consequence, we get:

$$\frac{\partial \lambda_1}{\partial y_1}\Big|_{(y_1,y_2)=(s,t)} = \frac{\partial \lambda_2}{\partial y_2}\Big|_{(y_1,y_2)=(t,s)} \qquad \forall (s,t) \in C$$

which upon integration proves Equation (156) to be true. Note that from the (macroscopic) point of view of Equation (155), there is also no reason for the diagonal elements corresponding to x_1 and x_2 to be different.

It may further seem that we have obtained nonzero off-diagonal elements in the diffusion tensor, which often gives rise to a nontrivial behaviour. However, due to symmetry, off-diagonal elements are actually zero. First, notice that Equation (157) also implies:

$$\frac{\partial \lambda_1}{\partial y_2}\Big|_{(y_1,y_2)=(s,t)} = \frac{\partial \lambda_2}{\partial y_1}\Big|_{(y_1,y_2)=(t,s)} \qquad \forall (s,t) \in C,$$

and this yields:

$$\int_C \frac{\partial \lambda_1}{\partial y_2} dS = \int_C \frac{\partial \lambda_2}{\partial y_1} dS.$$

We now show that $\int_C \frac{\partial \lambda_1}{\partial y_2} dS = 0$. Using the divergence theorem, we get:

$$\int_C \frac{\partial \lambda_1}{\partial y_2} dS = \int_C \nabla_y \cdot (0, \lambda_1) dS = \int_{\partial C} (0, \lambda_1) \cdot \hat{\boldsymbol{n}} dl = \int_{\partial C} \lambda_1 n_2 dl,$$

and using the periodicity of λ_1, we conclude:

$$\int_C \frac{\partial \lambda_1}{\partial y_2} dS = \int_U \lambda_1 n_2 dl.$$

For $(y_1, y_2) \in U$, we have $n_2(y_1, y_2) = -n_2(y_1, -y_2)$, and provided we can show:

$$\lambda_1(y_1, y_2) = \lambda_1(y_1, -y_2), \tag{158}$$

maximal mesh size	$\int_C \frac{\partial \lambda_1}{\partial y_1} dS$	$\int_C \frac{\partial \lambda_2}{\partial y_2} dS$	$\int_C \frac{\partial \lambda_1}{\partial y_2} dS$	$\int_C \frac{\partial \lambda_2}{\partial y_1} dS$
0.4	-0.11	-0.11	-2.4×10^{-4}	-2.2×10^{-4}
0.2	-0.11	-0.11	4.5×10^{-4}	4.2×10^{-4}
0.1	-0.12	-0.12	-2.0×10^{-4}	-2.0×10^{-4}
0.05	-0.13	-0.13	-3.4×10^{-6}	-3.7×10^{-6}
0.03	-0.13	-0.13	-3.0×10^{-7}	5.6×10^{-6}
0.02	-0.13	-0.13	9.8×10^{-7}	1.0×10^{-6}

Table 3.1.: Numerical confirmation that $\int_C \frac{\partial \lambda_1}{\partial y_2} dS = \int_C \frac{\partial \lambda_2}{\partial y_1} dS = 0$ and $\int_C \frac{\partial \lambda_1}{\partial y_1} dS = \int_C \frac{\partial \lambda_2}{\partial y_2} dS \approx -0.13$

we prove that $\int_C \frac{\partial \lambda_1}{\partial y_2} dS = 0$. To show this, we introduce a coordinate transformation $(y_1, y_2) \to (y_1, -y_2)$. In other words, define:

$$g(s,t) = \lambda_1(s,-t).$$

This function satisfies the same continuity equation $\frac{\partial^2 g}{\partial y_1^2} + \frac{\partial^2 g}{\partial (-y_2)^2} = \frac{\partial^2 g}{\partial y_1^2} + \frac{\partial^2 g}{\partial y_2^2} = 0$, the same periodicity conditions and the same boundary condition $n_1 \frac{\partial g}{\partial y_1} - n_2 \frac{\partial g}{\partial (-y_2)} = n_1 \frac{\partial g}{\partial y_1} + n_1 \frac{\partial g}{\partial (y_2)} = -n_1$ as λ_1. Because of our uniqueness results for λ_1, we conclude that $\lambda_1(s,-t) = \lambda_1(s,t)$, i.e. we have just proven Equation (158). This property can clearly be seen in Figure 3.18.

To support our symmetry arguments, we also compute these integrals numerically for a decreasing value of a maximal mesh size. The results are shown in Table 3.1.

Thus, we only need to solve the λ_1 problem (from now on called the unit cell problem) to obtain the homogenised equation (155).

Recall, that this analysis is valid only in the part of the domain occupied by the cylinders ($x_3 < h$). Outside this domain ($x_3 > h$), we are left with a simple diffusion equation:

$$\frac{\partial u_0}{\partial t} = \nabla_x \cdot \nabla_x u_0.$$

Note that we did not need to analyse the situation at $x_3 = 0$ separately, as u_0, u_1 and u_2 are all independent of y_3 for $0 < x_3 < h$, and thus nothing drives y_3-

variation at $x_3 = 0$. Moreover, the interface at $x_3 = h$ does not require special attention either (even though there exists a switch in the cylindrical surface boundary condition) - we simply impose that the homogenised solution and its flux are continuous.

3.2.2 *One-dimensional modelling*

If we assume that the initial and the macroscopic boundary conditions are independent of x_1 and x_2, then the same is true for the homogenised solution u_0. Thus, we have $\frac{\partial u_0}{\partial x_1} = \frac{\partial u_0}{\partial x_2} = 0$ everywhere in the domain, and this effectively yields a one-dimensional homogenised equation:

$$\frac{\partial u_0}{\partial t} = \frac{\partial^2 u_0}{\partial x_3^2} - \frac{2\pi K a}{1 - \pi a^2} u_0 \tag{159}$$

for $x_3 < h$, and:

$$\frac{\partial u_0}{\partial t} = \frac{\partial^2 u_0}{\partial x_3^2} \tag{160}$$

for $x_3 > h$. This way, the homogenised solution is only dependent on one spatial variable, i.e. distance from the root surface (x_3). Note that the same approach was chosen when modelling uptake by root hairs in [80], and that this way, the homogenised solution can (at least in principle) be compared with nutrient distributions extracted from experiments, as in [18] and [94] (water being the nutrient here).

In this section, we will study how well the solutions of this one-dimensional equation (equipped with various boundary conditions) approximate the corresponding full-geometry numerical simulations. Let us first consider a steady-state scenario, for which the numerical results will also be compared with exact solutions.

Steady state

We have:

$$0 = \frac{\partial^2 u_0}{\partial x_3^2} - \frac{2\pi K a}{1 - \pi a^2} u_0 \tag{161}$$

for $x_3 < h$, and:

$$0 = \frac{\partial^2 u_0}{\partial x_3^2} \tag{162}$$

for $x_3 > h$. Assuming a Dirichlet boundary condition $u(x_3 = 0) = u_{max} > 0$ (which can be used to model nutrient uptake by a field of crops where a fertiliser is applied to the top soil) leads to $u_0(x_3 = 0) = u_{max}$ for the homogenised solution. If we assumed $\lim_{x_3 \to \infty} u_0(x_3) = 0$ (modelling nutrients residing mostly in the top soil, e.g. phosphate), we would only be able to obtain a (unique) solution to this problem in the space of continuous functions (not continuously differentiable though). Truncating the domain at $x_3 = d$, and assuming $u_0(d) = 0$, we can find a unique solution to this problem in the space of continuously differentiable functions (so that not only the solution itself is continuous, but also its flux is), and the solution is:

$$u_0(x_3) = \begin{cases} Ae^{\lambda x_3} + (u_{max} - A)e^{-\lambda x_3} & \text{if } 0 < x_3 < h \\ C(x_3 - d) & \text{if } h < x_3 < d, \end{cases} \tag{163}$$

where $\lambda = \sqrt{\frac{2\pi K a}{1-\pi a^2}} > 0$. Matching solutions at $x_3 = h$, we get that $A = \frac{Q}{P}$, where:

$$Q = u_{max} e^{-\lambda h}\big[\lambda(d-h) - 1\big],$$

$$P = e^{\lambda h} - e^{-\lambda h} - \lambda e^{\lambda h}(h-d) - \lambda e^{-\lambda h}(h-d),$$

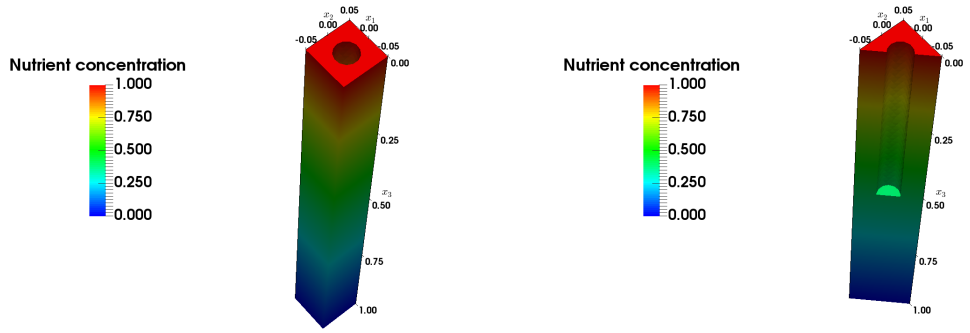
and finally:

$$C = A\lambda e^{\lambda h} - (u_{max} - A)\lambda e^{-\lambda h}.$$

For the full-geometry problem, we consider the steady-state version of Equation (129):

$$0 = \nabla^2 u, \tag{164}$$

and find the solution numerically in FEniCS [83] (we use FEniCS for all simulations in this chapter). Notice, that as we have assumed the initial and the boundary conditions to be independent of x_1 and x_2, it is sufficient to simulate Equation (164) in a three-dimensional unit cell (which only contains one cylinder and is shown in Figure 3.4), equipped with the cylindrical surface boundary condition (132). We used the following parameters: $\epsilon = 0.1$, $u_{max} = 1.0$, $K = 1.0$, $h = 0.5$, $d = 1.0$, and $a = 0.25$ (this can still be considered $O(1)$, as we know that a must by definition be less than 0.5). The resulting solution is shown in Figure 3.4, where we also introduce a clipped domain view, revealing



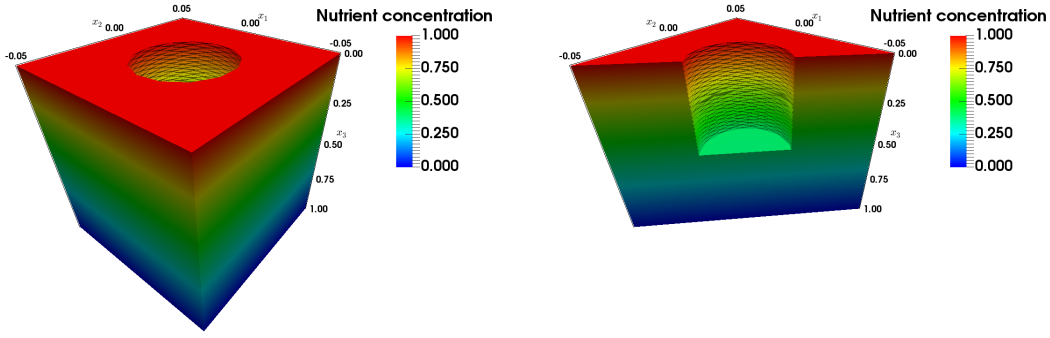
(a) Unit cell

(b) Clipped domain

Figure 3.4.: The steady state solution using the Dirichlet boundary conditions at $x_3 = 0$ and $x_3 = d$.

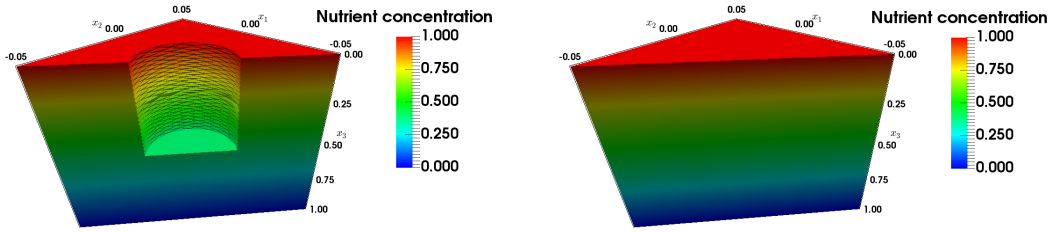
the behaviour at the cylindrical surface. From now onwards, we will mostly present results using the clipped domain.

Moreover, as the distance between the cylinders is assumed to be much smaller than the length of the cylinders, aspect ratio of this geometry makes it hard for us to clearly see certain features of these figures. Therefore, from now onwards, we will stretch the x_1 and x_2 axes, so that the aspect ratio is closer to 1 (see Figure 3.5). We compare this result to the numerical simulation of the homogenised equation with the same boundary conditions. The results are shown in Figure 3.6. Note that we do not use the equations (161) and (162) exactly - instead, we choose to artificially add diffusion in x_1 and x_2, which has no effect on the resulting solution, provided we do not introduce any x_1 or x_2 variation via initial or boundary conditions (we choose the constant initial condition everywhere, and zero-flux boundary conditions on all the boundaries of the cuboid that are not perpendicular to the direction of x_3). This way, the geometry for the homogenised problem can be chosen to be almost identical to the full-geometry (apart from the extracted cylinder), and the full-geometry and the homogenisation results are much easier to (visually) compare in FEniCS. We will use this approach throughout this and the next two chapters. Figure 3.6 demonstrates the main idea behind homogenisation - the solution to the homogenised equation is an average (in microscopic y_1 and y_2) of the solution to the full-geometry problem.



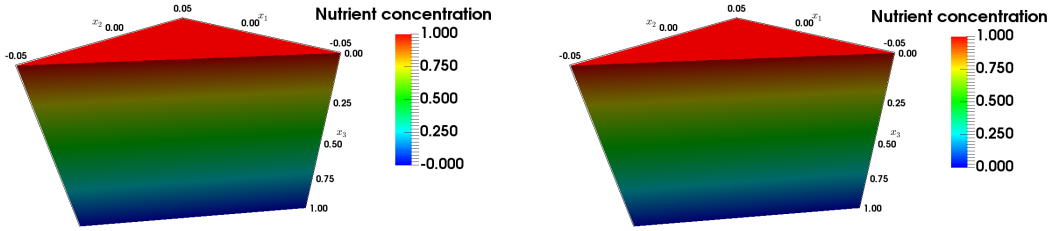
(a) Unit cell (b) Clipped domain

Figure 3.5.: The steady state solution using the Dirichlet boundary conditions at $x_3 = 0$ and $x_3 = d$. In order to obtain the aspect ratio of (approximately) 1, the x_1 and x_2 axes are stretched.



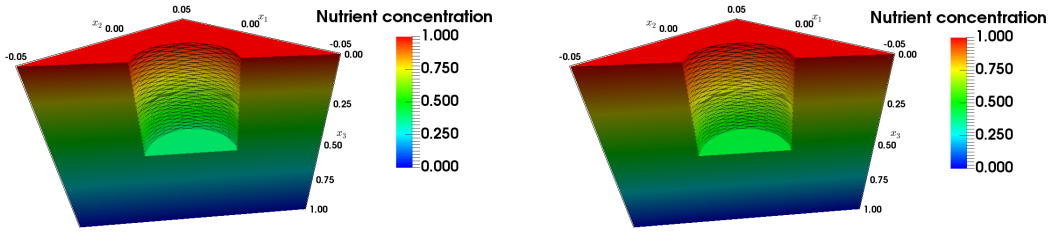
(a) Full-geometry numerics (FEniCS) (b) Homogenisation result (FEniCS)

Figure 3.6.: Comparison between the full-geometry numerics and the homogenisation solution for the steady-state scenario.



(a) Analytic solution (b) Numerics (FEniCS)

Figure 3.7.: Comparison between the analytic and the numerical solutions of the homogenised equation (steady states).



(a) With uptake (b) Without uptake

Figure 3.8.: The unit-cell simulations with and without the uptake.

We also compare the numerically obtained solution to the homogenised equation with the analytic solution as found above (Equation (163)). Figure 3.7 shows a strong agreement between the results. Figure 3.8 shows a comparison with a model without uptake (we achieved this by setting $K = 0.0$). This way, we can see what impact the nutrient uptake has on the overall solution. In order to see the difference more clearly, we plot the solution along a line with a start point at $(x_1, x_2, x_3) = (-0.05, -0.05, 0)$ and an end point at $(x_1, x_2, x_3) = (-0.05, -0.05, 1)$ - see Figure 3.9. From Figures 3.9 and 3.8 we see that even though the nutrient uptake has a nontrivial effect on the overall behaviour, this is mostly determined by the macroscopic gradient that we have imposed using the boundary conditions at $x_3 = 1.0$ and $x_3 = 0.0$. To soften

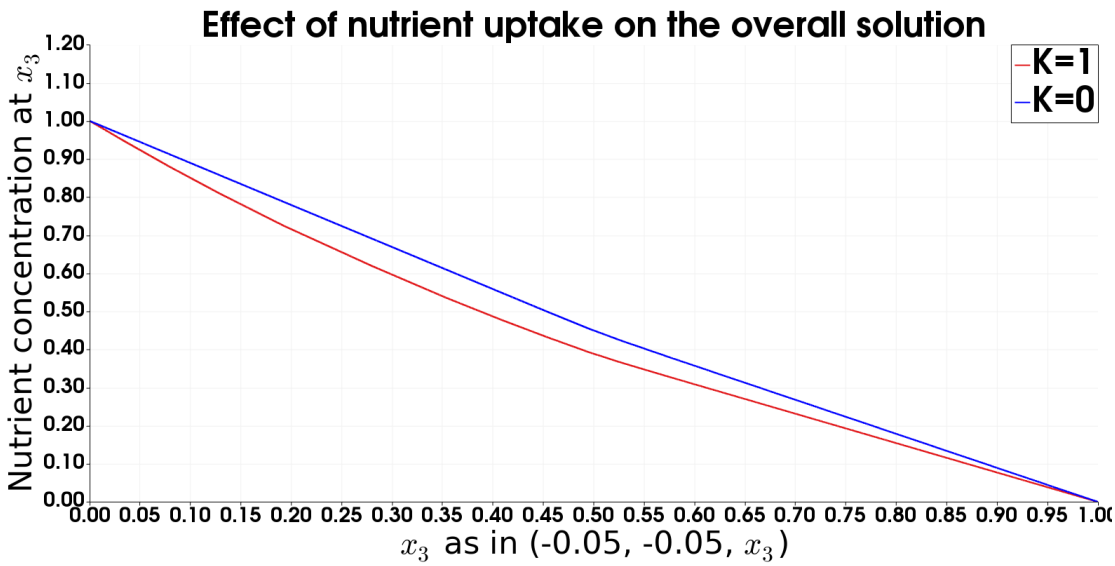


Figure 3.9.: Comparison with $K = 0$; solutions plotted along the edge of the unit cell.

this impact of boundary conditions (i.e. to enlarge the impact of the nutrient uptake), we next assume a zero-flux boundary condition at $x_3 = d$ (which may represent an impermeable layer at the bottom of the domain). This way, the analytic solution to the steady-state problem with $K = 0.0$ is constant everywhere - $u = 1.0$ (as we keep the boundary condition at $x_3 = 0$ the same), and the difference with the $K = 1.0$ case will be obvious.

Changed boundary condition at $x_3 = d$

We again assume Equation (161) for $x_3 < h$, Equation (162) for $x_3 > h$, and the boundary condition $u_0(x_3 = 0) = u_{max} > 0$. However, in this section, we impose:

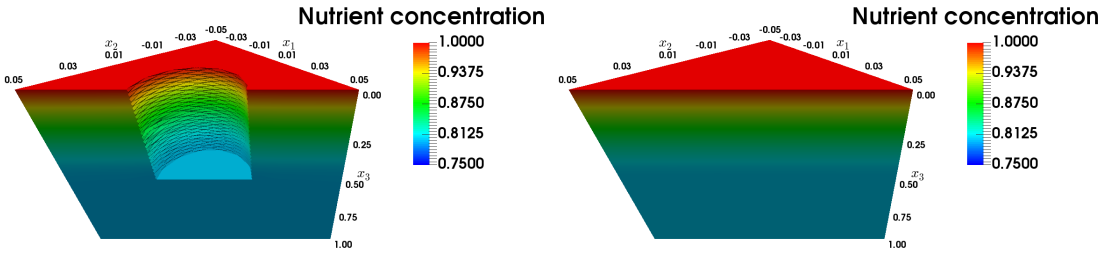
$$\frac{\partial u_0}{\partial x_3} = 0$$

at $x_3 = d$. For $x_3 > h$, this boundary condition together with Equation (162) leads to $u_0(x_3) = C_1$ for some constant C_1. For $x_3 < h$, Equation (161) gives:

$$u_0(x_3) = D_1 e^{\lambda x_3} + D_2 e^{-\lambda x_3},$$

where:

$$\lambda = \sqrt{\frac{2\pi K a}{1 - \pi a^2}} > 0. \tag{165}$$



(a) Full-geometry numerics (FEniCS) (b) Homogenisation result (FEniCS)

Figure 3.10.: Comparison between the full-geometry numerics and the homogenisation solution (steady states). The zero-flux boundary condition is applied at $x_3 = d$.

Using the boundary condition at $x_3 = 0$, we get $D_1 + D_2 = u_{max}$. To ensure that the solution is continuous at $x_3 = h$, we get $D_1 e^{\lambda h} + D_2 e^{-\lambda h} = C_1$, and to ensure the continuity of fluxes, we must have $D_1 e^{\lambda h} = D_2 e^{-\lambda h}$. This yields:

$$D_1 = u_{max} \frac{1}{1 + e^{2\lambda h}},$$

$$D_2 = u_{max} \frac{e^{2\lambda h}}{1 + e^{2\lambda h}},$$

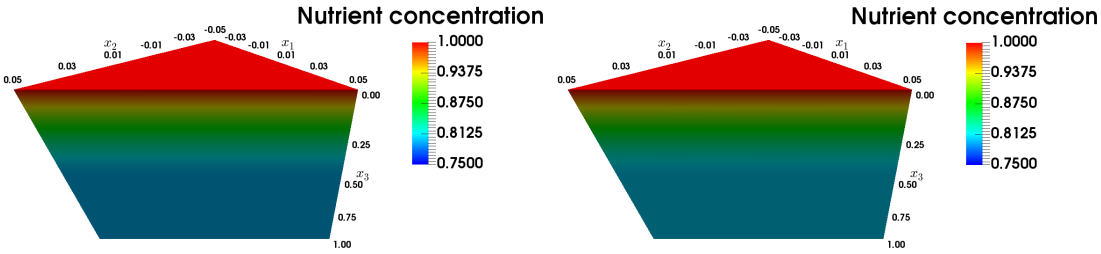
and:

$$C_1 = u_{max} \frac{2e^{\lambda h}}{1 + e^{2\lambda h}}. \tag{166}$$

We compared the analytic and the numerical solution of the homogenised equation using the same parameters as before. The results are shown in Figure 3.11 and a comparison with the full-geometry simulation is shown in Figure 3.10. Overall, the agreement is satisfactory.

The advantage of having an analytic solution is clearly visible here - for $x_3 > h$, the solution is given by a constant and we have an explicit formula - Equation (166) with λ defined by Equation (165) - describing how this constant depends on the parameters of our model. Fixing $h = 0.5$ and $u_{max} = 1.0$, we now investigate how C_1 depends on K and a.

First, we fix $a = 0.25$. Choosing $K = 0$ leads to $C_1 = u_{max}$, which is consistent with the no-uptake case. For $K \to \infty$, we get $\lambda \to \infty$, and thus $C_1 \to 0$ - the



(a) Analytic solution

(b) Numerics (FEniCS)

Figure 3.11.: Comparison between the analytic and the numerical solution of the homogenised equation (steady states). The zero-flux boundary condition is applied at $x_3 = d$.

uptake is so large, that no nutrient reaches $x_3 = h$. The dependence of C_1 on K is shown in Figure 3.12.

Now, we fix $K = 1$ and vary a. The results are shown in Figure 3.13. As expected, for $a \to 0$, $C_1 \to 1$ (the uptaking surface area approaches 0). For larger a, the uptake is larger too, and this C_1 is smaller. Let us note that the homogenised equation was derived using the assumption $a = O(1)$, and thus we cannot be certain about its validity for small a until we either do further analysis, or compare the full-geometry and the homogenised solutions. We will investigate the $a \ll 1$ limit in the next chapter.

From now onwards in this chapter, we will use $a = 0.25$, $K = 1$, and the zero-flux boundary condition at $x_3 = d$ (unless stated otherwise).

Time evolution

Let us go back to the time-dependent case (Equation $(159) - (160)$). Parameters remain the same - $\epsilon = 0.1$, $a = 0.25$, $K = 1$, $h = 0.5$, $d = 1.0$, and $u_{max} = 1.0$. We start with the initial condition (130), and we keep the nutrient concentration at $x_3 = 0$ fixed. From now on, we will mostly show solutions in a plane defined by $x_1 = x_2$, as introduced in Figure 3.14 (using the stretched coordinates as before). Moreover, we change the camera view as shown in Figure 3.15, and use this view (without axes labels) as default from now on.

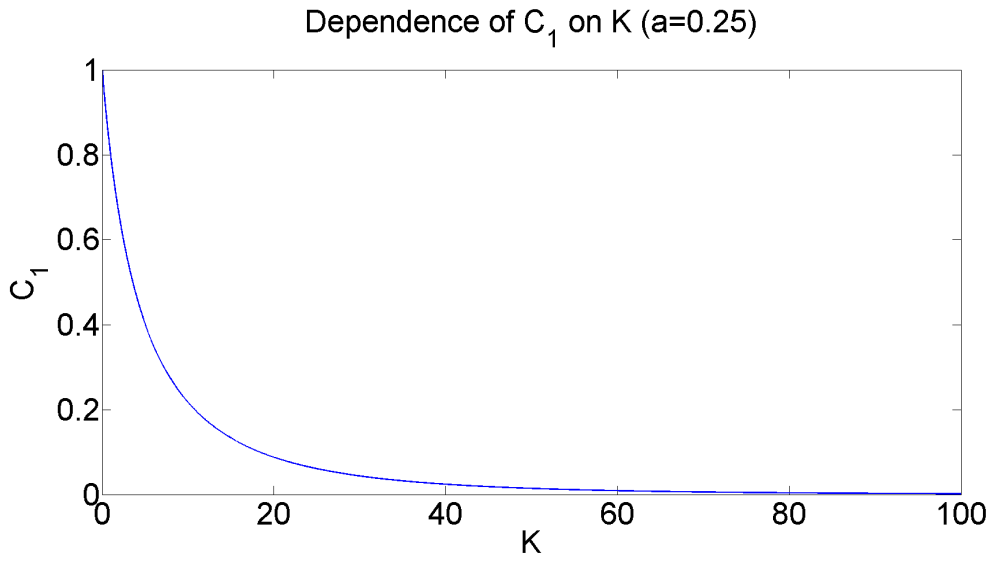


Figure 3.12.: Investigating how C_1 depends on K for $a = 0.25$ (fixed).

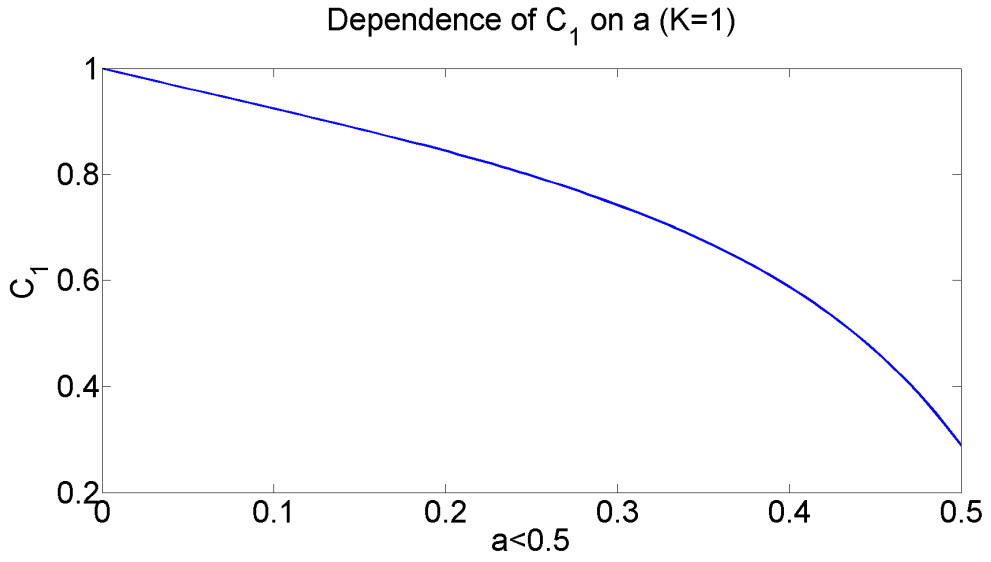
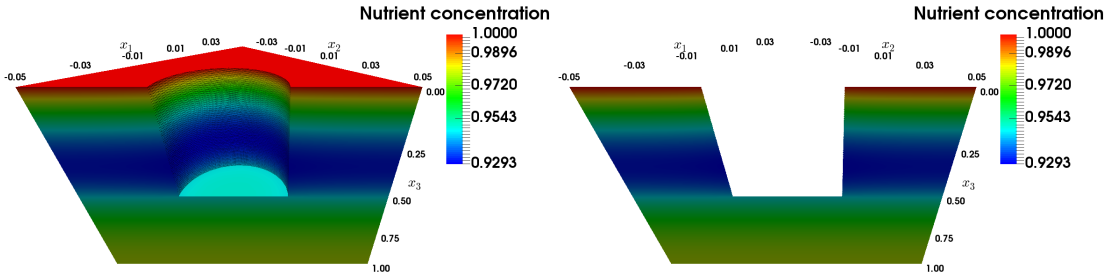
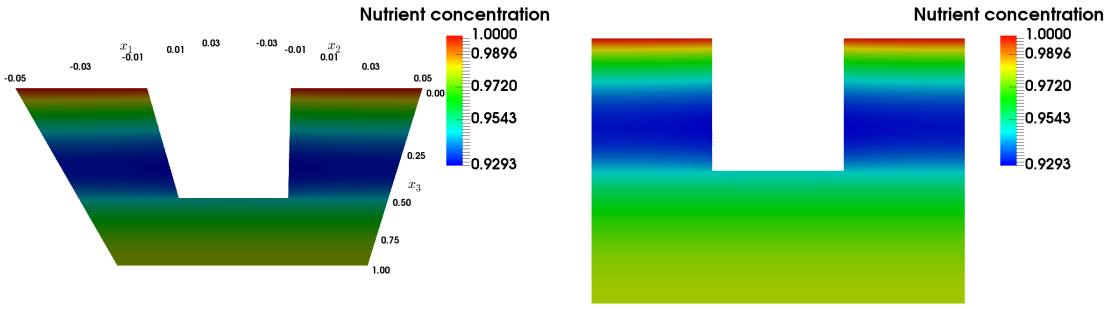


Figure 3.13.: Investigating how C_1 depends on a for $K = 1$ (fixed).



(a) Clipped domain (b) Solution in plane $x_1 = x_2$

Figure 3.14.: Introducing the plane view. Solution at $t = 0.1$.



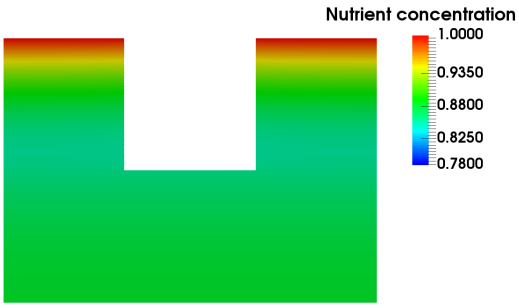
(a) Old view (b) New view

Figure 3.15.: Introducing the new camera view.

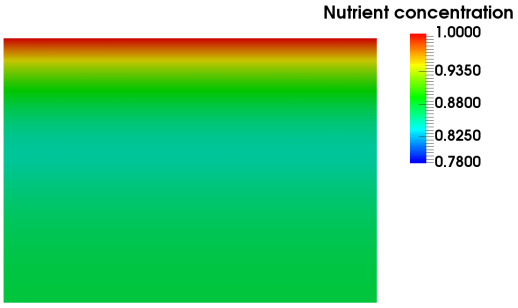
Figure 3.16 shows the solution to the full-geometry problem as well as to the homogenised equation at times $t = 0.5, 1.0, 2.0$, and what we observe is a gradual depletion of the nutrient from the domain until the steady state from previous section is reached. Again, notice the averaging property of homogenisation.

3.2.3 *Three-dimensional modelling*

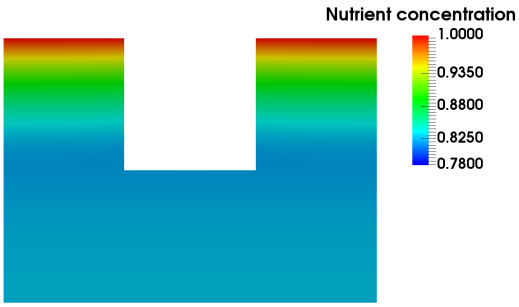
We now model a situation where a gradient in the (macroscopic) x_1 or x_2 is present, e.g. a nutrient is nonuniformly supplied to a field due to some special fertilisation treatment, or root hairs experience variable nutrient availability with changing distance along the root length.



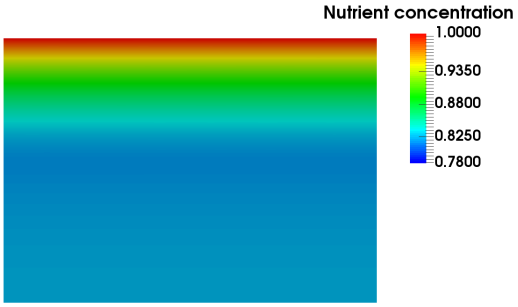
(a) Full geometry - $t = 0.5$



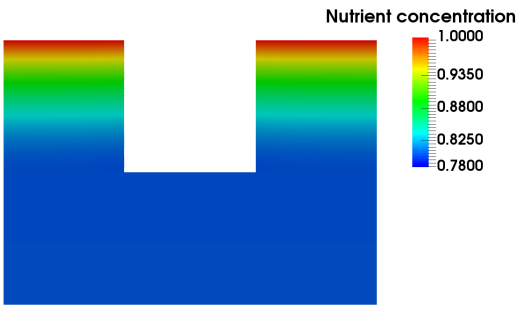
(b) Homogenisation - $t = 0.5$



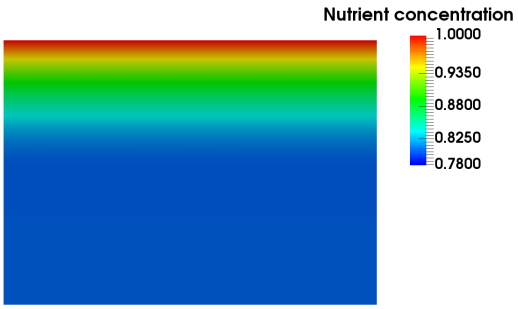
(c) Full geometry - $t = 1.0$



(d) Homogenisation - $t = 1.0$

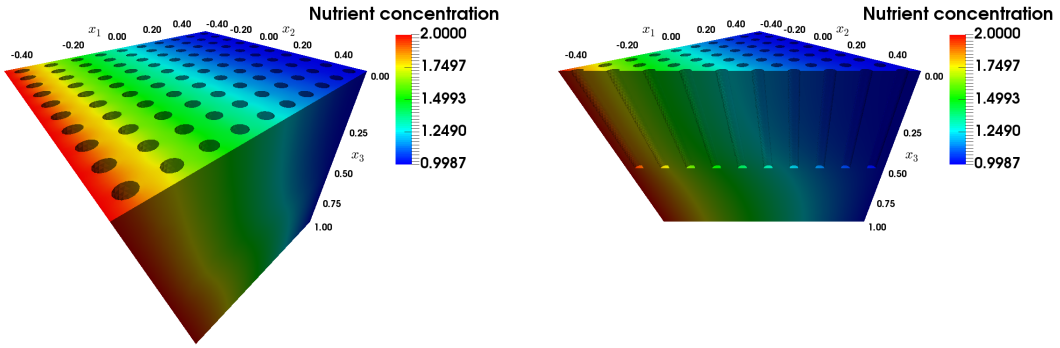


(e) Full geometry - $t = 2.0$



(f) Homogenisation - $t = 2.0$

Figure 3.16.: Comparison between the full-geometry solution and the homogenisation solution (time evolution).



(a) Whole domain

(b) Clipped domain

Figure 3.17.: Model with a macroscopic gradient in x_1 (steady state).

This can be modelled by imposing nonhomogeneous boundary conditions. We impose $u = u_l$ at $x_1 = -0.5$ and $u = u_r$ at $x_1 = 0.5$ with $u_l \neq u_r$. Supposing the domain is truncated as in the previous section, we impose zero-flux boundary conditions at $x_3 = 0$ and $x_3 = d$. At the remaining (macroscopic) boundary parts ($x_2 = -0.5$ and $x_2 = 0.5$), we impose zero-flux boundary conditions as well.

Steady state

We solved the steady-state case in FEniCS (using our default parameters). Note that as we have to perform the simulation on the whole domain here (in contrast with the case of no x_1 or x_2 variation, where it was sufficient to use the unit cell - see Section 3.2.2), we first show the full domain using standard (unstretched) variables. Figure 3.17 also shows the domain clipped along the plane $x_1 = x_2$. We want to compare this full-geometry result with the homogenisation result. In this case, we need to take into account the nonzero elements of matrix B (153), as these change the effective diffusion tensor D_{eff} (154) in Equation (155). Therefore, we simulate the unit cell problem for λ_1 (as discussed before, we do not need to do this for λ_2 separately; see Equations (143) and boundary conditions (144)). The results (normalised so that λ_1 attains a minimum equal to 0) are shown in Figure 3.18. From this simulation, we also calculated $\int_C \frac{\partial \lambda_1}{\partial y_1} dS \approx -0.13$. Using this value in the homogenised equation, we can compare this to the full-geometry numerics, and the results are

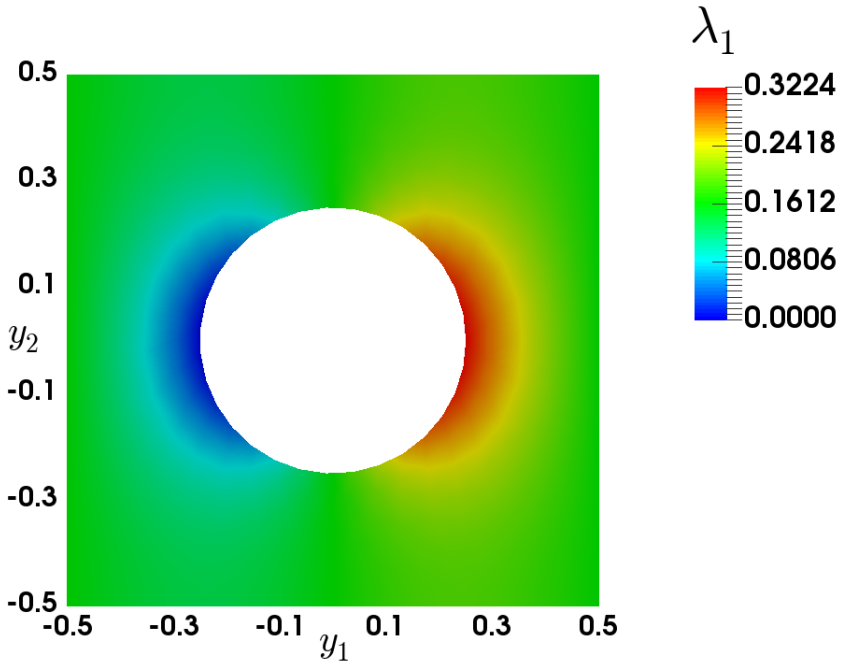
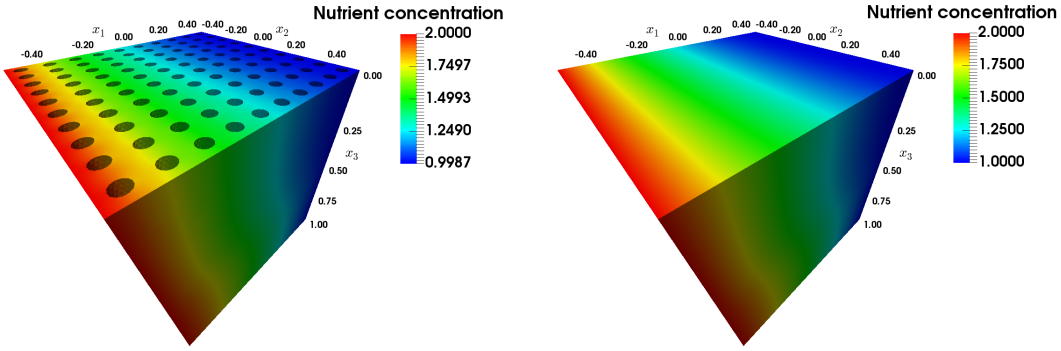


Figure 3.18.: Normalised solution to the unit cell problem for λ_1. The solution is independent of y_3, as shown before.

shown in Figure 3.19. Furthermore, we looked at $x_3 = const$ slices. The results are presented in Figure 3.20. Overall, homogenisation gives us the averaged behaviour we expect. To get a clearer comparison between the two models, we take one of the $x_3 = const$ slices as above (namely $x_3 = 0.0$), and we plot the solution along the line segment bounded by the end points $(-0.5, -0.5, 0.0)$ and $(0.5, 0.5, 0.0)$ (i.e. along the diagonal in the $x_3 = 0.0$ plane). This way, it is even easier to see, that the homogenisation solution is an average of the full-geometry solution (see Figure 3.21).

3.3 MODEL WITH CONVECTION

Apart from diffusing, a nutrient can often be convected, be it with the mass flow or with gravity (see Section 1.3.3). To study one example, we add convection (of varying strength) in the x_3 direction (this can be thought of as a



(a) Full-geometry numerics (FEniCS)

(b) Homogenisation result (FEniCS)

Figure 3.19.: Comparison between the full-geometry numerics and the homogenisation solution: model with a macroscopic variation in x_1 (steady state).

simple gravity term when modelling uptake by a field of crops) to Equation (129), and get a convection-diffusion equation:

$$\frac{\partial u}{\partial t} = \nabla^2 u - g\epsilon^n \frac{\partial u}{\partial x_3},$$

where $g = O(1)$, and we investigate which $n \in \mathbb{Z}$ yields a nontrivial convection term in the homogenised equation. The cylindrical surfaces boundary condition remains the same (because the direction of convection is perpendicular to the normal vector to the cylindrical surfaces; see Equation (132)). For $n \geq 1$, we get exactly the same equations at the first three orders as in the case without convection, and therefore the homogenised equation is the same too (convection is too weak to have any impact on the effective equation). For $n = 0$, we notice the first change at $O(1)$, where we obtain an additional term:

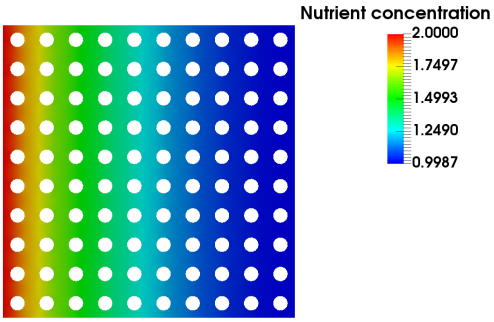
$$\frac{\partial u_0}{\partial t} = \nabla_x^2 u_0 + 2\nabla_x \cdot \nabla_y u_1 + \nabla_y^2 u_2 - g\frac{\partial u_0}{\partial x_3},$$

which after integration gives an effective equation:

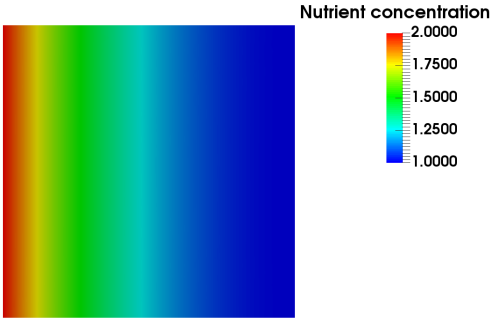
$$\frac{\partial u_0}{\partial t} = \nabla_x \cdot \left(D_{eff} \nabla_x u_0\right) - \frac{2\pi Ka}{1 - \pi a^2} u_0 - g\frac{\partial u_0}{\partial x_3}.$$

This holds in the $x_3 < h$ region, while for $x_3 > h$, we simply have:

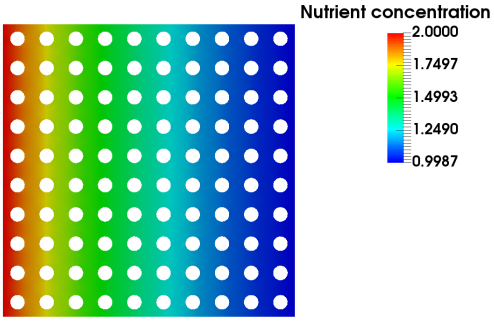
$$\frac{\partial u_0}{\partial t} = \nabla_x \cdot \nabla_x u_0 - g\frac{\partial u_0}{\partial x_3}.$$



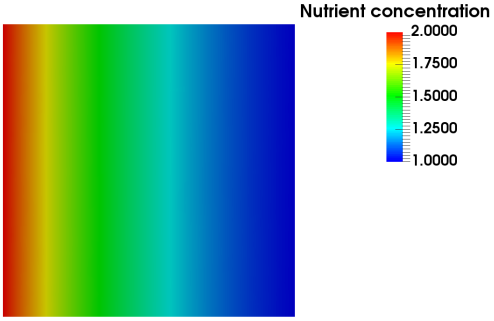
(a) Full geometry - slice at $x_3 = 0.00$



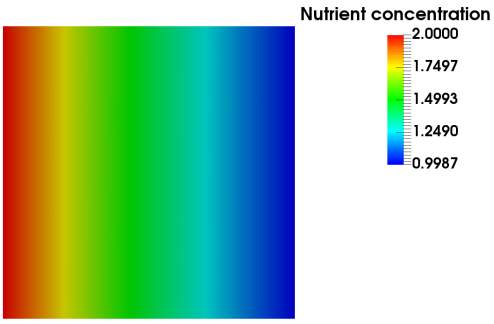
(b) Homogenisation - slice at $x_3 = 0.00$



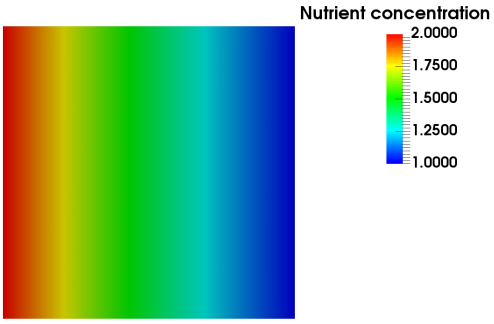
(c) Full geometry - slice at $x_3 = 0.45$.



(d) Homogenisation - slice at $x_3 = 0.45$.



(e) Full geometry - slice at $x_3 = 0.90$.



(f) Homogenisation - slice at $x_3 = 0.90$.

Figure 3.20.: Comparison between the full-geometry numerics and the homogenisation solution: model with a macroscopic variation in x_1 (steady state). Slices at $x_3 = const$. Note that $x_3 = 0.90$ is located outside of the root-hair zone.

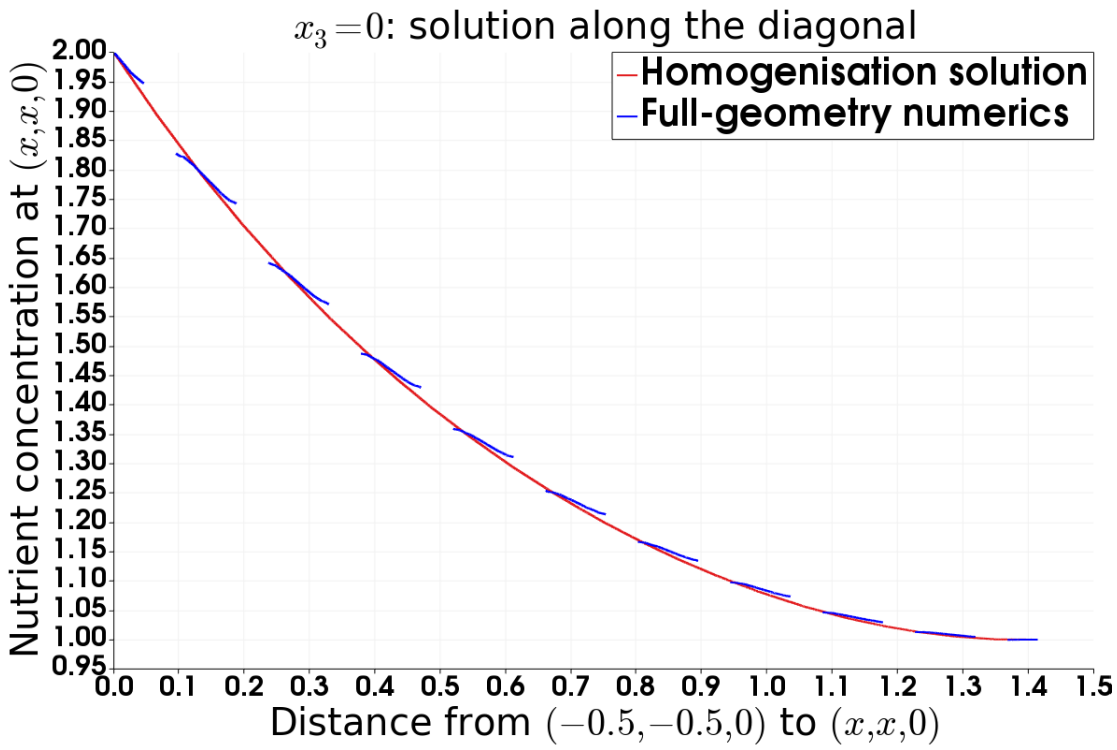


Figure 3.21.: Comparison between the full-geometry numerics and the homogenisation solution plotted along the diagonal within the $x_3 = 0.0$ slice. The $x-$axis represents the distance (measured on the macroscale) from one corner of this slice (-0.5,-0.5) to the opposite corner (0.5,0.5).

In the case of no macroscopic gradient in x_1 and x_2 introduced by initial or boundary conditions, we effectively get:

$$\frac{\partial u_0}{\partial t} = \frac{\partial^2 u_0}{\partial x_3^2} - \frac{2\pi K a}{1 - \pi a^2} u_0 - g \frac{\partial u_0}{\partial x_3}$$

for $x_3 < h$ and:

$$\frac{\partial u_0}{\partial t} = \frac{\partial^2 u_0}{\partial x_3^2} - g \frac{\partial u_0}{\partial x_3}$$

for $x_3 > h$. Figure 3.22 shows a simulation using $g = 1$. Figure 3.23 compares steady-state solutions for models with and without convection (see also Figure 3.16 for time evolution without convection). The convection term pulls more nutrient from the $x_3 = 0$ part of the boundary into the regions of uptake, which means that greater amounts of nutrient become available to the cylinders, and the total nutrient uptake by the cylinders is greater due to convection. Also, adding the convection term allows more nutrient to reach $x_3 = d$. This is a consequence of an interplay between the top boundary condition and the direction in which we have chosen the convection to be.

3.4 MICHAELIS-MENTEN BOUNDARY CONDITION

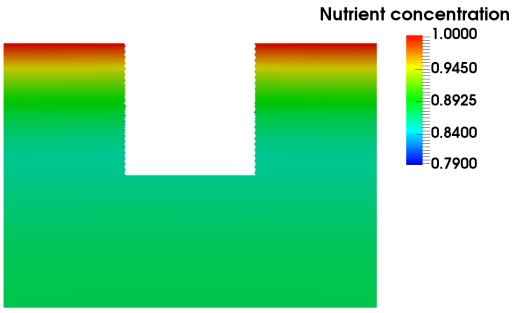
Uptake of most nutrients obeys Michaelis-Menten kinetics with an efflux term (see Section 1.3.4). Thus, we want to make sure that homogenisation gives us the averaged behaviour of the full problem for this boundary condition as well. We assume the same continuity equation (129), and the boundary condition (132) becomes:

$$\nabla u \cdot \hat{\boldsymbol{n}} = -\epsilon \frac{i_{max} u}{k_m + u} + \epsilon e,$$

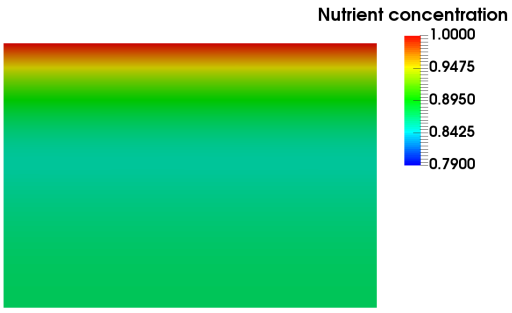
where i_{max} is the maximum influx rate (dimensionless), k_m is the Michaelis constant (dimensionless), and e is the efflux term (dimensionless; see Section 1.3.4)[3]. Using the multiscale ansatz (136), we get:

$$\frac{i_{max} u}{k_m + u} = \frac{i_{max} u_0}{k_m + u_0} + O(\epsilon).$$

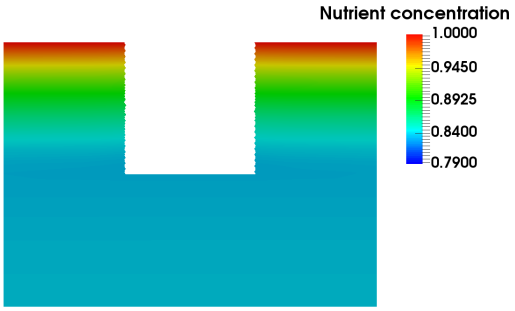
3 In the context of root hairs, the introduction of ϵ in the Michaelis-Menten as well as efflux term is justified in Section 1.4.4.



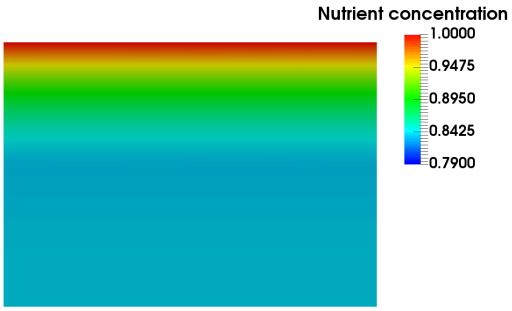
(a) Full-geometry solution - $t = 0.5$



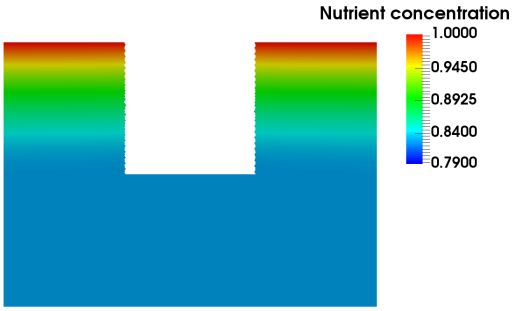
(b) Homogenisation solution - $t = 0.5$



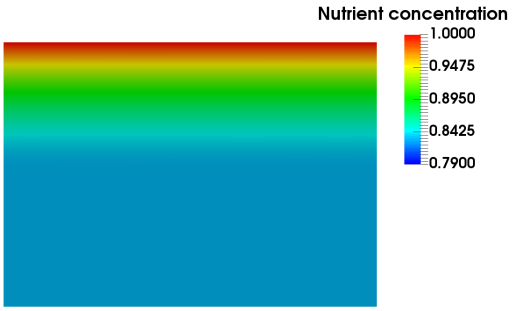
(c) Full-geometry solution - $t = 1.0$



(d) Homogenisation solution - $t = 1.0$

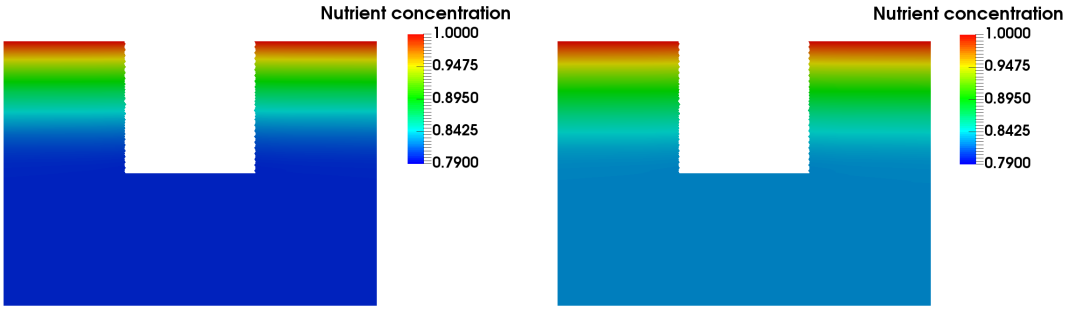


(e) Full-geometry solution - $t = 2.0$



(f) Homogenisation solution - $t = 2.0$

Figure 3.22.: Comparison between the full-geometry numerics and the homogenisation solution for the model with convection.



(a) Without convection

(b) With convection

Figure 3.23.: Comparison between the models with and without convection.

The first two orders are unchanged compared to the linear case, and we get $u_0 = u_0(t, \boldsymbol{x})$ as well as the ansatz (142) for u_1 (with the cell problems defined by the equations (143) and (144)). At the next order, we get the continuity equation (147), but the boundary condition (148) becomes:

$$\nabla_y u_2 \cdot \hat{\boldsymbol{n}} = -\frac{i_{max} u_0}{k_m + u_0} + e - \nabla_x u_1 \cdot \hat{\boldsymbol{n}}.$$

Repeating the same steps as before, we arrive at a nonlinear effective equation:

$$\frac{\partial u_0}{\partial t} = \nabla_x \cdot \left(D_{eff} \nabla_x u_0 \right) - \frac{2\pi a}{1 - \pi a^2} \left(\frac{i_{max} u_0}{k_m + u_0} - e \right)$$

for $x_3 < h$ and:

$$\frac{\partial u_0}{\partial t} = \nabla_x \cdot \nabla_x u_0$$

for $x_3 > h$.

3.4.1 *One-dimensional results*

Assuming no gradient in x_1 or x_2 is introduced by initial or boundary conditions, we effectively end up with:

$$\frac{\partial u_0}{\partial t} = \frac{\partial^2 u_0}{\partial x_3^2} - \frac{2\pi a}{1 - \pi a^2} \left(\frac{i_{max} u_0}{k_m + u_0} - e \right)$$

for $x_3 < h$ and:

$$\frac{\partial u_0}{\partial t} = \frac{\partial^2 u_0}{\partial x_3^2}$$

for $x_3 > h$. We choose $i_{max} = 1$ and $k_m = 1$ so that $\frac{i_{max}}{k_m} = 1$, which then equals K from the Robin-condition case (see Figure 3.16). This way, $\frac{i_{max}u}{k_m+u} < Ku$ for any $u > 0$. Moreover, the efflux term decreases the overall uptake too, and thus we expect the uptake to be smaller in the Michaelis-Menten case. We choose $e = 0.1$ so that the (Michaelis-Menten) influx dominates the efflux. FEniCS simulations are compared in Figure 3.24. Comparison with the steady-state solution using Robin boundary condition is given in Figure 3.25. It seems that at steady state, the concentration is higher in the whole slice for Michaelis-Menten boundary condition. Thus, we demonstrated our ability to apply homogenisation to problems that contain Michaelis-Menten boundary condition too.

3.5 NONLINEAR MODEL FOR WATER DYNAMICS

Water transport in the soil, which is often an important component of nutrient transport, obeys highly nonlinear differential equations due to the porous nature of the soil (see Section 1.3.3). The advantage of using the method of asymptotic expansions is that it can be easily applied to a nonlinear problem. Our starting point here will be Equation (87) from Section 2.6. We disregard the sink term as we plan to model uptake explicitly (using boundary conditions), and we nondimensionalise time and space as:

$$\tilde{t} = \frac{D_0}{L^2}t \qquad\qquad \tilde{\boldsymbol{x}} = \frac{1}{L}\boldsymbol{x}.$$

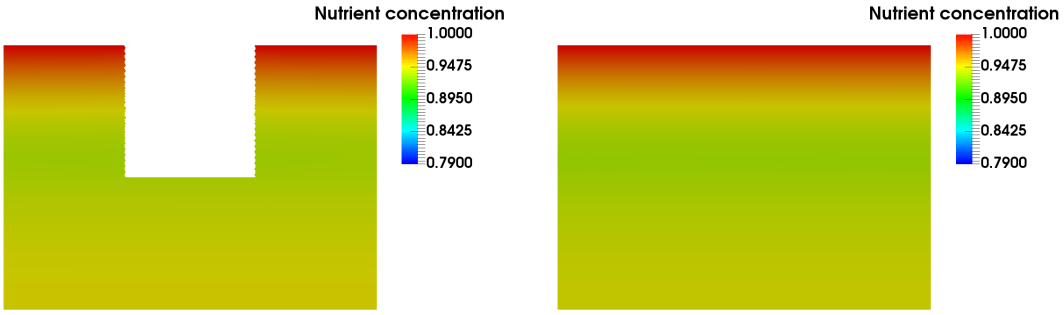
This leads to:

$$\phi\frac{\partial S}{\partial \tilde{t}} = \tilde{\nabla}\cdot\left[D(S)\nabla S - \frac{K_s L}{D_0}K(S)\hat{\boldsymbol{k}}\right].$$

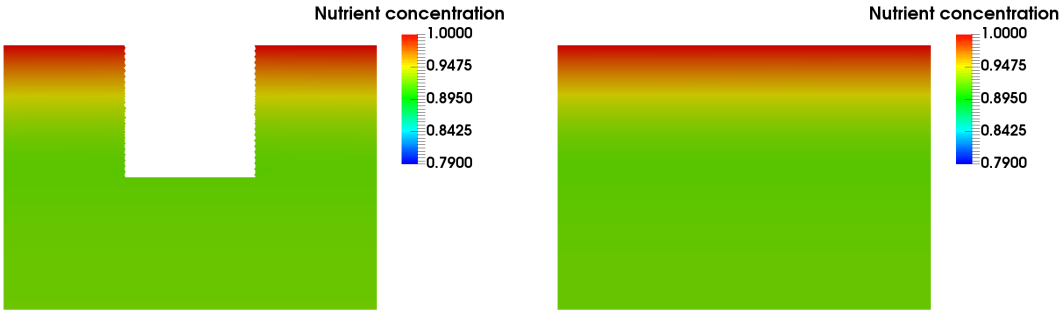
We drop tildes for convenience, and to unify notation with this chapter, we switch from S to u. We assume that $\frac{K_s L}{D_0} = \alpha = \epsilon^\beta$ for some β. This yields:

$$\phi\frac{\partial u}{\partial t} = \nabla\cdot\left[D(u)\nabla u - \epsilon^\beta K(u)\hat{\boldsymbol{k}}\right]$$

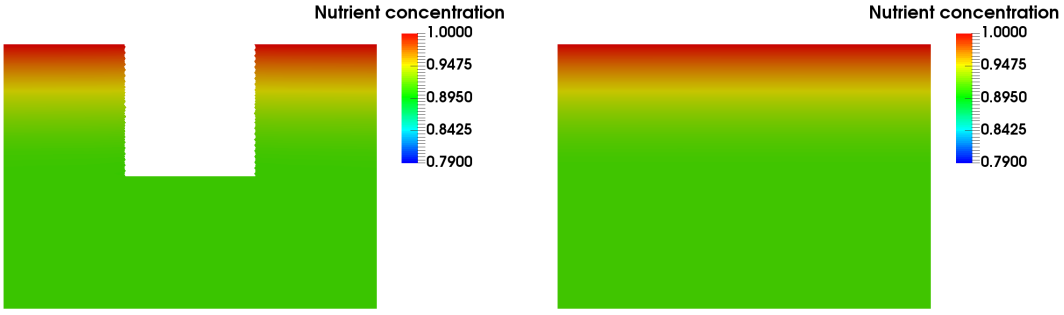
where $\hat{\boldsymbol{k}}$ is the downwards pointing unit vector, and $D(u)$ and $K(u)$ are nonlinear functions of the nutrient concentration u. We choose $D(u)$ and $K(u)$ to be the van Genuchten nonlinearities (as introduced in equations (85) and (86)).



(a) Full geometry - $t = 0.5$ (b) Homogenisation - $t = 0.5$

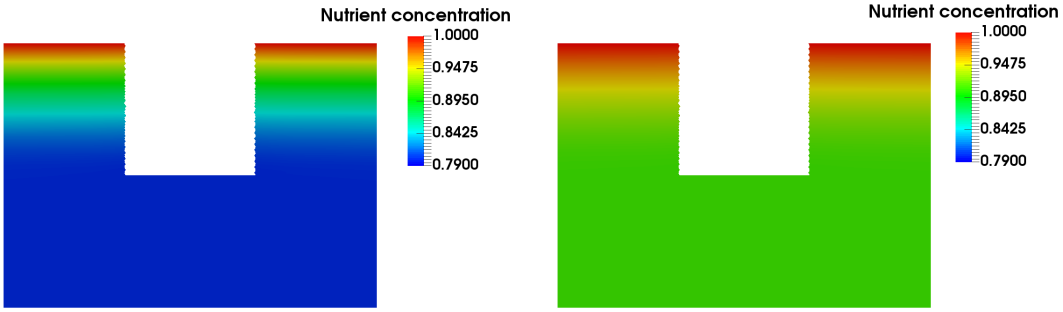


(c) Full geometry - $t = 1.0$ (d) Homogenisation - $t = 1.0$



(e) Full geometry - $t = 2.0$ (f) Homogenisation - $t = 2.0$

Figure 3.24.: Comparison between the full-geometry numerics and the homogenisation solution: model with the Michaelis-Menten boundary condition.



(a) Robin (b) Michaelis-Menten

Figure 3.25.: Comparison between the models with different cylindrical surface boundary conditions.

Guided by the linear model with convection, we focus on the case $\beta = 0$, which should lead to a nontrivial gravity term in the effective equation. We model uptake by a field of crops (so that the direction of gravity is perpendicular to the normal to the cylindrical root surfaces), and to make the root boundary condition simple yet realistic, we assume the flux at the root surfaces to be directly proportional to the available water content, i.e. $-D(u)\nabla u \cdot \hat{\boldsymbol{n}} = K\epsilon u$. Applying the same procedure as before, and writing $D(u)$ and $K(u)$ in the form of asymptotic expansions, we arrive at a continuity equation:

$$\left(\nabla_x + \frac{1}{\epsilon}\nabla_y\right) \cdot \left\{ \left\{ D(u_0) + \epsilon D'(u_0)u_1 + \frac{\epsilon^2}{2}\left[D''(u_0)u_1^2 + D'(u_0)2u_1\right] \right\} \right.$$

$$\left. \left(\nabla_x + \frac{1}{\epsilon}\nabla_y\right)\left[u_0 + \epsilon u_1 + \epsilon^2 u_2 + o(\epsilon^2)\right] - \left[K(u_0) + \epsilon K'(u_0)u_1 + o(\epsilon)\right]\hat{\boldsymbol{k}} \right\} =$$

$$\phi \frac{\partial\left[u_0 + o(1)\right]}{\partial t},$$

and a root surface boundary condition:

$$\left\{ D(u_0) + \epsilon D'(u_0)u_1 + \frac{\epsilon^2}{2}\left[D''(u_0)u_1^2 + D'(u_0)2u_2\right] \right\} \left(\nabla_x + \frac{1}{\epsilon}\nabla_y\right)$$

$$\left[u_0 + \epsilon u_1 + \epsilon^2 u_2 + o(\epsilon^2)\right] \cdot \hat{\boldsymbol{n}} = -K\epsilon\left[u_0 + o(1)\right].$$

As usual, we impose the periodic boundary conditions in y_1 and y_2 for u_0, u_1, and u_2. At each order, we then impose certain secularity conditions, so that

the solutions remain bounded.

At the leading order, we obtain a continuity equation $\nabla_y \cdot \left[D(u_0)\nabla_y u_0\right] = 0$, a root surface boundary condition $D(u_0)\nabla_y u_0 \cdot \hat{\boldsymbol{n}} = 0$, and the periodicity conditions in y_1 and y_2. Imposing secularity conditions:

$$\lim_{y_3 \to \infty} \frac{\partial u_0}{\partial y_3} = 0 = \lim_{y_3 \to -\infty} \frac{\partial u_0}{\partial y_3}$$

we see, that $u_0 = u_0(t, \boldsymbol{x})$ (independent of the microscale) is a solution to this problem. To show uniqueness, define Kirchhoff transform to be:

$$W(u_0)(t, \boldsymbol{y}, \boldsymbol{x}) = \int_0^{u_0(t,\boldsymbol{y},\boldsymbol{x})} D(\tau) d\tau,$$

so that:

$$\nabla_y^2 W = \nabla_y \cdot \left[D(u_0)\nabla_y u_0\right] = 0,$$

and:

$$\nabla_y W \cdot \hat{\boldsymbol{n}} = D(u_0)\nabla_y u_0 \cdot \hat{\boldsymbol{n}} = 0.$$

Furthermore, note that both W and $\frac{\partial W}{\partial y_1} = D(u_0)\frac{\partial u_0}{\partial y_1}$ are $1-$periodic with respect to y_1 due to the periodicity conditions imposed on u_0, and that the same reasoning applies to W, $\frac{\partial W}{\partial y_2} = D(u_0)\frac{\partial u_0}{\partial y_2}$, and $1-$periodicity with respect to y_2. Finally, $\frac{\partial W}{\partial y_3} = D(u_0)\frac{\partial u_0}{\partial y_3}$. Imposing secularity conditions:

$$\lim_{y_3 \to \infty} \frac{\partial W}{\partial y_3} = 0 = \lim_{y_3 \to -\infty} \frac{\partial W}{\partial y_3}$$

we see, that W satisfies the same conditions as g from Section 3.2.1, and therefore it must be independent of $\boldsymbol{y}$.

If we assume that there exists u_{max} such that:

$$u_0 \leq u_{max} < 1 \tag{167}$$

everywhere in the domain and for all times, then $D(u_0)$ is bounded (for van Genuchten nonlinearity). Looking back at the definition of W and recalling that (van Genuchten) $D(u_0)$ is positive everywhere except for $u_0 = 0$ leads to a conclusion, that u_0 independent of the microscale are truly the only possible solutions to this problem.

At $O(\epsilon)$, we arrive at a continuity equation:

$$D(u_0)\nabla_y^2 u_1 = \nabla_y \cdot \left[D(u_0)\nabla_y u_1\right] = 0$$

and a root boundary condition:

$$D(u_0)\big(\nabla_y u_1 \cdot \hat{\boldsymbol{n}}\big) = -D(u_0)\big(\nabla_x u_0 \cdot \hat{\boldsymbol{n}}\big).$$

Provided $D(u_0) \neq 0$, this becomes identical to the linear case, and thus we can use Ansatz (142) (together with the cell problems (143) and (144)). Note that to ensure $D(u_0) \neq 0$, we need to assume:

$$0 < u_{min} \leq u_0 \tag{168}$$

everywhere in the domain and for all times, which is an acceptable assumption provided the soil is not too dry.

At $O(\epsilon^2)$, we get a continuity equation:

$$\phi\frac{\partial u_0}{\partial t} = \nabla_x \cdot \big[D(u_0)\nabla_x u_0 - K(u_0)\hat{\boldsymbol{k}}\big] + \nabla_x \cdot \big[D(u_0)\nabla_y u_1\big] +$$
$$\nabla_y \cdot \Big[D(u_0)\big(\nabla_y u_2 + \nabla_x u_1\big) + D'(u_0)u_1\big(\nabla_y u_1 + \nabla_x u_0\big)\Big].$$

As in the linear case, we integrate over Y^N, use our knowledge from the previous orders to get:

$$2N(1-\pi a^2)\phi\frac{\partial u_0}{\partial t} = 2N(1-\pi a^2)\nabla_x \cdot \big[D(u_0)\nabla_x u_0 - K(u_0)\hat{\boldsymbol{k}}\big] +$$
$$2N\int_C \nabla_x \cdot \big[D(u_0)\nabla_y u_1\big]dS +$$
$$\int_{Y^N} \nabla_y \cdot \big[D(u_0)\big(\nabla_y u_2 + \nabla_x u_1\big) + D'(u_0)u_1\big(\nabla_y u_1 + \nabla_x u_0\big)\big]d\Omega,$$

and dividing by $2N(1-\pi a^2)$ we obtain:

$$\phi\frac{\partial u_0}{\partial t} = \nabla_x \cdot \big[D(u_0)\nabla_x u_0 - K(u_0)\hat{\boldsymbol{k}}\big] + \frac{1}{1-\pi a^2}\int_C \nabla_x \cdot \big[D(u_0)\nabla_y u_1\big]dS +$$
$$\frac{1}{2N(1-\pi a^2)}\int_{Y^N} \nabla_y \cdot \big[D(u_0)\big(\nabla_y u_2 + \nabla_x u_1\big) + D'(u_0)u_1\big(\nabla_y u_1 + \nabla_x u_0\big)\big]d\Omega. \tag{169}$$

Denoting:

$$\boldsymbol{\mathcal{F}} = D(u_0)\big(\nabla_y u_2 + \nabla_x u_1\big) + D'(u_0)u_1\big(\nabla_y u_1 + \nabla_x u_0\big),$$

the divergence theorem gives:

$$\frac{1}{2N(1-\pi a^2)}\int_{Y^N} \nabla_y \cdot \boldsymbol{\mathcal{F}}d\Omega = \frac{1}{2N(1-\pi a^2)}\int_{\partial Y^N} \boldsymbol{\mathcal{F}} \cdot \hat{\boldsymbol{n}}dS =$$

$$\frac{1}{2N(1-\pi a^2)}\int\limits_{y_3=\pm N}\boldsymbol{\mathcal{F}}\cdot\hat{\boldsymbol{n}}dS+\frac{1}{2N(1-\pi a^2)}\int\limits_{P^N\cup U^N}\boldsymbol{\mathcal{F}}\cdot\hat{\boldsymbol{n}}dS,$$

where we split the boundary as in the linear case. The integral over P^N is zero due to the periodic boundary conditions. Using the root surface boundary condition:

$$\Big[D(u_0)\big(\nabla_y u_2+\nabla_x u_1\big)+D'(u_0)u_1\big(\nabla_y u_1+\nabla_x u_0\big)\Big]\cdot\hat{\boldsymbol{n}}=-Ku_0,$$

we get:

$$\frac{1}{2N(1-\pi a^2)}\int\limits_{U^N}\boldsymbol{\mathcal{F}}\cdot\hat{\boldsymbol{n}}dS=-\frac{2\pi a}{1-\pi a^2}Ku_0.$$

Finally, looking at the remaining integral ($y_3=\pm N$) Note that all the expressions from $\boldsymbol{\mathcal{F}}$ containing u_0 and u_1 only (i.e. not containing u_2) are independent of y_3, and therefore when evaluated at any $(y_1,y_2,y_3=N)$, they give the same result as when evaluated at the corresponding $(y_1,y_2,y_3=-N)$. Considering that the outward pointing unit normal vector at $y_3=N$ is $(0,0,1)$, and the outward pointing unit normal vector at $y_3=-N$ is $(0,0,-1)$, integrals containing solely u_0 and u_1 cancel each other out, and multiplying by $2(1-\pi a^2)$ yields:

$$\frac{1}{N}\int\limits_{y_3=\pm N}\boldsymbol{\mathcal{F}}\cdot\hat{\boldsymbol{n}}dS=\frac{1}{N}\{\int\limits_{y_3=N}D(u_0)\frac{\partial u_2}{\partial y_3}dS-\int\limits_{y_3=-N}D(u_0)\frac{\partial u_2}{\partial y_3}dS\}.$$

By imposing secularity conditions:

$$\lim_{y_3\to\infty}\frac{\partial u_2}{\partial y_3}=0=\lim_{y_3\to-\infty}\frac{\partial u_2}{\partial y_3},$$

we get rid of these terms in the $N\to\infty$ limit, and Equation (169) becomes:

$$\phi\frac{\partial u_0}{\partial t}=\nabla_x\cdot\big[D(u_0)\nabla_x u_0-K(u_0)\hat{\boldsymbol{k}}\big]+$$
$$\frac{1}{1-\pi a^2}\int\limits_C\nabla_x\cdot\big[D(u_0)\nabla_y u_1\big]dS-\frac{2\pi Ka}{1-\pi a^2}u_0$$

Finally we notice, that from (142), one can derive:

$$\nabla_y u_1=M\nabla_x u_0,$$

where

$$M=\begin{pmatrix}\frac{\partial\lambda_1}{\partial y_1} & \frac{\partial\lambda_2}{\partial y_1} & 0\\ \frac{\partial\lambda_1}{\partial y_2} & \frac{\partial\lambda_2}{\partial y_2} & 0\\ 0 & 0 & 0\end{pmatrix}.$$

This gives an effective equation valid for $x_3 < h$:

$$\phi \frac{\partial u_0}{\partial t} = \nabla_x \cdot \left[D(u_0) D_{eff} \nabla_x u_0 - K(u_0) \hat{\boldsymbol{k}} \right] - \frac{2\pi a K}{1 - \pi a^2} u_0$$

(where D_{eff} is the matrix from the linear model section; see Equation (155)), and for $x_3 > h$, we get:

$$\phi \frac{\partial u_0}{\partial t} = \nabla_x \cdot \left[D(u_0) \nabla_x u_0 - K(u_0) \hat{\boldsymbol{k}} \right].$$

Thus, we obtained the same sink term, and the nonlinear diffusion term is modified by the same matrix as in the linear case.

3.5.1 *One-dimensional results*

If no x_1 and x_2 variation is introduced via initial or boundary conditions, we end up with a one-dimensional homogenised equation:

$$\phi \frac{\partial u_0}{\partial t} = \frac{\partial}{\partial x_3} \left[D(u_0) \frac{\partial u_0}{\partial x_3} \right] - K'(u_0) \frac{\partial u_0}{\partial x_3} - \frac{2\pi K a}{1 - \pi a^2} u_0$$

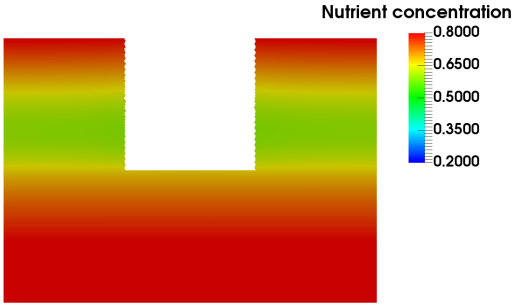
for $x_3 < h$ and:

$$\phi \frac{\partial u_0}{\partial t} = \frac{\partial}{\partial x_3} \left[D(u_0) \frac{\partial u_0}{\partial x_3} \right] - K'(u_0) \frac{\partial u_0}{\partial x_3}$$

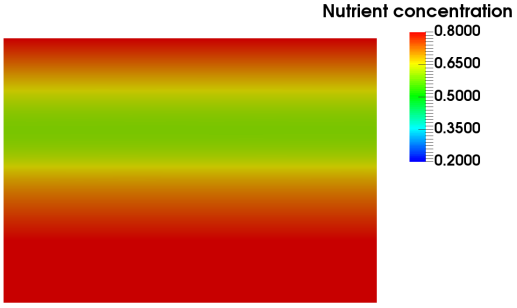
for $x_3 > h$. To avoid full-saturation condition $u = 1.0$ (recall the assumption (167)), we impose an initial condition $u(t = 0, \boldsymbol{x}) = u_{in} = 0.8$, and for consistency, we impose $u(t, x_1, x_2, 0) = 0.8$. Other parameter values remain the same. The results are presented in Figure 3.26. While regions in close proximity to $x_3 = 0.5$ are drying out fast due to the uptake, for regions in close proximity to $x_3 = 0.0$, this effect is weakened by the imposed Dirichlet boundary condition. Thus, we have shown that the method of homogenisation can be applied to certain nonlinear models as well, and we have confirmed that its averaging property extends to these models easily.

3.6 SUMMARY

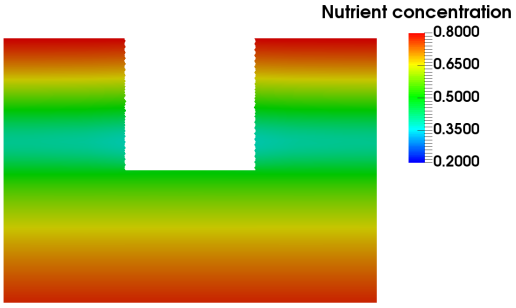
We showed how the theory of homogenisation can be applied to simplify modelling of nutrient uptake by periodic arrays of cylinders.



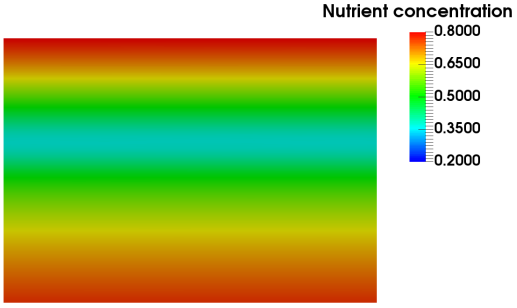
(a) Full geometry - $t = 0.1$.



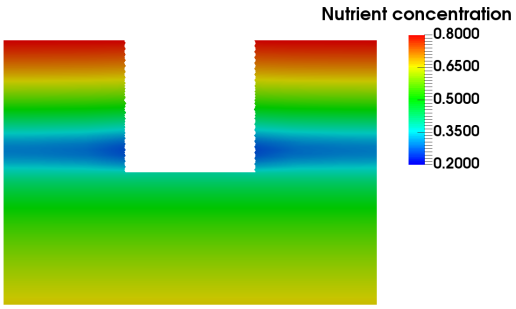
(b) Homogenisation - $t = 0.1$.



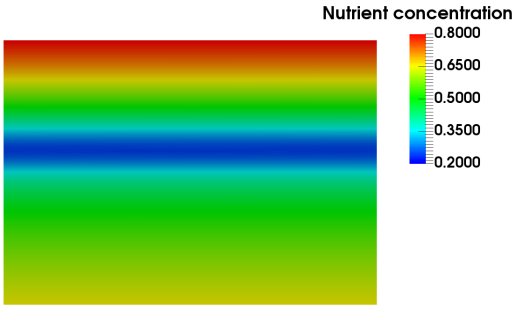
(c) Full geometry - $t = 0.5$



(d) Homogenisation - $t = 0.5$



(e) Full geometry - $t = 1.0$.



(f) Homogenisation - $t = 1.0$.

Figure 3.26.: Comparison between the full-geometry numerical solution and the homogenisation result for the model with van Genuchten nonlinearities.

We extended the framework from [80] to convection-diffusion equations, dealt with the Michaelis-Menten boundary condition as well as with the van Genuchten model describing water dynamics in the soil.
Let us also recall that many of the parameters used in this chapter were rather arbitrary - we were not interested in realistic, biologically or physically relevant parameters. Instead, we tried to emphasise the usefulness of homogenisation as a general concept, and our main intention was to introduce and develop the general framework of uptaking cylindrical surfaces. This framework will be used in the following two chapters of this thesis, in which we first study the limit of very sparse root hairs, and then investigate the effect of root hair length on nutrient uptake.
We are aware that some progress has been made on this topic by other authors before. Most notably, in [80], homogenisation was applied to a linear diffusion equation equipped with Michaelis-Menten boundary condition at the cylindrical surfaces to study nutrient uptake by root hairs. However, we still believe that our contributions introduced in this chapter are not negligible. To our knowledge, there has been no substantial research done so far to justify the use of homogenisation in this framework via direct comparison between the full-geometry simulations and the homogenisation results. Neither we have knowledge of researchers applying homogenisation study uptake by the cylindrical surfaces in the case of nontrivial macroscopic boundary conditions (as discussed in Section 3.2.3), nor we have encountered attempts to apply it to nonlinear water dynamics models (as studied in Section 3.5). Finally, in all the literature on this topic that we found, the scaling in the cylindrical surface boundary condition is stated without any effort to justify it, and thus we hope that our attempt on this justification (as found in Appendix A) can be considered valuable too.

4

NUTRIENT UPTAKE AND HOMOGENISATION: SPARSE HAIRS LIMIT

4.1 INTRODUCTION - THREE SPATIAL SCALES

When studying nutrient uptake by root hairs, an average distance between two neighbouring hairs (l) is not only much smaller than the length of the root which they grow on (L) - which introduces the homogenisation small parameter $\epsilon = \frac{l}{L} \ll 1$ - but it can also be much larger than the root hair radius (A) - this is especially true for very sparse root hairs. When two small parameters are present in a model, asymptotic expansions may disorder, which can result in distinct effective equations for different parameter regimes. Thus, it is important to investigate the case $0 < a = \frac{A}{l} \ll 1$ separately. First, we will briefly go back to the equations obtained in the previous chapter for the case where a was considered to be $O(1)$, and informally perform the $a \to 0$ limit in the effective equation (Section 4.2). Assuming $a = O(1)$, we will then study the $\epsilon \to 0$ limit using a simplified unit cell geometry (Section 4.3), which will allow us to obtain exact solutions for the $O(1)$, $O(\epsilon)$, and $O(\epsilon^2)$ cell problems. Later, we will introduce asymptotic expansions in a, and study the $a \ll 1$ limit behaviour of the solutions to the cell problems at different orders (in ϵ), first with the simplified geometry (Section 4.3), and then with the original geometry (Section 4.4). The analysis performed here will lead us to study two distinguished limits, which is done in Sections 4.6 and 4.7, and eventually we will arrive at a distinguished homogenised equation (239). Finally, in Section 4.8, we will numerically simulate the newly obtained limit,

and we will confirm that it gives a good approximation to the full-geometry problem for small a.

4.2 INFORMAL APPROACH

Assuming $\epsilon \to 0$ and $a = O(1)$, we arrived at Equation (155), with the effective diffusion tensor $D_{eff} = \frac{1}{1-\pi a^2} B + I$, and using symmetry arguments, we concluded:

$$B = \begin{pmatrix} \int_C \frac{\partial \lambda_1}{\partial y_1} dS & 0 & 0 \\ 0 & \int_C \frac{\partial \lambda_1}{\partial y_1} dS & 0 \\ 0 & 0 & 0 \end{pmatrix}.$$

As numerically demonstrated in Supporting information to [80], $\int_C \frac{\partial \lambda_1}{\partial y_1} dS \to 0$ as $a \to 0$, and therefore $B \to \mathbf{0}$ where $\mathbf{0}$ stands for a zero 3×3 matrix. Note, that this is true independent of the way K scales with a, because the cell problems are independent of K.

Assume $K = O(1)$ as $a \ll 1$. Then we have $-\frac{2\pi K a}{1-\pi a^2} \to 0$, and this results in a simple linear diffusion equation at the macroscale:

$$\frac{\partial u_0}{\partial t} = \nabla_x^2 u_0.$$

The sink term disappeared from the leading order, because (for fixed $\epsilon > 0$) we keep the uptake rate per unit surface area (K) fixed, and send the uptaking surface area to 0 via $a \ll 1$. This result is in accordance with the analysis from the previous chapter (see Figure 3.13).

However, using $K = O(\frac{1}{a})$ as $a \ll 1$, we arrive at a nontrivial sink term in the effective equation, i.e. $K = \frac{C}{a}$ with $C = O(1)$ yields:

$$\frac{\partial u_0}{\partial t} = \nabla_x^2 u_0 - 2\pi C u_0. \tag{170}$$

Moreover, an assumption $K = \frac{C}{a}$ for $C = O(1)$ corresponds to writing the hair surface boundary condition (132) as:

$$\nabla u \cdot \hat{\boldsymbol{n}} = -C \frac{\epsilon}{a} u. \tag{171}$$

Looking at biologically-realistic parameter values from [80], we see that a is usually $O(10^{-2})$, and using $\epsilon = 10^{-2}$, we get that $\frac{\epsilon}{a} = O(1)$. In order to

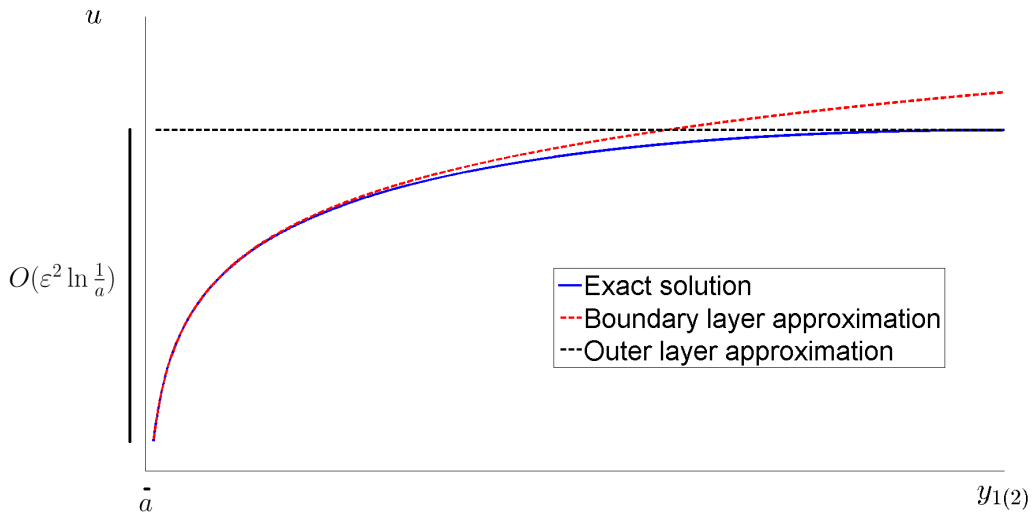


Figure 4.1.: The schematic representation of the depletion gradients close to the hair surfaces ($a \ll 1$).

justify the scaling in Equation (171), we therefore need to show that $\alpha = \frac{F_h L}{K_h D}$ is $O(1)$ or close to it (as this gives $C = O(1)$; compare with Equation (42)). As discussed in Section 1.4.4, when modelling phosphate uptake, α is $O(10^1)$ for wheat and at least three other plant species. Moreover, for maize, $\alpha = O(1)$ when modelling sulphur and magnesium uptake [119]. This suggests that the scalings used in this chapter are relevant in plant uptake modelling.

Assuming $K = \frac{C}{a}$ for $a \ll 1$, we enlarge the depletion gradients at the root hair surface. Furthermore, in the $a \ll 1$ limit, the microscale geometry sees the root hair as a point. Thus, we need to perform a separate analysis for a region in the vicinity of the origin ($r_y = 0$). We will refer to this region as a boundary layer (note that this is not a boundary layer in the standard sense of the word, but we will use this terminology, because the depletion gradients that we are interested in come from the boundary condition applied at the surface of the shrinking hair). Using the method of asymptotic expansions, we will later show (see Equations (186), (197) and (213)) that for $K(a) = \frac{C}{a}$, the microscopic variation in the nutrient concentration is $O(\epsilon^2 \ln \frac{1}{a})$, as shown schematically in Figure 4.1. Guided by the analysis from the previous chapter, we know that u_0, u_1, and u_2 are independent of y_3, and thus we assume the two-dimensional microscale geometry C as defined in Equation (133).

4.3 SIMPLER PROBLEM - FULL CIRCULAR SYMMETRY

Before we start analysing the model above, we start with a simpler problem. We assume our microscopic unit cell to be $C_a^c = \{(y_1, y_2) \in \mathbb{R}^2, a^2 \leq y_1^2 + y_2^2 \leq 1\}$, and impose a zero-flux boundary condition at $r_y (= \sqrt{y_1^2 + y_2^2}) = 1$ instead of the periodic boundary conditions (important here is that both conditions yield zero net flux into the unit cell from the outer boundary). We also introduce $C_0^c = \{(y_1, y_2) \in \mathbb{R}^2, y_1^2 + y_2^2 \leq 1\}$, which is the $a \to 0$ limit of the fully-circular unit cell geometry. This approach is not completely consistent with the periodic microstructure assumption, that we need for homogenisation, but it yields similar behaviour of cell problem solutions as in the original setting. Thus, using this simplification, we can obtain a valuable insight into the $a-$dependencies of terms at different orders (in ϵ) in an asymptotic expansion.

We start with the continuity equation (129) and the root hair boundary condition (132). As in the previous chapter, let $\boldsymbol{x}$ denote macroscopic (root length scale) variables, $(y_1, y_2) = \frac{(x_1, x_2)}{\epsilon}$ denote microscopic variables, and later on, we will introduce $(z_1, z_2) = \frac{(y_1, y_2)}{a}$ to be boundary layer microscopic variables ($z_1^2 + z_2^2 = 1$ corresponds to the root hair surface). Let $r_y = \sqrt{y_1^2 + y_2^2}$ represent the distance from the axis of the cylindrical root hair, $a = \frac{A}{l}$ be the quotient of the root hair radius (A) divided by the inter-hair distance (l). We first study the $\epsilon \ll 1$ limit, assuming $a = O(1)$ and $K = O(1)$. Later, we will proceed with the $a \ll 1$ case, and to obtain a nontrivial limit, we will assume that $K \to \infty$ as $a \ll 1$. As before, we search for a solution in the form of a multiscale ansatz:

$$u(t, \boldsymbol{x}; \epsilon, a) = u_0(t, \frac{\boldsymbol{x}}{\epsilon}, \boldsymbol{x}; a) + \epsilon u_1(t, \frac{\boldsymbol{x}}{\epsilon}, \boldsymbol{x}; a) + \epsilon^2 u_2(t, \frac{\boldsymbol{x}}{\epsilon}, \boldsymbol{x}; a) + o(\epsilon^2). \quad (172)$$

4.3.1 *Leading order*

At $O(1)$, we get:

$$0 = \nabla_y^2 u_0$$

together with an outer[1] boundary condition $\nabla_y u_0 \cdot \hat{\boldsymbol{n}} = 0$ at $y_1^2 + y_2^2 = 1$, and a hair boundary condition $\nabla_y u_0 \cdot \hat{\boldsymbol{n}} = 0$ at $y_1^2 + y_2^2 = a^2$. This problem only admits a solution independent of y_1 and y_2 (with possible dependency on a):

$$u_0(t, \boldsymbol{x}; a). \tag{173}$$

4.3.2 $O(\epsilon)$

At $O(\epsilon)$, we have:

$$\nabla_y^2 u_1 = 0,$$

a hair surface boundary condition:

$$\nabla_y u_1 \cdot \hat{\boldsymbol{n}} = -\nabla_x u_0 \cdot \hat{\boldsymbol{n}}$$

at $y_1^2 + y_2^2 = a^2$, and an outer boundary condition:

$$\nabla_y u_1 \cdot \hat{\boldsymbol{n}} = -\nabla_x u_0 \cdot \hat{\boldsymbol{n}}$$

at $y_1^2 + y_2^2 = 1$. We separate the microscale and the macroscale variables as:

$$u_1(t, y_1, y_2, \boldsymbol{x}; a) = f_1(t, \boldsymbol{x}; a) + \nabla_x u_0(t, \boldsymbol{x}; a) \cdot \boldsymbol{\lambda}(y_1, y_2; a),$$

and use polar coordinates r_y and φ at the microscale. The continuity equation yields:

$$\frac{1}{r_y} \frac{\partial}{\partial r_y} \{ r_y \frac{\partial \lambda_i}{\partial r_y} \} + \frac{1}{r_y^2} \frac{\partial^2 \lambda_i}{\partial \varphi^2} = 0$$

for $i \in \{1, 2, 3\}$. The hair surface boundary conditions give:

$$-\nabla_x u_0 \cdot \frac{\partial \boldsymbol{\lambda}}{\partial r_y} = -\frac{\partial u_1}{\partial r_y} = \nabla_x u_0 \cdot (\cos\varphi, \sin\varphi, 0)$$

at $r_y = a$, which simplifies to:

$$\frac{\partial \lambda_1}{\partial r_y} = -\cos\varphi \qquad \frac{\partial \lambda_2}{\partial r_y} = -\sin\varphi \qquad \frac{\partial \lambda_3}{\partial r_y} = 0.$$

Similarly, the outer boundary conditions give:

$$\nabla_x u_0 \cdot \frac{\partial \boldsymbol{\lambda}}{\partial r_y} = \frac{\partial u_1}{\partial r_y} = -\nabla_x u_0 \cdot (\cos\varphi, \sin\varphi, 0)$$

1 Note that we will investigate microscale boundary conditions here; these should not be mistaken with the macroscopic boundary conditions.

at $r_y = 1$, and this simplifies to:

$$\frac{\partial \lambda_1}{\partial r_y} = -\cos\varphi \qquad \frac{\partial \lambda_2}{\partial r_y} = -\sin\varphi \qquad \frac{\partial \lambda_3}{\partial r_y} = 0.$$

This suggests searching for the solutions in the following way:

$$\lambda_1(r_y, \varphi; a) = -\cos\varphi R_1(r_y; a) \qquad \lambda_2(r_y, \varphi; a) = -\sin\varphi R_2(r_y; a),$$

and clearly, $\lambda_3(r_y, \varphi; a) = 0$. This leads to:

$$r_y^2 R_1'' + r_y R_1' - R_1 = 0,$$

and the same equation holds for R_2. Furthermore, we get a hair surface boundary condition $R_1'(r_y = a) = 1$ and an outer boundary condition $R_1'(r_y = 1) = 1$. The same conditions hold for R_2, and thus: $R_1 = R_2 = R$. Using an ansatz $R(r_y; a) = A(a) r_y^n$, we get:

$$A(a) r_y^n (n^2 - 1) = 0,$$

which yields $n = \pm 1$. Thus, the solution is $R(r_y; a) = C_1(a) r_y + \frac{C_2(a)}{r_y}$. This means that $R'(r_y; a) = C_1(a) - \frac{C_2(a)}{r_y^2}$, and applying the boundary conditions leads to:

$$C_1(a) - \frac{C_2(a)}{a^2} = 1 = C_1(a) - C_2(a),$$

which yields $C_2(a) = 0$ and $C_1(a) = 1$. Therefore, the solution is $R(r_y; a) = R(r_y) = r_y$. We conclude:

$$u_1(t, y_1, y_2, \boldsymbol{x}; a) = f_1(t, \boldsymbol{x}; a) + \nabla_x u_0(t, \boldsymbol{x}; a) \cdot (-r_y \cos\varphi, -r_y \sin\varphi, 0). \quad (174)$$

4.3.3 $O(\epsilon^2)$

At $O(\epsilon^2)$, we get:

$$\nabla_y^2 u_2 = \frac{\partial u_0}{\partial t} - \nabla_x^2 u_0 - 2\nabla_x \cdot \nabla_y u_1,$$

and using:

$$\nabla_x \cdot \nabla_y u_1 = \{\frac{\partial^2}{\partial y_1 \partial x_1} + \frac{\partial^2}{\partial y_2 \partial x_2}\}\{-r_y \cos\varphi \frac{\partial u_0}{\partial x_1} - r_y \sin\varphi \frac{\partial u_0}{\partial x_2}\} =$$

$$-\frac{\partial}{\partial y_1}(r_y \cos\varphi)\frac{\partial^2 u_0}{\partial x_1^2} - \frac{\partial}{\partial y_2}(r_y \sin\varphi)\frac{\partial^2 u_0}{\partial x_2^2} = -\frac{\partial^2 u_0}{\partial x_1^2} - \frac{\partial^2 u_0}{\partial x_2^2},$$

we get:

$$\nabla_y^2 u_2 = \{\frac{\partial}{\partial t} + \frac{\partial^2}{\partial x_1^2} + \frac{\partial^2}{\partial x_2^2} - \frac{\partial^2}{\partial x_3^2}\}u_0$$

or:

$$\frac{\partial^2 u_2}{\partial r_y^2} + \frac{1}{r_y}\frac{\partial u_2}{\partial r_y} + \frac{1}{r_y^2}\frac{\partial^2 u_2}{\partial \varphi^2} = \{\frac{\partial}{\partial t} + \frac{\partial^2}{\partial x_1^2} + \frac{\partial^2}{\partial x_2^2} - \frac{\partial^2}{\partial x_3^2}\}u_0. \tag{175}$$

As a boundary condition at $r_y = a$ for u_2, we get:

$$\nabla_y u_2 \cdot \hat{\boldsymbol{n}} = -Ku_0 - \nabla_x u_1 \cdot \hat{\boldsymbol{n}},$$

and as we know that:

$$\nabla_x u_1 \cdot \hat{\boldsymbol{n}} = -\cos\varphi\frac{\partial f_1}{\partial x_1} - \sin\varphi\frac{\partial f_1}{\partial x_2} +$$

$$r_y\cos^2\varphi\frac{\partial^2 u_0}{\partial x_1^2} + r_y\sin^2\varphi\frac{\partial^2 u_0}{\partial x_2^2} + r_y\sin 2\varphi\frac{\partial^2 u_0}{\partial x_1\partial x_2},$$

this becomes:

$$\nabla_y u_2 \cdot \hat{\boldsymbol{n}} = -Ku_0 + \cos\varphi\frac{\partial f_1}{\partial x_1} + \sin\varphi\frac{\partial f_1}{\partial x_2} -$$

$$a\cos^2\varphi\frac{\partial^2 u_0}{\partial x_1^2} - a\sin^2\varphi\frac{\partial^2 u_0}{\partial x_2^2} - a\sin 2\varphi\frac{\partial^2 u_0}{\partial x_1\partial x_2}.$$

Assuming $K(a) = \frac{C}{a}$ for $C = O(1)$ (this way, we will be consistent with the analysis for the $a \ll 1$ case), this simplifies to:

$$-\frac{\partial u_2(r_y = a)}{\partial r_y} = -\frac{C}{a}u_0 + \cos\varphi\frac{\partial f_1}{\partial x_1} + \sin\varphi\frac{\partial f_1}{\partial x_2} -$$

$$a\cos^2\varphi\frac{\partial^2 u_0}{\partial x_1^2} - a\sin^2\varphi\frac{\partial^2 u_0}{\partial x_2^2} - a\sin 2\varphi\frac{\partial^2 u_0}{\partial x_1\partial x_2}$$

or:

$$\frac{\partial u_2(r_y = a)}{\partial r_y} = \frac{C}{a}u_0 - \cos\varphi\frac{\partial f_1}{\partial x_1} - \sin\varphi\frac{\partial f_1}{\partial x_2} +$$
$$a\cos^2\varphi\frac{\partial^2 u_0}{\partial x_1^2} + a\sin^2\varphi\frac{\partial^2 u_0}{\partial x_2^2} + a\sin 2\varphi\frac{\partial^2 u_0}{\partial x_1\partial x_2}. \tag{176}$$

As an outer boundary condition at $r_y = 1$ for u_2, we get:

$$\nabla_y u_2 \cdot \hat{\boldsymbol{n}} = -\nabla_x u_1 \cdot \hat{\boldsymbol{n}},$$

and as we know that:

$$\nabla_x u_1 \cdot \hat{\boldsymbol{n}} = +\cos\varphi\frac{\partial f_1}{\partial x_1} + \sin\varphi\frac{\partial f_1}{\partial x_2} -$$

$$r_y \cos^2\varphi \frac{\partial^2 u_0}{\partial x_1^2} - r_y \sin^2\varphi \frac{\partial^2 u_0}{\partial x_2^2} - r_y \sin 2\varphi \frac{\partial^2 u_0}{\partial x_1 \partial x_2},$$

this becomes:

$$\frac{\partial u_2(r_y = 1)}{\partial r_y} = -\cos\varphi \frac{\partial f_1}{\partial x_1} - \sin\varphi \frac{\partial f_1}{\partial x_2} + \cos^2\varphi \frac{\partial^2 u_0}{\partial x_1^2} + \sin^2\varphi \frac{\partial^2 u_0}{\partial x_2^2} + \sin 2\varphi \frac{\partial^2 u_0}{\partial x_1 \partial x_2}. \quad (177)$$

In attempt to solve Equation (175) equipped with the boundary conditions (176) and (177), we define:

$$v^*(t, y_1, y_2, \boldsymbol{x}; a) = -y_1 \frac{\partial f_1(t, \boldsymbol{x}; a)}{\partial x_1} - y_2 \frac{\partial f_1(t, \boldsymbol{x}; a)}{\partial x_2} = - r_y \cos\varphi \frac{\partial f_1}{\partial x_1} - r_y \sin\varphi \frac{\partial f_1}{\partial x_2}, \quad (178)$$

so that we have:

$$\nabla_y^2 v^* = 0$$

as well as:

$$\frac{\partial v^*}{\partial r_y} = -\cos\varphi \frac{\partial f_1}{\partial x_1} - \sin\varphi \frac{\partial f_1}{\partial x_2}$$

for any r_y. Therefore, by writing $u_2 = v^* + w$, our task reduces to finding a function w satisfying a continuity equation:

$$\frac{\partial^2 w}{\partial r_y^2} + \frac{1}{r_y}\frac{\partial w}{\partial r_y} + \frac{1}{r_y^2}\frac{\partial^2 w}{\partial \varphi^2} = \{\frac{\partial}{\partial t} + \frac{\partial^2}{\partial x_1^2} + \frac{\partial^2}{\partial x_2^2} - \frac{\partial^2}{\partial x_3^2}\} u_0, \quad (179)$$

a hair surface boundary condition:

$$\frac{\partial w}{\partial r_y} = \frac{C}{a} u_0 + a\cos^2\varphi \frac{\partial^2 u_0}{\partial x_1^2} + a\sin^2\varphi \frac{\partial^2 u_0}{\partial x_2^2} + a\sin 2\varphi \frac{\partial^2 u_0}{\partial x_1 \partial x_2} \quad (180)$$

at $r_y = a$, and an outer boundary condition:

$$\frac{\partial w}{\partial r_y} = \{\cos^2\varphi \frac{\partial^2}{\partial x_1^2} + \sin^2\varphi \frac{\partial^2}{\partial x_2^2} + \sin 2\varphi \frac{\partial^2}{\partial x_1 \partial x_2}\} u_0 \quad (181)$$

at $r_y = 1$. Notice further, that a function:

$$v^{**} = \frac{r_y^2}{2}\cos^2\varphi \frac{\partial^2 u_0}{\partial x_1^2} + \frac{r_y^2}{2}\sin^2\varphi \frac{\partial^2 u_0}{\partial x_2^2} + \frac{r_y^2}{2}\sin 2\varphi \frac{\partial^2 u_0}{\partial x_1 \partial x_2} = \frac{y_1^2}{2}\frac{\partial^2 u_0}{\partial x_1^2} + \frac{y_2^2}{2}\frac{\partial^2 u_0}{\partial x_2^2} + y_1 y_2 \frac{\partial^2 u_0}{\partial x_1 \partial x_2} \quad (182)$$

satisfies a continuity equation:

$$\nabla_y^2 v^{**} = \frac{\partial^2 u_0}{\partial x_1^2} + \frac{\partial^2 u_0}{\partial x_2^2},$$

a hair surface boundary condition:

$$\frac{\partial v^{**}(r_y = a)}{\partial r_y} = a\cos^2\varphi \frac{\partial^2 u_0}{\partial x_1^2} + a\sin^2\varphi \frac{\partial^2 u_0}{\partial x_2^2} + a\sin 2\varphi \frac{\partial^2 u_0}{\partial x_1 \partial x_2},$$

and an outer boundary condition:

$$\frac{\partial v^{**}(r_y = 1)}{\partial r_y} = \cos^2\varphi \frac{\partial^2 u_0}{\partial x_1^2} + \sin^2\varphi \frac{\partial^2 u_0}{\partial x_2^2} + \sin 2\varphi \frac{\partial^2 u_0}{\partial x_1 \partial x_2}.$$

This means that we can search for w in a form:

$$w = v + v^{**},$$

where we want v to satisfy a continuity equation:

$$\nabla_y^2 v = \frac{\partial u_0}{\partial t} - \frac{\partial^2 u_0}{\partial x_3^2}, \tag{183}$$

a hair surface boundary condition:

$$\frac{\partial v(r_y = a)}{\partial r_y} = \frac{C}{a} u_0, \tag{184}$$

and an outer boundary condition:

$$\frac{\partial v(r_y = 1)}{\partial r_y} = 0. \tag{185}$$

To ensure the existence of a solution to this problem, we integrate over the unit cell C_a^c, use the divergence theorem and the boundary conditions, and thus get a consistency condition (this is equivalent to the effective/homogenised equation from the previous chapter):

$$\pi(1-a^2)\{\frac{\partial u_0}{\partial t} - \frac{\partial^2 u_0}{\partial x_3^2}\} = \int\limits_{C_a^c} \nabla_y^2 v dS =$$

$$\int\limits_{\partial C_a^c} \nabla_y v \cdot \hat{\boldsymbol{n}} dl = -\int\limits_{r_y = a} \frac{C}{a} u_0 dl = -2\pi C u_0$$

or:

$$\frac{\partial u_0}{\partial t} = \frac{\partial^2 u_0}{\partial x_3^2} - \frac{2C}{1-a^2} u_0.$$

It follows from the symmetry of Problem $(183)+(184)+(185)$, that v is independent of φ, and we get:

$$\frac{\partial^2 v}{\partial r_y^2}+\frac{1}{r_y}\frac{\partial v}{\partial r_y}=-\frac{2C}{1-a^2}u_0,$$

which can also be written as:

$$\frac{\partial}{\partial r_y}\{r_y\frac{\partial v}{\partial r_y}\}=\{-\frac{2C}{1-a^2}u_0\}r_y,$$

and this leads to:

$$\frac{\partial v}{\partial r_y}=-\frac{C}{1-a^2}u_0 r_y+\frac{C^0}{r_y}.$$

Applying the boundary condition at $r_y=1$ yields:

$$C^0=\frac{C}{1-a^2}u_0,$$

which leads to:

$$v=-\frac{C}{1-a^2}u_0\{\frac{r_y^2}{2}-\ln r_y\}+f_2.$$

Thus, we conclude:

$$\begin{aligned}u_2(t,r_y,\varphi,\boldsymbol{x};a)=&-r_y\cos\varphi\frac{\partial f_1(t,\boldsymbol{x};a)}{\partial x_1}-r_y\sin\varphi\frac{\partial f_1(t,\boldsymbol{x};a)}{\partial x_2}+\\&\frac{r_y^2}{2}\cos^2\varphi\frac{\partial^2 u_0(t,\boldsymbol{x};a)}{\partial x_1^2}+\frac{r_y^2}{2}\sin^2\varphi\frac{\partial^2 u_0(t,\boldsymbol{x};a)}{\partial x_2^2}+\\&\frac{r_y^2}{2}\sin 2\varphi\frac{\partial^2 u_0(t,\boldsymbol{x};a)}{\partial x_1\partial x_2}-\frac{C}{1-a^2}u_0\{\frac{r_y^2}{2}-\ln r_y\}+f_2(t,\boldsymbol{x};a).\end{aligned}\quad(186)$$

Note, that the right-hand side of Equation (186) contains a term $\frac{C}{1-a^2}u_0\ln r_y$. In the $a\ll 1$ limit, this would mean that u_2 attains arbitrarily large negative values for $r_y=O(a)$ (i.e. close to the hair surfaces).

We have demonstrated our ability to obtain the exact solutions for u_0, u_1 and u_2 in the fully-circular case under the assumption $a=O(1)$[2]. We now study the $a\ll 1$ limit in the u_0, u_1 and u_2 problems for this case. This way, we will introduce the method of matched asymptotic expansions (see [60]) on the simpler geometry, and we will gain more insight into the matching procedure, which we will make use of later on, when analysing the periodic boundary

2 It is much more difficult to obtain such solutions in the case of the periodic boundary conditions, and thus the analysis from this section will help us in Section 4.4.

conditions case.

Note first, that writing the mentioned term from Equation (186) in a boundary layer variable $r_z = \frac{r_y}{a}$, we get:

$$\frac{C}{1-a^2} u_0 \ln(r_z a) = \frac{C}{1-a^2} u_0 \ln r_z - \frac{C}{1-a^2} u_0 \ln \frac{1}{a}.$$

As a consequence, we need to use asymptotic expansions in the powers of $\ln \frac{1}{a}$ (rather than a). The more detailed explanation of the importance of choosing this type of asymptotic expansion can be found in Section 4.3.4, where we will match boundary and outer layer solutions at $O(\epsilon^2)$.

Therefore, we assume an ansatz:

$$u_0(t, \boldsymbol{y}, \boldsymbol{x}; a) = u_{0,0}(t, \boldsymbol{y}, \boldsymbol{x}) + \frac{1}{\ln \frac{1}{a}} u_{0,1}(t, \boldsymbol{y}, \boldsymbol{x}) + \frac{1}{\ln^2 \frac{1}{a}} u_{0,2}(t, \boldsymbol{y}, \boldsymbol{x}) + o(\frac{1}{\ln^2 \frac{1}{a}})$$

for u_0 from the two-scale ansatz (172), and using the continuity equation and the boundary conditions from Section 4.3.1, we get the cell problems:

$$\nabla_y^2 u_{0,0} = \nabla_y^2 u_{0,1} = \nabla_y^2 u_{0,2} = 0$$

in C_0^c, equipped with the outer boundary conditions:

$$\nabla_y u_{0,0} \cdot \hat{\boldsymbol{n}} = \nabla_y u_{0,1} \cdot \hat{\boldsymbol{n}} = \nabla_y u_{0,2} \cdot \hat{\boldsymbol{n}} = 0$$

at $r_y = 1$. This yields:

$$u_0(t, \boldsymbol{y}, \boldsymbol{x}; a) = u_{0,0}(t, \boldsymbol{x}) + \frac{1}{\ln \frac{1}{a}} u_{0,1}(t, \boldsymbol{x}) + \frac{1}{\ln^2 \frac{1}{a}} u_{0,2}(t, \boldsymbol{x}) + o(\frac{1}{\ln^2 \frac{1}{a}}).$$

Equation (174) becomes:

$$u_1(t, y_1, y_2, \boldsymbol{x}; a) = f_1(t, \boldsymbol{x}; a) +$$

$$\nabla_x \{u_{0,0}(t, \boldsymbol{x}) + \frac{1}{\ln \frac{1}{a}} u_{0,1}(t, \boldsymbol{x}) + o(\frac{1}{\ln \frac{1}{a}})\} \cdot (-r_y \cos\varphi, -r_y \sin\varphi, 0).$$

As before, we write:

$$u_2 = v^* + v^{**} + v,$$

where v^* is defined by Equation (178), v^{**} is defined by Equation (182), and as a consequence, we want v to satisfy the continuity equation (183), the hair

surface boundary condition (184), and the outer boundary condition (185). Equation (183) becomes:

$$\frac{\partial^2 v}{\partial r_y^2} + \frac{1}{r_y}\frac{\partial v}{\partial r_y} + \frac{1}{r_y^2}\frac{\partial^2 v}{\partial \varphi^2} = \{\frac{\partial}{\partial t} - \frac{\partial^2}{\partial x_3^2}\}\{u_{0,0} + \frac{1}{\ln\frac{1}{a}}u_{0,1} + o(\frac{1}{\ln\frac{1}{a}})\}. \tag{187}$$

Writing this in the stretched variable $r_z = \frac{r_y}{a}$ ($\varphi_z = \varphi$) gives:

$$\frac{\partial^2 v}{\partial r_z^2} + \frac{1}{r_z}\frac{\partial v}{\partial r_z} + \frac{1}{r_z^2}\frac{\partial^2 v}{\partial \varphi^2} = a^2\{\frac{\partial}{\partial t} - \frac{\partial^2}{\partial x_3^2}\}\{u_{0,0} + \frac{1}{\ln\frac{1}{a}}u_{0,1} + o(\frac{1}{\ln\frac{1}{a}})\}. \tag{188}$$

Equation (184) becomes:

$$\frac{\partial v}{\partial r_y} = \frac{C}{a}\{u_{0,0} + \frac{1}{\ln\frac{1}{a}}u_{0,1} + o(\frac{1}{\ln\frac{1}{a}})\},$$

and using the stretched variable $r_z = \frac{r_y}{a}$, we get:

$$\frac{1}{a}\frac{\partial v}{\partial r_z} = \frac{C}{a}\{u_{0,0} + \frac{1}{\ln\frac{1}{a}}u_{0,1} + o(\frac{1}{\ln\frac{1}{a}})\},$$

which is applied at $r_z = 1$. This gives:

$$\frac{1}{a}\frac{\partial v(r_z = 1)}{\partial r_z} = \frac{C}{a}u_{0,0} + \frac{C}{a\ln\frac{1}{a}}u_{0,1} + o(\frac{1}{a\ln\frac{1}{a}}). \tag{189}$$

Equation (185) gives:

$$\frac{\partial v(r_y = 1)}{\partial r_y} = 0. \tag{190}$$

Next, we introduce outer[3] ($r_y = O(1)$) and boundary ($r_z = \frac{r_y}{a} = O(1)$) layer expansions for v.

4.3.4 *Boundary and outer layer solutions for v*

If we tried to find a solution using a boundary layer ansatz $v(r_z, \varphi; a) = v_0(r_z, \varphi) + O(a)$, we would get $\nabla_z^2 v_0 = 0$ and a hair surface boundary condition $\frac{\partial v_0}{\partial r_z} = Cu_{0,0}$, which has a solution $v_0 = Cu_{0,0}\ln r_z + D$. Writing this in the outer variable gives $Cu_{0,0}\ln r_y + Cu_{0,0}\ln\frac{1}{a} + D$. This way, we see more clearly why we need to use asymptotic expansions in the powers of $\ln\frac{1}{a}$ rather than a.

However, trying to find a solution using a boundary layer ansatz:

$$v(r_z, \varphi, a) = v_0(r_z, \varphi) + \frac{1}{\ln\frac{1}{a}}v_1(r_z, \varphi) + o(\frac{1}{\ln\frac{1}{a}}),$$

3 Again, note that the "outer" here refers to an outer layer within the microscale geometry.

we again get $v_0 = Cu_{0,0} \ln r_z = Cu_{0,0} \ln r_y + Cu_{0,0} \ln \frac{1}{a} + D$, and we do not have any $\ln \frac{1}{a}$ term in the outer expansion yet. This means that in order to match the boundary and the outer layer solutions, we have to include a $\ln \frac{1}{a}$ term in the outer ansatz. Note, that this term also appears once we write our expression for the exact u_2 in r_z variable (see Equation (186)). It is often called a switchback term in the theory of matched asymptotic expansions [60].

Thus, we assume a boundary layer ansatz:

$$v^B(r_z, \varphi, a) = \ln \frac{1}{a} v_0^B(r_z, \varphi) + v_1^B(r_z, \varphi) + o(1), \tag{191}$$

where from now onwards, the superscript ^{B} will represent the boundary layer approximation. From Equation (188) at $O(\ln \frac{1}{a})$, we get:

$$\frac{\partial^2 v_0^B}{\partial r_z^2} + \frac{1}{r_z} \frac{\partial v_0^B}{\partial r_z} + \frac{1}{r_z^2} \frac{\partial^2 v_0^B}{\partial \varphi^2} = 0,$$

and at $O(\frac{\ln \frac{1}{a}}{a})$ in the boundary condition (189):

$$-\frac{\partial v_0^B}{\partial r_z} = 0$$

at $r_z = 1$. This leads to a solution $v_0^B(r_z, \varphi) = B_0^B$.

Using an ansatz:

$$v^O(r_y, \varphi, a) = \ln \frac{1}{a} v_0^O(r_y, \varphi) + v_1^O(r_y, \varphi) + o(1) \tag{192}$$

for the outer solution (therefore the superscript ^{O}), we get at $O(\ln \frac{1}{a})$ from Equation (187):

$$\frac{\partial^2 v_0^O}{\partial r_y^2} + \frac{1}{r_y} \frac{\partial v_0^O}{\partial r_y} + \frac{1}{r_y^2} \frac{\partial^2 v_0^O}{\partial \varphi^2} = 0,$$

and from the outer ($r_y = 1$) boundary condition (Equation (190)):

$$\frac{\partial v_0^O}{\partial r_y} = 0.$$

This again leads to $v_0^O(r_y, \varphi) = B_0^O$.

At the next order we get:

$$\frac{\partial^2 v_1^B}{\partial r_z^2} + \frac{1}{r_z} \frac{\partial v_1^B}{\partial r_z} + \frac{1}{r_z^2} \frac{\partial^2 v_1^B}{\partial \varphi^2} = 0,$$

and a hair boundary condition ($r_z = 1$):

$$-\frac{\partial v_1^B}{\partial r_z} = -Cu_{0,0}.$$

This leads to $v_1^B(r_z, \varphi) = Cu_{0,0} \ln r_z + D_0^B$.

For the outer solution, we get:

$$\frac{\partial^2 v_1^O}{\partial r_y^2} + \frac{1}{r_y}\frac{\partial v_1^O}{\partial r_y} + \frac{1}{r_y^2}\frac{\partial^2 v_1^O}{\partial \varphi^2} = \frac{\partial u_{0,0}}{\partial t} - \frac{\partial^2 u_{0,0}}{\partial x_3^2},$$

and at $r_y = 1$:

$$\frac{\partial v_1^O}{\partial r_y} = 0.$$

Using symmetry, we see that v_1^O is independent of φ, and thus:

$$\frac{\partial^2 v_1^O}{\partial r_y^2} + \frac{1}{r_y}\frac{\partial v_1^O}{\partial r_y} = \frac{\partial u_{0,0}}{\partial t} - \frac{\partial^2 u_{0,0}}{\partial x_3^2},$$

which can also be written as:

$$\frac{\partial}{\partial r_y}\{r_y \frac{\partial v_1^O}{\partial r_y}\} = \{\frac{\partial u_{0,0}}{\partial t} - \frac{\partial^2 u_{0,0}}{\partial x_3^2}\} r_y,$$

and this leads to:

$$\frac{\partial v_1^O}{\partial r_y} = \frac{\frac{\partial u_{0,0}}{\partial t} - \frac{\partial^2 u_{0,0}}{\partial x_3^2}}{2} r_y + \frac{C_0^O}{r_y}.$$

Applying the boundary condition at $r_y = 1$ yields:

$$C_0^O = -\frac{\frac{\partial u_{0,0}}{\partial t} - \frac{\partial^2 u_{0,0}}{\partial x_3^2}}{2},$$

which leads to:

$$v_1^O = \frac{\frac{\partial u_{0,0}}{\partial t} - \frac{\partial^2 u_{0,0}}{\partial x_3^2}}{2}\{\frac{r_y^2}{2} - \ln r_y\} + D_0^O.$$

Thus, we have arrived at an outer layer approximation:

$$v^O = B_0^O \ln \frac{1}{a} + \frac{\frac{\partial u_{0,0}}{\partial t} - \frac{\partial^2 u_{0,0}}{\partial x_3^2}}{2}\{\frac{r_y^2}{2} - \ln r_y\} + D_0^O + o(1),$$

and a boundary layer approximation:

$$v^B = B_0^B \ln \frac{1}{a} + Cu_{0,0} \ln r_z + D_0^B + o(1).$$

4.3.5 *Matching for v*

We match these solutions using the intermediate variable method [60]. Using this method, one can determine the unknowns in the expansions by imposing

that the inner and outer expansions are of a similar form in an intermediate region where $a \ll r_y = ar_z \ll 1$ (for more details, see [60]). We define an intermediate variable $\eta = r_z a^\alpha = r_y a^{\alpha-1}$ with $0 < \alpha < 1$, and we rewrite both expansions in terms of η. For the outer solution, we get:

$$v^O = B_0^O \ln\frac{1}{a} + \frac{1}{2}\{\frac{\partial u_{0,0}}{\partial t} - \frac{\partial^2 u_{0,0}}{\partial x_3^2}\}\{\frac{1}{2}\eta^2 a^{2(1-\alpha)} - \ln\eta + (1-\alpha)\ln\frac{1}{a}\} +$$

$$D_0^O + o(1) = \ln\frac{1}{a}\{B_0^O + (1-\alpha)\frac{\frac{\partial u_{0,0}}{\partial t} - \frac{\partial^2 u_{0,0}}{\partial x_3^2}}{2}\} + D_0^O -$$

$$\frac{\frac{\partial u_{0,0}}{\partial t} - \frac{\partial^2 u_{0,0}}{\partial x_3^2}}{2}\ln\eta + o(1),$$

and for the boundary layer solution, we get:

$$v^B = B_0^B \ln\frac{1}{a} + Cu_{0,0}(\ln\eta + \alpha\ln\frac{1}{a}) + D_0^B + o(1) =$$

$$(B_0^B + \alpha C u_{0,0})\ln\frac{1}{a} + (Cu_{0,0}\ln\eta + D_0^B) + o(1).$$

We see that in order to match these expansions, we must have:

$$B_0^O - (\alpha-1)\frac{1}{2}(\frac{\partial u_{0,0}}{\partial t} - \frac{\partial^2 u_{0,0}}{\partial x_3^2}) = B_0^B + \alpha C u_{0,0}, \tag{193}$$

and

$$-\frac{1}{2}(\frac{\partial u_{0,0}}{\partial t} - \frac{\partial^2 u_{0,0}}{\partial x_3^2}) = Cu_{0,0}. \tag{194}$$

If we were in a periodic homogenisation framework (which we are not due to the fully-circular microscale geometry C^c), Equation (194) would give us the leading order macroscopic behaviour for u. Note that we lost the $\frac{\partial^2 u_{0,0}}{\partial x_1^2}$ and the $\frac{\partial^2 u_{0,0}}{\partial x_2^2}$ terms from the diffusion tensor here, because of the zero-flux boundary condition at $r_y = 1$ and two-scale asymptotic analysis rules. Substituting Equation (194) into Equation (193), we get:

$$B_0^O - Cu_{0,0} = B_0^B.$$

To fully determine the leading order solution, we still need to find B_0^O and D_0^O, but in order to do that, we would need to proceed to higher orders, and obtain effective equations there, which we will not do at this stage.

We have arrived at a boundary layer expansion:

$$v^B = (B_0^O - Cu_{0,0})\ln\frac{1}{a} + Cu_{0,0}\ln r_z + D_0^B + ...$$

and an outer layer expansion:

$$v^O = B_0^O \ln\frac{1}{a} - Cu_{0,0}\{\frac{r_y^2}{2} - \ln r_y\} + D_0^O + ...$$

We see that the outer expansion contains all the terms from the boundary layer expansion (as well as one additional term - $-Cu_{0,0}\frac{r_y^2}{2}$). Therefore, for the composite approximation (denoted by superscript ^{C} from now onwards), we get:

$$v^C = B_0^C \ln\frac{1}{a} - Cu_{0,0}\{\frac{r_y^2}{2} - \ln r_y\} + D_0^C, \tag{195}$$

where $B_0^C = B_0^O$. Recalling that $u_2 = v + v^* + v^{**}$, reintroducing the time and the macroscale dependencies, and dropping the superscript ^{C} we conclude:

$$u_2 = B_0(t,\boldsymbol{x})\ln\frac{1}{a} - Cu_{0,0}(t,\boldsymbol{x})\{\frac{r_y^2}{2} - \ln r_y\} +$$

$$\frac{r_y^2}{2}\cos^2\varphi\frac{\partial^2 u_0(t,\boldsymbol{x};a)}{\partial x_1^2} + \frac{r_y^2}{2}\sin^2\varphi\frac{\partial^2 u_0(t,\boldsymbol{x};a)}{\partial x_2^2} + \frac{r_y^2}{2}\sin 2\varphi\frac{\partial^2 u_0(t,\boldsymbol{x};a)}{\partial x_1\partial x_2} -$$

$$r_y\cos\varphi\frac{\partial f_1(t,\boldsymbol{x};a)}{\partial x_1} - r_y\sin\varphi\frac{\partial f_1(t,\boldsymbol{x};a)}{\partial x_2} + D_0(t,\boldsymbol{x}) + o(1),$$

which can also be written as:

$$u_2 = B_0(t,\boldsymbol{x})\ln\frac{1}{a} - Cu_{0,0}(t,\boldsymbol{x})\{\frac{r_y^2}{2} - \ln r_y\} +$$

$$\frac{r_y^2}{2}\cos^2\varphi\frac{\partial^2 u_{0,0}(t,\boldsymbol{x};a)}{\partial x_1^2} + \frac{r_y^2}{2}\sin^2\varphi\frac{\partial^2 u_{0,0}(t,\boldsymbol{x};a)}{\partial x_2^2} + \frac{r_y^2}{2}\sin 2\varphi\frac{\partial^2 u_{0,0}(t,\boldsymbol{x};a)}{\partial x_1\partial x_2} -$$

$$r_y\cos\varphi\frac{\partial f_1(t,\boldsymbol{x};a)}{\partial x_1} - r_y\sin\varphi\frac{\partial f_1(t,\boldsymbol{x};a)}{\partial x_2} + D_0(t,\boldsymbol{x}) + o(1). \tag{196}$$

As a check, note that using:

$$\frac{1}{1-a^2} = 1 + a^2 + a^4 + ...$$

for $a \ll 1$, our exact solution from Equation (186) can be written as:

$$u_2(t,r_y,\varphi,\boldsymbol{x};a) = -r_y\cos\varphi\frac{\partial f_1(t,\boldsymbol{x};a)}{\partial x_1} - r_y\sin\varphi\frac{\partial f_1(t,\boldsymbol{x};a)}{\partial x_2} +$$

$$\frac{r_y^2}{2}\cos^2\varphi\frac{\partial^2 u_{0,0}(t,\boldsymbol{x};a)}{\partial x_1^2} + \frac{r_y^2}{2}\sin^2\varphi\frac{\partial^2 u_{0,0}(t,\boldsymbol{x};a)}{\partial x_2^2} +$$

$$\frac{r_y^2}{2}\sin 2\varphi\frac{\partial^2 u_{0,0}(t,\boldsymbol{x};a)}{\partial x_1\partial x_2} - Cu_{0,0}\{\frac{r_y^2}{2} - \ln r_y\} + f_2(t,\boldsymbol{x};a) + o(1),$$

and writing:

$$f_2(t,\boldsymbol{x};a) = B_0(t,\boldsymbol{x})\ln\frac{1}{a} + D_0(t,\boldsymbol{x}) + o(1)$$

we see, that this approximation is identical to Equation (196).

In conclusion, our approximation (172) becomes:

$$\begin{aligned} u \sim \{u_{0,0}(t,\boldsymbol{x}) + \frac{1}{\ln\frac{1}{a}}u_{0,1}(t,\boldsymbol{x}) + ...\} + \epsilon f_1(t,\boldsymbol{x};a) + \\ \epsilon(-r_y\cos\varphi, -r_y\sin\varphi, 0)\cdot\nabla_x\{u_{0,0}(t,\boldsymbol{x}) + \frac{1}{\ln\frac{1}{a}}u_{0,1}(t,\boldsymbol{x}) + ...\} + \\ \epsilon^2\{B_0(t,\boldsymbol{x})\ln\frac{1}{a} - Cu_{0,0}(t,\boldsymbol{x})\{\frac{r_y^2}{2} - \ln r_y\} + D_0(t,\boldsymbol{x}) + \\ \frac{r_y^2}{2}\cos^2\varphi\frac{\partial^2 u_{0,0}(t,\boldsymbol{x})}{\partial x_1^2} + \frac{r_y^2}{2}\sin^2\varphi\frac{\partial^2 u_{0,0}(t,\boldsymbol{x})}{\partial x_2^2} + \frac{r_y^2}{2}\sin 2\varphi\frac{\partial^2 u_{0,0}(t,\boldsymbol{x})}{\partial x_1\partial x_2} - \\ r_y\cos\varphi\frac{\partial f_1(t,\boldsymbol{x};a)}{\partial x_1} - r_y\sin\varphi\frac{\partial f_1(t,\boldsymbol{x};a)}{\partial x_2} + ...\}. \end{aligned} \quad (197)$$

Note the $\ln r_y$ term; for $r_y = O(a)$ (i.e. close to the hair surface), this becomes $O(\ln a)$, which goes to $-\infty$ as $a \to 0$. Therefore, our expansion ceases to be uniform close to $r_y = a$ for $a \to 0$. Using the asymptotic analysis terminology, the expansion may disorder (depending on how fast ϵ and a approach 0).

To gain more insight into microscopic contributions at $O(\epsilon^2)$, we would wish to plot microscopically nontrivial terms in u_2 for decreasing a. Because of the $\ln r_y$ term, we would need to plot functions with the hair surface value decreasing to $-\infty$ as $a \to 0$. Therefore, before we go back to the periodic boundary conditions, we study $K(a)$ scalings which do not lead to these complications.

4.3.6 *Different scalings for $K(a)$*

If we had assumed $K(a) = C$, we would have ended up with the need of introducing powers of a in our asymptotic expansions (not just logarithms). Consistency conditions would have been different too (uptake is negligible at the leading order now), but apart from that, the procedure would have been similar. Let us study an interesting case $K(a) = \frac{C}{a\ln\frac{1}{a}}$. Repeating the same procedure as before, we arrive at an outer layer expansion:

$$v^O = \ln(\frac{1}{a})B_0^O + \frac{\frac{\partial u_{0,0}}{\partial t} - \frac{\partial^2 u_{0,0}}{\partial x_3^2}}{2}\{\frac{r_y^2}{2} - \ln r_y\} + D_0^O +$$

$$\frac{1}{\ln(\frac{1}{a})}\{\frac{\frac{\partial u_{0,1}}{\partial t}-\frac{\partial^2 u_{0,1}}{\partial x_3^2}}{2}\{\frac{r_y^2}{2}-\ln r_y\}+F_0^O\}+$$

$$\frac{1}{\ln^2(\frac{1}{a})}\{\frac{\frac{\partial u_{0,2}}{\partial t}-\frac{\partial^2 u_{0,2}}{\partial x_3^2}}{2}\{\frac{r_y^2}{2}-\ln r_y\}+H_0^O\}+o(\frac{1}{\ln^2(\frac{1}{a})}),$$

and a boundary layer expansion:

$$v^B=\ln\frac{1}{a}B_0^B+D_0^B+\frac{1}{\ln\frac{1}{a}}\{Cu_{0,0}\ln r_z+F_0^B\}+$$

$$\frac{1}{\ln^2\frac{1}{a}}\{Cu_{0,1}\ln r_z+H_0^B\}+o(\frac{1}{\ln^2(\frac{1}{a})}).$$

Using the intermediate variable $\eta = r_z a^\alpha = r_y a^{\alpha-1}$, the outer expansion becomes:

$$v^O=\ln(\frac{1}{a})B_0^O+\frac{1}{2}(\frac{\partial u_{0,0}}{\partial t}-\frac{\partial^2 u_{0,0}}{\partial x_3^2})(-\ln\eta-(\alpha-1)\ln\frac{1}{a})+D_0^O+$$

$$\frac{1}{\ln(\frac{1}{a})}\{\frac{1}{2}(\frac{\partial u_{0,1}}{\partial t}-\frac{\partial^2 u_{0,1}}{\partial x_3^2})(-\ln\eta-(\alpha-1)\ln\frac{1}{a})+F_0^O\}+$$

$$\frac{1}{\ln^2(\frac{1}{a})}\{\frac{1}{2}(\frac{\partial u_{0,2}}{\partial t}-\frac{\partial^2 u_{0,2}}{\partial x_3^2})(-\ln\eta-(\alpha-1)\ln\frac{1}{a})+H_0^O\}+o(\frac{1}{\ln^2\frac{1}{a}}),$$

and the boundary layer expansion becomes:

$$v^B=\ln\frac{1}{a}B_0^B+D_0^B+\frac{1}{\ln\frac{1}{a}}\{Cu_{0,0}(\ln\eta+\alpha\ln\frac{1}{a})+F_0^B\}+$$

$$\frac{1}{\ln^2\frac{1}{a}}\{Cu_{0,1}(\ln\eta+\alpha\ln\frac{1}{a})+H_0^B\}+o(\frac{1}{\ln^2\frac{1}{a}}).$$

To match these two expansions, we must impose:

$$B_0^B=B_0^O-\frac{1}{2}(\alpha-1)(\frac{\partial u_{0,0}}{\partial t}-\frac{\partial^2 u_{0,0}}{\partial x_3^2}), \tag{198}$$

$$D_0^B+\alpha Cu_{0,0}=D_0^O-\frac{1}{2}(\alpha-1)(\frac{\partial u_{0,1}}{\partial t}-\frac{\partial^2 u_{0,1}}{\partial x_3^2}), \tag{199}$$

$$\frac{1}{2}(\frac{\partial u_{0,0}}{\partial t}-\frac{\partial^2 u_{0,0}}{\partial x_3^2})=0, \tag{200}$$

$$F_0^B+\alpha Cu_{0,1}=F_0^O-\frac{1}{2}(\alpha-1)(\frac{\partial u_{0,2}}{\partial t}-\frac{\partial^2 u_{0,2}}{\partial x_3^2}), \tag{201}$$

and:

$$-\frac{1}{2}(\frac{\partial u_{0,1}}{\partial t} - \frac{\partial^2 u_{0,1}}{\partial x_3^2}) = Cu_{0,0}. \tag{202}$$

Combining Equation (200) (which tells us the leading order macroscopic behaviour) with Equation (198), we get $B_0^B = B_0^O$. Combining Equation (202) (which tells us the macroscopic behaviour at the next order) with Equation (199), we conclude $D_0^O = Cu_{0,0} + D_0^B$. If we proceeded to the next order, we would uncover:

$$-\frac{1}{2}(\frac{\partial u_{0,2}}{\partial t} - \frac{\partial^2 u_{0,2}}{\partial x_3^2}) = Cu_{0,1},$$

which altogether with Equation (201) (analogously to the previous orders) yields $F_0^O = F_0^B + Cu_{0,1}$. This way, we arrive at an outer expansion:

$$v^O(r_y; a) = B_0^O \ln\frac{1}{a} + D_0^O + \frac{1}{\ln\frac{1}{a}}\Big(- Cu_{0,0}(\frac{r_y^2}{2} - \ln r_y) + F_0^O \Big) + o(\frac{1}{\ln\frac{1}{a}}), \tag{203}$$

which is also a composite approximation to the solution (for similar reasons as in Section 4.3.5). Assume that no x_1 or x_2 variation is introduced via initial or boundary conditions. Then u_0 and f_1 are independent of x_1 and x_2, which means that $v^* = 0$ and $v^{**} = 0$. This leads to $u_2 = v$, and therefore the microscopically-varying part of u_2 (from now on denoted as $\underline{u_2}$) equals the microscopically-varying part of v (from now on denoted as $\underline{v}$):

$$\underline{u_2}(r_y; a) = \underline{v}(r_y; a) = \frac{1}{\ln\frac{1}{a}}\{-Cu_{0,0}(\frac{r_y^2}{2} - \ln r_y)\} + o(\frac{1}{\ln\frac{1}{a}}). \tag{204}$$

The behaviour of $u_{0,0}$ will be determined by the corresponding effective equations in combination with the imposed initial and boundary conditions. To shed some light on the microscopic behaviour of u_2 ($\underline{u_2}$), imagine we are at a point $(t, \boldsymbol{x})$ in time and (macroscopic) space, so that $Cu_{0,0} = 1.0$. Denote $\tilde{v}(r_y; a) = \frac{1}{\ln\frac{1}{a}}\{\ln r_y - \frac{r_y^2}{2}\}$ to be the leading order approximation to $\underline{v}(r_y; a)$ (evaluated at the mentioned point $(t, \boldsymbol{x})$). The dependence of $\tilde{v}(r_y; a)$ on a is shown in Figure 4.2. We observe sharp gradients as we approach the root hair surface ($r_y \to a$). These correspond to depletion zones due to the nutrient uptake by the root hairs. At the end of this chapter, we will show that using these higher order corrections we can approximate the behaviour of the full-geometry solution to a remarkable detail.

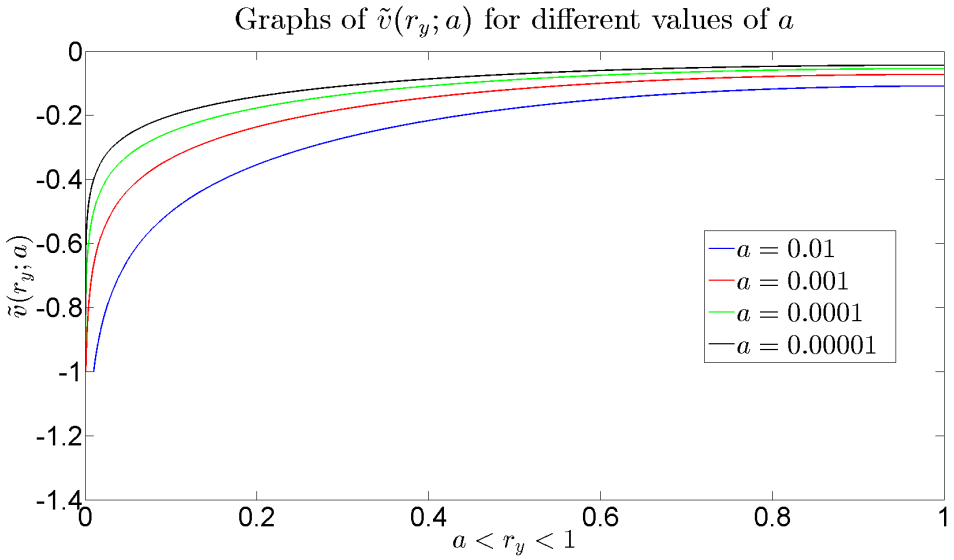


Figure 4.2.: Behaviour of $\tilde{v}(r_y; a)$ as $a \ll 1$

4.4 PERIODIC BOUNDARY CONDITIONS

We now go back to the periodic boundary conditions imposed at $y_1, y_2 = \pm\frac{1}{2}$. Again, $\boldsymbol{x}$ denotes the macroscopic variables, $(y_1, y_2) = \frac{(x_1, x_2)}{\epsilon}$ the microscopic variables (the inter-hair distance is equal to 1 in these variables), and we use $(z_1, z_2) = \frac{(y_1, y_2)}{a}$ for the boundary layer variables.

We start with the same continuity equation (129) equipped with the same Robin-type boundary condition (132) at the hair surfaces, and we search for a solution in the form of Ansatz (172). Similar to the fully-circular geometry case, we first make the $\epsilon \ll 1$ limit, after which we proceed with the $a \ll 1$ limit.

4.4.1 u_0

At $O(1)$, we get (assuming $a = O(1)$):

$$0 = \nabla_y^2 u_0 = \frac{\partial^2 u_0}{\partial y_1^2} + \frac{\partial^2 u_0}{\partial y_2^2}$$

together with the periodic boundary conditions in y_1 and y_2, and:

$$\nabla_y u_0 \cdot \hat{\boldsymbol{n}} = 0$$

at $y_1^2 + y_2^2 = a^2$. By the same reasoning as before, the subsequent $a \to 0$ limit analysis yields an expansion:

$$u_0(t, \boldsymbol{y}, \boldsymbol{x}; a) = u_{0,0}(t, \boldsymbol{x}) + \frac{1}{\ln \frac{1}{a}} u_{0,1}(t, \boldsymbol{x}) + o(\frac{1}{\ln \frac{1}{a}}). \tag{205}$$

4.4.2 u_1

At $O(\epsilon)$, we get (assuming $a = O(1)$):

$$\nabla_y^2 u_1 = 0,$$

and as the hair surface boundary condition, we obtain:

$$\nabla_y u_1 \cdot \hat{\boldsymbol{n}} = -\nabla_x u_0 \cdot \hat{\boldsymbol{n}}$$

applied at $r_y = a$. Proceeding with the $a \to 0$ limit, we examine the boundary layer (i.e. we rescale $(z_1, z_2) = \frac{(y_1, y_2)}{a}$), and get:

$$\nabla_z u_1 \cdot \hat{\boldsymbol{n}} = -a \nabla_x u_{0,0} \cdot \hat{\boldsymbol{n}} - \frac{a}{\ln \frac{1}{a}} \nabla_x u_{0,1} \cdot \hat{\boldsymbol{n}} + o(\frac{a}{\ln \frac{1}{a}}).$$

This leads to a boundary layer ansatz:

$$u_1^B = f_1^B(t, \boldsymbol{x}, a) + a\{\nabla_x u_{0,0}(t, \boldsymbol{x}) + \frac{1}{\ln \frac{1}{a}} \nabla_x u_{0,1}(t, \boldsymbol{x}) + o(\frac{1}{\ln \frac{1}{a}})\} \cdot \boldsymbol{\lambda}^B(z_1, z_2).$$

From $O(a)$, we have:

$$\nabla_z^2 \boldsymbol{\lambda}^B = \boldsymbol{0},$$

and a boundary condition:

$$\nabla_z \boldsymbol{\lambda}^B \cdot \hat{\boldsymbol{n}} = -\hat{\boldsymbol{n}}$$

applied at $r_z = 1$, which can also be written as:

$$\frac{\partial \boldsymbol{\lambda}^B}{\partial r_z} = (-\cos\varphi, -\sin\varphi).$$

The solutions are:

$$\lambda_1^B(r_z, \varphi) = -\cos\varphi(B(r_z + \frac{1}{r_z}) + r_z),$$

$$\lambda_2^B(r_z, \varphi) = -\sin\varphi(B(r_z + \frac{1}{r_z}) + r_z),$$

and:

$$\lambda_3^B(r_z, \varphi) = 0.$$

This leads to a boundary layer approximation:

$$u_1^B \sim f_1^B(t, \boldsymbol{x}, a) +$$

$$a\Big(-\cos\varphi\Big(r_z(B+1) + \frac{B}{r_z}\Big), -\sin\varphi\Big(r_z(B+1) + \frac{B}{r_z}\Big), 0) \cdot \nabla_x u_{0,0}(t, \boldsymbol{x}).$$

We now show that B must be -1, and the terms that increase (in absolute value) with increasing r_z thus disappear. Imagine $B \neq -1$. Then, we get an $ar_z \cos\varphi$ contribution in the boundary layer expansion. For the outer layer solution to match the boundary layer solution, we need to have an $r_y \cos\varphi = y_1$ contribution in the $r_y \to 0$ limit of the outer expansion. As the outer approximation needs to satisfy the periodic boundary conditions, it is impossible to have contributions of this form. Thus, we arrived at a contradiction.

This means that we must have $B = -1$, and we arrive at a boundary layer approximation:

$$u_1^B = f_1^B(t, \boldsymbol{x}, a) + a(\cos\varphi\frac{1}{r_z}, \sin\varphi\frac{1}{r_z}, 0) \cdot \nabla_x u_{0,0}(t, \boldsymbol{x}) +$$

$$\frac{a}{\ln\frac{1}{a}}(\cos\varphi\frac{1}{r_z}, \sin\varphi\frac{1}{r_z}, 0) \cdot \nabla_x u_{0,1}(t, \boldsymbol{x}) + ...$$

In the outer scaling, we have:

$$\nabla_y^2 u_1^O = 0,$$

and the periodic boundary conditions are imposed at $y_1, y_2 = \pm\frac{1}{2}$. To be able to match the boundary and the outer layer solutions (to find a matching for the $\frac{1}{r_z}$ term in particular), we need to use a similar ansatz for the composite solution, i.e.:

$$u_1^C = f_1^C(t, \boldsymbol{x}, a) + a^2\{\nabla_x u_{0,0}(t, \boldsymbol{x}) + \frac{1}{\ln\frac{1}{a}}\nabla_x u_{0,1}(t, \boldsymbol{x}) + o(\frac{1}{\ln\frac{1}{a}})\} \cdot \boldsymbol{\lambda}^C(y_1, y_2),$$

where $\boldsymbol{\lambda}^C(y_1, y_2)$ is defined on $[-\frac{1}{2}, \frac{1}{2}] \times [-\frac{1}{2}, \frac{1}{2}]$, and satisfies the periodicity conditions in y_1 and y_2. One might be tempted to impose a cell problem $\nabla_y^2 \boldsymbol{\lambda}^C = 0$. However, this is incorrect - there exist no non-constant solutions to this problem. The problem is that in the outer scaling, the hair boundary degenerates (in the $a \ll 1$ limit) to a single point. Moreover, with the periodic

boundary conditions, obtaining analytic solutions is much more troublesome (because circular symmetry is broken here). Therefore, the matching is performed in a slightly non-standard way. To be able to match with the boundary layer solution, we need to recover terms behaving as:

$$a\{(\cos\varphi\frac{1}{r_z},\sin\varphi\frac{1}{r_z},0)\cdot\nabla_x u_{0,0}(t,\boldsymbol{x})\}=\frac{a^2}{r_y}(\cos\varphi,\sin\varphi,0)\cdot\nabla_x u_{0,0}(t,\boldsymbol{x})$$

for $r_y\to 0$ in the outer solution. To achieve this, we notice that:

$$\frac{\partial}{\partial y_1}\{\ln r_y\}=\frac{\cos\varphi}{r_y},$$

$$\frac{\partial}{\partial y_2}\{\ln r_y\}=\frac{\sin\varphi}{r_y},$$

and we know that (assuming an unbounded geometry) $\ln r_y$ is a solution of:

$$\nabla_y^2 u=2\pi\delta_{(0,0)}(y_1,y_2),$$

where $\delta_{(0,0)}$ denotes the Dirac delta function in two dimensions concentrated at the origin, which is zero everywhere except for $(0,0)$, and whose integral over any domain containing $(0,0)$ is 1. In other words, $\frac{1}{2\pi}\ln r_y$ is Green's function for Laplace's operator in two dimensions (see [45]). This means that the solution of:

$$\nabla_y^2\boldsymbol{u}=2\pi\nabla_{y_1,y_2}\delta_{(0,0)}$$

with the periodic boundary conditions behaves as:

$$\boldsymbol{u}\sim\frac{1}{r_y}(\cos\varphi,\sin\varphi)$$

for $r_y\to 0$. Using this result we get the following cell problem (equipped with the periodic boundary conditions):

$$\nabla_y^2\boldsymbol{\lambda}^C=2\pi\nabla_y\delta_{(0,0)}.$$

Now that our cell problem at $O(\epsilon)$ is well defined, we obtained a composite approximation:

$$u_1^C=f_1^C(t,\boldsymbol{x},a)+a^2\nabla_x u_{0,0}(t,\boldsymbol{x})\cdot\boldsymbol{\lambda}^C(y_1,y_2)+\frac{a^2}{\ln\frac{1}{a}}\nabla_x u_{0,1}(t,\boldsymbol{x})\cdot\boldsymbol{\lambda}^C(y_1,y_2)+o(\frac{a^2}{\ln\frac{1}{a}}).\quad(206)$$

4.4.3 u_2

At $O(\epsilon^2)$, we get (assuming $a = O(1)$):

$$\nabla_y^2 u_2 = \frac{\partial u_0}{\partial t} - \nabla_x^2 u_0 - 2\nabla_x \cdot \nabla_y u_1,$$

which (using our knowledge of u_0 and u_1) becomes:

$$\nabla_y^2 u_2 = \frac{\partial u_{0,0}}{\partial t} - \nabla_x^2 u_{0,0} + \frac{1}{\ln \frac{1}{a}}\{\frac{\partial u_{0,1}}{\partial t} - \nabla_x^2 u_{0,1}\} + o(\frac{1}{\ln \frac{1}{a}}).$$

Writing this in the stretched coordinate $r_z = \frac{r_y}{a}$ ($\tilde{\varphi} = \varphi$) gives:

$$\frac{1}{a^2}\nabla_z^2 u_2 = \frac{\partial u_0}{\partial t} - \nabla_x^2 u_0 - \frac{2}{a}\nabla_x \cdot \nabla_z u_1$$

or (using the acquired knowledge of u_0 and u_1):

$$\frac{\partial^2 u_2}{\partial r_z^2} + \frac{1}{r_z}\frac{\partial u_2}{\partial r_z} + \frac{1}{r_z^2}\frac{\partial^2 u_2}{\partial \varphi^2} = o(\frac{a}{\ln \frac{1}{a}}).$$

At $r_y = a$, we get a boundary condition:

$$\nabla_y u_2 \cdot \hat{\boldsymbol{n}} = -Ku_0 - \nabla_x u_1 \cdot \hat{\boldsymbol{n}},$$

which in the stretched coordinate becomes:

$$\frac{1}{a}\nabla_z u_2 \cdot \hat{\boldsymbol{n}} = -Ku_0 - \nabla_x u_1 \cdot \hat{\boldsymbol{n}}$$

or (using our knowledge of the boundary layer u_0 and u_1):

$$\frac{\partial u_2}{\partial r_z} = a\{Ku_{0,0} + \frac{K}{\ln \frac{1}{a}}u_{0,1} + o(\frac{K}{\ln \frac{1}{a}}) +$$

$$\nabla_x f_0(t, \boldsymbol{x}) \cdot \hat{\boldsymbol{n}} + \frac{1}{\ln \frac{1}{a}}\nabla_x f_1(t, \boldsymbol{x}) \cdot \hat{\boldsymbol{n}} + o(\frac{1}{\ln \frac{1}{a}})\}.$$

Scaling assumption

Using the scaling assumption $K(a) = \frac{C}{a}$, our boundary condition becomes:

$$\frac{\partial u_2}{\partial r_z} = Cu_{0,0} + \frac{C}{\ln \frac{1}{a}}u_{0,1} + o(\frac{1}{\ln \frac{1}{a}})$$

applied at $r_z = 1$.

Assuming a boundary layer ansatz:

$$u_2^B(t, r_z, \varphi, \boldsymbol{x}; a) = \ln \frac{1}{a} v_0^B(t, r_z, \varphi, \boldsymbol{x}) + v_1^B(t, r_z, \varphi, \boldsymbol{x}) +$$

$$\frac{1}{\ln \frac{1}{a}} v_2^B(t, r_z, \varphi, \boldsymbol{x}) + o(\frac{1}{\ln \frac{1}{a}})$$

(recall the switchback term from Section 4.3.4), we get at $O(\ln \frac{1}{a})$:

$$\frac{\partial^2 v_0^B}{\partial r_z^2} + \frac{1}{r_z}\frac{\partial v_0^B}{\partial r_z} + \frac{1}{r_z^2}\frac{\partial^2 v_0^B}{\partial \varphi^2} = 0,$$

and at $O(\ln \frac{1}{a})$ in the hair surface boundary condition, we obtain:

$$\frac{\partial v_0^B}{\partial r_z} = 0$$

applied at $r_z = 1$. This yields a solution $v_0^B(t, r_z, \varphi, \boldsymbol{x}) = B_0^B(t, \boldsymbol{x})$.
At the next order, we get:

$$\frac{\partial^2 v_1^B}{\partial r_z^2} + \frac{1}{r_z}\frac{\partial v_1^B}{\partial r_z} + \frac{1}{r_z^2}\frac{\partial^2 v_1^B}{\partial \varphi^2} = 0,$$

which together with a hair surface boundary condition:

$$\frac{\partial v_1^B}{\partial r_z} = C u_{0,0}$$

at $r_z = 1$ leads to:

$$v_1^B(r_z, \varphi) = C u_{0,0} \ln r_z + D_0^B = C u_{0,0} \ln r_y + C u_{0,0} \ln \frac{1}{a} + D_0^B.$$

Similarly, at the following order, we get:

$$\frac{\partial^2 v_2^B}{\partial r_z^2} + \frac{1}{r_z}\frac{\partial v_2^B}{\partial r_z} + \frac{1}{r_z^2}\frac{\partial^2 v_2^B}{\partial \varphi^2} = 0,$$

which together with a hair surface boundary condition:

$$\frac{\partial v_2^B}{\partial r_z} = C u_{0,1}$$

at $r_z = 1$ leads to:

$$v_2^B(r_z, \varphi) = C u_{0,1} \ln r_z + F_0^B = C u_{0,1} \ln r_y + C u_{0,1} \ln \frac{1}{a} + F_0^B.$$

Thus, we obtain a boundary layer approximation:

$$u_2^B(t, r_z, \varphi, \boldsymbol{x}; a) = \ln \frac{1}{a} B_0^B(t, \boldsymbol{x}) + C u_{0,0} \ln r_z + D_0^B + \frac{1}{\ln \frac{1}{a}} \left(C u_{0,1} \ln r_z + F_0^B \right) + o(\frac{1}{\ln \frac{1}{a}}). \quad (207)$$

Using an outer layer ansatz:

$$u_2^O(t, r_y, \varphi, \boldsymbol{x}; a) = \ln \frac{1}{a} v_0^O(t, r_y, \varphi, \boldsymbol{x}) + v_1^O(t, r_y, \varphi, \boldsymbol{x}) + \frac{1}{\ln \frac{1}{a}} v_2^O(t, r_y, \varphi, \boldsymbol{x}) + ...,$$

we get at $O(\ln \frac{1}{a})$:

$$\nabla_y^2 v_0^O = 0,$$

which together with the periodic boundary conditions at $y_1, y_2 = \pm\frac{1}{2}$ leads to:

$$v_0^O(t, r_y, \varphi, \boldsymbol{x}) = B_0^O(t, \boldsymbol{x}).$$

At the next order in the outer layer approximation, we get:

$$\nabla_y^2 v_1^O = \frac{\partial u_{0,0}}{\partial t} - \nabla_x^2 u_{0,0} \tag{208}$$

together with the periodic boundary conditions at $y_1, y_2 = \pm\frac{1}{2}$. Writing the lowest-order, microscopically-nontrivial term from Ansatz (207) in the outer layer coordinate r_y yields:

$$C u_{0,0}(t, \boldsymbol{x}) \ln r_z = C u_{0,0}(t, \boldsymbol{x}) \ln \frac{r_y}{a} = C u_{0,0}(t, \boldsymbol{x}) \ln r_y + C u_{0,0}(t, \boldsymbol{x}) \ln \frac{1}{a}. \tag{209}$$

The emergence of the term $C u_{0,0}(t, \boldsymbol{x}) \ln \frac{1}{a}$ in Expression (209) suggests that the composite approximation for u will contain an $O(\epsilon^2 \ln \frac{1}{a})$ term. Thus, we are in danger that the two limits under consideration ($a \ll 1$, $\epsilon \ll 1$) might not commute, and in order to obtain the homogenised equation, we have to specify a scale-dependence between ϵ and $\ln \frac{1}{a}$. However, before we do that, let us proceed with our analysis and recover a homogenised equation (although it will not be valid for all the parameter regimes under consideration).

Expression (209) also suggests, that in order to ensure an appropriate matching between the solutions of the inner and the outer layer problems, we need to recover some terms for the outer solution behaving as:

$$C u_{0,0}(t, \boldsymbol{x}) \ln r_y$$

for $r_y = \sqrt{y_1^2 + y_2^2} \to 0$. Combining the fact that $\frac{1}{2\pi} \ln r_y$ is Green's function for Laplace's operator in two dimensions with the outer layer equation (208), we obtain a modified problem for composite v_1^C:

$$\nabla_y^2 v_1^C = \frac{\partial u_{0,0}}{\partial t} - \nabla_x^2 u_{0,0} + 2\pi C u_{0,0} \delta_{(0,0)} \tag{210}$$

equipped with the periodic boundary conditions. Recalling the Fredholm alternative (see [45]; alternatively integrate over the microscopic domain $C = (-\frac{1}{2}, \frac{1}{2}) \times (-\frac{1}{2}, \frac{1}{2})$ and apply the divergence theorem), we conclude that this problem admits a solution if and only if:

$$\int_C \{\frac{\partial u_{0,0}}{\partial t} - \nabla_x^2 u_{0,0} + 2\pi C u_{0,0} \delta_{(0,0)}\} dS = 0.$$

In other words, the solvability condition is:

$$\frac{\partial u_{0,0}}{\partial t} = \nabla_x^2 u_{0,0} - 2\pi C u_{0,0}. \tag{211}$$

By solving this equation, we obtain a leading order (in a) approximation to the homogenised solution. Substituting this result back to Equation (210) gives:

$$\nabla_y^2 v_1^C = 2\pi C u_{0,0}(\delta_{(0,0)} - 1). \tag{212}$$

Thus, we found a composite approximation (dropping the superscripts for convenience):

$$\begin{aligned} u(t, \boldsymbol{x}; \epsilon, a) \sim \{u_{0,0}(t, \boldsymbol{x}) + \frac{1}{\ln \frac{1}{a}} u_{0,1}(t, \boldsymbol{x}) + ...\} + \\ \epsilon\{f_1(t, \boldsymbol{x}, a) + a^2 \nabla_x u_{0,0}(t, \boldsymbol{x}) \cdot \boldsymbol{\lambda}(y_1, y_2) + \frac{a^2}{\ln \frac{1}{a}} \nabla_x u_{0,1}(t, \boldsymbol{x}) \cdot \boldsymbol{\lambda}(y_1, y_2) + ...\} + \\ \epsilon^2\{\ln \frac{1}{a} B_0(t, \boldsymbol{x}) + v_1(t, y_1, y_2, \boldsymbol{x}) + ...\} + ..., \end{aligned} \tag{213}$$

where v_1 satisfies Equation (212). We see that the same problem as in the fully-circular case is present here - $\epsilon^2 \ll 1$ is multiplied by $\ln \frac{1}{a} \gg 1$. Therefore, if we choose a and ϵ to approach 0 so that $\epsilon^2 \ln \frac{1}{a} = O(1)$, the $\epsilon^2 u_2$ term becomes as big as the u_0 term, and the homogenised equation will be changed (as will be shown in Section 4.7).

At the next order, we find a similar solvability condition:

$$\frac{\partial u_{0,1}}{\partial t} = \nabla_x^2 u_{0,1} - 2\pi C u_{0,1}. \tag{214}$$

4.4.4 *Different scalings for $K(a)$*

Before we deal with the case of non-commuting limits for $K(a) = \frac{C}{a}$, we study a different scaling for the uptake constant $K(a)$. Using our experience from

the fully-circular case, we assume $K(a) = \frac{C}{a \ln \frac{1}{a}}$. The hair boundary condition becomes:

$$\frac{\partial u_2}{\partial r_z} = \frac{C}{\ln \frac{1}{a}} u_{0,0} + \frac{C}{\ln^2 \frac{1}{a}} u_{0,1} + o(\frac{1}{\ln \frac{1}{a}})$$

applied at $r_z = 1$. Assuming a boundary layer ansatz:

$$u_2^B(t, r_z, \varphi, \boldsymbol{x}; a) = \ln \frac{1}{a} v_0^B(t, r_z, \varphi, \boldsymbol{x}) + v_1^B(t, r_z, \varphi, \boldsymbol{x}) + \frac{v_2^B(t, r_z, \varphi, \boldsymbol{x})}{\ln \frac{1}{a}} + o(\frac{1}{\ln \frac{1}{a}})$$

(recall the switchback term again), we get at $O(\ln \frac{1}{a})$:

$$\frac{\partial^2 v_0^B}{\partial r_z^2} + \frac{1}{r_z} \frac{\partial v_0^B}{\partial r_z} + \frac{1}{r_z^2} \frac{\partial^2 v_0^B}{\partial \varphi^2} = 0,$$

and at $O(\ln \frac{1}{a})$ in the hair boundary condition:

$$\frac{\partial v_0^B}{\partial r_z} = 0$$

at $r_z = 1$. This leads to $v_0^B(t, r_z, \varphi, \boldsymbol{x}) = B_0^B(t, \boldsymbol{x})$.

Using an outer layer ansatz:

$$u_2^O(t, r_y, \varphi, \boldsymbol{x}; a) = \ln \frac{1}{a} v_0^O(t, r_y, \varphi, \boldsymbol{x}) + v_1^O(t, r_y, \varphi, \boldsymbol{x}) + \frac{v_2^O(t, r_y, \varphi, \boldsymbol{x})}{\ln \frac{1}{a}} + ...,$$

we get at $O(\ln \frac{1}{a})$:

$$\frac{\partial^2 v_0^O}{\partial r_y^2} + \frac{1}{r_y} \frac{\partial v_0^O}{\partial r_y} + \frac{1}{r_y^2} \frac{\partial^2 v_0^O}{\partial \varphi^2} = 0,$$

which together with the periodic boundary conditions at $y_1, y_2 = \pm \frac{1}{2}$ yields:

$$v_0^O(t, r_y, \varphi, \boldsymbol{x}) = B_0^O(t, \boldsymbol{x}).$$

Moving to the next order, we get:

$$\frac{\partial^2 v_1^B}{\partial r_z^2} + \frac{1}{r_z} \frac{\partial v_1^B}{\partial r_z} + \frac{1}{r_z^2} \frac{\partial^2 v_1^B}{\partial \varphi^2} = 0,$$

which together with the hair surface boundary condition:

$$\frac{\partial v_1^B}{\partial r_z} = 0$$

at $r_z = 1$ leads to $v_1^B(t, r_z, \varphi, \boldsymbol{x}) = D_0^B(t, \boldsymbol{x})$. For the outer solution at this order, we get:

$$\nabla_y^2 v_1^O = \frac{\partial u_{0,0}}{\partial t} - \nabla_x^2 u_{0,0}$$

equipped with the periodic boundary conditions. Recalling the Fredholm alternative, we arrive at a solvability condition:

$$\frac{\partial u_{0,0}}{\partial t} = \nabla_x^2 u_{0,0}.$$

Notice that now the uptake term does not impact on the leading order behaviour anymore - dividing the existing $K(a)$ by $\ln \frac{1}{a}$ we made the uptake term too weak. We conclude that $v_1^O(t, r_y, \varphi, \boldsymbol{x}) = D_0^O(t, \boldsymbol{x})$.
At the next order, we find:

$$\frac{\partial^2 v_2^B}{\partial r_z^2} + \frac{1}{r_z}\frac{\partial v_2^B}{\partial r_z} + \frac{1}{r_z^2}\frac{\partial^2 v_2^B}{\partial \varphi^2} = 0$$

together with the hair surface boundary condition ($r_z = 1$):

$$\frac{\partial v_2^B}{\partial r_z} = C u_{0,0}.$$

This leads to:

$$v_2^B = C u_{0,0} \ln r_z + F_0^B = C u_{0,0} \ln r_y + C u_{0,0} \ln \frac{1}{a} + F_0^B.$$

Now, the $C u_{0,0} \ln \frac{1}{a}$ term will have impact on D_0^O (or D_0^B); it will not interfere with B_0^B and B_0^O anymore. As we have seen before, the $C u_{0,0} \ln r_y$ term causes changes in the formulation of the composite solution problem. We get:

$$\nabla_y^2 v_2^C = \frac{\partial u_{0,1}}{\partial t} - \nabla_x^2 u_{0,1} + 2C\pi u_{0,0}\delta_{(0,0)} \tag{215}$$

equipped with the periodic boundary conditions. Integration over the unit cell C gives a solvability condition:

$$\frac{\partial u_{0,1}}{\partial t} = \nabla_x^2 u_{0,1} - 2C\pi u_{0,0}. \tag{216}$$

As we already know the governing equation for $u_{0,0}$, this becomes an effective (macroscopic) equation for $u_{0,1}$. Thus, we obtain a two-term approximation (in a) to the homogenised solution:

$$u_0 \sim u_{0,0} + \frac{1}{\ln \frac{1}{a}} u_{0,1}.$$

4.5 CHECKING

In this section, we first go back to the fully-circular case with the zero-flux boundary conditions at $r_y = 1$, and check whether the matching procedure introduced in the periodic boundary conditions case gives the same results here. Then, we check the accuracy of numerical solutions of Poisson's equation with a Dirac sink term in FEniCS, as such solutions will be needed in future.

4.5.1 *Consistency between matching procedures*

Recall that under the scaling assumption $K = \frac{C}{a \ln \frac{1}{a}}$ (and assuming that no gradient in x_1 and x_2 is introduced via initial or boundary conditions), we arrived (in the fully-circular case) at the first nontrivial microscopic contribution (204) for $v = u_2$.

We want to show that the new matching rule is consistent with the standard one (i.e. that the resulting behaviour is the same), and this can be shown only in the case of the fully-circular microgeometry C_a^c. Thus, we apply the new matching rule to this case.

We go back to the boundary and outer layer continuity equations (188), (187), and the outer boundary condition (190). The hair surface boundary condition (189) was derived using $K = \frac{C}{a}$, and thus we replace it with:

$$-\frac{1}{a}\frac{\partial v}{\partial r_z} = -\frac{C}{a \ln \frac{1}{a}} u_{0,0} - \frac{C}{a \ln^2 \frac{1}{a}} u_{0,1} + o(\frac{1}{a \ln^2 \frac{1}{a}}).$$

Assuming a boundary layer ansatz:

$$v^B(t, r_z, \varphi, \boldsymbol{x}; a) = \ln \frac{1}{a} v_0^B(t, r_z, \varphi, \boldsymbol{x}) + v_1^B(t, r_z, \varphi, \boldsymbol{x}) +$$

$$\frac{1}{\ln \frac{1}{a}} v_2^B(t, r_z, \varphi, \boldsymbol{x}) + o(\frac{1}{\ln \frac{1}{a}}),$$

and an outer layer ansatz:

$$v^O(t, r_y, \varphi, \boldsymbol{x}; a) = \ln \frac{1}{a} v_0^O(t, r_y, \varphi, \boldsymbol{x}) + v_1^O(t, r_y, \varphi, \boldsymbol{x}) +$$

$$\frac{1}{\ln \frac{1}{a}} v_2^O(t, r_y, \varphi, \boldsymbol{x}) + o(\frac{1}{\ln \frac{1}{a}}),$$

we get at the leading order:

$$\nabla_y^2 v_0^O = 0,$$

which together with the outer boundary condition $\frac{\partial v_0^O}{\partial r_y} = 0$ at $r_y = 1$ yields $v_0^O = B_0^O(t, \boldsymbol{x})$. In the boundary layer, we obtain:

$$\nabla_z^2 v_0^B = 0,$$

and a hair surface boundary condition $\frac{\partial v_0^B}{\partial r_z} = 0$ at $r_z = 1$, which implies $v_0^B = B_0^B(t, \boldsymbol{x})$.

At the next order, the boundary layer gives $\nabla_z^2 v_1^B = 0$ together with $\frac{\partial v_1^B}{\partial r_z} = 0$, which implies $v_1^B = D_0^B(t, \boldsymbol{x})$, i.e. we do not observe the logarithmic behaviour in the boundary layer solution at this order. Therefore, an equation for the outer layer:

$$\nabla_y^2 v_1^O = \frac{\partial u_{0,0}}{\partial t} - \frac{\partial^2 u_{0,0}}{\partial x_3^2}$$

is also a composite solution equation, and it is equipped with a boundary condition:

$$\nabla_y v_1^O \cdot \hat{\boldsymbol{n}} = 0$$

at $r_y = 1$. To derive a consistency condition, we integrate the composite solution equation over C_0^c (the area of which equals $\pi \times 1^2 = \pi$), use the divergence theorem, and get:

$$\pi\{\frac{\partial u_{0,0}}{\partial t} - \frac{\partial^2 u_{0,0}}{\partial x_3^2}\} = \int\limits_{C_0^c} \nabla_y^2 v_1^O dS = \int\limits_{\partial C_0^c} \nabla_y v_1^O \cdot \hat{\boldsymbol{n}} dl = \int\limits_0^{2\pi} 0 d\varphi = 0.$$

This implies:

$$\frac{\partial u_{0,0}}{\partial t} = \frac{\partial^2 u_{0,0}}{\partial x_3^2},$$

which agrees with our result (200).

At the following order, the boundary layer gives a continuity equation:

$$\nabla_z^2 v_2^B = 0$$

and a hair surface boundary condition:

$$\frac{\partial v_2^B}{\partial r_z} = C u_{0,0}.$$

This gives $v_2^B(t, r_z, \varphi, \boldsymbol{x}) = Cu_{0,0}(t, \boldsymbol{x}) \ln r_z + F_0^B(t, \boldsymbol{x})$. Writing this in r_y leads to a delta function term in a composite equation:

$$\nabla_y^2 v_2^C = \frac{\partial u_{0,1}}{\partial t} - \frac{\partial^2 u_{0,1}}{\partial x_3^2} + 2\pi C u_{0,0} \delta_{(0,0)}, \tag{217}$$

which is equipped with a boundary condition:

$$\nabla_y v_2^C \cdot \hat{\boldsymbol{n}} = 0 \tag{218}$$

applied at $r_y = 1$. Integrating the continuity equation over C_0^c, and following steps similar to the previous order, we get:

$$\pi \frac{\partial u_{0,1}}{\partial t} = \pi \frac{\partial^2 u_{0,1}}{\partial x_3^2} - \pi 2 C u_{0,0},$$

and dividing by π yields:

$$\frac{\partial u_{0,1}}{\partial t} = \frac{\partial^2 u_{0,1}}{\partial x_3^2} - 2 C u_{0,0}.$$

This solvability condition is the same as the one from Equation (202), and it is similar to the periodic boundary condition case (216). The sink term from the fully-circular case (202) is not multiplied by π (whereas it is multiplied by π in the unit square case (216)), because the area of a circle with a radius of 1 is $\pi 1^2 = \pi$ (in contrast with the area of a square with a unit side - $1^2 = 1$). Therefore, the π factors in the fully-circular case cancel out as we have seen. Moreover, as already mentioned in the fully-circular analysis section, we lose the $\frac{\partial^2 u_{0,1}}{\partial x_1^2}$ and the $\frac{\partial^2 u_{0,1}}{\partial x_2^2}$ terms in the diffusion tensor.

We now substitute the consistency equation at this order into Equation (217), and get:

$$\nabla_y^2 v_2^C = 2(\pi \delta_{(0,0)} - 1) C u_{0,0} \tag{219}$$

equipped with the boundary condition (218) applied at $r_y = 1$. It is easy to see that a solution to such problem is $Cu_{0,0}\{\ln r_y - \frac{r_y^2}{2}\} + g(t, \boldsymbol{x})$. Comparing with Equation (204) we see that the new matching method gives microscopic behaviour consistent with the standard matching rule. Having done this check, we trust the new matching method also for the case of the square unit cell, for which it is much more difficult to obtain analytical results.

4.5.2 *Checking numerics for Dirac delta function*

Later on in this chapter, we will derive a distinguished limit, and compare it with the effective equation (211) including higher order approximations (see Section 4.8.1). To make this comparison, we need to solve Poisson's equation with a Dirac sink term, similar to the one from Equation (219). For the periodic boundary conditions, obtaining analytical results is nontrivial, and thus we will need to solve the equation numerically. Therefore, we check if the analytical result (which is easily obtained for the fully-circular domain C_0^c) agrees well with the numerical result (obtained using FEniCS).

For simplicity's sake, assume we want to find a function $\psi(r_y, \varphi)$, defined on C_0^c, satisfying:

$$\nabla_y^2 \psi = 2(\pi \delta_{(0,0)} - 1)$$

in C_0^c, and a zero-flux boundary condition:

$$\frac{\partial \psi}{\partial r_y} = 0$$

at $r_y = 1$. We now check that:

$$\psi = \ln r_y - \frac{r_y^2}{2} + C_\psi \tag{220}$$

is the analytic solution of this problem (for yet undetermined constant C_ψ). For any $r_y > 0$, differentiation with respect to r_y and multiplication by r_y gives $r_y \frac{d\psi}{r_y} = 1 - r_y^2$. By evaluating at $r_y = 1$, we confirm that $\frac{\partial \psi}{\partial r_y} = 0$ at the outer boundary. The subsequent differentiation and division by r_y yields $\nabla_y^2 \psi = \frac{1}{r_y} \frac{d}{dr_y} \left(r_y \frac{d\psi}{dr_y} \right) = -2$, and the $2\pi\delta_{(0,0)}$ term causes the logarithmic behaviour ($\ln r_y$).

Due to circular symmetry of this problem and freedom in choosing the constant C_ψ, we can replace the zero-flux boundary condition with a Dirichlet boundary condition $\psi = 0$ at $r_y = 1$. Solving this problem numerically in FEniCS yields a solution shown in Figure 4.3. To check the consistency with the numerical solution, we must choose $C_\psi = \frac{1}{2}$ for the analytic solution (220). We now check whether the FEniCS solution is a good approximation for the analytic result. Because of the circular symmetry and the resulting fact that the solution is independent of φ, we only plot the solutions (at selected points) along

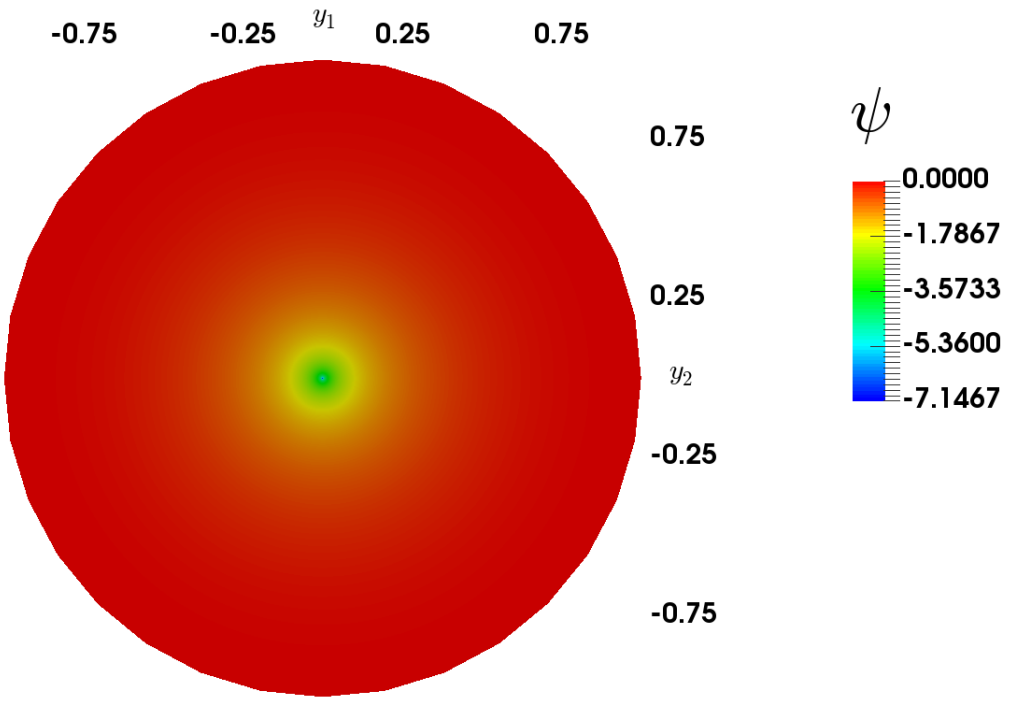


Figure 4.3.: Numerical solution for ψ (FEniCS).

the line segment starting at a point $(0.0, 0.0)$ and ending at a point $(1.0, 0.0)$. In general, the agreement is satisfactory. However, we observe errors towards $r_y = 0$. This is expected because $\lim_{r_y \to 0} \psi(r_y) = -\infty$, and numerically, we always deal with a finite mesh size, which cannot fully capture the point sink effect. Figure 4.5 shows a situation zoomed-in close to $r_y = 0$ (we also selected more points at which the solution is plotted in order to capture these deviations more clearly). In Section 4.8.1, we will need to know the solution behaviour close to $r_y = a$ in particular. From the analysis so far, we see that as long as we remain in the parameter regime where $a \geq 0.001$, we can (despite the small errors) be fairly confident about our numerics. If one wishes to study $a < 0.001$, the numerics needs to be made more precise by making the mesh size much smaller close to the origin (i.e. where Dirac delta function is operating).

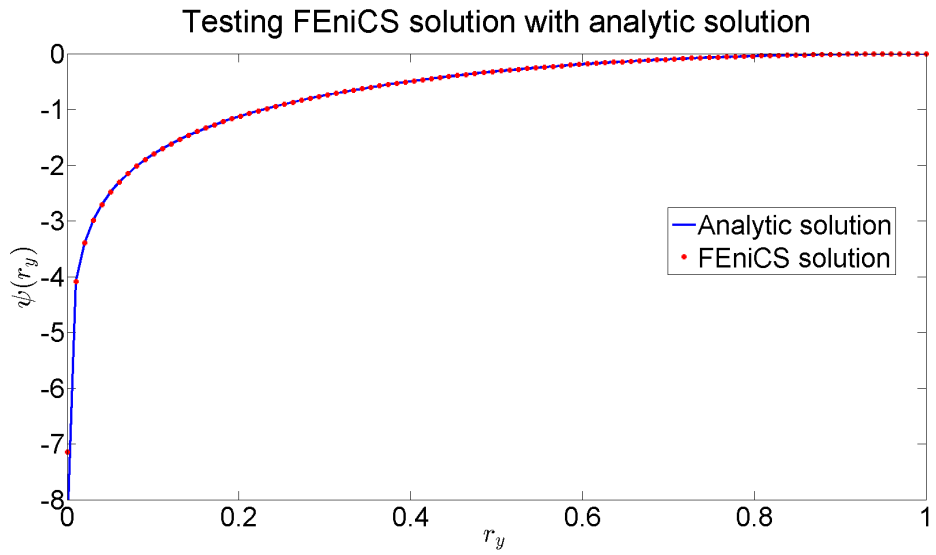


Figure 4.4.: Comparison between the FEniCS solution and the analytic solution for ψ.

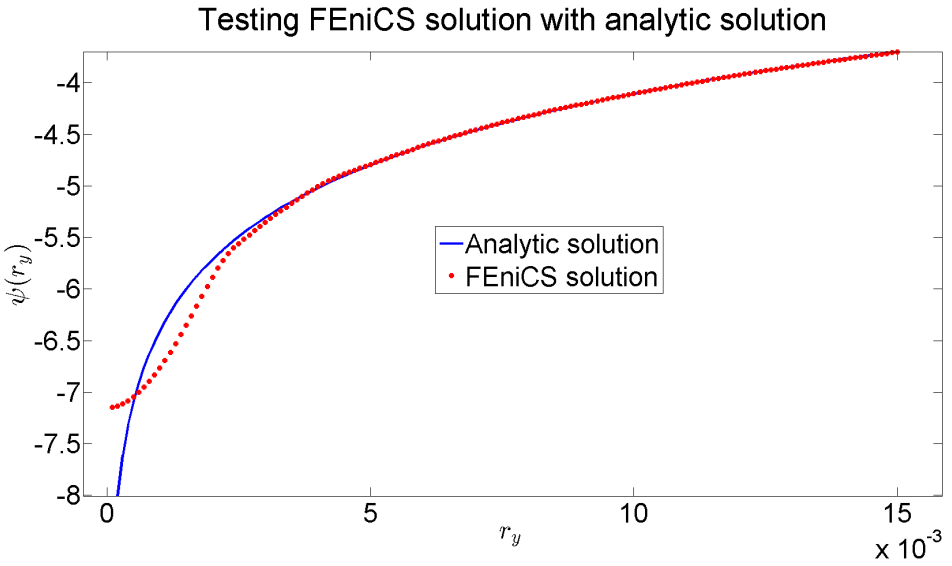


Figure 4.5.: Comparison between the FEniCS solution and the analytic solution for ψ (zoom).

4.6 FIRST NONUNIFORMITY: $\epsilon = \frac{\lambda}{\ln \frac{1}{a}}$

As mentioned in Section 4.4.3, our asymptotic expansion loses validity, if we have:

$$\epsilon = \frac{\lambda}{\ln \frac{1}{a}} \tag{221}$$

as $a \ll 1$ for $\lambda = O(1)$. This is equivalent to $a = e^{-\frac{\lambda}{\epsilon}}$ as $\epsilon \ll 1$. In this setting, a and ϵ are no longer independent small parameters but approach zero with a prescribed behaviour. Thus, we need to do the whole analysis once again. We start with Equation (129), and (assuming $K(a) = \frac{C}{a}$) the root surface boundary condition becomes:

$$\nabla_y u \cdot \hat{\boldsymbol{n}} = -\frac{C}{a}\epsilon^2 u = -Ce^{\frac{\lambda}{\epsilon}}\epsilon^2 u$$

applied at $r_y = a = e^{-\frac{\lambda}{\epsilon}}$. Introducing a two-scale ansatz:

$$u(t, \boldsymbol{x}, \epsilon) = u_0(t, \frac{x_1}{\epsilon}, \frac{x_2}{\epsilon}, \boldsymbol{x}) + \epsilon u_1(t, \frac{x_1}{\epsilon}, \frac{x_2}{\epsilon}, \boldsymbol{x}) + \epsilon^2 u_2(t, \frac{x_1}{\epsilon}, \frac{x_2}{\epsilon}, \boldsymbol{x}) + \epsilon^3 u_3(t, \frac{x_1}{\epsilon}, \frac{x_2}{\epsilon}, \boldsymbol{x}) + o(\epsilon^3), \tag{222}$$

where u_0, u_1, u_2 and u_3 satisfy the periodicity conditions in y_1 and y_2, this changes to a continuity equation:

$$\epsilon^2\{\frac{\partial u_0}{\partial t} + \epsilon\frac{\partial u_1}{\partial t} + o(\epsilon)\} =$$

$$\{\nabla_y^2 + 2\epsilon\nabla_y \cdot \nabla_x + \epsilon^2\nabla_x^2\}\{u_0 + \epsilon u_1 + \epsilon^2 u_2 + \epsilon^3 u_3 + o(\epsilon^3)\}$$

and a hair surface boundary condition:

$$\{\nabla_y + \epsilon\nabla_x\}\{u_0 + \epsilon u_1 + \epsilon^2 u_2 + \epsilon^3 u_3 + o(\epsilon^3)\} \cdot \hat{\boldsymbol{n}} = -Ce^{\frac{\lambda}{\epsilon}}\epsilon^2\{u_0 + \epsilon u_1 + o(\epsilon)\}.$$

Studying the boundary layer (i.e. using $r_z = \frac{r_y}{a} = r_y e^{\frac{\lambda}{\epsilon}}$), we get:

$$\epsilon^2\{\frac{\partial u_0^B}{\partial t} + \epsilon\frac{\partial u_1^B}{\partial t} + o(\epsilon)\} =$$

$$\{e^{\frac{2\lambda}{\epsilon}}\nabla_z^2 + 2\epsilon e^{\frac{\lambda}{\epsilon}}\nabla_z \cdot \nabla_x + \epsilon^2\nabla_x^2\}\{u_0^B + \epsilon u_1^B + \epsilon^2 u_2^B + \epsilon^3 u_3^B + o(\epsilon^3)\}$$

and a hair surface boundary condition:

$$\{e^{\frac{\lambda}{\epsilon}}\nabla_z + \epsilon\nabla_x\}\{u_0^B + \epsilon u_1^B + \epsilon^2 u_2^B + \epsilon^3 u_3^B + o(\epsilon^3)\} \cdot \hat{\boldsymbol{n}} =$$

$$-C\epsilon^2 e^{\frac{\lambda}{\epsilon}} \{u_0^B + \epsilon u_1^B + o(\epsilon)\}$$

applied at $r_z = 1$. All this leads to boundary layer equations:

$$\nabla_z^2 u_0^B = \nabla_z^2 u_1^B = \nabla_z^2 u_2^B = \nabla_z^2 u_3^B = 0,$$

and to hair surface boundary conditions:

$$\nabla_z u_0^B \cdot \hat{\boldsymbol{n}} = \nabla_z u_1^B \cdot \hat{\boldsymbol{n}} = 0 \quad \nabla_z u_2^B \cdot \hat{\boldsymbol{n}} = -C u_0^B \quad \nabla_z u_3^B \cdot \hat{\boldsymbol{n}} = -C u_1^B.$$

This means that $u_0^B = u_0^B(t, \boldsymbol{x})$, $u_1^B = u_1^B(t, \boldsymbol{x})$, $u_2^B = C u_0^B \ln r_z + D_2^B$, and $u_3^B = C u_1^B \ln r_z + D_3^B$.

For the outer layer approximation, we always impose the periodic boundary conditions at $y_1, y_2 = \pm\frac{1}{2}$, and at the leading order, we get a continuity equation:

$$\nabla_y^2 u_0^O = 0,$$

which yields $u_0^O = u_0^O(t, \boldsymbol{x})$. Using this information, the continuity equation at the next order reads:

$$\nabla_y^2 u_1^O = 0,$$

which means $u_1^O = u_1^O(t, \boldsymbol{x})$. Using information from previous orders, we get at the next order:

$$\nabla_y^2 u_2^O = \frac{\partial u_0^O}{\partial t} - \nabla_x^2 u_0^O. \tag{223}$$

Finally, proceeding to the following order, we get:

$$\nabla_y^2 u_3^O + 2\nabla_y \cdot \nabla_x u_2^O = \frac{\partial u_1^O}{\partial t} - \nabla_x^2 u_1^O. \tag{224}$$

To match terms at $O(\epsilon^2)$, we write the boundary layer solution at this order in the outer variable:

$$u_2^B = C u_0^B \ln r_z + D_2^B = C u_0^B \ln r_y + C u_0^B \frac{\lambda}{\epsilon} + D_2^B.$$

This suggests that the $C u_0^B \lambda$ term will be promoted to $O(\epsilon)$. Moreover, in order to account for the contribution of $C u_0^B \ln r_y$ as $r_y \to 0$ in the composite solution, we need to correct Equation (223) in the following way:

$$\nabla_y^2 u_2^C = \frac{\partial u_0^O}{\partial t} - \nabla_x^2 u_0^O + 2\pi C u_0^B \delta_{(0,0)}, \tag{225}$$

where the Dirac term ensures the required logarithmic behaviour. A solvability condition for Equation (225) reads:

$$\frac{\partial u_0^O}{\partial t} = \nabla_x^2 u_0^O - 2\pi C u_0^B, \tag{226}$$

and substituting this result back into Equation (225) gives:

$$\nabla_y^2 u_2^C = 2\pi C u_0^B \Big(\delta_{(0,0)} - 1\Big). \tag{227}$$

The solution of Equation (227) can be written as:

$$u_2^O = D_2^O(t, \boldsymbol{x}) + 2\pi C u_0^B(t, \boldsymbol{x})\psi(\boldsymbol{y}), \tag{228}$$

where $\psi(\boldsymbol{y})$ satisfies:

$$\nabla_y^2 \psi = \delta_{(0,0)} - 1. \tag{229}$$

Substituting information from previous orders into Equation (224) yields:

$$\nabla_y^2 u_3^O + 4\pi C \nabla_y \psi \cdot \nabla_x u_0^B = \frac{\partial u_1^O}{\partial t} - \nabla_x^2 u_1^O. \tag{230}$$

Thus, we have derived an outer layer approximation:

$$u_0^O(t, \boldsymbol{x}) + \epsilon u_1^O(t, \boldsymbol{x}) + \epsilon^2 \Big(D_2^O(t, \boldsymbol{x}) + 2\pi C u_0^B(t, \boldsymbol{x})\psi(\boldsymbol{y})\Big) + \epsilon^3 u_3^O(t, \boldsymbol{x}, \boldsymbol{y}) + \cdots, \tag{231}$$

where $\psi(\boldsymbol{y})$ satisfies Equation (229), and a boundary layer approximation:

$$\begin{aligned} u_0^B(t, \boldsymbol{x}) + \epsilon u_1^B(t, \boldsymbol{x}) + \epsilon^2 D_2^B(t, \boldsymbol{x}) + \epsilon^2 C u_0^B(t, \boldsymbol{x}) \ln r_z + \\ \epsilon^3 D_3^B(t, \boldsymbol{x}) + \epsilon^3 C u_1^B(t, \boldsymbol{x}) \ln r_z + \cdots \end{aligned} \tag{232}$$

Writing the boundary layer approximation in the outer variable gives:

$$\begin{aligned} &u_0^B(t, \boldsymbol{x}) + \epsilon u_1^B(t, \boldsymbol{x}) + \epsilon^2 D_2^B(t, \boldsymbol{x}) + \epsilon^2 C u_0^B(t, \boldsymbol{x}) \ln r_y + \epsilon^2 C u_0^B(t, \boldsymbol{x}) \frac{\lambda}{\epsilon} + \\ &\epsilon^3 D_3^B(t, \boldsymbol{x}) + \epsilon^3 C u_1^B(t, \boldsymbol{x}) \ln r_y + \epsilon^3 C u_1^B(t, \boldsymbol{x}) \frac{\lambda}{\epsilon} + \cdots = \\ &u_0^B(t, \boldsymbol{x}) + \epsilon \Big(u_1^B(t, \boldsymbol{x}) + \lambda C u_0^B(t, \boldsymbol{x})\Big) + \\ &\epsilon^2 \Big(D_2^B(t, \boldsymbol{x}) + \lambda C u_1^B(t, \boldsymbol{x}) + C u_0^B(t, \boldsymbol{x}) \ln r_y\Big) + \cdots \end{aligned} \tag{233}$$

Comparing the outer expansion (231) with Expansion (233) at the leading order gives a matching condition $u_0^O(t, \boldsymbol{x}) = u_0^B(t, \boldsymbol{x}) = u_0^C(t, \boldsymbol{x})$, and substituting this result into Equation (226) gives:

$$\frac{\partial u_0^C}{\partial t} = \nabla_x^2 u_0^C - 2\pi C u_0^C. \tag{234}$$

Notice that we obtained the same macroscopic equation as we did for $u_{0,0}$ in Section 4.4.3 (see Equation (211)). Substituting this result back to Equation (225), we get:

$$\nabla_y^2 u_2^C = 2\pi C u_0^C \{\delta_{(0,0)} - 1\}. \tag{235}$$

Comparing the outer expansion (231) with Expansion (233) at the next order yields:

$$u_1^C = u_1^O = u_1^B + C\lambda u_0^B = u_1^B + C\lambda u_0^C.$$

Following a similar procedure as before, we get from Equation (230):

$$\nabla_y^2 u_3^C = \frac{\partial u_1^O}{\partial t} - \nabla_x^2 u_1^O - 4\pi C \nabla_y \psi \cdot \nabla_x u_0^B + 2\pi C u_1^B \delta_{(0,0)} =$$

$$\frac{\partial u_1^C}{\partial t} - \nabla_x^2 u_1^C - 4\pi C \nabla_y \psi \cdot \nabla_x u_0^C + 2\pi C \left(u_1^C - C\lambda u_0^C \right) \delta_{(0,0)},$$

and integration gives an equation different from the previously obtained equation for $u_{0,1}$ (214); we observe additional contributions coming from the u_2^O term and the fact that $u_1^B \neq u_1^C$. This fictitious discrepancy can be easily explained. This time, ϵ and $\frac{1}{\ln \frac{1}{a}}$ are of the same order. Thus, recalling our expansion:

$$u \sim \left\{ u_{0,0} + \frac{1}{\ln \frac{1}{a}} u_{0,1} + ... \right\} + \epsilon \left\{ u_{1,0} + ... \right\} + \epsilon^2 \left\{ \ln \frac{1}{a} u_{2,0} + ... \right\}$$

we see that the equation for what is now u_1^O will contain contributions from what used to be $u_{0,1}$, $u_{1,0}$ and $u_{2,0}$. Thus, the new term $-4\pi C \nabla_y \psi \cdot \nabla_x u_0^C$ comes from the fact that ϵ and $\frac{1}{\ln \frac{1}{a}}$ are now of the same order. The $-C\lambda u_0^C$ term emerges, because the $\epsilon^2 \ln \frac{1}{a} u_{2,0}$ term is promoted to $O(\epsilon)$. Thus, if we want to know the macroscale behaviour of u_1^C, we need to know the microscale behaviour of u_2^C, i.e. we need to solve Equation (235). It is possible to do this (e.g. numerically), but we will not attempt it here.

4.7 NEXT NONUNIFORMITY: $\epsilon^2 = \frac{\lambda}{\ln \frac{1}{a}}$

We now study the next nonuniformity; we assume:

$$\epsilon^2 = \frac{\lambda}{\ln \frac{1}{a}} \tag{236}$$

as $a \ll 1$ for $\lambda = O(1)$. This is equivalent to $a = e^{-\frac{\lambda}{\epsilon^2}}$ as $\epsilon \ll 1$. We start with Equation (129), and assuming $K(a) = \frac{C}{a}$, the root surface boundary condition becomes:

$$\nabla_y u \cdot \hat{\boldsymbol{n}} = -\frac{C}{a}\epsilon^2 u = -Ce^{\frac{\lambda}{\epsilon^2}}\epsilon^2 u$$

applied at $r_y = a = e^{-\frac{\lambda}{\epsilon^2}}$. Using Ansatz (222), we get a boundary layer ($r_z = \frac{r_y}{a} = r_y e^{\frac{\lambda}{\epsilon^2}}$) continuity equation:

$$\epsilon^2\{\frac{\partial u_0^B}{\partial t} + \epsilon\frac{\partial u_1^B}{\partial t} + o(\epsilon)\} =$$

$$\{e^{\frac{2\lambda}{\epsilon^2}}\nabla_z^2 + 2\epsilon e^{\frac{\lambda}{\epsilon^2}}\nabla_z \cdot \nabla_x + \epsilon^2\nabla_x^2\}\{u_0^B + \epsilon u_1^B + \epsilon^2 u_2^B + \epsilon^3 u_3^B + o(\epsilon^3)\},$$

and a hair surface boundary condition:

$$\{e^{\frac{\lambda}{\epsilon^2}}\nabla_z + \epsilon\nabla_x\}\{u_0^B + \epsilon u_1^B + \epsilon^2 u_2^B + \epsilon^3 u_3^B + o(\epsilon^3)\} \cdot \hat{\boldsymbol{n}} =$$

$$-C\epsilon^2 e^{\frac{\lambda}{\epsilon^2}}\{u_0^B + \epsilon u_1^B + o(\epsilon)\}$$

is applied at $r_z = 1$. Notice, that at the first four orders, we obtain the same continuity equations and the same hair surface boundary conditions as in the previous section, and thus we conclude the same boundary layer approximation (232). As nothing changes in the outer layer continuity equation compared to the previous section (and the periodic boundary conditions remain the same too), following the same steps we arrive at the same outer layer approximation (231). However, writing the boundary layer approximation (232) in the outer variable yields:

$$\begin{aligned} &u_0^B(t,\boldsymbol{x}) + \epsilon u_1^B(t,\boldsymbol{x}) + \epsilon^2 D_2^B(t,\boldsymbol{x}) + \epsilon^2 C u_0^B(t,\boldsymbol{x})\ln r_y + \epsilon^2 C u_0^B(t,\boldsymbol{x})\frac{\lambda}{\epsilon^2} + \\ &+ \epsilon^3 D_3^B(t,\boldsymbol{x}) + \epsilon^3 C u_1^B(t,\boldsymbol{x})\ln r_y + \epsilon^3 C u_1^B(t,\boldsymbol{x})\frac{\lambda}{\epsilon^2} + \cdots = \\ &= \Big(u_0^B(t,\boldsymbol{x}) + \lambda C u_0^B(t,\boldsymbol{x})\Big) + \epsilon\Big(u_1^B(t,\boldsymbol{x}) + \lambda C u_1^B(t,\boldsymbol{x})\Big) + \cdots \end{aligned} \tag{237}$$

Comparing (231) with (237) at the leading order gives:

$$u_0^C(t,\boldsymbol{x}) = u_0^O(t,\boldsymbol{x}) = u_0^B(t,\boldsymbol{x}) + \lambda C u_0^B(t,\boldsymbol{x}),$$

and substituting this result into Equation (225) (which remains unchanged compared to the previous section) gives:

$$\nabla_y^2 u_2^C = \frac{\partial u_0^C}{\partial t} - \nabla_x^2 u_0^C + \frac{2\pi C}{1 + C\lambda}u_0^C\delta_{(0,0)}. \tag{238}$$

Integrating over the unit cell gives:

$$\frac{\partial u_0^C}{\partial t} = \nabla_x^2 u_0^C - \frac{2\pi C}{1 + C\lambda} u_0^C, \tag{239}$$

which is distinct from the homogenised equation we derived previously (see Equation (211)) - the sink term is divided by $1 + C\lambda$. Substituting this result back to Equation (238), we get:

$$\nabla_y^2 u_2^C = \frac{2\pi C}{1 + C\lambda} u_0^C (\delta_{(0,0)} - 1). \tag{240}$$

Notice as a check, that sending λ to 0 in Equation (239), we recover the homogenised equation from the previous section as expected (because this should be equivalent to the $\epsilon = \frac{O(1)}{\ln \frac{1}{a}}$ case; if $\epsilon \ln \frac{1}{a} = O(1)$, then $\lambda = \epsilon^2 \ln \frac{1}{a} \ll 1$).

4.8 TESTING THE NEW LIMIT

We now test whether the new limit (239) approximates the full-geometry simulations better than the previously found effective equation (211) in the parameter regimes identified by our asymptotic analysis. As the $\epsilon^2 \ln \frac{1}{a} = O(1)$ scaling predicts very small values of a, which cause the problem to be numerically challenging, we choose $\epsilon = 0.5$ so that $a = 0.01$ gives $\lambda = \epsilon^2 \ln \frac{1}{a} = 0.25 * \ln 100 \approx 1.15$, and this can be considered of order 1. The domain geometry for $a = 0.01$ is shown in Figure 4.6. We further assume $K(a) = \frac{C}{a}$ with $C = 1.0$, a dimensionless root hair length $h = 0.5$, and a dimensionless far-field distance $d = 1.0$. As for the macroscopic boundary conditions, we impose a constant nutrient supply at a fixed distance from the root surface ($u(x_3 = d) = 1.0$) and zero-flux boundary conditions at all the remaining macroscopic boundary parts. Using these boundary conditions, we get the same solution behaviour in each unit cell (as introduced in Figure 3.4). Therefore, from now onwards, we only simulate and show solution behaviour within a single cell.

Guided by our analysis, we fix $\epsilon = 0.5$ and make a smaller, until the full-geometry solution starts to deviate from the homogenised solution given by Equation (211). We then show the solutions in the clipped domain (as introduced in Figure 3.4).

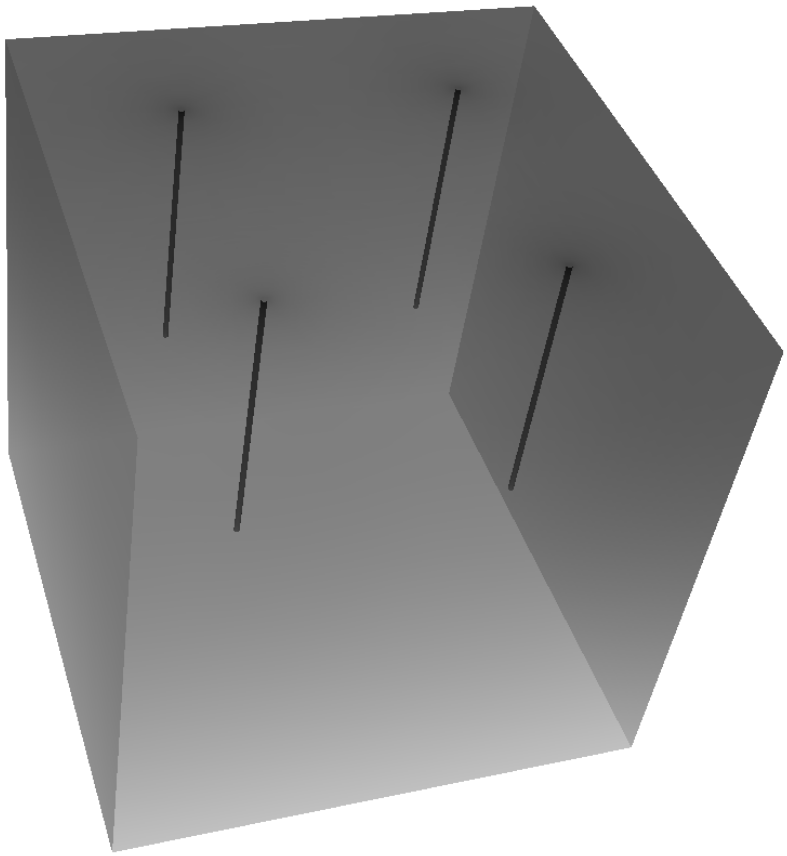
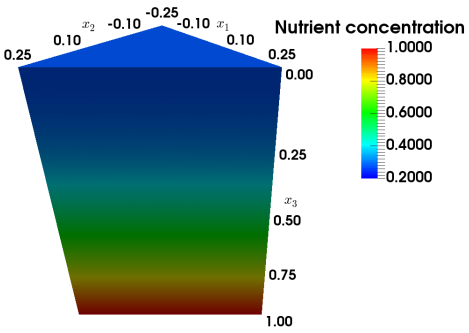
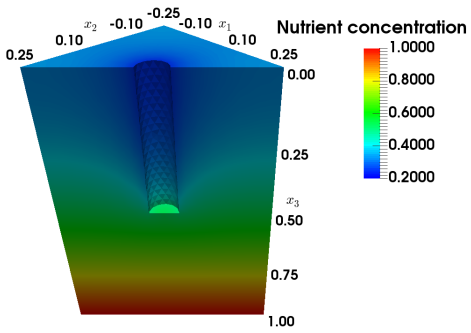


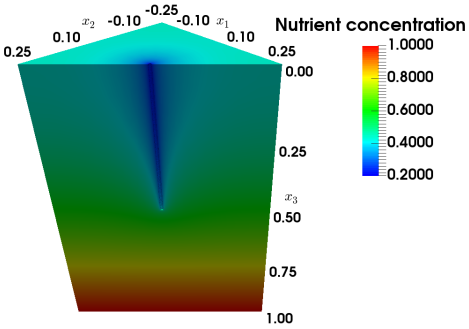
Figure 4.6.: The domain geometry for $a = 0.01$ and $\epsilon = 0.5$.



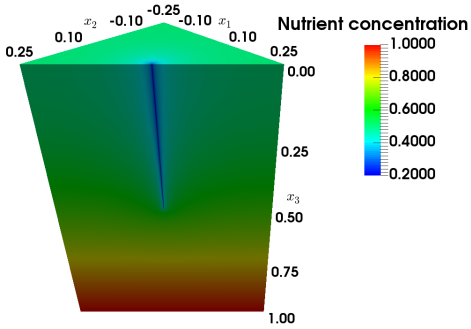
(a) Homogenisation: $a \gg e^{-\frac{1}{\epsilon^2}}$



(b) Full-geometry: $a = 0.1$, $\epsilon^2 \ln \frac{1}{a} \approx 0.58$



(c) Full-geometry: $a = 0.01$, $\epsilon^2 \ln \frac{1}{a} \approx 1.15$



(d) Full-geometry: $a = 0.001$, $\epsilon^2 \ln \frac{1}{a} \approx 1.73$

Figure 4.7.: The steady-state solutions of the full-geometry model for decreasing a deviate from the solution of Equation (211) (clipped domain).

While for $a = 0.1$, Equation (211) still gives a reasonably good average of the full-geometry numerics, for $a = 0.01$ we clearly observe deviations, and these deviations are even more significant for $a = 0.001$. The change thus truly seems to occur close to $\epsilon^2 \ln \frac{1}{a} = 1$.

The analysis from this chapter implies, that for any scaling satisfying $a \gg e^{-\frac{1}{\epsilon^2}}$ as $\epsilon \to 0$, the homogenised equation is the same as found in Section 4.6 (which is the same as Equation (211)).

We now compare these solutions at a fixed distance from the root surface. First, we fix $x_3 = 0.0$ and plot the solutions along a diagonal in this plane (similar to what we did in Figure 3.21 but this time only within a single cell). This way, we study behaviour at the root surface, and the results for decreasing a are shown in Figure 4.8. Recall that homogenisation should yield a solution where any microscopic variations are averaged out. Keeping this in mind, it seems that the behaviour for $a = 0.1$ is best described by Equation (211). For $a = 0.01$ and $a = 0.001$, the newly obtained limit might be giving us a better approximation of the averaged full-geometry solution. However, this is not clear from Figure 4.8, because a root-hair-zone behaviour is presented here, and the hair surfaces gradient is too large (especially for $a \ll 1$) for us to assess the validity of the two homogenisation limits. Therefore, we also study the situation outside of the root hair zone (at $x_3 = 0.75$). From the results shown in Figure 4.9 it seems that the new limit performs slightly better for $a = 0.01$. For $a = 0.001$, the superiority of the new model can be stated with confidence.

4.8.1 *Approximation using higher orders*

We have shown how one can use the two-scale asymptotic expansions to obtain homogenised equations, which give a behaviour averaged over the microscale. However, one can also use the formal asymptotic analysis to uncover microscopic variations, which tell us more about nutrient depletion close to the hair surface, as can be seen in Figure 4.8. We now study the microscopic behaviour of the two distinct $a \to 0$ limits obtained in Sections 4.6 and 4.7.

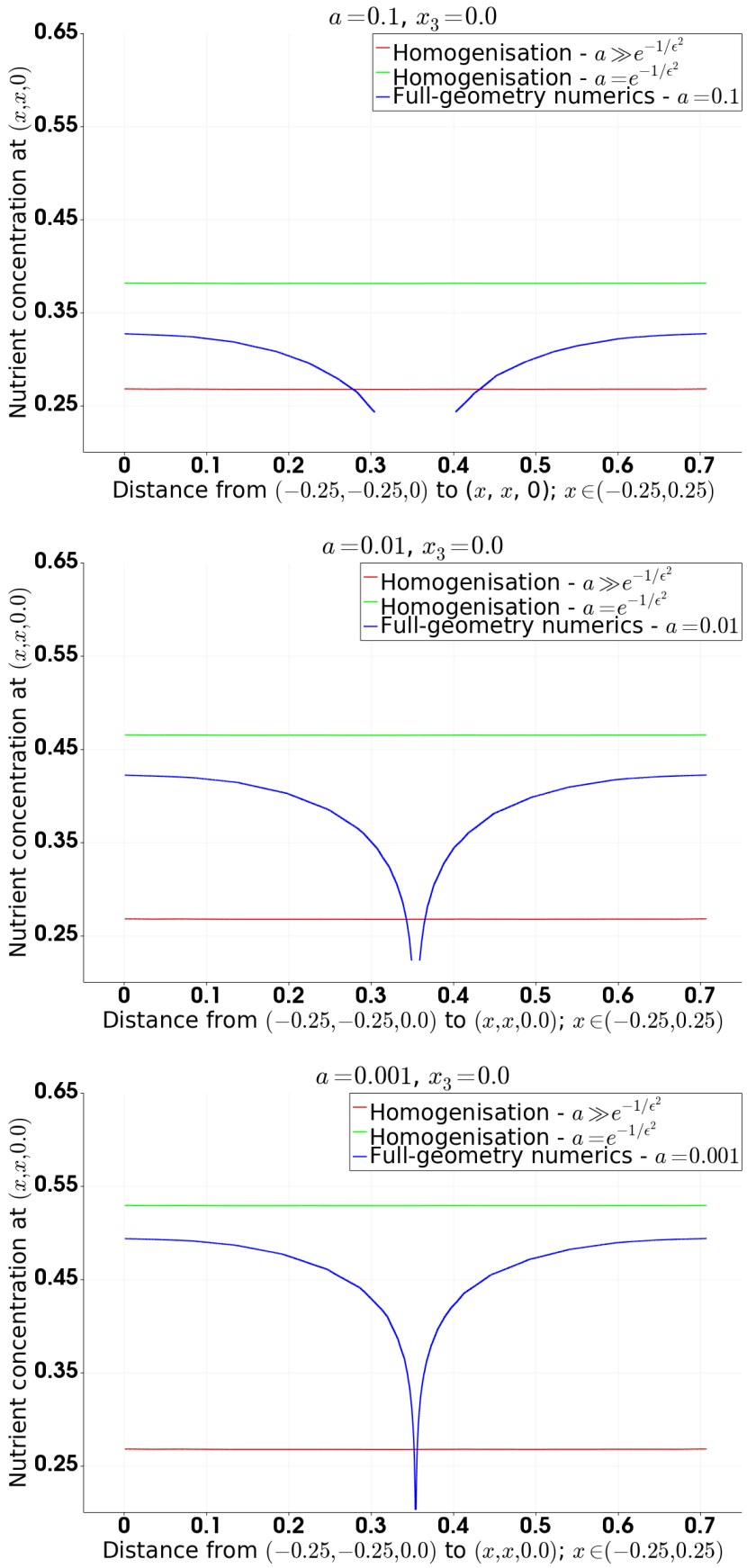


Figure 4.8.: Comparison of the steady-state solutions at the root surface.

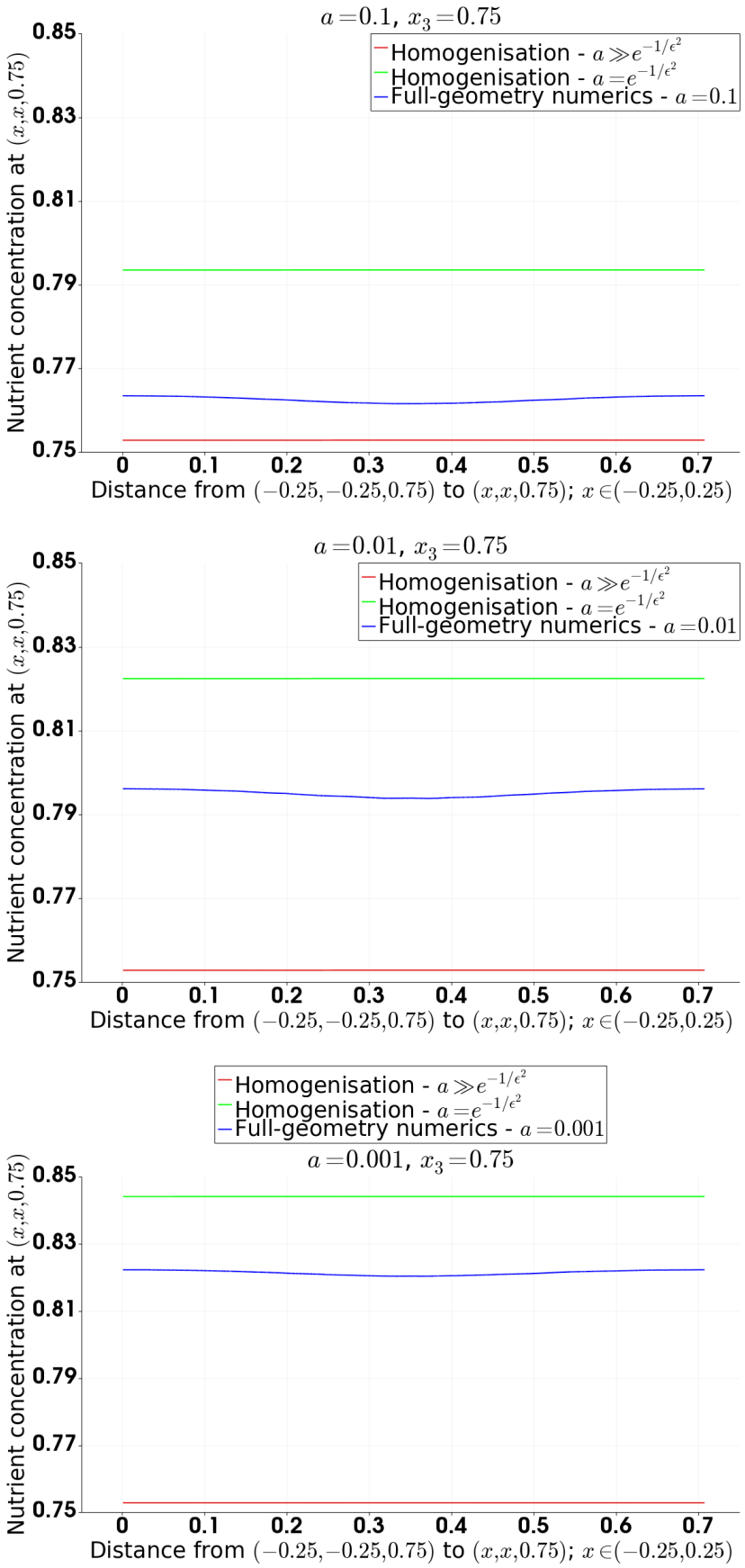


Figure 4.9.: Comparison of the steady-state solutions out of the hair zone.

From the analysis in these sections, we know that assuming no x_1 or x_2 variation is introduced via initial or macroscopic boundary conditions, we get an approximation:

$$u(t, x_1, x_2, x_3; \epsilon) \sim u_0(t, x_3) + \epsilon f_1(t, x_3) + \epsilon^2 u_2(t, \frac{x_1}{\epsilon}, \frac{x_2}{\epsilon}, x_3),$$

i.e. the first microscopically-nontrivial contribution comes at $O(\epsilon^2)$ (for both $a = e^{-\frac{1}{\epsilon}}$ and $a = e^{-\frac{1}{\epsilon^2}}$). For the $a = e^{-\frac{1}{\epsilon}}$ case (which we from now on denote by a superscript ^{A}), u_2^A must satisfy:

$$\nabla_y^2 u_2^A = 2\pi C u_0^A (\delta_{(0,0)} - 1),$$

whereas for $a = e^{-\frac{\lambda}{\epsilon^2}}$ (which we denote by a superscript ^{B}), we have:

$$\nabla_y^2 u_2^B = \frac{2\pi C}{1 + C\lambda} u_0^B (\delta_{(0,0)} - 1),$$

with $\lambda = \epsilon^2 \ln \frac{1}{a} = O(1)$ (see the equations (235) and (240)). Thus, in the former case, we can write:

$$u_2^A(t, y_1, y_2, x_3) = f_2^A(t, x_3) + 2\pi C u_0^A(t, x_3) \mu^A(y_1, y_2),$$

in the latter case, we can write:

$$u_2^B(t, y_1, y_2, x_3) = f_2^B(t, x_3) + \frac{2\pi C}{1 + C\lambda} u_0^B(t, x_3) \mu^B(y_1, y_2),$$

and we want μ^A and μ^B to satisfy:

$$\nabla_y^2 \mu^A = \delta_{(0,0)} - 1 = \nabla_y^2 \mu^B$$

in C_0, together with the periodicity conditions at $y_1, y_2 = \pm\frac{1}{2}$. Note that the equation and the boundary conditions for μ^A and μ^B are exactly the same, and the solution is unique up to a constant.

Thus, we obtain two three-term approximations:

$$\tilde{u}^A(t, x_1, x_2, x_3; \epsilon) = u_0^A(t, x_3) + \epsilon f_1^A(t, x_3) + \epsilon^2 \left(f_2^A(t, x_3) + 2\pi C u_0^A(t, x_3) \mu^A(\frac{x_1}{\epsilon}, \frac{x_2}{\epsilon}) \right) \quad (241)$$

and:

$$\tilde{u}^B(t, x_1, x_2, x_3; \epsilon) = u_0^B(t, x_3) + \epsilon f_1^B(t, x_3) + \epsilon^2 \left(f_2^B(t, x_3) + \frac{2\pi C}{1 + C\lambda} u_0^B(t, x_3) \mu^B(\frac{x_1}{\epsilon}, \frac{x_2}{\epsilon}) \right). \quad (242)$$

For a thorough comparison, we would need to know the macroscopic behaviour of the f_1 and f_2 terms, which is tedious to obtain. However, we are mostly interested in seeing how well the microscopic terms describe variations observed in the full-geometry numerics. Thus, denoting u_{full} to be the solution of the full-geometry problem, we make simplifying assumptions that for all t and x_3:

$$u_{full}(t, 0.5 \times \epsilon, 0.5 \times \epsilon, x_3) = u_0^A(t, x_3) + \epsilon f_1^A(t, x_3) + \epsilon^2 f_2^A(t, x_3) =$$

$$u_0^B(t, x_3) + \epsilon f_1^B(t, x_3) + \epsilon^2 f_2^B(t, x_3)$$

(where $(x_1, x_2) = (0.5 \times \epsilon, 0.5 \times \epsilon)$ corresponds to a value in the corner of the unit cell domain), and we impose:

$$\mu^A(0.5, 0.5) = \mu^B(0.5, 0.5) = 0$$

(so that the full-geometry numerics value is equal to the values of both two-scale approximations at the corner of the domain). We now compare $\tilde{u}^A$ and $\tilde{u}^B$ with the full-geometry numerics u_{full}.

Assuming no dependence on the macroscopic x_1, x_2, the approximation (213) reveals that the leading order microscopic contribution comes at $O(\epsilon^2)$, and it obeys the cell equation (212) for any $a \gg e^{-\frac{1}{\epsilon^2}}$. Thus, our approximation (241) is equally valid for any $a \gg e^{-\frac{1}{\epsilon^2}}$.

Steady-state results at the root surface ($x_3 = 0$) for decreasing a are shown in Figure 4.10. We plot the solutions along a line segment starting at a point $(0.0, 0.0, 0.0)$ and ending at a point $(0.25, 0.25, 0.0)$. Even though the situation is a bit unclear for $a = 0.1$, we can easily see that the new model gives a better approximation for $a = 0.01$, and the difference between the approximations is even more magnified for $a = 0.001$.

Now we fix $a = 0.001$ (for which the new limit seems to perform well at the root surface) and study whether the new approximation is applicable for a non-zero distance from the root surface. Figure 4.11 shows the situation for two distinct distances from the root surface ($x_3 = 0.2, 0.4$ - the situation for $x_3 = 0.0$ can be seen in Figure 4.10). The new limit gives a better approximation again.

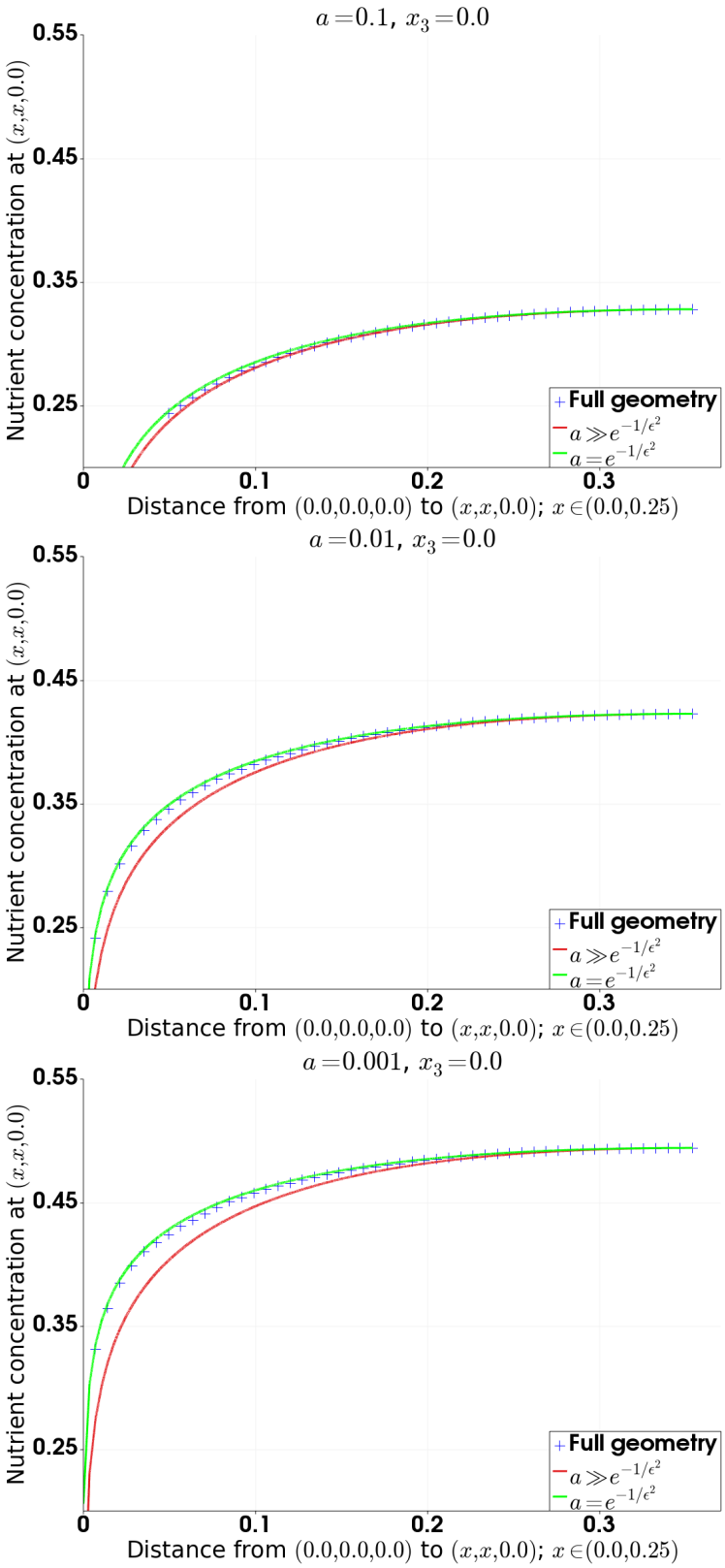


Figure 4.10.: Comparison of the steady-state solutions at the root surface using the higher-order microscopic behaviour (decreasing a).

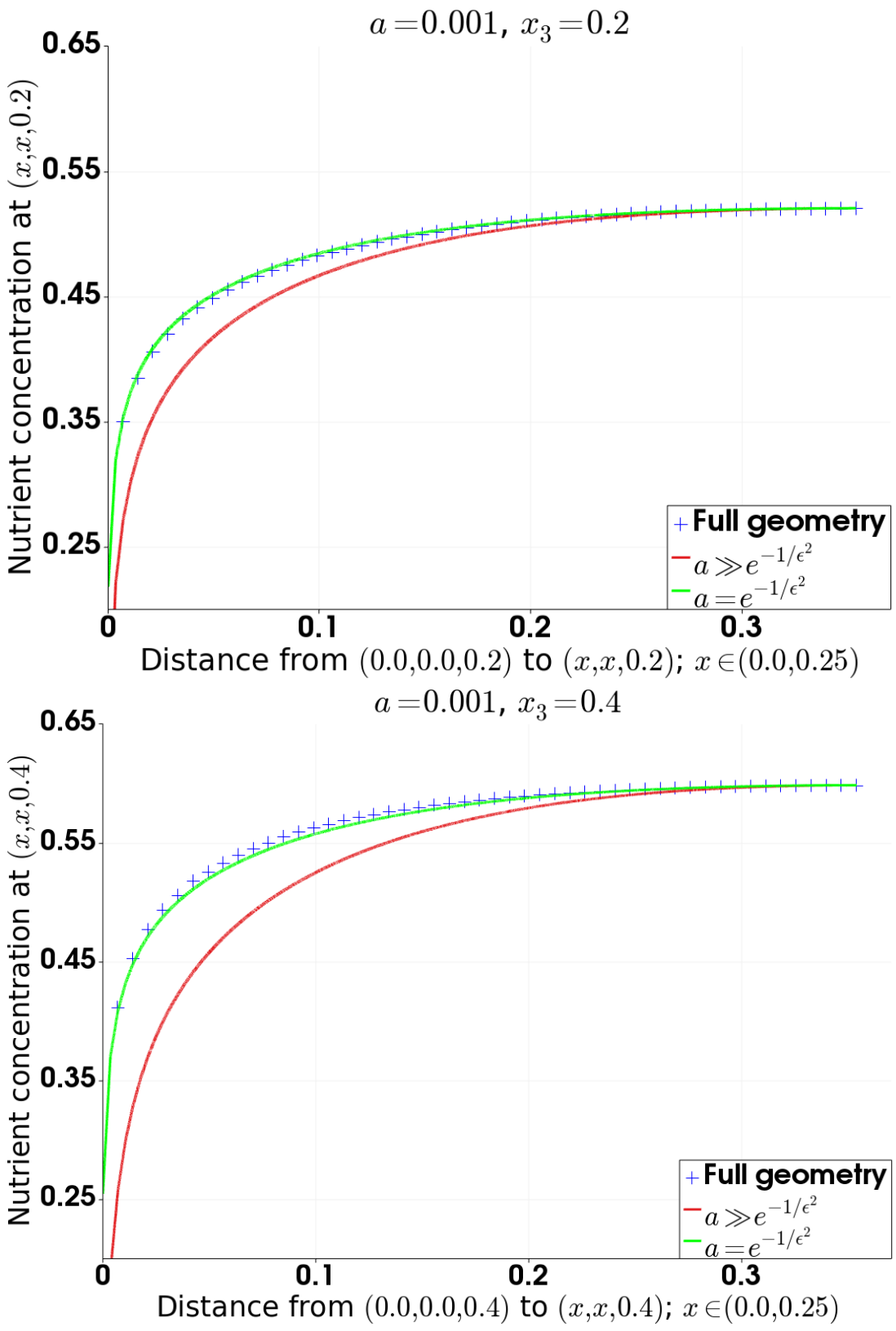


Figure 4.11.: Comparison of the steady-state solutions at varying distance from the root surface using the higher-order microscopic behaviour ($a = 0.001$).

4.8.2 *Time evolution*

So far, we have only compared the steady-state solutions. However, using the two-scale analysis, we can model time evolution to these steady states as well, and the results are shown in Figure 4.12. The new model performs better for all chosen times.

4.9 SUMMARY

To summarise this chapter, we have shown that the presence of another small parameter (a) may lead to erroneous results when solving models of nutrient uptake by root hairs using the method of homogenisation. We described how this new parameter influences behaviour at different orders of ϵ. Then, we found the new limit (239), which is achieved for $\lambda = \epsilon^2 \ln \frac{1}{a} = O(1)$. Subsequent comparisons between the full-geometry simulations and the numerical solutions to the homogenised equations confirmed the results obtained using formal asymptotics. However, for modelling real root hairs, taking ϵ as large as 0.1 (i.e. modelling a small piece of root with 10 root hairs only), this scaling leads to $a = e^{-\frac{\lambda}{\epsilon^2}} = e^{-100} \approx 3.72 \times 10^{-44}$ (using $\lambda = 1$). This value seems too small for any practical applications at the moment.

Let us note that after we had obtained most of our results from this chapter, we discovered that similar homogenisation limits were rigorously found in [56]. Here, the authors studied the Poisson equation in domains perforated by thin tubes (with a slightly more general cross-section geometry) equipped with a general nonlinear Robin-type boundary condition. However, we still consider our results from this chapter to be of importance. Firstly, we used the formal method of asymptotic expansions, which provides us with a desirable validation of the rigorous results from [56], sheds light on the orders at which different processes act, and makes the results available to broader audience. In addition, we considered a time-dependent problem, and studied higher order approximations as well. Finally, the asymptotic analysis was supported with numerical results, which confirmed its validity.

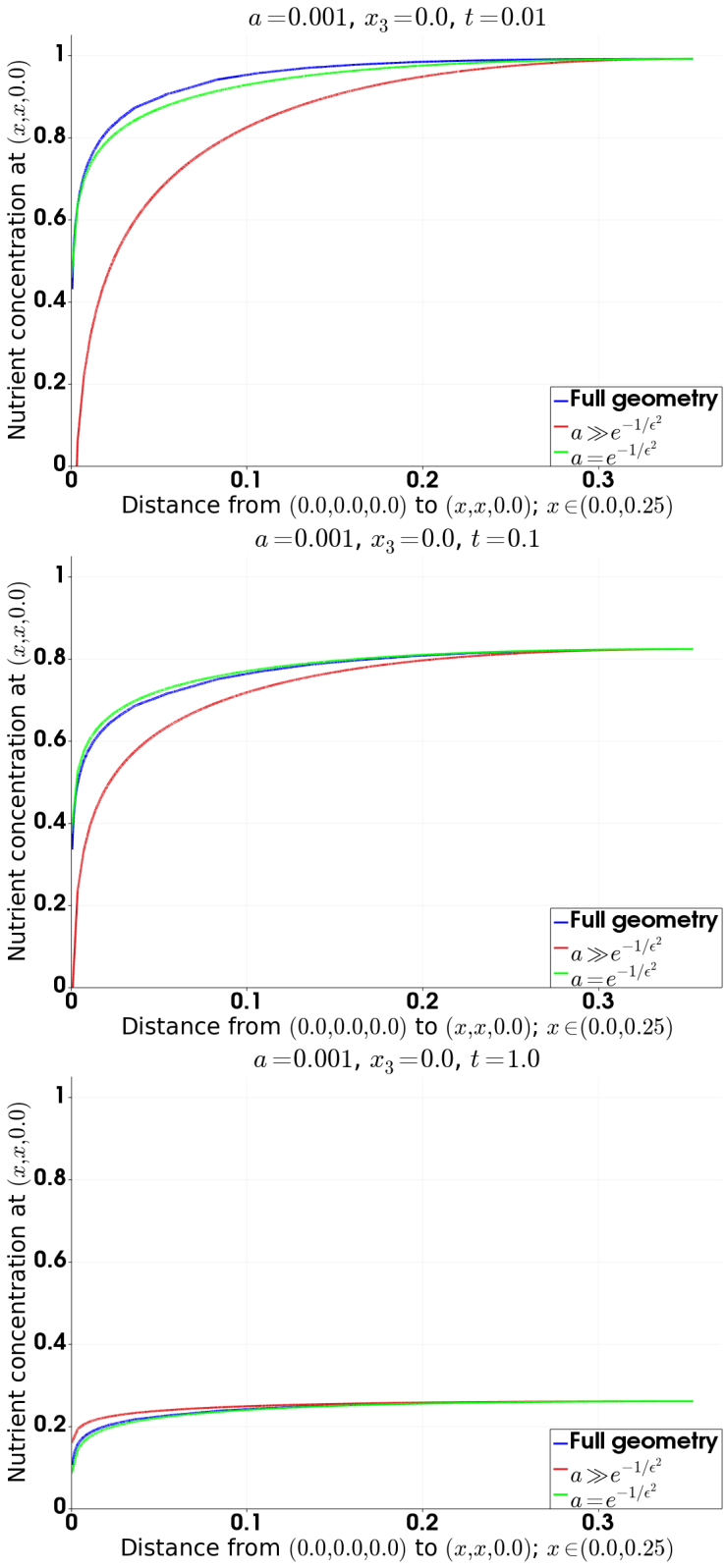


Figure 4.12.: Comparison between the models at different times ($x_3 = 0.0$). We used $a = 0.001$, $C = 1.0$, and assumed a zero-flux boundary condition at $x_3 = 1.0$ (instead of the Dirichlet boundary condition; this can be used to model inter-root competition).

5

EFFECTS OF ROOT CURVATURE ON HAIR UPTAKE MODELS

5.1 INTRODUCTION

In preceding chapters, we always started with the assumption, that the root surface is flattened (rolled) out. However, it is not clear how the flattening-out process changes the equations involved.

If the length of a root hair is of the same order of magnitude as (or much greater than) the radius of the root (which is usually the case; see [80] or Section 1.4.4), then the distance between the tips of two neighbouring hairs is of the same order of magnitude as (or much greater than) an inter-hair distance measured along the root surface. This suggests that changes in governing equations caused by the rolling-out process may result in a changed effective (homogenised) equation.

First, we investigate the case in which the root hair length is much smaller than the root radius and study changes in resulting homogenised equations. Then, we move on to the case where the hair length is comparable to the root radius. In the final section of this chapter, we compare derived effective models with full-geometry simulations.

We assume for simplicity that the distance between the hairs neighbouring along the root's circumference h equals the distance along the root's main axis h_0 (to our knowledge, the same assumption was used in all studies of hair uptake via homogenisation so far). We start with a domain shown in Figure 5.1. Note that notation used in this chapter is analogous to the one used in Section

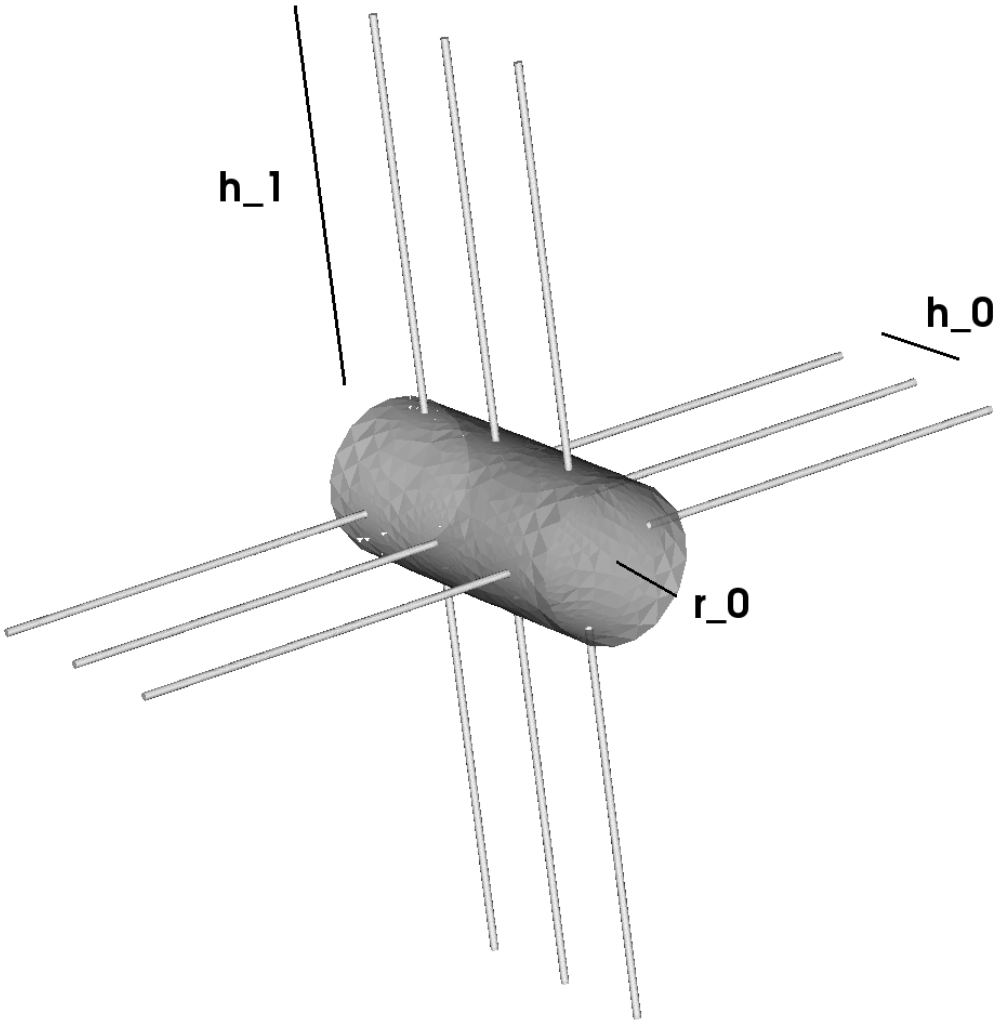


Figure 5.1.: The curved root surface and the most important parameters in this chapter. The four hairs per each layer are chosen rather arbitrarily, and this parameter will be changed in future.

2.6.3. We start with the dimensional continuity equation (127), the hair surface boundary condition (128), and a constant initial condition $\bar{u}(\bar{t} = 0) = \bar{u}_{in}$.

5.2 SHORT ROOT HAIRS

We nondimensionalise using the length of the root hair (h_1). Thus, we get a dimensionless root radius $\frac{r_0}{h_1} =: \frac{1}{\delta}$, and we assume $\delta \ll 1$. We further get a dimensionless inter-hair distance (in an azimuthal angle direction, which we denote by θ here) $\frac{h}{h_1}$ and a dimensionless root length $\frac{H}{h_1}$.

We first make a limit $\delta \to 0$ (in dimensional variables, this corresponds to $r_0 \to \infty$; keeping h_1 fixed), which describes the rolling-out process. At this stage, we keep $\epsilon = \frac{h}{h_1}$ (or h in dimensional variables) fixed, which means that as $\delta \to 0$, we get more and more root hairs along the circumference of the root, so that the distance between them is held constant. After that, we let $\epsilon \to 0$ ($h \to 0$ keeping h_1 fixed), which is a homogenisation condition.

Starting with dimensional cartesian coordinates $(\bar{w}_1, \bar{w}_2, \bar{w}_3)$, we nondimensionalise as:

$$(\bar{w}_1, \bar{w}_2, \bar{w}_3) = h_1(w_1, w_2, w_3) \qquad \bar{t} = \frac{h_1^2}{D}t \qquad \bar{u} = \bar{u}_{in}u$$

and get a continuity equation:

$$\frac{\partial u}{\partial t} = \nabla_w^2 u, \tag{243}$$

where $\nabla_w = (\frac{\partial}{\partial w_1}, \frac{\partial}{\partial w_2}, \frac{\partial}{\partial w_3})$, a hair boundary condition:

$$\nabla_w u \cdot \hat{\boldsymbol{n}} = -\frac{Bh_1}{D}u = -\frac{Bh_1^2}{hD}\frac{h}{h_1}u = -A\epsilon u \tag{244}$$

with $A = \frac{Bh_1^2}{hD}$, and:

$$u(t = 0) = 1.$$

Writing the continuity equation in cylindrical coordinates:

$$r_w = \sqrt{w_1^2 + w_2^2} \qquad \theta_w = \arctan\frac{w_2}{w_1} \qquad w_3 = w_3,$$

we get:

$$\frac{\partial u}{\partial t} = \frac{1}{r_w}\frac{\partial}{\partial r_w}\{r_w\frac{\partial u}{\partial r_w}\} + \frac{1}{r_w^2}\frac{\partial^2 u}{\partial \theta_w^2} + \frac{\partial^2 u}{\partial w_3^2}.$$

Now, we transform the coordinates in the following fashion (which corresponds to the rolling-out process):

$$r_w = \frac{1}{\delta} + x_3 \qquad \frac{\theta_w}{\delta} = x_1 \qquad x_2 = w_3, \tag{245}$$

and we get:

$$\frac{\partial u}{\partial t} = \frac{\partial^2 u}{\partial x_3^2} + \frac{\delta}{1 + \delta x_3}\frac{\partial u}{\partial x_3} + \frac{\delta^2}{(1 + \delta x_3)^2}\frac{\partial^2 u}{\partial x_1^2}(\frac{1}{\delta})^2 + \frac{\partial^2 u}{\partial x_2^2}$$

or:

$$\frac{\partial u}{\partial t} = \frac{\partial^2 u}{\partial x_3^2} + \frac{\delta}{1 + \delta x_3}\frac{\partial u}{\partial x_3} + \frac{1}{(1 + \delta x_3)^2}\frac{\partial^2 u}{\partial x_1^2} + \frac{\partial^2 u}{\partial x_2^2}. \tag{246}$$

For $\delta \ll 1$, we have:

$$\frac{\delta}{1+\delta x_3} = \delta(1 - x_3\delta + (x_3\delta)^2 - (x_3\delta)^3 + ...) = \delta - x_3\delta^2 + x_3^2\delta^3 - x_3^3\delta^4 + ...,$$

$$\frac{1}{(1+\delta x_3)^2} = 1 - 2x_3\delta + 3(x_3\delta)^2 - 4(x_3\delta)^3 + ...,$$

and thus we get:

$$\begin{aligned}\frac{\partial u}{\partial t} =& \frac{\partial^2 u}{\partial x_3^2} + (\delta - x_3\delta^2 + O(\delta^3))\frac{\partial u}{\partial x_3} + \\ & (1 - 2x_3\delta + 3(x_3\delta)^2 - 4(x_3\delta)^3 + O(\delta^4))\frac{\partial^2 u}{\partial x_1^2} + \frac{\partial^2 u}{\partial x_2^2}.\end{aligned} \tag{247}$$

Finally, we introduce $\epsilon = \frac{h}{h_1}$ as the homogenisation small parameter, $y_1 = \frac{1}{\epsilon}x_1 = \frac{h_1}{h}x_1$ and $y_2 = \frac{1}{\epsilon}x_2$ as the microscale variables in the two-scale ansatz (136) (from previous analysis, we know that the microscale geometry is effectively two-dimensional), and using the two-scale differential operators, we get:

$$\begin{aligned}\frac{\partial(u_0 + o(1))}{\partial t} &= \frac{\partial^2(u_0 + o(1))}{\partial x_3^2} + (\delta + O(\delta^2))\frac{\partial(u_0 + o(1))}{\partial x_3} + \\ & (1 - 2x_3\delta + 3(x_3\delta)^2 - 4(x_3\delta)^3 + O(\delta^4)) \times \\ \{\frac{1}{\epsilon^2}&\frac{\partial^2(u_0 + \epsilon u_1 + \epsilon^2 u_2 + o(\epsilon^2))}{\partial y_1^2} + \frac{2}{\epsilon}\frac{\partial^2(u_0 + \epsilon u_1 + o(\epsilon))}{\partial y_1 \partial x_1} + \frac{\partial^2(u_0 + o(1))}{\partial x_1^2}\} + \\ \{\frac{1}{\epsilon^2}&\frac{\partial^2(u_0 + \epsilon u_1 + \epsilon^2 u_2 + o(\epsilon^2))}{\partial y_2^2} + \frac{2}{\epsilon}\frac{\partial^2(u_0 + \epsilon u_1 + o(\epsilon))}{\partial y_2 \partial x_2} + \frac{\partial^2(u_0 + o(1))}{\partial x_2^2}\}.\end{aligned} \tag{248}$$

5.2.1 *Transforming the hair boundary condition*

We now transform the hair boundary condition. Using the dimensionless cartesian coordinates (w_1, w_2, w_3), the surface of a root hair pointing in the $\hat{\boldsymbol{w}}_1$ direction is given as:

$$F(w_1, w_2, w_3) = w_3^2 + w_2^2 = (\frac{r_1}{h_1})^2, \tag{249}$$

which means:

$$\nabla_w F = (0, 2w_2, 2w_3),$$

and this implies that a vector:

$$\frac{(0, w_2, w_3)}{(w_2^2 + w_3^2)^{\frac{1}{2}}} = \frac{(0, w_2, w_3)}{\frac{r_1}{h_1}}$$

is normal to this surface, and its norm is 1. For $w_3 > 0$, we want the w_3 component of the outward pointing unit vector normal to the hair surface to be negative. Therefore, the outward pointing unit normal vector is:

$$\hat{\boldsymbol{n}} = -\frac{h_1}{r_1}(0, w_2, w_3),$$

which can be written in the cylindrical coordinates as:

$$\hat{\boldsymbol{n}} = -\frac{h_1}{r_1}(0, r_w \sin\theta_w, w_3). \tag{250}$$

The nabla operator in the cartesian coordinates reads:

$$\nabla_w u = (\frac{\partial u}{\partial w_1}, \frac{\partial u}{\partial w_2}, \frac{\partial u}{\partial w_3}) = (\frac{\partial u}{\partial r_w}\frac{\partial r_w}{\partial w_1} + \frac{\partial u}{\partial \theta_w}\frac{\partial \theta_w}{\partial w_1}, \frac{\partial u}{\partial r_w}\frac{\partial r_w}{\partial w_2} + \frac{\partial u}{\partial \theta_w}\frac{\partial \theta_w}{\partial w_2}, \frac{\partial u}{\partial w_3}),$$

which can be substituted (together with Equation (250)) into the boundary condition (244) to give:

$$\begin{aligned} -A\epsilon u = &-\frac{h_1}{r_1}(0, r_w \sin\theta_w, w_3)\cdot \\ &(\frac{\partial u}{\partial r_w}\frac{\partial r_w}{\partial w_1} + \frac{\partial u}{\partial \theta_w}\frac{\partial \theta_w}{\partial w_1}, \frac{\partial u}{\partial r_w}\frac{\partial r_w}{\partial w_2} + \frac{\partial u}{\partial \theta_w}\frac{\partial \theta_w}{\partial w_2}, \frac{\partial u}{\partial w_3}). \end{aligned} \tag{251}$$

Using:

$$r_w = \sqrt{w_1^2 + w_2^2} \qquad \theta_w = \arctan\frac{w_2}{w_1},$$

we get:

$$\frac{\partial r_w}{\partial w_2} = \frac{w_2}{\sqrt{w_1^2 + w_2^2}} = \sin\theta_w \qquad \frac{\partial \theta_w}{\partial w_2} = \frac{1}{1 + (\frac{w_2}{w_1})^2}\frac{1}{w_1} = \frac{w_1}{w_1^2 + w_2^2} = \frac{\cos\theta_w}{r_w},$$

which after substituting into Equation (251) yields:

$$A\epsilon u = \frac{h_1}{r_1}(\frac{\partial u}{\partial r_w} r_w \sin^2\theta_w + \frac{\partial u}{\partial \theta_w}\sin\theta_w \cos\theta_w + \frac{\partial u}{\partial w_3} w_3).$$

Now, we change to the cartesian coordinates according to Transformation (245) and get:

$$\frac{A\epsilon r_1 u}{h_1} = \frac{\partial u}{\partial x_3}(\frac{1}{\delta} + x_3)\sin^2\delta x_1 + \frac{\partial u}{\partial x_1}\frac{1}{\delta}\sin\delta x_1 \cos\delta x_1 + \frac{\partial u}{\partial x_2} x_2.$$

Downscaling to the microscale variables $(y_1, y_2) = \frac{(x_1, x_2)}{\epsilon}$, we get:

$$\frac{A\epsilon r_1 u}{h}\frac{h}{h_1} = \frac{\partial u}{\partial x_3}(\frac{1}{\delta} + x_3)\sin^2\delta\epsilon y_1 + \frac{1}{\epsilon}\frac{\partial u}{\partial y_1}\frac{1}{\delta}\sin\delta y_1\epsilon\cos\delta\epsilon y_1 + \frac{1}{\epsilon}\frac{\partial u}{\partial y_2}\epsilon y_2. \quad (252)$$

Denoting $U = \frac{r_1 A}{h}$, recalling that $\sin\delta\epsilon y_1\cos\delta\epsilon y_1 = \frac{1}{2}\sin 2\delta\epsilon y_1$, and using Taylor expansions (as both δ and ϵ are small):

$$\sin\delta\epsilon y_1 = \delta\epsilon y_1 - \frac{(\delta\epsilon y_1)^3}{6} + O((\epsilon\delta)^5)$$

$$\sin 2\delta\epsilon y_1 = 2\delta\epsilon y_1 - \frac{4}{3}(\delta\epsilon y_1)^3 + O((\epsilon\delta)^5),$$

we get:

$$U\epsilon^2 u = \frac{\partial u}{\partial x_3}(\frac{1}{\delta} + x_3)((\delta\epsilon y_1)^2 - \frac{(\delta\epsilon y_1)^4}{3} + O((\epsilon\delta)^6)) +$$
$$\frac{1}{\epsilon}\frac{\partial u}{\partial y_1}\frac{1}{\delta}(\delta\epsilon y_1 - \frac{2}{3}(\delta\epsilon y_1)^3 + O((\epsilon\delta)^5)) + \frac{\partial u}{\partial y_2}y_2.$$

Simplifying, we conclude:

$$U\epsilon^2 u = \frac{\partial u}{\partial x_3}(\delta\epsilon^2 y_1^2 + O((\epsilon\delta)^2)) + \frac{\partial u}{\partial y_1}(y_1 - \frac{2}{3}\epsilon^2\delta^2 y_1^3 + O((\epsilon\delta)^4)) + \frac{\partial u}{\partial y_2}y_2. \quad (253)$$

Multiscale expansions and operators ($\epsilon = \frac{h}{h_1} \ll 1$) give:

$$U\epsilon^2(u_0 + o(1)) = \frac{\partial}{\partial x_3}(u_0 + o(1))(\delta\epsilon^2 y_1^2 + O((\epsilon\delta)^2)) +$$
$$(y_1 - \frac{2}{3}\epsilon^2\delta^2 y_1^3 + O((\epsilon\delta)^4))(\frac{\partial}{\partial y_1} + \epsilon\frac{\partial}{\partial x_1})(u_0 + \epsilon u_1 + \epsilon^2 u_2 + o(\epsilon^2)) +$$
$$y_2(\frac{\partial}{\partial y_2} + \epsilon\frac{\partial}{\partial x_2})(u_0 + \epsilon u_1 + \epsilon^2 u_2 + o(\epsilon^2)). \quad (254)$$

5.2.2 *Homogenisation*

To uncover the microscale geometry, we rewrite Equation (249) in the cylindrical coordinates as:

$$w_3^2 + r_w^2\sin^2\theta_w = (\frac{r_1}{h_1})^2$$

and use the rolling-out Transformation (245) to get:

$$x_2^2 + (\frac{1}{\delta} + x_3)^2\sin^2\delta x_1 = (\frac{r_1}{h_1})^2.$$

For $\delta \ll 1$ we know:

$$\sin \delta x_1 = \delta x_1 - \frac{(\delta x_1)^3}{6} + O(\delta^5),$$

which gives:

$$x_2^2 + (\frac{1}{\delta^2} + \frac{2}{\delta} x_3 + x_3^2)(\delta^2 x_1^2 + O(\delta^4)) = (\frac{r_1}{h_1})^2$$

or:

$$x_2^2 + (x_1^2 + O(\delta)) = (\frac{r_1}{h_1})^2.$$

Sending δ to 0 yields:

$$x_2^2 + x_1^2 = (\frac{r_1}{h_1})^2,$$

and downscaling gives:

$$(\epsilon y_2)^2 + \epsilon^2 y_1^2 = (\frac{r_1}{h})^2 (\frac{h}{h_1})^2 = \epsilon^2 (\frac{r_1}{h})^2$$

or:

$$y_2^2 + y_1^2 = (\frac{r_1}{h})^2.$$

This defines a circle in the (y_1, y_2)-plane centered at $(0, 0)$ with a radius of $\frac{r_1}{h} = a$, which is identical to the microscale geometry from Figure 3.3. Note that for the $\delta = O(1)$ case which we will study in the next section, the microscopic hair boundary changes into an ellipse (see derivations in Section 5.3 or Figure 5.11).

In the $\delta \to 0$ limit, the boundary condition (254) becomes:

$$U\epsilon^2(u_0 + o(1)) = y_1(\frac{\partial}{\partial y_1} + \epsilon \frac{\partial}{\partial x_1})(u_0 + \epsilon u_1 + \epsilon^2 u_2 + o(\epsilon^2)) +$$

$$y_2(\frac{\partial}{\partial y_2} + \epsilon \frac{\partial}{\partial x_2})(u_0 + \epsilon u_1 + \epsilon^2 u_2 + o(\epsilon^2)),$$

and Equation (248) reduces to:

$$\frac{\partial(u_0 + o(1))}{\partial t} = \frac{1}{\epsilon^2} \frac{\partial^2(u_0 + \epsilon u_1 + \epsilon^2 u_2 + o(\epsilon^2))}{\partial y_1^2} + \frac{2}{\epsilon} \frac{\partial^2(u_0 + \epsilon u_1 + o(\epsilon))}{\partial y_1 \partial x_1} +$$

$$\frac{\partial^2(u_0 + o(1))}{\partial x_1^2} + \frac{1}{\epsilon^2} \frac{\partial^2(u_0 + \epsilon u_1 + \epsilon^2 u_2 + o(\epsilon^2))}{\partial y_2^2} +$$

$$\frac{2}{\epsilon} \frac{\partial^2(u_0 + \epsilon u_1 + o(\epsilon))}{\partial y_2 \partial x_2} + \frac{\partial^2(u_0 + o(1))}{\partial x_2^2} + \frac{\partial^2(u_0 + o(1))}{\partial x_3^2}.$$

Thus, we have recovered the same microscale geometry and governing equations as those we started with in the previous chapters (compare with the continuity equation (137) and the hair boundary condition (138)).

However, the expansion $u \approx u_0 + \epsilon u_1 + \epsilon^2 u_2 + o(\epsilon^2)$ is not always appropriate as the following example demonstrates. Assume $\delta = \epsilon^{\frac{1}{2}}$. At $O(\epsilon^{-2})$, we get $u_0 = u_0(t, \boldsymbol{x})$, which is consistent with the continuity equation at $O(\epsilon^{-\frac{3}{2}})$: $-2x_3 \frac{\partial^2 u_0}{\partial y_1^2} = 0$. At $O(\epsilon^{-1})$, we get (using the fact that u_0 is independent of the microscale) $\nabla_y^2 u_1 = 0$, which together with the usual hair surface boundary condition implies that u_1 has a nontrivial microscopic behaviour (see Equation (142)). However, this is in contradiction with the continuity equation at $O(\epsilon^{-\frac{1}{2}})$: $-2x_3 \frac{\partial^2 u_1}{\partial y_1^2} = 0$. Thus, we need to consider more general asymptotic expansions, containing exponents that are not natural numbers.

Therefore, we go back to Equation (247) and the hair boundary condition (253). Assume $\delta = \mu\epsilon^\gamma$ with $\mu = O(1)$ and $\gamma > 0$. Using the two-scale operators, we get a continuity equation:

$$\begin{aligned}\frac{\partial u}{\partial t} =& \frac{\partial^2 u}{\partial x_3^2} + o(1) + \{\frac{1}{\epsilon^2}\frac{\partial^2 u}{\partial y_2^2} + \frac{2}{\epsilon}\frac{\partial^2 u}{\partial y_2 \partial x_2} + \frac{\partial^2 u}{\partial x_2^2}\} + \\ & (1 - 2x_3\mu\epsilon^\gamma + 3(x_3\mu\epsilon^\gamma)^2 - 4(x_3\mu\epsilon^\gamma)^3 + O(\epsilon^{4\gamma})) \times \\ & \{\frac{1}{\epsilon^2}\frac{\partial^2 u}{\partial y_1^2} + \frac{2}{\epsilon}\frac{\partial^2 u}{\partial y_1 \partial x_1} + \frac{\partial^2 u}{\partial x_1^2}\}\end{aligned} \tag{255}$$

and a hair surface boundary condition:

$$U\epsilon^2 u = o(\epsilon^2) + (y_1 + o(\epsilon^2))(\frac{\partial u}{\partial y_1} + \epsilon\frac{\partial u}{\partial x_1}) + y_2(\frac{\partial u}{\partial y_2} + \epsilon\frac{\partial u}{\partial x_2}). \tag{256}$$

Furthermore, we can rewrite the continuity equation as:

$$\begin{aligned}\frac{\partial u}{\partial t} =& \frac{\partial^2 u}{\partial x_3^2} + \\ & \{\frac{1}{\epsilon^2}\frac{\partial^2 u}{\partial y_1^2} + \frac{2}{\epsilon}\frac{\partial^2 u}{\partial y_1 \partial x_1} + \frac{\partial^2 u}{\partial x_1^2}\} + \{\frac{1}{\epsilon^2}\frac{\partial^2 u}{\partial y_2^2} + \frac{2}{\epsilon}\frac{\partial^2 u}{\partial y_2 \partial x_2} + \frac{\partial^2 u}{\partial x_2^2}\} + o(1) + \\ & (-2x_3\mu\epsilon^\gamma + 3(x_3\mu\epsilon^\gamma)^2 - 4(x_3\mu\epsilon^\gamma)^3 + O(\epsilon^{4\gamma}))\{\frac{1}{\epsilon^2}\frac{\partial^2 u}{\partial y_1^2} + \frac{2}{\epsilon}\frac{\partial^2 u}{\partial y_1 \partial x_1} + \frac{\partial^2 u}{\partial x_1^2}\}.\end{aligned}$$

Apart from the last line, this equation is identical to the one studied in previous chapters. Thus, any (potential) new terms can only originate from the last line of this equation.

We already know that a homogenised equation is obtained using $O(\epsilon^2)$ terms from the boundary condition. However, we see that all terms up to this order are unchanged (independent of the choice of γ). Therefore, it is sufficient to focus on the continuity equation. Here, in order to obtain the homogenised equation, one needs to expand up to $O(1)$. Notice that for any $\gamma > 0$, assuming ansatz $u = u_0 + o(1)$, we always conclude that u_0 is independent of the microscopic variables. This also means that we can rewrite Equation (255) as:

$$\frac{\partial u}{\partial t} = \frac{\partial^2 u}{\partial x_3^2} + \{\frac{1}{\epsilon^2}\frac{\partial^2 u}{\partial y_1^2} + \frac{2}{\epsilon}\frac{\partial^2 u}{\partial y_1 \partial x_1} + \frac{\partial^2 u}{\partial x_1^2}\} + \{\frac{1}{\epsilon^2}\frac{\partial^2 u}{\partial y_2^2} + \frac{2}{\epsilon}\frac{\partial^2 u}{\partial y_2 \partial x_2} + \frac{\partial^2 u}{\partial x_2^2}\} + o(1) + (-2x_3\mu\epsilon^\gamma + 3(x_3\mu\epsilon^\gamma)^2 - 4(x_3\mu\epsilon^\gamma)^3 + O(\epsilon^{4\gamma}))\{\frac{1}{\epsilon^2}\frac{\partial^2 u}{\partial y_1^2} + \frac{2}{\epsilon}\frac{\partial^2 u}{\partial y_1 \partial x_1}\}, \tag{257}$$

and we can focus solely on new terms coming from the last line of this equation.

Now, we get rid of one more term. We prove that there can be no $u_\alpha \epsilon^\alpha$ term in the asymptotic expansion with a nontrivial microscopic behaviour for $\alpha < 1$. Suppose such a term exists. Assume further that α is the smallest number with this property. From $O(\epsilon^\alpha)$ in the boundary condition (256), we get $\nabla_y u_\alpha \cdot \hat{\boldsymbol{n}} = 0$. From $O(\epsilon^{-2+\alpha})$ in Equation (257), we get $\nabla_y^2 u_\alpha = 0$. These conditions together with the periodic boundary conditions in y_1 and y_2 imply that u_α is independent of the microscale, which is in contradiction with

our assumption, that u_α has a nontrivial microscopic behaviour. Thus, we can rewrite Equation (257) as:

$$\begin{aligned}
\frac{\partial u}{\partial t} =& \frac{\partial^2 u}{\partial x_3^2} + \{\frac{1}{\epsilon^2}\frac{\partial^2 u}{\partial y_1^2} + \frac{2}{\epsilon}\frac{\partial^2 u}{\partial y_1 \partial x_1} + \frac{\partial^2 u}{\partial x_1^2}\} + \{\frac{1}{\epsilon^2}\frac{\partial^2 u}{\partial y_2^2} + \frac{2}{\epsilon}\frac{\partial^2 u}{\partial y_2 \partial x_2} + \frac{\partial^2 u}{\partial x_2^2}\} + \\
& (-2x_3\mu\epsilon^\gamma + 3(x_3\mu\epsilon^\gamma)^2 - 4(x_3\mu\epsilon^\gamma)^3 + O(\epsilon^{4\gamma}))\frac{1}{\epsilon^2}\frac{\partial^2 u}{\partial y_1^2} + o(1) = \\
& \frac{\partial^2 u}{\partial x_3^2} + \{\frac{1}{\epsilon^2}\frac{\partial^2 u}{\partial y_1^2} + \frac{2}{\epsilon}\frac{\partial^2 u}{\partial y_1 \partial x_1} + \frac{\partial^2 u}{\partial x_1^2}\} + \{\frac{1}{\epsilon^2}\frac{\partial^2 u}{\partial y_2^2} + \frac{2}{\epsilon}\frac{\partial^2 u}{\partial y_2 \partial x_2} + \frac{\partial^2 u}{\partial x_2^2}\} + \\
& (-2x_3\mu\epsilon^{-2+\gamma} + 3\epsilon^{-2+2\gamma}(x_3\mu)^2 - 4\epsilon^{-2+3\gamma}(x_3\mu)^3 + O(\epsilon^{-2+4\gamma}))\times \\
& \frac{\partial^2(u_1\epsilon + ... + u_\alpha\epsilon^\alpha + ...)}{\partial y_1^2} + o(1) = \\
& \frac{\partial^2 u}{\partial x_3^2} + \{\frac{1}{\epsilon^2}\frac{\partial^2 u}{\partial y_1^2} + \frac{2}{\epsilon}\frac{\partial^2 u}{\partial y_1 \partial x_1} + \frac{\partial^2 u}{\partial x_1^2}\} + \{\frac{1}{\epsilon^2}\frac{\partial^2 u}{\partial y_2^2} + \frac{2}{\epsilon}\frac{\partial^2 u}{\partial y_2 \partial x_2} + \frac{\partial^2 u}{\partial x_2^2}\} + \\
& (-2x_3\mu\epsilon^{-1+\gamma} + 3\epsilon^{-1+2\gamma}(x_3\mu)^2 - 4\epsilon^{-1+3\gamma}(x_3\mu)^3 + O(\epsilon^{-1+4\gamma}))\times \\
& \frac{\partial^2(u_1 + ... + u_\alpha\epsilon^{\alpha-1} + ...)}{\partial y_1^2} + o(1),
\end{aligned} \tag{258}$$

and all new terms will come from the last two lines of this equation. Having expressed the continuity equation this way, it is easy to keep track of any new terms arising at various orders as we make γ smaller and smaller. The new terms can only be nontrivial in case some u_α from Equation (258) is nontrivially dependent on y_1. As we have seen before, $O(\epsilon^{-1})$ in the continuity equation gives $\nabla_y^2 u_1 = 0$, and $O(\epsilon)$ in the boundary condition gives $\nabla_y u_1 \cdot \hat{\boldsymbol{n}} = -\nabla_x u_0 \cdot \hat{\boldsymbol{n}}$, which results in:

$$u_1 = \nabla_x u_0 \cdot \boldsymbol{\lambda^0}(y_1, y_2) + f_1(t, \boldsymbol{x}), \tag{259}$$

where $\boldsymbol{\lambda^0} = (\lambda_1^0, \lambda_2^0, 0)$, λ_1^0 and λ_2^0 satisfy Laplace's equation, the usual periodicity conditions and the hair surface boundary conditions $\nabla_y \lambda_1^0 \cdot \hat{\boldsymbol{n}} = -n_1$, $\nabla_y \lambda_2^0 \cdot \hat{\boldsymbol{n}} = -n_2$. These cell problems are identical to those described in Section 3.2.1; here we used the superscript ^{0}, because we will soon derive many other cell problems, the solutions of which will be denoted by superscripts ^{1}, ^{2}, ^{3} etc. This means that u_1 is the lowest order term in the asymptotic expansion for u with a nontrivial microscopic behaviour.

Using our knowledge of u_β for $\beta < 1$, we can rewrite the continuity equation one last time, putting all terms not needed for homogenisation in $o(1)$:

$$\begin{aligned}\frac{\partial u_0}{\partial t} =& \frac{\partial^2 u_0}{\partial x_3^2} + \{\frac{1}{\epsilon^2}\frac{\partial^2(\epsilon u_1 + o(\epsilon))}{\partial y_1^2} + 2\frac{\partial^2 u_1}{\partial y_1 \partial x_1} + \frac{\partial^2 u_0}{\partial x_1^2}\} + \\ & \{\frac{1}{\epsilon^2}\frac{\partial^2(\epsilon u_1 + o(\epsilon))}{\partial y_2^2} + 2\frac{\partial^2 u_1}{\partial y_2 \partial x_2} + \frac{\partial^2 u_0}{\partial x_2^2}\} + o(1) + \\ & (-2x_3\mu\epsilon^{-1+\gamma} + 3\epsilon^{-1+2\gamma}(x_3\mu)^2 - 4\epsilon^{-1+3\gamma}(x_3\mu)^3 + O(\epsilon^{-1+4\gamma}))\times \\ & \frac{\partial^2(u_1 + ... + u_\alpha \epsilon^{\alpha-1} + ...)}{\partial y_1^2}.\end{aligned} \tag{260}$$

From this expression containing all possible $O(1)$ terms in the continuity equation (integrating which we obtain the homogenised equation), it is easy to identify the values of γ which yield the new terms. The condition states:

$$-1 + m\gamma = 0 \qquad \forall m \in \mathbb{N}$$

or:

$$\gamma = \frac{1}{m}.$$

This gives a sequence $\gamma = 1, \frac{1}{2}, \frac{1}{3}, \frac{1}{4}, ...$ We now analyse the situation for γ decreasing from arbitrarily large values down to zero.

Case $\gamma > 1$

If $\gamma > 1$, no new terms arise up to $O(1)$, and we arrive at the same homogenised equation (155).

Case $\gamma = 1$

At $O(\epsilon^{-1})$, we observe no changes (this is true for any $\gamma > 0$). At $O(1)$, we find a new term $-2x_3\mu\frac{\partial^2 u_1}{\partial y_1^2}$, and using the separation of scales from Equation (259), this becomes:

$$-2x_3\mu\{\frac{\partial u_0}{\partial x_1}\frac{\partial^2 \lambda_1^0}{\partial y_1^2} + \frac{\partial u_0}{\partial x_2}\frac{\partial^2 \lambda_2^0}{\partial y_1^2}\}.$$

We now show that integrating both terms from the previous equation over the unit cell we get zero. Using the divergence theorem, we get:

$$\int_C \frac{\partial^2 \lambda_1^0}{\partial y_1^2} dS = \int_C \nabla \cdot (\frac{\partial \lambda_1^0}{\partial y_1}, 0) dS = \int_{\partial C} (\frac{\partial \lambda_1^0}{\partial y_1}, 0) \cdot \hat{\mathbf{n}} dl = \int_U \frac{\partial \lambda_1^0}{\partial y_1} n_1 dl,$$

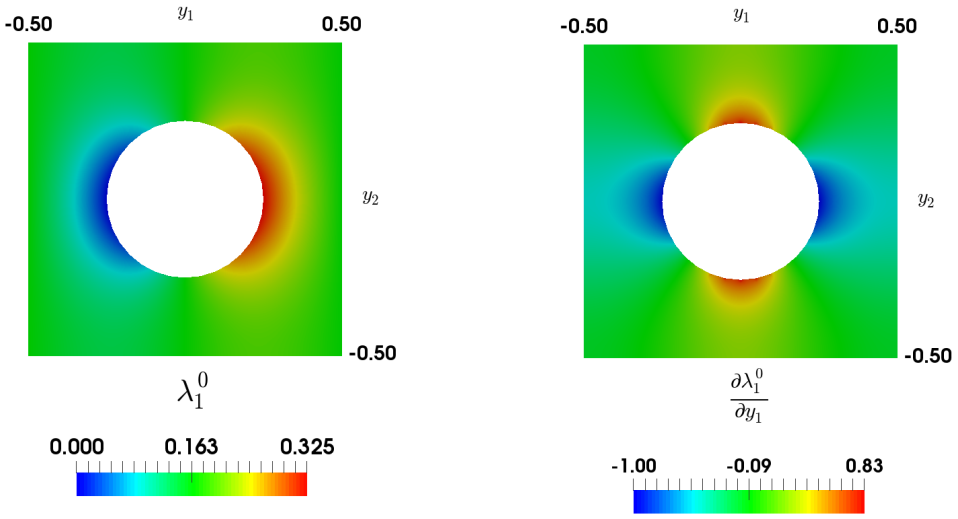


Figure 5.2.: The solution of the first unit cell problem and its derivative with respect to y_1.

where in the last step, we used the periodic flux condition for λ_1^0 (recall that U is the uptaking part of the two-dimensional unit cell boundary as defined in Equation (151)). Similarly:

$$\int_C \frac{\partial^2 \lambda_2^0}{\partial y_1^2} dS = \int_C \nabla \cdot (\frac{\partial \lambda_2^0}{\partial y_1}, 0) dS = \int_{\partial C} (\frac{\partial \lambda_2^0}{\partial y_1}, 0) \cdot \hat{\boldsymbol{n}} dl = \int_U \frac{\partial \lambda_2^0}{\partial y_1} n_1 dl.$$

Thus, the question of whether the new terms integrate out to zero or not can be answered by calculating certain integrals over the root hair part of the boundary. It remains to show, that:

$$\int_U \frac{\partial \lambda_1^0}{\partial y_1} n_1 dl = 0 = \int_U \frac{\partial \lambda_2^0}{\partial y_1} n_1 dl.$$

Figure 5.2 shows λ_1^0 and $\frac{\partial \lambda_1^0}{\partial y_1}$ numerically computed in FEniCS. This figure suggests us to think that $\frac{\partial \lambda_1^0}{\partial y_1}$ is even in y_1, i.e. that for any (s,t) belonging to the unit cell, we have:

$$\frac{\partial \lambda_1^0(s,t)}{\partial y_1} = \frac{\partial \lambda_1^0(-s,t)}{\partial y_1}. \tag{261}$$

As it is easy to see that the first component of the outward pointing unit normal vector at the hair surface n_1 is odd in y_1 ($n_1(s,t) = -n_1(-s,t)$), we conclude:

$$\int_U \frac{\partial \lambda_1^0}{\partial y_1} n_1 dl = 0.$$

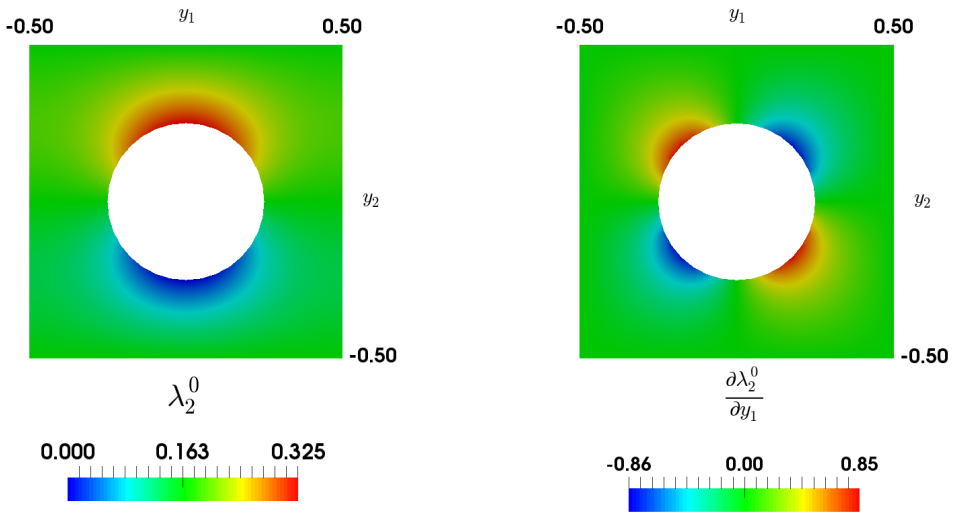


Figure 5.3.: The solution of the second unit cell problem and its derivative with respect to y_1.

Let us briefly note that the relationship (261) stems from a fact that λ_1^0 can be written as the sum of a function odd in y_1 and a constant (which originates from the symmetries of our geometry, continuity equation and boundary conditions, and can be shown using techniques similar to those presented in Section 3.2.1), and from a well-known rule stating that the derivative of an odd function is even.

Similar to the previous analysis, Figure 5.3 suggests that $\frac{\partial \lambda_2^0}{\partial y_1}$ is odd in y_2, i.e. for any (s,t) belonging to the unit cell, we have:

$$-\frac{\partial \lambda_2^0(s,t)}{\partial y_1} = \frac{\partial \lambda_2^0(s,-t)}{\partial y_1}. \tag{262}$$

The first component of the outward pointing unit normal vector at the hair surface n_1 is even in y_2 ($n_1(s,t) = n_1(s,-t)$), and therefore:

$$\int_U \frac{\partial \lambda_2^0}{\partial y_1} n_1 dl = 0.$$

The relationship (262) stems from a fact that λ_2^0 can be written as the sum of a function odd in y_2 and a constant (which again originates from the symmetries of our geometry, continuity equation and boundary conditions).

We have shown that the new terms in the $\gamma = 1$ case yield 0 when integrated over the microscale, and thus do not affect the effective equation.

Case $\gamma \in (\frac{1}{2}, 1)$

At $O(1)$ in the continuity equation (260), we get a new term: $-2x_3\mu\frac{\partial^2 u_{2-\gamma}}{\partial y_1^2}$. At $O(\epsilon^{-\gamma})$ in the continuity equation (260), we get:

$$\nabla_y^2 u_{2-\gamma} = 0$$

(as $-1+\gamma > -\gamma$ in this case), and from the boundary condition (256) at $O(\epsilon^{2-\gamma})$, we know:

$$\nabla_y u_{2-\gamma} \cdot \hat{\boldsymbol{n}} = -\nabla_x u_{1-\gamma} \cdot \hat{\boldsymbol{n}}.$$

Knowing that $u_{1-\gamma}$ is independent of the microscale, we conclude:

$$u_{2-\gamma} = \nabla_x u_{1-\gamma}(t, \boldsymbol{x}) \cdot \boldsymbol{\lambda^0}(y_1, y_2) + f_{2-\gamma}(t, \boldsymbol{x}),$$

where $f_{2-\gamma}(t, \boldsymbol{x})$ is a yet unknown function, and $\boldsymbol{\lambda^0}$ obeys the same unit cell problems as those considered in the $\gamma = 1$ case. Substituting $\gamma = 1$, we recover the same term as in the previous section. As shown therein, the new term integrates to 0.

Case $\gamma = \frac{1}{2}$

We already briefly mentioned the problem with the $\gamma = \frac{1}{2}$ case. To solve this problem, we now use an expansion:

$$u \approx u_0 + \epsilon^{\frac{1}{2}} u_{\frac{1}{2}} + \epsilon u_1 + \epsilon^{\frac{3}{2}} u_{\frac{3}{2}} + \epsilon^2 u_2 + o(\epsilon^2).$$

At $O(1)$ in Equation (260), we get two new terms:

$$-2\mu x_3 \frac{\partial^2 u_{\frac{3}{2}}}{\partial y_1^2}$$

and

$$+3\mu^2 x_3^2 \frac{\partial^2 u_1}{\partial y_1^2}.$$

From previous sections we know that the second term integrates out to 0.
At $O(\epsilon^{-\frac{1}{2}})$ in Equation (260), we find:

$$\nabla_y^2 u_{\frac{3}{2}} = 2\mu x_3 \frac{\partial^2 u_1}{\partial y_1^2} = 2\mu x_3 \nabla_x u_0 \cdot (\frac{\partial^2 \lambda_1^0}{\partial y_1^2}, \frac{\partial^2 \lambda_2^0}{\partial y_1^2}, 0),$$

and at $O(\epsilon^{\frac{3}{2}})$ in the boundary condition (256), we get:

$$\nabla_y u_{\frac{3}{2}} \cdot \hat{\boldsymbol{n}} = -\nabla_x u_{\frac{1}{2}} \cdot \hat{\boldsymbol{n}}.$$

This yields:

$$u_{\frac{3}{2}} = (\lambda_1^0(y_1, y_2), \lambda_2^0(y_1, y_2)) \cdot (\frac{\partial u_{\frac{1}{2}}}{\partial x_1}, \frac{\partial u_{\frac{1}{2}}}{\partial x_2}) + 2\mu x_3 \nabla_x u_0 \cdot \boldsymbol{\lambda^1} + f_{\frac{3}{2}}(t, \boldsymbol{x}),$$

where $\boldsymbol{\lambda^1} = (\lambda_1^1, \lambda_2^1)$ satisfies continuity equations:

$$\nabla_y^2 \lambda_1^1 = \frac{\partial^2 \lambda_1^0}{\partial y_1^2} \qquad \nabla_y^2 \lambda_2^1 = \frac{\partial^2 \lambda_2^0}{\partial y_1^2}, \tag{263}$$

and hair surface boundary conditions:

$$\nabla_y \lambda_1^1 \cdot \hat{\boldsymbol{n}} = 0 = \nabla_y \lambda_2^1 \cdot \hat{\boldsymbol{n}}. \tag{264}$$

Thus, the first term becomes:

$$-2\mu x_3 \frac{\partial^2 u_{\frac{3}{2}}}{\partial y_1^2} = -2\mu x_3 \{(\frac{\partial^2 \lambda_1^0}{\partial y_1^2}, \frac{\partial^2 \lambda_2^0}{\partial y_1^2}) \cdot (\frac{\partial u_{\frac{1}{2}}}{\partial x_1}, \frac{\partial u_{\frac{1}{2}}}{\partial x_2}) +$$

$$2\mu x_3 (\frac{\partial u_0}{\partial x_1}, \frac{\partial u_0}{\partial x_2}) \cdot (\frac{\partial^2 \lambda_1^1}{\partial y_1^2}, \frac{\partial^2 \lambda_2^1}{\partial y_1^2})\}$$

From previous sections we know that the first term on the right-hand side of this equation integrates out to 0. We now show that the same applies to the second term on the right-hand side. As before, it suffices to show that:

$$\int_U \frac{\partial \lambda_1^1}{\partial y_1} n_1 dl = 0 = \int_U \frac{\partial \lambda_2^1}{\partial y_1} n_1 dl.$$

Figure 5.4 shows λ_1^1 and $\frac{\partial \lambda_1^1}{\partial y_1}$ numerically computed in FEniCS. This figure suggests that $\frac{\partial \lambda_1^1}{\partial y_1}$ is even in y_1, and using $n_1(s,t) = -n_1(-s,t)$ for any (s,t) belonging to the hair surface, we conclude:

$$\int_U \frac{\partial \lambda_1^1}{\partial y_1} n_1 dl = 0.$$

The reason for $\frac{\partial \lambda_1^1}{\partial y_1}$ being even in y_1 is that λ_1^1 is odd in y_1 (up to a constant). This can be shown using symmetry arguments similar to those introduced in Section 3.2.1 and requires the forcing term on the right-hand side of Poisson's

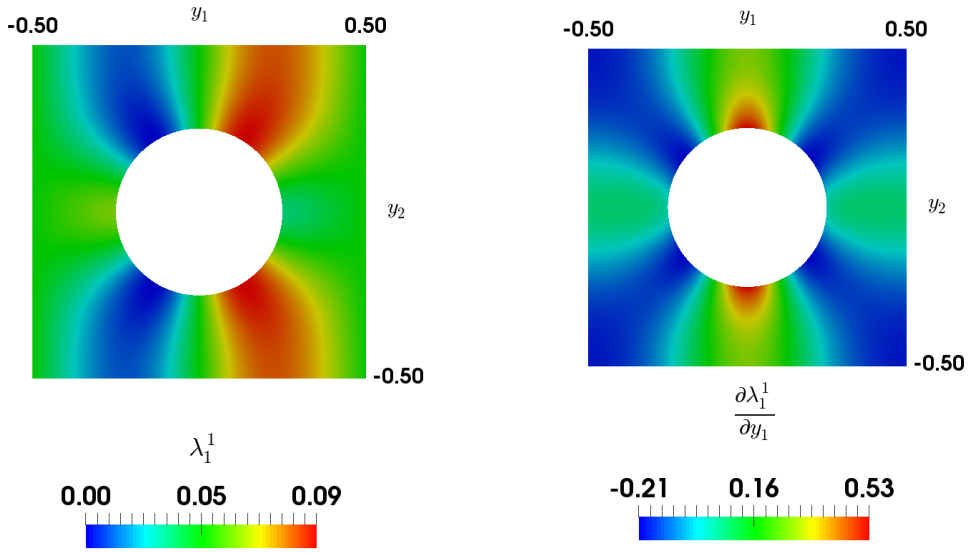


Figure 5.4.: The solution of the λ_1^1 (unit cell) problem and its derivative with respect to y_1.

equation for λ_1^1 (i.e. $\frac{\partial^2 \lambda_1^0}{\partial y_1^2}$) to be odd in y_1 [1]. This is caused by the already shown fact that $\frac{\partial \lambda_1^0}{\partial y_1}$ is even in y_1 (see Equation (261) and the reasoning in the $\gamma = 1$ case).

Figure 5.5 shows λ_2^1 and $\frac{\partial \lambda_2^1}{\partial y_1}$ numerically computed in FEniCS. This figure suggests that $\frac{\partial \lambda_2^1}{\partial y_1}$ is odd in y_2, and using $n_1(s,t) = n_1(s,-t)$ for any (s,t) belonging to the hair surface, we conclude:

$$\int_U \frac{\partial \lambda_2^1}{\partial y_1} n_1 dl = 0.$$

The reason for $\frac{\partial \lambda_2^1}{\partial y_1}$ being odd in y_2 is that λ_2^1 is odd in y_2 (up to a constant). This can be shown using symmetry arguments similar to those presented in Section 3.2.1 and requires the forcing term on the right-hand side of Poisson's

1 Denoting $f(y_1, y_2) = -\lambda_1^1(-y_1, y_2)$ we have:

$$\nabla_y^2 f(y_1, y_2) = -(\frac{\partial^2 \lambda_1^1}{\partial y_1^2}(-y_1, y_2) + \frac{\partial^2 \lambda_1^1}{\partial y_2^2}(-y_1, y_2)) =$$

$$-\frac{\partial^2 \lambda_1^0}{\partial y_1^2}(-y_1, y_2) = \frac{\partial^2 \lambda_1^0}{\partial y_1^2}(y_1, y_2),$$

provided $\frac{\partial^2 \lambda_1^0}{\partial y_1^2}$ is odd in y_1. f satisfies the same conditions as λ_1^1, and uniqueness yields that λ_1^1 is odd in y_1 (up to a constant).

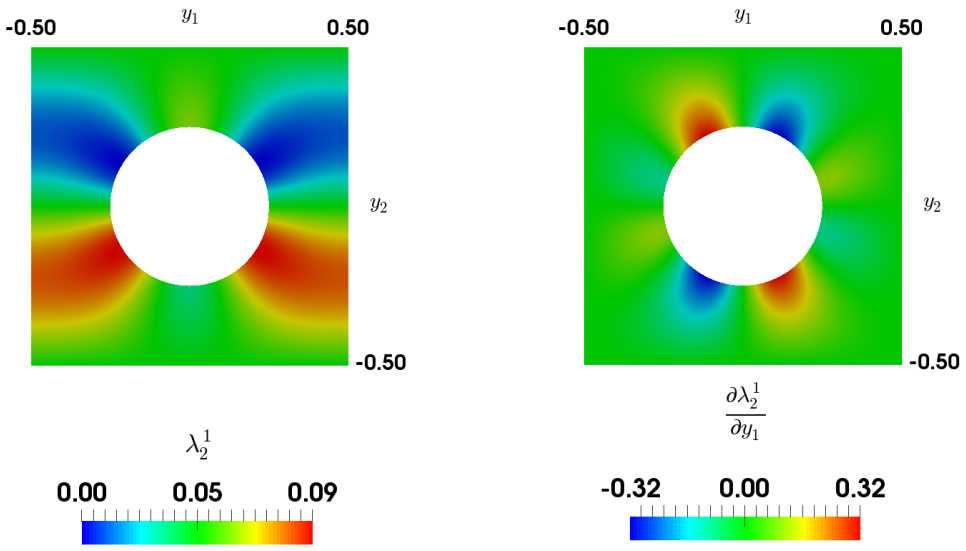


Figure 5.5.: The solution of the λ_2^1 (unit cell) problem and its derivative with respect to y_1.

equation for λ_2^1 (i.e. $\frac{\partial^2 \lambda_2^0}{\partial y_1^2}$) to be odd in y_2 [2]. This is caused by the already shown fact that $\frac{\partial \lambda_2^0}{\partial y_1}$ is odd in y_2.
Therefore, none of the new terms changes the homogenised equation.

Case $\gamma \in (\frac{1}{3}, \frac{1}{2})$

At $O(1)$, we get two new terms:

$$-2x_3\mu\frac{\partial^2 u_{2-\gamma}}{\partial y_1^2}$$

and:

$$+3x_3^2\mu^2\frac{\partial^2 u_{2-2\gamma}}{\partial y_1^2}.$$

From $O(\epsilon^{-2\gamma})$ in the continuity equation (260), we get:

$$\nabla_y^2 u_{2-2\gamma} = 0,$$

2 Denoting $g(y_1, y_2) = -\lambda_2^1(y_1, -y_2)$ we have:

$$\nabla_y^2 g(y_1, y_2) = -(\frac{\partial^2 \lambda_2^1}{\partial y_1^2}(y_1, -y_2) + \frac{\partial^2 \lambda_2^1}{\partial y_2^2}(y_1, -y_2)) =$$

$$-\frac{\partial^2 \lambda_2^0}{\partial y_1^2}(y_1, -y_2) = \frac{\partial^2 \lambda_2^0}{\partial y_1^2}(y_1, y_2),$$

provided $\frac{\partial^2 \lambda_2^0}{\partial y_1^2}$ is odd in y_2. g satisfies the same conditions as λ_2^1, and uniqueness yields that λ_2^1 is odd in y_2 (up to a constant).

and at $O(\epsilon^{2-2\gamma})$ in the boundary condition (256), we find:

$$\nabla_y u_{2-2\gamma} \cdot \hat{\boldsymbol{n}} = \nabla_x u_{1-2\gamma} \cdot \hat{\boldsymbol{n}},$$

which suggests that:

$$u_{2-2\gamma} = \nabla_x u_{1-2\gamma} \cdot \boldsymbol{\lambda^0} + f_{2-2\gamma}(t, \boldsymbol{x}).$$

From $O(\epsilon^{-\gamma})$ in the continuity equation (260), we get:

$$\nabla_y^2 u_{2-\gamma} = 2x_3\mu \frac{\partial^2 u_{2-2\gamma}}{\partial y_1^2} = 2x_3\mu \nabla_x u_{1-2\gamma} \cdot (\frac{\partial^2 \lambda_1^0}{\partial y_1^2}, \frac{\partial^2 \lambda_2^0}{\partial y_1^2}),$$

and at $O(2-\gamma)$ in the boundary condition (256), we find:

$$\nabla_y u_{2-\gamma} \cdot \hat{\boldsymbol{n}} = \nabla_x u_{1-\gamma} \cdot \hat{\boldsymbol{n}},$$

which implies:

$$u_{2-\gamma} = \boldsymbol{\lambda^0} \cdot \nabla_x u_{1-\gamma} + 2\mu x_3 \boldsymbol{\lambda^1} \cdot \nabla_x u_{1-2\gamma} + f_{2-\gamma}(t, \boldsymbol{x}).$$

Therefore, the new terms become:

$$-2x_3\mu \frac{\partial^2 u_{2-\gamma}}{\partial y_1^2} = -2x_3\mu \{\frac{\partial^2 \boldsymbol{\lambda^0}}{\partial y_1^2} \cdot \nabla_x u_{1-\gamma} + 2\mu x_3 \frac{\partial^2 \boldsymbol{\lambda^1}}{\partial y_1^2} \cdot \nabla_x u_{1-2\gamma}\}$$

and

$$+3x_3^2\mu^2 \frac{\partial^2 u_{2-2\gamma}}{\partial y_1^2} = +3x_3^2\mu^2 \nabla_x u_{1-2\gamma} \cdot \frac{\partial^2 \boldsymbol{\lambda^0}}{\partial y_1^2}.$$

As shown in the previous section, all these terms integrate out to 0. Moreover, note that after substituting $\gamma = \frac{1}{2}$, we recover the results from the previous section. Because of these analogies, there is no need to do the $\gamma = \frac{1}{N}$ cases separately, and from now onwards, we study γ belonging to intervals that include their greater endpoint.

Case $\gamma \in (\frac{1}{4}, \frac{1}{3}]$

At $O(1)$, we get three new terms, namely $-2x_3\mu \frac{\partial^2 u_{2-\gamma}}{\partial y_1^2}$, $+3x_3^2\mu^2 \frac{\partial^2 u_{2-2\gamma}}{\partial y_1^2}$ and $-4x_3^3\mu^3 \frac{\partial^2 u_{2-3\gamma}}{\partial y_1^2}$.

At $O(\epsilon^{-3\gamma})$ in the continuity equation (260), we get:

$$\nabla_y^2 u_{2-3\gamma} = 0,$$

and at $O(\epsilon^{2-3\gamma})$ in the boundary condition (260), we find:

$$\nabla_y u_{2-3\gamma} \cdot \hat{\boldsymbol{n}} = -\nabla_x u_{1-3\gamma} \cdot \hat{\boldsymbol{n}},$$

which means:

$$u_{2-3\gamma} = \boldsymbol{\lambda^0} \cdot \nabla_x u_{1-3\gamma} + f_{2-3\gamma}.$$

At $O(\epsilon^{-2\gamma})$ in the continuity equation (260), we get:

$$\nabla_y^2 u_{2-2\gamma} = 2x_3\mu \frac{\partial^2 u_{2-3\gamma}}{\partial y_1^2} = 2x_3\mu \nabla_x u_{1-3\gamma} \cdot \frac{\partial^2 \boldsymbol{\lambda^0}}{\partial y_1^2},$$

and at $O(\epsilon^{2-2\gamma})$ in the boundary condition (256), we find:

$$\nabla_y u_{2-2\gamma} \cdot \hat{\boldsymbol{n}} = -\nabla_x u_{1-2\gamma} \cdot \hat{\boldsymbol{n}},$$

which implies:

$$u_{2-2\gamma} = \boldsymbol{\lambda^0} \cdot \nabla_x u_{1-2\gamma} + 2x_3\mu \nabla_x u_{1-3\gamma} \cdot \boldsymbol{\lambda^1} + f_{2-2\gamma}.$$

At $O(\epsilon^{-\gamma})$ in the continuity equation (260), we find:

$$\nabla_y^2 u_{2-\gamma} = 2x_3\mu \frac{\partial^2 u_{2-2\gamma}}{\partial y_1^2} - 3x_3^2\mu^2 \frac{\partial^2 u_{2-3\gamma}}{\partial y_1^2} =$$

$$2x_3\mu \{ \frac{\partial^2 \boldsymbol{\lambda^0}}{\partial y_1^2} \cdot \nabla_x u_{1-2\gamma} + 2x_3\mu \nabla_x u_{1-3\gamma} \cdot \frac{\partial^2 \boldsymbol{\lambda^1}}{\partial y_1^2} \} - 3x_3^2\mu^2 \frac{\partial^2 \boldsymbol{\lambda^0}}{\partial y_1^2} \cdot \nabla_x u_{1-3\gamma},$$

and from $O(\epsilon^{2-\gamma})$ in the boundary condition (256), we get:

$$\nabla_y u_{2-\gamma} \cdot \hat{\boldsymbol{n}} = -\nabla_x u_{1-\gamma} \cdot \hat{\boldsymbol{n}},$$

which leads to:

$$u_{2-\gamma} = \boldsymbol{\lambda^0} \cdot \nabla_x u_{1-\gamma} + \{2x_3\mu \nabla_x u_{1-2\gamma} - 3x_3^2\mu^2 \nabla_x u_{1-3\gamma}\} \cdot \boldsymbol{\lambda^1} +$$

$$(2x_3\mu)^2 \nabla_x u_{1-3\gamma} \boldsymbol{\lambda^2} + f_{2-\gamma},$$

where $\boldsymbol{\lambda^2} = (\lambda_1^2, \lambda_2^2)$ satisfies continuity equations:

$$\nabla_y^2 \lambda_1^2 = \frac{\partial^2 \lambda_1^1}{\partial y_1^2} \qquad \nabla_y^2 \lambda_2^2 = \frac{\partial^2 \lambda_2^1}{\partial y_1^2} \tag{265}$$

and hair surface boundary conditions:

$$\nabla_y \lambda_1^2 \cdot \hat{\boldsymbol{n}} = 0 = \nabla_y \lambda_2^2 \cdot \hat{\boldsymbol{n}}. \tag{266}$$

Therefore, the three new terms become:

$$-2x_3\mu\frac{\partial^2 u_{2-\gamma}}{\partial y_1^2} = -2x_3\mu\{\frac{\partial^2 \boldsymbol{\lambda^0}}{\partial y_1^2}\cdot\nabla_x u_{1-\gamma}+$$

$$\{2x_3\mu\nabla_x u_{1-2\gamma} - 3x_3^2\mu^2\nabla_x u_{1-3\gamma}\}\cdot\frac{\partial^2 \boldsymbol{\lambda^1}}{\partial y_1^2} + (2x_3\mu)^2\nabla_x u_{1-3\gamma}\frac{\partial^2 \boldsymbol{\lambda^2}}{\partial y_1^2}\}$$

$$3x_3^2\mu^2\frac{\partial^2 u_{2-2\gamma}}{\partial y_1^2} = 3x_3^2\mu^2\{\frac{\partial^2 \boldsymbol{\lambda^0}}{\partial y_1^2}\cdot\nabla_x u_{1-2\gamma} + 2x_3\mu\nabla_x u_{1-3\gamma}\cdot\frac{\partial^2 \boldsymbol{\lambda^1}}{\partial y_1^2}\}$$

and

$$-4x_3^3\mu^3\frac{\partial^2 u_{2-3\gamma}}{\partial y_1^2} = -4x_3^3\mu^3\frac{\partial^2 \boldsymbol{\lambda^0}}{\partial y_1^2}\cdot\nabla_x u_{1-3\gamma}$$

We know that the terms containing $\frac{\partial^2 \boldsymbol{\lambda^0}}{\partial y_1^2}$ or $\frac{\partial^2 \boldsymbol{\lambda^1}}{\partial y_1^2}$ integrate out to 0. Therefore, the only possible change in the homogenised equation might come from the $\frac{\partial^2 \boldsymbol{\lambda^2}}{\partial y_1^2}$ term. However, the situation here is analogous to the previous section. To see that, we compare the continuity equations (263) with the continuity equations (265).

To show that the $\frac{\partial^2 \lambda_1^1}{\partial y_1^2}$ term integrates out to 0, it was sufficient to show that $\frac{\partial^2 \lambda_1^0}{\partial y_1^2}$ is odd in y_1. We further showed that $\frac{\partial \lambda_1^1}{\partial y_1}$ is even in y_1, which implies that $\frac{\partial^2 \lambda_1^1}{\partial y_1^2}$ is odd in y_1, and this is the right-hand-side forcing term in the continuity equation for λ_1^2 (265). As the hair boundary conditions are unchanged (compare Equation (264) with Equation (266)), and the periodicity conditions remain the same, we conclude that the $\frac{\partial^2 \lambda_1^2}{\partial y_1^2}$ term integrates out to 0.

To show that the $\frac{\partial^2 \lambda_2^1}{\partial y_1^2}$ term yields 0 after integration, it was sufficient to show that $\frac{\partial^2 \lambda_2^0}{\partial y_1^2}$ is odd in y_2. In the same section we also showed that $\frac{\partial \lambda_2^1}{\partial y_1}$ is odd in y_2, which implies that $\frac{\partial^2 \lambda_2^1}{\partial y_1^2}$ is odd in y_2 as well, and this is the right-hand side of the continuity equation for λ_2^2 (265). By the same reasoning, we get that the $\frac{\partial^2 \lambda_2^2}{\partial y_1^2}$ term integrates out to 0.

Having gained some insight into the problem, we now proceed with the general case.

Case $\gamma \in (\frac{1}{N+1}, \frac{1}{N}]$

At $O(1)$ in the continuity equation (260), we get N new terms: $-2x_3\mu\frac{\partial^2 u_{2-\gamma}}{\partial y_1^2}$, $+3x_3^2\mu^2\frac{\partial^2 u_{2-2\gamma}}{\partial y_1^2}$,..., $(-1)^N(N+1)x_3^N\mu^N\frac{\partial^2 u_{2-N\gamma}}{\partial y_1^2}$. This is caused by a fact that for

$\gamma \in (\frac{1}{N+1}, \frac{1}{N}]$, we have $2 - N\gamma \in [1, \frac{N+2}{N+1})$, which is an acceptable range for α (recall that we need $\alpha \geq 1$ - see Equation (260)). However, $2 - (N+1)\gamma \in [\frac{N-1}{N}, 1)$, and we have already shown that the terms u_α for $\alpha < 1$ are independent of the microscale.

From $O(\epsilon^{-N\gamma})$ in the continuity equation (260), we get:

$$\nabla_y^2 u_{2-N\gamma} = 0,$$

and at $O(\epsilon^{2-N\gamma})$ in the boundary condition (256), we find:

$$\nabla_y u_{2-N\gamma} \cdot \hat{\boldsymbol{n}} = -\nabla_x u_{1-N\gamma} \cdot \hat{\boldsymbol{n}},$$

which means:

$$u_{2-N\gamma} = \boldsymbol{\lambda^0} \cdot \nabla_x u_{1-N\gamma} + f_{2-N\gamma}.$$

From $O(\epsilon^{-(N-1)\gamma})$ in the continuity equation (260), we get:

$$\nabla_y^2 u_{2-(N-1)\gamma} = 2x_3\mu \frac{\partial^2 u_{2-N\gamma}}{\partial y_1^2} = 2x_3\mu \nabla_x u_{1-N\gamma} \cdot \frac{\partial^2 \boldsymbol{\lambda^0}}{\partial y_1^2},$$

and at $O(\epsilon^{2-(N-1)\gamma})$ in the boundary condition (256), we find:

$$\nabla_y u_{2-(N-1)\gamma} \cdot \hat{\boldsymbol{n}} = -\nabla_x u_{1-(N-1)\gamma} \cdot \hat{\boldsymbol{n}},$$

which implies:

$$u_{2-(N-1)\gamma} = \boldsymbol{\lambda^0} \cdot \nabla_x u_{1-(N-1)\gamma} + 2x_3\mu \nabla_x u_{1-N\gamma} \cdot \boldsymbol{\lambda^1} + f_{2-(N-1)\gamma}.$$

From $O(\epsilon^{-(N-2)\gamma})$ in the continuity equation (260), we know:

$$\nabla_y^2 u_{2-(N-2)\gamma} = 2x_3\mu \frac{\partial^2 u_{2-(N-1)\gamma}}{\partial y_1^2} - 3x_3^2\mu^2 \frac{\partial^2 u_{2-N\gamma}}{\partial y_1^2} =$$

$$2x_3\mu \{ \frac{\partial^2 \boldsymbol{\lambda^0}}{\partial y_1^2} \cdot \nabla_x u_{1-(N-1)\gamma} + 2x_3\mu \nabla_x u_{1-N\gamma} \cdot \frac{\partial^2 \boldsymbol{\lambda^1}}{\partial y_1^2} \} -$$

$$3x_3^2\mu^2 \frac{\partial^2 \boldsymbol{\lambda^0}}{\partial y_1^2} \cdot \nabla_x u_{1-N\gamma},$$

and at $O(\epsilon^{2-(N-2)\gamma})$ in the boundary condition (256), we uncover:

$$\nabla_y u_{2-(N-2)\gamma} \cdot \hat{\boldsymbol{n}} = -\nabla_x u_{1-(N-2)\gamma} \cdot \hat{\boldsymbol{n}},$$

which leads to:

$$u_{2-(N-2)\gamma} = \boldsymbol{\lambda^0} \cdot \nabla_x u_{1-(N-2)\gamma} + \{2x_3\mu\nabla_x u_{1-(N-1)\gamma} - 3x_3^2\mu^2\nabla_x u_{1-N\gamma}\} \cdot \boldsymbol{\lambda^1} +$$

$$(2x_3\mu)^2\nabla_x u_{1-N\gamma}\boldsymbol{\lambda^2} + f_{2-(N-2)\gamma}.$$

At $O(\epsilon^{-(N-3)\gamma})$ in the continuity equation (260), we find:

$$\nabla_y^2 u_{2-(N-3)\gamma} = 2x_3\mu\frac{\partial^2 u_{2-(N-2)\gamma}}{\partial y_1^2} - 3x_3^2\mu^2\frac{\partial^2 u_{2-(N-1)\gamma}}{\partial y_1^2} + 4x_3^3\mu^3\frac{\partial^2 u_{2-N\gamma}}{\partial y_1^2} =$$

$$2x_3\mu\{\frac{\partial^2\boldsymbol{\lambda^0}}{\partial y_1^2} \cdot \nabla_x u_{1-(N-2)\gamma} + \{2x_3\mu\nabla_x u_{1-(N-1)\gamma} -$$

$$3x_3^2\mu^2\nabla_x u_{1-N\gamma}\} \cdot \frac{\partial^2\boldsymbol{\lambda^1}}{\partial y_1^2} + (2x_3\mu)^2\nabla_x u_{1-N\gamma}\frac{\partial^2\boldsymbol{\lambda^2}}{\partial y_1^2}\} -$$

$$3x_3^2\mu^2\{\frac{\partial^2\boldsymbol{\lambda^0}}{\partial y_1^2} \cdot \nabla_x u_{1-(N-1)\gamma} + 2x_3\mu\nabla_x u_{1-N\gamma} \cdot \frac{\partial^2\boldsymbol{\lambda^1}}{\partial y_1^2}\} +$$

$$4x_3^3\mu^3\frac{\partial^2\boldsymbol{\lambda^0}}{\partial y_1^2} \cdot \nabla_x u_{1-N\gamma},$$

and from $O(\epsilon^{2-(N-3)\gamma})$ in the boundary condition (256), we get:

$$\nabla_y u_{2-(N-3)\gamma} \cdot \hat{\boldsymbol{n}} = -\nabla_x u_{1-(N-3)\gamma} \cdot \hat{\boldsymbol{n}}.$$

We can write the form of $u_{2-(N-3)\gamma}$ in the usual way, introducing $\boldsymbol{\lambda^3}$ with zero-flux boundary conditions at the hair surface, the periodicity conditions at $y_1, y_2 = \pm\frac{1}{2}$, and continuity equations:

$$\nabla_y^2\lambda_1^3 = \frac{\partial^2\lambda_1^2}{\partial y_1^2} \qquad \nabla_y^2\lambda_2^3 = \frac{\partial^2\lambda_2^2}{\partial y_1^2}$$

in the unit cell C.

Uncovering the behaviour of every next term is becoming more and more tedious. We could attempt to write a general $u_{2-i\gamma}$ term. However, this is not necessary. Let us, instead, write down the new terms discussed so far:

$$(-1)^N(N+1)x_3^N\mu^N\frac{\partial^2 u_{2-N\gamma}}{\partial y_1^2} = (-1)^N(N+1)x_3^N\mu^N\frac{\partial^2\boldsymbol{\lambda^0}}{\partial y_1^2} \cdot \nabla_x u_{1-N\gamma}$$

$$(-1)^{N-1}Nx_3^{N-1}\mu^{N-1}\frac{\partial^2 u_{2-(N-1)\gamma}}{\partial y_1^2} =$$

$$(-1)^{N-1}Nx_3^{N-1}\mu^{N-1}\{\frac{\partial^2\boldsymbol{\lambda^0}}{\partial y_1^2} \cdot \nabla_x u_{1-(N-1)\gamma} +$$

$$2x_3\mu\nabla_x u_{1-N\gamma}\cdot\frac{\partial^2\boldsymbol{\lambda^1}}{\partial y_1^2}\}$$

$$(-1)^{N-2}(N-1)x_3^{N-2}\mu^{N-2}\frac{\partial^2 u_{2-(N-2)\gamma}}{\partial y_1^2}=$$

$$(-1)^{N-2}(N-1)x_3^{N-2}\mu^{N-2}\{\frac{\partial^2\boldsymbol{\lambda^0}}{\partial y_1^2}\cdot\nabla_x u_{1-(N-2)\gamma}+$$

$$\{2x_3\mu\nabla_x u_{1-(N-1)\gamma}-3x_3^2\mu^2\nabla_x u_{1-N\gamma}\}\cdot\frac{\partial^2\boldsymbol{\lambda^1}}{\partial y_1^2}+(2x_3\mu)^2\nabla_x u_{1-N\gamma}\frac{\partial^2\boldsymbol{\lambda^2}}{\partial y_1^2}\}$$

$$(-1)^{N-3}(N-2)x_3^{N-3}\mu^{N-3}\frac{\partial^2 u_{2-(N-3)\gamma}}{\partial y_1^2}=$$

$$(-1)^{N-3}(N-2)x_3^{N-3}\mu^{N-3}\{\frac{\partial^2\boldsymbol{\lambda^0}}{\partial y_1^2}\cdot\nabla_x u_{1-(N-3)\gamma}+$$

$$\{2x_3\mu\nabla_x u_{1-(N-2)\gamma}-3x_3^2\mu^2\nabla_x u_{1-(N-1)\gamma}+4x_3^3\mu^3\nabla_x u_{1-N\gamma}\}\cdot\frac{\partial^2\boldsymbol{\lambda^1}}{\partial y_1^2}+$$

$$\frac{\partial^2\boldsymbol{\lambda^2}}{\partial y_1^2}\cdot\{-2(2\mu x_3 3\mu^2 x_3^2\nabla_x u_{1-N\gamma})+(2\mu x_3)^2\nabla_x u_{1-(N-1)\gamma}\}+$$

$$\frac{\partial^2\boldsymbol{\lambda^3}}{\partial y_1^2}\cdot\nabla_x u_{1-N\gamma}(2x_3\mu)^3\}$$

...

It is not crucial to write all the new terms explicitly. The key idea is that all microscale contributions contained in these new terms are of a form $\frac{\partial^2\boldsymbol{\lambda^i}}{\partial y_1^2}$ for $i\in\{0,1,2,...,N-1\}$. We now show that all these terms integrate out to 0.

CHANGES TO THE HOMOGENISED EQUATION We have already shown that the $\frac{\partial^2\boldsymbol{\lambda^0}}{\partial y_1^2}$ and $\frac{\partial^2\boldsymbol{\lambda^1}}{\partial y_1^2}$ terms integrate out to 0. For $m\geq 2$, we have:

$$\nabla_y^2\boldsymbol{\lambda^m}=\frac{\partial^2\boldsymbol{\lambda^{m-1}}}{\partial y_1^2}$$

equipped with the periodic boundary conditions and:

$$\nabla_y\lambda_1^m\cdot\hat{\boldsymbol{n}}=0=\nabla\lambda_2^m\cdot\hat{\boldsymbol{n}}$$

as the hair boundary conditions.

As we saw in previous sections, if $\frac{\partial^2\lambda_1^{m-1}}{\partial y_1^2}$ is odd in y_1, then $\frac{\partial^2\lambda_1^m}{\partial y_1^2}$ is odd in y_1 as well. As we have shown that $\frac{\partial\lambda_1^0}{\partial y_1}$ is even in y_1, it follows that $\frac{\partial^2\lambda_1^0}{\partial y_1^2}$ is odd in y_1,

and thus $\frac{\partial^2 \lambda_1^m}{\partial y_1^2}$ for any $m \in \mathbb{N}_0$ is odd in y_1 too. As a consequence, all the $\frac{\partial^2 \lambda_1^m}{\partial y_1^2}$ terms give 0 after the integration.

Similarly, we saw that if $\frac{\partial^2 \lambda_2^{m-1}}{\partial y_1^2}$ is odd in y_2, then $\frac{\partial^2 \lambda_2^m}{\partial y_1^2}$ is odd in y_2 as well. As we have shown that $\frac{\partial \lambda_2^0}{\partial y_1}$ is odd in y_2, it follows that $\frac{\partial^2 \lambda_2^0}{\partial y_1^2}$ is odd in y_2, and thus $\frac{\partial^2 \lambda_2^m}{\partial y_1^2}$ for any $m \in \mathbb{N}_0$ is odd in y_2 too. As a consequence, all the $\frac{\partial^2 \lambda_2^m}{\partial y_1^2}$ terms integrate out to 0.

To summarise, we uncovered infinitely many new terms impacting $O(1)$ in the continuity equation as $\gamma \to 0$ (i.e. as δ becomes larger and larger compared with ϵ). This condition can be interpreted as increasing the length of the root hairs (while still keeping it much smaller than the root radius and much larger than the distance between the hairs). We have also shown that all these new terms yield 0 after integration in the microscopic variables, and therefore, the homogenised equation remains the same.

5.3 $\delta = O(1)$

Here, we study the case where the root hair length is comparable to the root radius. We will not be able to use all the Taylor series from previous sections, as we now have $\delta = \frac{h_1}{r_0} = O(1)$. Having unrolled the root surface, we arrived at Equation (246), and as we cannot expand the $\frac{\delta}{1+\delta x_3}$ as well as $\frac{1}{(1+\delta x_3)^2}$ terms now, we only downscale to the microscopic variables, and get:

$$\frac{\partial u}{\partial t} = \frac{\partial^2 u}{\partial x_3^2} + \frac{\delta}{1+\delta x_3}\frac{\partial u}{\partial x_3} + \frac{1}{(1+\delta x_3)^2}\frac{\partial^2 u}{\partial y_1^2}\frac{1}{\epsilon^2} + \frac{\partial^2 u}{\partial y_2^2}\frac{1}{\epsilon^2}. \tag{267}$$

Moreover, we arrived at the hair surface boundary condition (252). Even though we do not assume $\delta \ll 1$ here, we are still interested in the $\epsilon \ll 1$ limit. Therefore (and because $\delta = O(1)$), we can still use the Taylor expansions, and we end up with:

$$\begin{aligned} U\epsilon^2 u =& \frac{\partial u}{\partial x_3}(\delta\epsilon^2 y_1^2 + x_3\delta^2\epsilon^2 y_1^2 + O(\epsilon^4)) + \\ & \frac{\partial u}{\partial y_1}(y_1 - \frac{2}{3}\epsilon^2\delta^2 y_1^3 + O(\epsilon^4)) + \frac{\partial u}{\partial y_2}y_2. \end{aligned} \tag{268}$$

5.3 $\delta = O(1)$

We wish to uncover, what a microscale geometry looks like in this case. From previous discussions, we know:

$$w_3^2 + w_2^2 = (\frac{r_1}{h_1})^2,$$

which is equivalent to:

$$w_3^2 + r_w^2 \sin^2 \theta_w = (\frac{r_1}{h_1})^2.$$

Transforming this to the rolled-out coordinates gives:

$$x_2^2 + (\frac{1}{\delta} + x_3)^2 \sin^2 \delta x_1 = (\frac{r_1}{h_1})^2,$$

and downscaling leads to:

$$\epsilon^2 y_2^2 + (\frac{1}{\delta} + x_3)^2 \sin^2 \delta \epsilon y_1 = (\frac{r_1}{h})^2 \epsilon^2.$$

This can (using a Taylor expansion as we assume $\epsilon \ll 1$) be written as:

$$\epsilon^2 y_2^2 + (\frac{1}{\delta} + x_3)^2 \{(\delta \epsilon y_1)^2 + O(\epsilon^4)\} = (\frac{r_1}{h})^2 \epsilon^2,$$

and dividing by ϵ^2, we conclude:

$$y_2^2 + (\frac{1}{\delta} + x_3)^2 \{(\delta y_1)^2 + O(\epsilon^2)\} = (\frac{r_1}{h})^2.$$

In the $\epsilon \to 0$ limit, we get:

$$y_2^2 + (1 + \delta x_3)^2 y_1^2 = (\frac{r_1}{h})^2,$$

which can be rewritten as:

$$\frac{y_2^2}{(\frac{r_1}{h})^2} + \frac{y_1^2}{(\frac{r_1}{h}\frac{1}{1+\delta x_3})^2} = 1, \tag{269}$$

and we know that this is an equation for an ellipse with a semi-major axis of length $\frac{r_1}{h}$ oriented in the y_2-direction and a semi-minor axis of length $\frac{r_1}{h}\frac{1}{1+\delta x_3}$ oriented in the y_1-direction (see Figure 5.11). Note that we again denote the uptaking part of the microscale boundary described by Equation (269) by U. As we know that our ellipse is given by the equation:

$$G(y_1, y_2) = \frac{y_2^2}{(\frac{r_1}{h})^2} + \frac{y_1^2}{(\frac{r_1}{h}\frac{1}{1+\delta x_3})^2} - 1 = 0,$$

we can easily compute:

$$\nabla_y G = (\frac{2y_1}{(\frac{r_1}{h}\frac{1}{1+\delta x_3})^2}, \frac{2y_2}{(\frac{r_1}{h})^2})$$

and conclude that a unit vector normal to this ellipse at a point (y_1, y_2) is proportional to a vector $((1+\delta x_3)^2 y_1, y_2)$; in other words:

$$\hat{\boldsymbol{n}} = \beta(y_1, y_2, x_3)((1+\delta x_3)^2 y_1, y_2), \tag{270}$$

where:

$$\beta(y_1, y_2, x_3) = -((1+\delta x_3)^4 y_1^2 + y_2^2)^{-\frac{1}{2}} \tag{271}$$

(for an outward pointing unit normal vector, β must be taken negative). Now, everything is in place for us to start with the homogenisation procedure.
Using the two-scale operators in the continuity equation (267) (multiplied by ϵ^2), we get:

$$\epsilon^2\frac{\partial u}{\partial t} = \epsilon^2\frac{\partial^2 u}{\partial x_3^2} + \epsilon^2\frac{\delta}{1+\delta x_3}\frac{\partial u}{\partial x_3} + \frac{1}{(1+\delta x_3)^2}\{\frac{\partial^2 u}{\partial y_1^2} + 2\epsilon\frac{\partial^2 u}{\partial y_1 \partial x_1} + \epsilon^2\frac{\partial^2 u}{\partial x_1^2}\} +$$
$$\{\frac{\partial^2 u}{\partial y_2^2} + 2\epsilon\frac{\partial^2 u}{\partial y_2 \partial x_2} + \epsilon^2\frac{\partial^2 u}{\partial x_2^2}\},$$

and using these operators in the boundary condition (268), we conclude:

$$U\epsilon^2 u = \frac{\partial u}{\partial x_3}(\delta\epsilon^2 y_1^2 + x_3\delta^2\epsilon^2 y_1^2 + O(\epsilon^4)) +$$
$$\{\frac{\partial u}{\partial y_1} + \epsilon\frac{\partial u}{\partial x_1}\}(y_1 - \frac{2}{3}\epsilon^2\delta^2 y_1^3 + O(\epsilon^4)) + \{\frac{\partial u}{\partial y_2} + \epsilon\frac{\partial u}{\partial x_2}\}y_2.$$

Assuming the usual two-scale ansatz:

$$u = u_0 + \epsilon u_1 + \epsilon^2 u_2 + o(\epsilon^2),$$

we get a continuity equation:

$$\begin{aligned}
&\epsilon^2\frac{\partial(u_0 + o(1))}{\partial t} = \epsilon^2\frac{\partial^2(u_0 + o(1))}{\partial x_3^2} + \epsilon^2\frac{\delta}{1+\delta x_3}\frac{\partial(u_0 + o(1))}{\partial x_3} + \\
&\frac{1}{(1+\delta x_3)^2}\{\frac{\partial^2(u_0 + \epsilon u_1 + \epsilon^2 u_2 + o(\epsilon^2))}{\partial y_1^2} + 2\epsilon\frac{\partial^2(u_0 + \epsilon u_1 + o(\epsilon))}{\partial y_1 \partial x_1} + \\
&\epsilon^2\frac{\partial^2(u_0 + o(1))}{\partial x_1^2}\} + \\
&\{\frac{\partial^2(u_0 + \epsilon u_1 + \epsilon^2 u_2 + o(\epsilon^2))}{\partial y_2^2} + 2\epsilon\frac{\partial^2 u_0 + \epsilon u_1 + o(\epsilon)}{\partial y_2 \partial x_2} + \epsilon^2\frac{\partial^2(u_0 + o(1))}{\partial x_2^2}\}
\end{aligned} \tag{272}$$

and a hair boundary condition:

$$\begin{aligned} &U\epsilon^2(u_0 + o(1)) = (\delta y_1^2 + x_3\delta^2 y_1^2 + O(\epsilon^2))\epsilon^2 \frac{\partial(u_0 + o(1))}{\partial x_3} + \\ &(y_1 - \frac{2}{3}\epsilon^2\delta^2 y_1^3 + O(\epsilon^4))\{\frac{\partial(u_0 + \epsilon u_1 + \epsilon^2 u_2 + o(\epsilon^2))}{\partial y_1} + \\ &\epsilon\frac{\partial(u_0 + \epsilon u_1 + o(\epsilon))}{\partial x_1}\} + \\ &y_2\{\frac{\partial(u_0 + \epsilon u_1 + \epsilon^2 u_2 + o(\epsilon^2))}{\partial y_2} + \epsilon\frac{\partial(u_0 + \epsilon u_1 + o(\epsilon))}{\partial x_2}\}. \end{aligned} \tag{273}$$

5.3.1 *Leading order*

At $O(1)$ in the continuity equation (272), we get:

$$0 = \frac{1}{(1+\delta x_3)^2}\frac{\partial^2 u_0}{\partial y_1^2} + \frac{\partial^2 u_0}{\partial y_2^2},$$

and integration over the unit cell gives:

$$0 = \int_C \nabla_y \cdot (\frac{1}{(1+\delta x_3)^2}\frac{\partial u_0}{\partial y_1}, \frac{\partial u_0}{\partial y_2})dS = \int_{\partial C} (\frac{1}{(1+\delta x_3)^2}\frac{\partial u_0}{\partial y_1}, \frac{\partial u_0}{\partial y_2}) \cdot \hat{\boldsymbol{n}} dl =$$

$$\int_U (\frac{1}{(1+\delta x_3)^2}\frac{\partial u_0}{\partial y_1}, \frac{\partial u_0}{\partial y_2}) \cdot ((1+\delta x_3)^2 y_1, y_2)\beta(y_1, y_2, x_3)dl =$$

$$\int_U (y_1\frac{\partial u_0}{\partial y_1} + y_2\frac{\partial u_0}{\partial y_2})\beta(y_1, y_2, x_3)dl,$$

where we first used the divergence theorem, then the imposed periodic boundary conditions, and finally Equation (270). $O(1)$ in the boundary condition reads:

$$y_1\frac{\partial u_0}{\partial y_1} + y_2\frac{\partial u_0}{\partial y_2} = 0,$$

which proves consistency between the continuity equation and the hair boundary condition at this order. As before, u_0 independent of the microscale satisfies the continuity equation as well as all the boundary conditions at this order. Analogous to what we did in Section 3.2.1, one could show that this solution is unique (up to a constant). We omit this proof for the sake of brevity, and the same applies to the next orders.

5.3.2 $O(\epsilon)$

At $O(\epsilon)$ in the continuity equation (using the information from $O(1)$), we get:

$$0 = \frac{1}{(1+\delta x_3)^2}\frac{\partial^2 u_1}{\partial y_1^2} + \frac{\partial^2 u_1}{\partial y_2^2},$$

and at $O(\epsilon)$ in the hair boundary condition, we find:

$$y_1\frac{\partial u_1}{\partial y_1} + y_2\frac{\partial u_1}{\partial y_2} = -y_1\frac{\partial u_0}{\partial x_1} - y_2\frac{\partial u_0}{\partial x_2}.$$

Therefore, we use an ansatz:

$$u_1(t, y_1, y_2, \boldsymbol{x}) = \nabla_x u_0 \cdot \boldsymbol{\chi}(y_1, y_2; x_3) + f_1(t, \boldsymbol{x}),$$

where $\boldsymbol{\chi} = (\chi_1, \chi_2, 0)$. Note that the unit cell geometry is parameterised by x_3 here, because the length of the semi-minor axis of the ellipse is dependent on x_3. Substituting this ansatz into the continuity equation at this order gives:

$$(\frac{1}{(1+\delta x_3)^2}\frac{\partial^2 \boldsymbol{\chi}}{\partial y_1^2} + \frac{\partial^2 \boldsymbol{\chi}}{\partial y_2^2}) \cdot \nabla_x u_0 = 0,$$

which is satisfied by imposing:

$$\frac{1}{(1+\delta x_3)^2}\frac{\partial^2 \boldsymbol{\chi}}{\partial y_1^2} + \frac{\partial^2 \boldsymbol{\chi}}{\partial y_2^2} = 0. \tag{274}$$

Substituting the ansatz into the boundary condition at this order yields:

$$(y_1\frac{\partial \boldsymbol{\chi}}{\partial y_1} + y_2\frac{\partial \boldsymbol{\chi}}{\partial y_2}) \cdot \nabla_x u_0 = (-y_1, -y_2) \cdot \nabla_x u_0,$$

from which we get:

$$\beta(y_1, y_2; x_3)((1+\delta x_3)^2 y_1 \frac{1}{(1+\delta x_3)^2}\frac{\partial \boldsymbol{\chi}}{\partial y_1} + y_2\frac{\partial \boldsymbol{\chi}}{\partial y_2}) \cdot \nabla_x u_0 =$$

$$\beta(y_1, y_2; x_3)(-y_1, y_2) \cdot \nabla_x u_0.$$

This yields:

$$\hat{\boldsymbol{n}} \cdot (\frac{1}{(1+\delta x_3)^2}\frac{\partial \boldsymbol{\chi}}{\partial y_1}, \frac{\partial \boldsymbol{\chi}}{\partial y_2}) = \beta(y_1, y_2, x_3)(-y_1, -y_2). \tag{275}$$

Integrating Equation (274) gives:

$$\boldsymbol{0} = \int_C \nabla \cdot (\frac{1}{(1+\delta x_3)^2}\frac{\partial \boldsymbol{\chi}}{\partial y_1}, \frac{\partial \boldsymbol{\chi}}{\partial y_2}) dS = \int_{\partial C} \hat{\boldsymbol{n}} \cdot (\frac{1}{(1+\delta x_3)^2}\frac{\partial \boldsymbol{\chi}}{\partial y_1}, \frac{\partial \boldsymbol{\chi}}{\partial y_2}) dl =$$

$$\int_U \hat{\boldsymbol{n}} \cdot (\frac{1}{(1+\delta x_3)^2}\frac{\partial \boldsymbol{\chi}}{\partial y_1}, \frac{\partial \boldsymbol{\chi}}{\partial y_2}) dl = \int_U \beta(y_1, y_2, x_3)(-y_1, -y_2) dl,$$

where we first used the divergence theorem, then the imposed periodic boundary conditions on $\boldsymbol{\chi}$, and finally the hair boundary condition (275). Using symmetry arguments, it is straight-forward to show that the integral yields a zero vector. This stems from simple observations that $\beta(y_1, y_2, x_3)$ is even in both y_1 and y_2, whereas $-y_1$ is odd in y_1 and $-y_2$ is odd in y_2. Thus, we have shown consistency between the continuity equation and the hair boundary condition at $O(\epsilon)$. The uniqueness argument is analogous to the one from Section 3.2.1.

5.3.3 $O(\epsilon^2)$

From $O(\epsilon^2)$ in the continuity equation (272), we get:

$$\frac{1}{(1+\delta x_3)^2}\frac{\partial^2 u_2}{\partial y_1^2} + \frac{\partial^2 u_2}{\partial y_2^2} = \frac{\partial u_0}{\partial t} - \frac{\partial^2 u_0}{\partial x_3^2} - \frac{1}{(1+\delta x_3)^2}\frac{\partial^2 u_0}{\partial x_1^2} - \frac{\partial^2 u_0}{\partial x_2^2} - \frac{\delta}{1+\delta x_3}\frac{\partial u_0}{\partial x_3} - \frac{2}{(1+\delta x_3)^2}\frac{\partial^2 u_1}{\partial y_1 \partial x_1} - 2\frac{\partial^2 u_1}{\partial y_2 \partial x_2},$$

which upon integration over the microscale gives:

$$\begin{aligned}\int_C \frac{1}{(1+\delta x_3)^2}\frac{\partial^2 u_2}{\partial y_1^2} + \frac{\partial^2 u_2}{\partial y_2^2} dS = A(x_3)\{\frac{\partial u_0}{\partial t} - \frac{\partial^2 u_0}{\partial x_3^2} - \frac{1}{(1+\delta x_3)^2}\frac{\partial^2 u_0}{\partial x_1^2} - \\ \frac{\partial^2 u_0}{\partial x_2^2} - \frac{\delta}{1+\delta x_3}\frac{\partial u_0}{\partial x_3}\} - 2\{\frac{1}{(1+\delta x_3)^2}(\frac{\partial^2 u_0}{\partial x_1^2}\int_C \frac{\partial \chi_x}{\partial y_1} dS + \\ \frac{\partial^2 u_0}{\partial x_1 \partial x_2}\int_C \frac{\partial \chi_y}{\partial y_1} dS) + (\frac{\partial^2 u_0}{\partial x_1 \partial x_2}\int_C \frac{\partial \chi_x}{\partial y_2} dS + \frac{\partial^2 u_0}{\partial x_2^2}\int_C \frac{\partial \chi_y}{\partial y_2} dS)\}, \quad (276)\end{aligned}$$

where $A(x_3)$ is the surface area of a unit cell at a distance x_3 from the root surface. Using the divergence theorem, the periodicity conditions and the form of the outward pointing unit normal vector, we calculate the left-hand side to be:

$$\int_C \nabla_y \cdot (\frac{1}{(1+\delta x_3)^2}\frac{\partial u_2}{\partial y_1}, \frac{\partial u_2}{\partial y_2}) dS = \int_{\partial C} \hat{\boldsymbol{n}} \cdot (\frac{1}{(1+\delta x_3)^2}\frac{\partial u_2}{\partial y_1}, \frac{\partial u_2}{\partial y_2}) dl =$$

$$\int_U \beta(y_1, y_2, x_3)\{y_1\frac{\partial u_2}{\partial y_1} + y_2\frac{\partial u_2}{\partial y_2}\} dl.$$

Looking at $O(\epsilon^2)$ in the boundary condition (273), we see:

$$y_1\frac{\partial u_2}{\partial y_1} + y_2\frac{\partial u_2}{\partial y_2} = Uu_0 - \delta(1+\delta x_3)y_1^2\frac{\partial u_0}{\partial x_3} - y_1\frac{\partial u_1}{\partial x_1} - y_2\frac{\partial u_1}{\partial x_2},$$

and substituting this into the previous equation gives:

$$\int_C \nabla_y \cdot (\frac{1}{(1+\delta x_3)^2}\frac{\partial u_2}{\partial y_1}, \frac{\partial u_2}{\partial y_2})dS = \int_U \beta(y_1, y_2, x_3)\{Uu_0 - \delta(1+\delta x_3)y_1^2\frac{\partial u_0}{\partial x_3} -$$

$$y_1\frac{\partial u_1}{\partial x_1} - y_2\frac{\partial u_1}{\partial x_2}\}dl = Uu_0\int_U \beta(y_1, y_2, x_3)dl -$$

$$\delta(1+\delta x_3)\frac{\partial u_0}{\partial x_3}\int_U \beta(y_1, y_2, x_3)y_1^2 dl -$$

$$\int_U \beta(y_1, y_2, x_3)\{y_1\frac{\partial f_1}{\partial x_1} + y_2\frac{\partial f_1}{\partial x_2}\}dl - \int_U \beta(y_1, y_2, x_3)((1+\delta x_3)^2 y_1, y_2)\cdot$$

$$(\frac{1}{(1+\delta x_3)^2}(\frac{\partial^2 u_0}{\partial x_1^2}\chi_1 + \frac{\partial^2 u_0}{\partial x_1 \partial x_2}\chi_2), \frac{\partial^2 u_0}{\partial x_1 \partial x_2}\chi_1 + \frac{\partial^2 u_0}{\partial x_2^2}\chi_2)dl.$$

Using symmetry arguments similar to the previous section and the fact that f_1 is independent of the microscale variables, we get:

$$\int_U \beta(y_1, y_2, x_3)\{y_1\frac{\partial f_1}{\partial x_1} - y_2\frac{\partial f_1}{\partial x_2}\}dl = 0,$$

and using the divergence theorem (and the periodic boundary conditions for χ_1 and χ_2), we conclude:

$$\int_C \nabla_y \cdot (\frac{1}{(1+\delta x_3)^2}\frac{\partial u_2}{\partial y_1}, \frac{\partial u_2}{\partial y_2})dS = Uu_0\int_U \beta(y_1, y_2, x_3)dl -$$

$$\delta(1+\delta x_3)\frac{\partial u_0}{\partial x_3}\int_U \beta(y_1, y_2, x_3)y_1^2 dl -$$

$$\int_C \nabla_y \cdot (\frac{1}{(1+\delta x_3)^2}(\frac{\partial^2 u_0}{\partial x_1^2}\chi_1 + \frac{\partial^2 u_0}{\partial x_1 \partial x_2}\chi_2), \frac{\partial^2 u_0}{\partial x_1 \partial x_2}\chi_1 + \frac{\partial^2 u_0}{\partial x_2^2}\chi_2)dS =$$

$$Uu_0\int_U \beta(y_1, y_2, x_3)dl - \delta(1+\delta x_3)\frac{\partial u_0}{\partial x_3}\int_U \beta(y_1, y_2, x_3)y_1^2 dl -$$

$$\int_C \{\frac{1}{(1+\delta x_3)^2}(\frac{\partial^2 u_0}{\partial x_1^2}\frac{\partial \chi_1}{\partial y_1} + \frac{\partial^2 u_0}{\partial x_1 \partial x_2}\frac{\partial \chi_2}{\partial y_1}) + \frac{\partial^2 u_0}{\partial x_1 \partial x_2}\frac{\partial \chi_1}{\partial y_2} + \frac{\partial^2 u_0}{\partial x_2^2}\frac{\partial \chi_2}{\partial y_2}\}dS. \quad (277)$$

Finally, we compare Equation (276) with Equation (277), and get:

$$A(x_3)\{\frac{\partial u_0}{\partial t} - \frac{\partial^2 u_0}{\partial x_3^2} - \frac{1}{(1+\delta x_3)^2}\frac{\partial^2 u_0}{\partial x_1^2} - \frac{\partial^2 u_0}{\partial x_2^2} - \frac{\delta}{1+\delta x_3}\frac{\partial u_0}{\partial x_3}\} -$$

$$2\{\frac{1}{(1+\delta x_3)^2}(\frac{\partial^2 u_0}{\partial x_1^2}\int\limits_C \frac{\partial \chi_1}{\partial y_1}dS + \frac{\partial^2 u_0}{\partial x_1 \partial x_2}\int\limits_C \frac{\partial \chi_2}{\partial y_1}dS) + (\frac{\partial^2 u_0}{\partial x_1 \partial x_2}\int\limits_C \frac{\partial \chi_1}{\partial y_2}dS +$$

$$\frac{\partial^2 u_0}{\partial x_2^2}\int\limits_C \frac{\partial \chi_2}{\partial y_2}dS)\} = Uu_0\int\limits_U \beta(y_1, y_2, x_3)dl -$$

$$\delta(1+\delta x_3)\frac{\partial u_0}{\partial x_3}\int\limits_U \beta(y_1, y_2, x_3)y_1^2 dl -$$

$$\int\limits_C \{\frac{1}{(1+\delta x_3)^2}(\frac{\partial^2 u_0}{\partial x_1^2}\frac{\partial \chi_1}{\partial y_1} + \frac{\partial^2 u_0}{\partial x_1 \partial x_2}\frac{\partial \chi_2}{\partial y_1}) + \frac{\partial^2 u_0}{\partial x_1 \partial x_2}\frac{\partial \chi_1}{\partial y_2} + \frac{\partial^2 u_0}{\partial x_2^2}\frac{\partial \chi_2}{\partial y_2}\}dS,$$

which can also be written as:

$$\frac{\partial u_0}{\partial t} = \frac{\partial^2 u_0}{\partial x_3^2} + \frac{1}{(1+\delta x_3)^2}\frac{\partial^2 u_0}{\partial x_1^2} + \frac{\partial^2 u_0}{\partial x_2^2} + \frac{\delta}{1+\delta x_3}\frac{\partial u_0}{\partial x_3} +$$

$$\frac{1}{A(x_3)}\int\limits_C \{\frac{1}{(1+\delta x_3)^2}(\frac{\partial^2 u_0}{\partial x_1^2}\frac{\partial \chi_1}{\partial y_1} + \frac{\partial^2 u_0}{\partial x_1 \partial x_2}\frac{\partial \chi_2}{\partial y_1}) +$$

$$\frac{\partial^2 u_0}{\partial x_1 \partial x_2}\frac{\partial \chi_1}{\partial y_2} + \frac{\partial^2 u_0}{\partial x_2^2}\frac{\partial \chi_2}{\partial y_2}\}dS +$$

$$\frac{1}{A(x_3)}\{Uu_0\int\limits_U \beta(y_1, y_2, x_3)dl - \delta(1+\delta x_3)\frac{\partial u_0}{\partial x_3}\int\limits_U \beta(y_1, y_2, x_3)y_1^2 dl\}. \quad (278)$$

This is our new homogenised equation. We are already familiar with most of these terms as they are analogous to the terms in Equation (155); they are just slightly modified due to the changed geometry. The only really new term is:

$$-\frac{1}{A(x_3)}\delta(1+\delta x_3)\frac{\partial u_0}{\partial x_3}\int\limits_U \beta(y_1, y_2, x_3)y_1^2 dl. \quad (279)$$

In the next section, we compare full-geometry simulations with the standard homogenisation result as well as with the new result obtained for $\delta = O(1)$.

5.4 SIMULATIONS

Starting with a full-geometry model, we set the parameters for modelling phosphate uptake by a wheat root in solution culture (see Section 1.2.2). Note that the new homogenised equation is valid in the case of other nutrients, plants and environments as well.

5.4.1 *Robin boundary condition*

Dimensional model

We start with a (dimensional) linear diffusion equation:

$$\frac{\partial \bar{u}}{\partial \bar{t}} = \bar{\nabla} \cdot \{D \bar{\nabla} \bar{u}\},$$

equipped with a Robin-type hair surface boundary condition:

$$D \bar{\nabla} \bar{u} \cdot \hat{\boldsymbol{n}} = -\mu_h \bar{u},$$

a Robin-type root surface boundary condition:

$$D \bar{\nabla} \bar{u} \cdot \hat{\boldsymbol{n}} = -\mu_r \bar{u},$$

and an initial condition:

$$\bar{u}(\bar{t} = 0) = \bar{u}_{in}. \tag{280}$$

We take $D = 10^{-5}\,\mathrm{cm}^2\,\mathrm{s}^{-1} = 10^{-3}\,\mathrm{mm}^2\,\mathrm{s}^{-1}$ to be the diffusion coefficient of phosphate in the solution culture (as in [80]). As discussed before (see Section 1.3.4), the uptake of a nutrient is usually modelled using a Michaelis-Menten boundary condition with an efflux term. In order for the efflux from the root to be negligible, we need the initial phosphate concentration to be reasonably large. At the same time, we need the initial concentration to be small enough (preferably smaller than K_m), so that we can approximate the Michaelis-Menten term with the linear (Robin) one. We do not investigate the exact conditions under which these assumptions are satisfied, as we will study Michaelis-Menten model with efflux at the end of this chapter.

Provided the mentioned assumptions are satisfied, we get that the parameter μ_r is equal to $\frac{I_{max}}{K_m}$ from the Michaelis-Menten model (see Equation (23)). For a wheat plant, this can be estimated (using rounded values $I_{max} \approx 2 \times 10^{-7}\,\mu\mathrm{mol}\,\mathrm{cm}^{-2}\,\mathrm{s}^{-1}$ and $K_m = 2 \times 10^{-3}\,\mu\mathrm{mol}\,\mathrm{cm}^{-3}$ from [80]) as:

$$\mu_r = 10^{-4}\,\mathrm{cm}\,\mathrm{s}^{-1} = 10^{-3}\,\mathrm{mm}\,\mathrm{s}^{-1}.$$

Due to the general agreement within the scientific community that one of the main functions of root hairs is the acquisition of nutrients (see Section 1.2.1),

it seems natural to assume that the density of (e.g. phosphate) transporters (see Section 1.3.4) will be higher in these cells. As a typical root hair is twenty times thinner than a typical wheat root [80], and we did not find any data estimating μ_h, we assume that the hair uptake constant is twenty times higher than that of the non-hair root surface, i.e. $\mu_h = 2 \times 10^{-2}\,\mathrm{mm\,s^{-1}}$. Later on, when studying the Michaelis-Menten boundary condition, we use the same uptake parameters for the hairs as we do for the root surface to confirm that the new model gives better results in this case too.

We will mostly be interested in how δ (the hair length divided by the root radius) affects the validity of the homogenisation result (155) when compared with the new model. Thus, we will vary δ from 0.1 to 10, which is still realistic especially for phosphate-starved plants (see [51]). Keeping this variation in mind, it seems reasonable to impose a zero-flux boundary condition at $r_\infty = 20r_0 = 2\,\mathrm{mm}$, where r_0 denotes the radius of the root as before. We assume the inter-hair distance of $h_0 = 0.1\,\mathrm{mm}$, the hair radius of $r_1 = 0.005\,\mathrm{mm}$, and the root segment of length $H = 1\,\mathrm{mm}$ (we are mostly interested in studying the effects of the root surface curvature, and thus we do not need to study longer segments) - these are all standard values as found in (e.g.) [80]. The parameter values are summarised in Table 5.1. Assuming the constant initial condition (280), we introduce no macroscopic variation in the θ (azimuthal angle) direction, and it is thus possible to restrict our attention from the full geometry (as in Figure 5.1) to a single wedge containing only 1 root hair in each layer (see Figure 5.6), which makes simulations computationally cheaper. Defining θ^* to be an angle between two planes forming the vertical boundaries of this wedge, we choose θ^* so that the distance between the root hairs along the circumference of the root is equal to the inter-hair distance along the main axis of the root, i.e. $\theta^* r_0 = h = h_0$, which yields:

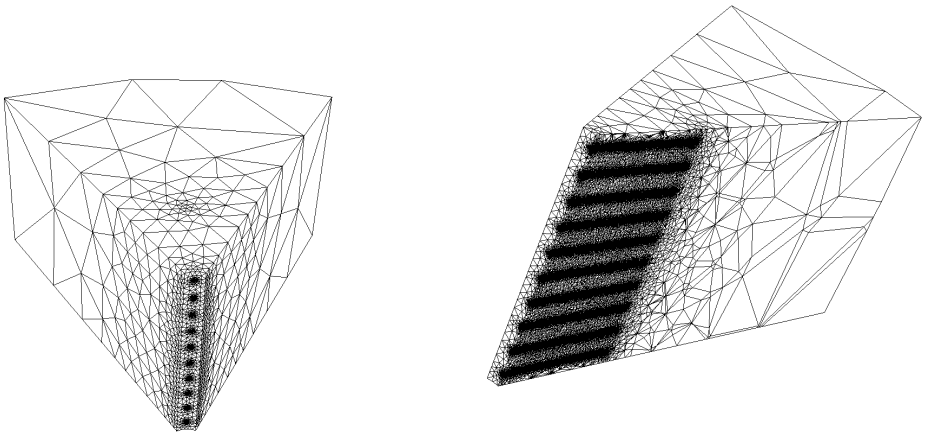
$$\theta^* = \frac{h_0}{r_0} = 1,$$

where r_0 and h_0 are taken from Table 5.1.

At the top and the bottom part of the boundary (i.e the two ends of the root segment) as well as at the two side planes of the wedge (representing mid-distance to the neighbouring hairs), we impose zero-flux boundary conditions.

Parameter	value	unit
D	0.001	$\mathrm{mm}^2\ \mathrm{s}^{-1}$
I_{max}	2×10^{-7}	$\mu\mathrm{mol}\ \mathrm{cm}^{-2}\ \mathrm{s}^{-1}$
K_m	2×10^{-3}	$\mu\mathrm{mol}\ \mathrm{cm}^{-3}$
E	1×10^{-8}	$\mu\mathrm{mol}\ \mathrm{cm}^{-2}\ \mathrm{s}^{-1}$
μ_r	0.001	$\mathrm{mm}\ \mathrm{s}^{-1}$
μ_h	0.02	$\mathrm{mm}\ \mathrm{s}^{-1}$
r_∞	2	mm
r_0	0.1	mm
h_0	0.1	mm
r_1	0.005	mm
H	1	mm

Table 5.1.: The parameter values for phosphate uptake by wheat. Most values are estimated from [80]. The values for μ_r, μ_h, r_∞ and H are justified in the main text.



(a) Wedge. (b) Clipped wedge.

Figure 5.6.: Restricting attention to the single wedge. Using the clipped domain, we see the (finely-meshed) hair surfaces.

Finally, we assume no macroscopic gradient in phosphate concentration along the root axis.

Nondimensionalisation

We wish to compare the new effective model with the full-geometry simulations using the curved geometry (not the flattened one). Therefore, we nondimensionalise as:

$$(\bar{w}_1, \bar{w}_2, \bar{w}_3) = h_1(w_1, w_2, w_3), \quad \bar{t} = \frac{h_1^2}{D}t, \quad \bar{u} = \bar{u}_{in}u,$$

and get a continuity equation:

$$\frac{\partial u}{\partial t_{h_1}} = \nabla_{h_1}^2 u,$$

an initial condition:

$$u(t = 0) = 1,$$

a hair surface boundary condition:

$$\nabla_{h_1} u \cdot \hat{\boldsymbol{n}} = -\frac{\mu_h h_1}{D}u = -\epsilon\frac{h_1^2\mu_h}{hD}u = -\epsilon K_{h_1}u,$$

a root surface boundary condition:

$$\nabla_{h_1} u \cdot \hat{\boldsymbol{n}} = -\frac{\mu_r h_1}{D}u$$

and a zero-flux boundary condition:

$$\nabla_{h_1} u \cdot \hat{\boldsymbol{n}} = 0$$

everywhere else. Note that we use the subscript $_{h_1}$ in $K_{h_1} = \frac{h_1^2 \mu_h}{hD}$ (the uptake constant), ∇_{h_1} and t_{h_1} to emphasise that the macroscale variables and the time were nondimensionalised with respect to the hair length h_1 to distinguish this case from what we did in Chapter 3 (see Equation (132)). In that chapter, neglecting the root surface curvature (i.e. assuming the geometry from Figure 3.1) and assuming no macroscopic variation along the root axis (i.e. in what now is the w_3 direction) as well as in the angular direction θ, we derived the homogenisation result (see Equation (159)):

$$\frac{\partial u_0}{\partial t_L} = \frac{\partial^2 u_0}{\partial x_{3,L}^2} - \frac{2\pi K_L a}{1 - \pi a^2} u_0,$$

where $a = \frac{r_1}{h_0} = \frac{0.005 \text{ mm}}{0.1 \text{ mm}} = 0.05$, and the subscript $_L$ in $x_{3,L}$, t_L and $K_L (= \frac{L^2 B}{lD})$ suggests nondimensionalisation with respect to the root segment length L (in this chapter denoted by H). As we nondimensionalise with respect to h_1 in this case, we conclude the effective equation:

$$\frac{\partial u_0}{\partial t_{h_1}} = \frac{\partial^2 u_0}{\partial x_{3,h_1}^2} - \frac{2\pi K_{h_1} a}{1 - \pi a^2} u_0. \tag{281}$$

However, we also want to vary the hair length in our simulations, and thus it is practically simpler to nondimensionalise (both space and time) with respect to the (fixed) $r_\infty = 2$ mm. The full-geometry model in this setting consists of a continuity equation:

$$\frac{\partial u}{\partial t_{r_\infty}} = \nabla_{r_\infty}^2 u,$$

an initial condition:

$$u(t_{r_\infty} = 0) = 1,$$

a hair surface boundary condition:

$$\nabla_{r_\infty} u \cdot \hat{\boldsymbol{n}} = -\frac{\mu_h r_\infty}{D} u,$$

a root surface boundary condition:

$$\nabla_{r_\infty} u \cdot \hat{\boldsymbol{n}} = -\frac{\mu_r r_\infty}{D} u,$$

and a zero-flux boundary condition:

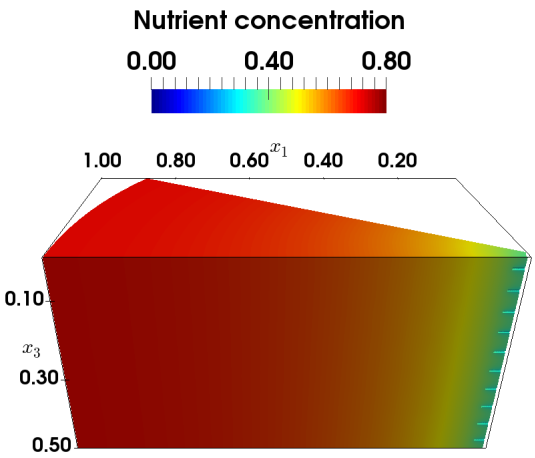
$$\nabla_{r_\infty} u \cdot \hat{\boldsymbol{n}} = 0$$

applied everywhere else. Transforming to the new dimensionless variables and coming back to the curved geometry from Figure 5.6, the effective equation (281) becomes:

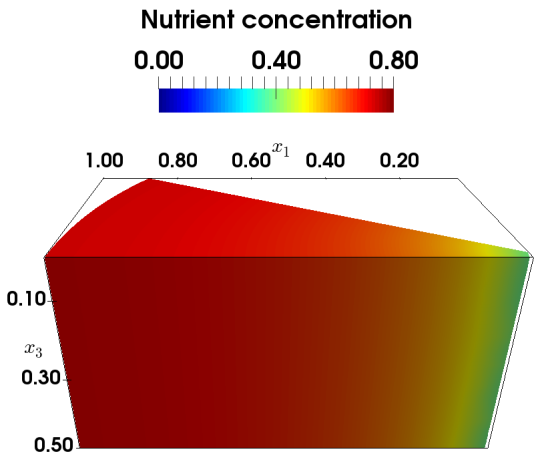
$$\frac{\partial u_0}{\partial t_{r_\infty}} = \nabla^2_{r_\infty} u_0 - \frac{2\pi K_{r_\infty} a}{1 - \pi a^2} u_0, \tag{282}$$

where $K_{r_\infty} = \frac{r_\infty^2 \mu_h}{hD}$, and the sink term is acting in the region of the wedge (see Figure 5.6), for which the dimensionless (with respect to r_∞) cylindrical radius r_{r_∞} is smaller than $\frac{r_0+h_1}{r_\infty}$. We compare the full-geometry simulations with the standard homogenisation result (282) (from now on referred to as a short-hairs limit) at (dimensionless) time $t_{r_\infty} = 1$ for $\delta = 0.5, 1.0, 2.0, 5.0$. From now onwards, we drop the subscript $_{r_\infty}$, bearing in mind that the model is nondimensionalised with respect to r_∞. From Figure 5.7, we see that for small δ ($= 0.5, 1.0$), the short-hairs homogenisation limit gives us a good approximation for the full-geometry simulation. However, starting from $\delta \approx 2$, the approximation gets worse, and for $\delta = 5.0$ the standard homogenisation limit gives results very far from an averaged behaviour (see Figure 5.8). The reason is that the root hairs are assumed to explore the surrounding soil to the same extent independent of the distance from the root, which is clearly wrong. In other words, for any fixed distance from the root surface, we have the same hair surface area taking up the nutrient, but the amount of available nutrient increases with this distance (linearly in the case of a constant nutrient concentration everywhere) simply because of the increase in the surrounding soil volume.

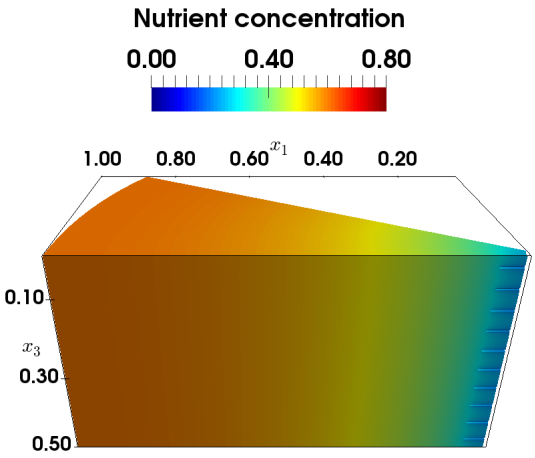
Note further that if δ is $O(1)$ or larger, the distance between the hair tips is significantly greater than the inter-hair distance at the root surface, and the space between the hairs is not sufficiently explored. One can study depletion gradients at the hair surfaces using cylindrical slices at a specified distance from the root surface (e.g. at the tips of the hairs), as shown in Figure 5.9 for $\delta = 1$ and $\delta = 10$ ($t = 1$). We now check whether the newly derived effective equation gives a better approximation in the $\delta = 5.0$ case.



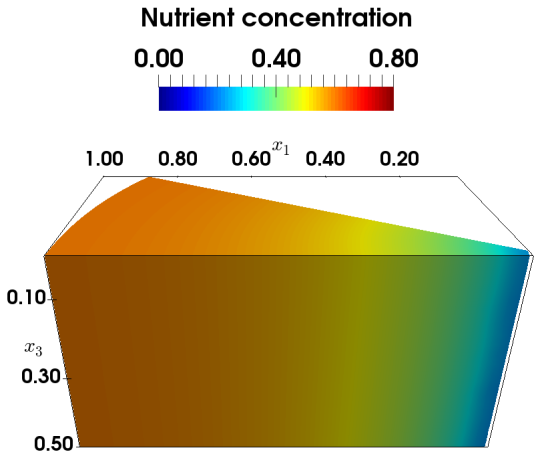
(a) Full-geometry numerics, $\delta = 0.5$



(b) Short-hairs homogenisation limit, $\delta = 0.5$

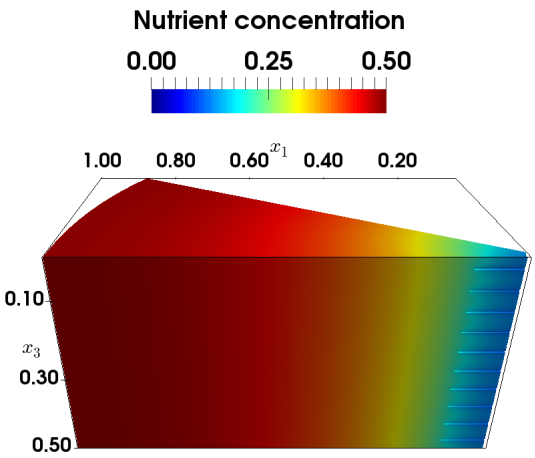


(c) Full-geometry numerics, $\delta = 1.0$

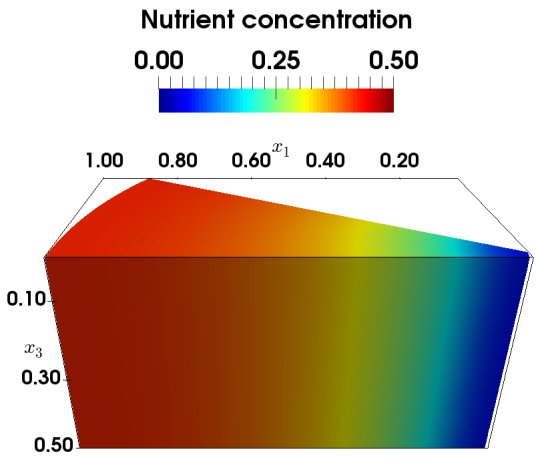


(d) Short-hairs homogenisation limit, $\delta = 1.0$

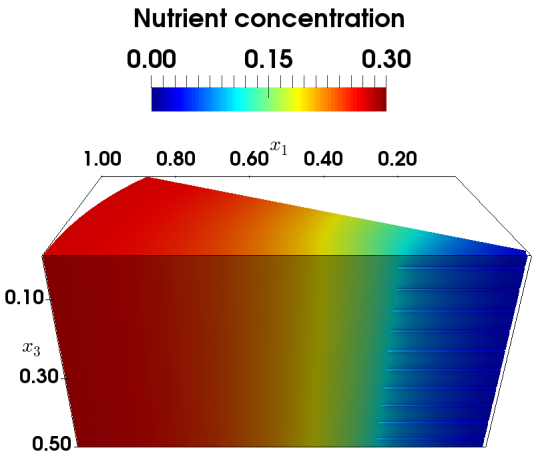
Figure 5.7.: Comparison between the full-geometry numerics and the short-hairs homogenisation result at $t = 1$ ($\delta = 0.5, 1.0$).



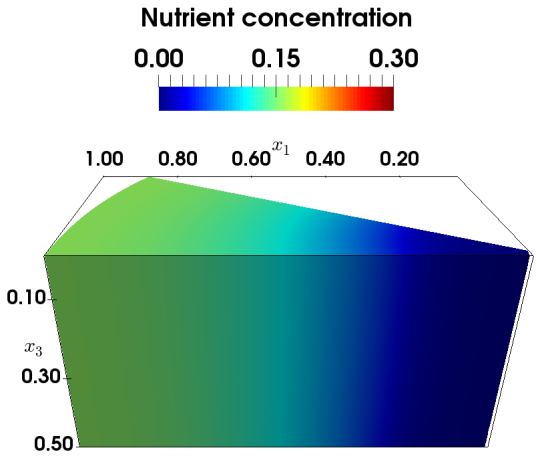
(a) Full-geometry numerics, $\delta = 2.0$



(b) Short-hairs homogenisation limit, $\delta = 2.0$

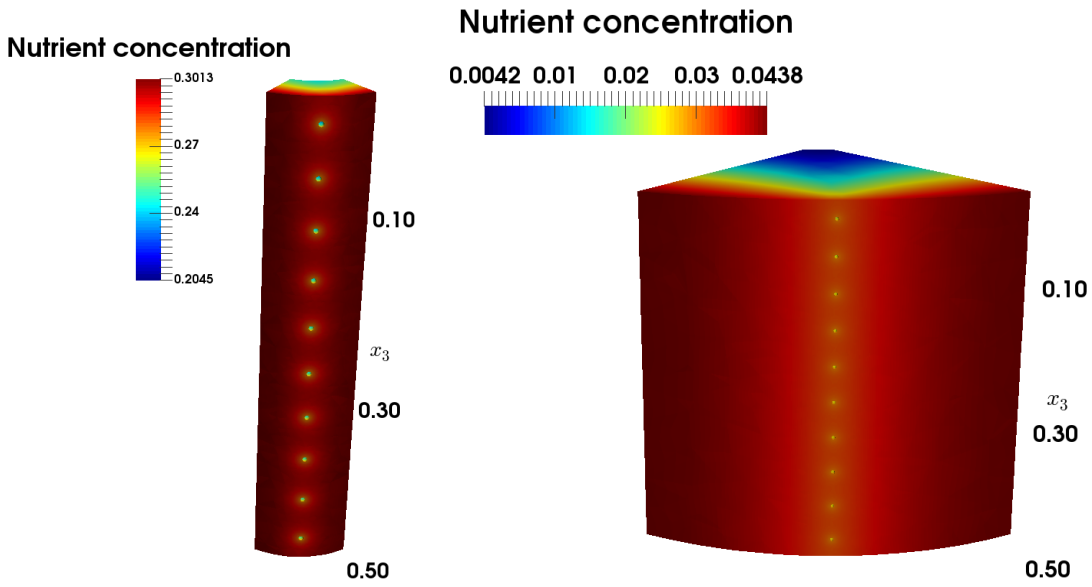


(c) Full-geometry numerics, $\delta = 5.0$



(d) Short-hairs homogenisation limit, $\delta = 5.0$

Figure 5.8.: Comparison between the full-geometry numerics and the short-hairs homogenisation result at $t = 1$ ($\delta = 2.0, 5.0$).



(a) $\delta = 1.0$ (b) $\delta = 10.0$

Figure 5.9.: The depletion gradients at the tips of the hairs for varying δ ($t = 1$).

NEW MODEL

Assuming that u_0 is independent of the macroscopic x_1 and x_2, Equation (278) becomes:

$$\frac{\partial u_0}{\partial t_{h_1}} = \frac{\partial^2 u_0}{\partial x_{3,h_1}^2} + \frac{\delta}{1+\delta x_{3,h_1}} \frac{\partial u_0}{\partial x_{3,h_1}} + \frac{1}{A(x_{3,h_1})} \{ U u_0 \int_U \beta(y_1, y_2, x_{3,h_1}) dl -$$

$$\delta(1+\delta x_{3,h_1}) \frac{\partial u_0}{\partial x_{3,h_1}} \int_U \beta(y_1, y_2, x_{3,h_1}) y_1^2 dl \}$$

The

$$\frac{1}{A(x_{3,h_1})} \{ U u_0(t, x_{3,h_1}) \int_U \beta(y_1, y_2, x_{3,h_1}) dl -$$

$$\delta(1+\delta x_{3,h_1}) \frac{\partial u_0(t, x_{3,h_1})}{\partial x_{3,h_1}} \int_U \beta(y_1, y_2, x_{3,h_1}) y_1^2 dl \}$$

term depends on t_{h_1}, x_{3,h_1} and δ. Fixing $\delta = 5$, $\delta x_{3,h_1}$ ranges from 0 to 5 (see Transformation (245), where the nondimensionalisation was performed with respect to h_1). As we cannot compute these integrals for uncountably many x_{3,h_1}, we split the domain into 6 subdomains as demonstrated in Figure 5.10. Nondimensionalising with respect to r_{ff}, we have $\frac{r_0}{r_\infty} < r < \frac{r_0+0.2*h_1}{r_\infty}$ for the first, $\frac{r_0+0.2*h_1}{r_\infty} < r < \frac{r_0+0.4*h_1}{r_\infty}$ for the second, $\frac{r_0+0.4*h_1}{r_\infty} < r < \frac{r_0+0.6*h_1}{r_\infty}$ for the

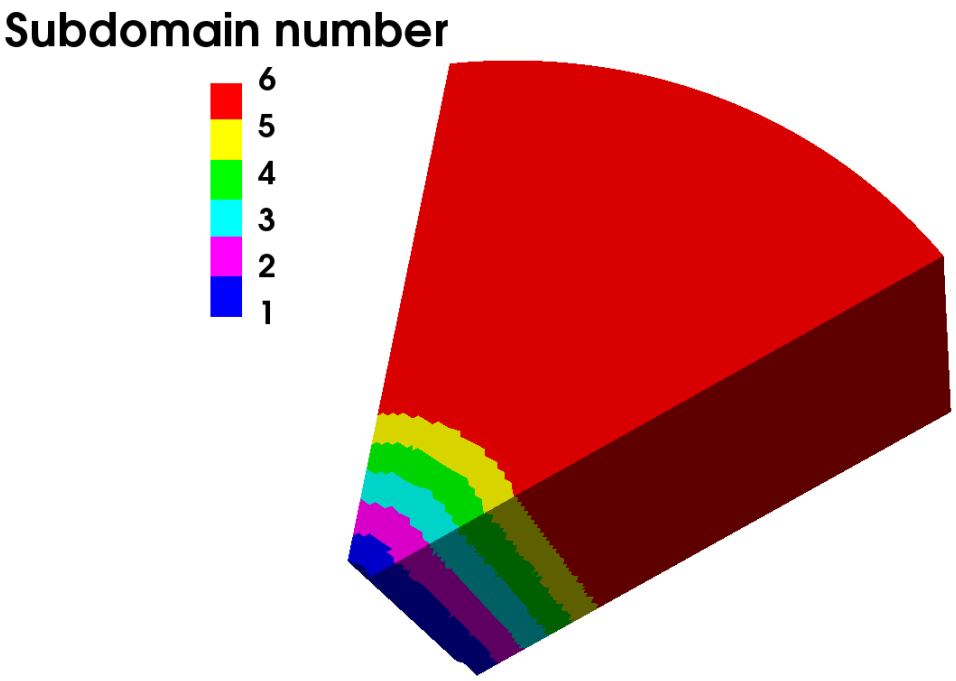
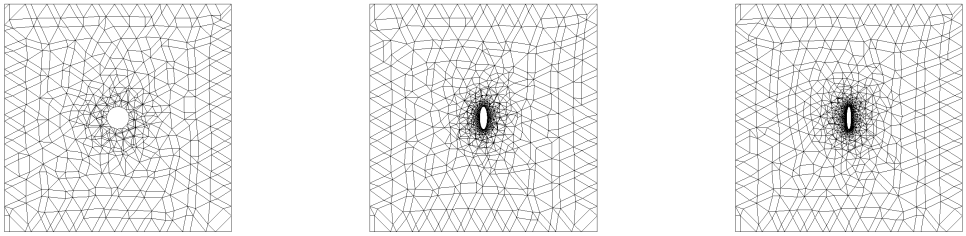


Figure 5.10.: The domain is divided into 6 subdomains. Colour indicates the subdomain number.

third, $\frac{r_0+0.6*h_1}{r_\infty} < r < \frac{r_0+0.8*h_1}{r_\infty}$ for the fourth, and $\frac{r_0+0.8*h_1}{r_\infty} < r < \frac{r_0+h_1}{r_\infty}$ for the fifth subdomain. The last (sixth) subdomain (zone without hairs) satisfies $\frac{r_0+h_1}{r_\infty} < r < 1$. In our simulations, the newly derived terms are chosen to be constant in each subdomain. To calculate the new terms for the first subdomain, we use the unit cell geometry corresponding to $x_3 = 0$, for the second subdomain, we use the unit cell geometry corresponding to $x_{3,h_1} = 0.2$, and so on. Finally, for the sixth subdomain, there is no sink term as it does not contain root hairs at all. Some of these unit cell geometries are shown in Figure 5.11. Table 5.2 summarises the numerically computed values of the studied integrals for different subdomains. We now briefly discuss the relative importance of the two terms $Uu_0 \int_U \beta dl$ and $\delta(1+\delta x_{3,h_1})\frac{\partial u_0}{\partial x_{3,h_1}} \int_U y_1^2 \beta dl$. As we do not have any prior knowledge of u_0 and $\frac{\partial u_0}{\partial x_{3,h_1}}$, and as we are mostly interested in the respective magnitudes of the two terms, we compare $U|\int_U \beta dl|$ with $\delta(1+\delta x_3)|\int_U y_1^2 \beta dl|$.



(a) $x_{3,h_1} = 0.0$ (b) $x_{3,h_1} = 0.4$ (c) $x_{3,h_1} = 0.8$

Figure 5.11.: Different unit cell geometries for varying x_{3,h_1} ($\delta = 5$).

Subdomain i	$\int_{U_i} \beta dl$	$\int_{U_i} y_1^2 \beta dl$
1	-6.34	-0.00764
2	-3.14	-0.00098
3	-2.14	-0.00029
4	-1.61	-0.00012
5	-1.29	-0.00006

Table 5.2.: Numerically-computed integral values.

Looking back into the analysis from this chapter, we see that $U = \frac{r_1 A}{h} = \frac{r_1}{h}\frac{Bh_1^2}{hD}$, and noting that the parameter B is now denoted as μ_h, we conclude:

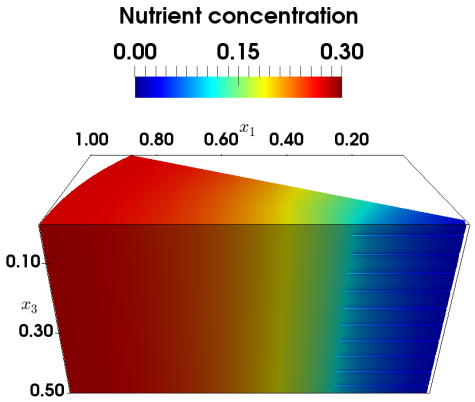
$$U = \frac{r_1 \mu_h h_1^2}{Dh^2} \approx 2.5.$$

As $\delta = 5$, the $\delta(1+\delta x_3)$ term ranges from 5 to 30. All these calculations together with Table 5.2 yield an estimate $U|\int_U \beta dl| > 2$ for the first term, and an estimate $\delta(1+\delta x_3)|\int_U y_1^2 \beta dl| < 0.05$ for the second term. This suggests that the (truly new) $\delta(1+\delta x_3)\frac{\partial u_0}{\partial x_3}\int_U y_1^2 \beta dl$ term has smaller impact on the effective equation than the $Uu_0\int_U \beta dl$ term, which is only the modified version of a term known from the flattened-root-surface case.

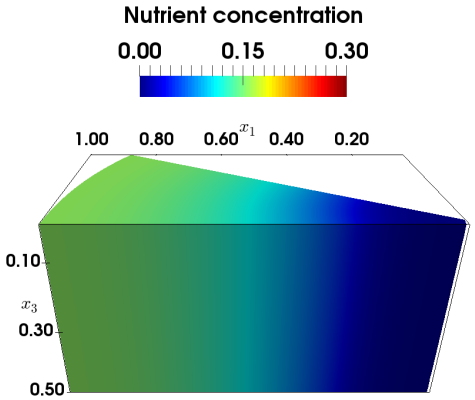
Now, we compare the full-geometry, the short-hairs-limit homogenisation, and the new model for $\delta = 5.0$. The new model performs much better - see Figure 5.12.

5.4.2 *More realistic models*

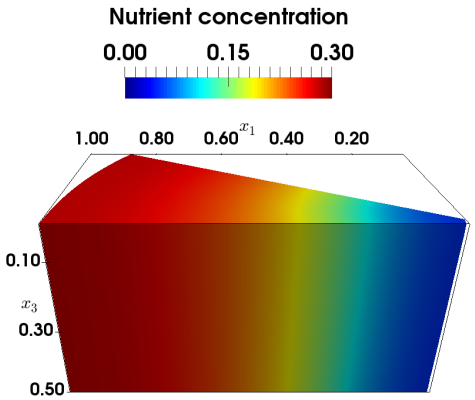
From now onwards, we assume that the root surface uptake can be described by the same Michaelis-Menten parameters ($K_{m,h} = K_{m,r}$, $I_{max,h} = I_{max,r}$) as the root hair surface uptake. The linear hair boundary condition from previous section only serves as a good approximation of the Michaelis-Menten kinetics assuming low nutrient concentrations. Moreover, under this assumption, the efflux from the root becomes non-negligible. Therefore, we now impose a low initial nutrient concentration everywhere, and we add a constant efflux term to our model, which yields a nonzero steady state. Finally, we assume that the root and the hair efflux rates are the same, and we use a rounded value $E_h = E_r = 10^{-8}\,\mu\text{mol}\,\text{cm}^{-2}\,\text{s}^{-1}$ from [80].



(a) Full-geometry numerics



(b) Short-hairs limit



(c) New model

Figure 5.12.: Comparison with the new model in which the sink term is dependent on the distance from the root surface. Errors in the short-hairs limit simulation are obvious for $\delta = 5.0$ ($t = 1.0$).

Linear model with efflux

We assume (compare with [80] as well as with the dimensional equations from the previous section) a continuity equation:

$$\frac{\partial \bar{u}}{\partial \bar{t}} = \bar{\nabla} \cdot \{D \bar{\nabla} \bar{u}\},$$

a hair surface boundary condition:

$$D \bar{\nabla} \bar{u} \cdot \hat{\boldsymbol{n}} = -\mu_h \bar{u} + E_h,$$

where $\mu_h = \frac{E_h}{K_h}$, a root surface boundary condition:

$$D \bar{\nabla} \bar{u} \cdot \hat{\boldsymbol{n}} = -\mu_h \bar{u} + E_h,$$

and an initial condition:

$$\bar{u}(\bar{t} = 0) = \bar{u}_{in} = 0.1 \times K_h.$$

Using this initial condition (and the fact that there exists no nutrient source in the model, which suggests that the concentration will never exceed $\bar{u}_{in}$), we restrict ourselves to the case where the linear model approximates the physical reality well, as demonstrated in Figure 5.13, where we compare the Michaelis-Menten function with its linear approximation (including the constant efflux term). We nondimensionalise as before:

$$(\bar{w}_1, \bar{w}_2, \bar{w}_3) = h_1 (w_1, w_2, w_3), \quad \bar{t} = \frac{h_1^2}{D} t, \quad \bar{u} = \bar{u}_{in} u,$$

and get a continuity equation:

$$\frac{\partial u}{\partial t_{h_1}} = \nabla_{h_1}^2 u,$$

an initial condition:

$$u(t = 0) = 1,$$

a hair surface boundary condition:

$$\nabla_{h_1} u \cdot \hat{\boldsymbol{n}} = -\frac{\mu_h h_1}{D} u + \frac{E_h h_1}{\bar{u}_{in} D} = -\epsilon \frac{h_1^2 \mu_h}{hD} u + \epsilon \frac{E_h h_1^2}{h \bar{u}_{in} D} = -\epsilon K u + \epsilon e_h$$

and a root surface boundary condition:

$$\nabla_{h_1} u \cdot \hat{\boldsymbol{n}} = -\frac{\mu_h h_1}{D} u + \frac{E_h h_1}{\bar{u}_{in} D}.$$

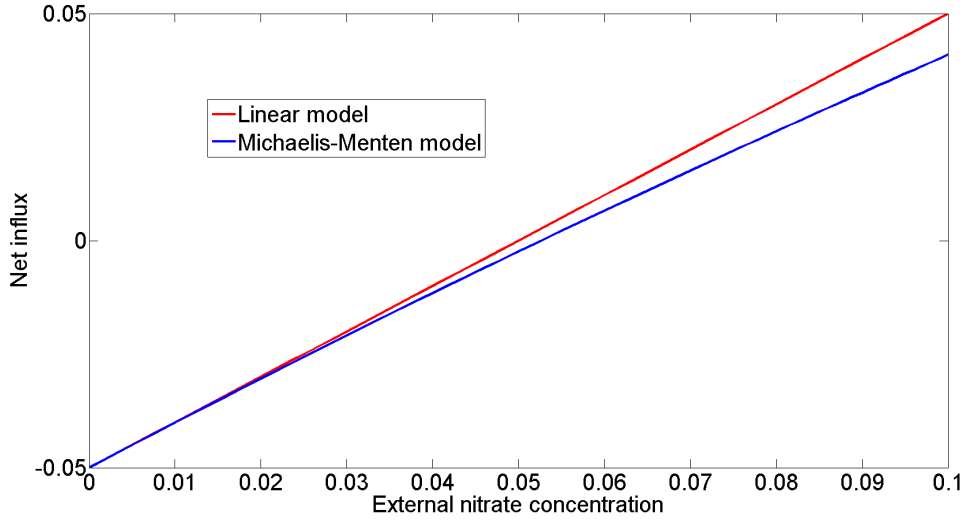


Figure 5.13.: Assessing the validity of the linear approximation.

The short-hairs homogenisation limit gives:

$$\frac{\partial u_0}{\partial t_{h_1}} = \nabla^2_{h_1} u_0 - \frac{2\pi K a}{1-\pi a^2} u_0 + \frac{2\pi a e_h}{1-\pi a^2},$$

which (scaling the space and the time with respect to r_∞) leads to:

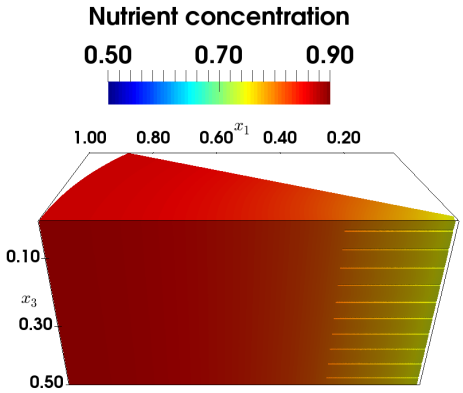
$$\frac{\partial u_0}{\partial t_{r_\infty}} = \nabla^2_{r_\infty} u_0 - (\frac{r_\infty}{h_1})^2 \frac{2\pi K a}{1-\pi a^2} u_0 + (\frac{r_\infty}{h_1})^2 \frac{2\pi a e_h}{1-\pi a^2}.$$

Assuming that u_0 is independent of the macroscopic x_1 and x_2, the new model yields:

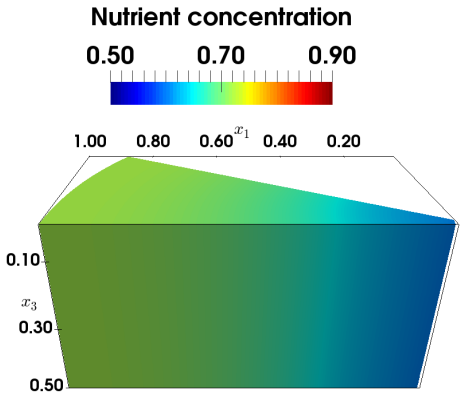
$$\frac{\partial u_0}{\partial t_{h_1}} = \frac{\partial^2 u_0}{\partial x^2_{3,h_1}} + \frac{\delta}{1+\delta x_{3,h_1}} \frac{\partial u_0}{\partial x_{3,h_1}} + \frac{1}{A(x_{3,h_1})} \times$$

$$\{(U u_0 - \frac{r_1}{h} e_h) \int_U \beta(y_1, y_2, x_{3,h_1}) dl - \delta(1+\delta x_{3,h_1}) \frac{\partial u_0}{\partial x_{3,h_1}} \int_U \beta(y_1, y_2, x_{3,h_1}) y_1^2 dl\},$$

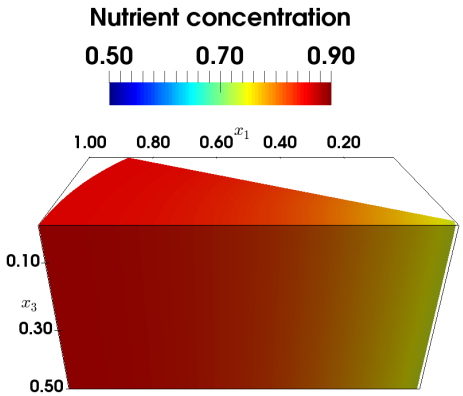
where $U = \frac{r_1}{h} K$. We compare all three models and conclude that the new model again approximates the full-geometry simulation better (see Figure 5.14). Compared to the model without efflux (see Figure 5.12), we see higher nutrient concentrations everywhere, which is simply a consequence of the efflux term.



(a) Full-geometry numerics



(b) Short-hairs limit



(c) New model

Figure 5.14.: Comparison with the new effective equation for $\delta = 5.0$ (the model with efflux; $t = 1.0$).

Michaelis-Menten uptake

Finally, we impose Michaelis-Menten boundary condition:

$$D\bar{\nabla}\bar{u}\cdot\hat{\boldsymbol{n}} = -\frac{I_{max,h}\bar{u}}{K_{m,h}+\bar{u}} + E_h,$$

and assume that the same parameters apply to both the root and the hair surfaces. Nondimensionalising as before yields a hair boundary condition:

$$\nabla_{h_1}u\cdot\hat{\boldsymbol{n}} = -\frac{I_{max,h}h_1u}{D(K_{m,h}+\bar{u}_{in}u)} + \frac{E_hh_1}{\bar{u}_{in}D} = -\epsilon\frac{h_1^2I_{max,h}u}{hD(K_{m,h}+\bar{u}_{in}u)} + \epsilon\frac{E_hh_1^2}{h\bar{u}_{in}D} =$$

$$-\epsilon\frac{\tilde{I}u}{1+\frac{\bar{u}_{in}}{K_{m,h}}u} + \epsilon e_h,$$

where $\tilde{I} = \frac{h_1^2I_{max,h}}{hDK_{m,h}}$[3] (compare with the previous section), and a root boundary condition:

$$\nabla_{h_1}u\cdot\hat{\boldsymbol{n}} = -\frac{I_{max,h}h_1u}{D(K_{m,h}+\bar{u}_{in}u)} + \frac{E_hh_1}{\bar{u}_{in}D}.$$

The short-hairs homogenisation limit gives:

$$\frac{\partial u_0}{\partial t_{r_\infty}} = \nabla^2_{r_\infty}u_0 - (\frac{r_\infty}{h_1})^2\frac{2\pi\tilde{I}a}{1-\pi a^2}\frac{u_0}{1+\frac{\bar{u}_{in}}{K_{m,h}}u_0} + (\frac{r_\infty}{h_1})^2\frac{2\pi ae_h}{1-\pi a^2},$$

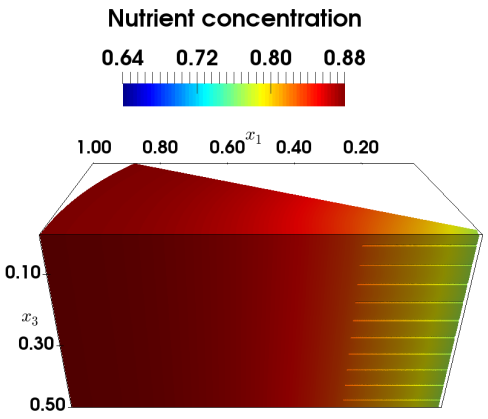
and the new model reads:

$$\frac{\partial u_0}{\partial t_{h_1}} = \frac{\partial^2u_0}{\partial x^2_{3,h_1}} + \frac{\delta}{1+\delta x_{3,h_1}}\frac{\partial u_0}{\partial x_{3,h_1}} + \frac{1}{A(x_{3,h_1})}\{(U\frac{u_0}{1+\frac{\bar{u}_{in}}{K_{m,h}}u_0} - \frac{r_1}{h}e_h)\times$$

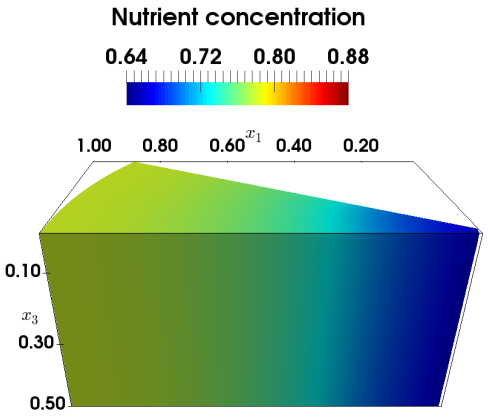
$$\int\limits_U \beta(y_1,y_2,x_{3,h_1})dl - \delta(1+\delta x_{3,h_1})\frac{\partial u_0}{\partial x_{3,h_1}}\int\limits_U \beta(y_1,y_2,x_{3,h_1})y_1^2dl\}$$

where $U = \frac{r_1}{h}\tilde{I}$. As before, we simulate the short-hairs limit result as well as the new model and see how these compare with the full-geometry simulation. The results are shown in Figure 5.15. As a consistency check, we compare the Michaelis-Menten model with the linear one. Figure 5.13 suggests that the uptake term for the linear model is greater compared with the Michaelis-Menten model for any nutrient concentration.

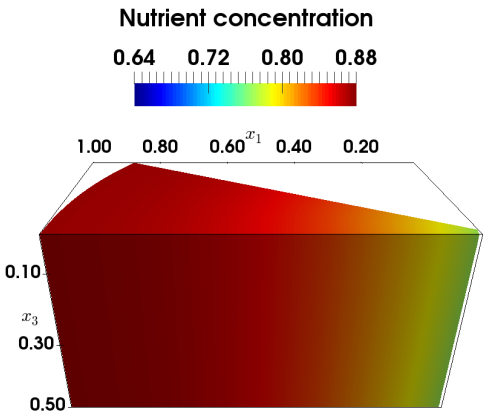
3 Using values from [80] (see also Section 1.4.4), we get that $\frac{I_{max,h}}{hDK_{m,h}}$ is usually $O(10^3\ \text{cm}^{-2})$ or $O(10^4\ \text{cm}^{-2})$. Given that in this chapter we mostly use $0.01\ \text{cm} \le h_1 \le 0.1\ \text{cm}$, we conclude that $\tilde{I}$ can range from $O(10^{-1})$ to $O(10^2)$, which covers the $O(1)$ range.



(a) Full-geometry numerics



(b) Short-hairs limit



(c) New model

Figure 5.15.: Comparison with the new effective equation for $\delta = 5.0$ (the Michaelis-Menten model; $t = 1.0$).

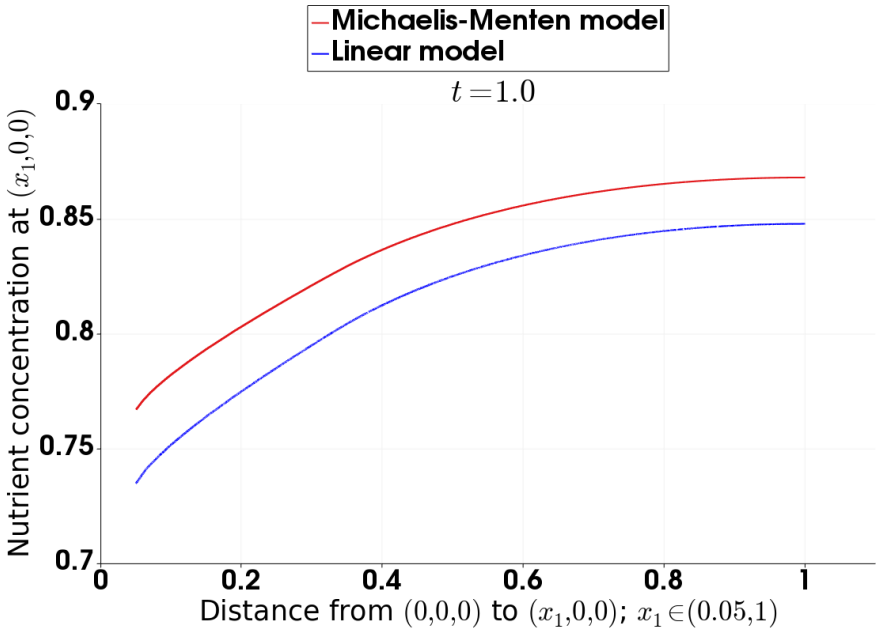
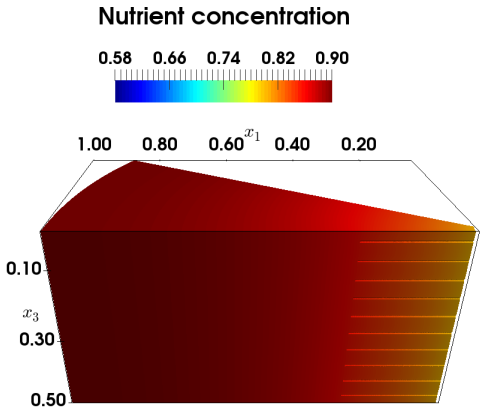


Figure 5.16.: The linear model takes up more nutrient.

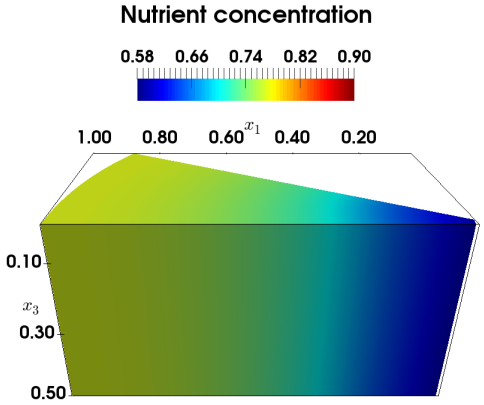
Therefore, we expect the overall uptake for the linear model to be greater than for the Michaelis-Menten model, and as a consequence, we expect the remaining nutrient concentration at (e.g.) $t_{(r_\infty)} = 1$ for the linear model to be lower. We compare the new limit for the two models, and the nutrient concentrations plotted against the increasing distance from the root axis can be found in Figure 5.16. Using the Michaelis-Menten term, we can model higher initial nutrient concentration as well. We chose $\bar{u}_{in} = 3K_m$, and the results are shown in Figure 5.17.

5.5 SUMMARY

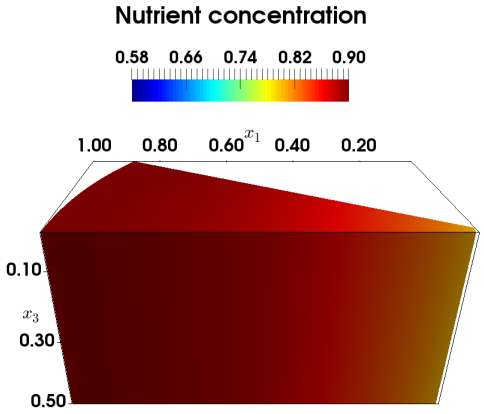
Studying the effects of the root hair length on uptake processes, we first analysed the limit of very short hairs, and we confirmed that the resulting effective equation is the same as the one we derived in Chapter 3 (see Equation (155)). Then, we studied the case $\delta = O(1)$ and derived the new effective equation (278). In the final section of this chapter, this equation was shown to give a better approximation to the full-geometry numerical simulations when compared with Equation (155) for various hair surface boundary conditions.



(a) Full-geometry numerics



(b) Short-hairs limit



(c) New model

Figure 5.17.: Comparison with the new effective equation for $\delta = 5.0$ using $\bar{u}_{in} = 3K_m$ (the Michaelis-Menten model; $t = 1.0$).

6

NITRATE TRANSPORTERS AND UPTAKE

6.1 INTRODUCTION

In the remaining chapters of this thesis, we will move from the root hairs uptake to different topics and show how even very simple upscaling methods can prove useful in plant uptake modelling.
Nitrate is the dominant form of nitrogen in many agricultural soils [25], and readily leaches down into groundwater as pollution [134]. Therefore, optimising the uptake of nitrate by crops could have large effects on the global nitrogen cycle. While genes encoding nitrate transporters (see Section 1.3.4) have been discovered [49], and the structures mostly determined [131], relatively little is known about how the properties of the transporters influence root uptake at larger scales. Understanding how the numbers and ratio of low and high affinity transporters (as introduced in Section 6.1.2) influence total root uptake would be an important goal to optimise nitrate uptake kinetics.
Therefore, this chapter is dedicated to models of nitrate uptake via low and high affinity transporters.

6.1.1 *Michaelis-Menten*

Nutrient uptake by plants is often modelled using the Michaelis-Menten framework (as introduced in Section 1.3.4). In its simplest form, it states:

$$I = \frac{I_{max} c}{K_m + c}, \tag{283}$$

where I denotes plant nutrient influx, I_{max} is the maximal value of this influx, c is the external nutrient concentration, and K_m is the Michaelis constant (concentration at which the plant influx is one half of the maximal influx). Note that instead of I_{max}, one often finds in the literature, V_{max} (e.g. [25]) or F_m (e.g. [122]) denoting the maximal influx rate. As discussed in [136], even though the original justification for this formalism was an enzymatic nature of nutrient transport, it has now become clear that the complexity of plant architecture and (perhaps more importantly) the variety of transporters (see Section 1.3.4) involved makes this reasoning questionable. Values of I_{max} and K_m are usually estimated from experiments in which the depletion of nitrate in solution culture caused by plant uptake is measured at different time points. The units of I_{max} are thus given on the basis of root length [21], surface area [150], or mass [89]. It is often not clear how these root segment level parameters (I_{max}, K_m) arise from the transporter level parameters and what their biological interpretation is. From now on, we refer to the root segment level as macroscale, and the transporter level as microscale.

In the literature for phytoplankton nutrient uptake, I_{max} and K_m have repeatedly been derived using concepts of ion-transporter encounter rate and handling time (see Section 6.2.1), and we shall use this approach to derive a model for nitrate uptake at a single transporter level in Section 6.2.2. This model will then be upscaled in the simplest way possible (multiplying by the transporter density) to the root segment scale.

6.1.2 *Low and high affinity transporters*

The existence of (at least) two distinct nitrate transport mechanisms in plants has long been suspected, based on experimental observations of uptake at low and high external nutrient concentration [44]. High affinity transporters (HATs) have small values of K_m and dominate uptake at low nutrient concentrations, whereas low affinity transporters (LATs) have large values of K_m and dominate at high nutrient concentrations [25]. Most empirical studies suggest that LAT uptake is a linear function of external concentration for all its bio-

logically relevant values [25]. Despite that, in this chapter, we propose that the apparent linearity results from a Michaelis-Menten behaviour with a very large K_m, and we shall use the Michaelis-Menten form for LAT uptake too.
Both LATs and HATs can either be constitutively expressed or are inducible by the external nitrate concentration [49].
We know of no research relating the Michaelis-Menten parameters observed in experiments and their microscopic counterparts derived using handling time and encounter rate concepts. This problem is studied in Section 6.2.

6.1.3 *Efflux*

As often observed in experiments, there exists a concentration c_{min} below which a plant cannot uptake nitrate [11] (the same applies to many other nutrients; see [8] for instance). As a consequence, Equation (283) is modified as follows:

$$I = \frac{I_{max}(c - c_{min})}{K_m + (c - c_{min})} \tag{284}$$

(see [39] or Section 1.3.4). Many authors have neglected c_{min} in their modelling (e.g. [43]) - substituting $c_{min} = 0$ mM in Equation (284), we recover Equation (283). While I_{max} and K_m have been derived before (see Section 6.2.1), we could not find a mechanistic justification for c_{min} in the available literature. The most obvious explanation seems be to be that this is the concentration at which the influx via transporters is exactly balanced by the nutrient efflux from the root, which is usually observed at very low external concentrations. Therefore, introducing E as the efflux, we consider the model:

$$I = \frac{I_{max}c}{K_m + c} - E \tag{285}$$

from [21] to be more physiologically insightful (in comparison with Equation (284)). However, the reason for the observed efflux is rarely mentioned. Moreover, to our knowledge, there has been no attempt to predict the observed values of c_{min} from the underlying mechanistic assumptions about the efflux term E. Furthermore, it is not clear what the effects of a particular distribution between the low and the high affinity transporters on the macroscopic parame-

ter c_{min} are. Therefore, in Section 6.3, we will search for an optimal transporter production strategy for a plant, i.e. how many low and high affinity transporters a plant should produce to maximise the overall uptake.
From now on, we distinguish between the microscopic and the macroscopic parameters by using bars for the latter ($\bar{I}_{max}$, $\bar{K}_m$, $\bar{c}_{min}$ for macroscopic parameters and I_{max}, K_m, E for microscopic parameters).

6.2 DERIVATION OF $\bar{I}_{max}$ AND $\bar{K}_m$

We start with a brief literature review of nitrate uptake by phytoplankton (see [102]) and its modelling.

6.2.1 *Nutrient uptake by phytoplankton - literature review*

In [5], a model for nutrient uptake by a single uptake site in phytoplankton is derived using concepts of handling time and encounter rate. Upscaling to an organism scale (a single phytoplankton cell in this case) is simply done via multiplying the resulting uptake by the number of uptake sites per cell. The resulting $\bar{I}_{max}$ and $\bar{K}_m$ are of the following form: $\bar{I}_{max} = \frac{n}{h}$, where n is a number of uptake sites and h is a handling time (defined as the time required to transport one ion across the plasma membrane); $\bar{K}_m = \frac{1}{A\mathcal{V}h}$, where A is surface area of a single uptake site and $\mathcal{V}$ is a mass transfer coefficient. This way, we directly see how the physiological and physical parameters A, n, h and $\mathcal{V}$ affect the Michaelis-Menten parameters.
In [102], Michaelis-Menten uptake into a spherical cell surface was combined with a model for diffusion of a nutrient towards this cell. A steady-state assumption was made and the nutrient flux through the cell membrane was calculated assuming balance between the diffusive flux from far-field and the influx via transport sites. This enabled the authors to model diffusion-limited situations as well [1]. The steady-state influx is found to be a root of a quadratic

1 sometimes a boundary layer exists close to the cell surface in which nutrient concentration is smaller than the bulk concentration, which may limit the uptake

equation in this case.

In [6], this approach was combined with an approach using the handling times and the encounter rates (similar to [5]), so that a better understanding of Michaelis-Menten parameters (in terms of physiological and physical parameters) is achieved. Even though the influx is again the root of the quadratic equation (discussed in the previous paragraph), for both very small and very large cells (compared to the characteristic length scale of this reaction-diffusion process), the authors derived an approximation in which the influx depends on the far-field concentration in the Michaelis-Menten form.

In [13], the Michaelis-Menten functional form for uptake at the root segment scale is obtained using an analogy with enzyme kinetics, where the role of enzymes is played by the transporters. Furthermore, the dependence of the number of uptake sites on the local nutrient concentration is taken into account here.

The latest development in this field is summarised in [47] and [128]. A similar approach in modelling plant nutrient foraging behaviour can also be found in [91].

In the next section, we proceed in the direction similar to the aforementioned papers, in attempting to model nitrate uptake by plants.

6.2.2 *Application to root uptake modelling*

In this chapter, superscripts ^{L} and ^{H} correspond, respectively, to the low and high affinity transporters. In addition, h denotes the handling time required to process one nitrate ion and c the external nitrate concentration.

Following [6], we assume that $f^H(t)$ denotes a fraction of high affinity transporters which are occupied in transporting nitrate at time t. Assuming that a^H is an acquisition rate (a rate at which a single unoccupied transporter acquires ions [6]), we get the following equation for the time evolution of $f^H(t)$:

$$N^H \frac{df^H}{dt} = N^H a^H c(1 - f^H) - \frac{N^H f^H}{h^H},$$

where N^H is the number of high affinity transporters (per unit root surface area), and similarly, an analogous equation for high affinity transporters can be obtained. Dividing by N^H, we have:

$$\frac{df^H}{dt} = a^H c(1 - f^H) - \frac{f^H}{h^H}.$$

Assuming we start with $f^H(0) = 1$ (all HATs are occupied in transport), this implies that $\frac{df^H}{dt}(t = 0) = -\frac{1}{h^H}$. As mentioned in [5], the transport rates do not exceed 100 s^{-1}, therefore, we can estimate the handling time per one ion per transporter to be $h^H = 0.01$ s. Thus, we assume that the equilibration of the dynamics between the occupied and the unoccupied transporters is achieved very quickly compared with other time scales involved (both nitrate depletion and changing of the molecular apparatus are assumed to take hours; the same assumption was made in [13]) and because of that, we may neglect this process in our modelling. Using quasi-steady-state assumption $\frac{df^H}{dt} = 0$, we obtain:

$$f^H = \frac{a^H c h^H}{a^H c h^H + 1},$$

and the total uptake by high affinity transporters contained in a unit root surface area is therefore:

$$\bar{I}^H = \frac{N^H f^H}{h^H} = N^H \frac{a^H c}{a^H c h^H + 1} = \frac{N^H}{h^H} \frac{c}{c + \frac{1}{a^H h^H}} = \bar{I}^H_{max} \frac{c}{\bar{K}^H_m + c}. \tag{286}$$

The same reasoning applies to the low affinity transporters and therefore, the total influx is:

$$\bar{I} = \bar{I}^L + \bar{I}^H.$$

From the previous analysis, it is not clear what the acquisition rate a is. To answer this question, we look at a single transporter scale in the same fashion as introduced in [5]. Let A denote the area occupied by a single transporter unit within the plasma membrane, and let $\mathcal{V}^H$ denote a mass transfer coefficient, representing the velocity at which nitrate ions arrive at the root surface (say by diffusion). During a time interval of length T_1, a single high affinity transporter encounters m^H ions:

$$m^H = T_1 A^H \mathcal{V}^H c,$$

and processing these ions requires an amount of time given by:

$$T_2^H = m^H h^H.$$

Therefore, an uptake rate for a single high affinity transporter is given by:

$$I^H = \frac{m^H}{T_1 + T_2^H} = \frac{A^H \mathcal{V}^H c}{1 + h^H A^H \mathcal{V}^H c} = \frac{\frac{1}{h^H} c}{\frac{1}{h^H A^H \mathcal{V}^H} + c} = \frac{I_{max}^H c}{K_m^H + c}. \tag{287}$$

This way, we have derived a Michaelis-Menten model for a nitrate uptake by a single high affinity transporter using concepts of handling time and encounter rate. We see that the microscopic maximum uptake rate (per single transporter) is:

$$I_{max}^H = \frac{1}{h^H}, \tag{288}$$

and the microscopic half-saturation constant is:

$$K_m^H = \frac{1}{h^H A^H \mathcal{V}^H}. \tag{289}$$

As both I_{max}^H and K_m^H are proportional to $\frac{1}{h^H}$, we get a linear relationship between I_{max}^H and K_m^H:

$$I_{max}^H = A^H \mathcal{V}^H K_m^H. \tag{290}$$

Upscaling the influx rate

The simplest way to upscale Equation (287) to the root segment scale is multiplying by the number of high affinity transporters per unit root surface area N^H to get:

$$\bar{I}^H = \frac{\frac{N^H}{h^H} c}{\frac{1}{h^H A^H \mathcal{V}^H} + c}.$$

Comparing this with (286), we see that $A\mathcal{V}$ corresponds to a. Without looking into molecular details, it seems natural to assume $A^H \approx A^L$.

Macroscopic maximum uptake rate (per unit root surface area) is:

$$\bar{I}_{max}^H = \frac{N^H}{h^H} \tag{291}$$

and the macroscopic half-saturation constant is:

$$\bar{K}_m^H = \frac{1}{h^H A^H \mathcal{V}^H}. \tag{292}$$

Again, we get a linear relationship at the macroscopic scale:

$$\bar{I}_{max}^H = N^H A^H \mathcal{V}^H \bar{K}_m^H. \tag{293}$$

COMPARISON WITH EXPERIMENTAL DATA

We now check, whether the simple upscaling of microscopic I_{max} via multiplication by the transporters density (Equation (291)) gives the macroscopic $\bar{I}_{max}$ comparable to the empirically obtained values using $h = 0.01$ s from [5].

From [63], we know that the density of glutamate transporters in the neuronal cells of rats range from 2000 to 8000 transporters per μm^2. Even though this is a completely different biological system, in this section, we would only like to check if the $\bar{I}_{max}$ value upscaled from the transporter scale is roughly of the same order of magnitude as empirical values I_{max}^{emp} from the literature. As we could not find any data on the density of nitrate transporters in a biological system more closely related to plant root cells, we decided to use this range and estimate nitrate transporters density on the plant root surface to be 5000 transporters per μm^2 which is equal to 5×10^{13} transporters per dm^2.

Therefore, Equation (291) predicts the maximum influx rate to be:

$$\bar{I}_{max} = \frac{N}{h} = 5 \times 10^{15}\,\mathrm{dm}^{-2}\,\mathrm{s}^{-1} = 1.8 \times 10^{19}\,\mathrm{dm}^{-2}\,\mathrm{h}^{-1} \approx$$

$$0.2989 \times 10^{-4}\,\mathrm{mol}\,\mathrm{dm}^{-1}\,\mathrm{h}^{-1} \approx 30\,\mu\mathrm{mol}\,\mathrm{dm}^{-2}\,\mathrm{h}^{-1},$$

which is of the same order of magnitude as the empirical value from [39]:

$$I_{max}^{emp} = 1\,\mu\mathrm{mol}\,\mathrm{m}^{-2}\,\mathrm{s}^{-1} = 36\,\mu\mathrm{mol}\,\mathrm{dm}^{-2}\,\mathrm{h}^{-1},$$

and this suggests that the simple upscaling we used may be sufficient (keeping in mind the inadequacy of the biological tissue we guessed the density parameter from).

In [13], the Michaelis-Menten kinetics was derived using the quasi-steady-state assumption for enzyme kinetics problem (transporters playing the role of enzymes). In our notation, results from [13] read:

$$\bar{I}_{max}^{H} = k_2^H N^H, \tag{294}$$

where k_2^H denotes the transporter-ion complex dissociation (unbinding) rate, and:

$$\bar{K}_m^H = \frac{k_2^H}{k_1^H}, \tag{295}$$

where k_1^H denotes the transporter-ion encounter (binding) rate. The $\bar{I}_{max}^H$ parameter is only dependent on (proportional to) the dissociation rate, which is expected, as in the case where nutrient availability is non-limiting, the uptake rate is only dependent on the processing time for single ion (and not on the encounter rate). More interestingly perhaps, K_m is not only proportional to the dissociation rate, but also inversely proportional to the encounter rate - if the encounter rate is large, then K_m is small.
The meaning of expressions (291) and (294) is identical, provided $k_2^H = \frac{1}{h^H}$, which implies that the meaning of expressions (292) and (295) is identical, provided $k_1^H = A^H \mathcal{V}^H$. The linear relation (293) in this framework states:

$$\bar{I}_{max}^H = N^H k_1^H \bar{K}_m^H, \tag{296}$$

All formulae in this section hold for LATS analogously.

6.3 DERIVATION OF $\bar{c}_{min}$

We derived $\bar{I}_{max}$ and $\bar{K}_m$ using the concepts of encounter rate and handling time. However, we have not yet been able to derive the $\bar{c}_{min}$ parameter. As mentioned in [25], certain studies suggest that internal (cytoplasmic) concentration (c_i) is held constant ($3 - 5$ mM) by homeostatic effects, and we use this assumption in our analysis. We now try to validate a hypothesis that the observed $\bar{c}_{min}$ is a result of steady state balance between the influx via transporters on one hand and the root efflux on the other. For simplicity, we assume that the efflux is mostly due to lower external concentration compared to the internal concentration.

6.3.1 *General Michaelis-Menten boundary condition*

Most of the experiments aiming to determine the Michaelis-Menten uptake parameters were performed in hydroponics (see [43], [150], or Section 1.2.2). Thus, we normally do not expect sharp depletion gradients to be created in the proximity of the root surfaces, as nutrient diffusion is usually fast com-

pared to the uptake. To model this situation, we can average out the small variations in the spatial domain, which yields an ordinary differential equation in which the nitrate concentration is solely dependent on time (not space) and we will use this approach throughout this chapter. Nevertheless, in this section, we present a derivation of the Michaelis-Menten boundary condition in the most general way because we think that it provides us with an important insight into the root uptake modelling.

In the standard derivation of the diffusion equation from a random walk, we assume that in each time step, we either move one step to the left with probability $\frac{1}{2}$ or one step to the right with probability $\frac{1}{2}$. Let $x = 0$ represent the root surface, h the spatial step, τ the time step, and suppose all these quantities are already dimensionless. Assume that a nitrate ion at the root surface at time t moves one step to the right (away from the root) with probability $\frac{1}{2}$, or is taken in by a transporter with probability $\phi_1(u(0,t),h)$ (where $u(0,t)$ is nitrate concentration at the root surface at time t and ϕ_1 is yet unspecified function), or enters root through the plasma membrane with probability $\phi_2(u(0,t),h)$ (where ϕ_2 is yet unspecified function), or remains at the root surface with probability $\frac{1}{2} - \phi_1(u(0,t),h) - \phi_2(u(0,t),h)$. Assume further, that a single ion from inside the root can also diffuse out of the root through plasma membrane with probability $\phi_2(u_{in}(t),h)$ (where $u_{in}(t)$ is internal nitrate concentration at time t). Then we can write:

$$\begin{aligned} u(0,t+\tau) = \frac{1}{2}u(h,t) + \\ (\frac{1}{2} - \phi_1(u(0,t),h) - \phi_2(u(0,t),h))u(0,t) + \phi_2(u_{in}(t),h)u_{in}. \end{aligned} \tag{297}$$

It is natural to assume that the probability of an uptake event or of an ion crossing the plasma membrane in a very short time is very small; the longer the time interval is, the more of these events are expected. Therefore, we assume $\lim_{h\to 0}\phi_1(u,h) = \lim_{h\to 0}\phi_2(u,h) = 0$, and we write:

$$\phi_1(u,h) = h^\alpha f_1(u) \qquad \phi_2(u,h) = h^\beta f_2(u), \tag{298}$$

with $\alpha, \beta > 0$. Assuming $\tau \ll 1$, $h \ll 1$, a parabolic scaling $\tau = \gamma h^2$ ($\gamma = O(1)$[2]), and using Taylor expansions, we obtain from Equation (297):

$$u(0,t) + \gamma h^2 \frac{\partial u(0,t)}{\partial t} + O(h^4) = \frac{1}{2}\{u(0,t) + h\frac{\partial u(0,t)}{\partial x} + O(h^2)\} +$$
$$(\frac{1}{2} - \phi_1(u(0,t),h) - \phi_2(u(0,t),h))u(0,t) + \phi_2(u_{in}(t),h)u_{in}(t),$$

or:

$$o(h) = \frac{1}{2}h\frac{\partial u(0,t)}{\partial x} - \\ \phi_1(u(0,t),h)u(0,t) - \phi_2(u(0,t),h)u(0,t) + \phi_2(u_{in}(t),h)u_{in}(t). \tag{299}$$

Assume first, that:

$$\phi_{1,2}(u,h) = hf_{1,2}(u). \tag{300}$$

which corresponds to $\alpha = \beta = 1$ in (298). From $O(h)$ we get:

$$\frac{1}{2}\frac{\partial u(0,t)}{\partial x} = f_1(u(0,t))u(0,t) + f_2(u(0,t))u(0,t) - f_2(u_{in}(t))u_{in}(t).$$

Recalling that $f_2(u)$ relates to the probability of an ion crossing plasma membrane via diffusion, the simplest assumption to make is that f_2 is constant. This leads to:

$$\frac{\partial u(0,t)}{\partial x} = 2f_1(u(0,t))u(0,t) + \kappa\{u(0,t) - u_{in}(t)\},$$

where we have chosen:

$$\kappa = 2f_2. \tag{301}$$

Similarly, if we choose $f_1(u)$ (which relates to the transporter uptake probability) to be constant ($f_1(u) = \frac{1}{2}C$), the transporter-uptake part of the boundary condition becomes of Robin type (as first introduced in Equation (21)):

$$\frac{\partial u}{\partial x} = Cu + \kappa\{u - u_{in}\}.$$

Note that by choosing [3]:

$$f_1(u) = \frac{i_{max}}{2(k_m + u)}, \tag{302}$$

2 γ corresponds to $\frac{1}{D}$ where D is the resulting dimensionless diffusion constant for the external medium. The parabolic scaling is standard when deriving the diffusion equation, and this is related to the fact that the diffusion equation is first-order in time and second-order in space.

3 We chose i_{max} and k_m instead of I_{max} and K_m here, because the units in which these quantities are measured differ.

we can incorporate the effects of competition of nitrate ions for uptake sites into our modelling - due to the limited number of sites available for the uptake, the higher the nitrate concentration is, the smaller the probability of a specific nitrate ion to be transported. Therefore, this choice leads to a Michaelis-Menten boundary condition:

$$\frac{\partial u}{\partial x} = \frac{i_{max} u}{k_m + u} + \kappa\{u - u_{in}\}$$

at the root surface. Having derived the boundary condition under the assumption (300), we now proceed with all the remaining limits (298). We are not yet interested in a specific biologically-relevant regime; we would rather like to explore how weakening (or strengthening) of the processes in our modelling affects the resulting root surface boundary condition. In the remainder of this section, we assume that Equation (302) models the transporters uptake and Equation (301) describes the plasma membrane crossing.

Assume $1 < \alpha, \beta$. From the leading order in Equation (299), we get a zero-flux boundary condition $\frac{\partial u}{\partial x} = 0$ which is expected, because we made both the transporters uptake rate and the membrane crossing rate too small - at the leading order, all nitrate ions are reflected back into the external medium.

Assume $\alpha < 1, \beta$. This means that the transporters uptake dominates, and the leading order in Equation (299) gives $0 = u f_1(u) = \frac{i_{max} u}{2(k_m + u)}$, which gives a Dirichlet boundary condition $u = 0$ - all nitrate ions are immediately transported into the root.

Assume $\beta < 1, \alpha$. The leading order gives $0 = f_2(u)u - f_2(u_{in})u_{in} = \frac{\kappa}{2}(u - u_{in})$. This leads to a Dirichlet boundary condition $u = u_{in}$. With passive crossing of the plasma membrane being the dominant process, balance is established by equating the external and the internal concentrations.

Assume $\alpha = 1 < \beta$. From the leading order, we get $\frac{\partial u}{\partial x} = \frac{i_{max} u}{k_m + u}$ - gradient at the root surface is governed by the Michaelis-Menten kinetics and the efflux is negligible.

Assume $\beta = 1 < \alpha$. The leading order gives $\frac{\partial u}{\partial x} = \kappa(u - u_{in})$. As the transporters uptake is negligible now, gradient at the root surface is determined by the concentration gradient between the internal and the external concentration.

Assume $\alpha = \beta < 1$. The leading order gives $\frac{i_{max}u}{k_m+u} = \kappa(u_{in} - u)$ and the balance is established between the transporters uptake and the cross-membrane diffusion. This leads to a quadratic equation for u which has solutions:

$$u_{\pm} = \frac{-(k_m - u_{in} + \frac{i_{max}}{\kappa}) \pm \sqrt{(k_m - u_{in} + \frac{i_{max}}{\kappa})^2 + 4k_m u_{in}}}{2}.$$

It is easy to see that $\left|k_m - u_{in} + \frac{i_{max}}{\kappa}\right| < \sqrt{(k_m - u_{in} + \frac{i_{max}}{\kappa})^2 + 4k_m u_{in}}$, and therefore $u_- < 0$ (which is nonphysical) and $u_+ > 0$. Therefore, the only physiologically relevant boundary condition is:

$$u = \frac{-(k_m - u_{in} + \frac{i_{max}}{\kappa}) + \sqrt{(k_m - u_{in} + \frac{i_{max}}{\kappa})^2 + 4k_m u_{in}}}{2}.$$

Thus we have shown how to derive all relevant root surface boundary conditions using the random walk approach. In the remaining part of this thesis, we will be mostly interested in the $\alpha = \beta < 1$ case.

6.3.2 *High and low affinity transport modelling*

The modelling from the previous section is not sufficient to describe the nitrate uptake fully, because we know of at least two distinct nitrate uptake kinetics in plants. Thus, we model nitrate uptake by low and high affinity transporters with a possible diffusion across the plasma membrane with permeability P [97]. Transporters of both types follow the Michaelis-Menten kinetics. We do not assume the linear relationship between I_{max} and K_m (290) from the beginning, as this has not been fully validated by experiments yet. Instead, we assume that HATS have low values for both K_m and I_{max}, and LATS have high values for both K_m and I_{max}, i.e.:

$$K_m^H < K_m^L \tag{303}$$

and

$$I_{max}^H < I_{max}^L. \tag{304}$$

We further assume that a plant can produce a limited number of low (N^L) and high (N^H) affinity transporters per unit root surface area so that the total number of transporters per unit root surface area is fixed:

$$N = N^L + N^H. \tag{305}$$

We study how different distributions of low and high affinity transporters affect nitrate uptake. Note that in this thesis, we assume the densities of low and high affinity transporters to be constant in time. However, plants do change these densities with their developmental stage and in response to external nitrate concentration [89]. We plan to incorporate these effects in future research.

First, we focus on the steady-state scenario where we try to shed more light on the effect that the parameters I_{max} and K_m have on the Michaelis-Menten functional form, so that we can understand more clearly why low affinity transporters dominate at high nitrate concentrations and vice versa. Parameter values and their units are not important at this stage - we will use realistic values after we introduce and explain the basic concepts.

6.3.3 *Steady state scenario*

We start with a steady-state assumption:

$$N^L \frac{I^L_{max} c_{ss}}{K^L_m + c_{ss}} + N^H \frac{I^H_{max} c_{ss}}{K^H_m + c_{ss}} = P(c_i - c_{ss}) \tag{306}$$

where c_{ss} is an external nitrate concentration, so that the total intake by the low ($N^L \frac{I^L_{max} c_{ss}}{K^L_m + c_{ss}}$) and the high ($N^H \frac{I^H_{max} c_{ss}}{K^H_m + c_{ss}}$) affinity transporters together is balanced with an efflux due to nitrate diffusion across the plasma membrane ($P(c_i - c_{ss})$ - where P is the membrane permeability). Our task here is to find an optimal N^L so that c_{ss} (which we solve for) is minimal, assuming the constraint (305). In other words, we want the plant to use as much of the external nitrate as possible. This is similar to the concept of R^* - a concentration at which a nutrient ceases to be extractable from [133] - which was shown to be crucial for the survival of a species.

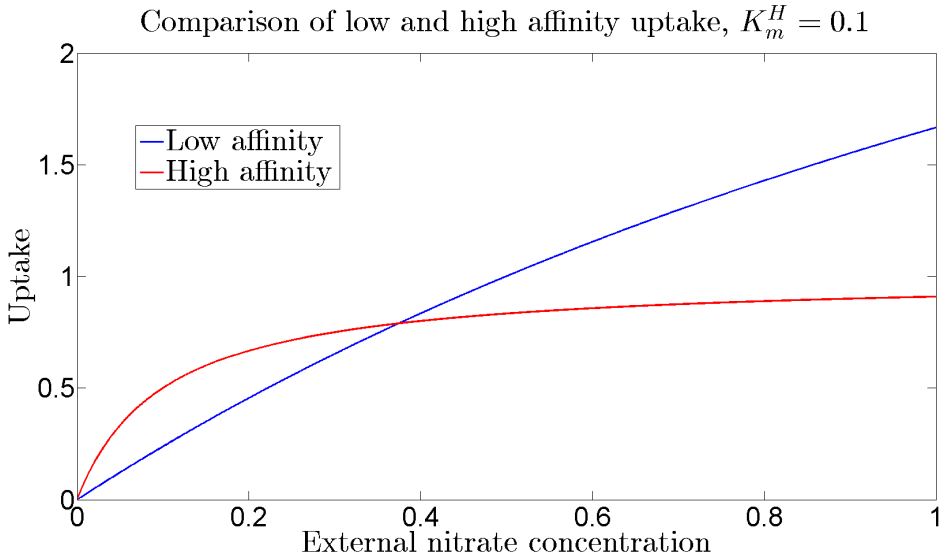


Figure 6.1.: Comparison of the Michaelis-Menten functions for LATs and HATs assuming $\frac{K_m^L}{K_m^H} = 20$ and $\frac{I_{max}^L}{I_{max}^H} = 5$.

First of all, we notice that $c^{**} = 0$ always satisfies a condition that the uptake by a single high and low affinity transporter at this external concentration is the same (namely zero)[4]. Next, assuming (304), any other value satisfying this condition obeys:

$$\frac{I_{max}^L}{K_m^L + c^*} = \frac{I_{max}^H}{K_m^H + c^*}.$$

This leads to the following dependence of c^* on the Michaelis-Menten parameters:

$$c^* = \frac{K_m^L I_{max}^H - K_m^H I_{max}^L}{I_{max}^L - I_{max}^H}, \tag{307}$$

which is positive if and only if $K_m^L I_{max}^H - K_m^H I_{max}^L$ is positive, or equivalently:

$$\frac{K_m^L}{K_m^H} > \frac{I_{max}^L}{I_{max}^H}. \tag{308}$$

Using (arbitrary) parameters $I_{max}^L = 5$, $I_{max}^H = 1$, $K_m^L = 2$ and varying K_m^H, we uncovered two distinct cases, which are depicted in Figures 6.1 and 6.2.

If $\frac{K_m^L}{K_m^H} \leq \frac{I_{max}^L}{I_{max}^H}$, then it is advantageous for the root to produce low affinity transporters only - these uptake more nitrate for the entire range of external concentrations, and thus the resulting external concentration at the steady state is minimalised by taking all the transporters to be of low affinity type.

4 Note that $c^{**} = 0$ is clearly not a solution of the steady-state equation (306)

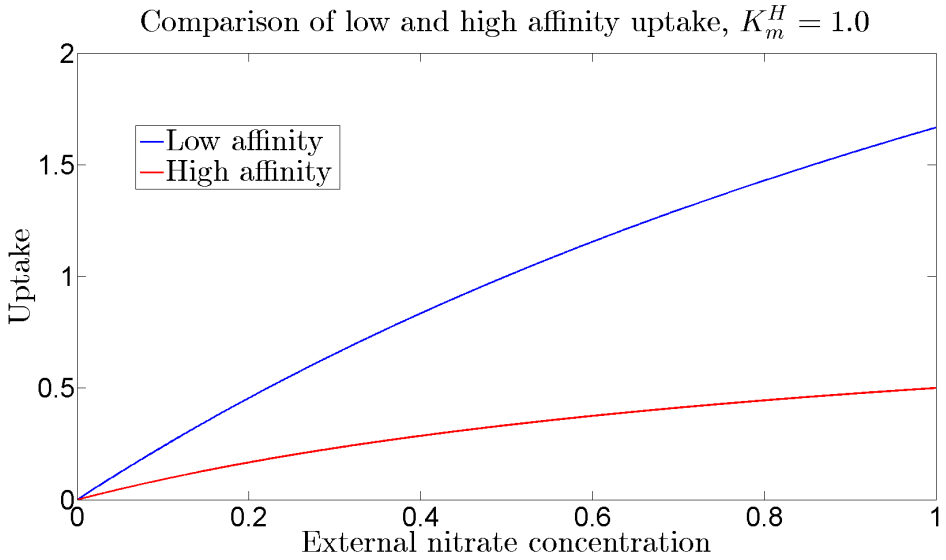


Figure 6.2.: Comparison of the Michaelis-Menten functions for LATs and HATs assuming $\frac{K_m^L}{K_m^H} = 2$ and $\frac{I_{max}^L}{I_{max}^H} = 5$.

For $\frac{K_m^L}{K_m^H} > \frac{I_{max}^L}{I_{max}^H}$, we have $c^* = \frac{K_m^L I_{max}^H - K_m^H I_{max}^L}{I_{max}^L - I_{max}^H} > 0$. Rewriting Equation (306), we get:

$$N^L \frac{I_{max}^L c_{ss}}{K_m^L + c_{ss}} + N^H \frac{I_{max}^H c_{ss}}{K_m^H + c_{ss}} + P c_{ss} = P c_i, \tag{309}$$

which represents the steady state scenario. Left-hand side can be interpreted as the total influx into the root, and the right-hand side as the efflux from the root. Substituting c^* (for c_{ss}) into the left-hand (influx) side of Equation (309), we can get three different outcomes:

1. The steady state condition (309) is satisfied
2. Influx dominates
3. Efflux dominates

In the steady-state situation (case 1.), it does not matter whether the plant produces HATs or LATs, because $c_{ss} = c^* = \frac{K_m^L I_{max}^H - K_m^H I_{max}^L}{I_{max}^L - I_{max}^H}$ here.
If the influx is larger than the efflux (case 2.), then c_{ss} at the steady state will be lower than c^*. This suggests that the optimal strategy for a plant is to produce HATs only.
If the efflux is larger than the influx (case 3.), then c_{ss} at the steady state will be higher than c^*. This suggests that the optimal strategy for a plant is to produce

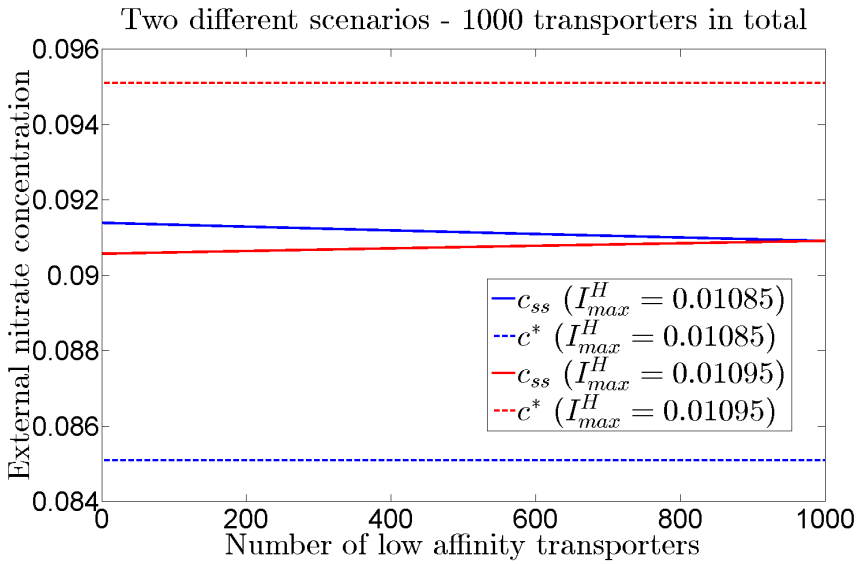


Figure 6.3.: For $I^H_{max} = 0.01085$ (blue), the steady-state concentration (for any value of N^L; solid line) is greater than c^* (dashed line), and therefore it is advantageous for the plant to produce LATs only. However, a slight increase in I^H_{max} gives the opposite outcome (red), and HATs-only becomes the optimal strategy for minimising c_{ss}.

LATs only.

We solved the cubic equation (306) and plotted the only positive root c_{ss} as a function of N^L. Using parameters $N = 1000$, $K^H_m = 1$, $K^L_m = 1000$, $I^L_{max} = 10$, $c_i = 1.0$, $P = 1.0$ and varying I^H_{max}, we managed to obtain the cases 2 and 3. Parameter values are chosen rather arbitrarily at the moment - the only assumptions made are stated in the equations (303), (304), and (308). Note, that the condition (308) implies $I^H_{max} > I^L_{max}\frac{K^H_m}{K^L_m} = 0.01$, which together with (304) means:

$$0.01 < I^H_{max} < 10. \tag{310}$$

We found that $I^H_{max} = 0.01085$ and $I^H_{max} = 0.01095$ give the two different scenarios (cases 2. and 3.), and the results are shown in Figure 6.3 (the corresponding MATLAB code can be found in Appendix C)). Using this steady-state approach, one can tell whether it is advantageous for a plant to produce LATs only or HATs only. However, this dichotomy is not observed in real plants. To obtain non-trivial quotient between N^L and N^H, we need to incorporate time evolution into our modelling. Imagine, we start with very high external nitrate

concentration. At this stage, roots mostly need LATs (which usually have large I_{max}) to uptake the surrounding nitrate as quickly as possible. However, as we approach low nitrate concentrations, HATs become more efficient. To capture these effects, we need to minimise depletion time alongside minimising the external concentration at the steady state. Minimisation of the depletion time requires LATs whereas minimisation of the steady-state external concentration may require HATs (provided $c_{ss} < c^*$).

6.3.4 *Time evolution to the steady state*

Imagine a unit volume of the solution in which roots are located with a typical root surface area as found in hydroponic experiments and nitrate being actively taken up via HATs and LATs. Again, we do not consider the spatial nitrate flows and we do not model competition for nitrate between plants or between different roots of the same plant. Thus, our model does not involve spatial variables, and we may think of it as being averaged across the mentioned unit solution volume. The resulting equation states:

$$\frac{dc}{dt} = -N^L \rho \frac{I^L_{max} c}{K^L_m + c} - N^H \rho \frac{I^H_{max} c}{K^H_m + c} - P\rho(c - c_i), \tag{311}$$

and for the initial condition, we assume:

$$c(t = 0) = c_{in}.$$

Here, $c(t)$ is the external nitrate concentration (we dropped the subscript *ss* as we model the time evolution now; mM), N^L is the number of LATs per unit root surface area (dm^{-2}), ρ is a typical root surface area density as found in hydroponic experiments (dm^2 of root surface per dm^3 of the solution volume), I^L_{max} is the maximum influx rate in the Michaelis-Menten kinetics (mmol of nitrate per h per transporter), K^L_m is the Michaelis half-saturation constant in mM, c_i is the internal nitrate concentration in mM (which is held constant as in the steady-state case), and P is the membrane permeability (mmol of nitrate per dm^2 of root surface per h per unit difference in nitrate concentration - this is consistent with the standard units for membrane permeability, i.e. dm

Parameter	Value
K_m^H	1.0
I_{max}^H	0.03
c_{in}	10.0
c_i	1.0
I_{max}^L	10.0
K_m^L	1000.0
ρ	1.0
P	1.0
N	1000

Table 6.1.: Toy model parameter values.

h^{-1}). This way $P\rho(c - c_i)$ is the amount of nitrate (in mmol) taken up in the unit solution volume (dm^3) per h. The constants with superscript H have analogous meaning to those with superscript L, and they refer to the HATs. We assume $N^L + N^H = N$, where N is fixed as before.

6.3.5 *Toy model*

In order to show the variety of behaviour our model can capture, we first simulate a toy model using the same arbitrary parameters as before, and then use realistic parameters for the specific case of nitrate uptake in the next section. The parameter values for the toy problem are summarised in Table 6.1. As parameters are chosen arbitrarily, their units are also irrelevant at this stage. We have chosen $c_{in} = 10.0$ so that we start with a concentration higher than the internal concentration $c_i = 1.0$. $I_{max}^H = 0.03$ is chosen to satisfy condition (310), and also to satisfy $I_{max}^H \geq 0.01095$ (otherwise we may never reach external concentration at which HATs are more efficient than LATS). Figure 6.4 shows time evolution of external nitrate concentration for some of the possible values of N^L. We see that the external nitrate concentration is always decreasing with time which is due to the uptake via transporters. The higher the value of N^L is,

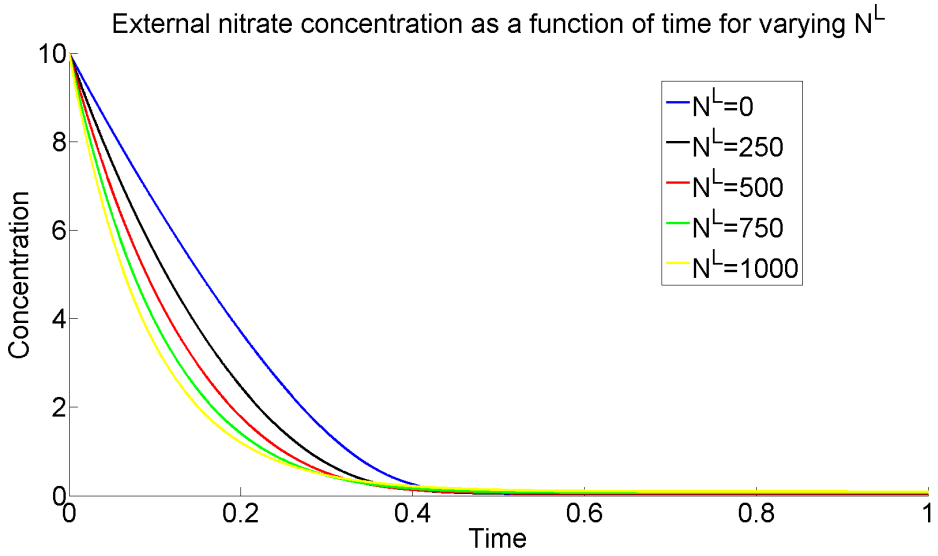


Figure 6.4.: Time evolution to the steady state for the toy model of nitrate uptake by HATs and LATs.

the faster we approach the steady state. However, increase in N^L also causes the steady state to be slightly higher (as it corresponds to a decrease in N^H). This is clearly visible when we zoom in on the behaviour close to the steady states as shown in Figure 6.5. We also plot the external nitrate concentration as a function of both time and N^L.

Depletion time

For this chapter, we define depletion time to be the time needed for an external concentration to drop from a given high initial concentration down to a fixed percentage (referred to as tolerance from now onwards) above the steady state value. The depletion time is plotted in the Figure 6.7 (choosing 1% as the tolerance value). We see that the depletion time is below 0.44 for every choice of N^L. Thus, we can fix $T = 0.44$ (and call it a reference time from now onwards), and study the remaining external nitrate concentration at this time point. The results for varying N^L are shown in the Figure 6.8 and comparison with the steady state concentration is also made. Minimum in remaining nitrate concentration at $t = 0.44$ is obtained for $N^L \approx 270\,\mathrm{dm}^{-2}$. Naturally, this value will depend on the choice of the reference time, which in turn depends on the time scale of the biological process under consideration.

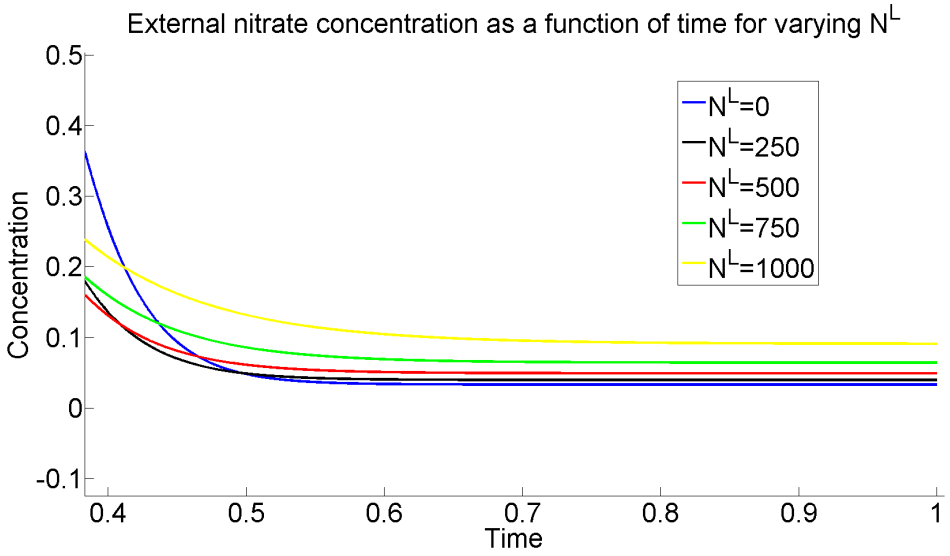


Figure 6.5.: Time evolution to the steady state for the toy model of nitrate uptake by HATs and LATs (zoom).

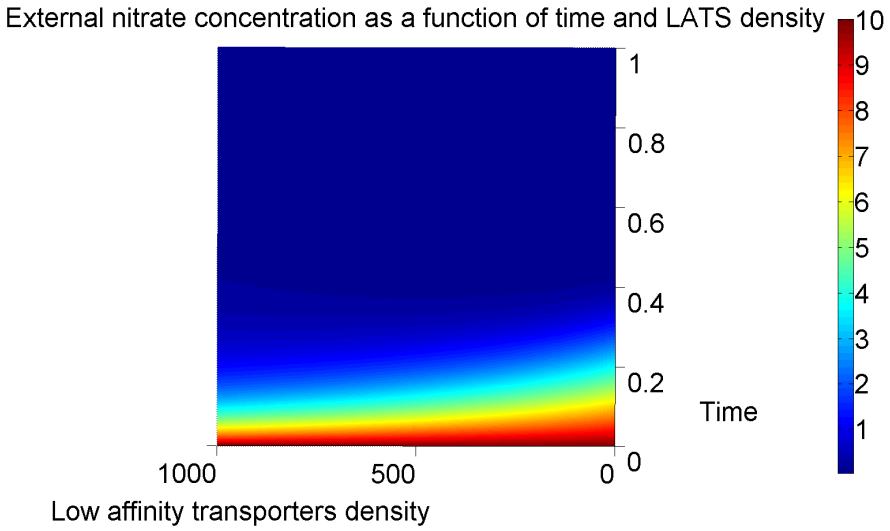


Figure 6.6.: The external nitrate concentration as a function of time and N^L for the toy model of nitrate uptake by HATs and LATs.

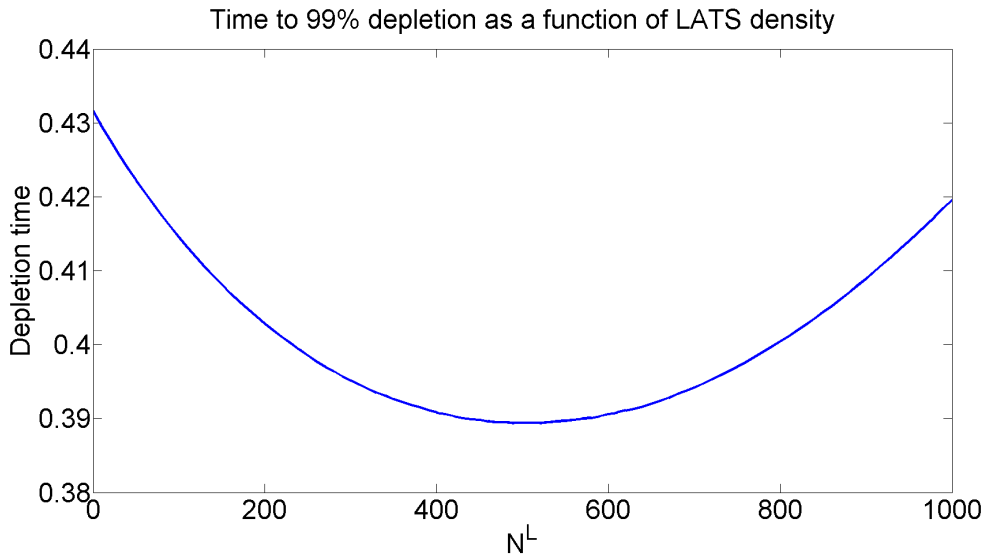


Figure 6.7.: Global minimum in depletion time for the toy model is achieved for a nontrivial low/high affinity transporters distribution - at $N^L \approx 505$ (which corresponds to $N^H = 495$).

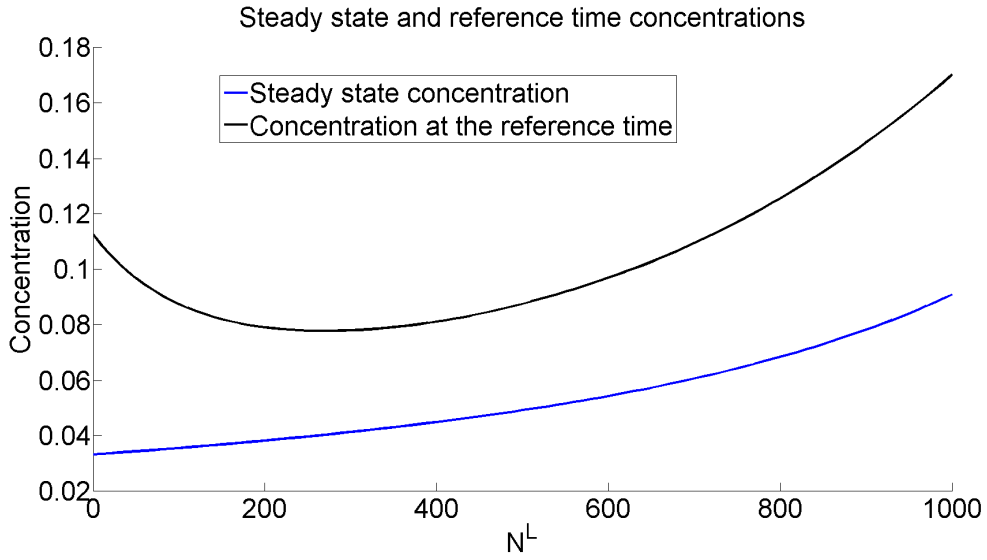


Figure 6.8.: Remaining nitrate concentration at the reference time and the corresponding steady states for the toy model.

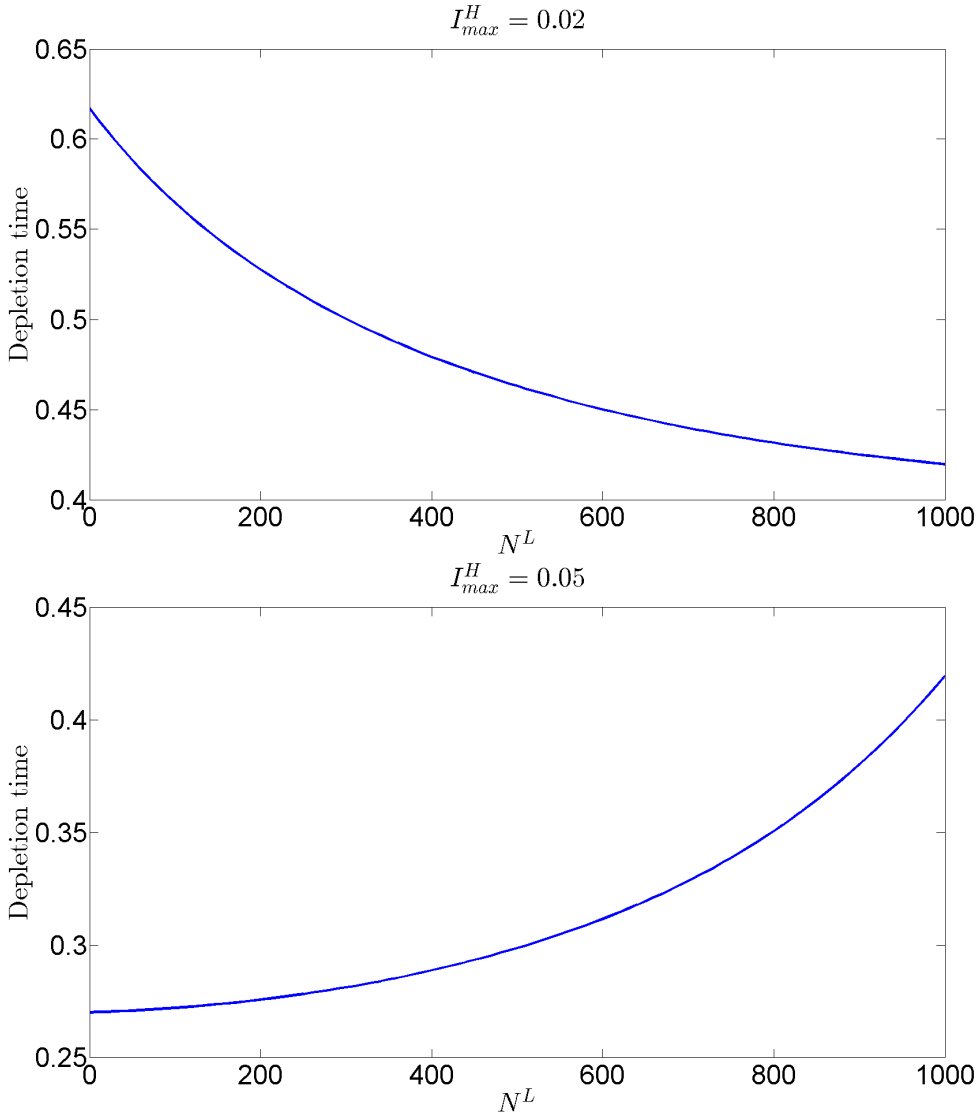


Figure 6.9.: Depletion times for $I^H_{max} = 0.02$ and $I^H_{max} = 0.05$ (toy model).

Note that we had to pick $I^H_{max} = 0.03$ very carefully in order to show that a non-trivial low-high affinity transporters distribution can give a global minimum in depletion time. Figure 6.9 shows that a small change in I^H_{max} can result in HATs/LATs-only being the optimal strategy. If we choose slightly smaller I^H_{max}, the depletion time is minimised by taking LATs only, and if we choose slightly higher I^H_{max}, the HATs-only strategy becomes optimal.

Now that we have explained all the basic ideas, we introduce biologically and physically relevant parameters.

6.3.6 *Model with realistic parameters*

Let us look back into the equations (294) and (295). The simplest of all possible interpretations of the differences in I_{max} and K_m between HATs and LATs is that LATs possess high dissociation rate k_2 (i.e. short handling time) and the opposite is true for HATs. This yields both Michaelis-Menten parameters (I_{max} and K_m) higher for LATs. From now onwards, we assume that this is true, and that the encounter rate is the same for HATS and LATS, even though the alternative explanation (that HATs attract/bind nitrate ions better than LATs, i.e. HATS have higher encounter rate k_1) is also worth keeping in mind.

Problem with the linear relationship assumption

The assumption of linear relationship between I_{max} and K_m at the microscale (Equation (290)) together with the assumption of the same area occupied by a HAT and a LAT unit ($A^H = A^L$), leads to an unexpected conclusion, namely that a single low affinity transporter unit is more efficient compared to a single high affinity unit at any external nitrate concentration. To see this, assume $K_m = \beta I_{max}$ and denote $g(I_{max}) = \frac{I_{max}c}{\beta I_{max}+c}$. Then $g'(I_{max}) = \frac{c^2}{(\beta I_{max}+c)^2}$ which is positive for any (fixed) $c > 0$. This (altogether with a simple fact that the uptake rate is 0 for $c = 0$ independent of I_{max}) leads to the dominance of LAT uptake at any nitrate concentration. Another way to see this is by looking at Equation (307) - assuming $K_m = \beta I_{max}$ holds for HATs and LATs with the same β gives $c^* = c^{**} = 0$, and as there is no positive concentration for which the uptake rate by a single HAT unit equals that by a LAT unit, LATs uptake more for any positive concentration. This seems to be in contradiction with the standard understanding of LATS and HAT uptake behaviour.

One explanation for this may be, that HATs are somehow cheaper for a plant to produce, and thus they can be produced in greater amounts compared to LATs. From [23] and [22], we see that the atNRT2.1 transporter (high affinity) has a molecular weight of 57709.4 daltons (1 dalton is approximately equal to 1.66×10^{-27} kg), which is less than 63981.1 daltons (molecular weight of the atNRT1.2 transporter; low affinity). This way, including carbon cost in

our calculations may help resolve these apparent contradictions. Furthermore, maintenance and functioning of a single LAT unit may be more expensive than that of a HAT unit (e.g. energy expenditure per one transported ion). This all would mean that even though a single HAT uptakes less than a single LAT at any nitrate concentrations, at low nitrate concentrations, it is advantageous for a plant to produce HATs (in greater amounts) because the difference between the (per transporter) uptake rates is very small in this range.
Independent of what the true reason for LATs being "more expensive" is, this means:

$$C^L N^L + C^H N^H = B = const, \tag{312}$$

where (vaguely speaking) C^L presents a cost of a single LAT unit, C^H a cost of a single HAT unit, and B total cost a plant can pay, which represents a limited plant budget, determined by (e.g.) available carbon. Thus, the constraint (305) is modified to be:

$$N^L + \alpha N^H = N, \tag{313}$$

where $\alpha = \frac{C^H}{C^L}$ and $N = \frac{B}{C^L}$. Applying this constraint, the time evolution equation (311) becomes:

$$\frac{dc}{dt} = -N^L \rho \frac{I^L_{max} c}{K^L_m + c} - \frac{N - N^L}{\alpha} \rho \frac{I^H_{max} c}{K^H_m + c} - P\rho(c - c_i). \tag{314}$$

It still remains to determine the constants α and N.

Parameter estimation

First, we estimate α. For concentrations much higher than K^H_m, HATs operate practically at the maximum influx rate. At the same time, as discussed in Section 6.1.2, LAT uptake in the millimolar range exhibits linear increase with the external nitrate concentration, and the influx is thus modelled as:

$$I = a_{ic} c + b_{ic},$$

where the constant term b_{ic} corresponds to HATs operating at the maximum influx rate, and the $a_{ic}c$ term presents the linear approximation to the Michaelis-Menten kinetics of LATs with very high K^L_m (which holds for concentrations much smaller than K^L_m). The subscript $_{ic}$ indicates that we are dealing with the

intermediate concentrations (high enough so that HATs operate at the maximum rate but low enough so that LATs kinetics is close to linear). The linear approximation for small concentrations gives:

$$a_{ic} \approx \frac{\bar{I}^L_{max}}{\bar{K}^L_m} = \frac{N^L_{ic} I^L_{max}}{K^L_m} = \frac{N^L_{ic} I^H_{max}}{K^H_m} = \frac{\alpha N^L_{ic} \bar{I}^H_{max}}{N \bar{K}^H_m}, \tag{315}$$

where we first used the linear relationship between I_{max} and K_m, then the standard transitions between the microscopic and macroscopic Michaelis-Menten parameters, and finally the assumption that almost all transporters are of the high affinity type for $c = O(K^H_m)$. Using this assumption, we substituted $N^L = 0$ in the constraint (313), which yields the upper bound for HATs density $N^H_{max} = \frac{N}{\alpha}$. Rearranging Equation (315) gives:

$$\alpha \approx \frac{a_{ic} N \bar{K}^H_m}{N^L_{ic} \bar{I}^H_{max}}. \tag{316}$$

Moreover, assuming that the constant term b_{ic} is caused by HATs operating at the maximum influx rate, and that almost all transporters are of the high affinity type for $c = O(K^H_m)$, we get:

$$\frac{b_{ic}}{\bar{I}^H_{max}} = \frac{N^H_{ic}}{N^H_{max}} = \frac{(N - N^L_{ic})/\alpha}{N/\alpha} = \frac{N - N^L_{ic}}{N},$$

which yields:

$$\frac{N}{N^L_{ic}} = \frac{\bar{I}^H_{max}}{\bar{I}^H_{max} - b_{ic}}. \tag{317}$$

Substituting (317) into Equation (316), we conclude:

$$\alpha = \frac{a_{ic} \bar{K}^H_m}{\bar{I}^H_{max}} \frac{\bar{I}^H_{max}}{\bar{I}^H_{max} - b_{ic}} = \frac{a_{ic} \bar{K}^H_m}{\bar{I}^H_{max} - b_{ic}}.$$

From [89] (in which nitrogen uptake by oilseed rape is modelled), we get $a^g_{ic} \approx 0.007\,\mathrm{dm^3\,h^{-1}\,g^{-1}}$, $b^g_{ic} \approx 20\,\mu\mathrm{mol\,h^{-1}\,g^{-1}}$ and (for inducible HATS) $\bar{I}^{H,g}_{max} = 135\,\mu\mathrm{mol\,h^{-1}\,g^{-1}}$, $\bar{K}^H_m = 85\,\mu\mathrm{M}$ (these parameters are often given per gram of root dry weight - we denote such parameters with a superscript ^{g}). These values yield $\alpha \approx 0.005$.

For LATs, we choose $\bar{K}^L_m$ high enough ($\bar{K}^L_m = 100$ mM), so that for concentrations of order 1 mM, the linear approximation is very close to the Michaelis-Menten kinetics. Corresponding $\bar{I}^L_{max}$ is calculated as follows:

$$\bar{I}^{L,g}_{max} = \bar{K}^L_m a^g_{ic} = 0.7\,\mathrm{mmol\,h^{-1}\,g^{-1}}.$$

It remains to estimate N from Equation (313). For very low concentrations, we assume that no LATs are produced, and that HATs are produced in the greatest amounts, i.e. $N = \alpha N^H_{max}$. As mentioned in Section 6.2.2, [63] gives the density of glutamate transporters in the neuronal cells of rats ranging from 2000 to 8000 transporters per μm^2. We pick $N^H_{max} = 8000$ transporters per μm^2, which equals $N^H_{max} = 8 \times 10^{13}\ dm^{-2}$, and conclude $N = 4 \times 10^{11}\ dm^{-2}$. Note that the resulting behaviour will actually be independent of N^H_{max}, because having no information on the density of transporters, we will define I^H_{max} and I^L_{max} simply by downscaling (i.e. dividing by the corresponding density) empirical values from the literature (see equations (318) and (319))[5].

To transform the influx units given per gram of root dry weight to those given per root surface area, we introduce specific root surface area A_g, which is defined as the root surface area divided by its dry weight. From [37], we get an estimate of 400 m g^{-1} for the specific root length of the oilseed rape, which combined with the mean root radius of 0.03 cm estimated from [73], yields the specific root surface area $A_g \approx 400 \times 2 \times \pi \times 0.0003\ m^2\ g^{-1} \approx 75\ dm^2\ g^{-1}$. Furthermore, taking 19 cm^{-2} from [37] as a value for the root length density for the oilseed rape plant, we estimate:

$$\rho = 2 \times \pi \times 0.03 \times 19\ cm^{-1} \approx 3.6\ cm^{-1} = 36\ dm^{-1}.$$

To get the maximum influx rates on the surface area basis, we simply divide by the specific root surface area, and get:

$$\bar{I}^L_{max} = \frac{\bar{I}^{L,g}_{max}}{A_g} \approx 9.3\ \mu mol\ h^{-1}\ dm^{-2} \qquad \bar{I}^H_{max} = \frac{\bar{I}^{H,g}_{max}}{A_g} = 1.8\ \mu mol\ h^{-1}\ dm^{-2}.$$

To find the microscopic (i.e. per transporter) maximum influx rate of HATs, we simply divide the maximum macroscopic HAT influx rate $\bar{I}^H_{max}$ by the corresponding HAT density N^H_{max}, and obtain:

$$I^H_{max} = \frac{\bar{I}^H_{max}}{N^H_{max}} = 2.25 \times 10^{-14}\ \mu mol\ h^{-1}, \tag{318}$$

5 In other words, imagine that the real value of N^H_{max} is actually γ times greater than the chosen value. Then the same is true for N, N^H_{min}, and N^L_{max} (N^H_{min} and N^L_{max} will be defined later in this section). Moreover, I^H_{max} and I^L_{max} are γ times smaller than the values calculated using the original N^H_{max}. The important thing from the perspective of Equation (311) is that irrespective of the choice of N^H_{max}, both $N^H_{max} I^H_{max} = \bar{I}^H_{max}$ and $N^L_{max} I^L_{max} = \bar{I}^L_{max}$ remain unchanged.

which roughly corresponds to 4 nitrate ions transported per second.

As we have already noted, even at very high nitrate concentrations, a non-zero HAT density is present - let us denote this density N^H_{min}. We can obtain an approximation for N^H_{min} by comparing the maximal HAT uptake rate $\bar{I}^{H,g}_{max}$ (achieved at the maximal transporter density N^H_{max}) with the HAT contribution at high nitrate concentrations b^g_{ic}, i.e.:

$$N^H_{min} = \frac{b^g_{ic}}{\bar{I}^{H,g}_{max}} N^H_{max} \approx 1.2 \times 10^{13}\,\mathrm{dm}^{-2}.$$

The corresponding LAT density is $N^L_{max} = N - \alpha N^H_{min} = 3.4 \times 10^{11}\,\mathrm{dm}^{-2}$. Therefore, to obtain a microscopic maximum influx rate of LATs, we need to divide the maximum macroscopic LAT influx rate $\bar{I}^L_{max}$ by the corresponding LAT density N^L_{max}, and get:

$$I^L_{max} = \frac{\bar{I}^L_{max}}{N^L_{max}} \approx 2.7 \times 10^{-11}\,\mu\mathrm{mol\,h}^{-1}, \tag{319}$$

which is approximately 4500 nitrate ions transported per second.

As before, we assume $K^H_m = \bar{K}^H_m$ and $K^L_m = \bar{K}^L_m$.

From [109] and [110], we know that the estimates of the nitrate permeability coefficient of the plasma membrane range from $1.8 \times 10^{-11}\,\mathrm{m\,s}^{-1}$ to $10^{-9}\,\mathrm{m\,s}^{-1}$, or equivalently from $6.48 \times 10^{-7}\,\mathrm{dm\,h}^{-1}$ to $3.6 \times 10^{-5}\,\mathrm{dm\,h}^{-1}$. We choose $P = 1 \times 10^{-5}\,\mathrm{dm\,h}^{-1}$.

The parameter values are summarised in Table 6.2.

Simulations

As the main check, we want the steady state concentration $\bar{c}_{min}$ measured and used in previous nitrate studies to be the same (or at least of the same order) as the one extracted from the model as a steady-state concentration. The $\bar{c}_{min}$ values measured in [150] range approximately from 1 to 5 µM. On the other hand, the authors of [39] used a value $\bar{c}_{min} = 0.1\,\mu\mathrm{M}$ in their modelling. As the information on $\bar{c}_{min}$ from the existing literature seems a bit ambiguous, we accept any $\bar{c}_{min}$ values higher than 0.1 µM and lower than 5 µM, but hope to get $\bar{c}_{min}$ in the experimentally-measured range from [150].

Moreover, we need to check that our modelling predicts the depletion time

Parameter	Value	Units
K_m^H	0.085	mM
I_{max}^H	2.25×10^{-17}	mmol h^{-1}
c_i	3	mM
I_{max}^L	2.7×10^{-14}	mmol h^{-1}
K_m^L	100	mM
ρ	36.0	dm^{-1}
P	1.0×10^{-5}	dm h^{-1}
α	0.005	-
N	4×10^{11}	dm^{-2}

Table 6.2.: Realistic parameter values for nitrate uptake by oilseed rape plant. Various sources (see the main text).

(time required to reach $\bar{c}_{min}$) in the same order as that observed in hydroponic experiments, which typically means up to 10 hours, provided we start with a relatively low initial concentration (e.g. 0.25 mM in [77]).

Simulation results using the parameters from Table 6.2 and $c_{in} = 0.25$ mM are shown in Figures 6.10 – 6.12. The corresponding MATLAB code can be found in Appendix C. The time of depletion is close to the experimental value of 10 hours from [77].

The steady-state concentrations (which we expect to correspond to the $\bar{c}_{min}$ value) range up to approximately 125 µM (Figure 6.11). However, for real plants at such low concentration, we assume that no LATs are present anymore. Zooming into the region $N^L \approx 0$, we get an estimate of $\bar{c}_{min} \approx 1.5$ µM (see Figure 6.13), which is within the range measured in [150]. All these figures suggest that HATs are more efficient in the uptake from the very beginning (i.e. for any external nitrate concentration ≤ 0.25 mM).

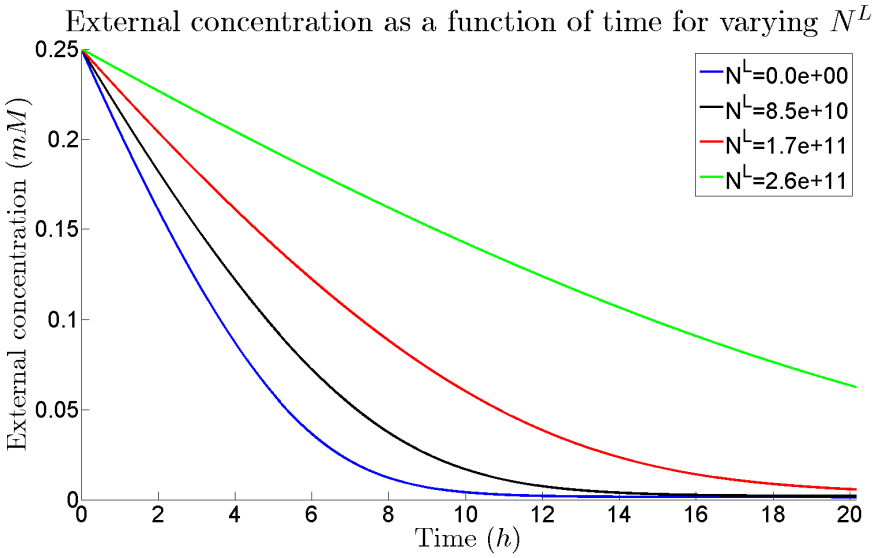


Figure 6.10.: Time evolution to the steady state for the model of nitrate uptake by LATs and HATs.

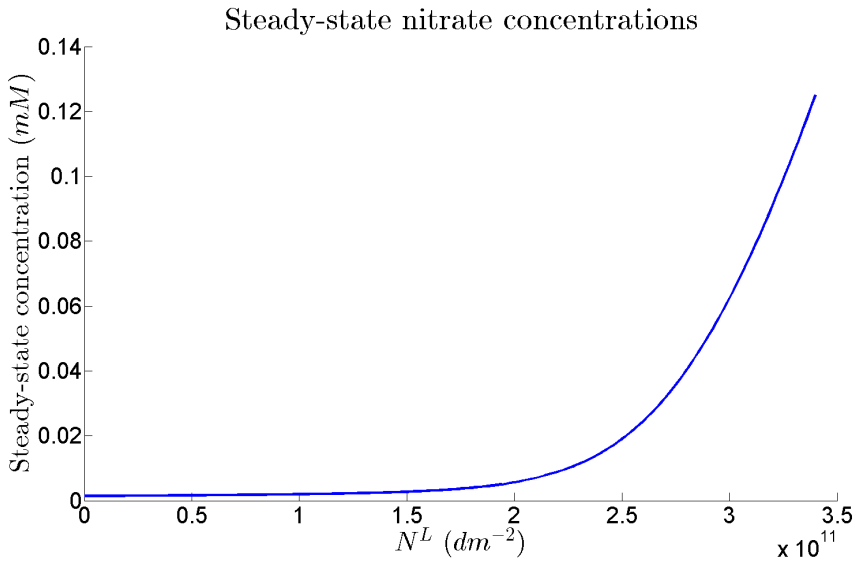


Figure 6.11.: Steady state concentration as a function of N^L for the model of nitrate uptake by LATs and HATs.

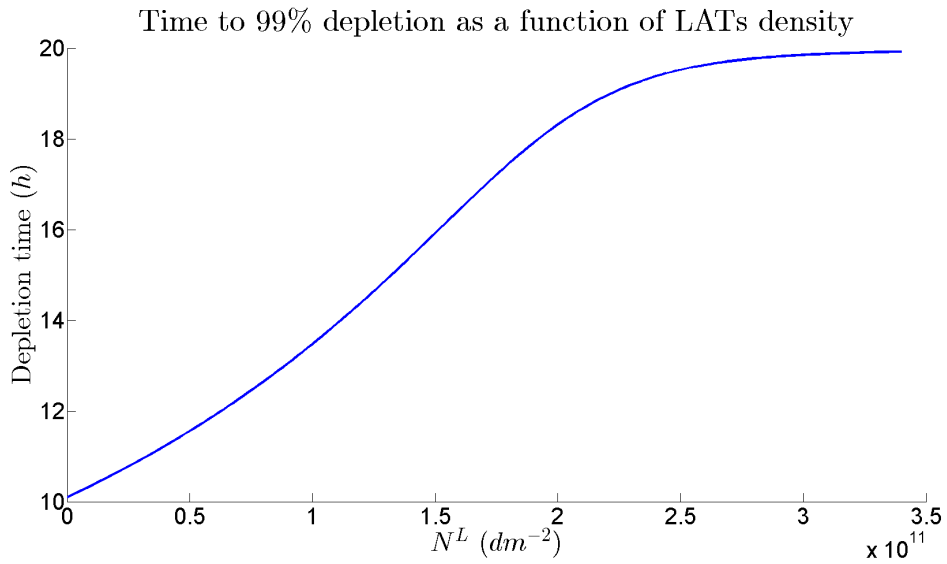


Figure 6.12.: Depletion time as a function of N^L for the model of nitrate uptake by LATs and HATs.

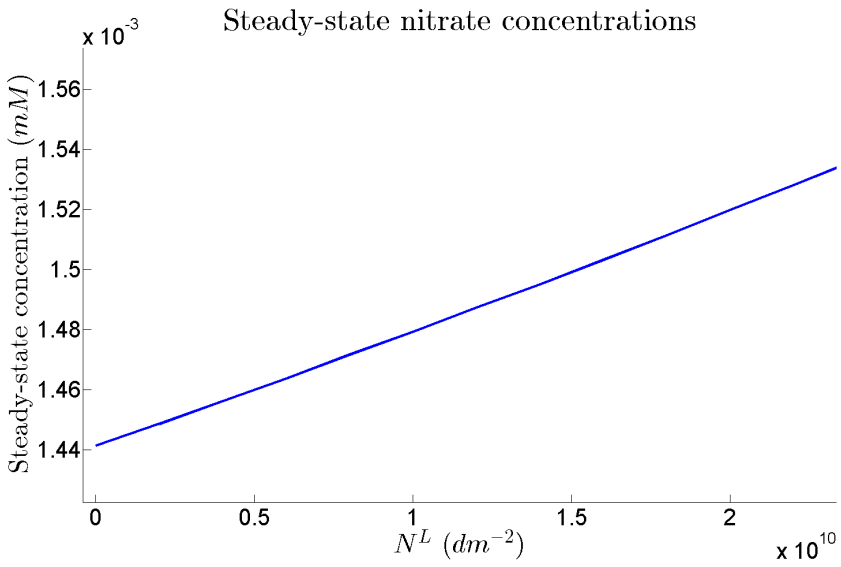
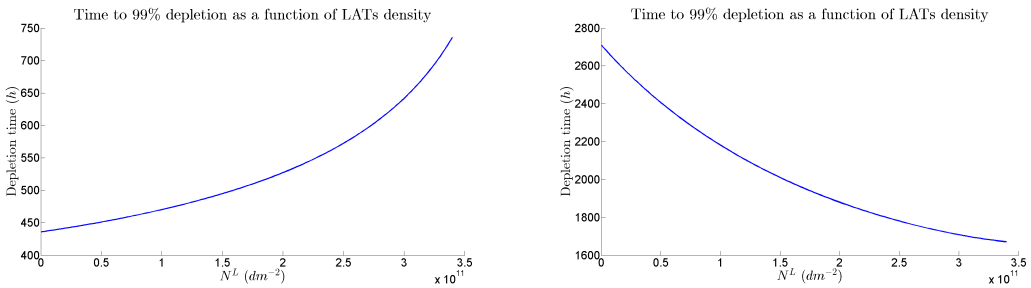


Figure 6.13.: Steady state concentration as a function of N^L (zoomed-in to the relevant region).



(a) $c_{in} = 30$ mM (b) $c_{in} = 300$ mM

Figure 6.14.: Depletion time as a function of N^L for $c_{in} = 30$ mM and $c_{in} = 300$ mM.

To see this more clearly, we now calculate the non-zero concentration c^*, at which the overall uptake rate is independent of whether the plant produces LATs or HATs only (under the constraint (313)). At this concentration, we have:

$$N\frac{I^L_{max}c^*}{K^L_m + c^*} = \frac{N}{\alpha}\frac{I^H_{max}}{K^H_m + c^*},$$

which yields:

$$c^* = \frac{I^H_{max}K^L_m - \alpha I^L_{max}K^H_m}{\alpha I^L_{max} - I^H_{max}} \approx 20 \text{ mM}. \tag{320}$$

Below this concentration, HATs are more efficient, which explains the results from Figures 6.10 – 6.12. Therefore, a nontrivial optimal HAT/LAT distribution can only be obtained using $c_{in} > 20$ mM. Figure 6.14 shows the depletion time as a function of the LATs density for $c_{in} = 30$ mM and $c_{in} = 300$ mM. We see that the HATs-only strategy is optimal for $c_{in} = 30$ mM and the LATs-only strategy is optimal for $c_{in} = 300$ mM. Choosing $c_{in} = 100$ mM leads to a nontrivial optimal LAT/HAT distribution ($\approx 2.3 \times 10^{11}$ dm^{-2}) minimising the depletion time as shown in Figures 6.15 – 6.17. The depletion times from Figures 6.17 and 6.14 are very high, because of the imposed initial nitrate concentrations. Such (high) concentrations are very rarely found in both the soil and the hydroponic experiments.

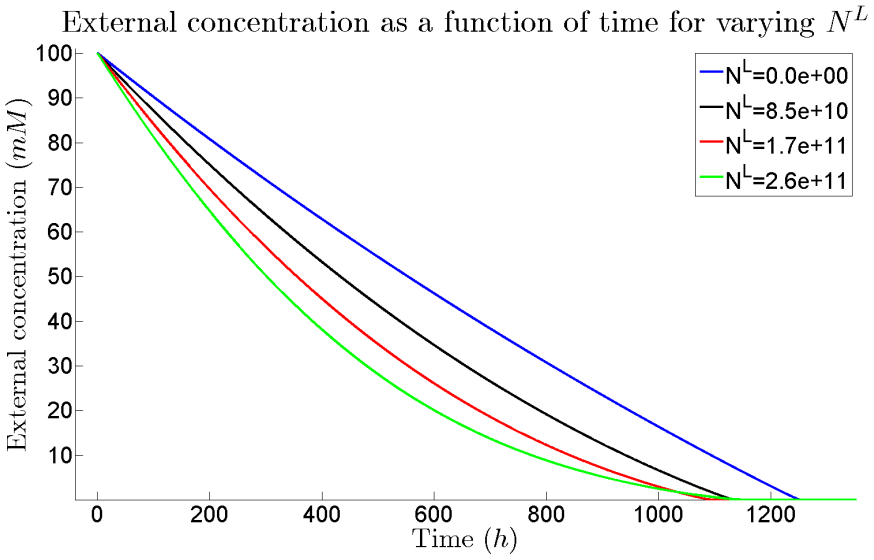


Figure 6.15.: Time evolution to the steady state for $c_{in} = 100$ mM.

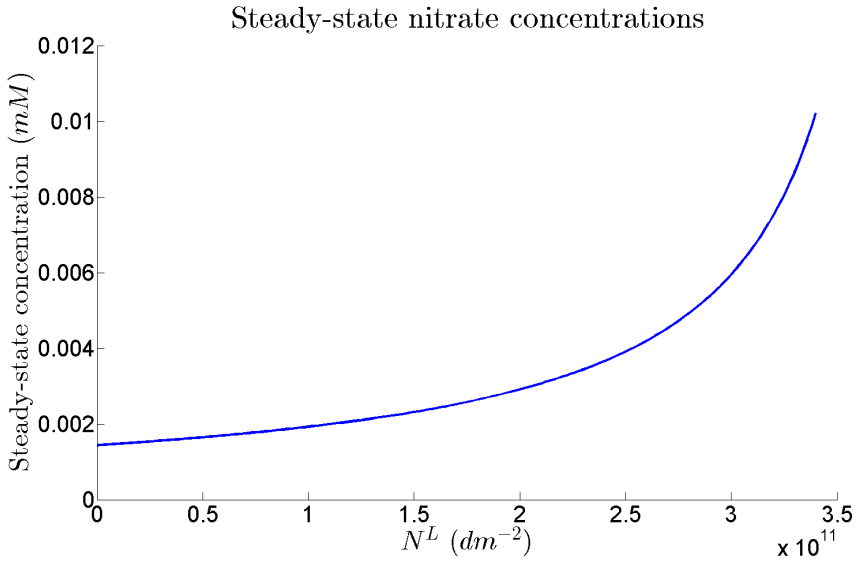


Figure 6.16.: Steady state concentrations as a function of N^L for $c_{in} = 100$ mM.

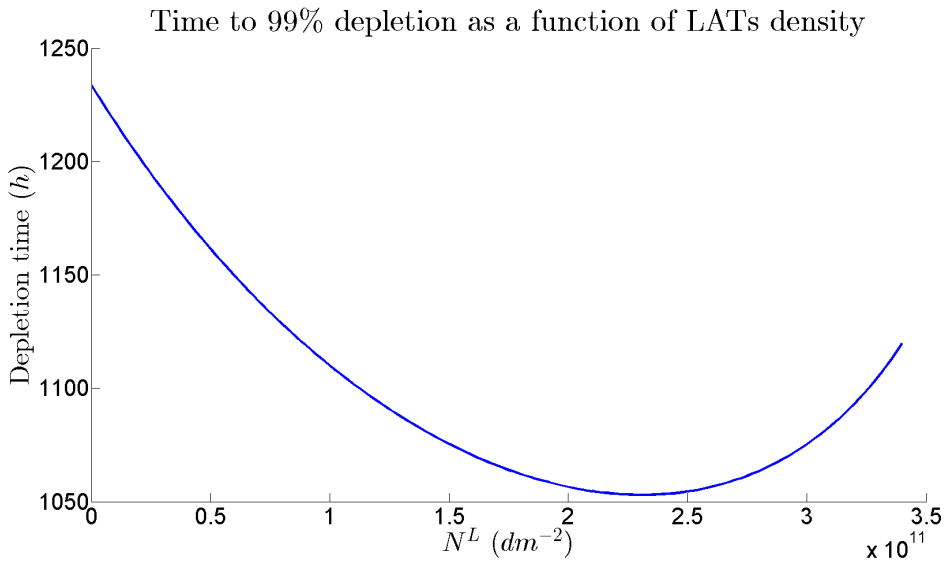


Figure 6.17.: Depletion time as a function of N^L for $c_{in} = 100$ mM.

6.4 SUMMARY

Using an approach analogous to the one found in phytoplankton uptake modelling literature ([5], [6]), we derived the Michaelis-Menten uptake condition for a single transporter and showed that using a very simple upscaling, we can get values of the macroscopic maximum influx rate with the same order of magnitude as those measured empirically at the plant or the root scale. Then, we studied how the irreducible nitrate concentration $\bar{c}_{min}$ observed in experiments can be derived as a steady-state value balancing the uptake via transporters with the root efflux using a simple toy model. Later, we introduced realistic parameters and concluded that such model yields the depletion time and the $\bar{c}_{min}$ values close to the experimental values. As already mentioned, we have not seen a similar calculation of the $\bar{c}_{min}$ value from basic principles (and subsequent comparison with experimental values) anywhere in the literature.

7

HORIZONTALLY AVERAGED MODELS OF ROOT SYSTEM UPTAKE

7.1 INTRODUCTION

Multiple root architecture models have been developed in recent decades (as discussed in Section 1.5). Using these models, it is possible to fully capture the root system growth as well as its interactions with the environment in three dimensions. However, a more detailed description of the underlying processes usually comes with an increased computational demands. Therefore, researchers often (implying some way of averaging in horizontal plane) use water uptake models which are only dependent on depth x_3, and thus are one-dimensional in space, which reduces the computation time and memory usage (see Section 1.3.4). As the fate of nitrate in soil is most often determined by the water dynamics (due to its high solubility; see Section 1.2.3), in this chapter, we will assess the suitability of horizontally averaged root system models for simulating water and nitrate uptake by real root systems.

We use real root systems, which were all grown and scanned in Hounsfield facility at the University of Nottingham using X-ray computed tomography. Note that these root systems are all of the same wheat genotype. Using RootNav (software allowing reconstruction of root system architecture from raw data input images [111]), Marcus Griffiths (then a PhD student at the University of Nottingham) segmented the root images, and then used RooTh - software developed by James Johnson (then a PhD student at the University of Nottingham) - for skeletonising (generating a structured description of the

root system without losing any important information; sometimes referred to as thinning) these root systems. The resulting data is thus smaller, easier to store and amenable to further analysis. This geometry was then imported into SimRoot (introduced in Section 1.5.1) using a module developed by Nathan Mellor (then a postdoctoral fellow at the University of Nottingham) which generates static root systems. After this the equations modelling water and nitrate dynamics were numerically solved using SWMS-3D code as implemented in SimRoot (discussed in Section 1.5.1). In the original version of SimRoot, the amount of nutrient taken up feeds into a simple canopy growth model, which then feeds back into the water uptake model in the form of a growing transpirational demand (as explained in Section 1.2.3). With the static-root-system version of SimRoot, we naturally assume that the canopy size is fixed as well, which yields a constant transpiration rate. This assumption may be a good approximation when modelling short-term water/nutrient uptake or the case of mature root systems (where growth slowed down and can thus be neglected).

From these simulations, we extract average water content and average nitrate concentration with depth. Moreover, from the obtained root images we extract root length distributions with depth for various root classes (primary, seminal, lateral and fine lateral roots) and we use this information when forming sink (uptake) terms in one-dimensional water and nitrate dynamics models in MATLAB. Results from these models are then compared with those from SimRoot. If average water/nitrate distribution in the one-dimensional model follows that of the three-dimensional model closely, then the (faster) one-dimensional model can be used (e.g.) to calculate overall uptake by a given root system. Note that we could not find any class-specific nitrate uptake parameters estimates for a wheat plant in the available literature, and thus we used default (maize) SimRoot parameters (and therefore also default class-specific root radii).

Due to technological progress as well as an increase in root-scanning facilities throughout the world, we expect to see a rise in available fully three-dimensional root system architecture data.

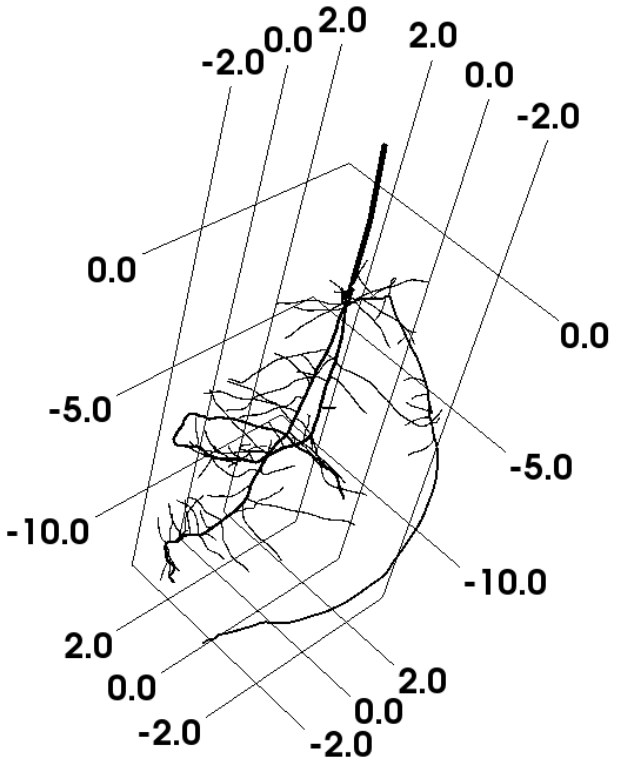


Figure 7.1.: A wheat root system numbered as 600 (in centimetres).

Using one-dimensional models such as those introduced in this chapter, we hope to address questions of the architecture impact on water and nitrate uptake in much faster way. Subsequently, this may help in certain optimisation problems, e.g. finding an optimal root length distribution for nitrate capture.

7.2 EXTRACTION OF DATA FROM ROOT IMAGES

To fully capture nitrate uptake, we need to incorporate depth-dependent root system characteristics (such as root length with depth or root surface area with depth) into our averaged model. We extracted these data from .xml representations of these root systems using python scripts. We started with a typical scanned root system numbered as 600 (shown Figure 7.1), for which the extracted root length distribution with depth is shown in Figure 7.2. Note that

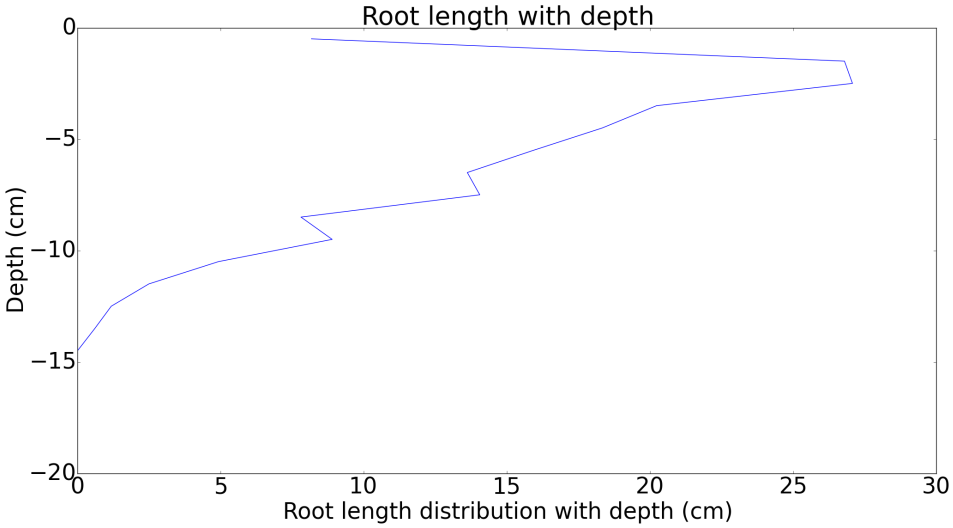


Figure 7.2.: The root length distribution with depth for the root system 600.

the small kinks in Figure 7.2 are purely a consequence of the chosen (vertical) width of the regions in which we count the overall root length[1], and have no biological meaning. Note also that even though mathematicians and statisticians may be more used to plots with swapped x and y axes (compared to Figure 7.2), we stick to the choice of axes from Figure 7.2 throughout this chapter, as by doing this we follow the convention that depth is plotted on the (negative) y axis, which seems to be standard in most agricultural studies (to give just a few examples, see [82], [2], [46] or [28]).

Different root classes may have different uptake properties (radii, transporter densities and others). Therefore, one may also need to extract separate root length distributions for primary, seminal, lateral or fine lateral roots. These are shown in Figure 7.12.

1 By choosing this width to be smaller, we should in general obtain more accurate descriptions of the given root system, and therefore more accurate one-dimensional models. However, later on in this chapter, we will confirm that the chosen width of 1 cm already gives a reasonably good approximation to the three-dimensional model.

7.3 WATER UPTAKE BY STATIC ROOT SYSTEMS

To model water dynamics, SimRoot solves an equation:

$$\frac{\partial \theta}{\partial t} = \nabla \cdot \Big(K \nabla h + K \nabla x_3 \Big) - S, \tag{321}$$

where K is the hydraulic conductivity function (of van Genuchten type, introduced in Section 2.6), h is the capillary pressure head and S is the sink term modelling water uptake [129] (see also Section 1.3.4). This is the same as the Richards' equation introduced in Section 1.3.3, noting that SWMS-3D (and therefore SimRoot) has the x_3 coordinate oriented opposite the direction of gravity [129]. We solve this equation in rectangular cuboid denoted Ω_S and defined as:

$$\left\{ (x_1, x_2, x_3) \in \mathbb{R}^3, x_1^{min} \leq x_1 \leq x_1^{max}, x_2^{min} \leq x_2 \leq x_2^{max}, x_3^{min} \leq x_3 \leq x_3^{max} \right\}.$$

The fixed total transpiration (as explained in Section 7.1) means that a fixed amount of water is taken in per day. Denote $\rho(x_1, x_2, x_3)$ to be a root length distribution (cm of root length per cm^3 of soil volume) and T to be a transpiration rate constant (cm^3 of water per day). Defining:

$$\hat{\rho}(x_3) = \int_{x_1^{min}}^{x_1^{max}} \int_{x_2^{min}}^{x_2^{max}} \rho \, dx_2 dx_1$$

one gets:

$$\int_{x_3^{min}}^{x_3^{max}} \hat{\rho}(x_3) dx_3 = L^T,$$

where L^T is the total root length of a given root system. In our static SimRoot version, we assume that the amount of in-taken water is equally distributed over the entire root system so that the uptake rate per unit root length is the same everywhere (not taking into account local water content). This can be expressed as:

$$S(x_1, x_2, x_3) = \frac{\rho(x_1, x_2, x_3) T}{L^T}. \tag{322}$$

Figure 7.3 shows water depletion zones. We now wish to obtain an averaged, one-dimensional (depth-dependent) model.

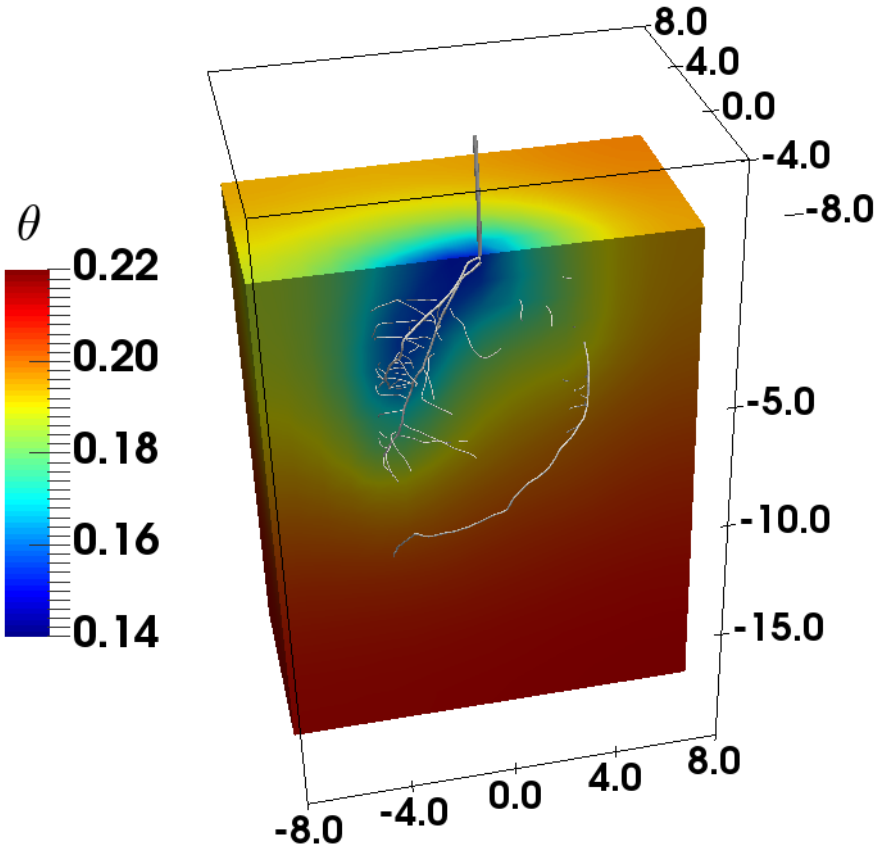


Figure 7.3.: Water depletion zones close to root surfaces in the modified SimRoot; a slice through the soil domain. Colours represent the varying water content - blue indicates the driest soil.

In order to do that, we will from now onwards assume that horizontal variations in water content are small enough so that they can be neglected in subsequent calculations (and therefore, the one-dimensional model thus obtained should give results close to the averaged results from the three-dimensional model). This assumption is justified as long as the soil water content is maintained sufficiently close to the full saturation (in other words, as long as we do not model very dry soils) [11].

First, we integrate Equation (321) in horizontal coordinates, divide by the surface area of a horizontal cross-section ($A = \left(x_1^{max} - x_1^{min}\right) \times \left(x_2^{max} - x_2^{min}\right)$; recall that we want to obtain an averaged behaviour), and get:

$$\begin{aligned}\frac{\partial \overline{\theta}}{\partial t} = \frac{1}{A}\int\limits_{x_1^{min}}^{x_1^{max}}\int\limits_{x_2^{min}}^{x_2^{max}} \frac{\partial \theta}{\partial t} dx_2 dx_1 = \frac{1}{A}\int\limits_{x_1^{min}}^{x_1^{max}}\int\limits_{x_2^{min}}^{x_2^{max}} \Big(\nabla \cdot \Big(K\nabla h + K\nabla x_3\Big) - \\ S\Big) dx_2 dx_1 = \frac{1}{A}\int\limits_{x_1^{min}}^{x_1^{max}}\int\limits_{x_2^{min}}^{x_2^{max}} \left(\frac{\partial}{\partial x_1}, \frac{\partial}{\partial x_2}\right) \cdot \left(K\Big(\frac{\partial h}{\partial x_1}, \frac{\partial h}{\partial x_2}\Big)\right) dx_2 dx_1 + \\ \frac{1}{A}\int\limits_{x_1^{min}}^{x_1^{max}}\int\limits_{x_2^{min}}^{x_2^{max}} \left(\frac{\partial}{\partial x_3}\Big(K\frac{\partial h}{\partial x_3} + K\Big) - S\right) dx_2 dx_1,\end{aligned} \tag{323}$$

where we have defined $\overline{\theta}(t, x_3) = \frac{1}{A}\int\limits_{x_1^{min}}^{x_1^{max}}\int\limits_{x_2^{min}}^{x_2^{max}} \theta(t, x_1, x_2, x_3) dx_2 dx_1$ to be the averaged water content distribution with depth and then we simply used the definition of the divergence operator. Using divergence theorem (in two dimensions), we get:

$$\begin{aligned}\frac{1}{A}\int\limits_{x_1^{min}}^{x_1^{max}}\int\limits_{x_2^{min}}^{x_2^{max}} \left(\frac{\partial}{\partial x_1}, \frac{\partial}{\partial x_2}\right) \cdot \left(K\Big(\frac{\partial h}{\partial x_1}, \frac{\partial h}{\partial x_2}\Big)\right) dx_2 dx_1 = \\ \frac{1}{A}\int\limits_{\partial A(x_3)} K\left(\frac{\partial h}{\partial x_1}, \frac{\partial h}{\partial x_2}\right) \cdot \hat{\boldsymbol{n}}_{2d} dl,\end{aligned} \tag{324}$$

where we defined:

$$A(y) = \left\{(x_1, x_2, x_3) \in \mathbb{R}^3, x_1^{min} \leq x_1 \leq x_1^{max}, x_2^{min} \leq x_2 \leq x_2^{max}, x_3 = y\right\},$$

$\partial A(x_3)$ denotes boundary of this set, and $\hat{\boldsymbol{n}}_{2d}$ denotes a two-dimensional, outward pointing unit normal vector. The boundary integral from Equation (324)

can be neglected due to the assumption of small water content variations in the horizontal direction (which is equivalent to the assumption of small capillary pressure head variations in the horizontal direction). Using this approximation, Equation (323) becomes:

$$\frac{\partial \overline{\theta}}{\partial t} = \frac{1}{A} \int_{x_1^{min}}^{x_1^{max}} \int_{x_2^{min}}^{x_2^{max}} \left(\frac{\partial}{\partial x_3} \left(K \frac{\partial h}{\partial x_3} + K \right) - S \right) dx_2 dx_1 =$$

$$\frac{1}{A} \frac{\partial}{\partial x_3} \int_{x_1^{min}}^{x_1^{max}} \int_{x_2^{min}}^{x_2^{max}} \left(K \frac{\partial h}{\partial x_3} + K \right) dx_2 dx_1 - \overline{S} = \frac{\partial}{\partial x_3} \left(K(\overline{h}) \frac{\partial \overline{h}}{\partial x_3} + K(\overline{h}) \right) - \overline{S}, \quad (325)$$

where we again assumed that the horizontal variation in the water content can be neglected. The bars (again) denote averaging in horizontal variables, i.e.:

$$\overline{S}(x_3) = \frac{1}{A} \int_{x_1^{min}}^{x_1^{max}} \int_{x_2^{min}}^{x_2^{max}} S(x_1, x_2, x_3) dx_2 dx_1$$

and:

$$\overline{h}(t, x_3) = \frac{1}{A} \int_{x_1^{min}}^{x_1^{max}} \int_{x_2^{min}}^{x_2^{max}} h(t, x_1, x_2, x_3) dx_2 dx_1.$$

Using the sink term (322), Equation (325) gives:

$$\frac{\partial \overline{\theta}}{\partial t} = \frac{\partial}{\partial x_3} \left(K(\overline{h}) \frac{\partial \overline{h}}{\partial x_3} + K(\overline{h}) \right) - \frac{T}{AL^T} \int_{x_1^{min}}^{x_1^{max}} \int_{x_2^{min}}^{x_2^{max}} \rho(x_1, x_2, x_3) dx_2 dx_1 =$$

$$\frac{\partial}{\partial x_3} \left(K(\overline{h}) \frac{\partial \overline{h}}{\partial x_3} + K(\overline{h}) \right) - \frac{T}{AL^T} \hat{\rho} = \frac{\partial}{\partial x_3} \left(K(\overline{h}) \frac{\partial \overline{h}}{\partial x_3} + K(\overline{h}) \right) - \frac{T}{L^T} \overline{\rho}. \quad (326)$$

This way, we clearly see how the overall (or the averaged) root length distribution with depth enters the sink term. We used a code solving Richards' equation in one dimension (depth) without a sink term (i.e. water uptake) using MATLAB solver titled pdepe as found in [64]. We further wrote a python script calculating averages of water content in horizontal slices from SimRoot output files. This way, we can compare the two models.

As default, we assumed that the soil domain Ω_S is given by $x_1^{min} = -8$ cm, $x_1^{max} = 8$ cm, $x_2^{min} = -8$ cm, $x_2^{max} = 8$ cm, $x_3^{min} = -20$ cm and $x_3^{max} = 0$ cm. Default soil water parameter values used are $\theta_r = 0.067$ as the residual water

Parameter	x_1^{min}	x_1^{max}	x_2^{min}	x_2^{max}	x_3^{min}	x_3^{max}
Value	-8	8	-8	8	-20	0
Unit	cm	cm	cm	cm	cm	cm

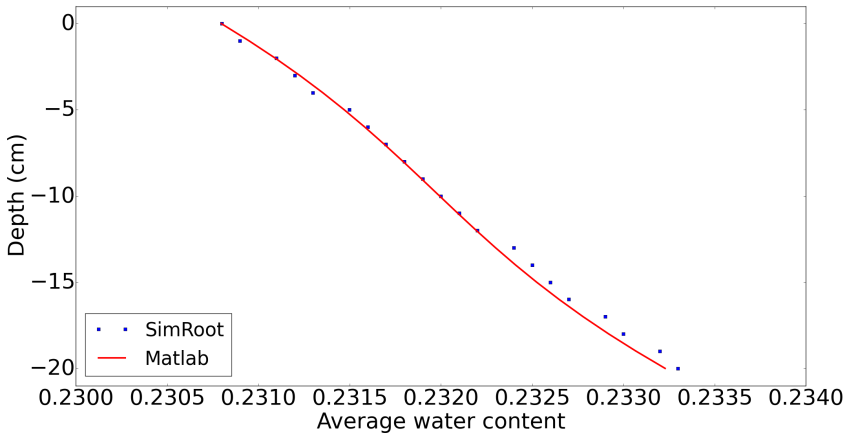
Table 7.1.: Default geometric parameters for water uptake.

Parameter	θ_r	ϕ	α	n	K_s	θ_{in}
Value	0.067	0.46	0.02	1.41	10.8	0.232
Unit	$-$	$-$	cm^{-1}	$-$	$\mathrm{cm\ d}^{-1}$	$-$

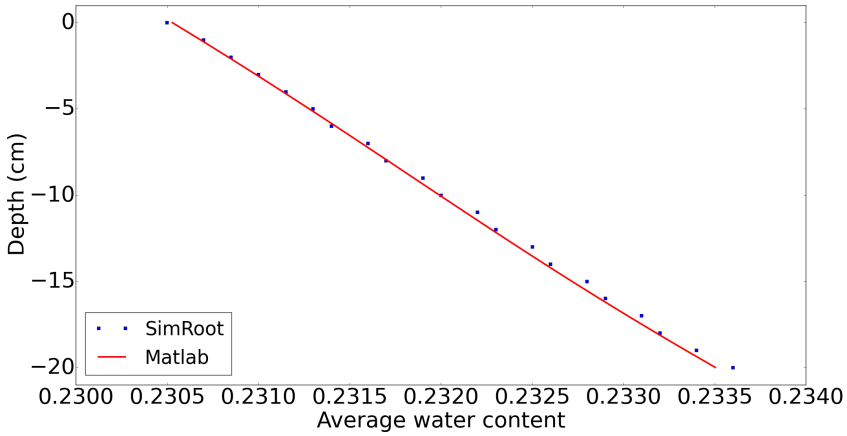
Table 7.2.: Default soil water parameters.

content, $\phi = 0.46$ as porosity, $K_s = 10.8\,\mathrm{cm\,d}^{-1}$ as the saturated hydraulic conductivity, and $\theta_{in} = 0.232$ as the (constant) initial water content. We use van Genuchten parameters $n = 1.41$ (this is equal to $\frac{1}{1-m}$ for m introduced in Section 2.6) and $\alpha = 0.02\,\mathrm{cm}^{-1}$ (this determines the water retention curve, i.e. the relationship between the soil water content and the capillary pressure head; for more details, see [142]). These are all typical values for Silt Loam soil - compare with Section 2.6.

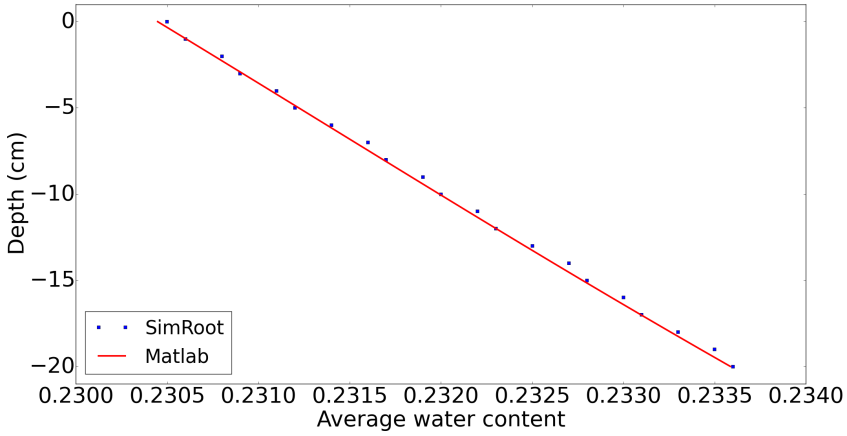
Default geometry parameters are summarised in Table 7.1 and soil water parameters in Table 7.2. Before modelling water uptake using depth-dependent sink terms, we would like to check whether the Richards equation as implemented in SimRoot is consistent with the implementation from [64]. To do this, we set the transpiration rate to zero in SimRoot. We show the results after 5, 10, and 15 days, starting with constant water content with depth. We assume zero-flux boundary conditions at both the top and the bottom part of the boundary ($x_3 = -20$ cm as well as $x_3 = 0$ cm). We observe that the water content is slowly reaching the steady state in which the balance between the gravity and the diffusion term is achieved (see Figure 7.4). The small deviations from smoothness in the SimRoot case can be explained by a rather coarse mesh used and therefore, we do not consider these to be important.



(a) Time = 5 days



(b) Time = 10 days



(c) Time = 15 days

Figure 7.4.: Comparison between the models without transpiration for an increasing time.

Now we wish to include the sink term from Equation (322) in our modelling and compare the resulting behaviour with the one obtained from SimRoot. In order to justify the need for inclusion of root length distribution into our model, we first compare both models with another (MATLAB) model, in which we implement what we will call a Boolean sink term from now onwards. This term is depth-dependent, but attains two values only - a zero and a non-zero value. The non-zero value is chosen so that the total water uptake is the same for all models and is applied at depths, where at least one root is present. Denoting L^R to be the maximal depth at which roots are present (sometimes referred to as the rooting depth [28]), this means:

$$\overline{S}_{sw}(x_3) = \begin{cases} \frac{T}{L^R} & \text{for } -L^R < x_3 < 0\,\text{cm} \\ 0 & \text{for } -20\,\text{cm} < x_3 < -L^R. \end{cases} \tag{327}$$

Assuming a constant transpiration rate $T = 5\,\text{cm}^3\,\text{d}^{-1}$ (which makes the per-unit-surface uptake rate approximately of the same order as the value used in Section 2.6.2), we impose a free-drainage condition at the bottom of the soil domain (introduced in Equation (50)). Comparison between these three models for Root System 600 clearly shows that inclusion of the root length information is necessary to realistically describe water dynamics (see Figure 7.5). To make sure that the agreement between the models is not just a coincidence, we used 3 other root systems from our collection (numbered 555, 593 and 615 and displayed in Figure 7.6). Comparison between the models for these root systems is shown in Figure 7.7.

7.4 NITRATE UPTAKE

Dynamics of soil nitrate is even more complex than that of water. As explained in Section 1.2.3, nitrate is mostly (dissolved in and thus) advected with water in the mass flow so the continuity equation for nitrate is coupled with that for water. Nitrate further diffuses within the solution to places of lower concentration and can be adsorbed to or desorbed from the soil surfaces. Moreover, it can undergo various transformations (e.g. biodegradation).

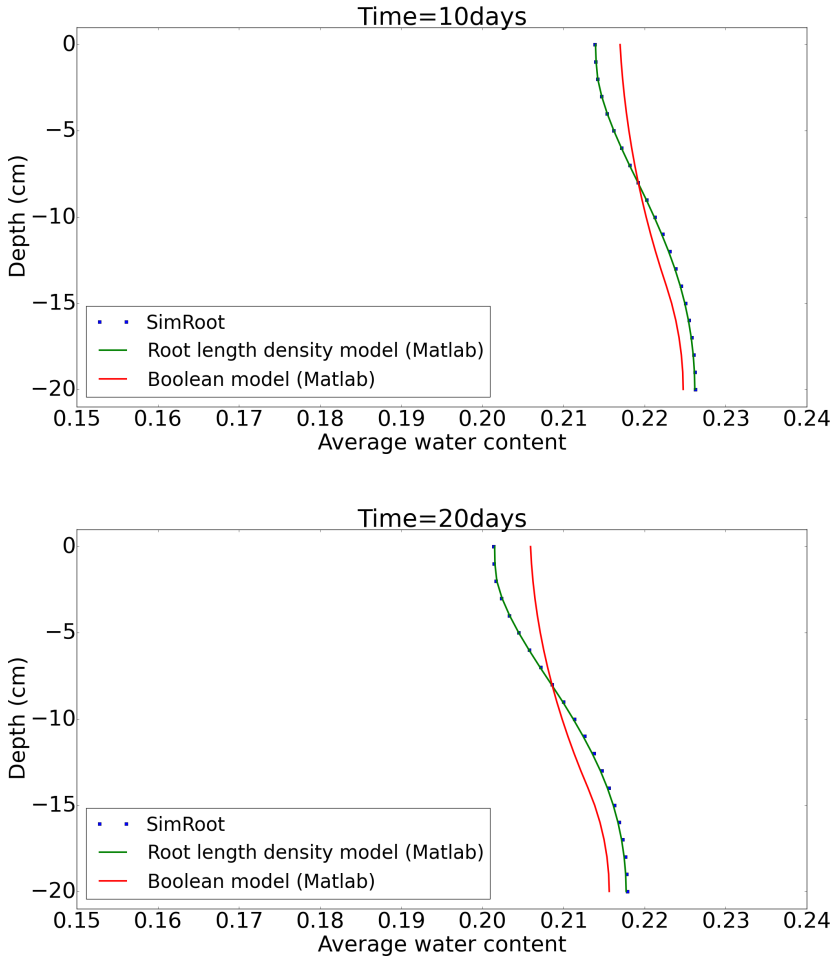
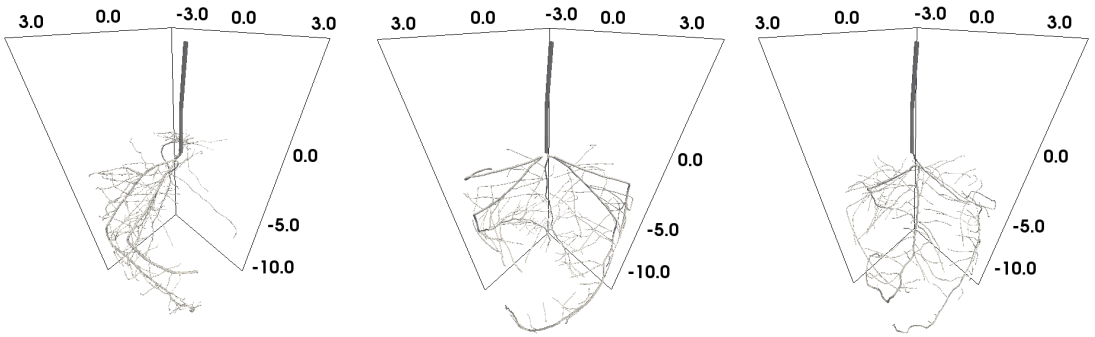


Figure 7.5.: Comparison with the Boolean model. The root length distribution is clearly relevant.



(a) 555 (b) 593 (c) 615

Figure 7.6.: Other root systems used in simulations.

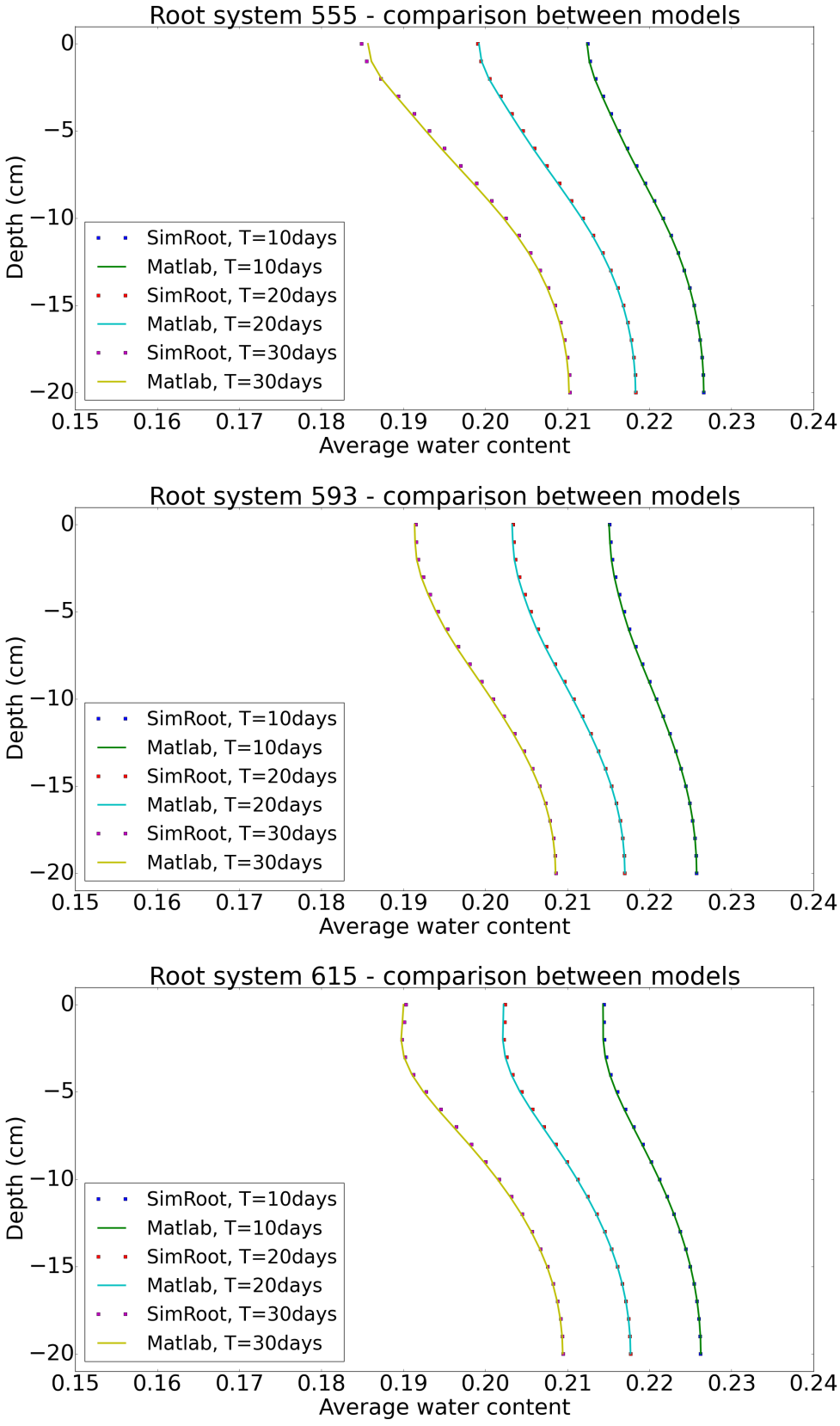


Figure 7.7.: Comparison between the models with water uptake.

Finally, nitrate is uptaken by plant roots and this process usually follows the Michaelis-Menten kinetics (see Section 1.3.4).

In SWMS-3D, assuming instantaneous equilibration between the nitrate dissolved in the water solution and that adsorbed to the soil particles (as outlined in Section 1.3.3), this leads to:

$$-\theta R\frac{\partial c}{\partial t} - q_i\frac{\partial c}{\partial x_i} + \frac{\partial}{\partial x_i}\{\theta D_{ij}\frac{\partial c}{\partial x_j}\} + Fc + G = 0, \tag{328}$$

where c denotes the nitrate concentration (in SWMS-3D, this is defined as mass per unit solution volume), $\boldsymbol{q}$ the water flux, D_{ij} the diffusion tensor, $R = 1 + \frac{\rho k}{\theta}$ with ρ being the soil bulk density and k being the soil buffer power[2]. Note that we used the so-called Einstein summation convention, which means that repeated indices are summed over implicitly. Furthermore, we have:

$$F = \mu_w\theta + \mu_s\rho k + S$$

$$G = \gamma_w\theta + \gamma_s\rho - Sc_s,$$

where μ_w, μ_s, γ_w and γ_s are four constants describing the production and degradation processes, S is the water sink term as in Equation (321) and c_s is the Michaelis-Menten term simulating nitrate uptake (for detailed derivation, see [129]). Note that, forgetting the Fc and G terms, and assuming an isotropic diffusion tensor (i.e. the diagonal terms are all equal and the off-diagonal terms are zero), Equation (328) is equivalent to Equation (12) derived in Section 1.3.3.

Under further assumptions that $\mu_w = \mu_s = 0$, $\gamma_w = \gamma_s = 0$, and $k = 0$ (this serves as a good approximation because nitrate is not a highly sorbed nutrient; see Section 1.2.3), we get:

$$-\theta\frac{\partial c}{\partial t} - q_i\frac{\partial c}{\partial x_i} + \frac{\partial}{\partial x_i}\{\theta D_{ij}\frac{\partial c}{\partial x_j}\} + Sc - Sc_s = 0,$$

and from [129], we know that:

$$\theta D_{ij} = D_T|\boldsymbol{q}|\delta_{ij} + (D_L - D_T)\frac{q_j q_i}{|\boldsymbol{q}|} + \theta D_d\tau\delta_{ij},$$

2 Note that the adsorbed concentration s in the model from [129] is dimensionless and the corresponding dimensional variable is achieved via multiplying this quantity by the soil bulk density ρ. As the soil buffer power is still defined as $k = \frac{s}{c}$ (cf. Equation (11)), the soil buffer power is given in units of volume per unit mass here.

where D_T and D_L are so-called transverse and longitudinal dispersivities, D_d is the diffusion coefficient and τ is so-called tortuosity factor defined as:

$$\tau = \frac{\theta^{\frac{7}{3}}}{\theta_s^2}$$

(for more details, see [129] and references therein). Assuming that horizontal variation in the water content θ is negligible (and therefore, the same applies to the water flux $\boldsymbol{q}$), we get:

$$\theta D_{ij} \approx 0 \quad \text{for } i \neq j$$

and:

$$\theta D_{11} = D_T|\boldsymbol{q}| + \theta D_d\tau \quad \theta D_{22} = D_T|\boldsymbol{q}| + \theta D_d\tau \quad \theta D_{33} = D_L|\boldsymbol{q}| + \theta D_d\tau.$$

The SimRoot version we used differs from the described model in an important aspect, namely that the Michaelis-Menten term is not multiplied by the water sink term, i.e.:

$$-\theta\frac{\partial c}{\partial t} - q_i\frac{\partial c}{\partial x_i} + \frac{\partial}{\partial x_i}\{\theta D_{ij}\frac{\partial c}{\partial x_j}\} + Sc - N_s = 0, \tag{329}$$

where the sink term N_s is defined as:

$$\begin{gathered} N_s = 2\pi\frac{I_{max}c(x_1,x_2,x_3)}{K_m + c(x_1,x_2,x_3)}\times \\ \Big(r_s\rho_s(x_1,x_2,x_3) + r_p\rho_p(x_1,x_2,x_3) + r_l\rho_l(x_1,x_2,x_3) + r_f\rho_f(x_1,x_2,x_3)\Big), \end{gathered} \tag{330}$$

where I_{max} and K_m are the Michaelis-Menten parameters (see Section 1.3.4). Note, that I_{max} is given on the per root surface area basis here, and thus needs to be multiplied by the corresponding root surface area distributions. This way, the radii (r) and the root length distributions (ρ) of the four different root classes - seminal, primary, lateral and fine lateral roots - are separately introduced.

Furthermore, Equation (329) can be rewritten as:

$$\theta\frac{\partial c}{\partial t} = \nabla\cdot\{\theta\boldsymbol{D}\nabla c\} - \boldsymbol{q}\cdot\nabla c + Sc - N_s,$$

where the tensor $\theta\boldsymbol{D}$ is defined as:

$$\theta\boldsymbol{D} = \begin{pmatrix} D_T|\boldsymbol{q}| + \theta D_d\tau & 0 & 0 \\ 0 & D_T|\boldsymbol{q}| + \theta D_d\tau & 0 \\ 0 & 0 & D_L|\boldsymbol{q}| + \theta D_d\tau \end{pmatrix}.$$

Thus, we obtained a reaction-advection-diffusion equation, which can (using Equation (321)) be written as:

$$\frac{\partial(\theta c)}{\partial t} = \nabla \cdot \{\theta \boldsymbol{D} \nabla c\} - \boldsymbol{q} \cdot \nabla c + Sc - N_s + \frac{\partial \theta}{\partial t} c = \\ \nabla \cdot \{\theta \boldsymbol{D} \nabla c\} - \boldsymbol{q} \cdot \nabla c + Sc - N_s - (\nabla \cdot \boldsymbol{q})c - Sc = \nabla \cdot \{\theta \boldsymbol{D} \nabla c - c\boldsymbol{q}\} - N_s. \tag{331}$$

As θc represents nitrate content per unit soil volume, $-\{\theta \boldsymbol{D} \nabla c - c\boldsymbol{q}\}$ represents the nitrate flux and $-N_s$ the nitrate uptake. For boundary conditions, we impose zero nitrate flux at all non-root parts of the boundary:

$$-\{\theta \boldsymbol{D} \nabla c - c\boldsymbol{q}\} \cdot \hat{\boldsymbol{n}} = 0.$$

Finally, we assume constant initial nitrate concentration $c(t = 0) = c_{in}$ everywhere.

7.4.1 *Averaged model for nitrate*

Denote $\overline{c}(t, z)$, $\overline{q}(t, z)$ to be the averaged nitrate concentration with depth and the averaged water flux with depth. Analogous to the averaging in the water section, we assume that the horizontal variations of θ and c are negligible, we integrate Equation (331) in the horizontal variables x_1, x_2, and we divide by the horizontal cross-sectional area to get:

$$\frac{1}{A} \int_{x_1^{min}}^{x_1^{max}} \int_{x_2^{min}}^{x_2^{max}} \frac{\partial(\theta c)}{\partial t} dx_2 x_1 = \frac{1}{A} \int_{x_1^{min}}^{x_1^{max}} \int_{x_2^{min}}^{x_2^{max}} \Big(\nabla \cdot \{\theta \boldsymbol{D} \nabla c - c\boldsymbol{q}\} - N_s \Big) dx_2 x_1. \tag{332}$$

First, we have:

$$\frac{1}{A} \int_{x_1^{min}}^{x_1^{max}} \int_{x_2^{min}}^{x_2^{max}} \frac{\partial(\theta c)}{\partial t} dx_2 x_1 = \frac{\partial}{\partial t} \Big(\frac{1}{A} \int_{x_1^{min}}^{x_1^{max}} \int_{x_2^{min}}^{x_2^{max}} (\theta c) dx_2 x_1 \Big) = \frac{\partial(\overline{\theta c})}{\partial t},$$

and assuming that the horizontal variation of θ and c is negligible, we get $\overline{\theta c} \approx \overline{\theta}\,\overline{c}$.

Next, for the right-hand side of Equation (332), we get:

$$\frac{1}{A} \int_{x_1^{min}}^{x_1^{max}} \int_{x_2^{min}}^{x_2^{max}} \Big(\nabla \cdot \{\theta \boldsymbol{D} \nabla c - c\boldsymbol{q}\} - N_s \Big) dx_2 x_1 =$$

$$\frac{1}{A}\Big\{\int_{x_1^{min}}^{x_1^{max}}\int_{x_2^{min}}^{x_2^{max}}\Big(\frac{\partial}{\partial x_1},\frac{\partial}{\partial x_2}\Big)\cdot\Big(\Big(D_T|\boldsymbol{q}|+\theta D_d\tau\Big)\Big(\frac{\partial c}{\partial x_1},\frac{\partial c}{\partial x_2}\Big)-$$

$$c\Big(q_1,q_2\Big)\Big)+\Big(\frac{\partial}{\partial x_3}\Big(\big(D_L|\boldsymbol{q}|+\theta D_d\tau\big)\frac{\partial c}{\partial x_3}-cq_3\Big)-N_s\Big)dx_2x_1\Big\},$$

and divergence theorem gives:

$$\frac{1}{A}\int_{x_1^{min}}^{x_1^{max}}\int_{x_2^{min}}^{x_2^{max}}\Big(\frac{\partial}{\partial x_1},\frac{\partial}{\partial x_2}\Big)\cdot\Big(\Big(D_T|\boldsymbol{q}|+\theta D_d\tau\Big)\Big(\frac{\partial c}{\partial x_1},\frac{\partial c}{\partial x_2}\Big)-c\Big(q_1,q_2\Big)\Big)dx_2dx_1=$$

$$\frac{1}{A}\int_{\partial A(x_3)}\Big(\Big(D_T|\boldsymbol{q}|+\theta D_d\tau\Big)\Big(\frac{\partial c}{\partial x_1},\frac{\partial c}{\partial x_2}\Big)-c\Big(q_1,q_2\Big)\Big)\cdot\hat{\boldsymbol{n}}_{2d}dl\approx 0,$$

because we assume $\frac{\partial c}{\partial x_1}$, $\frac{\partial c}{\partial x_2}$, q_1 and q_2 to be negligible. Thus, the averaged equation (332) becomes:

$$\frac{\partial(\overline{\theta}\overline{c})}{\partial t}=\frac{1}{A}\int_{x_1^{min}}^{x_1^{max}}\int_{x_2^{min}}^{x_2^{max}}\Big(\frac{\partial}{\partial x_3}\Big(\big(D_L|\boldsymbol{q}|+\theta D_d\tau\big)\frac{\partial c}{\partial x_3}-cq_3\Big)-N_s\Big)dx_2x_1=$$

$$\frac{\partial}{\partial x_3}\Big(\frac{1}{A}\int_{x_1^{min}}^{x_1^{max}}\int_{x_2^{min}}^{x_2^{max}}\Big(\big(D_L|\boldsymbol{q}|+\theta D_d\tau\big)\frac{\partial c}{\partial x_3}-cq_3\Big)dx_2x_1\Big)-\overline{N_s}=$$

$$\frac{\partial}{\partial x_3}\Big(\Big(D_L\overline{|\boldsymbol{q}|}+\overline{\theta}D_d\tau(\overline{\theta})\Big)\frac{\partial\overline{c}}{\partial x_3}-\overline{cq_3}\Big)-\overline{N_s},$$

where in the final step we used the assumptions that θ and c vary negligibly in the horizontal directions. The assumption on θ yields $q_1, q_2 \approx 0$, which in turn leads to $|\boldsymbol{q}| \approx |q_3|$. The same assumption leads to the conclusion that the horizontal variation of q_3 is small, which yields $\overline{|q_3|} \approx |\overline{q_3}|$. Finally, assuming negligibility of the horizontal variation of c, we get from Equation (330):

$$\overline{N_s}(t,x_3)=2\pi\frac{I_{max}\overline{c}(t,x_3)}{K_m+\overline{c}(t,x_3)}\Big(r_s\overline{\rho_s}(x_3)+r_p\overline{\rho_p}(x_3)+r_l\overline{\rho_l}(x_3)+r_f\overline{\rho_f}(x_3)\Big).\quad(333)$$

All this yields an averaged equation:

$$\frac{\partial(\overline{\theta}\overline{c})}{\partial t}=\frac{\partial}{\partial x_3}\{(D_L|\overline{q}|+\overline{\theta}D_d\tau(\overline{\theta}))\frac{\partial\overline{c}}{\partial x_3}-\overline{cq}\}-$$

$$2\pi\frac{I_{max}\overline{c}}{K_m+\overline{c}}\Big(r_s\overline{\rho_s}+r_p\overline{\rho_p}+r_l\overline{\rho_l}+r_f\overline{\rho_f}\Big),$$

where we dropped the subscript 3 in q_3, as this model is one-dimensional in space. The zero-flux boundary conditions at the top and the bottom boundary parts become:

$$\{D_L|\overline{q}| + \overline{\theta} D_d \tau(\overline{\theta})\} \frac{\partial \overline{c}}{\partial x_3} - \overline{cq} = 0,$$

and the initial condition is $\overline{c}(t = 0) = c_{in}$. Now, we need to extract the root length distributions with depth for different root classes and compare the (horizontally-averaged) SimRoot and the MATLAB results. Before we do that, we wish to improve our understanding of SimRoot functioning, and achieve control over errors that SimRoot produces. Therefore, we start with simulations of nitrate uptake for simpler root systems.

7.4.2 *Single cylindrical root*

We study water and nitrate uptake by a single cylindrical root of length 10 cm (this value is arbitrary) and radius 0.0325 cm (a value that SimRoot uses for the primary root radius of the maize plant) positioned in the centre of soil domain, stretching from top to bottom. For soil domain, we assume $x_1^{min} = -4$ cm, $x_1^{max} = 4$ cm, $x_2^{min} = -4$ cm, $x_2^{max} = 4$ cm, $x_3^{min} = -10$ cm and $x_3^{max} = 0$ cm, as shown in Figure 7.11. For modelling the nitrate dynamics in soil, we chose the default SimRoot parameters - $D_L = 1$ cm, $D_T = 0.5$ cm, $D_d = 1.6416$ cm^2 d^{-1}, and we assumed a constant initial nitrate concentration $c_{in} = 4$ mM. To model the primary root nitrate uptake, we used default SimRoot Michaelis-Menten parameters $I_{max} = 1.92$ µmol cm^{-2} d^{-1}, $K_m = 16.1 \times 10^{-3}$ µmol ml^{-1} $= 16.1 \times 10^{-3}$ mM, $c_{min} = 1.0 \times 10^{-3}$ µmol ml^{-1} $= 1.0 \times 10^{-3}$ mM, and we assumed a fixed total transpiration of 0.1 cm^3 d^{-1} (to account for a much smaller root system). Nitrate dynamics values are summarised in Table 7.3. The results of the SimRoot model averaged across the horizontal cross-sections 3 and 6 days from the beginning of the simulation are shown in Figure 7.8. As expected, the average nitrate concentration is decreasing with time due to the uptake. However, we want the curves to be smoother. In attempt to solve this issue, we change the mesh size in SimRoot from 1 cm to 0.2 cm and obtain a smoother solution. Figure 7.9 presents a comparison with the one-dimensional model.

Parameter	D_L	D^T	D_d	I_{max}	K_m	c_{min}
Value	1.0	0.5	1.6416	1.92	16.1×10^{-3}	10^{-3}
Unit	cm	cm	$cm^2\ d^{-1}$	$\mu mol\ cm^{-2}\ d^{-1}$	mM	mM

Table 7.3.: Default nitrate dynamics parameters in SimRoot.

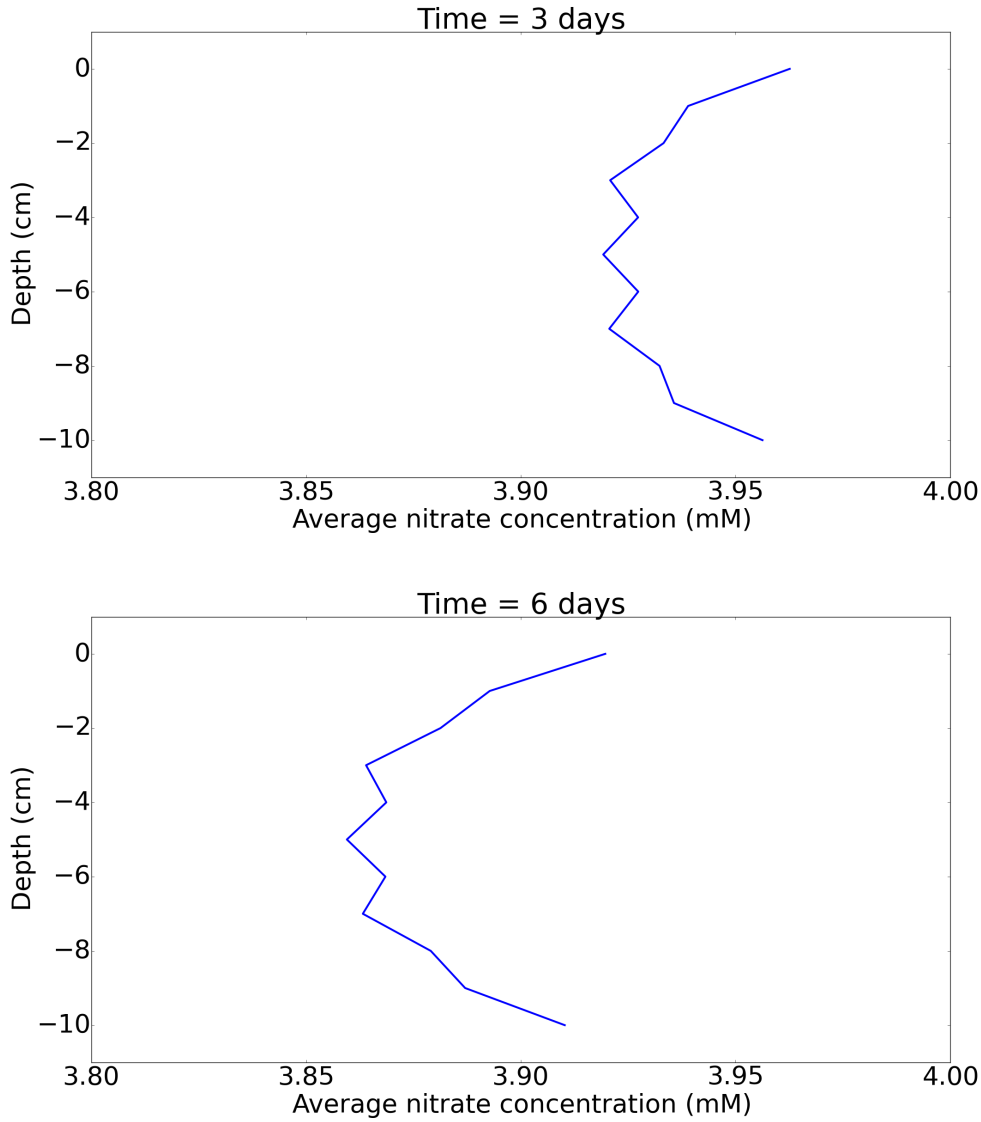


Figure 7.8.: The results of nitrate uptake simulation in SimRoot using the simple root system.

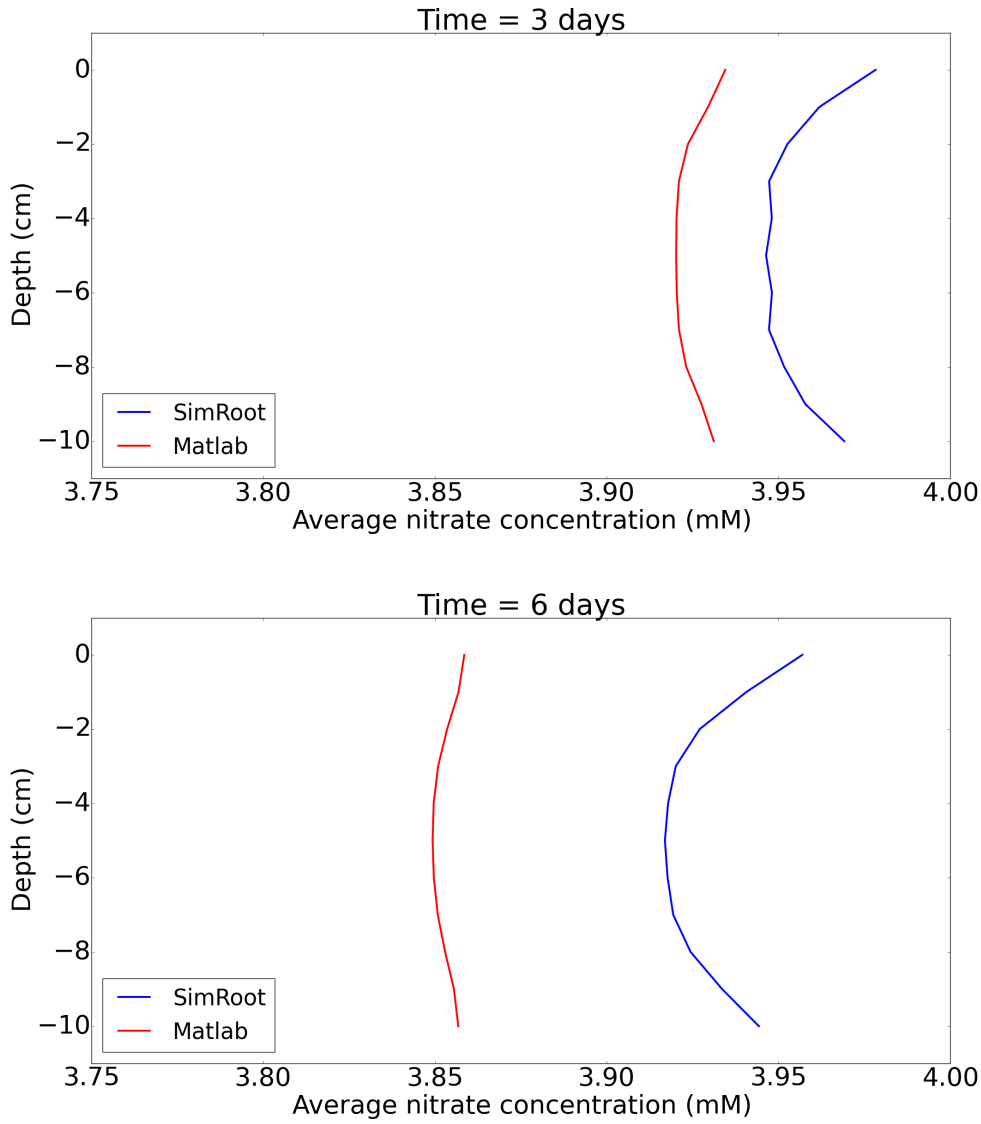


Figure 7.9.: Comparison of nitrate models for the simple root system using a finer mesh in SimRoot.

Even though the curves are smoother now, the observed differences cannot be neglected. To address this problem, we add more points in the root geometry definition (using root segments of length 0.1 cm rather than 1 cm), and the results are shown in Figure 7.10. The differences can now be considered small (in the sense that we can regard our understanding of the functioning of SimRoot as sufficient). The errors towards $x_3 = 0$ cm and $x_3 = -10$ cm are most likely caused by the presence of the boundary, and we expect these errors to decrease with further refinements of the root or of the soil meshes.

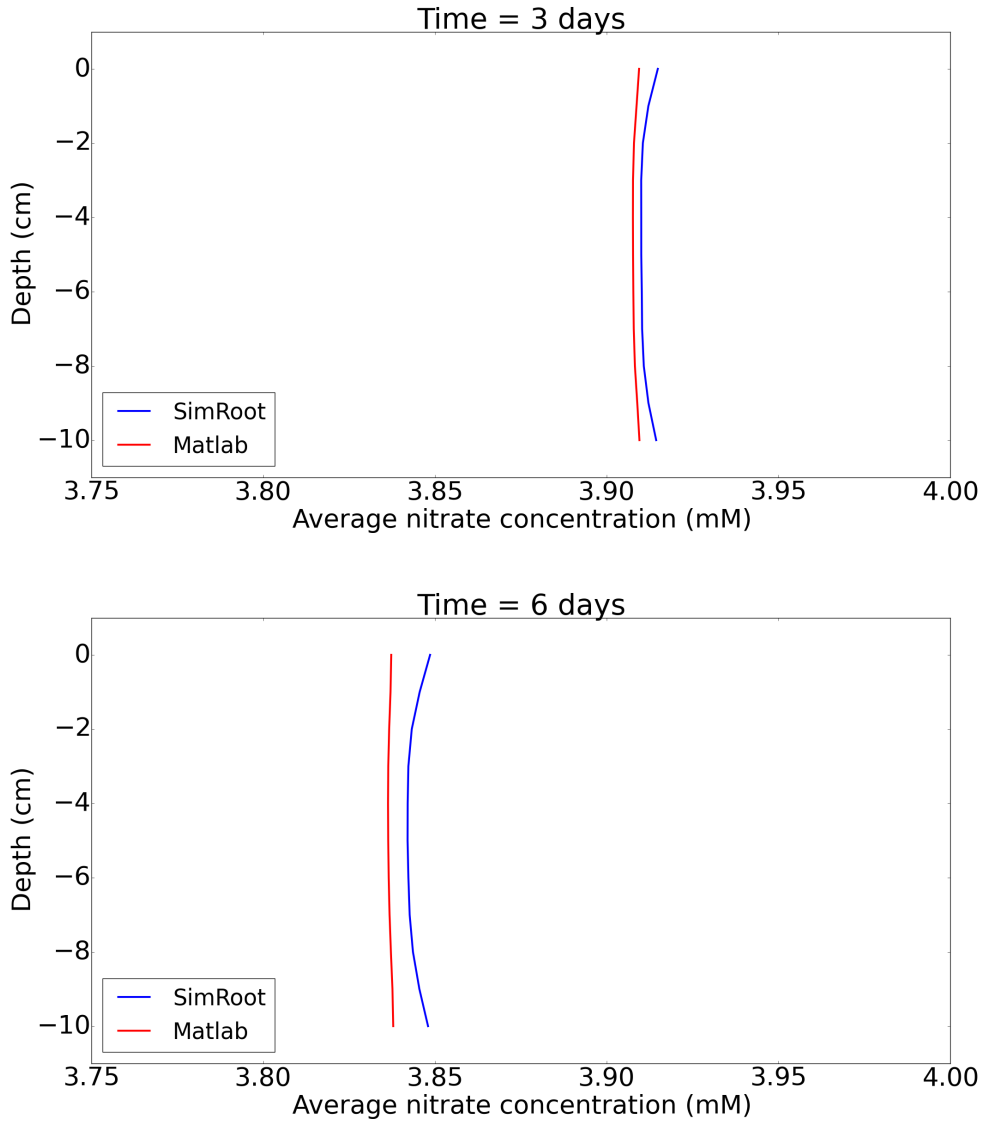


Figure 7.10.: Comparison of nitrate models for the simple root system using a finer mesh in SimRoot, and a finer root geometry definition.

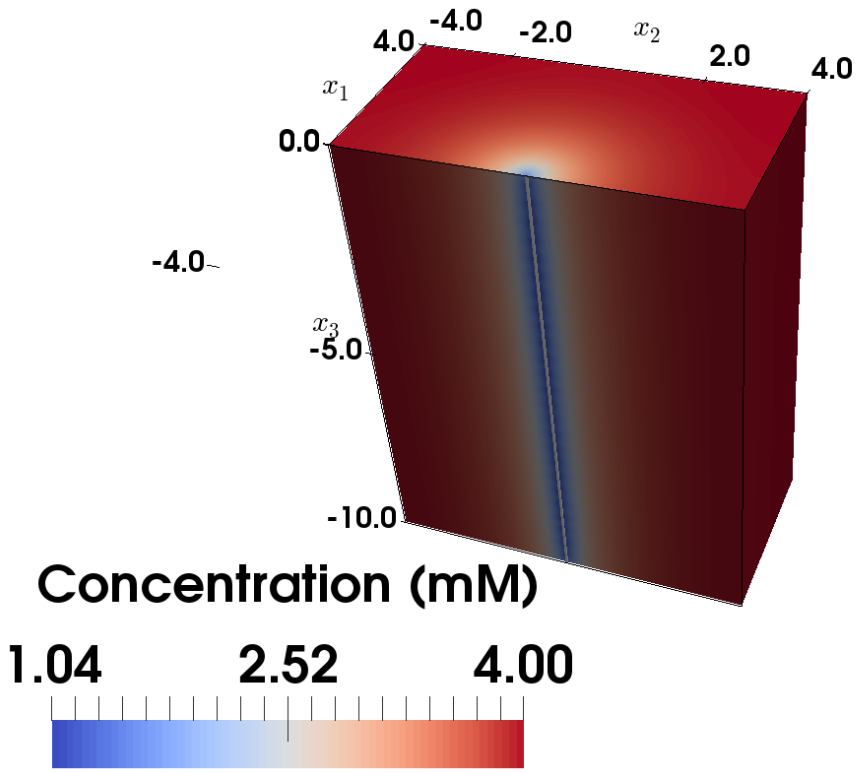


Figure 7.11.: Remaining soil nitrate concentration after 6 days of uptake (the simple root system).

Note that the minimum concentration after 6 days is still much greater than $K_m = 16.1 \times 10^{-3}$ mM (see Figure 7.11). Therefore, the uptake rate at the root surface is very close to I_{max}, and so is the uptake rate in the one-dimensional model (using the averaged nitrate concentration). If we considered more significant depletion gradients (by considering larger time scales or larger root surface area densities), we would need to adjust the one-dimensional equation by (e.g.) changing the Michaelis-Menten term.

7.4.3 *Real root systems*

We now show how the two models compare for the real root systems introduced in previous sections. We assume constant initial nitrate concentration $c_{in} = 4$ mM, total transpiration rate $T = 5\,\mathrm{cm}^3\,\mathrm{d}^{-1}$ and soil domain defined by the values from Table 7.1. Furthermore, we use the water parameters from Table 7.2 and the nitrate parameters from Table 7.3. Follow-

ing the maize model from SimRoot, we impose the nitrate uptake parameters from Table 7.3 on seminal roots, and for all lateral roots we impose $I^2_{max} = 1.27\,\mu\text{mol cm}^{-2}\,\text{d}^{-1}$, $K^2_m = 2.7 \times 10^{-3}\,\mu\text{mol ml}^{-1} = 2.7 \times 10^{-3}$ mM, $c^2_{min} = 1.7 \times 10^{-3}\,\mu\text{mol ml}^{-1} = 1.7 \times 10^{-3}$ mM. We calculate nitrate concentration distribution (with depth) 6 hours from the start of the simulation for both models, and the results are shown in Figure 7.12). The agreement between the two models is generally good, and we assume the observed differences (especially for Root System 555) to be most likely caused by numerical inaccuracies. We can also calculate the total root length for the four root systems, and we approximately get: 388 cm (555), 282 cm (593), 170 cm (600) and 241 cm (615). Even without doing further analysis, Figure 7.12 suggests that the longest root system (555) takes up the largest amount of nitrate and that the shortest root system (600) takes up the smallest amount of nitrate.

Note that SimRoot uses local (i.e. root surface) nitrate concentrations to evaluate the Michaelis-Menten term representing the nitrate uptake. On the other hand, the one-dimensional model uses averaged nitrate concentration, which can be substantially different from (greater than) the root surface concentrations, which makes the uptake larger. As we started with a fairly high nitrate concentration (4 mM), after 6 hours from the start of the simulation, the minimum nitrate concentration (for Root System 555, this is approximately 1.04 mM - see Figure 7.13) is still much higher than $K_m = 0.0161$ mM or $K^2_m = 0.0027$ mM. Therefore, the difference between the nitrate uptake rate calculated using the root surface concentration and the uptake rate calculated using the averaged concentration is almost negligible (they are both very close to the maximum uptake rate I_{max}), and thus we get similar outcomes from both models.

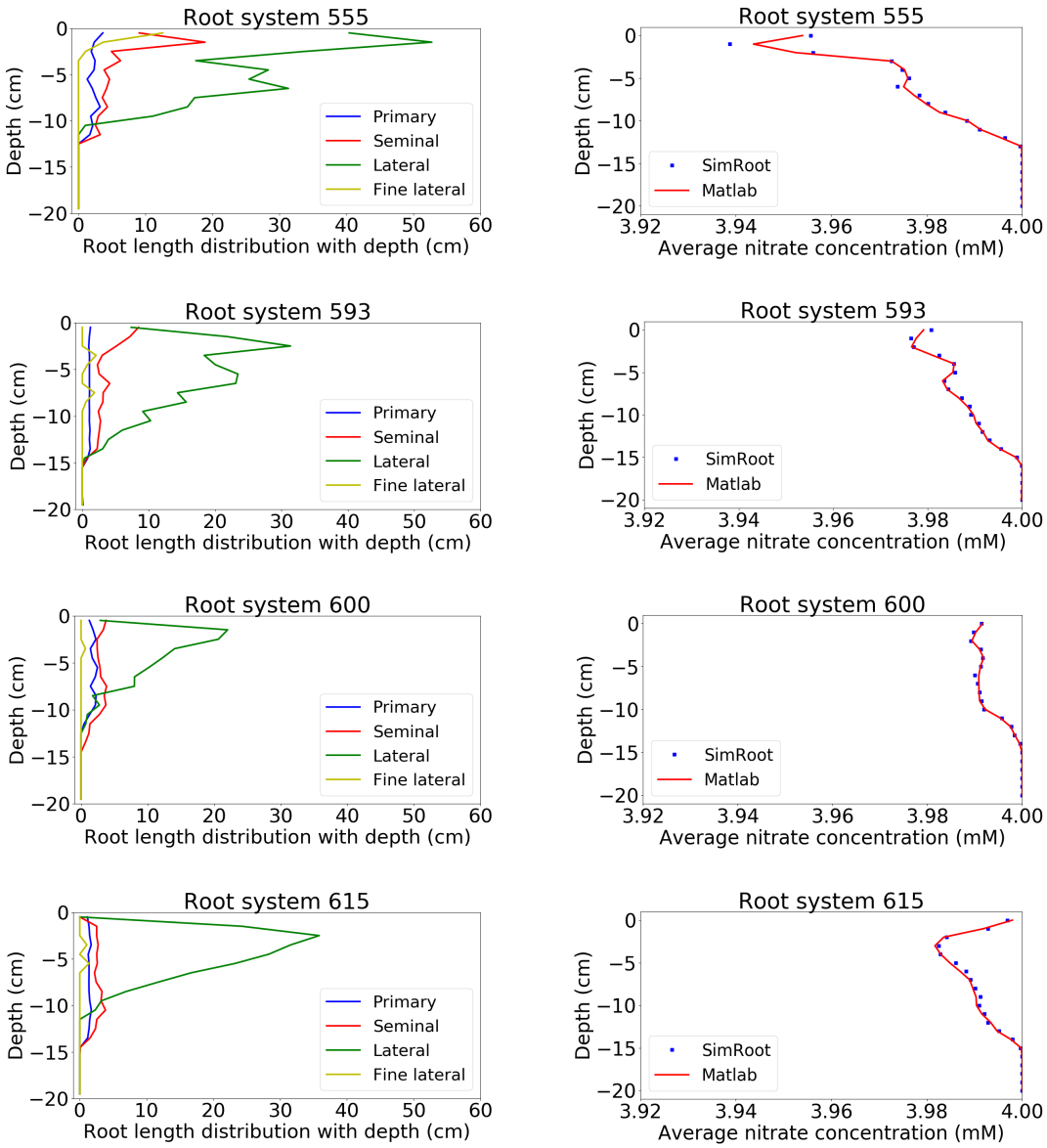


Figure 7.12.: The nitrate concentration distributions with depth after 6 hours of uptake (real root system geometries). Root length distributions with depth (separately for different root classes) of these root systems are shown for comparison.

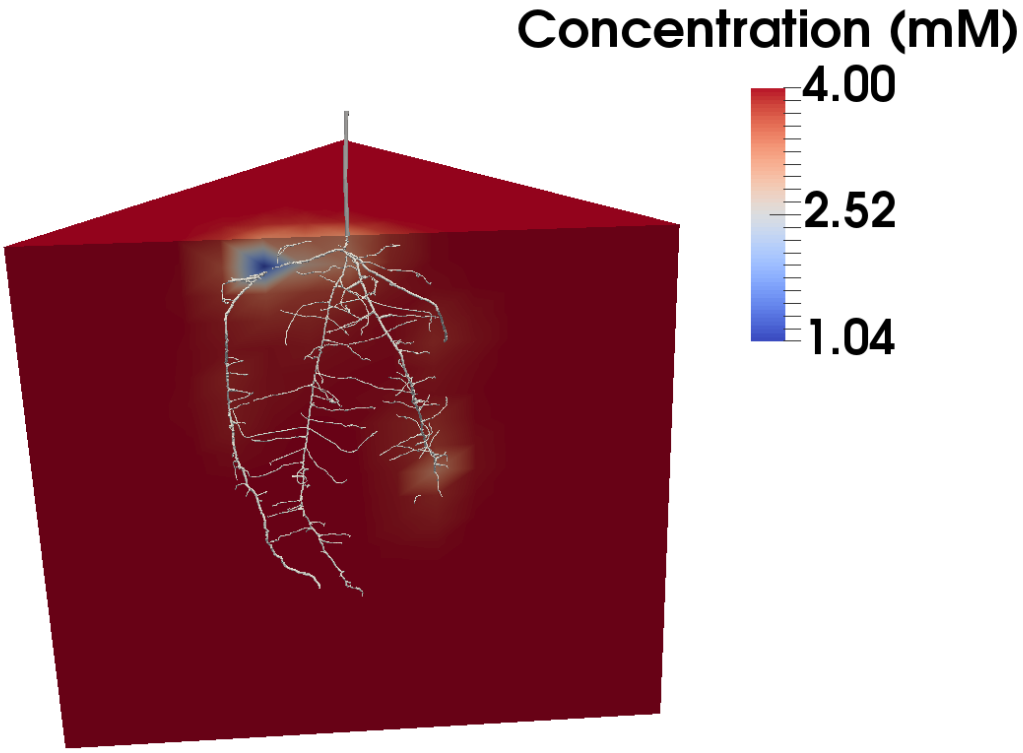


Figure 7.13.: Using $c_{in} = 4$ mM, after 6 hours, the depletion can still be neglected in the nitrate uptake calculations (root system 555).

7.5 SUMMARY

We have shown that under certain assumptions (static root systems, fixed transpiration rate, reasonably high water content and nitrate concentration), three-dimensional models of water and nutrient uptake are not necessary, and one can obtain reasonably good estimates of the overall uptake using horizontally-averaged (and therefore one-dimensional) models. In order to do that, it is sufficient to extract root length distributions with depth from the three-dimensional descriptions of the root systems, and use these distributions to form sink terms (representing the uptake) in the one-dimensional continuity equations for water and nitrate dynamics. As these equations are one-dimensional, they are computationally much less challenging than the fully three-dimensional models.

8

SUMMARY AND FUTURE WORK

8.1 SUMMARY

In this thesis, we studied water and nutrient uptake by plants at different spatial scales.

In Chapter 1, we introduced basic mathematical, physical and biological background in relation to plant-soil processes. The accuracy of uptake simulations in FEniCS and MATLAB was then tested in the first half of Chapter 2. In the second half of this chapter, we showed how one can address some important agricultural questions using very simple root geometries. First, we estimated the minimal rate of watering needed to keep the soil surrounding a single cylindrical root from drying. Then, assuming that the overall root volume (i.e. including the root hairs) is fixed, we found the inter-hair distance which maximises the water uptake.

In Chapter 3, we rederived the homogenisation result from [80] for the model of nutrient uptake by a periodic array of cylinders, and obtained other effective equations using different continuity equations and cylindrical surface boundary conditions. This way, we extended the modelling of nutrient uptake by root hairs from [80] to the modelling of uptake by a field of crops, and to the modelling of soil water dynamics using the van Genuchten model. The effective equations were later tested against full-geometry numerical simulations, and the averaging property of homogenisation was thus confirmed for all the continuity equations and boundary conditions under consideration (including the case of macroscopic variation in the direction of periodicity).

The framework from Chapter 3 was further modified in Chapter 4, where we assumed that the radius of the hair is very small compared to the inter-hair distance. The method of multiple scales in the $\epsilon^2 \ln \frac{1}{a} = O(1)$ case uncovered the new homogenisation limit (see Equation (239)). This new limit was then numerically compared with full-geometry numerics as well as with the previously obtained homogenisation limit. We further obtained asymptotic approximations with higher-order terms included, and compared these approximations with the full-geometry numerics. The numerical results were in accordance with the asymptotic analysis. Unfortunately, the $\epsilon^2 \ln \frac{1}{a} = O(1)$ scaling implies extremely small values of the a parameter (representing the quotient of the hair radius divided by the inter-hair distance), and such values are most likely not to be found in realistic root hair geometries.

In Chapter 5, we first justified (using asymptotic analysis) the usage of the unrolling assumption (i.e. the geometry from [80]) for the case where the hair length is much smaller than the root radius. Then we studied the case where the hair length is comparable to the root radius, and we derived a new homogenised equation in the unrolled variables (Equation (278)). In the curved geometry, this equation contains a sink term (representing the uptake) which is dependent on the distance from the root surface. As confirmed by numerical simulations, this new equation approximates the full-geometry model much better than the previously obtained limit.

In Chapter 6, we studied nitrate uptake via low and high affinity transporters (LATs and HATs), we showed how the (per-transporter) Michaelis-Menten uptake condition can be derived in different ways, and we investigated the implications for the functioning of LATs and HATs. Assuming that LATs have shorter per-ion handling times compared to HATs, the derivations yield higher values of both I_{max} and K_m for LATs, as usually observed in experiments. Multiplying by the density of the transporters, we upscaled the uptake rate from the transporter to the root segment scale, and obtained macroscopic values of I_{max} close to the experimental values. Finally, we introduced a simple ODE model for nitrate uptake and proposed that the experimentally-observed minimal nitrate concentration c_{min} is the result of a steady-state balance between

the uptake via transporters and the root efflux due to the presence of a nitrate concentration gradient. We concluded that the experimentally-obtained values of c_{min} and of the depletion time are of the same order as the values predicted by this model.

Finally, in Chapter 7, we showed that three-dimensional models of water and nutrient uptake can sometimes be replaced by horizontally-averaged models, which seem to predict the overall uptake satisfactorily.

8.2 FUTURE WORK

There are a number of ways in which our modelling could be improved in future. Even though the geometries used in Chapter 2 were rather simplistic, we still believe that they can provide us with an improved mechanistic understanding of uptake processes. In particular, provided a more-detailed understanding of carbon (and other) constraints for the growth of a root system is achieved in future, we still consider the geometry from Figure 2.2 to be a good starting point in studying the optimal inter-hair distance for the uptake of nutrients.

In future studies of uptake by root hairs via homogenisation, it may be useful to model the growth of the hairs. More importantly, we plan to implement the new model derived in Chapter 5 (which takes into account the curvature of the root surface; Equation (278)) into OpenSimRoot, and we hope that this model will from now on be used in other architectural models as well (such as those introduced in Section 1.5).

Due to the high complexity of nitrate uptake, there are many ways in which the modelling from Chapter 6 can be advanced. We made a few simplifying assumptions without having much detailed information on transporter densities, function or the energy constraints. To our knowledge, a lot of this information is still unknown and further experiments need to be performed.

As mentioned in Section 6.2.2, plant cells can change their molecular machinery within hours in response to changes in the external concentration [13], and this should be incorporated in future modelling. Furthermore, using di-

rect comparison with depletion experiments, various hypotheses about these changes can be tested (e.g. one can try to determine the external nitrate concentration which triggers the change from LATs to HATs using depletion times from experiments).

According to the solute dynamics theory as described in [97], chemical species (e.g. nitrate) move in response to a difference in the so-called chemical potential, which is a sum of several - activity, pressure, electrical and gravitational - components. The $-P\rho(c - c_i)$ term from Equation (311) corresponds to the activity component. While the gravitational and the pressure terms are usually negligible when modelling cross-membrane transport processes (see [97]), the electrical component may play a crucial role. Therefore, to obtain a more mechanistic description of the nitrate uptake, we plan to add the electrical component to our modelling in future.

If the diffusion of nitrate in a given medium is not sufficiently fast, depletion zones may be created close to the root surfaces, and we need to use spatial modelling. Finally, when modelling nitrate dynamics in soil, one needs to model the nonlinear mass flow with which the nitrate is advected, which adds extra complexity and further research is needed in this direction.

Similar to the uptake via the transporters, we consider our averaged models from Chapter 7 to be just the beginning of the story. These approximations have only been shown to be valid in very specific situations (see Section 7.5). This opens many possibilities for future research and many model modifications can be introduced.

To make the water uptake modelling from Section 7.3 more realistic, we need to make the water uptake dependent on the local water content in the soil, which can (in theory) be implemented in the averaged models. Furthermore, the latest version of SimRoot (similar to some other architectural models) contains the model of the root hydraulic architecture from [35] (see [108]), and thus the morphology of the root system is fully taken into account. It is not clear at the moment whether the averaged models will be capable of capturing these processes or the fully three-dimensional models are necessary.

If we observe sharp depletion gradients in nitrate concentration in SimRoot (so

that the root surface concentration is of the same order as K_m or lower), then it is very likely that the averaged model will give erroneous results, because the averaged concentration is probably much higher than the root surface concentration, and therefore, the uptake rate calculated using the averaged concentration is higher than the rate calculated using the root surface concentration. Therefore, it seems useful to investigate in which ways the sink term for the one-dimensional model needs to be modified to take into account these effects.

All models in Chapter 7 assumed a static root system, which can only be justified when modelling mature plants, or when using short time scales, i.e. situations in which the root system growth and development can be neglected. In order to model younger root systems and longer time scales, one needs to take the growth into account, and to obtain a good one-dimensional approximation for the three-dimensional model, one needs a dynamic model for the one-dimensional representation of the root system, and time-dependent data to parameterise such a model.

The main advantage of the averaged models is that they are computationally faster. Therefore, we believe these models present a desirable approximation to the three-dimensional models, if one wishes to simulate uptake by many different root systems (e.g. in order to find an optimal root architecture for nitrate capture).

To conclude, we believe that there is a lot of potential for further applications of multiscale modelling to plant water and nutrient uptake.

A

APPENDIX A

A.1 JUSTIFICATION OF SCALINGS

Imagine a fixed box $B = \{(x_1, x_2, x_3) \in \mathbb{R}^3, 0 \leq x_1, x_2, x_3 \leq 1\}$. Now we subtract a periodic array of cylinders of radii $\epsilon \times a$ where a is a fixed number (radius of the cylinder divided by the distance between neighbouring cylinders) and $\epsilon \ll 1$ is a quotient of the inter-cylinder distance divided by the macroscopic length scale (which equals 1 in this case). This way, the number of cylinders in B is $\frac{1}{\epsilon^2}$, the total volume of cylinders in B is $\frac{1}{\epsilon^2}\pi a^2\epsilon^2 = \pi a^2$ (i.e. constant), and the total surface area $SA(\epsilon) = \frac{1}{\epsilon^2}2\pi a\epsilon = \frac{2\pi a}{\epsilon} \to \infty$ as $\epsilon \to 0$. Therefore, the overall surface area of these cylinders increases (to infinity) as we space them more and more densely, but their overall volume remains the same.

Denote $A(\epsilon)$ to be the box B minus the union of all the cylinders. Consider a diffusion process happening in $A(\epsilon)$ modelled using equation (129) in $A(\epsilon)$, and an uptake process happening at the cylindrical surfaces, described by a Robin-type boundary condition:

$$\nabla u \cdot \hat{\boldsymbol{n}} = -\psi(\epsilon) K u, \tag{334}$$

where ψ is yet to be determined. The key idea here is that we do not want the cylinders to uptake the nutrient instantaneously (as we add infinitely many of them). We integrate over $A(\epsilon)$ and use the divergence theorem to get:

$$\frac{dU}{dt} = \int_{A(\epsilon)} \nabla^2 u d\Omega = \int_{\partial A(\epsilon)} \nabla u \cdot \hat{\boldsymbol{n}} dS = \int_{R(\epsilon)} \nabla u \cdot \hat{\boldsymbol{n}} dS + \int_{\partial A(\epsilon) \setminus R(\epsilon)} \nabla u \cdot \hat{\boldsymbol{n}} dS$$

where we defined $U(t;\epsilon) = \int\limits_{A(\epsilon)} u(t,x_1,x_2,x_3;\epsilon)d\Omega$ to represent the overall nutrient content left in $A(\epsilon)$ at time t, and $R(\epsilon)$ is the part of the boundary, where the nutrient uptake takes place. Assuming the zero-flux condition at all the remaining parts of the boundary and imposing a constant initial condition, we end up with a symmetric case and get:

$$\frac{1}{\psi(\epsilon)}\frac{dU}{dt} = -\frac{1}{\epsilon^2}K\int\limits_{SC(\epsilon)} udS = -\frac{1}{\epsilon^2}K2\pi a\epsilon\bar{u}_{cyl} = -\frac{2\pi Ka}{\epsilon}\bar{u}_{root}$$

where $SC(\epsilon)$ stands for a single cylinder and $\bar{u}_{cyl}(t;\epsilon)$ denotes a nutrient concentration averaged across a single cylindrical surface (which is identical for all the cylinders due to the symmetry of our problem). In other words, we have:

$$\frac{dU}{dt} = -\frac{2\pi Ka\psi(\epsilon)}{\epsilon}\bar{u}_{cyl}(t;\epsilon)(= -\psi(\epsilon)SA(\epsilon)K\bar{u}_{cyl}(t;\epsilon)) \tag{335}$$

Let us start with the initial condition $u(0,x_1,x_2,x_3) = u_{in} = 1.0$ everywhere in $A(\epsilon)$ (parameter units as well as parameter values are not important here; we simply wish to introduce basic ideas rather than draw any biological conclusions). This means that $U(0) = \|A(\epsilon)\| = 1 - \pi a^2 > 0$ (clearly, $a < \frac{1}{\sqrt{\pi}}$). Thus we see, that in order to achieve a nontrivial limit (to avoid instantaneous uptake of the nutrient), we must have $\frac{\psi(\epsilon)\bar{u}_{cyl}(t^*,\epsilon)}{\epsilon} = O(1)$ as $\epsilon \ll 1$ where $t^* > 0$ is any fixed positive number (say $t^* = 1$). Therefore, in order to determine possible choices for $\psi(\epsilon)$ we proceed as follows: we pick any $m \in \mathbb{Z}$ so that $\psi(\epsilon) = \epsilon^m$. Then, we study the behaviour of $\bar{u}_{cyl}(1,\epsilon)$ as $\epsilon \ll 1$ using what we will call the unit box problem, consisting of continuity equation (129), boundary condition (334) at a single cylindrical surface, and zero-flux boundary conditions on the sides of the unit box (because of the zero-flux boundary condition at all the non-uptaking parts of the boundary, we expect the solution to be identical in all these unit boxes). Finally, we determine $\frac{\psi(\epsilon)\bar{u}_{cyl}(1,\epsilon)}{\epsilon}$ as $\epsilon \ll 1$, and if this appears to be $O(1)$, we conclude that our choice of $\psi(\epsilon)$ should lead to a nontrivial limit. This yields a condition:

$$\bar{u}_{cyl}(1,\epsilon) = O(\frac{\epsilon}{\psi(\epsilon)}). \tag{336}$$

Let us first study the case $\psi(\epsilon) = \epsilon^0$. Simulation results (using FEniCS [83]) for $\epsilon = 1.0$ and $K = 1$ at time $t = 1.0$ is shown in Figure A.1. From the symmetry

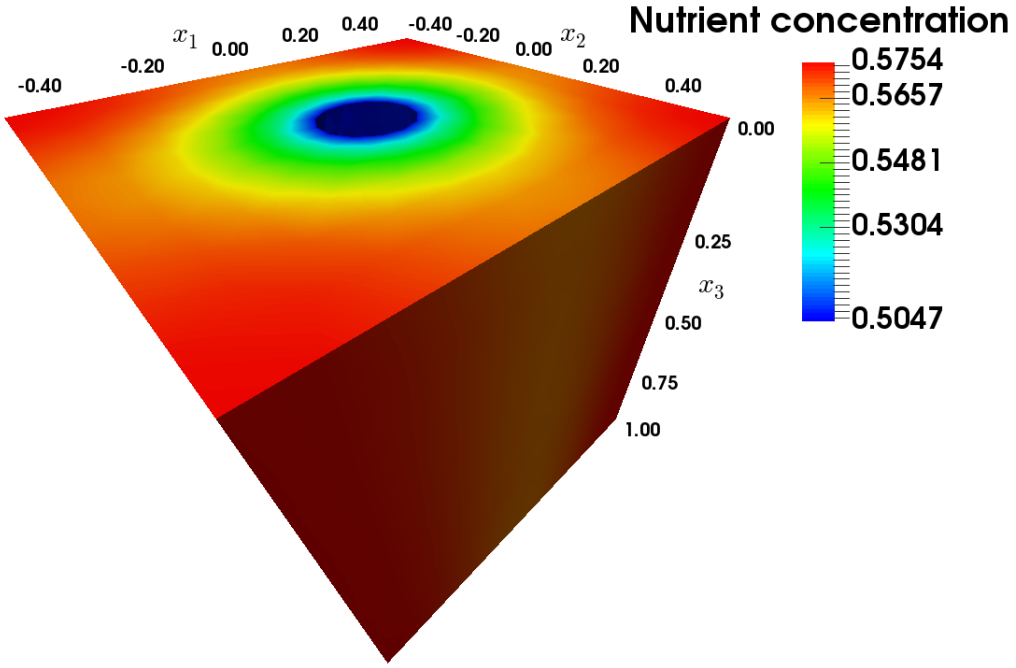


Figure A.1.: Nutrient concentration distribution at time $t = 1.0$ for $\epsilon = 1.0$ and $K = 1$.

of this problem we also get, that the solution is independent of x_3, which can also be seen using isosurfaces (surfaces of constant nutrient concentration) - see Figure $A.2$. Thus, from now on (in this appendix), we will only be interested in the solution behaviour within a slice $x_3 = c$ (for some constant c). Such slices for decreasing values of ϵ are shown in Figure $A.3$. From these figures we see, that the nutrient concentration does not vary significantly along the circular part of the boundary. This suggests that we can approximate $\bar{u}_{cyl}(1, \epsilon)$ by any value $u_{cyl}(1, \epsilon)$ at the cylindrical surface without making large errors.

To obtain a nontrivial scaling in the $m = 0$ case, we need $u_{cyl}(1, \epsilon)$ to be $O(\epsilon)$ as $\epsilon \to 0$ (see condition (336)). Results are shown in Table $A.1$. It seems that $u_{cyl}(1)$ decreases to zero with $\epsilon \to 0$ much faster than $O(\epsilon)$. Therefore, the proposed scaling is unacceptable.

The $m = 0$ scaling was inappropriate because the surface area of the cylinders was increasing to infinity (which is always true in our setting) and at the same time, the uptake rate by any unit cylindrical surface area was kept the same. Therefore, in order to get a nontrivial limit, we choose $m = 1$, i.e. $\psi(\epsilon) = \epsilon^1$.

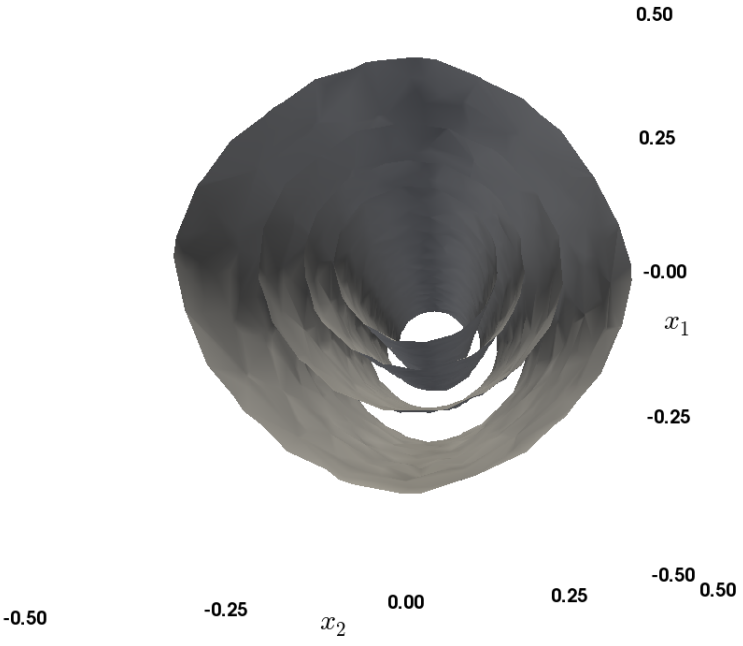
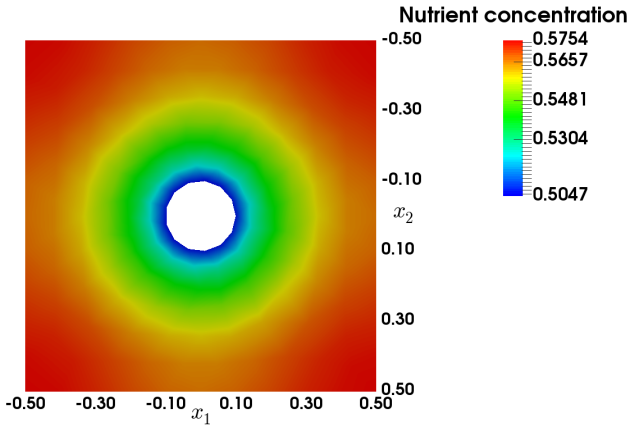


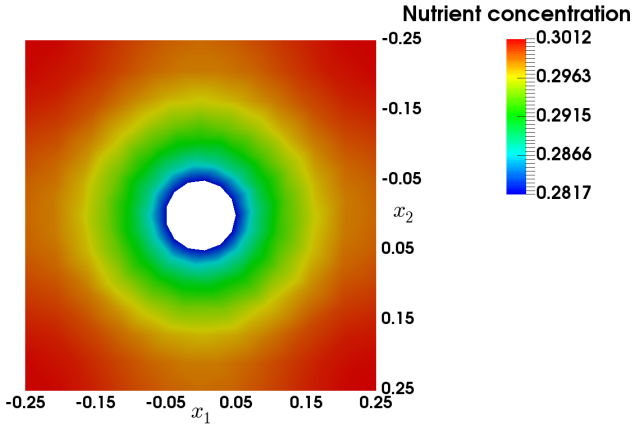
Figure A.2.: The isosurfaces for nutrient concentration at time $t = 1.0$ for $\epsilon = 1.0$ and $K = 1$.

ϵ	$u_{cyl}(1)$ for $m = 0$	$u_{cyl}(1)$ for $m = 1$	$u_{cyl}(1)$ for $m = 2$
1	5.1×10^{-1}	0.51	0.51
0.5	2.8×10^{-1}	0.52	0.72
0.25	8.2×10^{-2}	0.53	0.85
0.125	7.0×10^{-3}	0.53	0.92
0.0625	6.0×10^{-5}	0.53	0.96
0.03125	8.1×10^{-9}	0.53	0.98

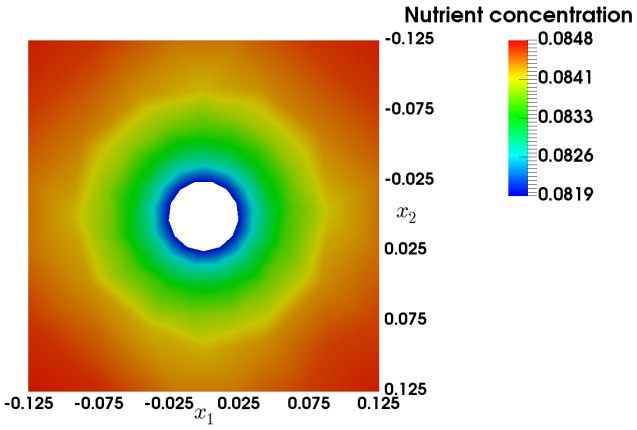
Table A.1.: $u_{cyl}(1, \epsilon)$ for different uptake scalings $\psi(\epsilon) = \epsilon^m$



(a) $\epsilon = 1.0$



(b) $\epsilon = 0.5$



(c) $\epsilon = 0.25$

Figure A.3.: Slice through the domain at $x_3 = 0.0$ for a decreasing value of ϵ. Notice the varying concentration range as well as the varying size of the unit cell.

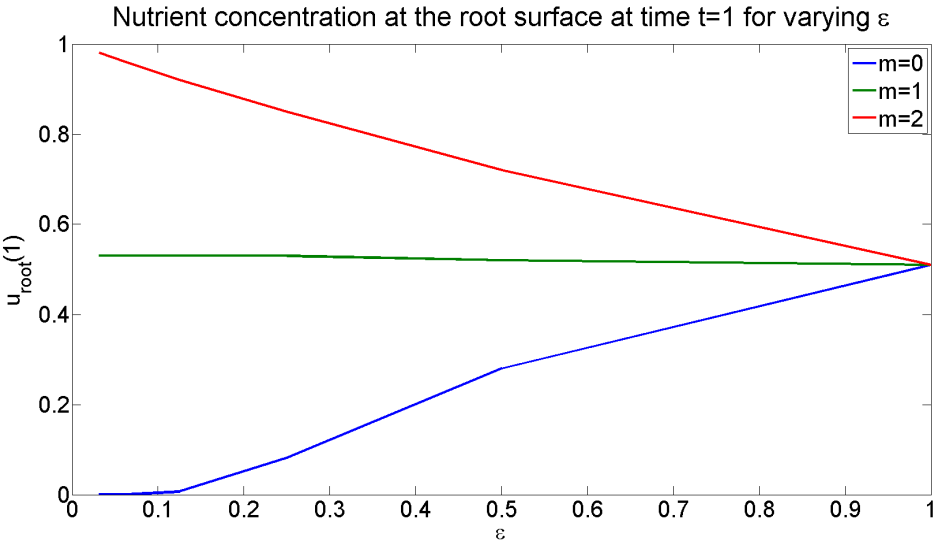


Figure A.4.: The nutrient concentration at the cylindrical surface at time $t = 1.0$ as a function of ϵ for varying m.

From condition (336), this scaling yields a nontrivial limit, if $u_{cyl}(1, \epsilon) = O(1)$ as $\epsilon \ll 1$. We calculate $u_{cyl}(1, \epsilon)$ numerically and the results are shown in Table $A.1$. Clearly, $u_{cyl}(1, \epsilon)$ is $O(1)$ and therefore, this is a scaling of interest. Furthermore, this is exactly the same scaling as the one used in Chapters 3, 4 and 5.

To finish this appendix, assume $m = 2$, i.e. $\psi(\epsilon) = \epsilon^2$. Equation (336) yields a condition $u_{cyl}(1, \epsilon) = O(\epsilon^{-1})$ as $\epsilon \ll 1$. Starting with $u_{in} = 1.0$ and having no nutrient source in $A(\epsilon)$, it is obvious that this can never happen. We calculate $u_{cyl}(1, \epsilon)$ numerically anyway and the results are shown in Table $A.1$. $u_{cyl}(1, \epsilon)$ appears to approach 1 as $\epsilon \to 0$ which is expected, as we have made the uptake rate very small and thus negligible in the first approximation. Clearly, $u_{cyl}(1, \epsilon)$ is $O(1)$ and therefore, this scaling is not interesting to us.

The behaviour of $u_{cyl}(t = 1, \epsilon)$ for different m is shown in Figure $A.4$. We conclude that if we picked any (real) $m < 1$ in $\psi(\epsilon) = \epsilon^m$, we would end up with instantaneous uptake as we made the uptake rate too large. Similarly, choosing $m > 1$ always leads to negligible uptake in the first approximation.

B

APPENDIX B

Listing B.1: Model without gravity: MATLAB code

```
function diffusion_cylinder_dirichlet

h.ro = 2;
h.r1 = 20;
h.length = h.r1-h.ro;
h.npts = 201;
h.dx = h.length/(h.npts-1);
h.dx2 = h.dx^2;
h.D = 2.5;
h.C1 = 0.5;
h.lambda = 0.0017;
xx = h.ro + [0:h.dx:(h.npts-1)*h.dx];
h.xx = xx';
ics = 0.5*ones(h.npts,1);

sol = 0.5+h.r1^2*h.lambda*log(xx/h.r1)/(2*h.D);

fin = 100;
nplots = 10;
t = 0;
tt = 0:(fin/nplots):fin;

figure(1)
clf
hold on
plot(xx,ics,'linewidth',1.5)
```

```
ylim([0 0.7])
title('Time evolution showing convergence to steady state','fontsize'
    ,40)
xlabel('r, polar radius','fontsize',35)
ylabel('\Phi, water content','fontsize',35)
set(gca,'FontSize',30)
pause(0.1)

ystore = ics;

for i=1:nplots
        tspan = [(i-1)*fin/nplots (2*i-1)*fin/(2*nplots) i*fin/nplots
            ];
        options = [];
        [t,y] = ode23(@molode,tspan,ics,options);
        ics = y(end,:)';
        plot(xx,ics,'linewidth',1.5)
    ylim([0 0.7])


        title('Convergence to steady state','fontsize',40)
    xlabel('r, polar radius','fontsize',35)
    ylabel('\Phi, water content','fontsize',35)
    ystore = [ystore, ics];
    pause(0.01)

end

plot(xx,ics,'linewidth',1.5)
plot(xx,sol,'r','linewidth',2.5)
100*abs(ics(1)-sol(1))/sol(1)

    function out1 = molode(t,y,flag)

        yxpdx = y([2:h.npts,h.npts-1]);
        yxmdx = y([2,1:h.npts-1]);
        % correction due to the flux condition at the left boundary
        yxmdx(1) = yxmdx(1) - h.r1^2*h.lambda*h.dx/(h.D*h.ro);
        xxpdx = (h.xx([2:h.npts,h.npts-1])+h.xx)/2;
```

```
        xxmdx = (h.xx([2,1:h.npts-1]) + h.xx)/2;
        diff = ((xxpdx.*(yxpdx-y) - xxmdx.*(y-yxmdx))./h.xx)/h.dx2;
        diff(end) = 0;
        out1 = h.D*diff;
    end
end
```

Listing B.2: Model with gravity: MATLAB code

```
function water_uptake_cylindrical_root_gravity
%% function to simulate (C=theta)
%   C_t = D (C_x3x3 + (1/r)(r C_r)_r) - K C_x3        (1)
% subject to
% % %   D C_x3(t,r,0)= K C(t,r,0), D C_x3(t,r,ho)= K C(t,r,ho)
                (2)
%   C(t,r_inf,z)= 0.25          (3)
%   C(t,r_0,z)= 0.0                         (4)
%
% simulation uses finite differences to approximate spatial
    derivatives
% and turn (1) into a system of ODEs, and then uses MATLABs ODE
    solvers to
% simulate those ODEs.

%% set up the model and numerical parameters
nr = 191; % resolution

ro = 0.1;

r1 = 2.0;

dr = (r1-ro)/(nr-1); % mesh size

ho = 1.0;

nz = 1+ho/dr;

dr2 = dr^2;

D = 1.0;
```

```
29
30 K = 1.0;
31
32 fin = 5;  % final time
33
34 nplots = 50; % number of plots
35
36 lambda = K/D*dr; % auxiliary variable for approximating the boundary
       conditions in x3 direction
37
38 %% set up vectors mapping to neighbouring mesh points
39 [i,j] = meshgrid(1:nz,1:nr)
40 im1 = i(:,[2 1:nz-1]);
41 ip1 = i(:,[2:nz nz-1]);
42 jm1 = j([2 1:nr-1],:);
43 jp1 = j([2:nr nr-1],:);
44 ij = reshape(sub2ind([nz nr],i,j)',nz*nr,1);
45 im1j = reshape(sub2ind([nz nr],im1,j)',nz*nr,1);
46 ip1j = reshape(sub2ind([nz nr],ip1,j)',nz*nr,1);
47 ijm1 = reshape(sub2ind([nz nr],i,jm1)',nz*nr,1);
48 ijp1 = reshape(sub2ind([nz nr],i,jp1)',nz*nr,1);
49
50 %% set up vectors mapping to boundary mesh points
51 [itop,jtop] = meshgrid(1,1:nr);
52 topbc = sub2ind([nz nr],itop,jtop);
53 [ibottom,jbottom] = meshgrid(nz,1:nr);
54 bottombc = sub2ind([nz nr],ibottom,jbottom);
55 [iright,jright] = meshgrid(1:nz,nr);
56 rightbc = sub2ind([nz nr],iright,jright);
57 [ileft,jleft] = meshgrid(1:nz,1);
58 leftbc = sub2ind([nz nr],ileft,jleft);
59
60 %% set up the spatial mesh
61 zz = o:dr:ho;
62 rr = ro:dr:r1;
63 [zzz,rrr] = meshgrid(zz,rr);
64
65 rr = reshape(rrr',nz*nr,1);
66
```

```
67
68
69  %% set up the initial conditions
70
71  far_field_water = 0.25;
72  ics= far_field_water*ones(1,nz*nr);
73  ics(1:nz)=0.0;
74
75  t = 0;
76
77  %% create a figure and plot initial conditions
78  f = figure(1)
79  clf
80  cla
81
82  cc = reshape(ics,nz,nr);
83  hh = imagesc(rr,zz,cc);
84  axis([0 2.1 -0.1 1.1]);
85
86  ylabel('$x_3$, depth','fontsize',30, 'Interpreter','latex')
87  xlabel('$r$, polar radius','fontsize',30, 'Interpreter','latex')
88  title('Water content','fontsize',30, 'Interpreter','latex')
89  set(gca,'fontsize',30)
90
91  colormap(jet)
92  caxis([0 0.3533])
93  hold on
94  hhh=colorbar;
95  set(hhh, 'ylim', [0 0.3533])
96  set(hhh, 'fontsize',30)
97  mkdir('FRAMES')
98
99
100 %% loop to simulate a time subinterval and plot output
101 for i=1:nplots
102         tspan = [(i-1)*fin/nplots (2*i-1)*fin/(2*nplots) i*fin/nplots
                ];
103         options = [];
104         [t,y] = ode23(@molode,tspan,ics,options);
```

```
105         ics = y(end,:)'
106     cc = reshape(ics,nz,nr)
107
108     imagesc(rr,zz,cc);
109     title(['Water content at time = ',num2str(t(end))],'fontsize',30)
110     print(['FRAMES/frame' num2str(i)],'-dpng')
111
112 end
113
114     %% nested function defining the ODEs
115     function out1 = molode(t,y,flag)
116
117         % approximate r + dr/2 and r - dr/2
118         rrpdro2 = (rr(ijp1) + rr)/2;
119         rrmdro2 = (rr(ijm1) + rr)/2;
120
121         % define y(r + dr) and y(r - dr)
122         yrpdr = y(ijp1);
123         yrmdr = y(ijm1);
124         yzpdz = y(ip1j);
125         yzmdz = y(im1j);
126
127         %approximate (1/r)(r C_r)_r by
128         % ((r + dr/2) C_r(r + dr/2) - (r - dr/2) C_r(r - dr/2))/(r dr
                )
129         diffr = ((rrpdro2.*(yrpdr-y) - rrmdro2.*(y-yrmdr))./rr)/dr2;
130
131         % boundary condition at x3=0
132         % D*c_x3 = K*c                                    (dz = dr in our
                case)
133         % D (c(dr) - c(-dr)) = 2*dr*K*c(0)
134         % c(dr) - c(-dr) = 2*dr*K/D*c(0)                   lambda :=dr*K/D
135         % c(-dr) = c(dr) - 2*lambda*c(0)
136         % yzmdz(topbc) = yzmdz(topbc) - 2*lambda*y(topbc);
137         % similar with boundary condition at x3=ho
138
139         yzmdz(topbc) = yzmdz(topbc)-2*lambda*y(topbc);
140         yzpdz(bottombc) = yzpdz(bottombc)+2*lambda*y(bottombc);
141
```

```
142
143          % diffusion with 'no-flux' bcs
144          diffz = (yzmdz + yzpdz - 2*y)/dr2;
145          % upwinding for advection term
146          dcdzdown = (y - y(im1j))/dr;
147
148          out1 = D*(diffz + diffr) - K*dcdzdown;
149
150          % dirichlet at the root and the outer boundary
151          out1(leftbc)=0;
152          out1(rightbc)=0;
153
154      end
155  end
```

C

APPENDIX C

Listing C.1: LATs and HATs uptake (steady state): two scenarios

```
NTotal = 1000; % parameter values
ImH = 0.01085;
ImL = 10;
KmH = 1;
KmL = 1000;
co = 1;
I = ImH/ImL; % nondimensional quantities
K = KmH/KmL;
A = 1/ImL;
roots1 = zeros(NTotal+1,1); % cubic equation has max three roots
roots2 = zeros(NTotal+1,1);
roots3 = zeros(NTotal+1,1);
% for each NL we calculate roots of the corresponding cubic equation
    using
% standard formulas, ImH = 0.01085;
for NL = 0:NTotal
  a = A*KmL;
  b = NL+I*(NTotal-NL)+A*KmL+A*KmL*K-A*co;
  c = K*NL+I*(NTotal-NL)+A*KmL*K-A*co-A*co*K;
  d = -A*co*K;
  deltao = b*b - 3*a*c;
  delta1 = 2*b*b*b - 9*a*b.*c+27*a*a*d;
  angle1 = atan(sqrt(4*deltao*deltao*deltao-delta1*delta1)/delta1)/3;
  cosofangle1 = cos(angle1);
  ReC1 = sqrt(deltao)*cosofangle1;
  root1 = -(b+2*ReC1)/(3*a);
```

```
26    angle2 = atan(sqrt(4*deltao*deltao*deltao-delta1*delta1)/delta1)
          /3+2*pi/3;
27    cosofangle2 = cos(angle2);
28    ReC2 = sqrt(deltao)*cosofangle2;
29    root2 = -(b+2*ReC2)/(3*a);
30    angle3 = atan(sqrt(4*deltao*deltao*deltao-delta1*delta1)/delta1)
          /3+4*pi/3;
31    cosofangle3 = cos(angle3);
32    ReC3 = sqrt(deltao)*cosofangle3;
33    root3 = -(b+2*ReC3)/(3*a);
34    tr = 18*a*b*c*d - 4*b*b*b*d + b*b*c*c - 4*a*c*c*c-27*a*a*d*d;
35    y1 = a*root1*root1*root1+b*root1*root1+c*root1+d;
36    y2 = a*root2*root2*root2+b*root2*root2+c*root2+d;
37    y3 = a*root3*root3*root3+b*root3*root3+c*root3+d;
38    roots1(NL+1)=root1;
39    roots2(NL+1)=root2;
40    roots3(NL+1)=root3;
41  end
42  ImH2 = 0.01095; % we only change ImH
43  I2 = ImH2/ImL;
44  roots12 = zeros(NTotal+1,1);
45  roots22 = zeros(NTotal+1,1);
46  roots32 = zeros(NTotal+1,1);
47  for NL = 0:NTotal % calculating roots for ImH = 0.01095;
48    a = A*KmL;
49    b2 = NL+I2*(NTotal-NL)+A*KmL+A*KmL*K-A*co;
50    c2 = K*NL+I2*(NTotal-NL)+A*KmL*K-A*co-A*co*K;
51    d = -A*co*K;
52    deltao2 = b2*b2 - 3*a*c2;
53    delta12 = 2*b2*b2*b2 - 9*a*b2.*c2+27*a*a*d;
54    angle12 = atan(sqrt(4*deltao2*deltao2*deltao2-delta12*delta12)/
          delta12)/3;
55    cosofangle12 = cos(angle12);
56    ReC12 = sqrt(deltao2)*cosofangle12;
57    root12 = -(b2+2*ReC12)/(3*a);
58    angle22 = atan(sqrt(4*deltao2*deltao2*deltao2-delta12*delta12)/
          delta12)/3+2*pi/3;
59    cosofangle22 = cos(angle22);
60    ReC22 = sqrt(deltao2)*cosofangle22;
```

```
61    root22 = -(b2+2*ReC22)/(3*a);
62    angle32 = atan(sqrt(4*delta02*delta02*delta02-delta12*delta12)/
          delta12)/3+4*pi/3;
63    cosofangle32 = cos(angle32);
64    ReC32 = sqrt(delta02)*cosofangle32;
65    root32 = -(b2+2*ReC32)/(3*a);
66    tr2 = 18*a*b2*c2*d - 4*b2*b2*b2*d + b2*b2*c2*c2 - 4*a*c2*c2*c2-27*a
          *a*d*d;
67    y1 = a*root12*root12*root12+b2*root12*root12+c2*root12+d;
68    y2 = a*root22*root22*root22+b2*root22*root22+c2*root22+d;
69    y3 = a*root32*root32*root32+b2*root32*root32+c2*root32+d;
70    roots12(NL+1)=root12;
71    roots22(NL+1)=root22;
72    roots32(NL+1)=root32;
73  end
74  x = linspace(0,NTotal,NTotal+1);
75  h1 = plot(x,roots2*KmL,'Color','b','LineWidth',3); % plot the
      positive dimensional roots, ImH = 0.01085
76  hold on
77  cstar = (KmL*ImH-KmH*ImL)/(ImL-ImH) % calculate c*, ImH = 0.01085
78  h2 = plot(x,cstar*ones(NTotal+1,1),'--','Color','b','LineWidth',3) %
      plot c*, ImH = 0.01085
79  h3 = plot(x,roots22*KmL,'Color','r','LineWidth',3); % plot the
      positive dimensional roots, ImH = 0.01095
80  cstar2 = (KmL*ImH2-KmH*ImL)/(ImL-ImH2) % calculate c*, ImH = 0.01095
81  h4 = plot(x,cstar2*ones(NTotal+1,1),'--','Color','r','LineWidth',3) %
       plot c*, ImH = 0.01095
82  h_legend=legend([h1',h2',h3',h4'],'c_{ss} (I_{max}^{H}=0.01085)','c
      ^{*} (I_{max}^{H}=0.01085)','c_{ss} (I_{max}^{H}=0.01095)','c^{*}
      (I_{max}^{H}=0.01095)')
83  set(h_legend,'FontSize',27);
84  rect = [0.70, 0.25, .25, .07];
85  set(legend, 'Position', rect);
86  set(gca,'FontSize',35);
87  xlabel('Number of low affinity transporters','FontSize', 40);
88  ylabel('External nitrate concentration','FontSize', 40);
89  title('Two different scenarios - 1000 transporters in total','
      FontSize', 40);
```

Listing C.2: LATs and HATs uptake: time evolution

```
KmL = 100;   %millimolar
IL = 0.7;    %millimole per hour per gram
KmH = 0.085; % 0.016 for constitutively expressed HATs; millimolar
IH = 0.135;  % 0.027 for constitutively expressed HATs; millimole per
    hour per gram
a_ic = IL/KmL; %dm^3 (hg)^-1
b_ic = 0.020; % millimole (hg)^-1
surfacepergram = 75.0; %total root surface per gram of root
IHH = IH/surfacepergram; %millimole per hour per dm^2 of root surface
ILL = IL/surfacepergram; %millimole per hour per dm^2 of root surface
alpha = 0.005; % 0.016 for constitutively expressed HATS;  alpha =
    a_ic*KmH/(IH - b_ic), dimensionless

NH_max = 80000000000000; % maximum number of HATs per dm^2 of root
    surface
NTotal = NH_max*alpha
%NH_min = b_ic/IH*NH_max
NH_min =12000000000000
NL_max = NTotal - alpha*NH_min
dN = NTotal/200;

ImH = IHH/NH_max;  % millimole per hour per transporter
ImL = ILL/NL_max;
I = ImH/ImL;
K = KmH/KmL;
newcstar = (KmL*ImH-alpha*KmH*ImL)/(alpha*ImL-ImH)

cin = 0.25;  %millimolar
theta = 1.0; % hydroponics
rho = 36.0;  % dm^2 of root surface per dm^3 of soil
co = 3; % millimolar
P = 0.00001; % dm^3 of solute per dm^2 of root surface per hour
C = P*rho/theta; % dm^3 of solute per dm^3 of soil per hour
A = P/ImL;

trialc = cin; % we first estimate depletion time roughly using NL =
    0;
trialt = 0;
```

```
35 NL = 0;
36
37 while trialc > cin/10
38     dt = abs(trialc/(-(NL*rho)*(ImL*trialc)/(KmL+trialc) - ((NTotal-
           NL)/alpha*rho)*(ImH*trialc)/(KmH+trialc) + C*(co-trialc)))
           /500;
39     trialt=trialt+dt;
40     trialc = trialc+dt*(-(NL*rho)*(ImL*trialc)/(KmL+trialc) - ((
           NTotal-NL)/alpha*rho)*(ImH*trialc)/(KmH+trialc) + C*(co-trialc
           ));
41 end
42
43 finaltime = 3*trialt; % we allow the simulation to run for three
       times longer than the estimated depletion time
44 halftime = zeros([NL_max/dN+1, 1],'double'); % depletion time
45 concatfinaltime = zeros([NL_max/dN+1,1],'double'); % steady states
46 figure(1);
47 plotStyle = {'b','k','r','g','y','b','k','r','g','y','b','k','r','g',
       'y','b','k','r','g','y','g'};
48 set(gca,'fontsize',30);
49 hold on;
50
51 for NL = 0:dN:NTotal
52
53 if NL > NL_max
54         break
55 end
56
57 t=[];
58 y=[];
59 t(1)=0;
60 y(1)=cin;
61
62 while t(end)<finaltime  % we simulate for each NL until the final
       time is reached
63     dt = abs(y(end)/(-(NL*rho)*(ImL*y(end))/(KmL+y(end)) - ((NTotal-
           NL)/alpha*rho)*(ImH*y(end))/(KmH+y(end)) + C*(co-y(end))))
           /5000;
64     t(end+1)=t(end)+dt;
```

```
    y(end+1) = y(end)+dt*(-(NL*rho)*(ImL*y(end))/(KmL+y(end)) - ((
        NTotal-NL)/alpha*rho)*(ImH*y(end))/(KmH+y(end)) + C*(co-y(end)
        ));
end

if mod(NL,NTotal/4)==0  % For specified NL, we plot the solutions
    plot(t,y,plotStyle{NL*4/NTotal+1},'Linewidth',3);
    title('External concentration as a function of time for varying $
       N^L$','FontSize',40, 'Interpreter','latex');
    xlabel('Time ($h$)','FontSize',35, 'Interpreter','latex');
    ylabel('External concentration ($mM$)','FontSize',35, '
        Interpreter','latex');
end

difference = cin - y(end);
threshold = y(end)+0.01*difference; % threshold value for the steady
    state, 99% depletion
t99 = finaltime;

for x = 1:length(t) % calculate depletion time
    if y(x) < threshold
        t99 = t(x);
        break
    end
end

concatfinaltime(NL/dN+1) = y(end);
halftime(NL/dN+1) = t99;
end

xlim([0,finaltime]);
halftime;
legend(['N^{L}=' num2str(0*NL_max/4,'%10.1e\n')],['N^{L}=' num2str(1*
    NL_max/4,'%10.1e\n')],['N^{L}=' num2str(2*NL_max/4,'%10.1e\n')],['
    N^{L}=' num2str(3*NL_max/4,'%10.1e\n')],['N^{L}=' num2str(4*NL_max
    /4,'%10.1e\n')]);
figure(2); % plot everything
hold on;
plot(0:dN:NL_max,halftime,plotStyle{1},'Linewidth',3);
```

```
96  title('Time to $99\%$ depletion as a function of LATs density','
        FontSize',40, 'Interpreter','latex');
97  xlabel('$N^{L}$ ($dm^{-2}$)','FontSize',35, 'Interpreter','latex');
98  ylabel('Depletion time ($h$)','FontSize',35, 'Interpreter','latex');
99  set(gca,'fontsize',30);
100 figure(3);
101 hold on;
102 plot(o:dN:NL_max,concatfinaltime,plotStyle{1},'Linewidth',3);
103 title('Steady-state nitrate concentrations','FontSize',40, '
        Interpreter','latex');
104 xlabel('$N^{L}$ ($dm^{-2}$)','FontSize',35, 'Interpreter','latex');
105 ylabel('Steady-state concentration ($mM$)','FontSize',35, '
        Interpreter','latex');
106 set(gca,'fontsize',30);
```

BIBLIOGRAPHY

[1] M. Abramowitz and I.A. Stegun. *Handbook of Mathematical Functions, tenth printing*. National Bureau of Standards, Washington, 1972.

[2] S.G.K. Adiku, C.W. Rose, R.D. Braddock, and H. Ozier-Lafontaine. On the simulation of root water extraction: examination of a minimum energy hypothesis. *Soil Science*, 165(3):226–236, 2000.

[3] Agriculture and Cereals & Oilseeds Horticulture Development Board. General guides on growing cereals and oilseeds, 2015. `https://cereals.ahdb.org.uk/crop-management/growth-guides.aspx`.

[4] S. Ahmed, T.N. Klassen, S. Keyes, M. Daly, D.L. Jones, M. Mavrogordato, I. Sinclair, and T. Roose. Imaging the interaction of roots and phosphate fertiliser granules using 4D X-ray tomography. *Plant and soil*, 401(1-2):125–134, 2016.

[5] D.L. Aksnes and J.K. Egge. A theoretical model for nutrient uptake in phytoplankton. *Mar. Ecol. Prog. Ser.*, 1991.

[6] R.A. Armstrong. Nutrient uptake rate as a function of cell size and surface transporter density: A Michaelis-like approximation to the model of Pasciak and Gavis. *Deep Sea Research Part I: Oceanographic Research Papers*, 55(10):1311 – 1317, 2008.

[7] M.J. Aston and D.W. Lawlor. The relationship between transpiration, root water uptake, and leaf water potential. *Journal of Experimental Botany*, 30(1):169, 1979.

[8] V.C. Baligar and S.A. Barber. Genotypic differences of corn for ion uptake. *Agronomy Journal*, 71(5):870–873, 1979.

[9] L.R. Band, J.A. Fozard, Ch. Godin, O.E. Jensen, T. Pridmore, M.J. Bennett, and J.R. King. Multiscale systems analysis of root growth and development: Modeling beyond the network and cellular scales. *Plant Cell*, pages 3892–3906, 2012.

[10] S.A. Barber. A diffusion and mass-flow concept of soil nutrient availability. *Soil Science*, 93(1):39–49, 1962.

[11] S.A. Barber. *Soil nutrient bioavailability: A mechanistic approach, 2nd ed.* John Wiley & Sons, 1995.

[12] A.J. Bloom, F.S. Chapin, and H.A. Mooney. Resource limitation in plants - an economic analogy. *Annual review of Ecology and Systematics*, 16(1):363–392, 1985.

[13] J.A. Bonachela, M. Raghib, and S.A. Levin. Dynamic model of flexible phytoplankton nutrient uptake. *Proceedings of the National Academy of Sciences*, 108(51):20633–20638, 2011.

[14] N.C. Brady and R.R. Weil. *The nature and properties of soils, 11th ed.* Prentice-Hall Inc. Upper Saddle River, New Jersey, 1996.

[15] R.H. Brooks and A.T. Corey. Hydraulic properties of porous media. *Hydrology Papers, Colorado State University*, 1964.

[16] M. Bruna and S.J. Chapman. Diffusion in spatially varying porous media. *SIAM Journal on Applied Mathematics*, 75(4):1648–1674, 2015.

[17] Y. Capdeboscq and M. Ptashnyk. Root growth: Homogenization in domains with time dependent partial perforations. *ESAIM: Control, Optimisation and Calculus of Variations*, 2012.

[18] A. Carminati, A.B. Moradi, D. Vetterlein, P. Vontobel, E. Lehmann, U. Weller, H.-J. Vogel, and S.E. Oswald. Dynamics of soil water content in the rhizosphere. *Plant and Soil*, page 163–176, 2010.

[19] D. Cioranescu and P. Donato. *An Introduction to Homogenization*. Oxford lecture series in mathematics and its applications. Oxford University Press, 1999.

[20] D. Cioranescu, P. Donato, and R. Zaki. The periodic unfolding method in perforated domains. *PORTUGALIAE MATHEMATICA*, 63(4):467–496, 2006.

[21] N. Claassen and S.A. Barber. A method for characterizing the relation between nutrient concentration and flux into roots of intact plants. *Plant Physiology*, 54(4):564–568, 1974.

[22] Phoenix Bioinformatics Corporation. The Arabidopsis information resource - gene model: AT1G08090.1, 2015. `https://www.arabidopsis.org/servlets/TairObject?type=gene&id=139048`.

[23] Phoenix Bioinformatics Corporation. The Arabidopsis information resource - gene model: AT1G69850.1, 2015. `https://www.arabidopsis.org/servlets/TairObject?type=gene&id=137886`.

[24] J. Crank. *The mathematics of diffusion*. Oxford university press, 1979.

[25] N.M. Crawford and A.D.M. Glass. Molecular and physiological aspects of nitrate uptake in plants. *Trends in Plant Science*, 3(10):389 – 395, 1998.

[26] K.R. Daly, S.D. Keyes, S. Masum, and T. Roose. Image based modeling of nutrient movement in and around the rhizosphere. *Journal of Experimental Botany*, pages 1–12, January 2016.

[27] K.R. Daly, S.R. Tracy, N.M.J. Crout, S. Mairhofer, T.P. Pridmore, S.J. Mooney, and T. Roose. Quantification of root water uptake in soil using X-ray computed tomography and image-based modelling. *Plant, cell & environment*, 2017.

[28] J.L. Dardanelli, J.T. Ritchie, M. Calmon, J.M. Andriani, and D.J. Collino. An empirical model for root water uptake. *Field Crops Research*, 87(1):59 – 71, 2004.

[29] P.R. Darrah, D.L. Jones, G.J.D. Kirk, and T. Roose. Modelling the rhizosphere: a review of methods for 'upscaling' to the whole-plant scale. *European Journal of Soil Science*, pages 13–25, 2006.

[30] S. Datta, Ch.M. Kim, M. Pernas, N.D. Pires, H. Proust, T. Tam, P. Vijayakumar, and L. Dolan. Root hairs: development, growth and evolution at the plant-soil interface. *Plant and Soil*, 346(1):1–14, Sep 2011.

[31] Y. Davit, Ch.G. Bell, H.M. Byrne, L.A.C. Chapman, L.S. Kimpton, G.E. Lang, K.H.L. Leonard, J.M. Oliver, N.C. Pearson, R.J. Shipley, et al. Homogenization via formal multiscale asymptotics and volume averaging: How do the two techniques compare? *Advances in Water Resources*, 62:178–206, 2013.

[32] P.G. Dennis, A.J. Miller, and P.R. Hirsch. Are root exudates more important than other sources of rhizodeposits in structuring rhizosphere bacterial communities? *FEMS Microbiology Ecology*, 72(3):313–327, 6 2010.

[33] A.J. Diggle. ROOTMAP - a model in three-dimensional coordinates of the growth and structure of fibrous root systems. *Plant and Soil*, September 1988.

[34] C. Doussan, L. Pagès, and A. Pierret. Soil exploration and resource acquisition by plant roots: an architectural and modelling point of view. *Agronomie*, 23(5-6):419–431, 2003.

[35] C. Doussan, L. Pagès, and G. Vercambre. Modelling of the hydraulic architecture of root systems: An integrated approach to water absorption - model description. *Annals of Botany*, pages 213–223, 1998.

[36] C. Doussan, A. Pierret, E. Garrigues, and L. Pagès. Water uptake by plant roots: II – Modelling of water transfer in the soil root-system with explicit account of flow within the root system – comparison with experiments. *Plant and Soil*, pages 99–117, 2006.

[37] M.F. Dreccer, A.H.C.M. Schapendonk, G.A. Slafer, and R. Rabbinge. Comparative response of wheat and oilseed rape to nitrogen supply: ab-

sorption and utilisation efficiency of radiation and nitrogen during the reproductive stages determining yield. *Plant and soil*, 220(1-2):189–205, 2000.

[38] V.M. Dunbabin, A.J. Diggle, Z. Rengel, and R. van Hugten. Modelling the interactions between water and nutrient uptake and root growth. *Plant and Soil*, pages 19–38, 2002.

[39] V.M. Dunbabin, S. McDermott, and A.G. Bengough. Upscaling from rhizosphere to whole root system: Modelling the effects of phospholipid surfactants on water and nutrient uptake. *Plant and Soil*, pages 57–72, 2006.

[40] V.M. Dunbabin, J.A. Postma, A. Schnepf, L. Pages, M. Javaux, L. Wu, D. Leitner, Y.L. Chen, Z. Rengel, and A.J. Diggle. Modelling root–soil interactions using three–dimensional models of root growth, architecture and function. *Plant Soil*, 2013.

[41] L. Dupuy, P.J. Gregory, and A.G. Bengough. Root growth models: towards a new generation of continuous approaches. *Journal of Experimental Botany*, pages 1–13, 2010.

[42] A. Einstein. *Investigations on the Theory of the Brownian Movement*. Courier Corporation, 1956.

[43] E. Epstein and C.E. Hagen. A kinetic study of the absorption of alkali cations by barley roots. *Plant Physiology*, 27(3):457–474, 1952.

[44] E. Epstein, D.W. Rains, and O.E. Elzam. Resolution of dual mechanisms of potassium absorption by barley roots. *Proceedings of the National Academy of Sciences*, 49(5):684–692, 1963.

[45] L.C. Evans. *Partial differential equations*, volume 19 of *Graduate Studies in Mathematics*. American Mathematical Society, Providence, RI, second edition, 2010.

[46] R.A. Feddes, H. Hoff, M. Bruen, T. Dawson, P. de Rosnay, P. Dirmeyer, R.B. Jackson, P. Kabat, A. Kleidon, A. Lilly, and A.J. Pitman. Modeling

root water uptake in hydrological and climate models. *Bulletin of the American Meteorological Society*, 82(12):2797–2809, 2001.

[47] Ø. Fiksen, M.J. Follows, and D.L. Aksnes. Trait-based models of nutrient uptake in microbes extend the Michaelis-Menten framework. *Limnology and Oceanography*, 58(1):193–202, 2013.

[48] A.H. Fitter. The topology and geometry of plant root systems: Influence of watering rate on root system topology in Trifolium pratense. *Annals of Botany*, 58(1):91, 1986.

[49] B.G. Forde. Nitrate transporters in plants: structure, function and regulation. *Biochimica et Biophysica Acta (BBA) - Biomembranes*, 1465(1–2):219 – 235, 2000.

[50] M.J. Foulkes, M.J. Hawkesford, P.B. Barraclough, M.J. Holdsworth, S. Kerr, S. Kightley, and P.R. Shewry. Identifying traits to improve the nitrogen economy of wheat: Recent advances and future prospects. *Field crop research*, pages 329–342, 2009.

[51] T.S. Gahoonia, D. Care, and N.E. Nielsen. Root hairs and phosphorus acquisition of wheat and barley cultivars. *Plant and Soil*, pages 181–188, 1997.

[52] W.R. Gardner. Dynamic aspects of water availability to plants. *Soil Science*, pages 63–73, 1960.

[53] W.R. Gardner. Modeling water uptake by roots. *Irrigation Science*, pages 109–114, 1991.

[54] Z. Ge, G. Rubio, and J.P. Lynch. The importance of root gravitropism for inter-root competition and phosphorus acquisition efficiency: Results from a geometric simulation model. *Plant and Soil*, pages 159–171, 2000.

[55] H.Ch.J. Godfray, J.R. Beddington, I.R. Crute, L. Haddad, D. Lawrence, J.F. Muir, J. Pretty, S. Robinson, S.M. Thomas, and C. Toulmin. Food security: The challenge of feeding 9 billion people. *Science*, pages 812–818, 2010.

[56] D. Gómez, M. Lobo, M.E. Pérez, T.A. Shaposhnikova, and M.N. Zubova. On critical parameters in homogenization of perforated domains by thin tubes with nonlinear flux and related spectral problems. *Mathematical Methods in the Applied Sciences*, 38(12):2606–2629, 2015.

[57] P.J. Gregory. Roots, rhizosphere and soil: the route to a better understanding of soil science? *European Journal of Soil Science*, pages 2–12, 2006.

[58] P.J. Gregory, M. McGowan, P.V. Biscoe, and B. Hunter. Water relations of winter wheat. *The Journal of Agricultural Science*, 93(2):494–494, 1979.

[59] D. Hillel. *Environmental soil physics*. San Diego, CA: Academic Press, 1998.

[60] E.J. Hinch. *Perturbation Methods*. Cambridge Texts in Applied Mathematics. Cambridge University Press, 1991.

[61] P. Hinsinger, A. Brauman, N. Devau, F. Gérard, Ch. Jourdan, J.-P. Laclau, E. Le Cadre, B. Jaillard, and C. Plassard. Acquisition of phosphorus and other poorly mobile nutrients by roots. Where do plant nutrition models fail? *Plant Soil*, pages 29–61, 2011.

[62] A. Hodge, G. Berta, C. Doussan, F. Merchan, and M. Crespi. Plant root growth, architecture and function. *Plant Soil*, pages 153–187, 2009.

[63] S. Holmseth, Y. Dehnes, Y.H. Huang, V.V. Follin-Arbelet, N.J. Grutle, M.N. Mylonakou, C. Plachez, Y. Zhou, D.N. Furness, D.E. Bergles, K.P. Lehre, and N.C. Danbolt. The density of EAAC1 (EAAT3) glutamate transporters expressed by neurons in the mammalian CNS. *The Journal of Neuroscience*, 32(17):6000–6013, 2012.

[64] E. Holzbecher. *Environmental modeling: using MATLAB, 2nd edition*. Springer Science & Business Media, 2012.

[65] S. Itoh and S.A. Barber. A numerical solution of whole plant nutrient uptake for soil-root systems with root hairs. *Plant and Soil*, 70(3):403–413, 1983.

[66] M. Janott, S. Gayler, A. Gessler, M. Javaux, Ch. Klier, and E. Priesack. A one-dimensional model of water flow in soil-plant systems based on plant architecture. *Plant Soil*, pages 233–256, 2011.

[67] M. Javaux, T. Schröder, J. Vanderborght, and H. Vereecken. Use of a three-dimensional detailed modeling approach for predicting root water uptake. *Vadose Zone Journal*, 7(3):1079–1088, 2008.

[68] S. Jiménez. *Homogenization of nonlinear partial differential equations*. PhD thesis, Louisiana State University, 2010.

[69] Ch. Jourdan and H. Rey. Modelling and simulation of the architecture and development of the oil-palm (Elaeis guineensis Jacq.) root system. *Plant and Soil*, pages 217–233, 1997.

[70] A. Merotto Jr. and C.M. Mundstock. Wheat root growth as affected by soil strength. *Revista Brasileira de Ciência do Solo*, 1999.

[71] S.D. Keyes, K.R. Daly, N.J. Gostling, D.L. Jones, P. Talboys, B.R. Pinzer, R. Boardman, I. Sinclair, A. Marchant, and T. Roose. High resolution synchrotron imaging of wheat root hairs growing in soil and image based modelling of phosphate uptake. *New Phytologist*, pages 1023–1029, 2013.

[72] S.D. Keyes, K.C. Zygalakis, and T. Roose. An explicit structural model of root hair and soil interactions parameterised by synchrotron X-ray computed tomography. *Bulletin of mathematical biology*, 79(12):2785–2813, 2017.

[73] C.G. Kjellström and H. Kirchmann. Dry matter production of oilseed rape (Brassica napus) with special reference to the root system. *The Journal of Agricultural Science*, 123(3):327–332, 1994.

[74] J. Kohanová, M. Martinka, M. Vaculík, P.J. White, M.-T. Hauser, and A. Lux. Root hair abundance impacts cadmium accumulation in Arabidopsis thaliana shoots. *Annals of botany*, 2018.

[75] T.W. Körner. *Fourier analysis*. Cambridge university press, 1989.

[76] C.P. Kumar and S. Mittal. Determination of soil hydraulic properties in a part of Hindon river catchment using SOILPROP software. *ISH Journal of Hydraulic Engineering*, 16(2):13–27, 2010.

[77] P. Lainé, A. Ourry, J. Macduff, J. Boucaud, and J. Salette. Kinetic parameters of nitrate uptake by different catch crop species: effects of low temperatures or previous nitrate starvation. *Physiologia plantarum*, 88(1):85–92, 1993.

[78] F.C. Landis and L.H. Fraser. A new model of carbon and phosphorus transfers in arbuscular mycorrhizas. *New Phytologist*, pages 466–479, 2008.

[79] H.P. Langtangen and A. Logg. *Solving PDEs in Python: The FEniCS Tutorial I*. Simula SpringerBriefs on Computing. Springer International Publishing, 2017.

[80] D. Leitner, S. Klepsch, M. Ptashnyk, A. Marchant, G.J.D. Kirk, A. Schnepf, and T. Roose. A dynamic model of nutrient uptake by root hairs. *New Phytologist*, 185(3):792–802, 2010.

[81] D. Leitner and A. Schnepf. Mathematics and rhizotechnology. Mathematical methods for upscaling of rhizosphere control mechanisms., 2015. `http://www.csc.univie.ac.at/rootbox/`.

[82] K.Y. Li, J.B. Boisvert, and R. De Jong. An exponential root-water-uptake model. *Canadian Journal of soil science*, 79(2):333–343, 1999.

[83] A. Logg, K.-A. Mardal, and G.N. Wells. *Automated Solution of Differential Equations by the Finite Element Method. The FEniCS Book*. Springer Berlin Heidelberg, Springer-Verlag Berlin Heidelberg, 2011.

[84] H.D. Lugo-Méndez, F.J. Valdés-Parada, M.L. Porter, B.D. Wood, and J.A. Ochoa-Tapia. Upscaling diffusion and nonlinear reactive mass transport in homogeneous porous media. *Transport in Porous Media*, 107(3):683–716, 2015.

[85] J.P. Lynch. Roots of the second Green Revolution. *Australian Journal of Botany*, page 493–512, 2007.

[86] J.P. Lynch, K.L. Nielsen, R.D. Davis, and A.G. Jablokow. SimRoot: Modelling and visualization of root systems. *Plant and Soil*, pages 139–151, 1997.

[87] X. Ma, M. Zarebanadkouki, Y. Kuzyakov, E. Blagodatskaya, J. Pausch, and B.S. Razavi. Spatial patterns of enzyme activities in the rhizosphere: Effects of root hairs and root radius. *Soil Biology and Biochemistry*, 118:69–78, 2018.

[88] Z. Ma, T.C. Walk, A. Marcus, and J.P. Lynch. Morphological synergism in root hair length, density, initiation and geometry for phosphorus acquisition in Arabidopsis thaliana: a modeling approach. *Plant and Soil*, 236(2):221–235, 2001.

[89] P. Malagoli, P. Lainé, E. Le Deunff, L. Rossato, B. Ney, and A. Ourry. Modeling nitrogen uptake in oilseed rape cv Capitol during a growth cycle using influx kinetics of root nitrate transport systems and field experimental data. *Plant Physiology*, 134(1):388–400, 2004.

[90] J.T. McCord. Application of second-type boundaries in unsaturated flow modeling. *Water Resources Research*, 27(12):3257–3260, 12 1991.

[91] G.G. McNickle and J.S. Brown. When Michaelis and Menten met Holling: towards a mechanistic theory of plant nutrient foraging behaviour. *AoB Plants*, 6, 2014.

[92] R. Metzner, A. Eggert, D. van Dusschoten, D. Pflugfelder, S. Gerth, U. Schurr, N. Uhlmann, and S. Jahnke. Direct comparison of MRI and X-ray CT technologies for 3D imaging of root systems in soil: potential and challenges for root trait quantification. *Plant methods*, 11(1):17, 2015.

[93] F.J. Molz. Models of water transport in the soil-plant system: A review. *Water Resources Research*, pages 1245–1260, 1981.

[94] A.B. Moradi, A. Carminati, D. Vetterlein, P. Vontobel, E. Lehmann, U. Welle, J.W. Hopmans, H.-J. Vogel, and S.E. Oswald. Three-dimensional visualization and quantification of water content in the rhizosphere. *New Phytologist*, pages 653–663, 2011.

[95] J.D. Murray. *Mathematical Biology*. Springer-Verlag, Berlin Heidelberg New York, 1993.

[96] R.B. Neumann and Z.G. Cardon. The magnitude of hydraulic redistribution by plant roots: a review and synthesis of empirical and modeling studies. *New Phytologist*, pages 337–352, 2012.

[97] P.S. Nobel. *Physicochemical and Environmental Plant Physiology*. Oxford Academic Press, 2009.

[98] B. Nowack, K.U. Mayer, S.E. Oswald, W. van Beinum, C.A.J. Appelo, D. Jacques, P. Seuntjens, F. Gerard, B. Jaillard, A. Schnepf, and T. Roose. Verification and intercomparison of reactive transport codes to describe root-uptake. *Plant Soil*, pages 305–321, 2006.

[99] P.H. Nye and P.B. Tinker. *Solute movement in the soil-root system*. Blackwell Scientific Publications, Oxford, 1977.

[100] S.E. Oswald, Ch. Tötzke, S. Haber-Pohlmeier, A. Pohlmeier, A.P. Kaestner, and E. Lehmann. Combining neutron and magnetic resonance imaging to study the interaction of plant roots and soil. *Physics Procedia*, 69:237–243, 2015.

[101] L. Pages, G. Vercambre, J.-L. Drouet, F. Lecompte, C. Collet, and J. Le Bot. Root Typ: a generic model to depict and analyse the root system architecture. *Plant and Soil*, pages 103–119, 2004.

[102] W.J. Pasciak and J. Gavis. Transport limitation of nutrient uptake in phytoplankton. *Limnology and Oceanography*, 19(6):881–888, 1974.

[103] J.B. Passioura. Water transport in and to roots. *Annual Review of Plant Physiology and Plant Molecular Biology*, pages 245–265, 1988.

[104] G.A. Pavliotis and A.M. Stuart. *Multiscale Methods: Averaging and homogenization*. Springer, 2007.

[105] D. Pflugfelder, R. Metzner, D. Dusschoten, R. Reichel, S. Jahnke, and R. Koller. Non-invasive imaging of plant roots in different soils using magnetic resonance imaging (MRI). *Plant Methods*, 13(1):102, 2017.

[106] J.R. Philip. The physical principles of soil water movement during the irrigation cycle. *Proc. Int. Congr. Irrig. Drain.*, pages 125–54, 1957.

[107] J.R. Philip. Plant water relations: Some physical aspects. *Annual Review of Plant Physiology*, pages 245–268, 1966.

[108] J.A. Postma, Ch. Kuppe, M.R. Owen, N. Mellor, M. Griffiths, M.J. Bennett, J.P. Lynch, and M. Watt. OpenSimRoot: widening the scope and application of root architectural models. *New Phytologist*, 215(3):1274–1286, 2017.

[109] P. Pouliquin, J.-C. Boyer, J.-P. Grouzis, and R. Gibrat. Passive nitrate transport by root plasma membrane vesicles exhibits an acidic optimal pH like the H^+-ATPase. *Plant Physiol.*, 122(1):265–274, 2000.

[110] P. Pouliquin, J. Grouzis, and R. Gibrat. Electrophysiological study with oxonol VI of passive NO_3^- transport by isolated plant root plasma membrane. *Biophys. J.*, 1999.

[111] M.P. Pound, A.P. French, J.A. Atkinson, D.M. Wells, M.J. Bennett, and T. Pridmore. RootNav: Navigating images of complex root architectures. *Plant Physiology*, 162(4):1802–1814, 2013.

[112] M. Ptashnyk. Derivation of a macroscopic model for nutrient uptake by hairy-roots. *Nonlinear Analysis: Real World Applications*, 11(6):4586 – 4596, 2010. Multiscale Problems in Science and Technology.

[113] M. Ptashnyk, T. Roose, and G.J.D. Kirk. Diffusion of strongly sorbed solutes in soil: a dual-porosity model allowing for slow access to sorption sites and time-dependent sorption reactions. *European Journal of Soil Science*, pages 108–119, 2010.

[114] P.A.C. Raats. Uptake of water from soils by plant roots. *Transport in Porous Media*, pages 5–28, 2007.

[115] D.K. Ray, N.D. Mueller, P.C. West, and J.A. Foley. Yield trends are insufficient to double global crop production by 2050. *PLOS ONE*, 2013.

[116] J.C. Reginato, D.A. Tarzia, and A. Cantero. On the free boundary problem for the Michaelis-Menten absorption model for root growth. II. High concentrations. *Soil Science*, pages 63–71, 1991.

[117] J.O. Reuss and G.S. Innis. A grassland nitrogen flow simulation model. *Ecology*, pages 379–388, 1977.

[118] L.A. Richards. Capillary conduction of liquids through porous mediums. *Journal of Applied Physics*, 1931.

[119] T. Roose. *Mathematical model of plant nutrient uptake*. PhD thesis, Mathematical Institute, Oxford University, 2000.

[120] T. Roose and A.C. Fowler. A mathematical model for water and nutrient uptake by plant root systems. *Journal of Theoretical Biology*, pages 173–184, 2004.

[121] T. Roose and A.C. Fowler. A model for water uptake by plant roots. *Journal of Theoretical Biology*, pages 155–171, 2004.

[122] T. Roose, A.C. Fowler, and P.R. Darrah. A mathematical model of plant nutrient uptake. *Mathematical Biology*, pages 347–360, 2001.

[123] T. Roose and G.J.D. Kirk. The solution of convection–diffusion equations for solute transport to plant roots. *Plant Soil*, pages 257–264, 2009.

[124] T. Roose and A. Schnepf. Mathematical models of plant-soil interaction. *Philosophical Transactions of the Royal Society A*, pages 4597–4611, 2008.

[125] J. Rubinstein and S. Torquato. Flow in random porous media: mathematical formulation, variational principles, and rigorous bounds. *Journal of fluid mechanics*, 206:25–46, 1989.

[126] M.J. Russell, O.E. Jensen, and T. Galla. Stochastic transport in the presence of spatial disorder: Fluctuation-induced corrections to homogenization. *Physical Review E*, 94(4), 2016.

[127] J. Schöberl. NETGEN An advancing front 2D/3D-mesh generator based on abstract rules. *Computing and Visualization in Science*, 1(1):41–52, 1997.

[128] A. Shaw, I. Takacs, K. Pagilla, R. Riffat, H. DeClippeleir, Ch. Wilson, and S. Murthy. Toward universal half-saturation coefficients: Describing extant K_S as a function of diffusion. *Water Environment Research*, 2015.

[129] J. Simunek, K. Huang, and M.Th. van Genuchten. The SWMS-3D code for simulating water flow and solute transport in three-dimensional variably-saturated media, 1995.

[130] W.A. Strauss. *Partial differential equations. An Introduction, Second edition*. Wiley New York, 2008.

[131] J. Sun, J.R. Bankston, J. Payandeh, T.R. Hinds, W.N. Zagotta, and N. Zheng. Crystal structure of the plant dual-affinity nitrate transporter NRT1.1. *Nature*, 507(7490), 2014.

[132] I.A. Taina, R.J. Heck, and T.R. Elliot. Application of X-ray computed tomography to soil science: A literature review. *Canadian Journal of Soil Science*, 88(1):1–19, 2008.

[133] D. Tilman. Constraints and tradeoffs: Toward a predictive theory of competition and succession. *Oikos*, 58(1):3–15, 1990.

[134] D. Tilman. Global environmental impacts of agricultural expansion: The need for sustainable and efficient practices. *Proceedings of the National Academy of Sciences*, 96(11):5995–6000, 1999.

[135] D. Tilman, K.G. Cassman, P.A. Matson, R. Naylor, and S. Polasky. Agricultural sustainability and intensive production practices. *Nature*, 418(6898):671, 2002.

[136] P.B. Tinker and P.H. Nye. *Solute movement in the rhizosphere*. Oxford University Press, New York, 2000.

[137] M.E. Toal, C. Yeomans, K. Killham, and A.A. Meharg. A review of rhizosphere carbon flow modelling. *Plant and Soil*, pages 263–281, 2000.

[138] D.K. Todd. *Ground water hydrology*. John Wiley and Sons, Inc, New York, 1959.

[139] S.R. Tracy, K.R. Daly, C.J. Sturrock, N.M.J. Crout, S.J. Mooney, and T. Roose. Three-dimensional quantification of soil hydraulic properties using X-ray Computed Tomography and image-based modeling. *Water Resources Research*, 51(2):1006–1022, 2015.

[140] M. van den Berg, P.M. Driessen, and R. Rabbinge. Water uptake in crop growth models for land use systems analysis: II. Comparison of three simple approaches. *Ecological Modelling*, pages 233–250, 2002.

[141] D. van Dusschoten, R. Metzner, J. Kochs, J.A. Postma, D. Pflugfelder, J. Bühler, U. Schurr, and S. Jahnke. Quantitative 3D analysis of plant roots growing in soil using magnetic resonance imaging. *Plant physiology*, pages pp–01388, 2016.

[142] M.Th. van Genuchten. A closed-form equation for predicting the hydraulic conductivity of unsaturated soils. *Soil Sci. Soc. Am. J.*, pages 892–898, 1980.

[143] Y. Waisel, A. Eshel, T. Beeckman, and U. Kafkafi. *Plant Roots: The Hidden Half, Third Edition*. Books in Soils, Plants, and the Environment Series. Taylor & Francis, 2002.

[144] T.C. Walk, E. van Erp, and J.P. Lynch. Modelling applicability of fractal analysis to efficiency of soil exploration by roots. *Annals of Botany*, pages 119–128, 2004.

[145] E. Wang and Ch.J. Smith. Modelling the growth and water uptake function of plant root systems: a review. *Australian Journal of Agricultural Research*, pages 501–523, 2004.

[146] T. Watanabe, S. Misawa, S. Hiradate, and M. Osaki. Root mucilage enhances aluminum accumulation in Melastoma malabathricum, an aluminum accumulator. *Plant Signaling and Behaviour*, pages 603–605, 2008.

[147] S. Whitaker. *Theory and Application of Transport in Porous Media: The Method of Volume Averaging*. Kluwer Academic London, 1999.

[148] F. Wichern, E. Eberhardt, J. Mayer, R.G. Joergensen, and T. Muller. Nitrogen rhizodeposition in agricultural crops: Methods, estimates and future prospects. *Soil Biology and Biochemistry*, pages 30–48, 2008.

[149] Worldometers. Current world population. `http://www.worldometers.info/world-population/`.

[150] L.M. York, M. Silberbush, and J.P. Lynch. Spatiotemporal variation of nitrate uptake kinetics within the maize (Zea mays L.) root system is associated with greater nitrate uptake and interactions with architectural phenes. *Journal of Experimental Botany*, 67(12):3763, 2016.

[151] A. Zhan and J.P. Lynch. Reduced frequency of lateral root branching improves N capture from low-N soils in maize. *Journal of Experimental Botany*, 66(7):2055, 2015.

[152] K.C. Zygalakis, G.J.D. Kirk, D.L. Jones, M. Wissuwa, and T. Roose. A dual porosity model of nutrient uptake by root hairs. *New Phytologist*, pages 676–688, 2011.

[153] K.C. Zygalakis and T. Roose. A simple mathematical model for investigating the effect of cluster roots on plant nutrient uptake. *The European Physical Journal Special Topics*, pages 103–118, 2012.